

# CRAFTING TISSUE COMPLEXITY

Pioneering Layerwise and Volumetric Biofabrication  
Strategies for Advanced *In Vitro* Models

Paulina Núñez Bernal



# **Crafting Tissue Complexity:**

**Pioneering Layerwise and Volumetric Biofabrication  
Strategies for Advanced *In Vitro* Models**

**Paulina Núñez Bernal**

Crafting Tissue Complexity:

*Pioneering Layerwise and Volumetric Biofabrication Strategies for Advanced In Vitro Models*

PhD Thesis Utrecht University

Financial support for printing this thesis was kindly provided by

The Netherlands Society for Biomaterials and Tissue Engineering (NBTE)

ISBN: 978-90-393-7622-5

DOI: 10.33540/2116

Author: Paulina Núñez Bernal

Cover design: Charlotte Brice and Valentina Bernal

Thesis layout: Madison J. Ainsworth

Printing: Ridderprint, the Netherlands

The research in this thesis is financially supported by the Horizon 2020 research and innovation program under the Grant Agreement No. 814444 (MEFISTO), and the European Research Council (ERC) under the European Union's Horizon 2020 research and innovation programme (grant agreement No. 949806, VOLUME-BIO).

Copyright © P. Núñez Bernal 2023. All rights reserved. No parts of this thesis may be reproduced, stored in a retrieval system of any nature, or transmitted in any form or by any means, without prior written consent of the author. The copyright of the articles that have been published has been transferred to the respective journals.

# **Crafting Tissue Complexity:**

## Pioneering Layerwise and Volumetric Biofabrication Strategies for Advanced In Vitro Models

### **Introduceren van Weefselcomplexiteit:**

Pioneren van Laagsgewijze en Volumetrische Biofabricatie  
Strategieën met als Toepassing Geavanceerde In Vitro Modellen

(met een samenvatting in het Nederlands)

### **Diseñando Tejidos Complejos:**

Estrategias Innovadoras de Biofabricación en Capas y  
Volumétricas para Modelos In Vitro Avanzados

(con resumen en Español)

### **Proefschrift**

ter verkrijging van de graad van doctor aan de  
Universiteit Utrecht  
op gezag van de  
rector magnificus, prof. dr. H.R.B.M. Kummeling,  
ingevolge het besluit van het college voor promoties  
in het openbaar te verdedigen op  
dinsdag 6 februari 2024 des ochtends te 10.15 uur

door

### **Paulina Núñez Bernal**

geboren op 4 maart 1995  
te Mexico City, Mexico

**Promotor:** Prof. dr. ir. J. Malda

**Co-promotoren:** Dr. ir. R. Levato

**Beoordelingscommissie:** Prof. dr. J.M. Beekman (voorzitter)  
Prof. dr. R. Masereeuw  
Prof. dr. ir. L. Moroni  
Prof. dr. A. Ovsianikov  
Prof. dr. D. Salvatori

**“Takin’ on a challenge is a lot  
like ridin’ a horse.  
If you’re comfortable while  
you’re doin’ it, you’re probably  
doin’ it wrong.”**

*-Ted Lasso*

# Table of Contents

Chapter 1: General Introduction and Thesis Outline	8	
<hr/>		
<b>Part I</b>	<b>Advanced Biofabrication Strategies to Enhance Resolution and Architectural Complexity of Biofabricated Tissue Mimics</b>	<b>28</b>
<hr/>		
Chapter 2: Hydrogel-Based Bioinks for Cell Electrowriting of Well-Organized Living Structures with Micrometer-Scale Resolution	30	
Chapter 3: Volumetric Bioprinting of Complex Living-Tissue Constructs within Seconds	56	
Chapter 4: Volumetric Printing Across Melt Electrowritten Scaffolds Fabricates Multi-Material Living Constructs with Tunable Architecture and Mechanics	80	
<hr/>		
<b>Part II</b>	<b>Development of Advanced <i>In Vitro</i> Model Platforms through Biofabrication Approaches</b>	<b>116</b>
<hr/>		
Chapter 5: Bioprinting of Human Liver-Derived Epithelial Organoids for Toxicity Studies	118	
Chapter 6: Volumetric Bioprinting of Organoids and Optically Tuned Hydrogels to Build Liver-Like Metabolic Biofactories	140	
Chapter 7: Volumetric Printing Hollow Bi-Chambered Heart Structures for the Next Generation of Clinically Relevant Cardiac <i>In Vitro</i> Models	180	



---

**Part III     Driving Tissue Biomimicry in Biofabricated Structures  
with Smart Biomaterials**     **204**

---

Chapter 8: Biofunctionalization of 3D Printed Collagen with Bevacizumab-Loaded Microparticles Targeting Pathological Angiogenesis     206

Chapter 9: Spatial-Selective Volumetric 4D Printing and Single-Photon Grafting of Biomolecules within Centimeter-Scale Hydrogels via Tomographic Manufacturing     238

Chapter 10: General Discussion and Future Perspectives     272

---

**Annex**     **290**

---

Thermal Shrinking of Biopolymeric Hydrogels for High Resolution Volumetric Printing     292

References     306

List of Abbreviations     336

English Summary/Nederlands Samenvatting/Resumen en Español     339

Acknowledgements     350

Publications     362

Curriculum Vitae     366





# **Chapter 1**

## **General Introduction and Thesis Outline**



## AN EMERGING PARADIGM-SHIFT IN THE DEVELOPMENT OF HUMAN IN VITRO MODELS FOR PRECLINICAL TESTING AND DISEASE MODELING

Since the dawn of medical science, understanding the exact mechanisms of disease has been pivotal in the development of effective treatment strategies, surgical interventions and more recently, personalized medicine. As the global average life expectancy increases, so does the incidence of chronic diseases, which carry a heavy economic toll on society and compromises patients' quality of life. In this growing population, this increase in the onset of diseases and the inherent biological variation of human beings which makes individual drug/treatment response highly variable, has put the drug discovery and development pipeline (**Figure 1**) to the test, calling for the adaptation of its rules and regulations to reduce the ever-increasing failure rates of new drugs. The staggering growth of the pharmaceutical industry in the last decades, and the high expenditure required to bring a new drug to the market (an estimated \$314 million to \$2.8 billion per drug from 2009-2018)<sup>[1]</sup>, is set to become an unsustainable issue in the coming years. The costs of the drug discovery process are further exacerbated due to the fact that an estimated 89% candidate drugs fail only after entering the highly costly clinical testing phase,<sup>[2]</sup> out of which 60-66% drugs fail to transition from Phase I clinical trials.<sup>[2,3]</sup> That is why, in recent years, far more attention has been focused on the preclinical testing phase of the pipeline, which most drugs still pass after a plethora of *in vitro* studies and *in vivo* studies on a wide variety of animal models. In this phase, most drug discovery testing culminates in animal testing, the current gold standard to ensure drug safety and efficacy before human trials.<sup>[4-7]</sup> However, ample research has demonstrated that no single animal model that can fully recapitulate the human condition, meaning that these models can easily fail to detect harmful or ineffective drugs due to their low predictability and thus bring about a significant translational gap.<sup>[4,5,7]</sup> From intra-species discrepancies in receptor specificity, immune reactivity, and drug metabolism, to the lack of diversity in inbred laboratory animals and the highly polarizing ethical issues that animal testing entails,<sup>[8]</sup> a general consensus on the need for more complex and predictive human disease models has emerged and become a priority for both scientists and policy makers in recent years.<sup>[5,6]</sup>

Supporting this paradigm shift in preclinical testing practices, various initiatives at national and European Union (EU)-wide levels have sought to develop programs to push forward the transition towards animal-free research. From the development of governmental initiatives like the Transitie Proefdiervrije Innovatie (TPI; transition animal-free innovation), to the creation of non-profit foundations such as Proefdiervrij in The Netherlands, the European Medicine Agency has also implemented steps to facilitate the adoption of New Approached Methodologies (NAMs) aimed to replace animal experimentation in pharmaceutical research. This, together with the congressional approval of the U.S. Food

and Drug Administration (FDA) Modernization Act 2.0 on January 2023, which allows for alternative complex *in vitro* model use in the advanced preclinical phases,<sup>[9]</sup> have recently opened the gateway to reduce the need for animal experimentation. However, in order to develop the next generation of *in vitro* platforms that can fill the ever-growing translational gap in our understanding of disease and the development of new drugs, it is first essential to understand the advantages and limitations of existing *in vitro* modeling techniques and leverage their translational potential.

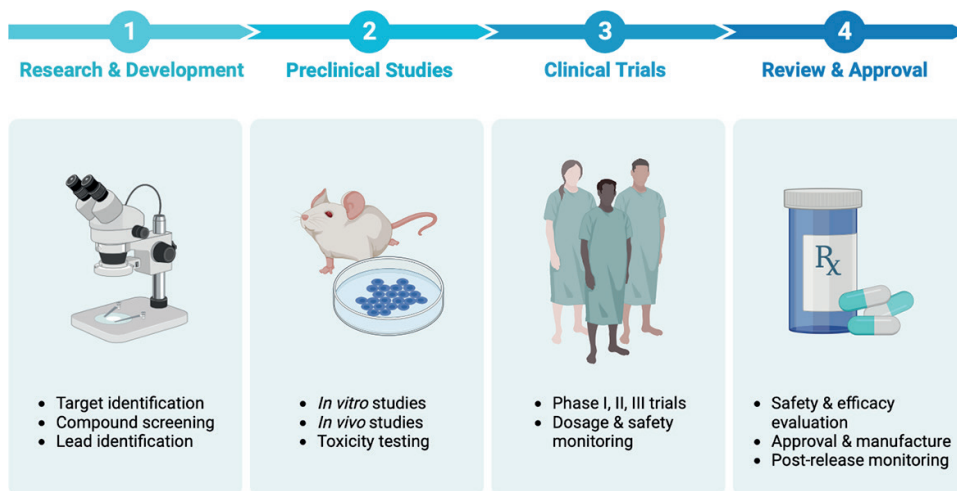


**Figure 1:** Schematic of the drug discovery and development pipeline including the 4 key phases of the process before entering the market: research and development, preclinical testing, clinical trials and review and approval stages. Created with BioRender.com.

## EXISTING *IN VITRO* MODELING APPROACHES CAPTURE DIFFERENT ASPECTS OF ORGAN AND TISSUE COMPLEXITY

The most widely used *in vitro* modeling approach for preclinical testing has been 2-dimensional (2D) monolayer cell culture. Here, single cells are grown on top of a substrate and cultured in optimized medium and environmental conditions that enable their growth. For pharmaceutical research, these systems represent the gold standard due to their cost effectiveness and high-throughput potential.<sup>[10-14]</sup> While the simplicity of these models provides an indispensable understanding of basic cellular phenomena, these 2D cultures do not adequately represent the physiological conditions of cells in the human body and thus lack the physiological relevance needed to understand systemic processes and multicellular responses involved in specific disease and treatment strategies. For example, the lack of oxygen, nutrient and waste gradients, and limited control over cell-cell and cell-extracellular matrix (ECM) interactions are crucial elements required to mimic native cellular behavior that cannot be replicated in two dimensions.<sup>[14-16]</sup> In the search for more

predictive, human-based *in vitro* models that better capture organ and tissue complexity, several tissue engineering approaches have been developed, each contributing different advantages to the modeling of human diseases (**Table 1**).

**Table 1:** Overview of in vitro modeling approaches including a brief description of their basic features, as well as their main advantages and limitations.

In vitro platform		Description
<b>2D cell culture</b>		One or more cell types grown on two-dimensional surfaces (coated or non-coated)
<b>3D cell culture</b>	<i>Hydrogels for cell encapsulation</i>	One or more cell types embedded within three-dimensional matrices
	<i>Spheroids</i>	Free-floating, self-assembled cellular aggregates growing in spheroid within biological fluids or extracellular matrix
	<i>Organoids</i>	Three-dimensional structures derived from (pluripotent) stem cells, progenitor, and/or differentiated cells that self-organize through cell-cell and cell-matrix interactions
<b>Bioreactors</b>		Manufactured devices that allow cell and tissue culture in carefully defined biological and physiological environments and employ mechanical means to influence biological processes
<b>Microphysiological systems</b>		Miniaturized models that mimic the structure and function of human organs or tissues and their respective interfaces
<b>Biofabricated models</b>		Biologically functional products with structural organization from living cells, bioactive molecules, biomaterials, cell aggregates or hybrid cell-material constructs, through bio-printing or bioassembly and subsequent tissue maturation processes



Advantages	Disadvantages
<ul style="list-style-type: none"> <li>- High throughput</li> <li>- Highly reproducible</li> <li>- Easy to automate culture and analysis</li> <li>- Low cost</li> </ul>	<ul style="list-style-type: none"> <li>- 2D cellular response differs from cells in a 3D microenvironment</li> <li>- Lack of physiological relevance</li> <li>- Limited cell-matrix interactions</li> </ul>
<ul style="list-style-type: none"> <li>- Wide range of materials from natural and synthetic origin</li> <li>- Provide 3D microenvironment that mimics the extracellular matrix</li> <li>- Versatile mechanical properties</li> <li>- Low cost</li> </ul>	<ul style="list-style-type: none"> <li>- Cell-friendly hydrogels often too soft to withstand high mechanical stresses</li> <li>- Lack the convoluted architectural organization of native tissues</li> <li>- Poor physiological relevance on their own</li> </ul>
<ul style="list-style-type: none"> <li>- Can comprise multiple cell types from target tissue</li> <li>- Exhibit cell-cell and cell-matrix interactions</li> <li>- Scalable production</li> <li>- Low cost</li> </ul>	<ul style="list-style-type: none"> <li>- Lack native tissue cell organization</li> <li>- Heterogeneity in size and shape</li> <li>- Dense cell aggregation limits oxygen and nutrient supply</li> </ul>
<ul style="list-style-type: none"> <li>- Self-renewal and self-assembly capabilities</li> <li>- Resembles native tissue organization</li> <li>- Genetic stability</li> <li>- Long-term, scalable expansion</li> <li>- Differentiation capabilities into multiple tissue/organ-specific cell lineages</li> </ul>	<ul style="list-style-type: none"> <li>- Low reproducibility</li> <li>- Poor control over shape and size</li> <li>- Lack of vasculature limits oxygen and nutrient supply</li> <li>- Golden-standard culture matrix is tumor-derived</li> </ul>
<ul style="list-style-type: none"> <li>- Provide dynamic culture conditions that lead to enhanced tissue-specific maturation</li> <li>- Scalable systems for high throughput screening</li> <li>- Introduction of dynamic flow enhance nutrient and oxygen supply</li> </ul>	<ul style="list-style-type: none"> <li>- Costly to set-up and scale</li> <li>- Complex operating methodologies require expert users</li> <li>- Limited control over microenvironmental and structural cues</li> </ul>
<ul style="list-style-type: none"> <li>- Accurate mimicry of tissue microenvironment</li> <li>- High physiological relevance</li> <li>- Incorporation of tissue-tissue and tissue-air interfaces allow modeling of tissue crosstalk</li> <li>- Incorporate biomechanical cues and sensors</li> <li>- Interconnected multi-organ-on-chip systems enable systemic studies of physiological processes</li> </ul>	<ul style="list-style-type: none"> <li>- Complex set-ups require expert users</li> <li>- Lacks multi-scale architectural properties of native tissues</li> <li>- Lack of standardization of fabrication and operation protocols</li> <li>- Costly to upscale production and continuous monitoring</li> </ul>
<ul style="list-style-type: none"> <li>- Highly customizable macro- and micro-structural architectures to mimic native-like organization and patient-specific shapes</li> <li>- Enables the integration of multiple cells and materials in a spatially controlled manner</li> <li>- Diverse range of existing bioprinting technologies with different process characteristics</li> <li>- Convergence into multitechnology approaches enhances construct complexity and stability</li> </ul>	<ul style="list-style-type: none"> <li>- Layerwise approaches require long printing times to create clinically relevant sized constructs</li> <li>- Layerwise approaches also pose limits on the design freedom of prints (i.e. overhangs and flowing structures)</li> <li>- Compromise between material printability and shape fidelity, and optimal cell growth often required.</li> </ul>

## 1 Bringing cell culture into the third dimension: development of advanced biological tools for *in vitro* model development

To increase the physiological relevance of existing cell-based models, research started to shift its focus towards more complex 3-dimensional (3D) cell culture strategies. These techniques range from encapsulating cellular structures within scaffolds (often aqueous soft matrices resembling the mechanobiological properties of native ECM like hydrogels), to developing cellular assemblies like spheroids and organoids that possess enhanced tissue/organ-specific functionalities based on their 3D organization.<sup>[11,12,14,15,17-19]</sup> These approaches have brought conventional cell culture into the third dimension, offering new tools to tune cell-cell and cell-ECM interactions *in vitro*, leading to more physiologically relevant microenvironments as compared to simple 2D monolayer cultures.<sup>[20-23]</sup> Spheroids can be defined as free-floating, self-assembled cellular aggregates growing in spheres within biological fluids or extracellular matrix.<sup>[24]</sup> These spheroids can in turn be composed of multiple cell types and form tight cell-to-cell and cell-ECM interactions within a few days.<sup>[25-28]</sup> Since spheroids can be produced with high-throughput, these cell aggregates have been used for tumor characterization and immunotherapy efficacy models,<sup>[25,28,29]</sup> to build liver units that model drug toxicity,<sup>[30,31]</sup> to model processes in diseased organs, such as cardiac scar tissue formation,<sup>[32]</sup> and to develop highly organized models of various complex tissues like those in the musculoskeletal system<sup>[33,34]</sup>. Despite the potential and wide range of applications of spheroids, these 3D tissue models have intrinsic limitations, such as maintaining spheroid morphology and uniformity, achieving homogenous nutrient and oxygen supply throughout spheroids and the difficulty in incorporating all the cell types relevant to complex tissues/organs in an organized fashion.<sup>[29]</sup>

Addressing the limitation of spheroids of mimicking the multicellular organization and resulting function of cell culture systems, the development of organoids takes a big leap towards recapitulating native tissue functions and organization. As defined by experts in the field, an organoid is “a three-dimensional structure derived from (pluripotent) stem cells, progenitor, and/or differentiated cells that self-organize through cell-cell and cell-matrix interactions to recapitulate aspects of the native tissue architecture and function *in vitro*”.<sup>[35]</sup> These structures exhibit high genetic stability and expansion yield, making them excellent candidates for tissue engineering of clinically relevant-sized structures that exhibit highly predictive functions compared to their native counterpart.<sup>[23,36-38]</sup> The striking cellular organization similarities to native tissues, and the possibility to obtain these cell assemblies from most tissues in the human body have made organoids one of the most promising preclinical model candidates in recent years, with great strides in the understanding of organ development,<sup>[36,39-42]</sup> as well as human genetic and developmental pathologies.<sup>[36,38,40-50]</sup> As organoids can also be obtained from primary cells (*i.e.*, obtained from biopsies) these tissue models have also facilitated the advancement of patient specific

biomedical research, and enabled further understanding and treatment development of rare diseases.<sup>[37,39,51]</sup> In combination with genome editing technologies<sup>[52–54]</sup> and other emerging biomedical tools, organoids are sure to bring about a revolution in the biomedical research field and have the potential to shape the next generation of *in vitro* models. Nonetheless, before incorporating these promising structures in the advanced preclinical testing phase some key limitations must be addressed. As with spheroid culture, control over the size and shape of organoids is difficult to homogenize, despite their high-throughput culture potential.<sup>[55]</sup> Furthermore, organoids lack a vasculature system that facilitates nutrient and oxygen supply, largely limiting their scalability to the millimeter-scale.<sup>[39,46,51]</sup> From a functional perspective, a key challenge lies in controlling the architecture of organoids during culture, a feature shown to significantly impact their maturation and biomimicry.<sup>[56]</sup> It is thus evident that the development of new technologies that facilitate the introduction of complex enveloping architectures to guide architecture and facilitate nutrient and oxygen supply is of utmost importance to bring this powerful biological tool into the forefront of preclinical research.

## **Incorporating dynamic culture in *in vitro* models: bioreactors and microphysiological systems**

During the processes of development, growth, and regeneration that the human body experience since the prenatal stage, biophysical cues and feedback loops in their extracellular environment are crucial. Over time, cells have to adapt to these stimuli by changing their spatial organization and constantly engaging in cytoskeletal and ECM remodeling.<sup>[57]</sup> These processes are all major contributors of emerging organ and tissue structure and function and are thus essential elements needed to achieve enhanced biomimicry of preclinical testing platforms. Despite the aforementioned developments in advanced 3D cell culture models, these systems alone do not provide these biophysical factors such as shear, compression and flow. To date, several biophysical stimuli have been shown to effectively modulate cell fate and behavior, including electrical,<sup>[58–61]</sup> acoustic,<sup>[62,63]</sup> magnetic,<sup>[64–68]</sup> and mechanical, the latter being the most widely studied in a wide array of tissues.<sup>[67,69–72]</sup> To incorporate this into *in vitro* platforms, the development of cell and tissue culture systems which recapitulate the dynamic *in vivo* environment has been another important step towards creating more predictive and accurate preclinical models.

Bioreactors are manufactured devices that allow cell and tissue culture in carefully defined biological and physiological environments and employ mechanical means to influence biological processes<sup>[73]</sup>. Bioreactors pose a promising step in biomedical research and drug discovery by developing standardized, long-term, and scalable *in vitro* culture methods which enable researchers to achieve higher levels of experimental reproducibility.

Moreover, these devices facilitate the incorporation of numerous biophysical cues to biological structures, therefore enhancing the recapitulation of *in vivo* environments.<sup>[73]</sup> Many different modalities of bioreactor exist,<sup>[73–77]</sup> for example, spinner flasks, which are automated stirring tanks that facilitate massive cellular expansion,<sup>[55,77]</sup> perfusable culture chambers that enable the introduction of dynamic flow throughout tissue models,<sup>[78,79]</sup> and culture chambers coupled to automated piston systems that enable continuous mechanical stimulation over time.<sup>[76]</sup> Thanks to 3D printing technologies highly customizable bioreactors can be designed for virtually any desired tissue-specific application.<sup>[80,81]</sup> Overall, these automated systems offer unique controllability of *in vitro* cell culture through customisable, physiologically relevant setups. Nonetheless, the introduction of more complex systems hinders the high-throughput possibilities of these platforms and introduces practical limitations that can hinder the widespread use of these technologies.

A subtype of microscale bioreactors, microphysiological systems (MPS) are another important *in vitro* modeling approach that enables the microscale recapitulation of functional units of tissues and organs.<sup>[82]</sup> These platforms also enable the introduction of flow and various biophysical stimuli, and importantly, are compatible with the incorporation of sensors for continuous monitoring of cellular processes.<sup>[83,84]</sup> The microscale nature of these devices, such as organ-on-a-chip (OoC) platforms allows for the maintenance of more physiological cell-to-media ratios, eliminating massive dilutions in signalling molecules that provide insight into cellular behavior.<sup>[85]</sup> OoCs are a type of MPS based upon a microfluidic device containing networks of perfusable microchannels able to direct and manipulate picoliter to milliliter volumes of fluids.<sup>[86]</sup> This technology exploits developments in microfabrication techniques such as lithography and replica moulding in polydimethylsiloxane (PDMS)<sup>[87]</sup> and other high resolution manufacturing technologies such as 3D printing.<sup>[88,89]</sup> These platforms may also be coupled with miniaturized biosensing and read-out capabilities.<sup>[90]</sup> These on-chip systems can incorporate tissue-specific 2D or 3D cell culture systems, organized in ways that mimic tissue-tissue or tissue-air interfaces. These features provide a high physiological relevance platform that, in combination with the high-throughput set-up and analysis potential, make for extremely promising platforms for preclinical testing.<sup>[85,91]</sup> These OoC have been developed to study a wide range of organs and tissues such as liver,<sup>[92]</sup> lung,<sup>[93,94]</sup> intestine,<sup>[95]</sup> kidney,<sup>[96,97]</sup> the blood brain barrier,<sup>[98,99]</sup> articular joint tissues,<sup>[100,101]</sup> as well as vascular structures.<sup>[102,103]</sup> Naturally, the study of single tissues or organs when it comes to evaluating the systemic effect of drugs in the drug discovery pipeline is a rather reductive approach, so progress in the MPS field seeks to incorporate this inter-organ communication through devices known as human multi-organ-on-a-chip (multi-OoC), which are currently a major focus of *in vitro* model research.<sup>[104–106]</sup> Nonetheless, despite MPS's comprehensive recapitulation of cell-cell, cell-stimuli and tissue-tissue interactions, a critical aspect is lacking in these high

physiological relevance systems: the intricate multi-scale architectural complexity that, *in vivo*, plays a critical role in tissue and disease development.

## BIOFABRICATION APPROACHES PROVIDE UNPARALLELED ARCHITECTURAL CONTROL OF TISSUE ENGINEERED MODELS

Despite the vast progress in enhancing the complexity of cellular organization through spheroid and organoid development, and the incorporation of tissue specific biophysical stimulation and multi-tissue interfaces with bioreactors and MPS, a key aspect in recapitulating native tissues lies in replicating their intricate micro- and macro-scale architecture. During development the cellular patterning and tissue architecture are key drivers of organ and tissue formation and the rise of their respective functions,<sup>[107-109]</sup> so being able to replicate these intricate elements is essential to achieve true physiological relevance in *in vitro* models. A technology-driven field that has come to the forefront of tissue engineering and regenerative medicine strategies in the last two decades is biofabrication, as it facilitates the precise patterning of cellularized materials into complex architectures.<sup>[110-112]</sup> Biofabrication, a multidisciplinary field that bridges biology, materials science and engineering, as recently highlighted in a consensus paper from the International Society for Biofabrication (ISBF), can be defined as: “*the automated generation of biologically functional products with structural organization from living cells, bioactive molecules, biomaterials, cell aggregates such as micro-tissues, or hybrid cell-material constructs, through Bioprinting or Bioassembly and subsequent tissue maturation processes*”.<sup>[110]</sup> As this area of research grows and increasingly attracts the interest for tissue engineering, a wide range of techniques have been developed, all towards creating highly organized tissue mimics with unprecedented architectural control.<sup>[111]</sup> From the first bioprinting studies using inkjet printing technology,<sup>[113]</sup> multiple bioprinting modalities have now been developed and commercialized, like extrusion-based bioprinting,<sup>[114-116]</sup> inkjet printing,<sup>[117,118]</sup> light or laser-based bioprinting,<sup>[119-122]</sup> electrohydrodynamic-based printing,<sup>[123-126]</sup> and more recently, volumetric, layerless bioprinting methods, developed for the first time within this thesis work (**Figure 2**).<sup>[127]</sup> Each of these modalities possess different key features such as printing resolution, design freedom and material requirements.<sup>[111,112,128-130]</sup> Moreover, recent trends towards the development of multi-modal biofabrication devices,<sup>[131]</sup> which combine multiple technologies into a single step (*i.e.*, first shown combining extrusion of thermoplastic materials with the extrusion of cell-laden hydrogels directly within the same construct), opens the door to the development of architecturally complex *in vitro* platforms where multi-cellular and multi-material structures can easily be created.

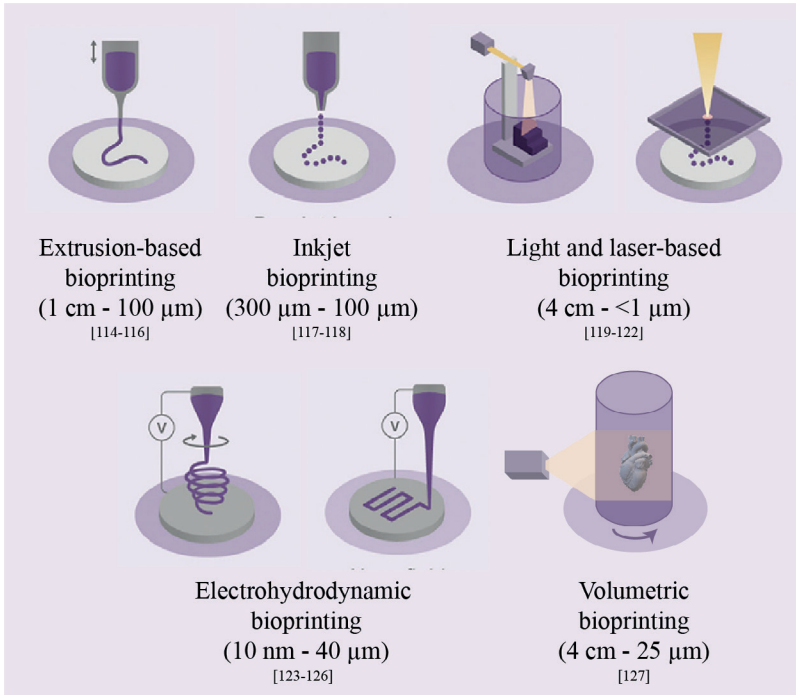


**Figure 2:** Graphical overview of the various categories of biofabrication approaches, with the range of achievable printing resolutions for each category. Adapted from [131].

Decades of research in the field of biofabrication have brought about exciting developments to the field of *in vitro* models and tissue engineering through the myriad of techniques and applications explored in several extensive reviews in the field.<sup>[109,111,112,132,133]</sup> The physiological relevance provided by biofabricated constructs, given their spatial control over cell and biomaterial patterning, has even made these approaches one of several named by the FDA Modernization Act 2.0 as a potential replacement strategy for animal experimentation in the preclinical phase of the drug development pipeline. However, despite the immense strides taken in the last years through a vast multidisciplinary effort, some drawbacks remain that may hinder the translation of these approaches to preclinical settings. Apart from the need for further automation and incorporation of machine learning to enhance the reproducibility and adoptability of 3D bioprinting approaches, various fundamental process limitations pose shorter-term issues that must be addressed to enhance the mimicry of multi-scale, highly organized organs and tissues. On the one hand, the majority of bioprinting approaches cannot yet mimic the single-cell resolutions (10 – 100  $\mu\text{m}$ )<sup>[134]</sup> required in many tissues, where cell orientation and alignment are key to their function. Multi-photon polymerization can reach submicron resolutions, but limited biocompatible materials are printable with this approach.<sup>[121]</sup> Development of high resolution, cell friendly approaches and compatible materials is crucial to overcome

this issue. Another important limitation is the extent of design freedom achievable with layer-by-layer bioprinting approaches. Despite the development of techniques to overcome the design limitations of these layered structures, such as embedded printing approaches,<sup>[135,136]</sup> these techniques are conventionally very time consuming when upscaling the size of printed constructs to clinically relevant sizes, and still pose some limits on printable designs such as free-floating components. Furthermore, ensuring the mechanical stability of bioprinted constructs has been a long-standing issue that may hinder the translation of these structures. Addressing these technological challenges will play a crucial role in the adoption of biofabrication approaches in the preclinical testing landscape.

**Technology-driven challenge**

In order to recapitulate the multiscale organization and architecture of native organs and tissues in clinically relevant-sized constructs, some key features must be introduced in the next generation of bioprinting technologies to enhance printing resolution and design freedom, reduce processing times and ensure mechanical stability of printed structures.

Regardless of these technical limitations, an exciting aspect of the biofabrication field is its compatibility with other *in vitro* modeling approaches. The process and material versatility of the various biofabrication approaches enable the introduction of complex 3D cell culture technologies like spheroids<sup>[32,137–140]</sup> and organoids,<sup>[141,142]</sup> which themselves hold immense preclinical potential but have specific material and processing requirements to ensure their optimal function. Their marriage with bioprinting technologies that allow for the precise patterning of these structures into physiologically relevant architectures can bring about functional patterns that more closely mimic human processes. For instance, Daly *et al.*,<sup>[32]</sup> and Bulanova *et al.*<sup>[143]</sup> have demonstrated that, through the bioprinting of functional tissue spheroids, cardiac and vascularized thyroid gland constructs, respectively, can be fabricated. The bioprinted cardiac spheroid structures could replicate distinct units of healthy and scarred cardiac tissue that, when shaped into specific arrangements, enabled the observation of physiological phenomena like impaired contractions, decreased calcium handling and significant activation delays in the contractions at the scarred tissue areas.<sup>[32]</sup> Vascularized thyroid constructs also exhibited native-like functionality *in vitro* and *in vivo*, demonstrating thermoregulatory activity and thyroxine hormone secretion when placed in a controlled architecture with predefined spheroid spacing.<sup>[143]</sup> While these converged approaches have brought about promising enhancements in the functionality of tissue engineered *in vitro* platforms, most of the functional biofabricated constructs developed to date are scaled down units of organs and tissues.<sup>[144]</sup> To increase the translational potential of these technologies and facilitate the study of large-scale processes such as biodistribution, the introduction of multiple tissue units and upscaling of bioprinted structures is necessary.<sup>[144,145]</sup> Following this essential upscaling step, the

1 introduction of dynamic culture systems can help enhance differential nutrient and oxygen supply to various tissue units, introduce biomechanical cues needed for salient functions and mimic tissue interfaces.<sup>[81,146]</sup> A key set of technologies to achieve this are MPS, where the convergence with biofabrication approaches has already brought about exciting developments by enabling the fabrication of intricate OoC systems without the need of additional processing steps or facilitating the direct printing of the tissue components inside the chip devices with higher spatial control than conventional molding and casting approaches.<sup>[147–150]</sup> Overall, it is evident that in order to take biofabrication approaches to the next level in the preclinical testing pipeline, the incorporation of other *in vitro* modeling techniques is fundamental.

**Application-driven challenge**

When it comes to recapitulating large, multicellular and multifunctional organs and tissues, biofabrication faces major challenges like the mimicking of cellular organization and self-assembly or the replication of native biophysical cues that may require the convergence of alternative technologies.

Even with the incorporation of various *in vitro* modeling approaches, an outstanding challenge in the field of biofabrication is that of the development of biomaterials that are compatible with both cells and different printing approaches that are also capable of recapitulating key biochemical and structural cues of native tissues.<sup>[18,120,128,130]</sup> In brief, the materials used for bioprinting applications in the presence of cells are termed bioinks (or bioresins in the case of light- and laser-assisted approaches). The term bioink has, in a separate publication, also been defined by the ISBF as: “*a formulation of cells suitable for processing by an automated biofabrication technology that may also contain biologically active components and biomaterials*.”<sup>[129]</sup> Ample research into the design and characterization of printable bioinks/bioresins has been carried out, with multiple reviews describing the optimal material properties and common materials used for different bioprinting modalities.<sup>[109,130,151]</sup> In particular, designing bioinks that provide high shape fidelity (maintenance of shape and long-term stability), while also acting as an optimal environment to facilitate and preferentially guide cell fate has been a major challenge in the field since its inception. To aid in the latter, the introduction of stimuli responsive hydrogels,<sup>[152,153]</sup> materials capable of binding bioactive compounds to replicate native chemical cues,<sup>[154–156]</sup> and mechanically versatile material platforms<sup>[157–161]</sup> that facilitate cellular growth and function of various cells and cellular assemblies like organoids and spheroids have been thoroughly investigated.



**Material-driven challenge**

Organ and tissue development are highly intricate processes that are highly reliant on intricately orchestrated spatiotemporal biochemical and structural cues. The development of bioink/bioresin platforms capable of mimicking these complex extracellular characteristics like bioactive factor delivery and patterning, as well as controllable structural changes is a major challenge in the field of biofabrication.

While the field of biofabrication has come a long way in the last decades, significant challenges (outlined in boxes above) remain that must be addressed to increase the biomimicry of biofabricated structures that can one day become the new golden standard for preclinical testing practices. In this thesis, several steps have been taken to tackle these challenges, resulting in the introduction of novel bioprinting techniques, tissue-specific advanced *in vitro* platforms and smart bioinks/bioresins.

**AIM AND OUTLINE OF THIS THESIS**

Considering the need for more complex preclinical models to bridge the existing translational gap between commonly used 2D *in vitro* models, animal testing and clinical trials, the overarching aim of this thesis is “to develop new biofabrication approaches, encompassing 3D bioprinting technologies, powerful biological building blocks, and smart biomaterials, that facilitate the development of advanced human *in vitro* models with native tissue-like functionality.”

To take the first steps into realizing this aim, several key aspects of biofabrication approaches are addressed in the following sub-aims:

- 1) To develop **novel bioprinting technologies** that tackle existing limitations of current strategies such as **reduced micro-scale printing resolution, limited design freedom** and **long processing times**
- 2) To apply these **bioprinting technologies in combination with advanced biological building blocks**, to develop the next generation of **organ-specific human *in vitro* models**
- 3) To develop advanced methods to **control cell fate regulation and/or material properties post-printing** through a new library of **smart biomaterials**

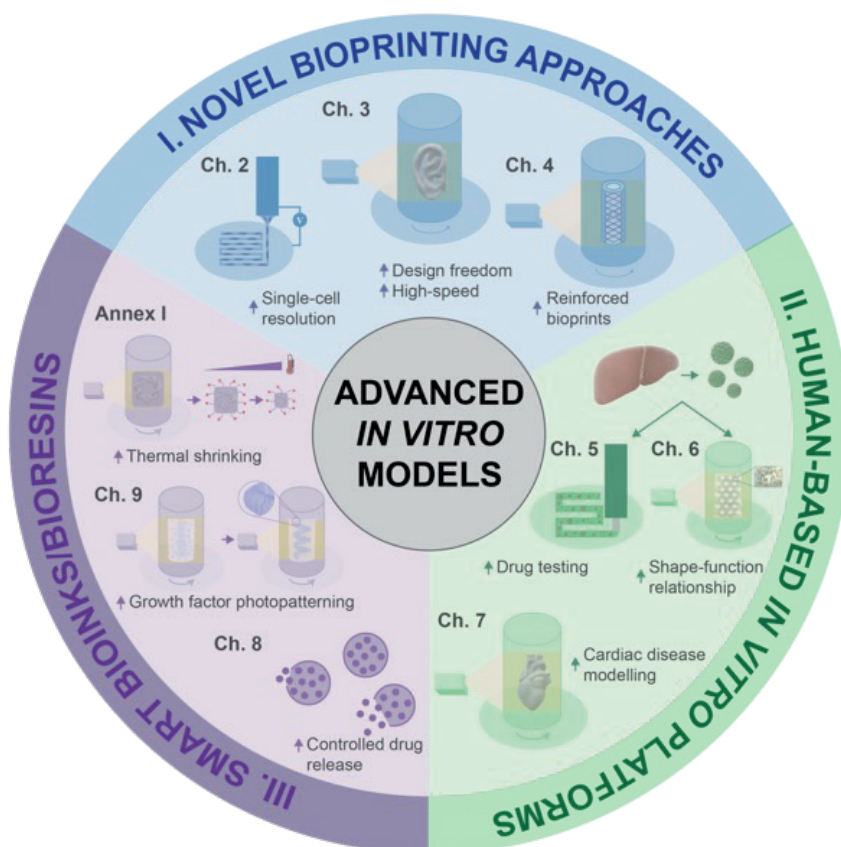


**Figure 3:** Graphical overview of the main topics covered in this thesis.

To address each sub-aim, this thesis is divided into three parts (**Figure 3**). **Part I** focuses on the development of advanced bioprinting techniques that address different limitations of existing bioprinting processes. In **Chapter 2**, the resolution limit of most conventional bioprinting approaches is tackled through the development of cell electrowriting (CEW), a new bioprinting approach that uses a voltage-driven printing head to fabricate high resolution, cell-laden hydrogel fibers with diameters comparable or even smaller than single cells (down to 5  $\mu\text{m}$ ). **Chapter 3** on the other hand, focuses on addressing the restricted design freedom exhibited by most layer-by-layer manufacturing approaches, as well as the long printing times required to create clinically-relevant sized constructs. The development of volumetric bioprinting (VBP) as a cell-friendly, layerless approach introduces a significant enhancement in design freedom of hydrogel-based constructs and enables the ultra-fast fabrication of centimeter-scale complex living structures. The hydrogel structures developed with this technique however, as observed with a variety of tissue engineering approaches, exhibit rather limited mechanical properties which may hinder the functionality and stability of these prints. To address this, **Chapter 4**

demonstrates the possibility to converge Volumetric Printing and Melt ElectroWriting in a new approach termed VolMEW. The introduction of cylindrical melt electrowritten scaffolds (precisely organized thermoplastic microfibers) into the VBP process results in the enhancement of mechanical properties of the complex printed hydrogel structures.

Transitioning the focus to the combination of biofabrication approaches with other *in vitro* modeling tools and their application for organ-specific *in vitro* model development, **Part II** highlights two target organs for which platforms of various complexity levels are developed: the liver and the heart. **Chapter 5** demonstrates the extrusion bioprinting of human liver-derived organoids in a gelatin based bioink into simple 3D structures that can be perfused with various toxic compounds. While the bioprinted model permits organoid differentiation and exhibits toxicity-dependent organoid death, the large and fragile organoids appear fragmented and exhibit significant cell death post-printing due to the shear stresses characteristic of extrusion printing techniques. To address this key limitation, while still harnessing the potential of organoid technology, **Chapter 6** shows, for the first time, the VBP of high-density organoid-laden structures which retain their morphology and function post-printing. Accurate printing of liver organoids into complex, structurally defined models and their incorporation into perfusable bioreactors shows the potential to modulate metabolic function based on the printed architecture, highlighting the importance of 3D shape in cellular function. In **Chapter 7**, a bi-chambered, multi-material heart model with native wall thickness gradients is volumetrically printed with induced pluripotent stem cell-derived cardiomyocytes, another powerful tool in cardiac tissue engineering. The design freedom of VBP enables the fabrication of numerous variations of the heart model to mimic different structural cardiomyopathies. Furthermore, an induced cryoinjury to mimic myocardial infarction showed promising biological signs of scar tissue formation and extracellular matrix remodeling, opening the door to the creation of clinically relevant cardiac *in vitro* models.

With promising observations regarding the use of VBP and other biofabrication approaches for *in vitro* model development, **Part III** focuses on further driving tissue mimicry of bioprinted structures through the development of new classes of smart biomaterials or “bioresins” that allow for the control of cell fate and/or structural properties of the material and cell culture environment. **Chapter 8** shows a controlled drug delivery tool through the fabrication of printable microcapsules. Incorporation of an anti-angiogenic drug into these particles showed a significant reduction in vessel growth in a highly angiogenic platform, and the addition of 3D printing allowed for the precise patterning of these particles in complex architectures. **Chapter 9** introduces a chemically editable gelatin norbornene (gelNOR) bioresin for VBP that not only exhibits highly tunable mechanical properties, but also enables the covalent attachment of thiolated proteins or growth factors with high spatiotemporal control. With this material, precise localized control over cell behavior is achieved and presents a first step towards mimicking complex developmental chemical

cues. In **Annex I** the library of VBP resins is further expanded through the development of thermoresponsive materials that exhibit temperature-dependent shrinking properties. These printable resins achieve the highest resolutions with VBP shown to date and exhibit great promise in the development of multi-scale bioprinted structures.

Finally, **Chapter 10** discusses the overarching key findings of this thesis and includes future perspectives of the presented works for the development of advanced *in vitro* models using biofabrication approaches.

Overall, these compiled works aim to demonstrate how, through the combination of various aspects in the biofabrication field (advanced printing approaches, human-based biological tools and smart materials), physiologically relevant *in vitro* platforms can be developed and take the next step towards filling the translational gap currently hindering drug development and disease modeling.

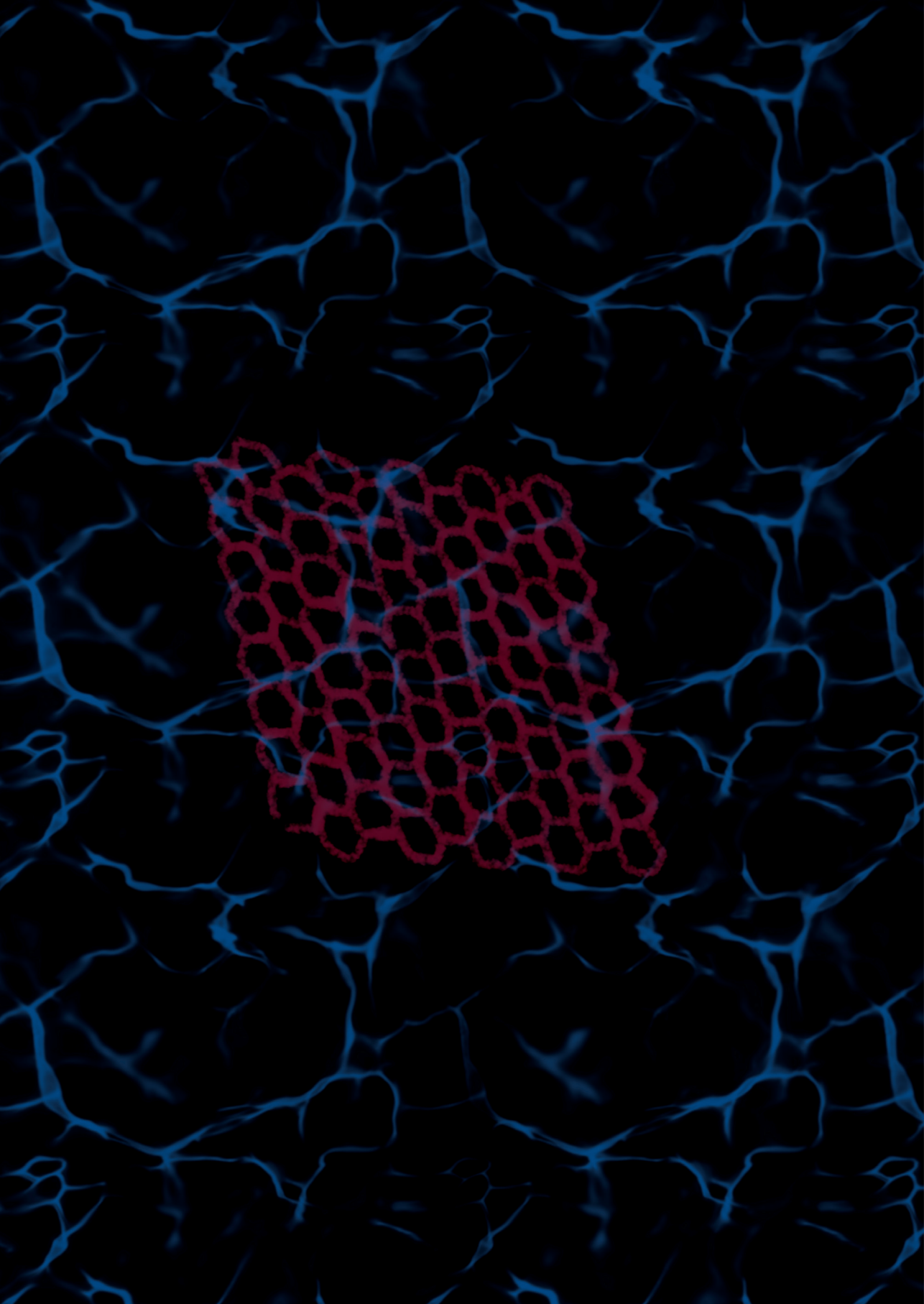




A vertical strip on the left side of the page shows a microscopic view of tissue, likely showing a network of cells or fibers in shades of blue and white. The rest of the page is white.

# Part I

**Advanced Biofabrication Strategies to  
Enhance Resolution and Architectural  
Complexity of Biofabricated Tissue  
Mimics**





# Chapter 2

## Hydrogel-Based Bioinks for Cell Electrowriting of Well-Organized Living Structures with Micrometer-Scale Resolution

Miguel Dias Castilho<sup>1,2\*</sup>, Riccardo Levato<sup>3,1\*</sup>, Paulina Núñez Bernal<sup>1</sup>, Myléne de Ruijter<sup>1</sup>, Christina Y. Sheng<sup>1</sup>, Joost van Duijn<sup>1</sup>, Susanna Piluso<sup>1,4</sup>, Keita Ito<sup>1,2</sup>, Jos Malda<sup>1,3</sup>

Published in: *Biomacromolecules*. 2021. 22(2)

<sup>1</sup> Department of Orthopedics, University Medical Center Utrecht, Utrecht University, Utrecht, The Netherlands

<sup>2</sup> Department of Biomedical Engineering, Eindhoven University of Technology, Eindhoven, The Netherlands

<sup>3</sup> Department of Clinical Sciences, Faculty of Veterinary Medicine, Utrecht University, Utrecht, The Netherlands

<sup>4</sup> Department of Developmental BioEngineering, Technical Medical Centre, University of Twente, Enschede, The Netherlands

\* Authors contributed equally to this work

## ABSTRACT

2 Bioprinting has become an important tool for fabricating regenerative implants and *in vitro* cell culture platforms. However, until today, extrusion-based bioprinting processes are limited to resolutions of hundreds of micrometers, which hamper the reproduction of intrinsic functions and morphologies of living tissues. This study describes novel hydrogel-based bioinks for cell electrowriting (CEW) of well-organized cell-laden fiber structures with diameters ranging from 5 to 40  $\mu\text{m}$ . Two novel photoresponsive hydrogel bioinks, that is, based on gelatin and silk fibroin, which display distinctly different gelation chemistries, are introduced. The rapid photomediated cross-linking mechanisms, electrical conductivity, and viscosity of these two engineered bioinks allow the fabrication of 3D ordered fiber constructs with small pores (down to 100  $\mu\text{m}$ ) with different geometries (*i.e.*, squares, hexagons, and curved patterns) of relevant thicknesses (up to 200  $\mu\text{m}$ ). Importantly, the biocompatibility of the gelatin- and silk fibroin-based bioinks enables the fabrication of cell-laden constructs, while maintaining high cell viability post printing. Taken together, CEW and the two hydrogel bioinks open up fascinating opportunities to manufacture microstructured constructs for applications in regenerative medicine and *in vitro* models that can better resemble cellular microenvironments.

**Keywords:** high-resolution bioprinting, photosensitive hydrogels, cell electrowriting

## INTRODUCTION

Bioprinting is an emerging technique for the fabrication of biological constructs that can be used in regenerative medicine (RM) and *in vitro* drug testing.<sup>[110]</sup> However, in an attempt to better mimic native tissues, there is an increasing demand to engineer structures with finer resolutions and further capture the hierarchical structure and composition of the native extracellular matrix.<sup>[111,162]</sup> This mimicking of the cellular microenvironment could provide new opportunities for the generation of constructs that can successfully exhibit functions at tissue and organ levels.<sup>[109,131,163]</sup> For example, intercellular interactions at the micro- to nanometer scale,<sup>[164]</sup> spatiotemporal changes in the ECM structure,<sup>[165,166]</sup> and mechanical and topographical cues provided by fibrillar ECM components are the well-known key drivers of cell behavior<sup>[167–169]</sup> and are the likely crucial elements for the engineering of functional, tissue-like constructs. Until today, the most well-established bioprinting processes, namely, extrusion-based,<sup>[170,171]</sup> droplet-based,<sup>[172]</sup> and light-assisted,<sup>[173]</sup> with the notable exception of two-photon polymerization,<sup>[174]</sup> are limited to resolutions close to tens of micrometers, which hamper the reproduction of such cellular microenvironments.

Recently, attempts have been made to achieve high-resolution biological constructs by using biofabrication processes, such as electrospinning<sup>[175–177]</sup> and electrohydrodynamic jetting.<sup>[178,179]</sup> In both methods, and differently from the conventional extrusion bioprinting techniques, material flow is driven by electrical forces that surpass the surface tension of the liquid ink, allowing for the fabrication of fibers with sizes smaller than the extrusion nozzle diameter.<sup>[180]</sup> Despite the high-intensity electrical field involved, these methods were found to be compatible with the processing of living cells, even showing initial steps toward the reconstruction of hierarchical structures embedding cardiomyocytes,<sup>[175]</sup> or cells from neural lineage.<sup>[181]</sup> Nevertheless, neither of these techniques could simultaneously meet the requirements to emulate the intrinsic morphologies and local composition of cellular microenvironments, that is, the three-dimensional (3D) patterning, the deposition of fibers with micron/submicron size diameters, and the maintenance of high cell viability. Despite the fact that electrospinning approaches are compatible with the generation of cell-laden microfibers, they could not be readily applied to organize the fibers into predefined 3D shapes because of the whipping instabilities of the electrified jet.<sup>[175,182]</sup> With electrohydrodynamic jetting, on the other hand, structures with more complex 3D patterns could be created, yet fabrication resolution was compromised.<sup>[178,183,184]</sup> In addition, most of the previous studies on nonthermal electrohydrodynamic jetting have been carried out with polysaccharide-based hydrogels, such as alginate, which present poor cell adhesive properties and limited mechanical toughness.<sup>[178,185]</sup> Thermal electrohydrodynamic jetting, on the other hand, has mostly been based on the use of synthetic polymers, such as poly(2-ethyl-2-oxazine) and ureido-pyrimidinone coupled

2

to poly(ethylene glycol),<sup>[179,184,186–188]</sup> which are not compatible with cell encapsulation. In particular, Melt Electrowriting (MEW) is a technique that has gained increased attention in RM because of its potential to engineer highly ordered fibrous scaffolds but until now is still limited to the use of biomaterial inks, that is, thermoplasts and hydrogel-based materials, without encapsulated cells, because of the high processing temperatures required. **Supplementary Table S1** in the Supporting Information summarizes the material platform, resolution, shape control, and cell encapsulation capabilities of previously reported electrohydrodynamic fabrication technologies.

There is a clear need for the development of biomaterial platforms that are compatible with processing through the application of strong electrical fields, allow for the fabrication of complex small-scale geometries, and support high viability of encapsulated cells. Protein-based natural-derived materials are promising candidates because of their inherent biocompatibility, bioactive signals, binding affinity for cells, and tunable mechanical properties. Here, we describe a new class of photo-cross-linkable bioinks based on proteinaceous polymers, namely, gelatin and silk fibroin, that are compatible with the abovementioned requirements and thus can enable the 3D writing of microscale, cell-laden fibers via a cell electrowriting process (CEW) (**Figure 1**). This process conjoins the principles of electrical-assisted material deposition with cell-laden hydrogel extrusion, moving beyond the existent nozzle-based bioprinting processes and MEW technology. We selected gelatin, as it is derived from collagen, the main organic constituent of the natural ECM of mammals,<sup>[189]</sup> and silk fibroin because of its unique mechanical properties and potential for cell encapsulation.<sup>[190,191]</sup> These protein-based polymers with complementary biological and mechanical properties could aid in further approaching the functional and structural properties of native cellular microenvironments, while additionally demonstrating the flexibility in material processing of the CEW for biofabrication.

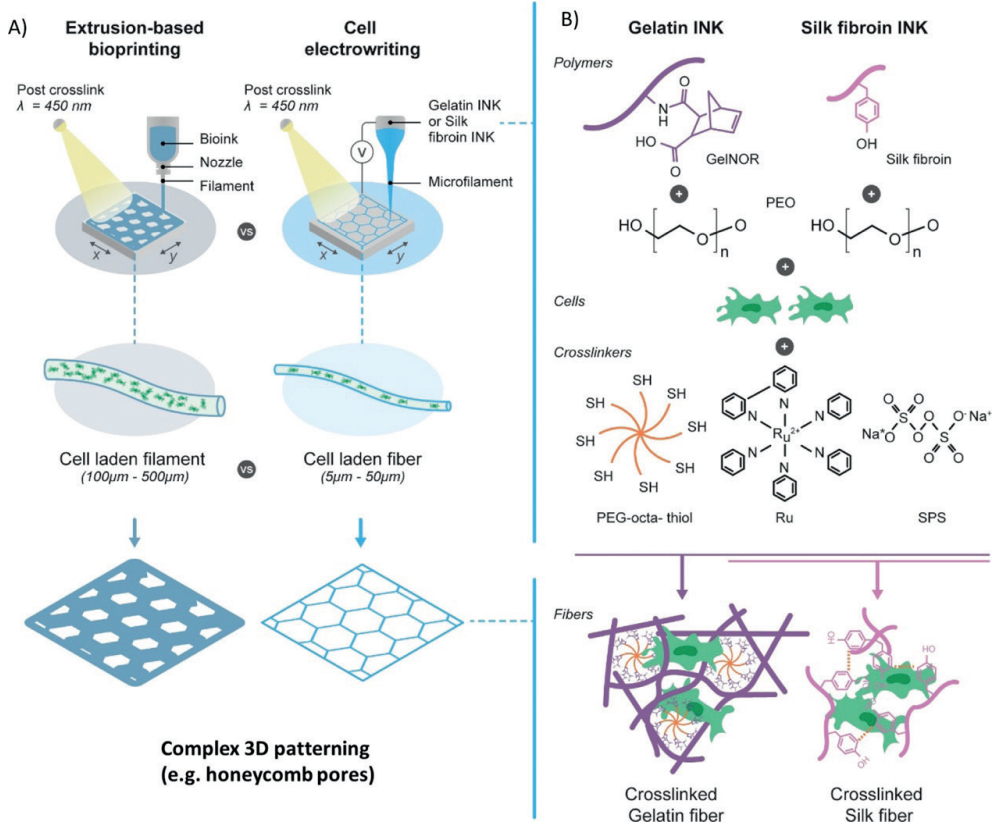


**Figure 1:** A) Comparison between conventional extrusion-based bioprinting and novel CEW process with respective differences in cell distribution and process resolution. B) Schematic of the developed gelatin and silk fibroin bioink compositions with their respective light photocrosslinking mechanism. Scheme illustrates the visible light-initiated orthogonal crosslinking of i) gelNOR with a PEG thiol cross-linker and ii) silk fibroin, in the presence of ruthenium and sodium persulfate. GelNOR and silk bioinks are compatible with both extrusion-based printing and CEW.

## RESULTS AND DISCUSSION

As a first step, the gelation kinetics, viscosity, and electrical conductivity of the CEW-compatible bioinks were tuned (**Figure 1A**). Clearly, fast gelation kinetics is paramount to form stable fibers with a reproducible diameter that can be effectively stacked into ordered 3D structures. Although this feature is also important for bioinks in conventional extrusion-based bioprinting, it poses a significant challenge for CEW, as the bioinks typically flow about 10–100 times faster within the electrohydrodynamic jet than within conventional extrusion-based bioprinting.<sup>[192]</sup> This results in a short latency time available to cross-link the jet before it is deposited onto the collector. Because of this short latency time, visible light-mediated thiol-ene click reactions and di-tyrosine oxidation

photochemistries were used. More specifically, norbornene-modified gelatin (gelNOR), which can form a hydrogel network through step growth polymerization in the presence of a multifunctional thiol crosslinker, and unmodified silk fibroin, which undergoes quick photochemical crosslinking because of the presence of tyrosine residues in its protein structure,<sup>[193]</sup> were selected as bioink platforms (**Figure 1B**). To accelerate the gelation kinetics, a two-component photoinitiator system was used, based on the mixture of tris(2,2-bipyridyl)dichlororuthenium(II) hexahydrate and sodium persulfate (Ru/SPS). Such a two-component system has been recently introduced for both extrusion- and light-based bioprinting processes in the fabrication of large tissue constructs with complex geometry, through a photoreactive process, which is only marginally affected by oxygen inhibition.<sup>[173,194,195]</sup> Photorheological analysis at different Ru/SPS ratios confirmed gelation of the gelNOR and silk fibroin bioinks within less than 30 s and 1.5 min of exposure to visible light, respectively (**Figure 2A**). This underscores the potential of these material combinations as inks for CEW, in view of the short latency times during which fiber crosslinking must occur. It is important to mention that a slight increase in the storage modulus of the gelNOR gels (but not of the silk gels) was observed, prior to the photo-exposure trigger. We attributed this to the high reactivity of the gelNOR system, as recently described by Soliman and colleagues,<sup>[196]</sup> and to the potential photo-exposure while placing the hydrogel materials on the rheometer.

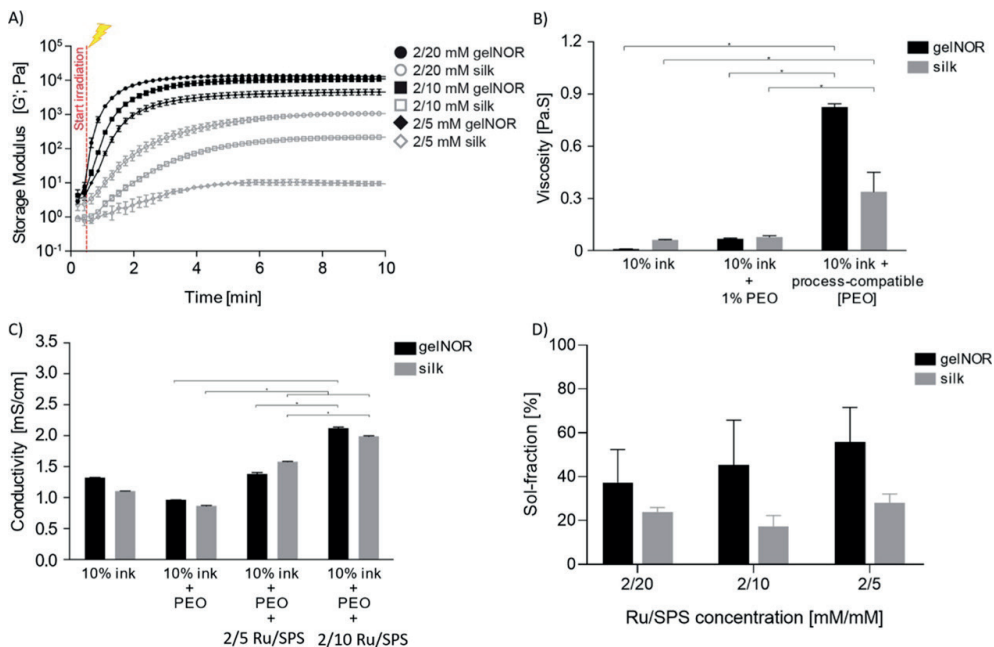


**Figure 2: Physical-chemical properties of gelNOR and silk fibroin bioink systems.** A) *In situ* photorheometry showing the storage modulus ( $G'$ ) of the bioinks as a function of time. Hydrogel samples were irradiated with visible light 30 s after the experiment started. B) Viscosity changes as a function of the bioinks' PEO concentration. C) Conductivity changes as a function of PEO concentration and Ru/SPS ratio. D) Sol-fraction changes as a function of Ru/SPS concentration.

C) Electrical conductivity of hydrogels as a function of both PEO and photoinitiator concentration. D) Sol fraction as a function of Ru/SPS photoinitiator concentration.\* indicates significant difference.

In parallel to the fast gelation requirement, CEW bioinks should possess high viscosity and moderate electrical conductivity to prevent Rayleigh instabilities and ensure steady jets. To enhance viscosity, gelNOR and silk fibroin were blended with polyethylene oxide (PEO) at increasing concentrations (1–6% w/v). The viscosity of the gelNOR–PEO and silk–PEO blends increased significantly compared to the gelNOR- and silk fibroin-only solutions when PEO concentrations exceeded 3.4% w/v. Maximum viscosities of 0.8 and 0.4 Pa·s were obtained for gelNOR and silk fibroin hydrogel systems with 6% w/v and 3.4% w/v PEO, respectively (**Figure 2B**). These PEO concentrations were required to prevent droplet formation and to thus allow a steady jet formation.

The electrical conductivity of the gelNOR and silk fibroin hydrogels, with and without PEO, was considerably higher (0.9–1.3 mS/cm, **Figure 2C**) than that of semiconductive fluids (<10–11 mS/cm)<sup>[197,198]</sup> that are considered ideal for steady jet formation under electrical fields. Nevertheless, our results demonstrate that these high conductivity values did not prevent stable jet formation, yet it did limit the continuous fiber collection to approximately 30 min. Based on our observations, this fabrication time was sufficient to collect satisfactory material volume without significant drying of the fibers. Additionally, the inclusion of 2/5 and 2/10 mM Ru/SPS resulted in a further increase of the conductivity of both hydrogel systems (1.5–2.3 mS/cm). This is likely due to the presence of sodium and persulfate ions from SPS in the aqueous medium of the ink. The presence of this compound determined a specific window within which the formation of a fluid jet at the spinneret was still possible (**Figure 2C**). Indeed, when the levels of SPS exceeded 10 mM, formation of a continuous jet was no longer observed, likely due to the excess of SPS ionic compounds and the resulting increase in electrical conductivity of the hydrogel. High crosslinking efficiency within such short latency time is of importance to ensure high printing resolution and cell embedding within the electrowritten filament. Therefore, the effect of SPS and PEO on the crosslinking efficiency of both CEW bioinks was investigated by quantifying the sol fraction upon the formation of the polymer network. Both bioink systems, 10% gelNOR + 6% PEO and 10% silk fibroin + 3.4% PEO, were able to form stable hydrogel fibers at 5 mM SPS concentration, which corresponded to an amount of uncrosslinked polymer of approximately 50% (**Figure 2D**). This sol fraction value is likely due, on one hand, to the presence of PEO macromolecules, which are not directly crosslinked in the hydrogel network, and on the other hand to the low SPS concentration used in the bioink. Ru/SPS mediates crosslinking of alkenes mainly via the generation of sulfate radicals,<sup>[194,195]</sup> whose concentration is dependent on the SPS content of the prepolymer solution. Lower sol fraction values could be achieved for 20 and 10 mM SPS; however, continuous fiber deposition could not be obtained, which limited further 3D scaffold fabrication.

In order to allow controlled patterning of the fibers with the embedded cells, we then focused on fine-tuning the key CEW instrument parameters: applied voltage, collector velocity, and dispensing pressure, with respect to the fiber alignment and fiber diameter (**Figure 3**). The applied voltage was first studied at a constant collector velocity (25 mm/s) and applied pressure (0.05 bar), as the combination of these parameters allowed the consistent deposition of homogeneous fibers, that is, without a jet break and minimal oscillation of fiber diameter within a jet. An increase in both fiber straightness and diameter was observed between 2.5 and 3.0 kV, with fibers from both gelNOR and silk fibroin hydrogel systems reaching full straightness (no visual fiber coiling) at 3.0 kV (**Figure 3Ai, Bii**). In contrast, coiling and reduction of the fiber diameter occurred when voltages between 3.0 and 5.0 kV were applied. The observed fiber coiling was likely due to an imbalance between the extrusion rate of the material and the velocity of the collector plate. Jet buckling and consequent fiber coiling typically occur when the jet velocity is higher than the collection velocity, as previously described for other direct writing electrofabrication methods.<sup>[199,200]</sup> By increasing the collector velocity from 25 to 50 mm/s, a reduction in fiber coiling and fiber diameter was consequently observed (**Figure 3Aii, Bii**). This suggests that an adequate balance between extrusion rate and collection velocity can prevent jet buckling and simultaneously reduce fiber diameter. For collector velocities between 25 and 50 mm/s, fiber diameters between 3 and 6  $\mu\text{m}$  for gelNOR, and 40–45  $\mu\text{m}$  for silk fibroin (**Figure 3Aii**), were obtained. The higher fiber diameter for the silk hydrogel system is most likely attributed to the precursor solution showing a viscosity about twofold lower than that of the gelNOR system. Regardless of these differences, the obtained fiber diameters are 1 to 2 orders of magnitude smaller than the fiber sizes previously reported for extrusion-based bioprinting ( $\approx 200 \mu\text{m}$ ).<sup>[201,202]</sup> Interestingly, the obtained fiber diameters approximate the size of a single cell (animal cell size  $\sim 10 \mu\text{m}$ ) and were suitable for cell encapsulation. The effect of the dispensing pressure was also investigated, yet straight fiber alignment was only observed within a narrow pressure range (**Figure 3Aiii**). Because of the low viscosity of both hydrogel systems, dispensing pressures above 0.05 bar resulted in excessive flow rates and consequent fiber coiling and fiber diameter oscillation. An overview of the effect of key hydrogel bioink material properties and CEW processing parameters on jet formation, as well as of the physical mechanisms governing the CEW process, is provided in **Supplementary Figures S1 and S6**, respectively.



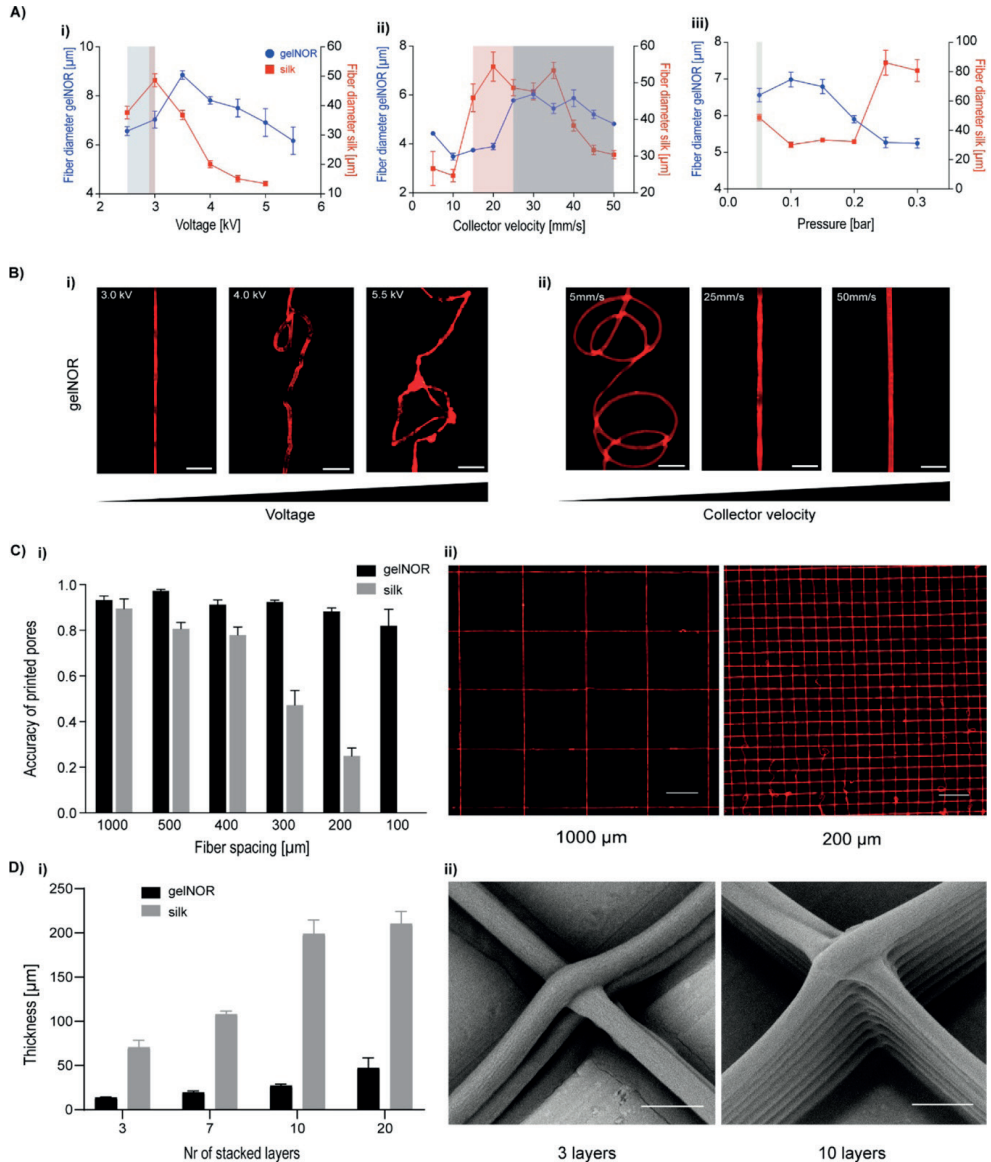


**Figure 3: Influence of key CEW processing parameters on fiber collection and 3D patterning for both cell-free gelNOR and silk fibroin hydrogel systems.** A) Effect of i) voltage, ii) collector velocity, and iii) air pressure on fiber diameter. Printability window is represented by background colors. B) Representative microscopic images of the effect of increasing i) voltage and ii) collector velocity on fiber morphology for the gelNOR hydrogel system. Scale bar = 50 μm. C) Print fidelity of fiber hydrogel 3D scaffolds. Ci) Accuracy of printed pores,  $A_{cc\ pore}$  as a function of scaffold pore size.  $A_{cc\ pore}$  was determined using a relative value obtained by the ratio between the design and fabricated pore area. In the case of no deviation between the printed and designed pore areas,  $A_{cc\ pore} = 1$ . Cii) Representative images of printed scaffolds with pore sizes of 1000 and 200 μm for gelNOR hydrogel. Scale bar = 500 μm. D) Scaffold thickness as a function of the number of stacked hydrogel layers. Di) Final scaffold thickness and Dii) representative scanning electron microscopy (SEM) images of scaffolds with 3 and 10 layers showing perfectly stacked hydrogel fibers at the vertices of squared pores. Scale bar = 10 μm.

Next, the patterning capacity of both gelNOR and silk hydrogels was investigated by manufacturing 3D scaffolds with square pore geometries of varying pore sizes, from 100  $\mu\text{m}$  to 1000  $\mu\text{m}$ , and varying scaffold thicknesses, from 1 to 30 layers (**Figure 3Ci, ii**). All scaffolds were fabricated under optimized fabrication parameters, that is, constant collector velocity of [25, 30] mm/s, voltages of 2.5 (gelNOR) and 3.0 (silk), air pressure of 0.05 bar, and cross-linking time with visible light (400–450 nm) during jet collection and after printing for approximately 5 min. Scaffolds with precisely configured square pores were obtained with minimum pore sizes of 100  $\mu\text{m}$  for gelNOR and 400  $\mu\text{m}$  for silk (accuracy of printed pores > 0.8). Smaller pore sizes could also be achieved, but this compromised the accuracy of printed constructs, resulting in higher deviations between the printed constructs and their digitally designed counterparts (data not shown). The lower print fidelity, and consequently larger pore sizes obtained for the silk ink, is most likely attributed to the lower viscosity and slower reactivity of this system. These two aspects combined resulted in less stable material collection during printing.

In addition, the ability to form scaffolds with curved fibers instead of straight fibers was also demonstrated (**Supplementary Figure S2**). Both bioink systems allowed the accurate writing of hemispherical shaped fiber scaffolds with a minimum interfiber distance of 200  $\mu\text{m}$ . We further observed that scaffolds with thicknesses of 50 and 200  $\mu\text{m}$  for the gelNOR and silk hydrogel systems, respectively, could be fabricated without significantly affecting the printing accuracy (**Figure 3Di, ii**). Above these thicknesses, accurate fiber placement and stacking were hampered, likely due to the residual charges accumulated in and onto the electrified jets,<sup>[203,204]</sup> resulting in repulsive Coulomb interactions between the new and previously deposited fibers. Importantly, the hydrogel systems and the CEW process allowed the fabrication of regularly structured biocompatible hydrogel scaffolds with unprecedented high resolution and geometrical accuracies. To the best of our knowledge, no other nozzle-based biofabrication approach or MEW technology has been able to process natural-derived protein-based hydrogels with a similar control over the spatial resolution of the fibers (**Supplementary Table S1**).

Subsequently, the swelling and mechanical characteristics of gelNOR and silk fibroin CEW scaffolds were investigated (**Figure 4**). The swelling behavior was studied by measuring the diametral changes of single CEW fibers when subjected to an aqueous environment over 7 days (**Figure 4A – C**). The diameter of gelNOR fibers increased by approximately 2.5-fold compared to that on day 0, reaching a maximum diameter of  $15.3 \pm 0.5 \mu\text{m}$  (**Figure 4A, C**), whereas silk fibroin fibers displayed an increase of only 1.1-fold, reaching a maximum diameter of  $55.9 \pm 9.5 \mu\text{m}$  (**Figure 4B**). Interestingly, both gelNOR and silk fibroin fibers reached the equilibrium swelling at day 1, after which no change in morphology was observed until day 7. After day 7, small fiber breakage and loss of fiber morphological structure started to be observed in both material systems, which indicate partial material degradation. This limited stability in aqueous environments after 7 days

could be improved by increasing the crosslink density (*i.e.*, polymer concentration and irradiation time), although at the cost of potentially reducing viability of encapsulated cells and their ability to synthesize new ECM. Further, the mechanical properties of gelNOR and silk fibroin CEW scaffolds were determined by nanoindentation testing carried out on CEW scaffolds at equilibrium swelling (**Figure 4D – G**). This mechanical testing method was selected because of its sensitivity to measure forces in the range of nano- to micro-Newtons and the suitability to characterize small-sized constructs, that is, on the scale of nano- to micrometers. The load–displacement curves of gelNOR and silk fibroin CEW scaffolds with three layers were compared with those of the scaffolds of the same composition prepared by conventional extrusion-based printing (**Figure 4D**, only representative images of CEW scaffolds are shown). We observed that the effective elastic modulus of gelNOR scaffolds (CEW,  $8.5 \pm 4.9$  kPa; extrusion,  $2.7 \pm 1.5$  kPa) was significantly lower than that of silk scaffolds (CEW,  $164.3 \pm 53.8$  kPa; extrusion,  $35.8 \pm 16.7$  kPa) (**Figure 4F, G**). Notably, the effective stiffness of CEW scaffolds was 3 (gelNOR) to 4.5 (silk) times higher than that found for extruded printed scaffolds. Such differences are likely due to the higher shear-induced alignment by the CEW process than by the conventional extrusion printing, which led to the generation of polymer fibers with a high degree of orientation and reduced number of polymer entanglements. In addition, the obtained effective stiffness is comparable to that reported for other alginate- and gelatin-based materials (4 kPa – 20 MPa)<sup>[205,206]</sup> but significantly lower for silk-based hydrogels (24–1864 MPa)<sup>[207]</sup> processed by other electrohydrodynamic processes (see also **Supplementary Table S1**). This is likely due to the methanol treatment used to stabilize silk fibroin fibers obtained with other electrohydrodynamic techniques, which induces the rearrangement of silk fibroin chains into  $\beta$ -sheet crystals. Although this treatment conveys the silk mechanical properties similar to those of native silk fibers, it would not be suitable for the stabilization of cell-laden fibers.<sup>[208]</sup> Importantly, all silk scaffolds showed a greater overall energy absorption than the gelNOR scaffolds, as observed from the different load–displacement response curves (**Figure 4D – E**). This confirms the improved ductile behavior of the presented silk fibroin bioink system in comparison with the conventionally used alginate hydrogel systems for electrohydrodynamic processes.

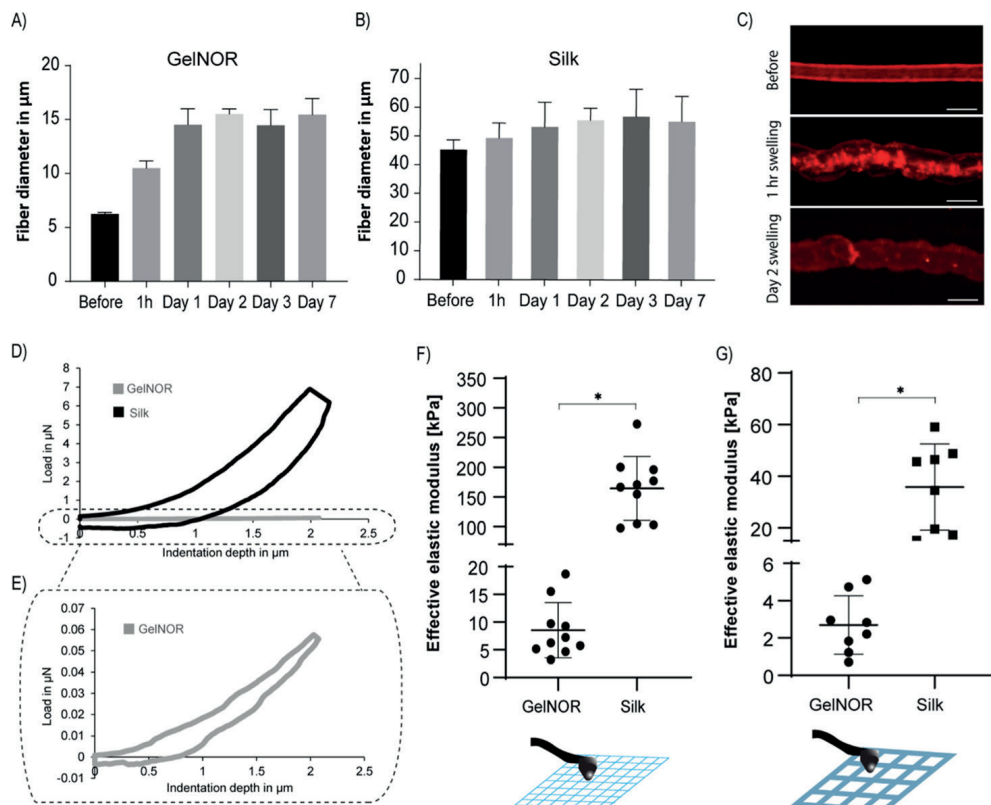
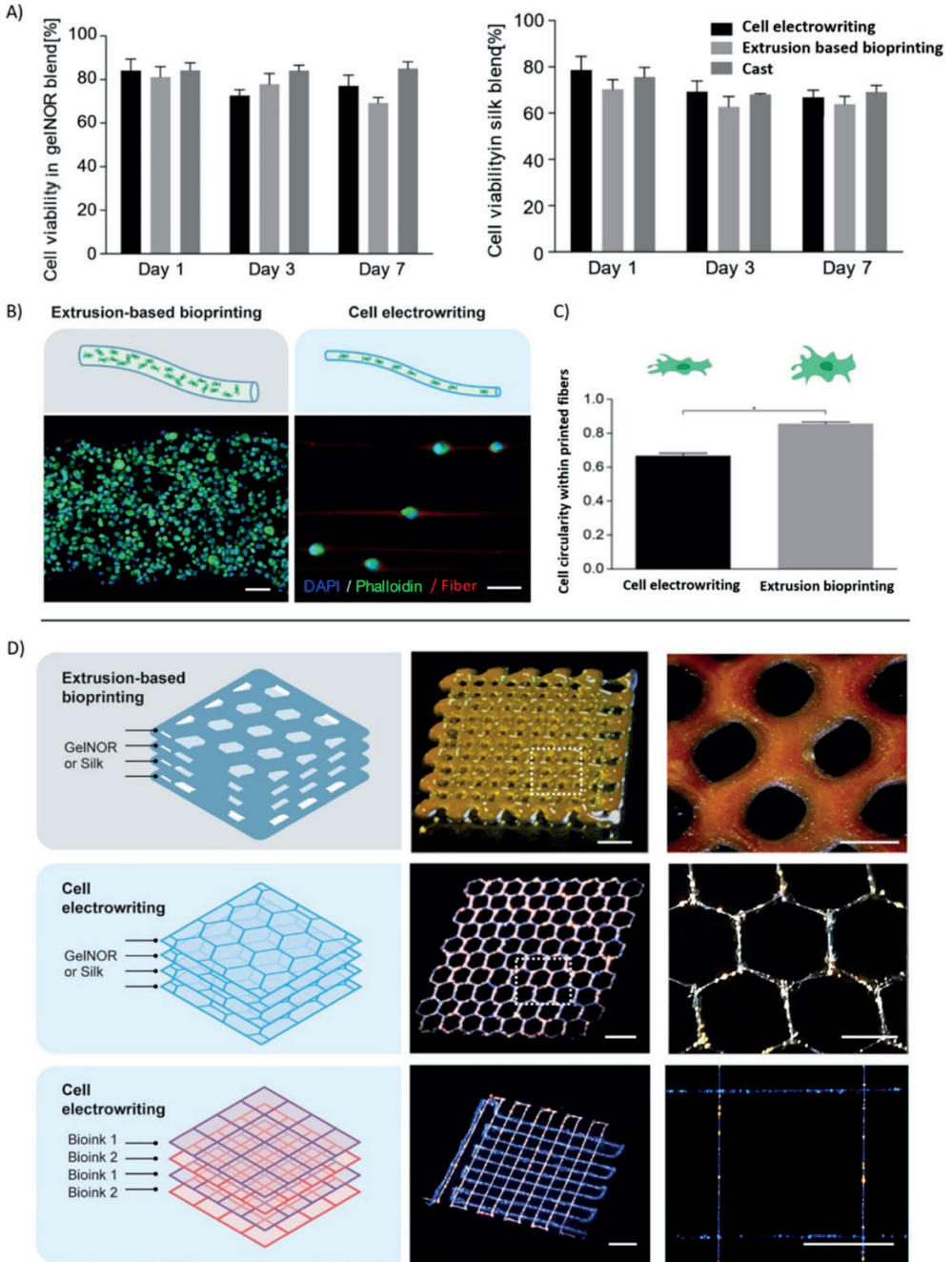


**Figure 4: Swelling and mechanical characteristics of CEW hydrogel fibers.** Swelling of A) gelNOR and B) silk fibroin-based cell-free hydrogel fiber before and after 1 hour, 1, 2, 3, and 7 days incubation in phosphate buffered saline (PBS). C) Representative images of swollen gelNOR fibers before and after 1 h and 2 days of swelling. D, E) Representative loading and unloading curves of CEW gelNOR and silk-based cell-free scaffolds measured by nanoindentation. Curves have been averaged over at least three measurements. F) Effective stiffness of CEW gelNOR and silk fibroin-based cell-free scaffolds and G) comparison with the scaffolds of same composition obtained by conventional extrusion bioprinting. All nanoindentation experiments were performed on scaffolds after 1 day of PBS immersion (equilibrium swelling).

Subsequently, the ability to pattern gelatin and silk fibroin hydrogels into 3D organized microfiber networks with encapsulated cells was assessed. For this, bone marrow-derived mesenchymal stromal cells (MSCs) were mixed within the ink precursors. Cell concentrations up to  $10^8$  cells/mL could successfully be processed, and cell-laden electrowritten microfibers could be obtained. Viability of the electrowritten cells was determined at 1, 3, and 7 days of culture post printing, revealing a high ratio of living cells ( $> 70\%$  at all time points) for both gelNOR and silk fibroin bioinks (**Figure 5A**). These values were comparable to those observed for conventional extrusion-based bioprinted and cast controls and were in line with previous works on different electrohydrodynamic techniques (**Supplementary Table S1**). Furthermore, the presence of the viscosity enhancer PEO in the gelNOR and silk fibroin-based CEW bioinks before and after incubation in PBS for 0,

24, and 72 h was studied (Figure S3). Analysis performed on the Fourier transform infrared spectroscopy (FTIR) spectra of gelNOR revealed the presence of peaks characteristic of polyethylene glycol (PEG)-thiol, namely the peaks indicative of the asymmetric and symmetric C–O–C stretching ( $\approx 1090$  and  $845\text{ cm}^{-1}$ , respectively), representative of the incorporation of the PEG-thiol cross-linker within the polymer network (**Supplementary Figure S3A**). Although the inherent presence of such molecules within the gelatin hydrogels renders the PEO removal upon washing of the gels difficult to assess by means of FTIR, the analysis of the peak area between the ether peaks and amide I ( $\approx 1650\text{ cm}^{-1}$ ) suggests that PEO residues may persist within the hydrogel after 3 days of washing (**Supplementary Figure S3C**). This is possibly due to the entrapment of PEO chains within the gelatin network. Although these data suggest that different washing protocols may be required to completely remove PEO, no significant effect on the cell metabolic activity was detected after 3 days of culture, indicating the overall safety of having this supplemental molecule as the viscosity enhancer (**Figure 5A**). Conversely, in the case of the silk fibroin hydrogels, PEO removal after 1 day of incubation in PBS was demonstrated, with the ratio between the area under the ether C–O–C stretching peak and the amide I band reaching values comparable to those of pristine silk (**Supplementary Figure S3B – D**). Taken together, these data show that the CEW process preserves cell viability, suggesting that the relatively high viscosity of the bioinks, the applied electric field, and the resulting shear stresses within the electrohydrodynamic jet did not induce significant damage to the cells. This is in agreement with previous works, which also indicated that living cells could be safely electrospun, reaching a minimum size of approximately  $10\text{ }\mu\text{m}$  in diameter, even though in such setups, differently from CEW, limited patterning control was observed (**Supplementary Table S1**).<sup>[175,181,209]</sup>



scaffolds and compared with conventional extrusion bioprinting. Cell electrowritten fibers exhibited single cells accurately aligned along the fiber pattern. Meanwhile, extrusion-bioprinted fibers exhibited multiple cells distributed homogeneously along the thickness of the filament. Scale bar = 20  $\mu\text{m}$ . D) Complex shape patterning of representative gelNOR-based electrowritten scaffolds with fluorescent nanoparticles. Cell electrowritten hexagon-shaped 3D scaffolds exhibited 2 times higher printing accuracy than the extruded printed scaffolds. CEW also allowed simultaneous printing of multiple bioinks in one single construct. Scale bars = 800  $\mu\text{m}$  (left panels) and 400  $\mu\text{m}$  (right panels).

We further investigated cell distribution and morphology within the gelNOR hydrogel system, as we hypothesized that smaller fiber diameters could alter these parameters substantially. In contrast to what is observed for the distribution of cells within large ( $\approx 300$   $\mu\text{m}$ ) hydrogel filaments obtained through conventional extrusion-based bioprinting, printed cells in gelNOR through the CEW process are accurately aligned following the deposition pattern of the fibers (**Figure 5B**). An interesting feature of the gelNOR CEW process is that each printed microfiber (diameter  $\approx 2\text{--}10$   $\mu\text{m}$ ) is significantly smaller than the size of an individual MSC in suspension ( $\approx 10\text{--}30$   $\mu\text{m}$ ).<sup>[210]</sup> Small, submicron features, such as grooves, pillars, and microfibers, are generally known to greatly affect cell morphology via contact guidance and spatial constriction.<sup>[211]</sup> However, from a morphological point of view, the electrowritten cells showed only a slight cytoskeletal deformation, yet no significant morphological changes in the nucleus, compared to the cells embedded in extrusion-based printed fibers, as observed by measuring cell circularity as a shape descriptor (**Figure 5C**). Interestingly, the bioinks, rather than providing a strict confinement for the embedded cells, simply appear to accommodate for the cell size, encapsulating them in a bead-and-necklace-like conformation.

In addition, fluorescent microparticles, with the size comparable to that of MSCs, were used to facilitate the visualization of “cell-laden” constructs with more complex geometries and material combinations (**Figure 5D**). The unique patterning capabilities of the CEW process were demonstrated by printing complex hexagonal pore structures (accuracy of printed pores  $> 0.8$ ), which could not be reproduced by conventional extrusion-based bioprinting (accuracy of printed pores  $< 0.4$ ) (**Figure 5D, Supplementary Figure S5**). The potential of the CEW process for multi-material fiber scaffold fabrication was further investigated by simultaneous printing of two gelNOR bioinks loaded with fluorescent particles displaying different emission wavelengths. Well-organized microstructures with square-shaped pores were successfully obtained (**Figure 5D**). This versatility of the CEW process is a powerful characteristic that can aid the generation of more relevant ECM-like microenvironments that combine different materials and cell types. Another important implication of our results is the potential development of multiple tissue-type microenvironments, as the investigated cells, MSCs, possess the ability to differentiate toward different lineages (*i.e.*, myoblasts, tendons, and neural-like cells). However, the remaining challenge is to maintain both the shape and stability of the fabricated cell-laden fibers over culturing periods longer than 7 days. Because of the reduced fiber size

(combined with potentially the relatively high sol-fraction in the gelNOR bioinks) and enzymatic activity during culture, strategies to accurately control the degradation kinetics and mechanical stability may be required.

## CONCLUSIONS

In summary, the unique biocompatibility of both the gelNOR and silk fibroin materials, their promising mechanical performance when compared with conventional extrusion bioprinting, the reduced cell-laden fiber sizes (5–40  $\mu\text{m}$ ), and the unprecedented resolution and patterning precision open promising avenues for the high-resolution printing of labile biological moieties and living cells. These remarkable features of the novel photoresponsive hydrogel bioinks and CEW process will allow to create microstructure scaffolds that can better resemble cellular microenvironments for RM (*i.e.*, muscle fibers, tendons, and nerve networks) and organ-on-a chip models. One of the fascinating applications of CEW is the creation of unique cell culture platforms for applications in developmental biology and drug discovery because the cellular microenvironment could now be further controlled by the resulting cell-laden fiber size, material composition, scaffold architecture, and mechanical properties.

## EXPERIMENTAL SECTION

*Materials:* The following materials were used: gelatin type A (bloom 180, Roth, Germany); 8-arm poly(ethylene glycol) thiol (MW: 10,000 g/mol; JenKem Technology, USA); tris(2,2'-bipyridyl)dichlororuthenium(II) hexahydrate (Ru; Sigma-Aldrich, The Netherlands); sodium persulfate (SPS; Sigma-Aldrich, The Netherlands); poly(ethylene oxide) (PEO; MW: 600,000–1,000,000 g/mol, Acros Organics, USA); silkworm cocoons (Wild Fibres, UK); and lithium bromide (Acros Organics, USA).

*GelNOR preparation:* GelNOR was synthesized as previously described.<sup>[212]</sup> Briefly, 10% w/v porcine gelatin type A (180 bloom; Roth, Germany) was dissolved in phosphate-buffered saline (PBS) at 50° C under constant stirring conditions. A 20% w/v of carbic anhydride (CA; Acros Organics, Japan) was added to the gelatin solution, and the pH was adjusted to 7.5–8.0 using 5 M sodium hydroxide (NaOH). The reaction was quenched after 24 h by the addition of 3 $\times$  PBS. After centrifugation at 4000 rpm to remove excess CA, gelNOR was dialyzed against deionized water (Milli-Q) at 5° C for 5 days, and water was refreshed 2 $\times$  per day. Finally, the solution was filter-sterilized and lyophilized. The degree of functionalization was 45%, as determined by fluoraldehyde assay, as previously reported.<sup>[212]</sup>

*Silk fibroin preparation:* Silk fibroin was extracted from *Bombyx mori* silkworm cocoons, as previously described.<sup>[191]</sup> Briefly, cut cocoons were boiled in an aqueous solution of



0.02 M  $\text{Na}_2\text{CO}_3$  for 30 min. The degummed fibers were dissolved in a 9.3 M LiBr (Sigma-Aldrich) solution at 70 °C for 1 h, followed by dialysis against water for 48 h, using cellulose dialyzing tubing (MWCO 3.5 kDa, Sigma-Aldrich). The resulting 6% w/v silk solution was concentrated to 16% w/v by dialysis against PEG (10 kDa, Sigma-Aldrich).

*Bioink preparation:* Stock gelNOR solutions were mixed with solutions having different PEO concentrations to obtain a blend with the final gelnor concentration of 10% and various PEO contents (1–6% w/v). A 10% w/v PEO stock solution was prepared by dissolving PEO powder in Milli-Q water. The gelnor/PEO blends were gently mixed at room temperature, followed by the addition of Ru and SPS at various ratios (2:5, 2:10, and 2:20). Concentrated silk solutions were prepared with the PEO concentrations same as the gelnor ink. The silk fibroin/PEO blend was mixed at 4 °C, followed by the addition of Ru and SPS at the same ratios as that of gelNOR.

*Rheological measurements:* Rheological characterizations of gelNOR, gelNOR/PEO, silk, and silk/PEO were performed on a rheometer (Discovery HR-2, TA instruments) fitted with a parallel plate of 20 mm in diameter, a gap distance of 0.5 mm, and equipped with a light-curing system. To determine the gelation time, the bioink solutions with different Ru/SPS ratios were placed between the two plates. *In situ* photorheometry was performed by using a visible light source, with light switched on 30 s after initiating the time sweep measurement. All measurements were performed within the linear viscoelastic region, at a strain of 1% and room temperature. The elastic modulus ( $G'$ ) and viscous modulus ( $G''$ ) were recorded as functions of time. To determine viscosity as a function of shear rate, the bioink solutions were placed between the parallel plates, and data were collected over a shear rate range between 1 and 1000  $\text{s}^{-1}$ . The photorheometry and hydrogel cross-linking experiments were conducted using a 600 lumen white lamp, with the wavelength range of 400–700 nm.

*Electrical conductivity:* The conductivity of the different hydrogel compositions was evaluated using a CDM230 conductivity meter (Radiometer Analytical, France). Calibration was first conducted using NaCl solutions (0.1 and 1% w/v).

*Sol-fraction analysis:* Crosslinking efficiency was assessed through sol-fraction analysis, as previously reported in the literature.<sup>[194]</sup> First, cylindrical gels ( $\varnothing = 6 \text{ mm} \times h = 2 \text{ mm}$ ) were prepared in custom-made Teflon molds and cross-linked by exposure to visible light irradiation (wavelength 400–450 nm) for 45 s. All cross-linked cylinders were weighted for their initial weight ( $m_{\text{in } t=0}$ ) and three lyophilized samples to obtain dry weights ( $m_{\text{dry } t=0}$ ). The remaining samples were incubated in PBS at 37 °C, freeze-dried, and weighted again ( $m_{\text{dry}}$ ). The sol-fraction was then determined as follows: sol fraction =  $((m_{\text{in } t=0} - m_{\text{dry}})/m_{\text{in } t=0})$ .

*FTIR spectroscopy:* Infrared (IR) spectra were obtained on a FTIR spectrometer (PerkinElmer Spectrum Two, with a universal ATR sampling accessory and equipped with a diamond

2 crystal, PerkinElmer Instruments, The Netherlands). The IR spectra were measured at room temperature in reflection mode, with the wavelength region from 4000 to 450  $\text{cm}^{-1}$ . GelNOR and silk-based CEW bioinks before and after incubation in PBS for 0, 24, and 72 h were analyzed. All samples were freeze-dried for 24 h before analysis. The FTIR spectra were processed for peak deconvolution, integration, and analysis with the OriginPro 8 software package (Origin Lab, USA). Upon identification of the key characteristic peaks of the macromolecules present in the hydrogel formulations, the area under the peaks was calculated. The presence of residual PEO within the hydrogels was estimated by calculating the ratio of the area under the peaks representing the asymmetric C–O–C stretch at 1090  $\text{cm}^{-1}$  (characteristic of the ether bonds in PEO) and the amide I band (characteristic of protein compounds like gelatin and silk).

*Cell electrowriting:* Hydrogel fabrication was performed with an in-house-built device (**Supplementary Figure S6**). Briefly, the hydrogel was loaded in a temperature-controlled printhead (temperature range 0–120° C) connected to a high-precision air pressure (0.01–2 bar, VPPE-3-1-1/8-2-010-E1 557771, Festo). The hydrogel was electrified with a high-voltage power supply (Heinzinger LNC 30000-2pos, 0–30 kV), and the electrified hydrogel fiber was collected in a computer-controlled high-precision XYZ stage (LG-motion, UK). The CEW device was protected by an acrylic box to ensure stable environmental conditions. All the fabrication experiments were performed at room temperature using glass syringes (3 mL, 25 G needle nozzle). Hydrogel jet formation as well as fiber diameter and morphology were investigated at an increasing voltage of [2–5] kV, for a constant velocity of 25 mm/s and pressure of 0.05 bar; at an increasing collection velocity of [5, 50] mm/s, for constant voltages of 2.5 kV (gelNOR) and 3 kV (silk) and pressure of 0.05 bar; and at an increasing pressure of [0.05–0.3] bar, for a constant collection velocity of 25 mm/s and voltages of 2.5 kV (gelNOR) and 3.0 kV (silk). Print fidelity and layer stacking experiments were performed at a constant collector velocity of [25–30] mm/s, voltages of 2.5 (gelNOR) and 3.0 (silk), and air pressure of 0.05 bar. All experiments were conducted at a constant collector distance of 5 mm, and the constructs were irradiated with visible light (400–450 nm) during jet collection and after printing for approximately 5 min. Square- and hexagon-shaped pore fabrication experiments were performed with the same CEW parameters. Jet and scaffold fabrications were monitored by digital USB microscopes.

*Extrusion-based bioprinting:* Extrusion printing of gelNOR and silk hydrogels was achieved by pneumatic dispensing with a CELLINK INKREDIBLE bioprinter (CELLINK, Sweden). Extrusion was performed at room temperature, with a 25 G needle tip, collector velocity of 10 mm/s, and an applied pressure of 0.9 bar. After printing, the constructs were irradiated with visible light (400–450 nm) for 5 min.

*Swelling and mechanical evaluation:* Swelling was evaluated by first immersing CEW fibers in PBS over 14 days, followed by imaging the fibers before and after 1 h, 1, 2, 3, 7, and 14 days

of immersion by fluorescence microscopy. The fiber diameter changes were measured at each time point. For simplicity, the fibers were assumed to expand in an isotropic manner. The mechanical behavior of the gelNOR and silk-based scaffolds obtained by CEW and extrusion-based printing was assessed by a displacement-controlled Piuma nanoindenter (Optics 11, The Netherlands). A probe with a spherical indenter tip with a radius of 28  $\mu\text{m}$  and a stiffness of 0.51 N/m was used. Probe displacement was set to 10% of the specimen thickness. The effective elastic modulus (stiffness) was derived by fitting the load–displacement curves to the Hertzian contact model, between 0 and 30% of the maximum load point. At least five scaffolds of each composition and fabrication process were tested.

*Fiber and scaffold imaging:* An Olympus BX51 fluorescent microscope (Olympus, The Netherlands) was used with a TRITC filter to obtain high-magnification images of the printed hydrogel fibers. Fluorescence microscopy for fiber quality analysis was performed through imaging the natural fluorescence exhibited by gelatin and silk polymers. Stereomicroscopy images of the fabricated 3D constructs were acquired with an Olympus stereomicroscope (Olympus Soft Imaging Solutions GmbH, The Netherlands). Accuracy of the hydrogel 3D constructs was also analyzed with SEM (Phenom Pro, Phenom-World, The Netherlands) at an acceleration voltage of 5–10 kV. Prior SEM imaging samples were gold-plated (2 nm) using a Q150R rotary-pumped sputter (Quorum Technologies, UK). Print fidelity was quantified using a relative value,  $A_{\text{cc pore}}$ , expressed by the following index:  $A_{\text{cc pore}} = A_{\text{fab}} / A_{\text{des}}$ , where  $A_{\text{fab}}$  is the fabricated pore area and  $A_{\text{des}}$  is the designed pore area. The pore areas were quantified using Image J.

*Cell isolation and culture:* Equine tissue samples and cells were obtained from deceased horse donors, donated to science by their owners, according to the guidelines of the Institutional Animal Ethical Committee. Equine-derived bone marrow-derived mesenchymal stromal cells (MSCs) were isolated as previously described.<sup>[213]</sup> After isolation, the cells were cultured in MSC expansion medium consisting of DMEM + GlutaMAX (Gibco, 31966, The Netherlands), supplemented with fetal bovine serum (FBS, 10% v/v, Gibco, 10270, The Netherlands), penicillin/streptomycin (1%, Gibco, The Netherlands), l-ascorbic acid-2-phosphate ( $0.2 \times 10^{-3}\text{M}$ , Sigma-Aldrich, The Netherlands), and basic fibroblast growth factor (1 ng mL<sup>-1</sup>, PeproTech, United Kingdom); the medium was refreshed twice per week. The cells were expanded until passage 4 and used at a density of  $10^8$  cells mL<sup>-1</sup> for both CEW and extrusion-based bioprinting.

*Cell viability:* Cell viability in printed fibers was quantified through a LIVE/DEAD assay (Calcein AM, ethidium homodimer-1, Life Technologies, The Netherlands) using a confocal microscope (Leica SPX8, Leica Systems, The Netherlands) for imaging after 1, 3, and 7 days in culture ( $n = 5$ ). Cast cell-laden hydrogels used as control groups were prepared using Teflon molds ( $\varnothing = 6 \text{ mm} \times h = 2 \text{ mm}$ ).

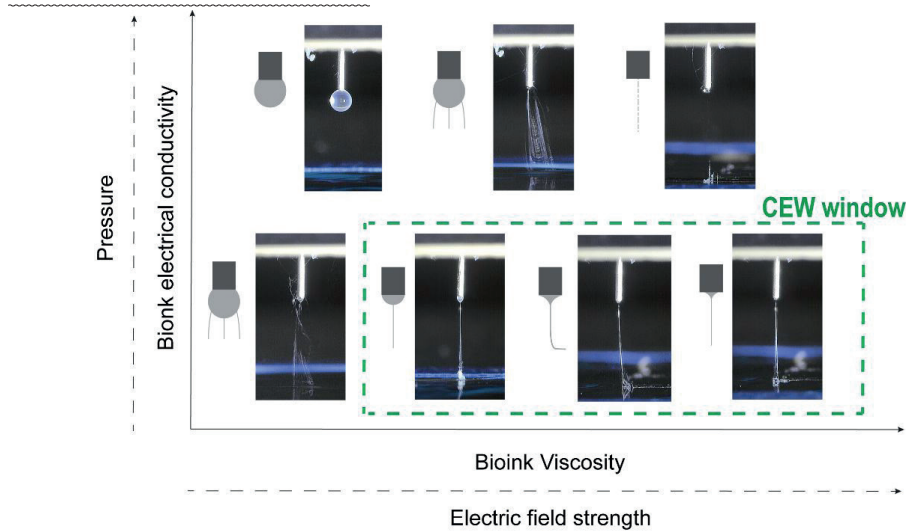
*Immunofluorescent stainings:* At days 1 and 7 after CEW and extrusion bioprinting, the

cell-laden constructs were fixed using 4% neutral buffered formalin. Following Triton-X membrane permeabilization, the samples were stained with phalloidin and DAPI. Images were captured using a Leica SP8X confocal microscope, and cell shapes were quantified using ImageJ.

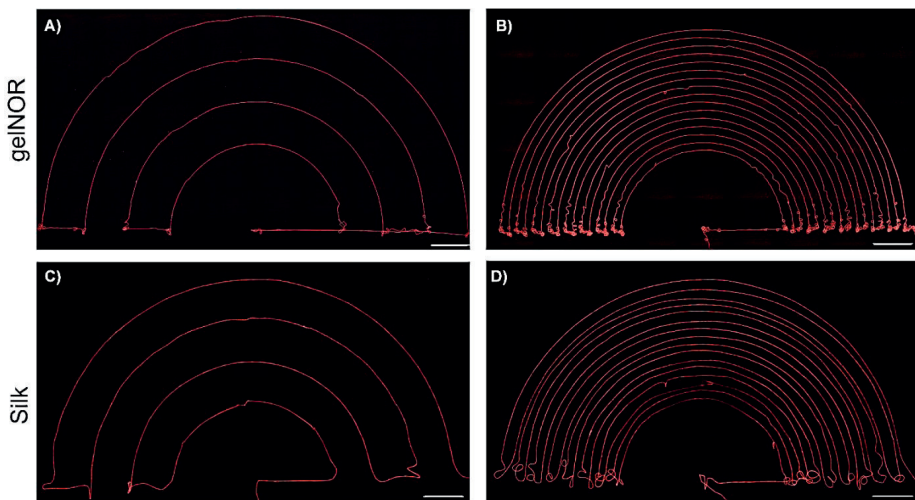
**2** *Statistical analysis:* All results are presented as mean  $\pm$  standard error of the mean. Statistical analyses were performed using GraphPad Prism 7.0 (GraphPad Software, USA). Differences between groups were assessed by a one-way ANOVA with a post hoc Bonferroni test. The differences were found to be significant when  $p < 0.05$ . For the FTIR analysis, the ratio between the areas under the asymmetric C–O–C and amide I peaks for each sample was compared to PEO-free hydrogel controls, performing a one-way ANOVA with Bonferroni post hoc correction. Values of  $p < 0.05$  indicated statistical significance.

## SUPPORTING INFORMATION

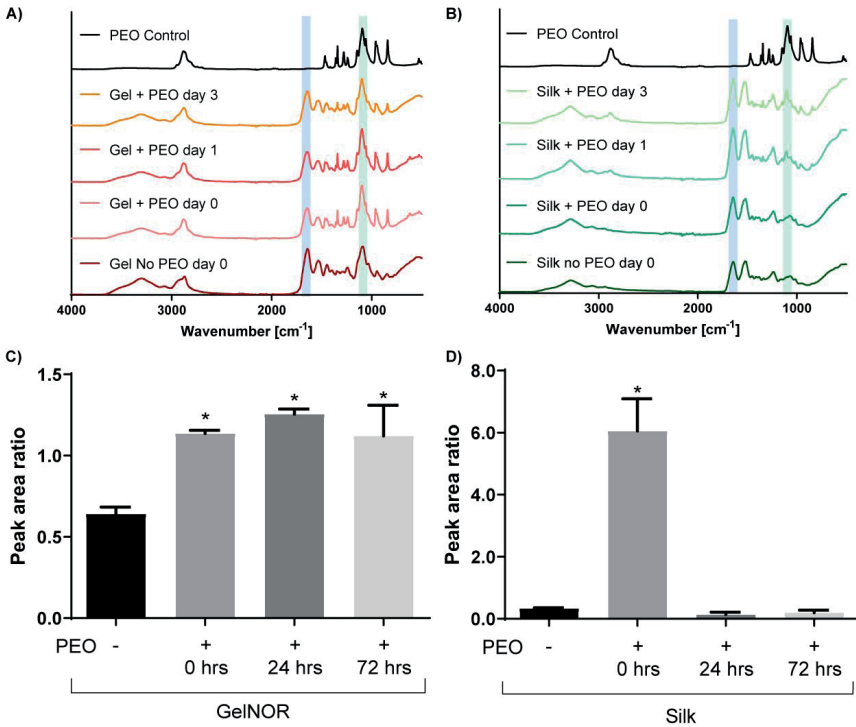
### Supplementary Figures



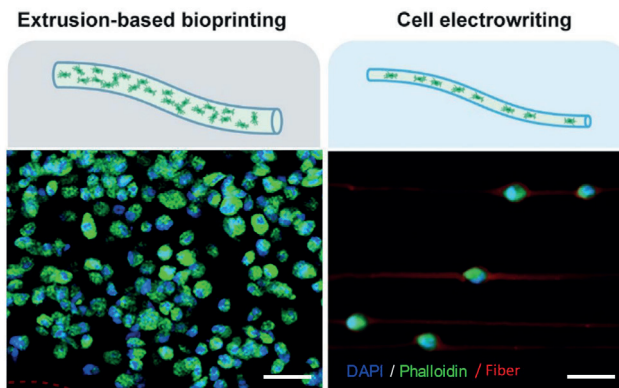
**Supplementary Figure S1:** Cell electrowriting (CEW) fabrication window. Effect of key hydrogel materials properties and CEW processing parameters on the electrified jet formation. Quantitative investigation of bioink electrical conductivity and viscosity, as well as dispensing pressure, high voltage and collector velocity on CEW jet formation and fiber morphology and diameter can be found in **Figures 2, 3**.



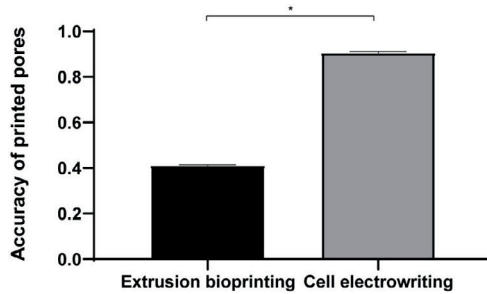
**Supplementary Figure S2:** Representative microscopy images of curved CEW fibers of gelINOR (top) and silk (bottom). Curved fibers could be produced with an interfiber spacing of A-C) 1000  $\mu\text{m}$  and B-D) 200  $\mu\text{m}$ . Scale bar = 1000  $\mu\text{m}$ .



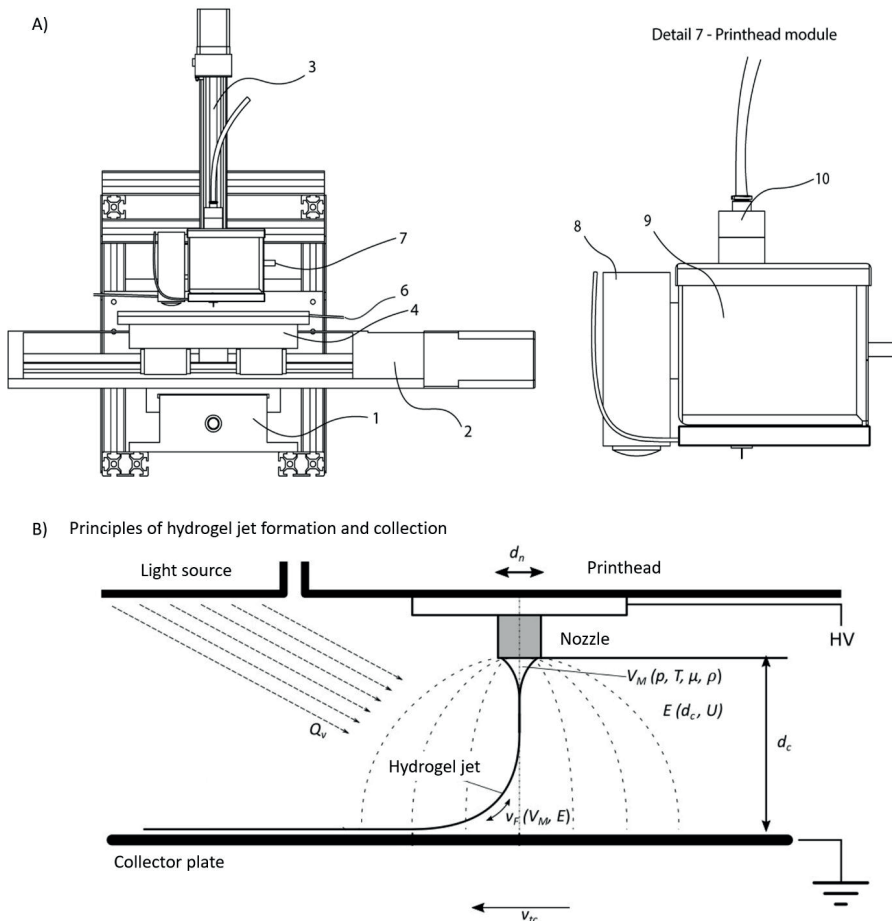
**Supplementary Figure S3:** FTIR analysis of hydrogels formed from the A) gelNOR and B) Silk-based CEW bioinks before and after incubation in PBS for 0, 24 and 72 hours. The amide I band and the major ether bond stretching band are highlighted in blue and green, respectively. The ratio between the area under the asymmetric C-O-C stretching peak and the amide I band shows C) presence of PEO within the gelNOR mixture, and D) release of PEO after 1-day of incubation in PBS for the silk-based bioinks.



**Supplementary Figure S4:** Representative fluorescence images of cells on gelNOR based cell-laden scaffolds obtained by conventional extrusion bioprinting (left) and CEW (right).



**Supplementary Figure S5:** Comparison of printing accuracy of gelNOR scaffolds produced by extrusion bioprinting and cell electrowriting. Accuracy was determined using a relative value,  $Acc_{\text{pore}}$ , obtained by the ratio between the design and fabricated pore area. In the case of no deviation between printed and designed pore areas,  $Acc_{\text{pore}} = 1$ .



**Supplementary Figure S6:** A) Schematic illustration of the custom-made CEW setup. The system comprises a XYZ computer-controlled stage (1-4), a grounded aluminium collector plate (4-6), a printhead module for photocrosslinkable inks (7) composed of a localized lighting source (8), a temperature-controlled chamber

(9) and a high precision air-pressure (10). B) Physics of CEW process. Governing mechanisms of hydrogel jet formation and collection during CEW are divided in two main steps, A) jet formation and B) jet collection and solidification. Jet formation starts by extruding a volume of a viscous hydrogel ( $V_M$ ) that is then stretched by an applied electrical field (E) created between the dispensing nozzle ( $d_n$ ) and collecting plate.  $V_M$  is dependent on extrusion pressure (p), hydrogel temperature (T), viscosity ( $\mu$ ) and electrical conductivity ( $\rho$ ); while electrical field is a function of the collecting distance ( $d_c$ ) and acceleration voltage (U). After jet formation, the hydrogel material solidifies by exposure to visible light (Qv) and straight hydrogel fibers are collected when the speed of the jet ( $v_j$ ) equals the speed of the collector plate ( $v_c$ ).

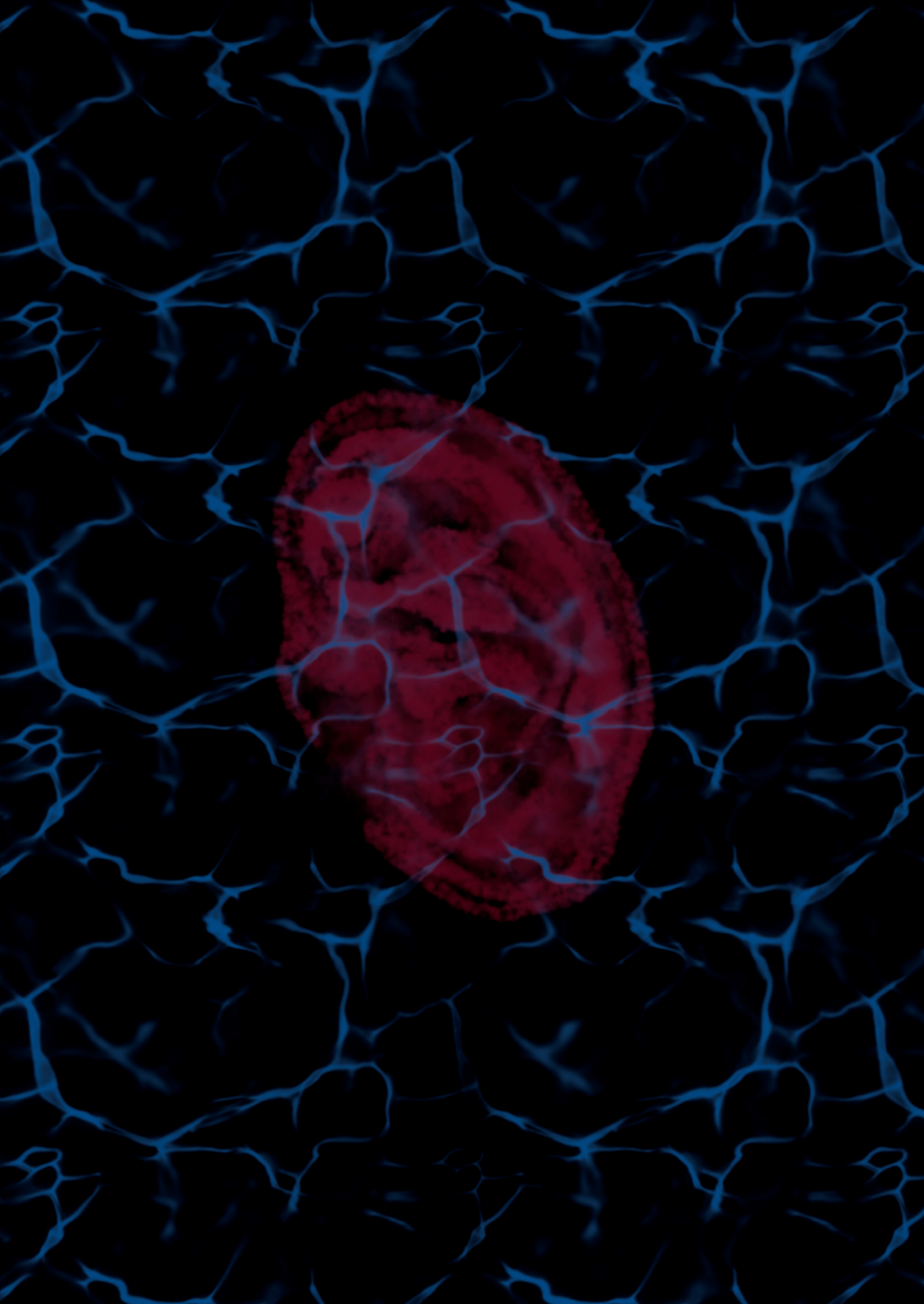
## Supplementary Tables

**Supplementary Table S1:** Summary of electrohydrodynamic techniques using polymer and hydrogel solutions

Electrohydrodynamic technique characteristics			Material System	Cell characteristics			Mechanical properties
System	Fiber size ( $\mu\text{m}$ )	Shape control	Composition	Cell encapsulation	Cell type	Viability (%)	Young modulus (MPa)
SE	35 - 45	No	Polyvinyl alcohol	Yes	hMSCs	1.3 - fold cell increase over 28d (proliferation only)	NE
SE	10 - 30	No	poly(dimethylsiloxane)	Yes	Astrocytes	67.7	NE
SE	0.3 - 0.5	No	Alginate w/ Polyethylene Oxide	Yes	HUVECs	90	0.004
SE	10	No	Alginate w/ Polyethylene Oxide	Yes	MSCs	60 - 80	0.07
SE	NE	No	Matrigel	Yes	Cardiomyocytes	80	NE
SE	NE	No	Matrigel	Yes	Mouse Neuroblastoma	80	NE
SE	0.8 - 5	No	Silkworm	NE	NE	NE	750
SE	1.2 - 2.4	No	Silkworm w/ Polyethylene Oxide	No	iPSC - MSCs	NE	24 - 1864
SE	70 - 100	Limited	Alginate w/ Polyethylene Oxide	Yes	Myoblasts	90	5
JW	120	Yes	poly(ethylene glycol) and poly(acrylic acid)	NE	NE	NE	NE
JW	6 - 50	Yes	poly(lactic-co-glycolic acid)	No	hMSCs	NE	NE
LEP	1 - 3	Limited	Polyethylene Oxide	Yes	Bacteria	NE	NE
LEP	2 - 4	Limited	Gelatin	NE	NE	NE	NE
LEP	1 - 10	Yes	Gelatin	No	Glioma cells	NE	20
NES	82.4	Yes	Alginate	Yes	HUVECs	95	NE
MEW	45	Yes	poly(2-ethyl-2-oxazine)	No	Fibroblasts	86	0.14 - 0.20
MEW	73.9	Yes	Ureido-pyrimidinonepoly(ethylene glycol)	No	No	No	No
CEW	3 - 6	Yes	Gelatin	Yes	MSCs	75	0.002
CEW	40 - 45	Yes	Silk fibroin	Yes	MSCs	70	0.16







# Chapter 3

## Volumetric Bioprinting of Complex Living-Tissue Constructs within Seconds

Paulina Núñez Bernal<sup>1\*</sup>, Paul Delrot<sup>2\*</sup>, Damien Loterie<sup>2\*</sup>, Yang Li<sup>1</sup>, Jos Malda<sup>1,3</sup>, Christophe Moser<sup>2</sup>, Riccardo Levato<sup>3,1</sup>

Published in: *Advanced Materials*. 2019. 31(42)

<sup>1</sup>Department of Orthopedics, University Medical Center Utrecht, Utrecht University, Utrecht, The Netherlands

<sup>2</sup>Laboratory of Applied Photonics Devices, École Polytechnique Fédérale Lausanne (EPFL), Lausanne, Switzerland

<sup>3</sup>Department of Clinical Sciences, Faculty of Veterinary Medicine, Utrecht University, Utrecht, The Netherlands

\* Authors contributed equally to this work

## ABSTRACT

Biofabrication technologies, including stereolithography and extrusion-based printing, are revolutionizing the creation of complex engineered tissues. The current paradigm in bioprinting relies on the additive layer-by-layer deposition and assembly of repetitive building blocks, typically cell-laden hydrogel fibers or voxels, single cells or cellular aggregates. The scalability of these additive manufacturing technologies is limited by their printing velocity, as lengthy biofabrication processes impair cell functionality. Overcoming such limitation, this study describes the volumetric bioprinting of clinically-relevant sized, anatomically-shaped constructs, in a time frame ranging from seconds to tens of seconds. An optical tomography-inspired printing approach, based on visible light projection, was developed to generate cell-laden tissue constructs with high viability (>85%) from gelatin-based photoresponsive hydrogels. Free-form architectures, difficult to reproduce with conventional printing, were obtained, including anatomically correct trabecular bone models with embedded angiogenic sprouts, and meniscal grafts. The latter underwent maturation *in vitro* as the bioprinted chondroprogenitor cells synthesized neo-fibrocartilage matrix. Moreover, free-floating structures were generated, as demonstrated by printing functional hydrogel-based ball-and-cage fluidic valves. Volumetric bioprinting permits to create geometrically complex, centimeter-scale constructs at an unprecedented printing velocity, opening new avenues for upscaling the production of hydrogel-based constructs and for their application in tissue engineering, regenerative medicine and soft robotics.

**Keywords:** biofabrication, tomographic laser prototyping, cell encapsulation, photopolymers, bioinks and bioresins

## INTRODUCTION

Living tissues owe their functionality predominantly to their complex architecture. The topographical and geometrical cues provided by the extracellular milieu, together with the precise and anisotropic spatial distribution of morphogens and biochemical signals, are well recognized as major determinants of cell fate both *in vitro* and *in vivo*.<sup>[162,214–216]</sup> Capturing such a shape-function relationship within engineered biomaterials holds great potential for the creation of new cell-instructive implants that can unlock the regenerative potential of embedded or recruited cells upon grafting *in situ*. Irregular and anisotropic architectures are fundamental, *i.e.*, in the load-bearing function of cancellous bone as the trabecular framework aligns along the main direction of stress,<sup>[217]</sup> in the shock-absorber function of menisci, where geometry and zonal architecture distribute applied loads,<sup>[218]</sup> or in the contractile function of cardiac and skeletal muscle, as cell alignment provides directionality for force generation.<sup>[219]</sup>

Biofabrication technologies are emerging as powerful tools to drive tissue regeneration. This is owed to their ability to accurately control the spatial orchestration of multiple cell types and biomaterials in an automated patterning process.<sup>[112,220]</sup> Although this discipline is still in its early stages of development, the presentation of optimized geometrical features and biomimetic architectures within biofabricated constructs, has shown remarkable achievements in the restoration of salient tissue functions even *in vivo*, for instance within biofabricated ovaries,<sup>[221]</sup> and thyroid glands.<sup>[143]</sup>

Despite such promising advances, new developments are necessary to enable the creation of large, clinically-relevant biofabricated grafts, with potential application for regenerative medicine in humans, produced with a high speed scalable process. Current (bio)printing and additive manufacturing methods include extrusion-based techniques, lithographic printing, *i.e.*, stereolithography (SLA) and digital light projection printing employing digital micromirror devices (DLP/DMD), laser-based methods and melt electrowriting. These all build three dimensional (3D) objects in a layer-by-layer fashion, typically patterning voxels or extruded fibers as essential building units.<sup>[112]</sup> This feature greatly limits the type of structures that can be generated, which often require supports to produce the complex hollow features and overhangs, typical of biological structures (*i.e.*, due to intrinsic porosity and the presence of vasculature). Importantly, these printing processes take considerable time, especially when large, centimeter-scale grafts need to be generated.<sup>[112]</sup> Such extended fabrication times impose the requirement to keep the cells in a printer cartridge or within a printed construct outside an optimal culture environment for long periods. This can cause significant stress to cells and substantially impair their functionality.<sup>[202,222]</sup> This issue becomes even more significant when larger constructs are generated with high-resolution printing methods, such as those involving co-printing of microfibers and cells<sup>[202]</sup> or two-photon polymerization.<sup>[223]</sup> Thus, overcoming these limitations of layer-by-

layer additive manufacturing in the field of tissue biofabrication is of great interest to open new avenues towards the successful generation of larger, clinically-relevant engineered constructs.

Volumetric printing technologies introduce a paradigm shift, as they enable the creation of entire objects at once, rather than through the sequential addition of basic building blocks. In this study, the concept of Volumetric BioPrinting (VBP) is introduced, enabling the fabrication of entire cell-laden constructs with arbitrary size and architecture within a time frame of seconds to tens of seconds. As recently implemented, volumetric additive manufacturing relies on the projection of a series of 2D patterned optical light fields within a volume of a photopolymer.<sup>[224,225]</sup> The 2D light patterns act cumulatively to produce an optical 3D dose distribution that triggers polymerization of the irradiated material into the desired object. In the first conceptualization of volumetric additive manufacturing, simple objects were fabricated by irradiating a photopolymer reservoir with a superposition of multiple beams coming from fixed, pre-determined orientations.<sup>[226]</sup> New volumetric printing processes, inspired by computed tomography (CT), enable the production of more complex objects by using 2D dynamic light fields.<sup>[224,225]</sup> Technical photopolymers, such as acrylates<sup>[225]</sup> and elastomeric resins<sup>[224]</sup> have been printed, showing the ability to resolve features down to 80  $\mu\text{m}$ .<sup>[224]</sup> However, the potential for regenerative medicine remains unexplored, and significant steps are required to further develop volumetric manufacturing into a cell printing technology.

## RESULTS AND DISCUSSION

In this work, we demonstrated the bioprinting of large living tissue constructs by processing cell-friendly hydrogel-based bio-resins with a volumetric, visible light laser-based printer. In our set-up, a three-dimensional light dose distribution is deposited into a cylindrical container of photopolymer gel to permit its spatially selective crosslink (**Figure 1A–B**). To build up this three-dimensional dose distribution, the resin container is set into rotation and synchronously irradiated with a sequence of two-dimensional light patterns, computed by a Radon transform,<sup>[227]</sup> applying the principles of medical tomographic imaging in reverse. In other words, the light patterns represent projections of the object to fabricate along multiple rotational angles of the cylindrical volume of photopolymer. These dynamic light patterns are displayed into the build volume by irradiating a DLP modulator with a 405 nm laser source. Although each light pattern exposes the whole build volume, the light dose resulting from a single exposure is insufficient to crosslink the resin.<sup>[224]</sup> The polymer solidifies only in selective areas where the accumulation of multiple angular exposures results in an absorbed dose overcoming the gelation threshold (as exemplified in **Supplementary Figure S1**). As a consequence, and differently to

the layerwise process of stereolithography, overcuring will always lead to off-target polymerization. Thus, identifying the minimum exposure time to gelate the 3D object within the optical field is paramount to optimize shape fidelity.

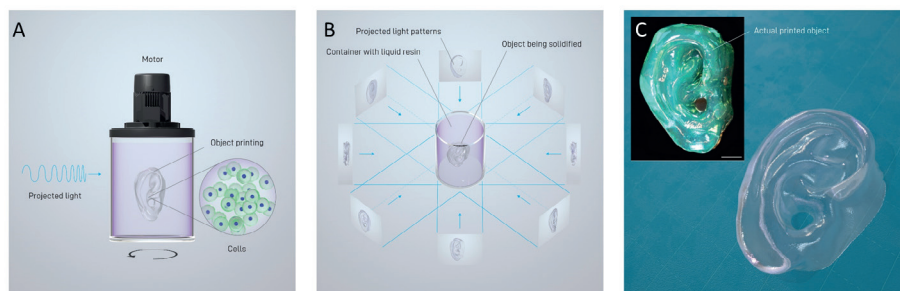


**Figure 1:** Overview of the volumetric bioprinting process, showing (A) the cell-laden gelRESIN reservoir connected to a rotating platform, (B) a schematic of tomographic projections, used to print the human auricle model, and (C) a rendering of the resulting printed hydrogel structure. The inset in (C) shows a stereomicrograph of the actual printed hydrogel, stained with Alcian Blue to facilitate visualization (printing time = 22.7 s; scale bar = 2 mm).

Several photo-responsive hydrogels have shown remarkable compatibility for cell encapsulation. Among them, gelatin methacryloyl (gelMA) has rapidly become a widely used and versatile bioink, for both extrusion-based and light-based fabrication.<sup>[228–231]</sup> Therefore, as a cell-friendly bioresin for volumetric printing, we designed a formulation based on gelMA dissolved in phosphate buffered saline (PBS), with lithium phenyl-2,4,6-trimethylbenzoyl-phosphinate (LAP) as photoinitiator for the free-radical polymerization of the methacryloyl moieties (gelRESIN). With this approach, complex, free-form structures could be generated within seconds from a volume of cell laden-hydrogels (**Figure 1C**). The chosen photoinitiator, LAP, exhibits a superior quantum efficiency and molar extinction coefficient at visible wavelength ( $\epsilon = 50\text{M}^{-1}\text{cm}^{-1}$  at 405 nm), compared with other initiators used so far for the volumetric printing of non-cell compatible resins.<sup>[224]</sup> Importantly, in volumetric printing, the whole build volume must be addressed by each light pattern for the object reconstruction to be accurate. This feature sets an upper limit on the photoinitiator concentration. In other words, when designing a resin composition for volumetric printing, the initiator concentration must be low enough for the light to penetrate through the whole volume, but high enough to allow the gel to polymerize. To achieve that, a light intensity value corresponding to at least 37% of the incoming light intensity to reach the opposite edge of the build volume was found to be sufficient (**Figure 2A**). Using the Beer-Lambert law, this is equivalent to  $\ln(10)\epsilon Dc = 1$ , where  $\epsilon$  is the photoinitiator molar extinction coefficient ( $\text{M}^{-1}\text{m}^{-1}$ ),  $D$  ( $m$ ) is the diameter of the cylindrical build volume diameter, and  $c$  the photoinitiator concentration ( $\text{mol m}^{-3}$ ).

Interestingly, the LAP concentration required to produce well-defined printed structures was only 0.037% w/v, a value considerably lower than what has commonly been used in previously reported additive bioprinting studies.<sup>[232–235]</sup> This reduces the potential toxicity risks that are correlated with high concentrations of this photoinitiator.<sup>[155,236]</sup>

First of all, VBP showed a promising volume accuracy, with printed human auricle models showing a volume variation of  $5.71 \pm 2.31\%$ , when comparing the printed constructs acquired via  $\mu$ CT and the original STL files. Remarkably, and in contrast to other additive bioprinting approaches, printing time is not bound to the dimensions of the construct. To quantify and compare the printing time, we printed an anatomical human auricle model that was first miniaturized (volume  $\approx 0.15 \text{ cm}^3$ ), then scaled two and three times (volume  $\approx 1.23$  and  $4.14 \text{ cm}^3$ , respectively). All VBP-printed models were fabricated within the same printing time (22.7 seconds). In extrusion-based bioprinting, the printing time increases cubically with the scaling factor, quickly reaching an unfavorable magnitude ( $>1\text{-}2$  hours) when cell-laden centimeter-scale objects are required without greatly compromising on resolution. Instead, in DLP processes (but not in conventional SLA) the printing time increases linearly as a function of the height of the construct, independently on the area to be printed in each individual layer (**Figure 2B**).<sup>[173]</sup> DLP processes can be accelerated by reducing the lifting time of each printed layer, as shown by the recent development of the Continuous Liquid Interface Printing (CLIP) method.<sup>[237]</sup> However, as calculated using our biocompatible gelRESIN, even when reducing the lifting time to zero, the overall fabrication time (10 seconds/layer with gelRESIN) would be one order of magnitude higher than that achieved with volumetric bioprinting (data not shown). Conversely, in volumetric bioprinting, the printing time can be consistently found in the range of tens of seconds, regardless of the volume of the construct, as long as the same irradiation intensity is supplied to the photopolymer. For example, to keep a constant printing time for a build volume scaled twice in each dimension, a laser output four times as powerful as that used for the unscaled volume is necessary. Furthermore, volumetric bioprinting results in seemingly artefact-free surface features, as illustrated by the smooth profile of the generated structures, including the printed auricle (**Figure 2Ci**, further discussion provided in the supplementary information). These volumetric printed parts reflect the nature of the digital model and reproduce its surface features more faithfully, especially when compared with additive technologies. In fact, extrusion-based and DLP bioprinting exhibit a typical filament- and voxel-riddled pattern respectively that introduce an artefactual surface roughness profile in the construct (**Figure 2Cii-iii**). The resolution of volumetric printing is limited by optical and chemical phenomena. The optical resolution of volumetric printing is determined by the effective pixel size of the projected images at the center of the build volume, along with the depth of focus which determines to what degree the optical resolution is maintained at the edge of the build volume. The effective pixel size is  $22.8 \mu\text{m}$  in our experiments, and with the current optics the resolution at the



edge of the volume is  $33\ \mu\text{m}$ . A number of effects, such as the diffusion of chemical species, can decrease the resolution of volumetric printing methods,<sup>[225]</sup> and steps to maximize resolution have been recently described.<sup>[224]</sup>

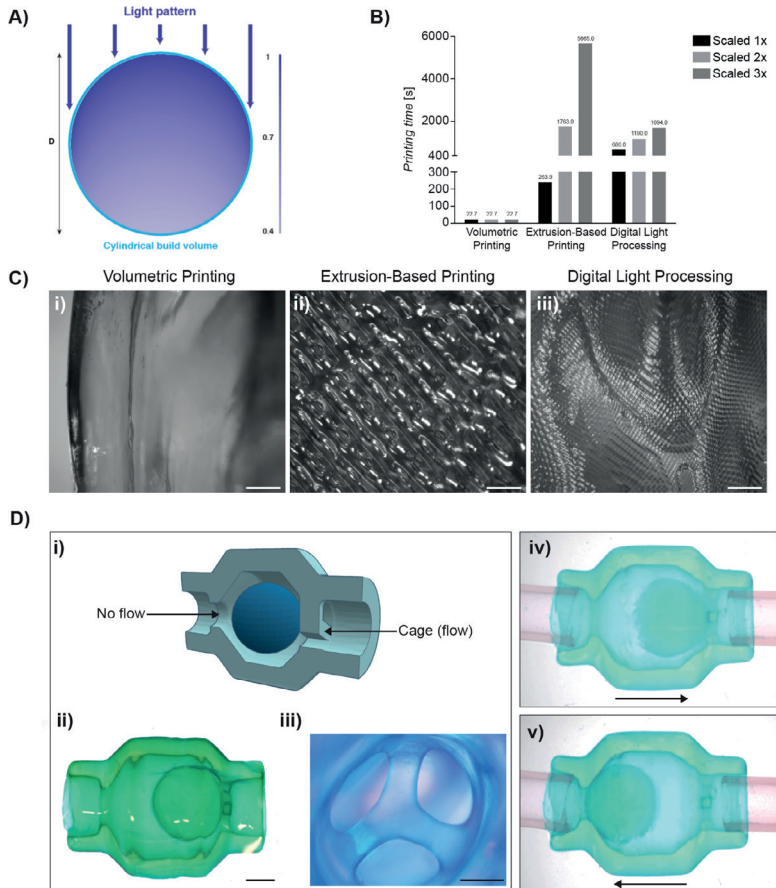


**Figure 2:** Main volumetric printing process parameters and printed construct features. A) Graphical representation of the light penetration pattern through the entire build volume in the presence of a photoinitiator. B) Fabrication time for the human auricle model scaled 1x ( $0.15\ \text{cm}^3$ ), 2x ( $1.23\ \text{cm}^3$ ) and 3x ( $4.14\ \text{cm}^3$ ) using different bioprinting techniques: volumetric printing, extrusion-based (bio)printing and digital light processing. C) Close-up images of the surface features of the auricle fabricated through i) volumetric printing, ii) extrusion-based printing and iii) digital light processing (scale bars =  $500\ \mu\text{m}$ ). D) Volumetric printing of a fluidic ball-cage valve with free-floating elements from a i) computer-generated 3D model of the valve. ii) Top-view of the printed valve (scale bar =  $2\text{mm}$ ), iii) close-up of the cage segment that permits flow (scale bar =  $1\text{mm}$ ), and video stills showing unidirectional flow functionality with an iv) open and a v) closed valve (black arrow represents the flow direction).

Moreover, we demonstrated the possibility, unique to volumetric bioprinting, to print free-floating parts without the need for sacrificial support materials or two-photon polymerization approaches. This feature is paramount to generate systems able to reversibly

3

modify their shape post-printing, and similar free-moving parts could be included also in structures printed with stimuli-responsive materials (often used in 4D printing),<sup>[238]</sup> for instance to facilitate shape changes. Hydrogel-based actuators are prevalently obtained by exploiting the swelling capability of hydrogels in response to osmolarity, temperature and pH,<sup>[238,239]</sup> and by endowing the materials with *i.e.*, magnetic or electrical stimuli responsive properties, for instance by introducing nanoparticles within the hydrogel bulk.<sup>[219,240]</sup> On the other hand, the freedom of design provided by volumetric bioprinting approaches permits the production of such actuators through the direct fabrication of movable or articulating parts. To confirm this, we printed a fluidic valve inspired by the ball-cage cardiac valve prosthesis<sup>[241]</sup> (**Figure 2Di-iii**). Such a model, unlike other valve designs such as the anatomically inspired bi- and tri-leaflets,<sup>[235]</sup> cannot be directly fabricated by extrusion or DLP/DMD technologies in the absence of sacrificial supports. When connected to a fluidic system, the valve could function correctly, enabling unidirectional flow within the circuit (**Figure 2Div-v**). This feature that can have potential applications in hydrogel-based microfluidics<sup>[235]</sup> or in hydrodynamic-actuated soft robots.<sup>[242]</sup> To achieve this type of complex constructs, the thermoreversible gelation of gelRESIN is particularly advantageous. In fact, printing in the gel state (at room temperature) is beneficial not only to prevent cell sedimentation during the fabrication step (**Supplementary Figure S2**), but also to provide positional stability to the construct, avoiding movement of printed parts due to potential changes in buoyancy post-crosslinking or due to the rotation of the photopolymer reservoir. Furthermore, experimental analysis of the cell sedimentation time prior to the thermal gelation, revealed that cells are homogeneously distributed throughout 2 cm-thick hydrogel volumes, even if the reversible gelation is triggered after 10 minutes after cell mixing. This result also suggests that, given the rapidity of the VBP process, homogenous cell suspension could be achieved even when processing alternative bioresins that lack the thermal gelation behavior of gelatin. Finally, after the material is selectively crosslinked, the unreacted hydrogel precursor is easily washed away in PBS or aqueous media at 37° C, and the printed object is post-cured, giving rise to a complete polymerization comparable to that of cast gelMA gels, as documented by the low sol fraction (**Supplementary Table S1**).

Notably, we demonstrated that living tissue constructs can be safely generated via volumetric bioprinting of gelRESIN without impacting cell survival. Structures with high cell viability (> 85% post-printing, **Figure 3Ai**) were created, with cells showing an increase in metabolic activity over time (**Figure 3Aii**). Chondroprogenitor cell viability was preserved at high levels across seven days of additional culture, with values comparable to those found for conventional hydrogel casting and other well-known bioprinting methods (no statistically significant differences, **Figure 3Aiii**). This result is also in line with several reports on safe and cytocompatible windows for radical-induced photopolymerization.<sup>[243–245]</sup> Additionally, as a nozzle-free method, volumetric bioprinting shows no risk of

shear stress-induced cell damage or phenotype alteration which could compromise the function of the biological construct post-printing, as previously reported for certain high-viscosity bioinks for extrusion-based and inkjet printing.<sup>[222,246,247]</sup>

Further building on these results, an anatomical trabecular bone model laden with bone marrow-derived mesenchymal stromal cells (MSCs) was bioprinted using a  $\mu$ CT scan of a bone explant as a blueprint (cylindrical construct, 8.5 x 9.3 mm, **Figure 3Bi-ii**). Generation of the trabecular architecture and the convoluted, interconnected porous network, goes beyond what can be created with conventional extrusion-based bioprinting. Using the volumetric printing approach, these structures were successfully reproduced with the smallest resolved feature measuring  $144.69 \pm 13.55 \mu\text{m}$  (**Supplementary Figure S3**). Likewise, we also showed the creation of fully perfusable hollow channels with an inner diameter of 200  $\mu\text{m}$  (**Supplementary Figure S4**). Overall, current resolution is comparable with the most accurate extrusion-based technologies, and has the potential to be further improved, as already demonstrated with conventional resins.<sup>[224]</sup>

In biofabrication, the printing of an accurate 3D architecture is only the first step of many. In order to enable post-printing tissue maturation (either *in vitro* or *in vivo*), cells need to retain high viability, differentiation capacity, and the ability to synthesize bioactive compounds and interact with other cells in their surroundings. After volumetric bioprinting, cells could be maintained in culture, and the expression of salient physiological functions was observed over time (**Figure 3C–D**). More specifically, MSCs within the printed trabecular bone model were successfully primed in osteogenic medium for 7 days, as mimic of the osteoblasts within native bone (O-MSCs) (Figure 3C). These generated structures also allowed for further top-down tissue engineering strategies. In this case, the complex porous network of the cell-laden trabecular model could also be seeded with additional cells post-printing. For this, we delivered endothelial colony forming cells (ECFCs) and MSCs into the pore network between the printed O-MSC-laden trabeculae to generate a heterocellular structure. A co-culture of osteogenically differentiating cells, vascular endothelial cells and supporting MSCs that act as pericytes (P-MSCs), was successfully generated. After 3 days of culture, the formation of early angiogenic sprouts, typical of blood capillary network precursors,<sup>[248]</sup> was observed. Additionally, the introduced P-MSCs co-aligned along these nascent ECFCs sprouts (**Figure 3Di-ii**), suggesting a pericyte-like supporting activity.<sup>[248]</sup> Importantly, the density of such networks of organized sprouts, relative to the available volume within the pores of the model, was higher than that of pre-capillary networks generated by control co-cultures of ECFCs and MSCs, when the bioprinted O-MSCs structure is not present (**Figure 3Diii, Supplementary Figure S5**). This phenomenon, together with the observation that these early capillaries began to invade the bone hydrogel matrix, suggests that the bioprinted O-MSCs have the ability to provide paracrine signals that promote the angiogenic process driven by ECFCs. These findings further support the notion that volumetric bioprinting allows for the realization of key cellular functions.

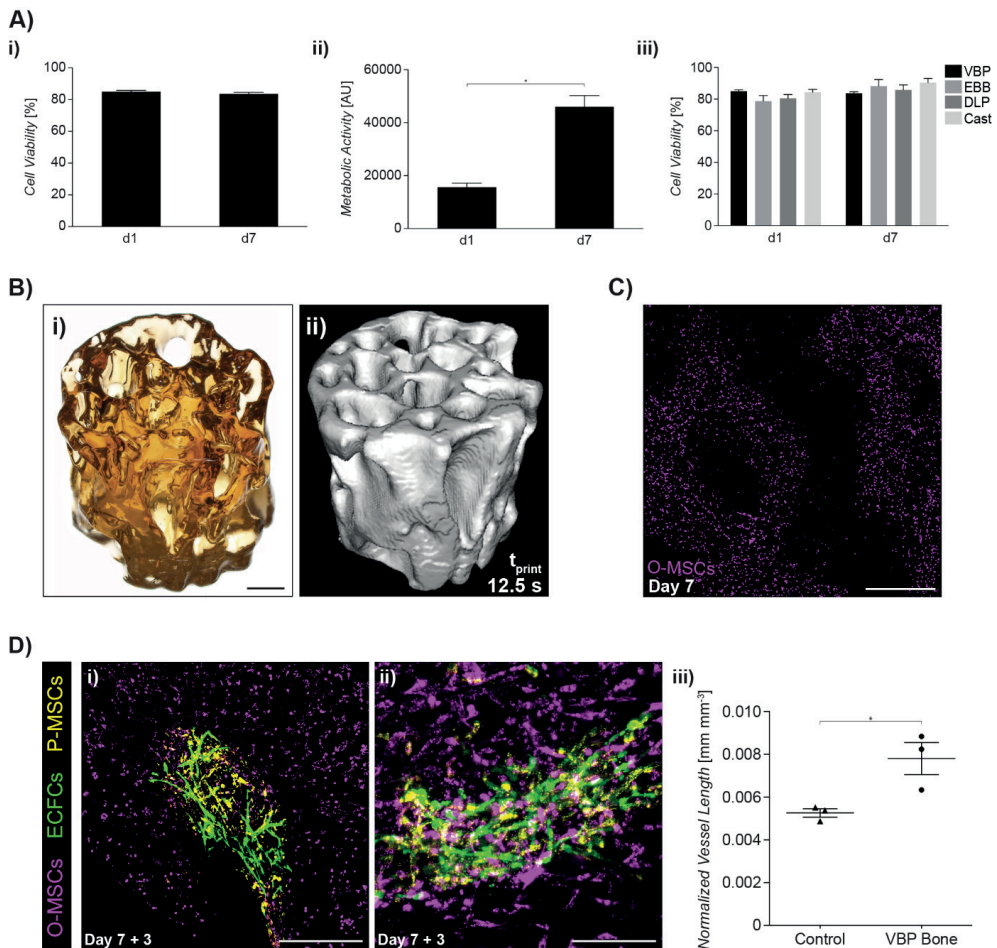


**Figure 3:** A) Volumetric bioprinted, ACPC-laden gelRESIN disc-shaped constructs were cultured for 7 days and exhibited i) high cell viability (> 85%), ii) increased metabolic activity over time and iii) comparable cell survival compared to hydrogel casting and other commonly used bioprinting techniques: extrusion-based bioprinting and digital light processing. B) A complex trabecular bone model was fabricated to examine the development of salient characteristics post-printing. i) The printed bone exhibited a porosity that extended throughout the extended 3D construct (scale bar = 2 mm), ii) as shown through  $\mu$ CT imaging. C) The O-MSC-laden (pink) bone construct was cultured for 7 days (scale bar = 1 mm). C) Constructs were then seeded with ECFCs (green) and P-MSCs (yellow) to induce capillary formation. i) ECFCs were shown to interconnect after 3 additional days of culture, filling the pores of the printed construct (scale bar = 500  $\mu\text{m}$ ), ii) and were also shown to begin invading the bone compartment of the construct (scale bar = 250  $\mu\text{m}$ ). iii) Vessel interconnectivity and length was also measured quantitatively and compared to a control 2D culture condition.

In order to facilitate the synthesis of new tissue matrix and its homogeneous distribution within a 3D hydrogel for regenerative medicine and tissue engineering applications, (bio)fabrication processes need to allow for the processing of high cell densities. While the described volumetric bioprinting approach can meet this requirement, inkjet-

and extrusion-based processes present a greater challenge, due to the risk of nozzle clogging and nutrient depletion within the cartridge during extended printing times.<sup>[249]</sup> Furthermore, the ability to process hydrogels in the gel state ensures prevention of sedimentation of embedded cells<sup>[250]</sup> and permits homogeneous cell distribution within the printed volume. To assess this potential and the ability of bioprinted cells to synthesize new-tissue matrix, a meniscus-shaped implant was printed from an anatomical scan (**Figure 4A**), encapsulating  $10^7$  articular chondroprogenitor cells (ACPCs)  $\text{mL}^{-1}$ . These multipotent cells showed increased metabolic activity over time (**Figure 4B**) and exhibited high cell viability throughout the bioprinted structure (**Supplementary Figure S6**). These meniscus-shaped constructs could be successfully maintained in culture for at least 28 days during which synthesis of neo-fibrocartilage matrix was observed (**Figure 4C**). Importantly, such neo-extracellular matrix (ECM) resulted in a functional increase of the mechanical properties of the meniscal graft, as measured by indentation. The compressive modulus increased from  $24.63 \pm 0.65$  kPa immediately after the volumetric printing process, until reaching values in the range of  $266.54 \pm 4.49$  kPa, comparable to native human fibrocartilage.<sup>[251]</sup> Newly synthesized glycosaminoglycans (GAGs) were distributed throughout the volume of the printed construct (**Figure 4D**). High amounts of collagen type I were also detected (**Figure 4E**), typical for the human menisci, as well as minor amounts of collagen type II (**Figure 4F**), analogue to the native tissue composition. To further promote the maturation of these constructs, which were cultured under static conditions, the use of dynamic loading systems or bioreactors could be of interest for future studies, for instance to induce physiological collagen fiber alignment.<sup>[252]</sup>

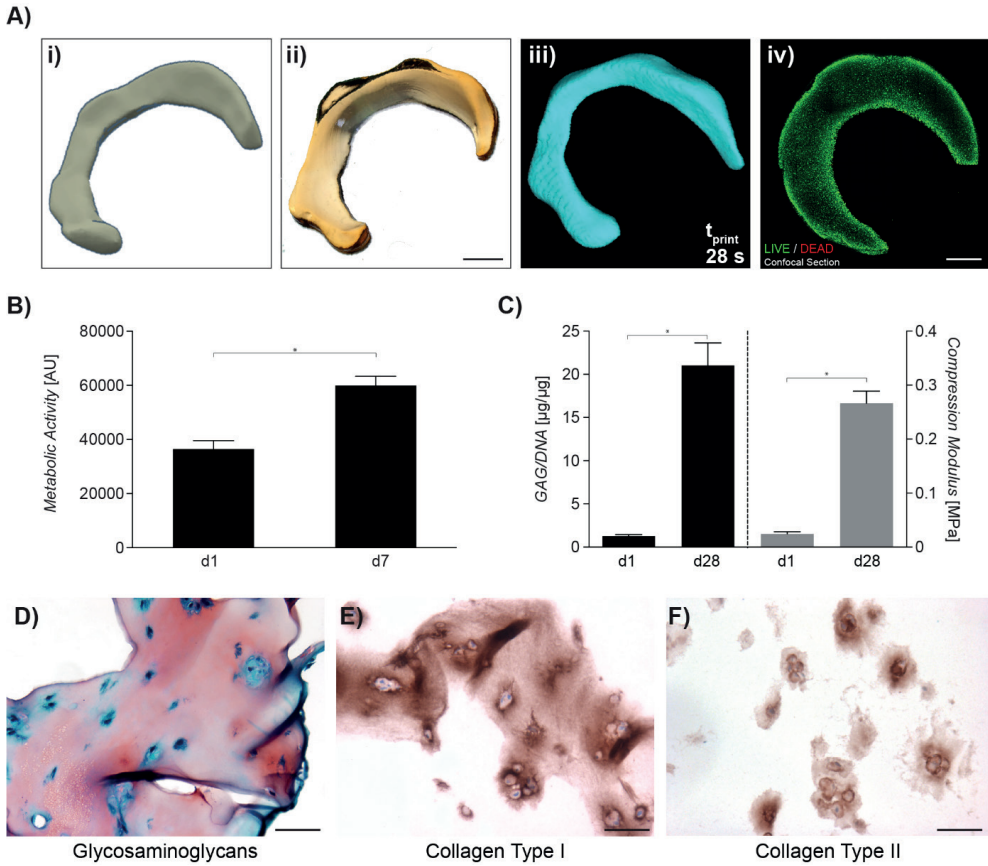


**Figure 4:** Long-term culture of meniscus-shaped, volumetric bioprinted constructs to assess matrix synthesis and neo-tissue formation. A) Meniscus constructs were printed from a i) computer-generated 3D model and ii) the resulting gelRESIN samples were cultured *in vitro* for 28 days (scale bars= 2 mm). iii) The 3D structure of the printed menisci was assessed through  $\mu\text{CT}$ , and iv) high cell viability throughout the construct was observed over a 7-day period. B) metabolic activity increased over a 7-day evaluation period. C) In terms of neo-tissue formation, the bioprinted constructs exhibited a significant increase in glycosaminoglycan production, as well as an increase of the meniscus compressive modulus over a 28-day culture period. Matrix components present in the native meniscus were shown to be present throughout the bioprinted constructs: D) glycosaminoglycans, E) extensive amounts of collagen type I and F) lower amounts of collagen type II (scale bars D–F= 50  $\mu\text{m}$ ).

## CONCLUSIONS

In summary, the results reported herein highlight the potential of volumetric printing as a novel, powerful and versatile biofabrication strategy. Its ability to rapidly create large, free-form cell-laden structures, can solve many of the key challenges in bioprinting and regenerative medicine. With dramatically reduced printing times compared to conventional bioprinting methods, obtaining high cell numbers to be loaded into the printer and

produce constructs with high cell density remain open challenges toward the fabrication of clinically-relevant grafts. This could potentially be tackled with the use of novel sources of adult stem cells,<sup>[253]</sup> as well as with further refinement of induced Pluripotent Stem Cell (iPSC) technology,<sup>[254,255]</sup> or of bioreactors for upscaling the production of regeneration-competent cells.<sup>[254,256]</sup> Additionally, with the adoption of volumetric bioprinting in the field of biofabrication, several future developments can be expected. Here, we selected gelMA as a resin, due to its well-established use in biofabrication approaches. However, there is virtually no limitation on the use of different photopolymers, and several photoresponsive natural or synthetic hydrogels could be optimized for this process (including but not limited to materials based on hyaluronan, PEG, alginate, or decellularized ECM) or even stimuli-responsive biomaterials for remote stimulation of the construct or controlled patterning of bioactive molecules.<sup>[156]</sup> Photochemistries alternative to methacryloyl addition polymerization could be employed as well, for instance thiol-ene step growth polymerization as used in DLP printing.<sup>[195]</sup> Next steps pertaining to the technology should introduce the potential for printing multiple materials within the same process, as this will be important to further mimic the heterogeneous composition of living tissues. For example, multi-material volumetric printing could be used to address the zonal architecture of certain tissues (*i.e.*, cartilage, menisci), create cell and material gradients, replicate biological interfaces, introduce vascularization in a single step, or even co-print mechanically strong polymers to reinforce the cell-laden bioprinted hydrogels. The rapid speed of volumetric bioprinting is an important benefit for the production of tissues and disease models. The generation of large constructs with arbitrary shape can aid patient-specific regenerative medicine, in light of potential translation of clinically relevant grafts. At the same time, drug discovery and testing typically requires testing of a large number of molecule combinations on identical models, which can easily be produced on a large scale with the proposed method, also reducing costs related to personnel and machine time necessary per constructs. It is hoped that this capability can complement and even reduce animal testing in the intermediate phases of drug development, leading to lower development costs and fewer ethical issues. Complemented by these perspectives for future developments, our results and the volumetric bioprinting technology proposed herein pave the way for the next generation of large and functional biofabricated grafts, with a wide array of envisioned applications for tissue regeneration, *in vitro* tissue and disease models, and soft robotics.

## EXPERIMENTAL SECTION

**Materials:** Gelatin methacryol (gelMA; 80% DoF) was synthesized as previously described, and used as a 10% w/v solution in PBS.<sup>[257]</sup> As photoinitiator, lithium phenyl(2,4,6-trimethylbenzoyl)phosphinate (LAP, Tokyo Chemical Industry, Japan) was dissolved in phosphate-buffered saline (PBS) at 0.037% (w/v) in the hydrogel to induce a photocrosslinking reaction. In cast gelMA controls, LAP was dissolved at 0.2% w/v. Post-photocrosslinking of printed samples was carried out in a solution containing tris(2,2-bipyridyl)dichlororuthenium(II) hexahydrate (Ru, 0.5 mM, Alfa Aesar, Germany) and sodium persulfate (SPS, 5 mM, Sigma Aldrich, The Netherlands).

**Volumetric printing procedure:** To achieve volumetric bioprinting, six 405-nm laser diodes D with a 6.4-W combined power (HL40033G, Ushio, Japan) were collimated and coupled by lenses L1, L2 and L3 (L1:f=3.1mm aspheric lens; L2:f=200mm lens; L3:3.1mm aspheric lens) in a square fiber F as illustrated in **Supplementary Figure S7**. The output of the fiber is then magnified and projected onto a digital micromirror device (DMD) via an aspheric lens and a set of orthogonal cylindrical lenses C1 and C2 (C1: f = 250mm cylindrical lens; C2: f = 300mm cylindrical lens). The surface of the DMD is imaged via a 4f-system (L5: f = 150mm lens and L6: f = 250 mm lens) into a Ø16.75mm cylindrical glass vial (V) containing the photopolymer (PR). In the Fourier plane of the afocal system, an aperture (A) blocks the unwanted diffraction orders from the DMD. To address the largest build volume possible, the glass vial V is immersed into a vat (VAT) containing a liquid matching the refractive index of the resin (in this study, water). Hence, the addressable volume inside the photopolymer is approximately 14mm x 14mm x 20mm. A feedback system was integrated in our volumetric printing setup by taking advantage of the transparency of the build volume. As shown in Supplementary Figure S6 a 671-nm laser (LAS; MLS-671-FN, CNI, China) is expanded by an afocal system (lenses L7 and L8) to match the build volume section. The build volume is subsequently imaged by a camera (CAM). The photoinitiators used in this study are not sensitive to the 671-nm imaging wavelength and this feedback system does not impact the printing parameters. The light patterns displayed during the volumetric printing process were calculated using a filtered back-projection algorithm,<sup>[224]</sup> as further detailed in the supplementary information.

**Sample processing post-volumetric printing:** Vials containing the printed constructs were heated to 37° C to melt the unpolymerized gelRESIN, and samples were washed with pre-warmed PBS, followed by 2.5 minutes of additional crosslinking in a Ru/SPS bath in PBS, under a visible light handheld lamp (130 lumen, Ansmann, Germany). Due to the transparency of the constructs printed with LAP, the Ru/SPS crosslinking system was chosen as it induces an orange staining of the hydrogels, thus facilitating their visualization, and is compatible to ensure homogenous crosslinking throughout large-scale printed constructs (**Supplementary Figure S8**).<sup>[258]</sup>



*Cell isolation and culture:* Equine tissue samples and cells were obtained from deceased horse donors, donated to science by their owner and according to the guidelines of the Institutional Animal Ethical Committee. Equine-derived articular chondroprogenitor cells (ACPCs) and bone marrow-derived MSCs were isolated as previously described.<sup>[259]</sup> The procedures to isolate human tissue and cells were approved by the research ethics committee of the University Medical Center Utrecht. Human MSCs were isolated from bone marrow aspirates obtained from consenting patients as previously described.<sup>[248]</sup> Endothelial colony-forming cells (ECFCs) were isolated from human cord blood (procedure was approved by the medical research ethics committee, University Medical Center Utrecht, informed consent was obtained from the mothers).<sup>[248]</sup> Details of the culture media are reported in the supplementary information.

*Viability in volumetric bioprinting:* ACPCs were harvested at passage 3, embedded in gelRESIN at a density of  $10^7$  cells  $\text{mL}^{-1}$ , and printed into disc constructs (1mm height x 5 mm diameter). These were cultured for 7 days in ACPC expansion medium, which was refreshed twice per week. Metabolic activity was measured with a resazurin assay (resazurin sodium salt, Alfa Aesar, Germany) and cell viability was evaluated using a LIVE/DEAD assay (Calcein, ethidium homodimer, Thermo Fischer Scientific, The Netherlands) after 1 and 7 days (n=5).

*Stereomicroscopy and computed tomography:* Macroscopic images were acquired using an Olympus SZ61 stereomicroscope coupled with an Olympus DP70 digital camera (Olympus Soft Imaging Solutions GmbH, The Netherlands). Micro-computed tomography ( $\mu\text{CT}$ ) scans were performed using a contrast agent (CA4+, MW = 1354 g/mol, q = +4) that was synthesized and kindly provided by the lab of Mark W. Grinstaff.<sup>[260]</sup> Printed constructs were incubated in a solution containing 10 mg  $\text{mL}^{-1}$  CA4+ in PBS for 3 hours, washed and briefly dried with tissue paper, prior to being scanned with a Quantum FX  $\mu\text{CT}$  scanner (voxel size = 20  $\mu\text{m}^3$ , 90 kV tube voltage, 200  $\mu\text{A}$  tube current, and 3 minutes of scan time, Perkin Elmer, USA). The volume of the resulting scans (n= 3 independent prints) was calculated using the “volume fraction” function of the BoneJ plugin for Image J (<http://bonej.org>).

*Comparison between different bioprinting technologies:* A human auricle model was scaled 1, 2 and 3x its original volume, and printing time was compared with extrusion-based and lithography based DLP bioprinting. For extrusion-based printing, gelRESIN was printed with a pneumatic-driven system (23G stainless steel nozzle, temperature = 18° C, feed rate = 10 mm  $\text{s}^{-1}$ , pressure = 0.12 MPa, 3DDiscovery, regenHU, Switzerland). For DLP printing, gelRESIN was printed with DLP station (v5, Atum 3D, The Netherlands) equipped with a 405 nm projector (layer exposure time = 10 s, intensity = 15 mW  $\text{cm}^2$ ). Although the printer permits a minimum resolution of 50  $\mu\text{m}$  in the Z direction, printing resolution was artificially worsened increasing the layer height to 300  $\mu\text{m}$ , to match the resolution

achievable with extrusion-based printing and greatly decrease the printing time. The surface profile of the constructs was assessed using the best available resolution and inks for extrusion and DLP printing enabling most accurate and defect-free prints. For extrusion printing, 40% w/v solution of Pluronic F-127 (Sigma Aldrich, The Netherlands) in PBS was printed (temperature = 21° C, feed rate = 20 mm s<sup>-1</sup>, pressure = 0.22 MPa). For DLP printing a bioresin based on polyvinyl alcohol methacrylate (PVA-MA, 10% w/v in PBS), enabling resolution between 25 and 50 μm was used as previously described.<sup>[173]</sup>

**3** *Fluidic experiments:* The printed ball and cage valves were connected at both ends to silicone tubing with the same outer diameter to the inner diameter of the ends of the valve, and the flexibility of the tubing prevented leakage from the connection. Perfusion with PBS either pristine or supplemented with 10 mg mL<sup>-1</sup> Cytodex 1 microbeads stained with Ponceau 4R to enhance visualization (diameter = 147-248 μm, GE Healthcare) was handled with a disposable syringe. Images and videos were taken with the aforementioned stereomicroscope.

*Trabecular bone bioprinting and culture:* Equine-derived MSCs were harvested at passage 3, labelled with cell labeling solution DiD (Vybrant cell labeling kit, Thermo Fischer Scientific, The Netherlands,  $\lambda_{\text{ex}} = 644 \text{ nm}$ ,  $\lambda_{\text{em}} = 665 \text{ nm}$ ) and embedded in gelRESIN at a density of  $1 \times 10^6 \text{ cells mL}^{-1}$ . Constructs were cultured for 7 days in osteogenic induction medium. Cell presence within the trabecular structures was imaged at day 7 via confocal laser scanning microscopy (SPX8, Leica Microsystems, The Netherlands). After this time, the pores of the bioprinted bone were seeded with human-derived ECFCs (passage 10) and supporting human-derived MSCs to act as pericytes (P-MSCs, passage 4) labeled with green fluorescent protein (GFP)<sup>[261]</sup> and DiL (Vybrant cell labeling kit,  $\lambda_{\text{ex}} = 549 \text{ nm}$ ,  $\lambda_{\text{em}} = 565 \text{ nm}$ ) respectively. To enable the formation of 3D capillaries within the porosity of the bone construct, these cells were injected together with matrigel (Growth Factor Reduced, Corning, USA, 1:1 dilution in endothelial media) at a density of  $4.5 \times 10^6 \text{ MSCs}$  and  $1.25 \times 10^6 \text{ ECFCs mL}^{-1}$ . Loaded samples were cultured in endothelial medium for additional 3 days, to observe the onset of angiogenic sprouts formation via confocal microscopy. The length of the angiogenic network formed by ECFCs was calculated using the Angiogenesis Analyzer plugin for ImageJ (<http://image.bio.methods.free.fr/ImageJ/?Angiogenesis-Analyzer-for-ImageJ>). Total length was normalized against the volume available for cell migration and sprouting. ECFCs and P-MSC seeded into 96 well plates in matrigel were used as controls.

*Bioprinted menisci and neo-tissue formation:* ACPCs were harvested at passage 3, embedded in gelRESIN at a density of  $10^7 \text{ cells mL}^{-1}$ , and bioprinted into meniscus-shaped constructs. Samples were cultured for 28 days in chondrogenic differentiation medium, which was refreshed twice per week. Samples were analyzed for metabolic activity (resazurin assay) and cell viability using a LIVE/DEAD assay after 1 and 7 days of culture (n= 3). Fibrocartilage formation potential was assessed by quantifying GAG (dimethylmethylene blue assay,

DMMB, Sigma Aldrich) and DNA (Picogreen Quant-iT, Thermo Fischer Scientific, The Netherlands) synthesis after 1 and 28 days of culture, as well as via Safranin-O, collagen I and collagen II histological staining on paraffin-embedded samples (n= 3). Details of the immunohistochemical procedures are reported in the supplementary methods. Compressive properties of the printed menisci were probed in an indentation-based compression test, with a Dynamic Mechanical Analyzer (DMA Q800, TA Instruments, The Netherlands), equipped with a cylindrical flat piston (diameter = 2 mm). Samples at days 1 and 28 of culture were subjected to a force ramp 0.5 N/min (n = 3-4). The compression modulus was calculated as the slope of the stress/strain curve in the 10% to 15% strain range.

*Statistics:* Results were reported as mean  $\pm$  standard error. Statistical analyses were performed using GraphPad Prism 7.0 (GraphPad Software, USA). For the quantitative data, single comparisons were assessed via a one or two-way ANOVA, followed by post-hoc Bonferroni correction to test differences between groups. When normality could not be assumed, non-parametric tests were performed. For the blood vessel length analysis, the quantification of the GAG/DNA ratio and the mechanical testing, a Mann-Whitney test was performed. Differences were found to be significant when  $p < 0.05$ .

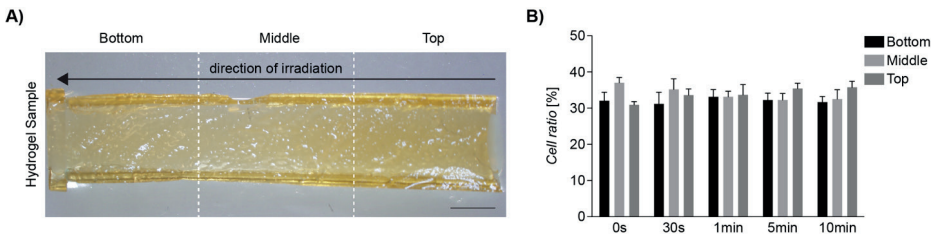
## SUPPORTING INFORMATION

### Supplementary Figures

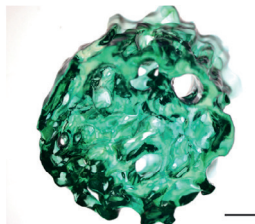
3



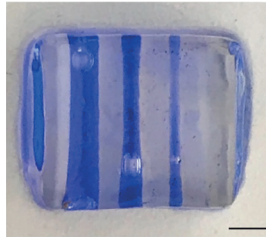
**Supplementary Figure S1:** Side view of the Utrecht Dom tower model printed using the volumetric printing technique. Model resin SR399 (Sartomer, France) and 0.63 mM Irgacure 819 (Sigma-Aldrich, Germany), was used to print this model for illustrative purposes.



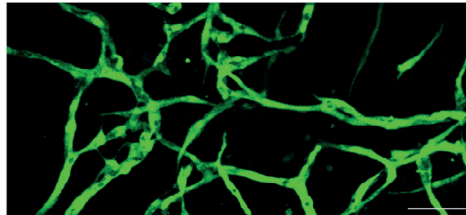
**Supplementary Figure S2:** Assessment of cell sedimentation at different waiting times after mixing of cells into the hydrogel solution. A) Macroscopic image of the hydrogel construct (scale bar = 2 mm). Dashed, white lines show the bottom, middle and top regions from which images were captured for cell quantification. Black arrow shows the direction from which the construct was irradiated. B) Quantification of cells in the different regions of the hydrogel construct after different waiting times. Values are expressed as the cell ratio in each region normalized against to total cell number within the whole section of the construct.



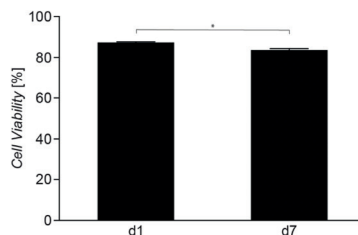
**Supplementary Figure S3:** Top view of the trabecular bone construct, as observed via optical stereomicroscopy. The hydrogel was stained with alcian blue to facilitate visualization. Scale bar = 1 mm.



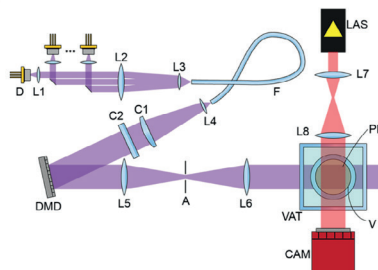
**Supplementary Figure S4:** Top view stereomicroscopy image of a gelRESIN hydrogel with embedded channels with decreasing inner diameter. Channels are perfused with an alcian blue solution to better visualize the open tubular vessels. Scale bar = 1 mm.



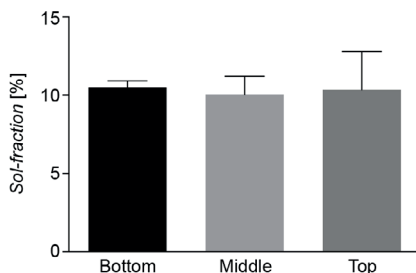
**Supplementary Figure S5:** Confocal microscopy (stitched tilescan), representing the pre-capillary network developed by the ECFC/P-MSC co-culture in the control condition (casted in matrigel in a tissue culture well). GFP channel, visualizing the ECFCs only. Scale bar = 100  $\mu\text{m}$ .



**Supplementary Figure S6:** Cell viability of the bioprinted meniscal constructs over the first week of culture in differentiation medium.



**Supplementary Figure S7:** Graphical representation of the volumetric printing set-up. Coupling the laser diodes in the square core fibers (CeramOptec WF 70x70/115/200/400N, core size: 70  $\mu\text{m}$  by 70  $\mu\text{m}$ , numerical aperture: 0.22) provides a homogeneous square output beam matching the rectangular aperture of the modulator, a digital micromirror device (DMD). The cylindrical lenses have different focal lengths, which allows adjusting the square beam from the fiber to the rectangular area of the DMD (Vialux V-7000 VIS). The DMD acts as a blazed grating, it was therefore rotated of approximately  $7^\circ$  to optimize its diffraction efficiency. When all the DMD pixels are in their 'ON' state, the power of the light beam sent into the vial is approximately 1.6 W.



**Supplementary Figure S8:** Sol-gel analysis of the bottom, middle and top regions of 2 cm-high hydrogel constructs.

## Supplementary Tables

**Supplementary Table S1:** Results of the sol-gel analysis for the casted and volumetric printed hydrogels.

Type of gel	Sol fraction [%]	Swelling [%]
gelMA (cast)	$12.069 \pm 1.965$	$8.190 \pm 0.221$
gelRESIN (printed)	$6.662 \pm 1.164$	$9.518 \pm 0.193$

**Supplementary Table S2.** Printing time (s) for the different gelRESIN constructs fabricated with volumetric printing technique.

Construct	Printing time (s)
Human ear	22.7
Fluidic valve (ball and cage)	21.5
Trabecular bone	12.5

## Supplementary Data

*Smoothness of the prints:* Though the light patterns used in our volumetric printing setup are produced with a similar pixelated DLP modulator as standard stereolithography printer, the structures printed with VBP exhibit a smoother surface profile than structures printed via stereolithography. This smoothness feature originates from the rotation of the container during the exposure with dynamic light patterns. The accumulation of different light intensities from multiple angles onto a local volume allows creating dose distributions along smooth profile rather than relying on elementary  $20\ \mu\text{m}$  cubic building blocks as in stereolithographic printers. Most importantly, stereolithography is a discrete layer-by-layer process creating step profiles whereas as the name indicates, in volumetric printing, the entire volume of the part is created at once.

## Supplementary Methods

*Calculation of the tomographic back-projections for the volumetric bioprinting process:* First, 3D models in STL format were converted to a three-dimensional voxel map, that is to say a 3D matrix where the values '1' indicate the presence of the object and '0' its absence at each particular location in space. For each 2D section of this matrix, projections were calculated over a 360° grid of angles with a spacing of 0.6°, using the 'radon' function in MATLAB (MathWorks, USA). This function numerically calculates the Radon transform:

$$\mathcal{R}f(t, \theta) = \int_{-\infty}^{+\infty} f(q \sin \theta + t \cos \theta; -q \cos \theta + t \sin \theta) dq$$

The projections were subsequently filtered with a Ram-Lak filter in the Fourier domain. This filter yields a set of projections which, when projected back into an empty volume, result in theory in a perfect reconstruction of the object. The calculated patterns having both negative and positive values, a simple threshold was used to set the negative values to 0 as physically, only positive light dose can be deposited inside the build volume.

*Quantification of cell distribution throughout large hydrogel constructs:* 1 mL cell-laden 10% gelMA solutions were left in its sol state for different periods of time (0 s, 30 s, 1 min, 5 min and 10 min) before thermal gelation was induced in a cold water-bath. The hydrogel solutions were then photocrosslinked into a 2 cm-high cylindrical structure using the Ru/SPS crosslinking system. Cells were labelled with nucleus staining solution DAPI after crosslinking and imaged at 3 different areas within each region of the cylinder (bottom, middle and top; n = 3) using an epifluorescence microscope. Cell distribution along the resulting gel cylinder was then quantified.

*ACPC expansion medium:* Dulbecco Modified Eagle Medium (DMEM) + GlutaMAX (Gibco, 31966, The Netherlands) supplemented with fetal bovine serum (FBS, 10% v/v, Gibco, 10270, The Netherlands), penicillin/streptomycin (1%, Gibco, The Netherlands), l-ascorbic acid-2-phosphate (0.2 × 10<sup>-3</sup> M, Sigma Aldrich, The Netherlands), and basic fibroblast growth factor (5 ng mL<sup>-1</sup>, PeproTech, United Kingdom).

*MSC expansion medium:* DMEM + GlutaMAX (Gibco, 31966, The Netherlands) supplemented with fetal bovine serum (FBS, 10% v/v, Gibco, 10270, The Netherlands), penicillin/streptomycin (1%, Gibco, The Netherlands).

*Osteogenic medium:* alpha-MEM (Gibco, 22561, The Netherlands) supplemented with 10% v/v FBS, 100 U mL<sup>-1</sup> penicillin, 100 µg mL<sup>-1</sup> streptomycin, 0.2 mM L-ascorbic acid-2-phosphate, 20 mM β-glycerol phosphate (Sigma-Aldrich, The Netherlands), 100nM dexamethasone (Sigma-Aldrich, The Netherlands).

*Endothelial medium:* Endothelial Growth Medium-2 (EGM-2, Lonza, The Netherlands) containing Endothelial Basal Medium-2 + SingleQuots (Lonza), 100 U mL<sup>-1</sup>-100 µg mL<sup>-1</sup> PenStrep, and 10% heat-inactivated FBS.

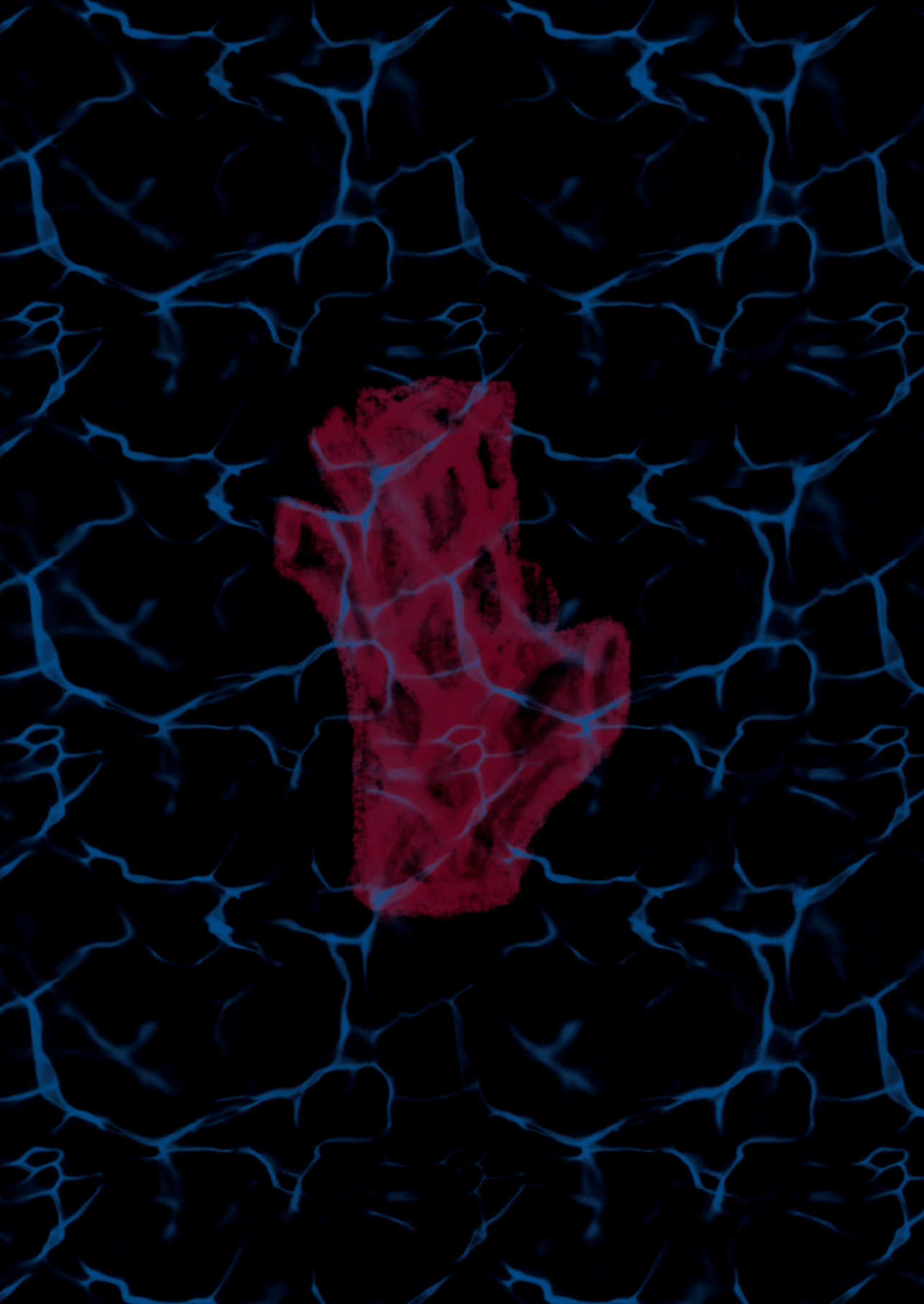
*Chondrogenic medium:* DMEM + GlutaMAX supplemented with 100 U mL<sup>-1</sup> penicillin, 100 µg mL<sup>-1</sup> streptomycin, 0.2 mM L-ascorbic acid-2-phosphate, ITS + Premix Universal Culture Supplement (1%, Corning, USA), dexamethasone ( $0.1 \times 10^{-6}$  M, Sigma Aldrich, The Netherlands) and recombinant human TGF-β1 (10 ng mL<sup>-1</sup>, PeproTech, USA).

*Immunohistochemistry for collagen type I and II:* Paraffin embedded samples were cut into 5 µm thick slices, deparaffinized with xylene and hydrated in ethanol graded solutions. Endogenous peroxidases were blocked with 0.3% v/v hydrogen peroxide. Antigen retrieval was performed with 1mg mL<sup>-1</sup> pronase and 10 mg mL<sup>-1</sup> hyaluronidase, for 30 minutes at 37° C. Sections were blocked with bovine serum albumin (5% w/v in PBS) for 1 hour at room temperature. Primary antibodies (anti-collagen type I, sc-8784, Santa Cruz Biotechnology, USA; anti-collagen type II, DSHB, II-II6B3, USA) were incubated overnight at 4°C. IgGs were used as isotype controls. Secondary antibody incubation was performed for 1 hour at room temperature, and staining was developed with with 3,3-diaminobenzidine-horseradish peroxidase (Sigma Aldrich, The Netherlands). Nuclei were counterstained with hematoxylin and the sections were mounted in DPX (Millipore, USA).

*Sol-fraction analysis of bioprinted constructs compared to cast controls:* Samples were either printed or cast (n=5) and the crosslinking efficiency and swelling capacity of the resulting hydrogel constructs were assessed as previously described.<sup>[173]</sup>







# Chapter 4

## **Volumetric Printing Across Melt Electrowritten Scaffolds Fabricates Multi-Material Living Constructs with Tunable Architecture and Mechanics**

Gabriel Größbacher<sup>1\*</sup>, Michael Bartolf-Kopp<sup>2\*</sup>, Csaba Gergely<sup>2\*</sup>, Paulina Núñez Bernal<sup>1\*</sup>, Sammy Florczak<sup>1</sup>, Mylène de Ruijter<sup>1</sup>, Núria Ginés Rodriguez<sup>1</sup>, Jürgen Groll<sup>2</sup>, Jos Malda<sup>1,3</sup>, Tomasz Jüngst<sup>2#</sup>, Riccardo Levato<sup>3,1#</sup>

Published in: *Advanced Materials*. 2023. 35(32)

<sup>1</sup> Department of Orthopedics, University Medical Center Utrecht, Utrecht University, Utrecht, The Netherlands

<sup>2</sup> Department of Functional Materials in Medicine and Dentistry, Institute of Functional Materials and Biofabrication (IFB), KeyLab Polymers for Medicine of the Bavarian Polymer Institute (BPI), University of Würzburg, Würzburg, Germany

<sup>3</sup> Department of Clinical Sciences, Faculty of Veterinary Medicine, Utrecht University, Utrecht, The Netherlands

\* Authors contributed equally to this work

# Indicates shared senior authorship

## ABSTRACT

Major challenges in biofabrication revolve around capturing the complex, hierarchical composition of native tissues. However, individual 3D printing techniques have limited capacity to produce composite biomaterials with multi-scale resolution. Volumetric bioprinting recently emerged as a paradigm-shift in biofabrication. This ultra-fast, light-based technique sculpts cell-laden hydrogel bioresins into three-dimensional structures in a layerless fashion, providing enhanced design freedom over conventional bioprinting. However, it yields prints with low mechanical stability, since soft, cell-friendly hydrogels are used. Herein, for the first time, the possibility to converge volumetric bioprinting with melt electrowriting, which excels at patterning microfibers, is shown for the fabrication of tubular hydrogel-based composites with enhanced mechanical behavior. Despite including non-transparent melt electrowritten scaffolds into the volumetric printing process, high-resolution bioprinted structures were successfully achieved. Tensile, burst and bending mechanical properties of printed tubes were tuned altering the electrowritten mesh design, resulting in complex, multi-material tubular constructs with customizable, anisotropic geometries that better mimic intricate biological tubular structures. As a proof-of-concept, engineered tubular structures were obtained by building tri-layered cell-laden vessels, and features (valves, branches, fenestrations) that could be rapidly printed using this hybrid approach. This multi-technology convergence offers a new toolbox for manufacturing hierarchical and mechanically tunable multi-material living structures.

**Keywords:** biofabrication, volumetric additive manufacturing, bioprinting hydrogels, melt electrowriting

## INTRODUCTION

In the quest to restore the function of damaged tissues, additive manufacturing technologies are continuously opening new avenues to better capture the complex composition and function of native biological architectures.<sup>[109]</sup> A central characteristic of biofabrication techniques is the ability to perform the automated and accurate simultaneous placement of living cells and materials (together also termed bioinks)<sup>[129]</sup> in custom-designed patterns. Fabrication can be performed by means of light-based printing, such as stereolithography and digital light processing,<sup>[173,262]</sup> extrusion-based,<sup>[263,264]</sup> droplet-based or inkjet printing,<sup>[265–267]</sup> and fiber reinforcing technologies.<sup>[268,269]</sup> All these technologies have their individual benefits and challenges with respect to resolution, shape-fidelity, cell-viability, compatible ranges of materials (inks or resins), and printing/processing time. Yet, while each technique excels in processing certain subsets of inks and object geometries, native biological tissues are characterized by their unique multicellular and multi-material composition, shape and hierarchical architecture, with features from the submicron to the macro-scale. Most importantly, both mechanical and biological function are intimately correlated to this multi-scale, multi-material hierarchy.<sup>[109]</sup> New directions in the biofabrication field hold the promise to bridge this gap by converging different (and previously incompatible) bioprocessing technologies,<sup>[131,270]</sup> with the aim to produce engineered tissue constructs that, by combining their benefits and range of achievable prints, better mimic salient features of their native counterparts, to eventually restore and replace damaged tissues.

Volumetric printing (VP) is a recently developed biofabrication technology to sculpt hydrogels into free-form 3D structures.<sup>[127]</sup> In VP, a hydrogel with the addition of a photocrosslinking agent is placed in a rotating platform and a light source (*i.e.*, a laser), in combination with a spatial light modulator (such as a digital micromirror device, DMD), is subsequently used to deliver a sequence of filtered tomographic back-projections onto this volume. The sum of the different projections rapidly generate an anisotropic, 3D light-dose distribution within the build volume, thereupon activating the polymerization reaction only in correspondence to the desired object.<sup>[224]</sup> This process is extremely fast (< 30 seconds to produce several cm<sup>3</sup> parts)<sup>[121]</sup> compared to conventional extrusion-based printing (20 min), while offering equal or greater resolution (40–200 μm) with higher spatial freedom.<sup>[127,224]</sup> Although promising, the materials used with volumetric printing are hydrogels, which are intrinsically soft, while most tissues in the body also need to account for mechanical stability and load bearing capacity. Techniques to mechanically stabilize soft hydrogels include the formation of interpenetrating polymer networks, the inclusion of nanoparticles, or the inclusion of fibrous reinforcements, such as structures produced via fused deposition modeling, electrospinning, and melt electrowriting (MEW).<sup>[271]</sup> In particular, MEW generates (sub)micrometer-scale fibers by applying a high voltage to the

polymer melt. Fibers are deposited onto a moving collector plate, allowing for control over fiber deposition and subsequent scaffold architecture.<sup>[123,271]</sup> Scaffolds made with MEW have proven to facilitate cell alignment,<sup>[272]</sup> and increase the mechanical stability of tissue engineered constructs.<sup>[273]</sup> This technique is compatible with printing a variety of thermoplastic materials,<sup>[274,275]</sup> whose biochemical composition can further be modified post-writing with surface coatings.<sup>[274,276,277]</sup> Recently, first steps have also demonstrated the possibility to print hydrogel-based fibers.<sup>[278]</sup> Notably, fiber deposition can be done on a flat collector plate but also on a mandrel for the fabrication of intricate tubular scaffolds.<sup>[279–281]</sup> Tubular geometries are of particular interest for biological applications, as they recur in many tissues, and can therefore be applied as scaffolds for blood vessels, airways, intestinal and tubular kidney structures,<sup>[282]</sup> among others.<sup>[280,281]</sup>

4 One of the drawbacks of MEW tubular scaffolds is that the inclusion of cells is generally done post-printing, either by direct seeding on top of the fiber strands, or by casting with a hydrogel carrier.<sup>[283–285]</sup> Promising composite structures have been produced, exploiting the unique ability of MEW to provide mechanical reinforcement to other cell-carrying materials.<sup>[202]</sup> However, since the cell-laden compartment can only be loaded in simple geometries following the electrowritten mesh pattern, replicating complex, branched and tortuous geometries typical of native tissues remains challenging.

In this work, we demonstrate for the first time the convergence of volumetric bioprinting with melt electrowriting, to pattern multiple materials and cell types in any custom-desired geometry even within opaque polymeric microfibrillar thermoplastic meshes. In shaping these novel hydrogel-cell-microfiber composites, as a proof-of-concept to demonstrate the applicability and versatility of this technology, we built a broad array of constructs that mimic key features of native blood vessels. The intricacy in design ranges from double-branched structures to multi-cellular and fenestrated, structurally reinforced scaffolds with tunable mechanical properties, and cell-laden architectures not possible with previously existing techniques alone.

## RESULTS AND DISCUSSION

The convergence of different 3D printing technologies has become a widely studied concept in the fields of biofabrication and tissue engineering, given the potential to exploit the advantages of different technologies to combine different classes of materials in a single object, and to create living, hierarchical structures.<sup>[131]</sup> In the present study, we aim to elucidate the potential and advantages offered by the convergence of volumetric printing (VP), which allows the fabrication of highly complex, centimeter-scale structures using hydrogel-based bioresins,<sup>[127]</sup> and melt electrowriting (MEW), which

allows the creation of highly organized fiber architectures having micron-scale resolution, uniquely able to confer outstanding mechanical properties to low-stiffness hydrogels. To accomplish this, tubular MEW scaffolds were first fabricated from poly- $\epsilon$ -caprolactone (PCL) and incorporated into a volumetric printing vial, which in turn was exposed to the tomographic light projections required to form a 3D object in tens of seconds (**Figure 1A**). As platforms to investigate the converged technique, termed VolMEW for simplicity of reference, materials widely used in the field of biofabrication for both technologies were employed in this study: PCL for MEW, given its previously established superior printing properties and medical grade nature,<sup>[274]</sup> and gelatin methacryloyl (gelMA) as a bioresin for VP, which has been shown to be a fast, high-resolution choice for this printing approach.<sup>[127,286]</sup> PCL itself, as a bulk material, features an *in vivo* degradation time of 1-2 years, depending on molecular weight, chemical modifications and shape into which it has been processed.<sup>[287]</sup> Thereby, the degradation kinetics is highly dependent on the exact type of sourced material and on the morphology of the scaffold. Previous work has shown residues of fused deposition modeling (FDM) processed PCL in an equine model up to 6 months after implantation within a cement blend.<sup>[288]</sup> For MEW, due to the thin fiber diameter and relatively high surface to volume ratio, the degradation kinetics will be quicker, although the exact degradation time will depend also on the anatomical location in which the biomaterial is implanted. Within the articular joint of a horse model, remnants of MEW meshes were clearly seen even after 6 months of implantation,<sup>[289]</sup> while in the periodontal region in a mouse model, histological evidence of persisting MEW fibers was detected at 6 weeks of implantation.<sup>[290]</sup> While there is evidence showing MEW scaffolds are stable over long *in vivo* implantation times, consistent data elucidating in details their degradation kinetic scaffold is currently lacking in the literature, and future research would be needed *i.e.*, before applying these materials as vascular grafts. In the present study, different MEW mesh architectures were successfully fabricated, with custom-designed i) pore shapes (*i.e.*, rhombic with 34° and 70° winding angles and hexagonal (**Figure 1Ai, B**)) and ii) thicknesses (*i.e.*, 20, 30, 40, and 60 printed layers). These tubular scaffolds were first placed into volumetric printer vials and guided in through a carbon fiber rod with controlled alignment (**Supplementary Figure S1**). Subsequently, the vials were loaded with gelMA. Due to the thermal gelation behavior characteristic of gelMA, the MEW mesh could be secured into its intended location and alignment even after removal of the support rod (**Figure 1Aii - iv**). With the MEW scaffold aligned within the printing vial, the VP process was conducted (**Figure 1Av, C**).

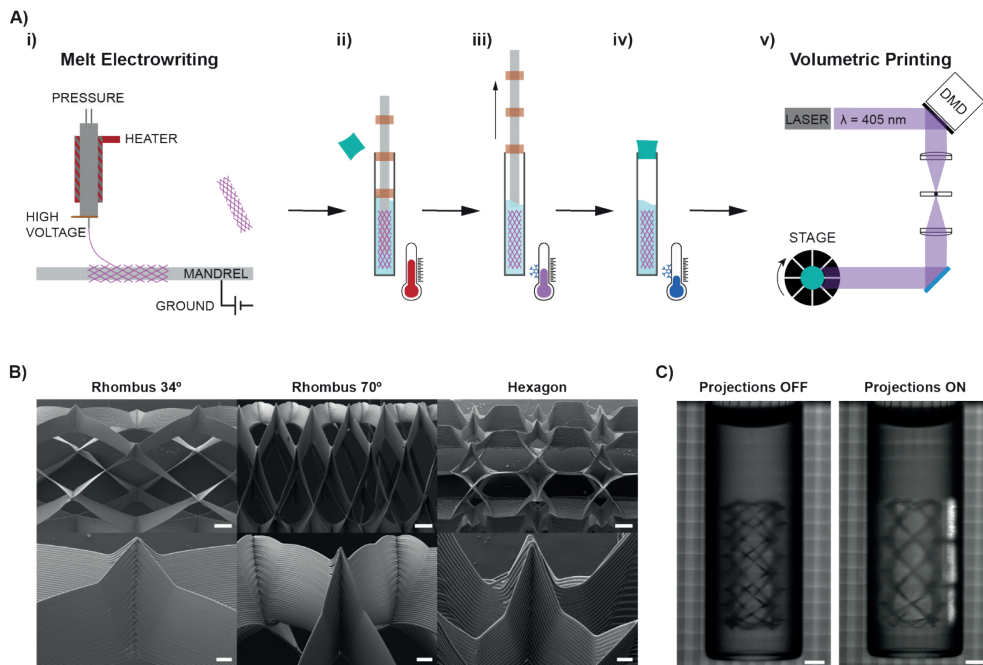


**Figure 1: Convergence of MEW and VP processes - VolMEW.** A) Graphical overview of i) the fabrication of tubular melt electrowritten scaffolds on a rod and their subsequent incorporation into the volumetric printing process by ii) first placing the MEW meshes in a vial of preheated gelatin methacryloyl solution using a carbon fiber rod with centering guides. iii) once the MEW tube is completely infused, the gelMA solution is gradually cooled as the mandrel is retracted without disrupting the gelling resin or the MEW mesh structure, iv) the vial is then fully gelled in ice water and v) placed in the volumetric printer. The same process can be applied in presence of cells, therefore performing a Volumetric Bioprinting (VBP) step. B) SEM images of three different pore structures of the tested MEW tubes (scale bars = 500  $\mu\text{m}$  (top panels) and 100  $\mu\text{m}$  (bottom panels)). C) Digital images of the volumetric printing vials containing gelMA and a fixed, centered MEW mesh when inserted into the printer and when light projections are initiated. Scale bar = 2 mm.

After establishing a simple and consistent method for setting up a hybrid VolMEW process, the effect of the opaque PCL meshes on the tomographic illumination imparted by VP was investigated to ensure the achievement of high-resolution prints (**Figure 2**). It was essential to first characterize this effect because the VP process relies on the undisturbed passage of tomographic light projections through the entire bioresin vat in order to induce specific photocrosslinking in the target regions. The presence of elements that attenuate or refract the light beams incoming from the spatial light modulator could therefore impair printing resolution. While the presence of scattering elements (*i.e.*, cells, particles) can be mitigated mixing the bioresin with refractive index matching compounds,<sup>[286]</sup> the effect of opaque structures had yet to be investigated. Previous research has demonstrated the possibility to perform volumetric prints around non-transparent objects, such as metallic rods. However, such prints were only achieved with bulky structures fully encasing the abovementioned rod and lack the fine features characteristic of volumetrically printed



objects.<sup>[225]</sup> In this study, the opacity of the PCL mesh provided a light attenuation effect by partially blocking the projection path in the regions where the PCL meshes align with the beam (occlusion points).

A custom-made setup to evaluate the light attenuation effect was devised. A laser (520 nm) was used to project a small pixel matrix through the center of a rotating VP vial containing the constructs with varying MEW pore architectures, or constructs with the same mesh geometry, but different layer heights. A photodetector was then placed on the opposite side of the vial, to determine the profile of the light beam passing through the hydrogel-soaked MEW mesh (**Figure 2A, Supplementary Figure S2**). The percentage of projected light intensity passing through each angle of the vial was calculated by integrating the normalized signal over a full rotation and represents the average percentage of light detected with MEW scaffold attenuations of different pore architectures (**Figure 2B**) and layer heights (**Figure 2C**). Compared to hydrogel-only control conditions, where  $94.9 \pm 2.0\%$  of light intensity could be detected after passing through the bioresin vial, all three MEW pore architectures: hexagons ( $80.9 \pm 5.3\%$ ) and rhombi with  $70^\circ$  ( $77.1 \pm 3.7\%$ ) and  $34^\circ$  ( $91.6 \pm 1.6\%$ ) winding angles, showed significantly lower percentages of detected light. As for the differences between architectures, the  $34^\circ$  rhomboid-shaped pore architecture showed the lowest attenuation effect, allowing significantly higher amounts of light passage compared to the hexagons and the  $70^\circ$  rhomboid. In presence of highly opaque fiber assemblies, such as the case of our MEW meshes, light travelling through the vial is primarily attenuated by the fibers, rather than scattered. Notably, precise printing has been demonstrated previously in presence of opaque occlusions, as, given that the light source has at least any  $180^\circ$  unobstructed view of the occluding object, tomographic reconstruction remains possible.<sup>[225]</sup> The light detection plots (**Figure 2Di, Supplementary Figure S3**) clearly visualize that the different architectures exhibit a series of steep dips where the light is partially blocked by each occlusion point (**Figure 2Dii**). Although the occlusion points coincide with a high local light attenuation, the average light passing through the vial is observed to be correlated with the pore size of the scaffold rather than the amount of total occlusion points per revolution. This hypothesis is supported by the significant difference in total percent transmitted light between  $34^\circ$  and  $70^\circ$ , where both have only four occlusion points per revolution, but the  $34^\circ$  rhomboid (8 pivot points) has a pore size of  $4.12 \text{ mm}^2$ , whereas  $70^\circ$  rhombi (8 pivot points) have a pore size of only  $1.01 \text{ mm}^2$ .<sup>[279]</sup> Using the same setup,  $34^\circ$  rhombi were selected to investigate the effect of layer height based on the observed least significant light attenuation for this architecture. Here, compared to the mesh-free control, the 20-layer scaffold ( $94.0 \pm 2.7\%$ ) did not significantly decrease the amount of transmitted light, as opposed to what was found for the 40- ( $91.6 \pm 1.6\%$ ) and 60- ( $88.4 \pm 2.2\%$ ) layer structures (**Figure 2C**). Overall, it should be noted that all these light attenuation profiles are compatible with the light transmission requirements identified in previous works, when performing volumetric

printing using gelMA and LAP as resin components (>37% of transmitted light across the vial).<sup>[127]</sup> The observed differences in light attenuation are likely caused by i) the increase in total electrowritten material, combined with ii) minor stacking errors over the entire layer height resulting in a larger occlusion zone. In addition, inherent to MEW on a rotating mandrel, each deposited layer could suffer from a minute layer shift, effectively creating a sloped and, therefore, thicker wall. Consequently, as this thicker wall rotates out of the field of view of the projected spot, it partly overcasts the detected light over a longer angular distance when compared to thinner PCL walls (**Supplementary Figure S4**).

Having shown that the degree of light attenuation can be controlled by pore architecture and layer height selection, the effect of shading on VP printing accuracy was assessed using 34° rhombic tubes at the different layer heights tested above. As a benchmark assay, we volumetrically printed cylinders with arbitrarily designed wall sizes to match the thickness of the MEW mesh ( $t_{\text{print}} = 14.8$  s). All three MEW-mesh wall thicknesses (20, 40, and 60 layers) were completely encapsulated within VP-printed gelMA cylinders of equal programmed thickness as the MEW scaffolds (**Figure 2E**). The thickness of the wall enveloping the 20- and 40-layer scaffolds ( $291 \pm 13$   $\mu\text{m}$  and  $550 \pm 16$   $\mu\text{m}$ , respectively) did not significantly differ from their respective target designs (MEW mesh thicknesses) ( $267 \pm 10$   $\mu\text{m}$  and  $537 \pm 1$   $\mu\text{m}$  for the 20- and 40-layer meshes, respectively), suggesting that the potential effect of light attenuation for these scaffolds can be easily avoided with the selected volumetric printing light dose settings (**Figure 2F**). However, this was not observed for the 60-layer scaffold, where the resulting wall thickness encapsulating this structure ( $1026 \pm 41$   $\mu\text{m}$ ) was significantly larger than the mesh itself ( $828 \pm 3$   $\mu\text{m}$ ) (**Figure 2F**). The significant decrease in printing accuracy is underpinned by the light attenuation observations described previously, as this scaffold had the most noticeable effect on the passage of light through the VP sample. It is hypothesized that the thicker scaffold experiences a higher sum of diffuse backscatter reflected from the opaque PCL fibers, resulting in lower precision in delivering the light dose along the projected pattern. Consequently, off-target regions of the bioink adjacent to the MEW mesh also reached the photopolymerization threshold. Despite this effect seen in the thicker MEW samples, it is noteworthy that all three mesh thicknesses allowed VP to occur and produced homogeneous cylindrical prints. Moreover, if thicker MEW scaffolds are required for specific applications, this information on the light attenuation profile could feed future algorithms to computationally correct the tomographic projections.

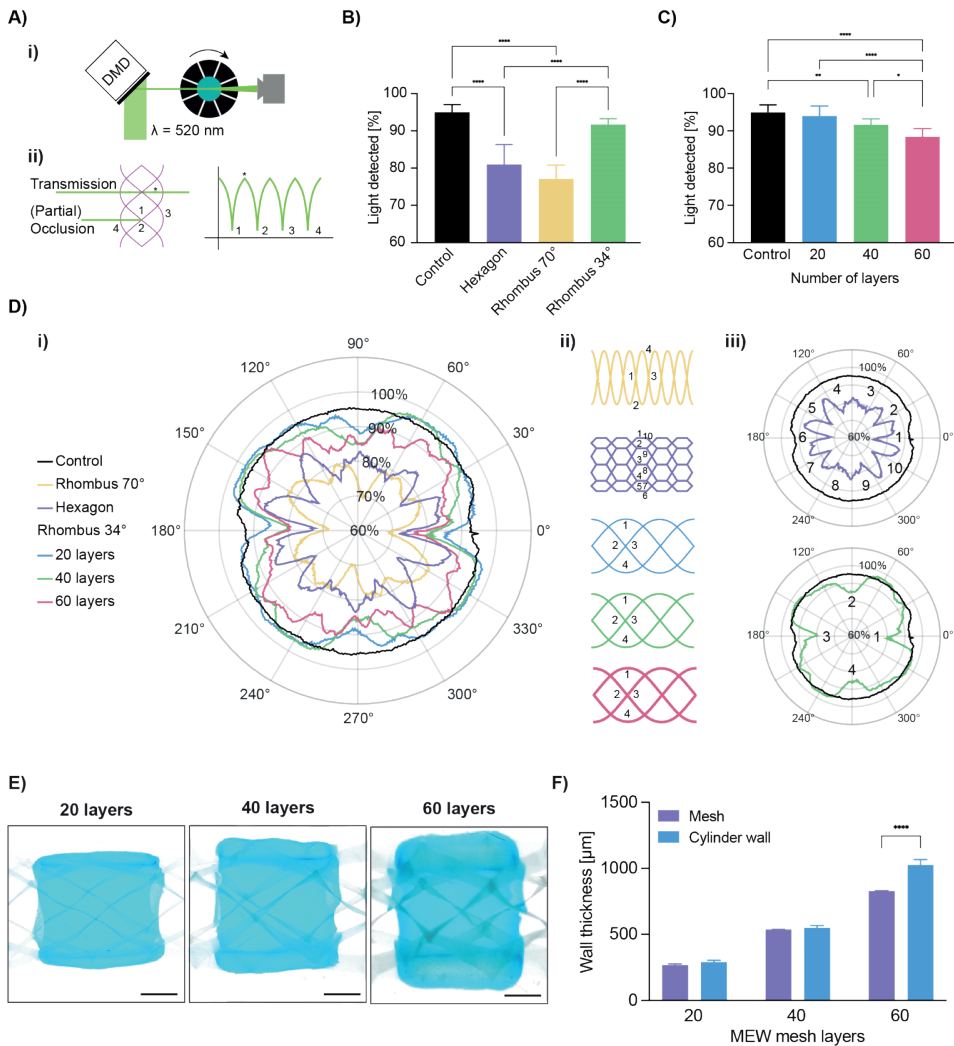


**Figure 2: Characterization of the effect of MEW tube incorporation on beam path homogeneity through gelMA-filled VP vials.** A) Graphical overview of the test setup used to evaluate the light attenuation effect of different architectures/layers of MEW meshes. i) A 520nm laser beam is used to project a pixel array through a VP vial containing gelatin and different MEW tube structures for one 360° rotation while a detector placed at the opposite end of the vial is captures the percentage of light passing through the vial at each angle of rotation. ii) Diagram of the numbered occlusion locations in a 34° rhombus, where the highest light attenuation is observed with an example transmission point (\*) and a corresponding graph. Based on the resulting light detection measurements per structure showing the percentage of light passing through the vial, the area under the curve is plotted for B) different mesh architectures: hexagons, rhombi with 70° and 34° winding angle and mesh-free controls, as well as for C) the 34° winding angle rhombus with different number of layers (20, 40 and 60). D) Time synchronous average percentage of light detected for the different mesh architectures and layer heights: hexagons (40 layers), rhombi with 70° (40 layers) and 34° (20, 40, 60 layers) winding angles and mesh-free controls (n=4). ii) Architectural mesh diagrams and their respective occlusion points. Each occlusion mesh point (represented by the troughs in the graph) is numbered and iii) examples are given for the corresponding

graphs. E) Stereomicroscope images of VP-printed tubes accurately encapsulating tubular MEW meshes of 20, 40 and 60 layers respectively (scale bars = 1 mm). F) Average wall thickness of the MEW meshes with different number of layers (20, 40 and 60) and the average wall thickness of the printed hydrogel surrounding these structures (n = 3, scale bars = 1 mm). \* =  $p < 0.05$ , \*\* =  $p < 0.01$ , \*\*\*\* =  $p < 0.0001$ .

In previous research focused on the VP technique for bioprinting applications, biocompatible bioresins obtained from hydrogel-based materials with relatively low mechanical stability have been used. On the one hand, these classes of hydrogels are desirable when it comes to maintaining cell viability and facilitating cell-to-cell communication.<sup>[127,286,291,292]</sup> On the other hand, these bioresins are often not strong enough to withstand the harsh mechanical environment found in native tissues, be it shear, tensile, or compressive forces. The VolMEW approach has the potential to overcome this challenge and enhance the mechanical stability of the printed structures, enabling a range of tissue-specific load-bearing applications in line with the mechanical stabilization that has been achieved when MEW was combined with extrusion-based bioprinting.<sup>[167,202]</sup> To determine the mechanical properties of the hybrid VolMEW constructs, the burst and tensile performance of the composite prints were tested.

First, the burst pressure of the tubes was assessed by connecting the VolMEW tubes to a custom-made test setup via microfluidics adapters and commercially available tubing (**Figure 3A, Supplementary Figure S5A**), Different from what was experienced with reinforced tubes, simply mounting constructs made from non-reinforced gelMA constructs to the adapters was difficult, as these prints tended to rupture while being secured in place. Vaseline was injected into the luminal cavity of the tubes and the pressure was recorded until failure. A significant difference in burst pressure was recorded for the different geometries, which displayed increased strength when compared to the gelMA-only controls (Control:  $0.66 \pm 0.32$  bar / Hexagon:  $1.14 \text{ bar} \pm 0.10$  bar /  $34^\circ$ :  $1.3 \pm 0.26$  bar /  $70^\circ$ :  $1.58 \pm 0.17$  bar) (**Figure 3B**). Overall, these results corroborate previous observations of hydrogel-infused tubular MEW scaffolds, which also showed enhanced tensile properties and resistance to flow-based pressures. Nevertheless, it should be noted that, in terms of absolute values, our results differ from previous burst pressure evaluations that have been done with heterotypic tubular graft systems as a balloon catheter has been used to inflate the construct.<sup>[284]</sup> To better capture the flow dynamics of a liquid exerting the pressure onto the lumen of the construct, and prevent drying out of the hydrogel, we opted for vaseline as a conductor for its incompressibility that would allow to exert the applied air pressure onto the construct and thus offer a form of comparison towards other comparable experimental setups with pressurized air. Vaseline also made it easier to notice small, damaged areas, as it formed ribbon-like shapes, which could be easily evaluated as failure of the construct (**Supplementary Figure S5B**). From a physiological perspective, the measured values are above the maximum arterial pressure, but below expected burst strength recordings for native vascular systems.<sup>[293]</sup> Nevertheless,

the measurements reveal the possibility of modifying these parameters by adapting the reinforcement geometry of the hybrid construct and adjusting the properties of the hydrogel via its composition. Moreover, it should be noted that, in a tissue engineering application, cells could be added to the printed scaffold prior to implantation, and the constructs could be subjected to an *in vitro* maturation step to finally match the desired mechanical properties for *in vivo* utilization.<sup>[294]</sup>

Next, a custom two-pin setup was mounted on a uniaxial tensile testing machine capable of cyclic motion and samples were mounted by inserting the pins through the lumen of the construct to perform radial tensile tests (**Figure 3C**). In this fashion, a motion similar to the dilation of blood vessels during systole could be replicated and recorded. This is a relevant parameter to quantify, because the compliance of a tubular construct is associated with the likelihood of graft occlusion and ultimately rejection, especially for small-diameter vascular structures.<sup>[295]</sup> Another advantage of testing circular constructs in radial tensile experiments is that it more closely approximates physiological mechanical properties compared to the planar axial method of cutting the tube longitudinally and clamping it onto the testing machine.<sup>[296]</sup> Conversion to stress and strain values were calculated using formulas previously used in wire myography.<sup>[297]</sup> In order to evaluate the tensile performance of the composite materials, samples were strained to 5 mm, which equates to 166% elongation, a value chosen as a reference point as it exceeds physiological vascular strain levels. **Figure 3D** illustrates the behavior of VolMEW constructs with different reinforcement geometries compared to unreinforced constructs. Each of the reinforcement geometries showed a different hysteresis curve over cyclic loading, and all of them allowed the VolMEW constructs to withstand a full cycle of stress loading, that instead resulted in failure for VP-only (gelMA-only) constructs. A significant overall increase was shown in the recorded peak stress values for all reinforcement strategies, with hexagonal pores ( $20.3 \pm 3.2$  kPa), rhombic pores with  $34^\circ$  ( $28.7 \pm 4.9$  kPa) and  $70^\circ$  ( $73.0 \pm 21.5$  kPa) winding angles, outperforming gelMA-only controls ( $5.2 \pm 2.1$  kPa). Overall, the strongest reinforcement in terms of Young's Modulus was provided by the  $70^\circ$  rhombic structure ( $10.8 \pm 3.3$  kPa) when compared to  $34^\circ$  rhombic ( $3.5 \pm 0.3$  kPa) and hexagonal ( $3.2 \pm 1.2$  kPa) structures (**Figure 3E**). The difference is likely caused by the specific pore sizes present in these MEW constructs as well as the compliance of the different repeating compartments in deforming along with the hydrogel during the tensile displacement. The effect of pore size of MEW meshes has already been characterized in previous studies.<sup>[279,298]</sup> The hexagonal constructs feature a higher stiffness compared to the rhomboid structures in radial deformation as an effect of their geometry, which is likely the main cause for the linear rise of stress in the recorded measurements and is supported by other studies on the influence of MEW geometries on their mechanical behavior.<sup>[299]</sup> The rhomboid structures illustrated a certain degree of flexibility depending on the winding angle, allowing the construct to behave elastically in the direction of radial

4

tensile deformation before transitioning to plastic deformation. This allows the rhomboid geometry to assume vastly different mechanical properties depending on the chosen winding angle.<sup>[300]</sup> The aforementioned effect is presented in the recorded difference between the 34° (Peak Stress  $28.7 \pm 4.9$  kPa / Young's Modulus  $3.5 \pm 0.3$  kPa) and 70° (Peak Stress  $73.0 \pm 21.5$  kPa / Young's Modulus  $10.8 \pm 3.3$  kPa) rhomboid orientations (**Figure 3D**). The deviation between the generated samples is minimal within their group (apart from the 70° rhomboid constructs), highlighting the stable manufacturing process of the VolMEW constructs. The hexagonal structures differ from the rhomboids in their elastic properties due to the higher number of crossover points and the overall stable hexagonal geometry, resulting in a nearly linear mechanical behavior over the entire displacement range. For biological applications connective tissues and blood vessel walls are typically characterized by tensile stress-strain curves with an initial toe region (**Supplementary Figure S6**), indicative of the gradual recruitment of the ECM fibers in the direction of the application of the stress, followed by a stiffer region at higher deformations. A similar profile can be obtained with the rhombic MEW reinforcements at low winding angles (34°), while stiffer meshes in the radial direction can be obtained at higher winding angles (70°).<sup>[300]</sup> To enable a comparison to natural tissues, two porcine coronary arteries were measured in the same fashion as the VolMEW constructs. When comparing the rhomboid constructs to the porcine coronary arteries, the 70° (Blood Vessel 1: 72.4 kPa / 70°: 75.5 kPa) and 34° (Blood Vessel 2: 38.7 kPa / 34°: 37.3 kPa) VolMEW constructs showed a good approximation of the maximum stress levels, while the 34° rhomboid reinforced constructs also showed a comparable overall curve trajectory to the physiological specimens (**Figure 3F**). Due to inter-patient variability and the wide range of mechanical properties that vessels display even when taken from adjacent anatomical locations,<sup>[301]</sup> these results underscore the versatility of the proposed VolMEW system to modulate the mechanical profile of the printed composite tubes in order to approximate physiological blood vessel mechanics and to utilize the mesh design to account for natural variation. In summary, the presence of the MEW scaffolds endows the otherwise mechanically weak hydrogel construct with superior mechanical properties, and stress-deformation profiles approaching those displayed by native vessels.

Based on these findings, combined with the previously established superior light attenuation performance, further experimentation focused on the 34° rhombus geometry. A major benefit of MEW is the highly organized manner of fabrication and the consistent stacking of fibers, enabling a high degree of reproducibility and an additional adjustment point for mechanical properties.<sup>[124,125]</sup> The evaluation of the effect of different layer heights for the 34° rhomboid constructs illustrated an increase of maximum recorded stress (20L:  $18.5 \pm 4.2$  kPa / 40L:  $34.3 \pm 3.3$  kPa / 60L:  $37.3 \pm 1.5$  kPa), as well as an increase of Young's Modulus. (20L:  $2.9 \pm 0.3$  kPa / 40L:  $3.3 \pm 1.1$  kPa / 60L:  $5.3 \pm 0.9$  kPa) (**Figure 3G, H**). Assessing the ability of the constructs to operate in a range of strains closer to

biological values over an extended period is a valuable metric to record when looking into the mechanical properties of tubular constructs. A 200-cycle displacement to 20 % strain was used, and it revealed an increase in stiffness as a function of the number of layers of the MEW reinforcement geometries (control:  $1 \pm 0.3$  kPa / 20L:  $3.6 \pm 0.2$  kPa / 40L:  $3.8 \pm 1$  kPa / 60L:  $6.0 \pm 1.3$  kPa), except for the difference between 20 and 40 layers, where the SD and limit of recording resolution prevented any discernible significance from being recorded (**Supplementary Figure S6C**). It should be noted that although we focused on PCL as the MEW platform material and gelMA as VBP material in this study, the mechanical properties of the MEW fiber reinforcements could also be tuned by utilizing different biomaterial inks.<sup>[302–304]</sup> Regardless of the choice of material used for the fibrous reinforcement, another aspect to keep in mind in composite materials is the strength of adhesion between the fibrous inclusions and the embedding matrix (the hydrogel). In our case, observing the fracture behavior of the composite materials under tensile testing, it is possible to appreciate how failure occurs predominantly within the GelMA component, with the formation of a crack longitudinal to the direction of the bar used to apply the mechanical stress (**Supplementary Figure S7**). Notably, the fracture does not occur at the interface between the GelMA and the PCL fibers, nor is it aligned with the fibers themselves. This suggests that the interfacial strength between the two materials is likely superior to the tensile strength of the GelMA itself. Despite of this, should it be necessary for future applications to further improve the hydrogel-MEW mesh adhesion, several strategies have been reported in the literature, including surface treatments to the PCL to improve hydrophilicity,<sup>[277]</sup> or the introduction of covalent bonding between the two components,<sup>[305]</sup> among other possibilities.

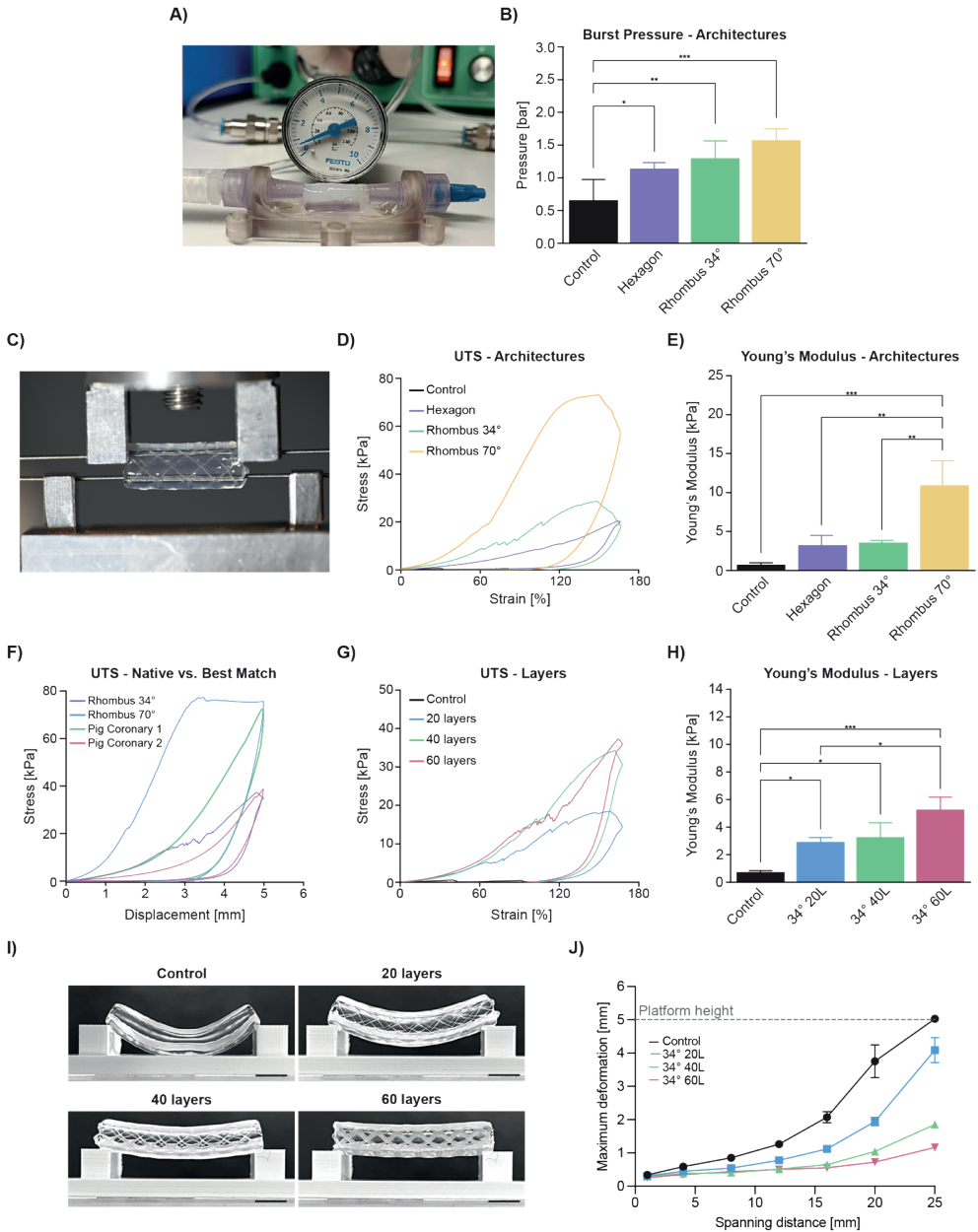


**Figure 3: Mechanical properties of VolMEW constructs with different mesh architectures and number of layers.** A) Photograph of the burst pressure test setup with the construct mounted and pressurized using part of a custom 3D printed bioreactor assembly. B) Burst pressure evaluation between different MEW reinforcement geometries (30 layers). C) Photograph of the customized mounting setup on the uniaxial tensile testing machine with the VolMEW construct in place. D) Ultimate tensile stress analysis for architectural differences between the tested MEW geometries (30 layers) within the VP tubes. Constructs were displaced to 5 mm, corresponding to 166% strain. E) Graphical depiction of Young's Moduli compared between MEW geometries (30 layers). F) Comparison



of VolMEW construct ultimate tensile stress (UTS) measurements with porcine coronary artery measurements obtained using the same tensile test setup and parameters. G) Ultimate tensile stress analysis of different layers of MEW construct reinforcement H) Graphical representation of Young's Moduli compared between different layers of MEW construct (34° rhombus geometry). I) Bending resistance was assessed by placing a volumetrically printed gelMA tube reinforced with 34° winding angle rhombus MEW meshes of different number of layers (0, 20, 40 and 60) on two 5 mm high columns spanning 25 mm in length to evaluate the maximum deformation of the printed construct (scale bars = 5 mm). J) Plotted average maximum deformation of control samples without MEW reinforcement and tubes reinforced with 34° winding angle rhombus MEW meshes of different number of layers (0, 20, 40 and 60; dotted line represents the maximum height of the columns on which the constructs were placed). \* =  $p < 0.05$ , \*\* =  $p < 0.01$ , \*\*\* =  $p < 0.001$ .  $n = 3$  for mean values, unless indicated otherwise.

In addition to tensile testing and burst pressure analyses, the shape stability of these VolMEW cylinders was assessed by evaluating their bending resistance. While a degree of bending flexibility can be desirable to manipulate the VolMEW tubes, unwanted collapse due to the inability of the tubes to sustain their own weight can be detrimental. The experiment was set up in a manner similar to the previously proposed filament collapse test, which has been used to evaluate the filament stability of extrusion-based printing materials.<sup>[306]</sup> Briefly, long (27.5 mm) composite tubes ( $t_{\text{print}} = 16.4$  s) were placed to bridge the distance across two columns spaced at increasing distance from each other (1–25 mm), and the gravity-induced flexural deformation of the tube was imaged and measured, as a function of the layer height (34° rhombic geometry) (**Figure 3I, J**). The most striking effect of the reinforcing MEW scaffolds was observed at the longest spanning distance of 25 mm. At this gap distance, where meshless 8% w/v gelMA cylinders completely collapse over the entire height of the column structure, increased resistance to bending is observed in the hybrid VolMEW samples as layer height increases (**Figure 3I, Supplementary Figure S8**). Spanning the largest gap of 25 mm, the 60-layer construct only underwent an average maximum deformation distance of  $1.16 \pm 0.04$  mm, significantly less than the 40- and 20-layer constructs ( $1.85 \pm 0.05$  mm and  $4.09 \pm 0.38$  mm respectively). A similar trend in bending resistance was also observed for some of the smaller spanning distances (20, 16 and 12 mm), down to the 8 mm gap and below, where the maximum deformation becomes undetectable across all samples (**Figure 3J**). Importantly for the versatility of this approach, it was also demonstrated that lower gelMA concentrations (*i.e.*, 5% w/v), which are often necessary for different cell types to thrive, the reinforcing effect of the MEW meshes is still evident in this bridging test (**Supplementary Figure S9, S10**). Overall, these mechanical evaluations confirm that the convergence of MEW with VP results in hybrid constructs exhibiting superior mechanical stability compared to pure gelMA constructs, thus enabling applications of these hydrogel-based constructs in a broader array of biologically relevant settings.

With a thorough understanding of the mechanical reinforcement provided by MEW fibers in the established VolMEW converged approach, the unique advantages of the VP process were further explored to create advanced and geometrically complex tubular structures (**Figure 4**). Attempting to introduce cell-laden hydrogels within tubular porous

structures, such as those produced by fused deposition modeling, melt electrowriting or solution electrospinning could be simply performed via casting in tubular molds. A major drawback of such casting approaches is the lack of precise control, which only allows the production of homogeneous cylindrical tubes consisting of a single gel layer (and thus a single layer of encapsulated cells). Alternative approaches are therefore needed to obtain, for instance, multilayered walls analogous to those found *in vivo* in vessels larger than 100  $\mu\text{m}$  in diameter. With the positional accuracy provided by VP, the relative orientation of the hydrogel layers in relation to the MEW mesh can be freely designed and modified (**Figure 4A**). This was demonstrated with prints in which the hydrogel layer reached the center of the mesh, leaving either the outer region of the scaffold gel-free (inner print; **Figure 4Ai, iii, v**) or its inner region gel-free (outer print; **Figure 4Aii, iv, vi**). Such structures would have potential applications in vascular tissue engineering by allowing a second layer of gel to be printed over the exposed region of the scaffold to guide cell attachment and directionality,<sup>[282,307]</sup> or to incorporate multiple materials and cell types within the same construct. Another physiologically relevant application of the positional control of hydrogel printing within the MEW mesh is the creation of micron-scale fenestrations (**Figure 4B**), features resembling, albeit at a larger scale than native structures, those commonly found in permeable vessels throughout the human body. These fenestrated vessel walls, already present in neovascular structures during development,<sup>[308]</sup> are abundant in different regions of the body where permeability is critical for nutrient and waste exchange, including the renal glomerulus,<sup>[309]</sup> intestinal blood vessels,<sup>[310]</sup> the nasal mucosa,<sup>[311]</sup> and are present in different areas of the central nervous system,<sup>[312]</sup> including the blood-brain barrier in certain neurological diseases including strokes.<sup>[313–315]</sup> Apart from these naturally occurring fenestrated structures, the clinical application of fenestrated stents for the repair of damaged vessels and aneurysms has also been a topic of interest, given the need to maintain transmembrane transport in the repaired vascular structures.<sup>[316–318]</sup> In this study, we have demonstrated how to generate similar types of leakage points throughout VolMEW printed tubes by taking advantage of the natural interactions at the interface between the bioprinted hydrogel structures and the MEW mesh (**Figure 4C**). During the fabrication of MEW scaffolds, intersecting print paths of the same layer (crossover points) create a local elevation due to more material being stacked on top of each other, while at the same time there is a sagging effect between two crossover points that further amplifies the elevation effect. These crossover points are herein exploited to create fenestrated structures (**Figure 4Ci**). To achieve this, hollow gelMA cylinders were volumetrically printed exactly in the center of a MEW scaffold, leaving the inner base of the mesh and the tip of the crossover points exposed, allowing for small fenestrations ( $\approx 10$ -micron range, comparable to the MEW fiber thickness) to form on the outer surface of the hydrogel layer (**Figure 4Cii, iii**). These small fenestrations were successfully produced throughout long tubular structures and remained perfusable, as evident by the outflow

of Alcian Blue stain through the exposed crossover points (**Figure 4D**). Importantly, the number and distribution of these fenestrations can be controlled by adjusting the number of pivot points of the MEW tubes, an easily adjustable parameter in the code used to fabricate these tubular scaffolds. It is clearly visible that the 4-pivot point scaffold (**Figure 4Di**) yields fewer fenestration regions compared to the 8-pivot point scaffolds (**Figure 4Dii**). The VP design alone was also tested to fabricate fenestration-like structures of decreasing size by stacking cylinders on top of each other with a minimum reproducible gap size of  $464 \pm 48 \mu\text{m}$  (**Figure 4Ei**). These cylinders remained bound together by the interwoven MEW fibers and also allowed lateral Alcian Blue outflow (**Figure 4Eii**). The combination of macroscale VP- and micron-scale crossover VolMEW fenestrations (as low as hundreds of nanometers)<sup>(125)</sup> could introduce hierarchical pore distribution with spatial control along the length of the tube, while spanning a wide range of pore sizes within the same hydrogel shell. It should be noted that the density of larger, VP-induced pores should be carefully controlled, as placing too many of these gaps in close proximity to each other could significantly affect the structural stability of the printed constructs. Furthermore, it is important to note that the resolution of these fenestrations is determined by the thickness of MEW fibers and does not match native fenestration sizes. However, this approach could be exploited for other *in vitro* applications that require the controlled creation of micro-scale pores, and further developed to more closely mimic native structure scales. These experiments further demonstrate the potential of the VolMEW convergence, as the incorporation of MEW constructs not only plays a mechanical role in VP printing, but can also be exploited to create more complex, native-like tubular structures when combined with the design freedom offered by volumetric printing.

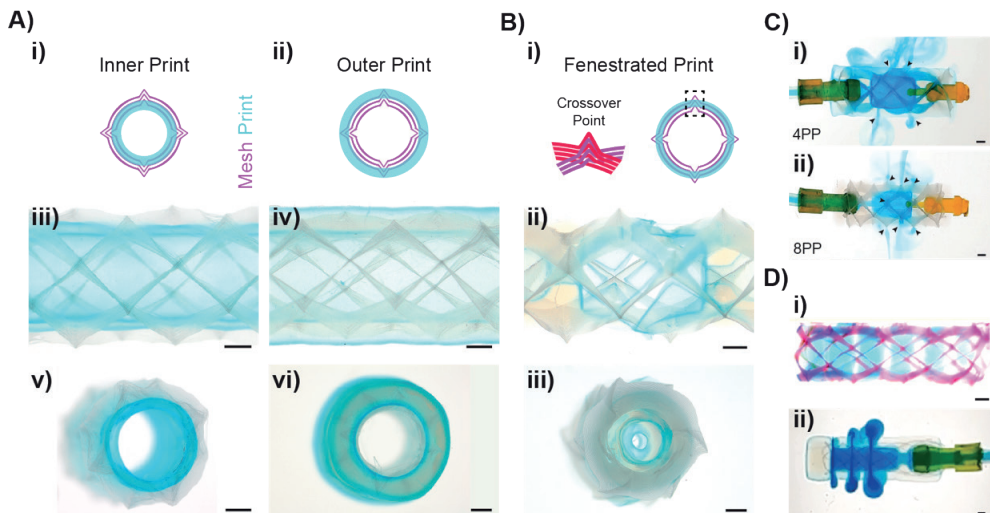


**Figure 4: Printing of complex tubular structures and fenestrations.** A) Graphical overview of possible i) inner and ii) outer printing strategies, in which the hydrogel embeds only the inner or outer region of the MEW construct respectively, leaving the rest exposed. Stereomicroscopic images of these iii, v) inner and iv, vi) outer

prints from iii, iv) top and v, vi) side views. B) VolMEW printing of fenestrated tubular constructs i) Graphical representation of the characteristic crossover points of tubular MEW meshes, and the resulting fenestrations when a thin layer of bioresin is printed exactly in the middle of the MEW construct. Stereomicroscopic images of the ii) top and iii) side views of such fenestrated structures. C) MEW induced fenestration showing local filtration at crossover points where the mesh pierces the hydrogel construct with i, ii) adjustable leakage over time based on the number of crossover points (black arrows) controlled by pivot points (PP). D) Circular fenestrations i) lightsheet maximum projection highlighting the ability to tailor fenestration size ii) light microscope image of the perfusable VolMEW construct with controlled leakage of Alcian Blue stain through the fenestrations, undisturbed by the presence of the MEW meshes. Scale bars = 1 mm.

In addition to introducing the freedom to control the degree of alignment and the presence of pores and fenestrations, the hybrid VolMEW approach also facilitates, for the first time, the integration of complex architectural structures in the outer and inner regions of the MEW-reinforced tubular structures (**Figure 5**). Current approaches, based on hydrogel casting and extrusion bioprinting do not easily allow for the integration of complex architectural elements around and within the pre-existing MEW mesh, mainly due to the presence of moving needles in extrusion printing, and the challenges of mold removal in the case of casting. By fully encapsulating the MEW scaffold in a single step using the VP approach, hydrogel regions with increased design freedom were created. Importantly, it was first shown that the light attenuation effect of the MEW mesh on the VP process explored in **Figure 2** did not affect the printing resolution of features within the tubular structures (**Figure 5A**). To do this, the differences in feature size of a sinusoidal strut running through the lumen of a VolMEW tube were evaluated in comparison to hydrogel-only prints (**Figure 5Ai,ii**). The average strut thickness between the mesh-free and reinforced constructs did not exhibit significant differences, thus further cementing the fact that the light attenuation induced by the MEW mesh did not hinder the VP process (**Figure 5Aiii**). To illustrate the ability to print distinct, high-resolution components within the MEW mesh in a more widely distributed manner, a tubular structure lined with villi-like pillars oriented in different angles was successfully resolved (**Figure 5B**). The villi structures were successfully resolved ( $232.3 \pm 35.5 \mu\text{m}$  average thickness), did not fuse to one another and could be designed to match physiological length to width ratios.<sup>[319,320]</sup> It should be noted that the purpose of these printed structure is to highlight the potential to resolve protrusions that can be easily produced within the PCL mesh-laden tubes via volumetric printing, but not with other approaches, and that native intestinal villi in humans show comparable dimension, but are present at higher densities. Next, to demonstrate the addition of complex geometries on the outer side of the VolMEW tubes, branching channels stemming from the reinforced tube were successfully printed ( $t_{\text{print}} = 18.5 \text{ s}$ ). Both the reinforced and non-reinforced channels were homogeneously perfused, as the porous MEW mesh allowed for a seamless connection between the channels, demonstrating the potential to create more complex and reinforced branching structures that are crucial to replicating native vascular networks (**Figure 5C**). Additionally, the ability to print complex structures within the lumen of VolMEW reinforced tubes was

demonstrated, a mathematically derived Schwarz D lattice was printed within the gelMA cylinder, as proof-of-concept design (**Figure 5D**). While these types of structures have previously been printed on a volumetric printer,<sup>[286]</sup> it is remarkable that, even in the presence of the opaque MEW mesh, these fully perfusable structures could be resolved with a printing accuracy of  $764 \pm 48 \mu\text{m}$  ( $t_{\text{print}} = 14.8 \text{ s}$ ).

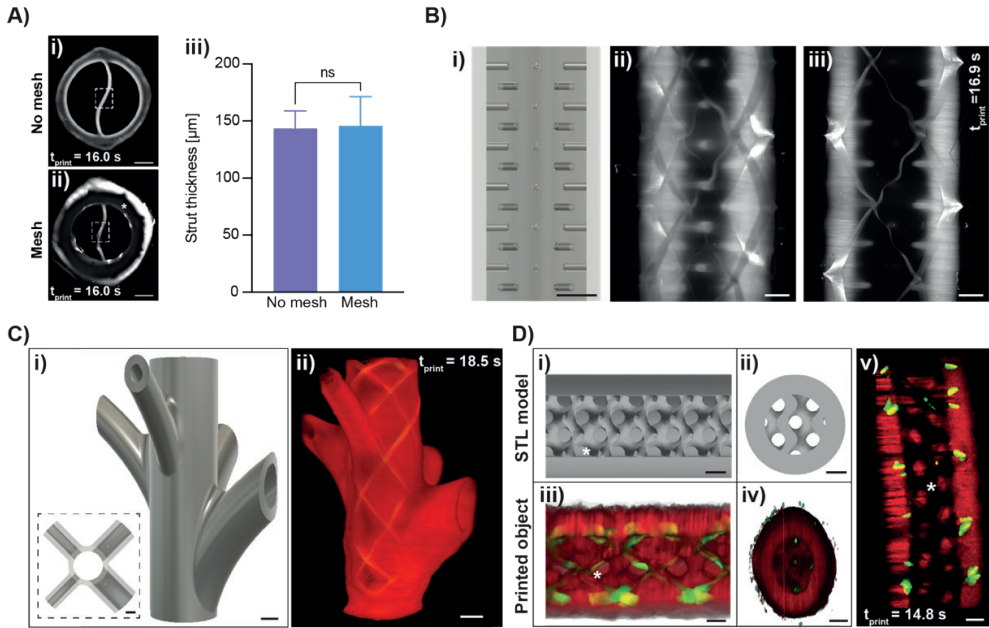


**Figure 5: High-resolution VolMEW printing demonstrating external and internal features of physiological relevance.** A) Printing resolution of positive features in mesh-free samples i) as shown through stereomicroscopy images and in the presence of a 40-layer MEW mesh ii) as shown in a lightsheet microscopy image (dotted-box represents the measured strut, asterisk represents the area in which the MEW mesh is embedded). iii) Comparison of printing resolution between mesh-free and mesh. B) Digital model of a tubular structure consisting of several interspaced villus-like structures protruding into the lumen of an open channel, and ii-iii) different lightsheet microscopy slices of the model showing the presence of villi throughout the tubular structure. C) Digital model of a branched structure with channels of different diameters (dotted box shows the top view of the model) and ii) 3D reconstruction of the printed structure from lightsheet microscopy imaging. Di-ii) A digital model of a VolMEW printed Schwarz D structure inside a cylinder containing the reinforcing MEW mesh from lateral and vertical cross-sectional views and iii-iv) the corresponding lightsheet 3D volume reconstructions and v) a central lightsheet fluorescence image of the printed structure with the gel structure (red) and the encapsulated MEW mesh (green) highlighting the high printing resolution within the inner diameter of the mesh. Scale bars = 1 mm.

The presented range of architectures printed within reinforced VolMEW tubes highlights the fact that the inherent freedom of design of VP is maintained in this hybrid approach, and can bring about important advantages to different applications in tissue engineering. Another of these advantages was the incorporation of customizable, modular components to the tubular models shown here, that could facilitate the direct connection of VolMEW structures into leak-free perfusion systems (**Figure 6**). The role of perfusion in

the development of native-like tissues has been thoroughly explored in the field of tissue engineering, with the development of dynamic perfusion bioreactors and microfluidic systems gaining increasing interest in the last years.<sup>[321]</sup> Here, a major challenge when working with soft hydrogels is ensuring a tight and leak-free perfusion that can be maintained for long-term. In conventional casting/molding approaches, incorporating customizable inlets comprising a combination of narrowing and opening lumen diameters that allow for these tight connections, is very difficult when not unfeasible, especially when using low stiffness hydrogels like the ones applied in this work. **Figure 6** demonstrates how VolMEW can leverage the design freedom offered by VP to create readily perfusable constructs by incorporating fitting inlets to the tubular prints shown throughout this manuscript. First, custom-made connectors consisting of an O-ring to seal the inlet point of the tubular structures were developed, and a negative of these structures was incorporated into the tubular structure 3D models (**Figure 6Ai,ii**). These modular constructs enabled the leak-free, sterile perfusion of simple tubular structures for up to 7 days under sterile conditions (tested in cell-free constructs), whereas the connector-free, straight tubes immediately exhibited multiple leakage points (Figure 6Aii,iii). To demonstrate the feasibility and functional advantages of these modular constructs, perfusable models showing asymmetric ( $t_{\text{print}} = 18.5$  s; **Figure 6B**) and symmetric ( $t_{\text{print}} = 16.0$  s; **Figure 6C**) narrowing of the VolMEW lumen to mimic stenosis were printed and could be immediately perfused. Continuous blood perfusion (**Figure 6Ciii**) through the symmetrical stenosis model resulted in a rapid blockage of flow at the stenotic region of the construct, and upon gentle flushing the formed blood clot could be observed occluding the narrow region of the construct (**Figure 6Civ**). To highlight the versatility of this modular approach, a simplified venous valve model (**Figure 6Di**) was successfully printed at high resolution within VolMEW reinforced tubes, with leaflets measuring  $232 \pm 10 \mu\text{m}$  ( $t_{\text{print}} = 11.9$  s) (**Figure 6Dii**). The valve, as found in the native structure, was able to control flow in a unidirectional manner in response to flow pressure, with the leaflets bending towards each other and closing, preventing flow in one direction (**Figure 6Diii**), but remaining unstressed and open in the other direction, allowing uninterrupted flow (**Figure 6Div**). In this case, a different shaped connector was used, further showing the versatility of the VP, moldless- and contactless approach, to accommodate for virtually any geometry. The male part of the connector, could be produced on-demand using DLP printing, and tailored to the perfused structure and perfusion flow rates necessary for specific applications as previously shown.<sup>[321]</sup>

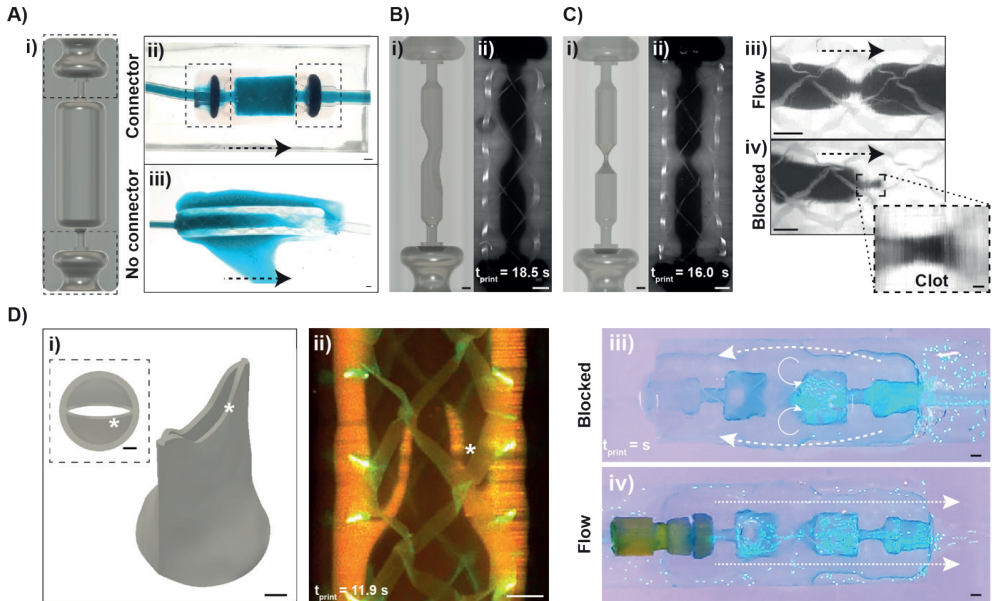


**Figure 6: Volumetric printing of custom connectors to create leak-free perfusable systems of physiological relevance with flow-dependent behavior.** Ai) Digital model of a custom-made connector printed as an inlet and outlet of a MEW-reinforced tubular structure (dotted line shows the connector area added to the tubular print model). Stereomicroscope images of VolMEW-printed tubes ii) with and iii) without the custom-made connector (dotted lines) ends as they are perfused with Alcian Blue solution to visualize leakage points: being perfused in a homogeneous manner (arrows indicate the direction of flow). Bi) A digital model of a VolMEW complex stenosis model showing asymmetrical channel narrowing along the length of the printed tube and ii) a lightsheet microscopy image showing the inside of the resulting printed channel. Bi) A digital model of a VolMEW stenosis model with symmetrical narrowing of the lumen and ii) a lightsheet microscopy image showing the inside of the resulting printed channel. iii) Constant perfusion (arrows represent the direction of flow) of blood through the symmetrical stenosis model showing iv) blockage of flow at the stenosis region after minutes due to the formation of a blood clot (shown at higher magnification in the dotted box). Di) Digital model of a simplified venous valve model and ii) a central lightsheet section of the printed construct showing the high resolution leaflets (\*) of the valve. iii-iv) Digital images of fluorescent beads perfused through the valve structure using a different fit of DLP-printed connectors, showing unidirectional flow (dotted lines show the outline of the printed construct and arrows indicate the direction of flow). Scale bars = 1 mm.

After successfully demonstrating the ability to print these different geometric features (complex branched structures, stenosis models, valves, etc.), create ready-to-perfuse systems and given the promising mechanical properties of the hybrid VolMEW scaffolds, the possibility of forming cell-laden constructs containing multiple cell types by both direct bioprinting and by post-print seeding was investigated. To make this possible, we devised a strategy to sequentially, volumetrically print multiple cell-laden hydrogel layers (**Figure 7A**), followed by a seeding phase in the lumen of the tube, resulting in a three-layer construct (**Figure 7B**). As a preparatory step, using a single fluorescently labeled suspension of human bone marrow-derived mesenchymal stromal cells (DiD-hbMSCs), it was shown that cell-laden gelMA resins could be printed to precisely envelop

the MEW scaffold ( $t_{\text{print}} = 14$  s), and the resulting hybrid, cellularized construct maintained high cell viability (**Supplementary Figure S11**) and could then be seeded with human umbilical vein endothelial cells (HUVECs) after printing (**Figure 7C**). This resulted in a two-layer construct with independent cell regions, an inner HUVEC layer (**Figure 7Di**) and a 3D gelMA layer encapsulating hbMSCs and the MEW scaffold to provide mechanical stability to the structure (**Figure 7Dii**). Next, we focused on providing a proof-of-concept demonstration of the possibility to perform volumetric printing across MEW meshes also in presence of cells, with the capacity to pattern multiple cell-types, mimicking the structuring of blood vessels. For this, three distinct cellular layers were fabricated using the hybrid VolMEW approach. Native macro-scale vessels, such as veins or arteries, have three distinct cell layers, the tunica intima, media, and externa, each consisting of different cell types (endothelial, smooth muscle, and fibroblasts, respectively) and matrix composition required for proper vessel function (**Figure 7E**). Our model tubular construct consisted of the previously described two-layer approach, but by adding a second VBP step with a new cell suspension (hbMSCs, which have the capability to differentiate towards smooth muscle cells and fibroblasts, in presence of the appropriate signals,<sup>[322–324]</sup> labeled with a different fluorescent dye, Dil), an outer cell and material layer was successfully printed, creating a three-layer architecture that approximates the layered structure of a native vessel (**Figure 7F, G**). Furthermore, the possibility of creating fenestrated, cellularized constructs was also demonstrated using the principles described in Figure 4. By first creating the first hydrogel layer as an inner print, leaving the outer edge of the vessel exposed, the second layer could still be printed within the MEW scaffold, leaving the small crossover points of the mesh exposed to the outside, creating the previously shown perfusable fenestrations in a cellularized model (**Figure 7H**). These final proof-of-principle prints demonstrate that the use of the VolMEW hybrid approach can be exploited in several ways to increase the complexity of current tissue engineered macrovascular-inspired structures. While our experiments constitute a feasibility study for VolMEW as a bioprinting tool, future work aiming to produce fully functional vessel should first focus on extended culture time under flow to promote endothelial cell maturation, optimizing a proper tri-culture media system to either feed directly printed endothelial, smooth muscle cells and fibroblasts, or to induce the differentiation of MSCs into smooth muscle and fibroblastic phenotypes. Several biofabrication approaches have been explored to create architecturally complex vessels,<sup>[325]</sup> including sacrificial extrusion templating,<sup>[326,327]</sup> coaxial extrusion bioprinting,<sup>[328]</sup> suspended bioprinting<sup>[329]</sup> and suspended sacrificial printing,<sup>[330]</sup> digital light projection printing,<sup>[235,331,332]</sup> and acoustic wave patterning.<sup>[62,333]</sup> Expanding on this toolkit, VolMEW introduces the ability to both tune the mechanical properties of the construct and to introduce custom-designed patterns of microfibers, which have been used in previous work to facilitate stromal cell alignment.<sup>[284]</sup> Notably, and with broad applications beyond of vascular-mimetic printing, VolMEW allows to



freely sculpt the hydrogel component, creating features that intertwine with the MEW mesh, or, for example, incorporate fenestrations and branches relevant for hierarchical networks,<sup>[325]</sup> and valve-like structures, of relevance to regulate flow and local pressure in vessels and more generally in fluidic components. While conventional approaches (*i.e.*, casting) are still suitable when producing simple, single component tubes, VolMEW does not require to build and remove a physical mold, therefore facilitating the fabrication step, and improving precision. This facilitates the incorporation of complex structures within and around the reinforced tubes that would pose significant complications for casting procedures. Additionally, by printing with tomographic light patterns, hydrogel layers thinner than the reinforcing MEW mesh can be easily obtained, as shown in **Figure 4**. These architectures can be printed in seconds with no need for support materials, incorporating a mechanically reinforcing MEW mesh without compromising print resolution. Moreover, while this study focused on the advantage of producing mechanically competent grafts even when using soft hydrogels for tissue culture, previous literature provide consistent data that certain cell types, including different types of muscle cells, are able to align following the directionality of the MEW fibers, even when these are embedded in a hydrogel matrix.<sup>[167,200,334]</sup> Future research on VolMEW could investigate this potential, for example to guide cell orientation in vessels including, *i.e.*, a smooth muscle cell layer. Freedom of design in this contactless printing approach allows to produce architectures that cannot be easily obtained with other methods, and can therefore be potentially applied to produce patient specific *in vitro* models, in which the effect of flow as a function of the (vascular) geometry, could be studied. This has implications, for instance, for systems to predict the kinetics of stenotic processes (in line with the proof of concept shown in Figure 6B-C), or even to produce personalized grafts for regenerative medicine. Overall, these features make VolMEW promising for the creation of next-generation tubular grafts with customizable designs that can be tailored to tissue-specific requirements and produced in high-throughput.

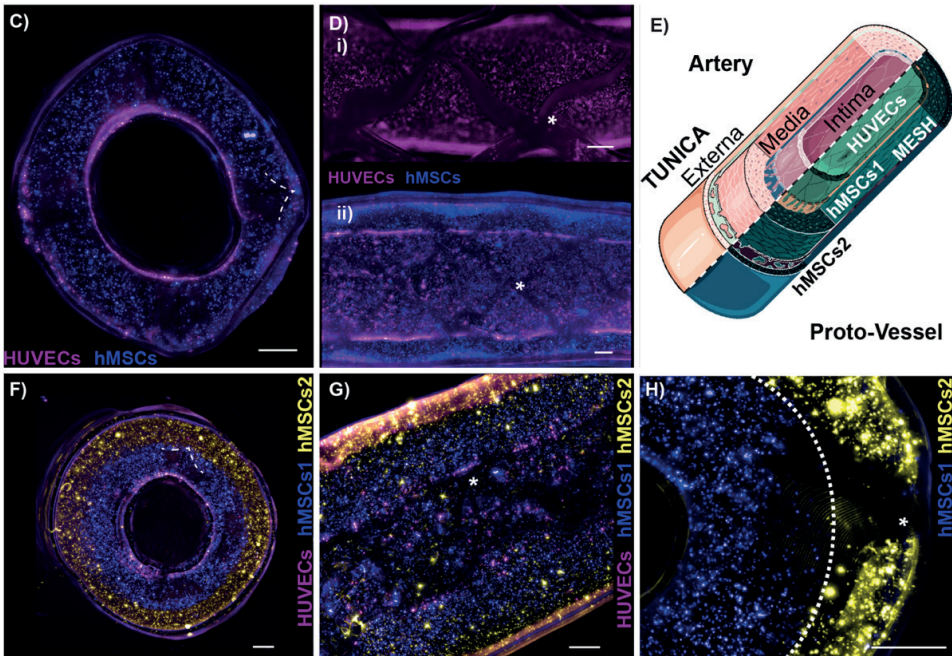
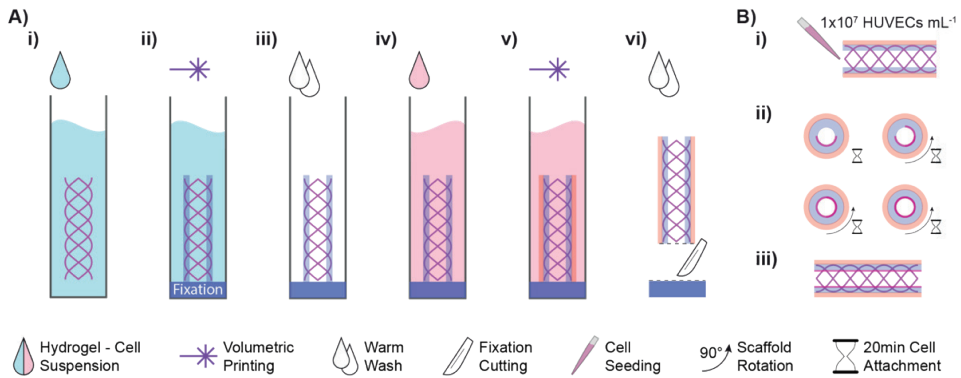


**Figure 7: Sequential VolMEW printing of cell-laden, multi-material and multi-layer tubular constructs.** A) Graphical overview of the multi-material VolMEW printing process with cell-laden bioresins. i) The MEW mesh is inserted as previously described followed by ii) VBP of the scaffold with an overexposed fixation, whereby the construct is firmly attached to the printing vial. After iii) washing the residual, uncrosslinked hydrogel, iv, v) the process is repeated with the second material. Finally, the vi) fixation is cut with a scalpel. B) Depiction of the HUVEC seeding process, where first i)  $1 \times 10^7$  cells  $\text{mL}^{-1}$  are pipetted into the construct, followed by ii) 20 minutes of incubation periods ending with  $90^\circ$  rotations. The process is repeated four times to homogeneously cover all sides to create iii) the final three-layer VolMEW construct. C) Perpendicular and Dii) longitudinal cross-sectional fluorescence images of a two-layer VolMEW-printed tubular construct consisting of VBP-printed hbMSCs (blue) in the gel layer encapsulating the MEW mesh and i) a HUVEC-seeded lumen (magenta) (dotted line represents the position of the MEW mesh crossover point). E) Diagram of native vessel structures compared to the VolMEW printed proto-vessels. F) Perpendicular and G) longitudinal cross-sectional fluorescence images of a tree-

layer VolMEW printed tubular construct consisting of VBP-printed hbMSCs (blue and yellow) in the gel layer encapsulating the MEW mesh and a HUVEC-seeded lumen (magenta). H) Sequentially printed multi-material construct with crossover points exposed, embedding the MEW mesh in both layers (asterisk represents the MEW mesh crossover point tip, and dotted line represents the separation between printed cell layers). Panel E was partly generated using Servier Medical Art, provided by Servier, licensed under a Creative Commons Attribution 3.0 unported license. Scale bars = 500  $\mu\text{m}$ .

## CONCLUSIONS

This study demonstrates, for the first time, the convergence of volumetric bioprinting with melt electrowriting to build geometrically complex objects with enhanced mechanical properties, even when using low stiffness bioresins commonly used in VP. In the first stage of the study, we presented the VolMEW setup, which takes advantage of the thermal gelation properties of gelMA and a custom-designed guide system to precisely place and align MEW constructs of different architectures. While the presence of MEW constructs in the VP vial is shown to attenuate the tomographic light path, VP-printed layers were successfully, and precisely sculpted onto and across the opaque microfibrinous meshes with high shape fidelity. Furthermore, the reinforcing effects observed in these converged printing constructs show mechanical advantages in flexural, burst and tensile strength compared to non-reinforced scaffolds, reducing the gap between these hybrid biofabricated constructs and native tubular tissues of biological relevance, such as vascular structures. This newly developed approach also retains the high printing speeds (< 20 seconds) and unparalleled design freedom associated with conventional VP. Exploiting this architectural freedom, an array of hierarchical, physiologically relevant constructs could be produced. This includes custom-designed and distributed wall fenestrations and complex printing of gyroid-structures, bifurcated channels and a functional venous valve model within the reinforced hydrogel tubes. As a proof-of-concept, the possibility of creating multi-material and multi-cellular structures through a sequential printing approach was also demonstrated. The three distinct layers found in native macro vessels (*i.e.*, veins and arteries) could be replicated in these reinforced, composite structures, demonstrating the potential to create hierarchical living constructs with the VolMEW approach. Notably, since the MEW meshes can be bulk produced and stored to printing, future applications can be envisioned, in which off-the-shelf mesh geometries could be readily loaded into a volumetric printer, to add the hydrogel and cellular components, just before their intended application. Overall, this novel technique poses the possibility of creating volumetric composite objects from materials with very different chemical and physical properties (hydrogels and thermoplastics) with enhanced mechanical properties and high design freedom. By leveraging the advantages of the MEW and VP technologies in the present approach, these findings also provide exciting opportunities for future hybrid applications with other opaque materials (*i.e.*, ceramics, metals) for advanced tissue engineering strategies.

## EXPERIMENTAL SECTION

*Materials:* For melt electrowriting, medical-grade polycaprolactone (PCL) (PURASORB PC 12, Corbion Inc., Gorinchem, The Netherlands) was used to fabricate the MEW tubular scaffolds. As a bioresin for volumetric (bio)printing, gelatin methacryloyl (93.5% DoF) was synthesized as previously reported<sup>[335]</sup> and used as 5% w/v (cellular experiments), 15% w/v (venous valve) and 8% w/v (all others) solution in phosphate-buffered saline (PBS). As photoinitiator, 0.1% w/v lithium phenyl(2,4,6-trimethylbenzoyl)phosphinate (LAP, Tokyo Chemical Industry, Japan) was supplemented to the hydrogel precursor solution to initiate the photocrosslinking reaction.

*Melt electrowriting of tubular structures with different geometries:* Tubular MEW constructs were processed using two custom-made melt electrowriting devices with a cylindrical and interchangeable collector. One device, used to fabricate tensile test specimens, employs an Aerotech axis system (PRO115) and the A3200 (Aerotech, USA) software suite as coding and machine operating interface. Polypropylene cartridges, and 22G flat-tip needles (Nordson EFD, USA) were used. The second device, used for all other experiments, has been described elsewhere<sup>[282]</sup> and was used with an electrically heated 3 mL glass syringe and a 25G needle. A modified code was developed similar to previous work,<sup>[279]</sup> to move the collector in translational and rotational directions for precise fiber placement onto a rotating steel mandrel at predetermined winding angles.

*Thermally controlled incorporation of tubular MEW meshes into volumetric printing setup:* In order to insert the tubular MEW scaffolds in a perfectly centered and reproducible manner, the scaffolds were transferred to 3mm pultruded carbon fiber rods (easycomposites, The Netherlands) matching the inner diameter of the MEW mesh. To center the rod inside a Ø10 mm cylindrical borosilicate glass vial compatible for use with the volumetric printer, small inserts were printed on a Perfactory 3 digital light projection (DLP) 3D printer (Envisiontec, Germany) using PIC100 resin to fit the rod and perfectly match the inner diameter of the vial. To fix the samples in the center of the vial, the tubular mesh was placed on the end of the insertion rod with 5mm offset. The printing vial was then filled with preheated (37°C) bioresin and the rod was inserted. The vial was subsequently placed in ice water up to the beginning of the insertion rod until gelation occurred. The gelled bioresin holds the tubular mesh firmly in place. The insertion rod is raised to the upper limit of the tubular mesh and the gelation process repeated, resulting in a centered sample.

*Volumetric (bio)printing process:* A commercial Tomolite v1.0 (Readily3D SA, Switzerland) volumetric printing setup was used to fabricate the hybrid VolMEW constructs. The gelMA bioresin-infused MEW meshes were prepared as described above in Ø10 mm cylindrical borosilicate glass vials and kept cool at 4° C to ensure that the resin remained thermally gelled. Custom-designed CAD files (Fusion360) were loaded and processed using the Readily3D Apparite software (b11409a). The average light intensity across all prints was

set at  $12.16 \text{ mW/cm}^2$ . Venous valve models were additionally printed using Apparite's proprietary settings for a bulk length of  $400 \mu\text{m}$  and a bulk multiplier of 2x. After printing, the thermally gelled bioresin was gently washed with pre-warmed PBS at  $37^\circ \text{C}$  to remove the uncrosslinked resin from the printed structure. To achieve homogeneous crosslinking and facilitate sample handling, the samples were immersed in a 0.01% w/v LAP solution and post-cured for 5 min in an UV oven (CI-1000, Ultraviolet Crosslinker,  $\lambda = 365 \text{ nm}$ ,  $I = 8 \text{ mW/cm}^2$  UVP, USA). All printed structures for mechanical analysis and complex geometries were printed at a gelMA concentration of 8% w/v, except for the venous valve model. For this structure, a 15% w/v GelMA concentration was selected for the sake of visualization and handling, as stiffer hydrogels provided higher yield strength of the printed leaflets, and therefore withstood higher pressures when flow was directed against the closed valve. All cell-laden constructs were printed at a gelMA concentration of 5% w/v.

*Measurements of MEW mesh light attenuation effect during VP:* Tubular MEW meshes were placed in cylindrical vials containing the gelMA resin. The vials were then placed within the print area of the volumetric printer and coupled to the rotary stage (Newmark RB-90). Index matching was achieved by immersing the vial in a square cuvette containing distilled water. A virtual beam was generated by encoding a circular region of on-sate pixels on a DMD (Vialux Hi-Speed V-7000) illuminated by a collimated 520nm source. This corresponded to a beam waist diameter of  $200 \pm 10 \mu\text{m}$ . The vial was positioned so that the virtual beam was incident on the central axis of the embedded MEW mesh and the vial. A biased photodetector (Thorlabs DET36A2) was positioned  $100 \pm 5 \text{ mm}$  behind the vial and was used to measure the relative intensity of the incident light after attenuation by the scaffold. A digital acquisition board (National Instruments USB-6001) was used to acquire the voltage signal from the photodiode. In order to perform the measurement, the virtual beam was turned on and the vial was rotated at a rate of  $36 \text{ deg sec}^{-1}$  over a full rotation. The resulting voltage signal from the photodiode was recorded at a sampling rate of 50 Hz. For each sample, this measurement was acquired at 3 locations on the MEW mesh, with the virtual beam being offset by +3 mm and -3 mm from its central position. The acquired data was normalized with 100% being the maximum amount of light detected across all runs. The runs were then rotated to start at the first peak using Savitzky-Golay filtering, followed by finding the first local maximum, and the resulting phase-matched raw data were averaged using time synchronous averaging (MATLAB R2022a). The area under the curve was approximated using discrete trapezoidal numerical integration and the data were normalized (deg) and plotted (MATLAB R2022a).

*Tensile testing of hybrid VolMEW constructs:* To determine the radial mechanical properties of the VolMEW constructs, a customized two-pin mounting setup was used on a dynamic mechanical tester (Electron-Force 5500, TA Instruments, USA). Two metal pins were inserted through the luminal cavity of the constructs and a radial tensile force was applied

during the test procedure (Figure 3A). Samples were measured in a 100-cycle waveform setup with a peak displacement of 18% strain with respect to the inner tube diameter. Construct measurements were evaluated after the initial hysteresis had subsided and the peak force had stabilized over several cycles. A second evaluation was a pull to 166% strain to elucidate the maximum stress values at beyond physiological values of small diameter blood vessels.

*Burst pressure analysis of VolMEW constructs:* A Vieweg DC 200 (Vieweg, Germany) dispenser, which uses pressurized air to dispense material, was used with a custom tubing array that included a pressure gauge for readout and a Luer connector to a custom-made bioreactor assembly part created by DLP printing on a Prusa SL1s resin printing system (Prusa, Czech Republic) with Dreve FotoDent guide 405 nm (Dreve, Germany). The resin was also used to fix VolMEW constructs liquid tight into the assembly part, a thin cover of FotoDent has been applied to the connectors and cured with a Prusa CW1 curing and washing station (Prusa, Czech Republic). Vaseline was then injected into the VolMEW construct through an attached printer cartridge (Nordson, USA) until the construct's lumen was completely filled with Vaseline. The opposing end of the assembly was then sealed off and air pressure applied via the printer cartridge by the dispenser until failure of the constructs could be observed by Vaseline breaking through the construct. Data collection was done by digital video recording of VolMEW constructs consisting of MEW meshes of different architectures and number of layers.

*Bending resistance evaluation of VolMEW constructs:* To evaluate the effect of MEW mesh incorporation on the bending resistance of the hydrogel constructs, 27.5 mm long VolMEW scaffolds were printed with meshes of rhombic pores with 34° winding angle consisting of different layer numbers (0, 20, 40 and 60). Based on the previously established filament collapse test developed to evaluate the shape fidelity of bioinks<sup>[306]</sup> similar 5mm column structures were printed from polylactic acid (PLA, MakerPoint) using a fused deposition modeling printer (Ultimaker S3, Ultimaker, The Netherlands) with gaps of 25, 20, 16, 12, 8 and 4 mm, to assess the maximum deformation of the printed structures as they spanned each gap distance. Maximum deformation was measured as the lowest point the sample bent downwards from the top of the column structure.

*Blood clotting assay in symmetric stenosis model:* Equine blood was collected in 3.2% citrated tubes at the Horse Clinic, Faculty of Veterinary Medicine, Utrecht University, as redundant sample from veterinary surgery practice, in accordance to the institutional ethical committee of Utrecht University. Citrate prevents blood from clotting immediately after extraction. To allow blood to clot again it needs to be recalcified previous to the experiment. The recalcification buffer consisted of 63.2 mM  $\text{CaCl}_2$  and 31.6 mM  $\text{MgCl}_2$ . Tubing used for blood perfusion was coated in a 200 mM  $\text{CaCl}_2$ , 0.1  $\mu\text{L mL}^{-1}$  Heparin, 1% BSA, 1% Glucose in HEPES solution overnight to prevent the blood from clotting in it. Blood

was continuously perfused through the symmetric stenosis model at a flow rate of  $0.58 \text{ mL min}^{-1}$  using a syringe pump (AL-2000, World Precision Instruments). The tubes were perfused for 10 minutes or until blockage was observed due to blood clotting. Videos and images of the perfused model were acquired with an Olympus SZ61 stereomicroscope coupled with an Olympus DP70 digital camera (Olympus Soft Imaging Solutions GmbH, The Netherlands).

*Cell isolation and culture:* Green fluorescent human umbilical vein endothelial cells (GFP-HUVECs; cAP-001GFP, Angioproteomie) were expanded in type I collagen precoated culture flasks in endothelial cell growth medium-2 (EGM-2) BulletKit medium (CC-3162, Lonza). Culture flasks were precoated with  $50 \mu\text{g mL}^{-1}$  collagen I rat tail (354236, Corning) in 0.01 M HCl for 1 hour at  $37^\circ\text{C}$ , followed by two washes with phosphate-buffered saline (PBS). GFP-HUVECS were used in experiments at passage 6-7 and cultured in EGM-2 medium for expansion and differentiation. Human bone marrow-derived mesenchymal stromal cells (hbMSCs) were isolated from bone marrow aspirates of consenting patients, as previously described.<sup>[336]</sup> Briefly, human bone marrow aspirates were obtained from the iliac crest of patients that were receiving spondylodesis or hip replacement surgery. Isolation and distribution were performed in accordance with protocols approved by the Biobank Research Ethics Committee (isolation 08-001, distribution protocol 18-739, University Medical Center Utrecht). Protocols used are in line with the principles embodied in the Declaration of Helsinki. MSCs were expanded in DMEM + GlutaMAX supplemented with FBS (10% v/v) and p/s 1%. The procedures for human tissue and cell isolation were approved by the Research Ethics Committee of the University Medical Center Utrecht.<sup>[336]</sup> All cells were cultured at  $37^\circ\text{C}$ , 5%  $\text{CO}_2$  and used at passage 4-5. HbMSCs were cultured in DMEM + GlutaMAX supplemented with FBS (10% v/v) and p/s 1%. All cells were cultured at  $37^\circ\text{C}$  and 5%  $\text{CO}_2$  and used at passage 4-5.

*Volumetric bioprinting of reinforced multilayered macrovessel-like structures:* Mechanically reinforced macrovessel structures mimicking the layered structure of native vessels (tunica intima, media and externa) were fabricated using a sequential bioprinting approach. The following procedure was used to fabricate two- and three-layer protovessel constructs. First, a 15mm hybrid VolMEW hollow tube was printed with  $1 \times 10^6 \text{ cells mL}^{-1}$  hbMSCs labeled with membrane staining DiD (ThermoFisher Scientific, The Netherlands) encapsulated in 5% w/v gelMA + 0.1% w/v LAP bioresin. In this first layer, a MEW scaffold (40 layers) with rhombic pores of  $34^\circ$  winding angle and 8 pivot points was incorporated and completely encapsulated by the printed gel layer of  $1050 \mu\text{m}$ . For the 3-layer structure, the sample was washed after the first printing step and re-infused in a bioresin suspension containing  $5 \times 10^5 \text{ cells mL}^{-1}$  hbMSCs labeled with membrane staining Dil (ThermoFisher Scientific, The Netherlands), and a second outer layer of  $800 \mu\text{m}$  was printed around the first cell layer. Samples were washed, post-cured for 5 minutes and cultured in hbMSC expansion medium overnight. The next day, the samples were placed on a rectangular

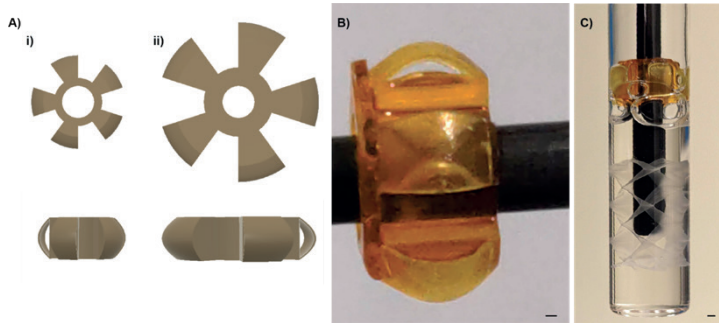
mold with a concave slot for the tube to rest on, and the channels were seeded with a suspension of  $1 \times 10^7$  cells  $\text{mL}^{-1}$  GFP-HUVECs. Samples were rotated  $90^\circ$  every 20 minutes, for a total span of 80 minutes to achieve homogeneous cell seeding across the lumen of the protovessel. To create a fenestrated 3-layer protovessel, the same protocol was used, but the total width of the two cell layers was reduced to allow for overprinting of the MEW mesh outside the gel sample. Lateral and longitudinal cross-sections of the samples were imaged after 7 days of culture in EGM-2 BulletKit medium using a Thunder imaging system (Leica Microsystems, Germany).

*Statistical analysis:* Results were reported as mean  $\pm$  standard deviation (S.D.). Statistical analysis was performed using GraphPad Prism 9.0 (GraphPad Software, USA). For tensile test results, Origin 2022 (OriginLab, USA) was used. Comparisons between experimental groups were assessed via one or two-way ANOVAs, followed by post hoc Bonferroni correction to test differences between groups. Non-parametric tests were used when normality could not be assumed. Differences were considered significant when  $p < 0.05$ . Significance is expressed on graphs as follows: \*  $p \leq 0.05$ , \*\*  $p \leq 0.01$ , \*\*\*  $p \leq 0.001$ , \*\*\*\*  $p \leq 0.0001$ .

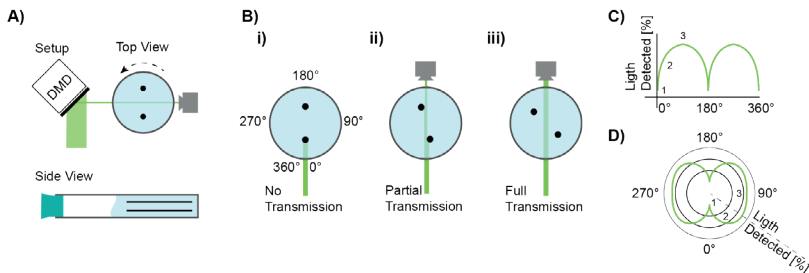


## SUPPORTING INFORMATION

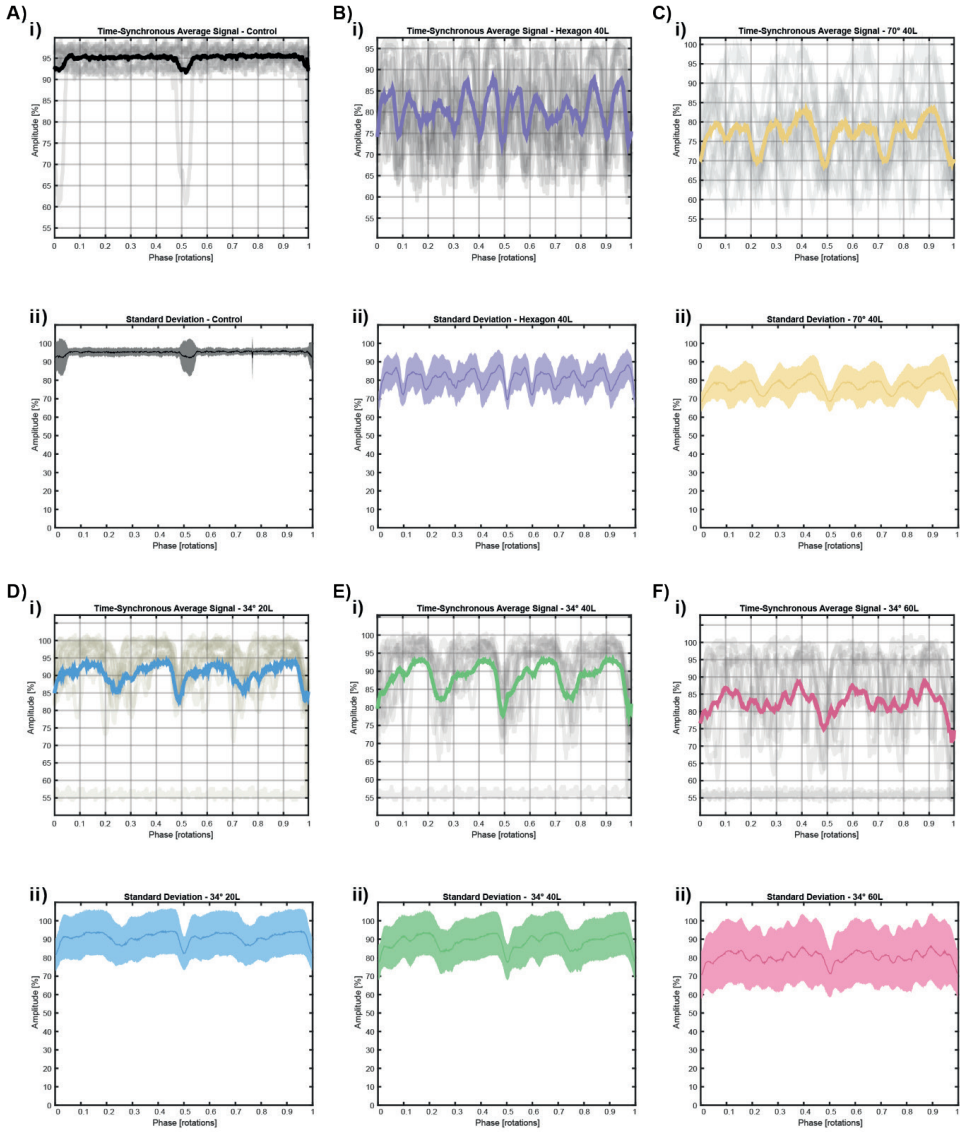
### Supplementary Figures



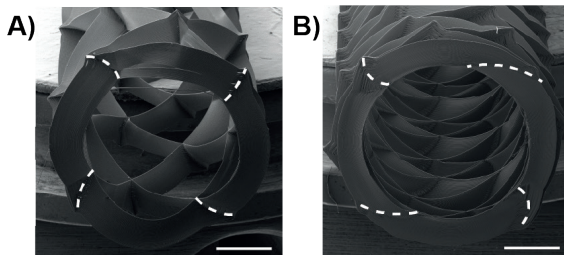
**Supplementary Figure S1:** DLP printed alignment guides for tubular MEW meshes with 150  $\mu\text{m}$  self centering wings. Ai,B) Winged guide for 10 mm and Aii) 20 mm Tomolite vials. B) Printed guide on carbon fiber rod for vial placement. C) Assembly with hydrogel in a vial prior to thermal gelation. Scale bars = 1mm.



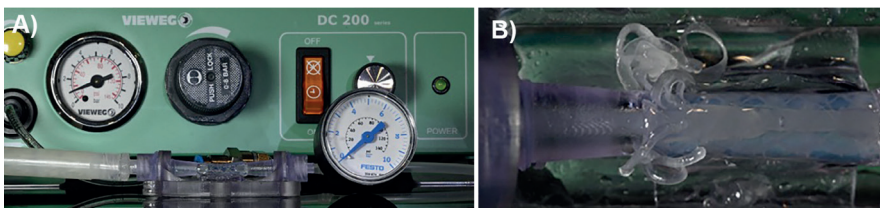
**Supplementary Figure S2:** Overview of the light attenuation setup from measurement to polar plot. A) Setup with two hypothetical rods as attenuating objects. B) Transmission profiles of light with i) no transmission, ii) partial transmission and iii) full transmission. The corresponding C) Cartesian and D) polar plots.



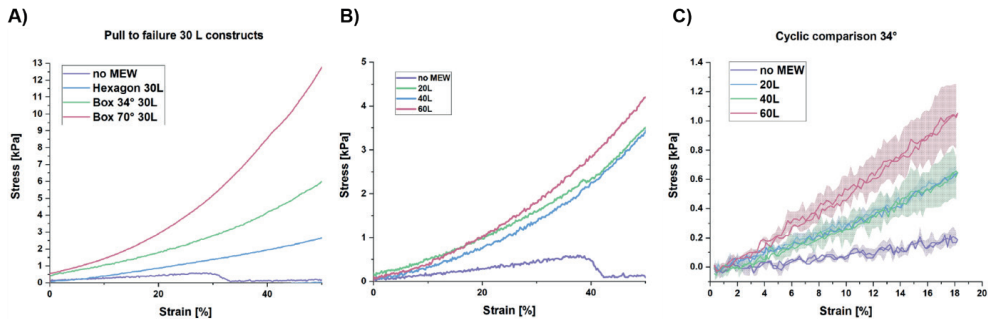
**Supplementary Figure S3:** i) Time synchronous average (tsa) data with data set lines (gray) and highlighted tsa (color) and ii) standard deviation for A) control, B) hexagonal (40L), C) 70° rhombus (40L), and 34° rhombi with D) 20-, E) 40-, and F) 60-layer heights.



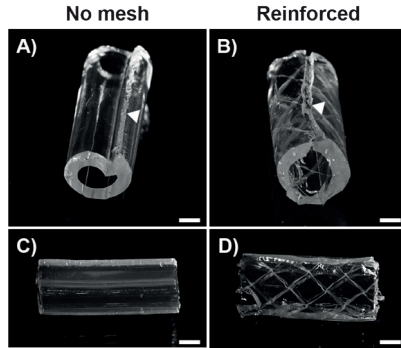
**Supplementary Figure S4:** A) 34° and B) 70° winding-angle scaffolds with the uncompensated layer-shifting of crossover points with increasing wall height (dashed lines; scale bars = 1 mm).



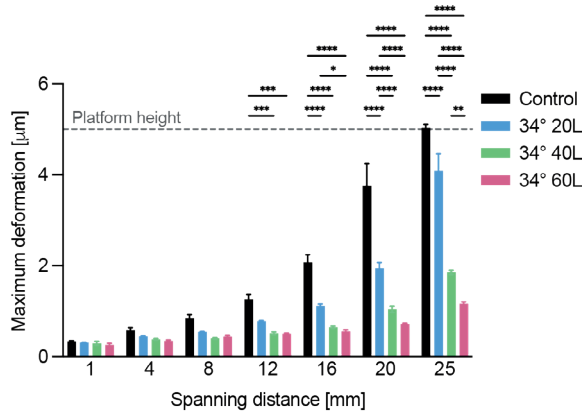
**Supplementary Figure S5:** A) Burst pressure test set-up and B) image of a failed construct and the characteristic ribbon-like appearance of Vaseline.



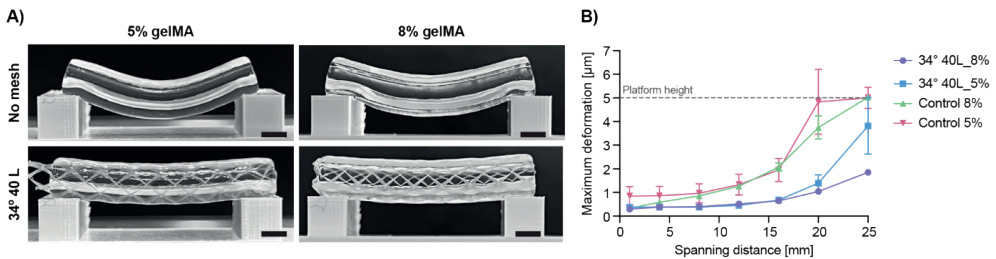
**Supplementary Figure S6:** UTS zoom of the relevant Young's Modulus region for A) different architectures and B) different layer heights. C) Cyclic radial stress-strain curves presented as their mean with SD values to illustrate the deviation within the same MEW reinforcement geometry.



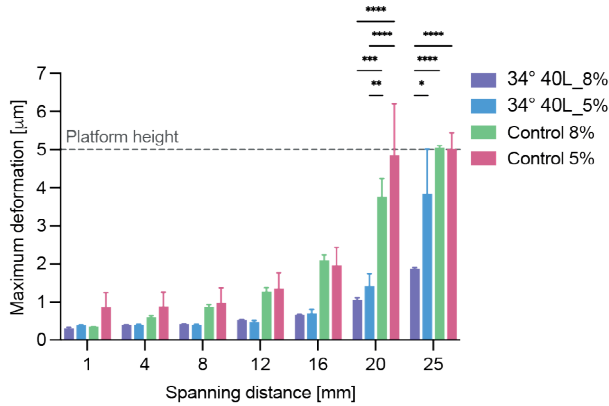
**Supplementary Figure S7:** Digital images of A,C) mesh-free and B,D) MEW-reinforced tubular structures after pull to failure test, shown from an inclined top view and lateral view to show the breaking behavior of the samples.



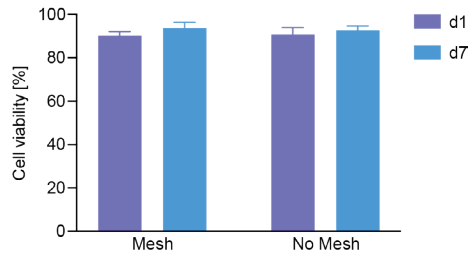
**Supplementary Figure S8:** Statistical information of bridging data shown in Figure 3J, showing two-way ANOVA analysis results for spanning-distance comparisons. \* =  $p < 0.05$ , \*\* =  $p < 0.01$ , \*\*\* =  $p < 0.001$ , \*\*\*\* =  $p < 0.0001$ .



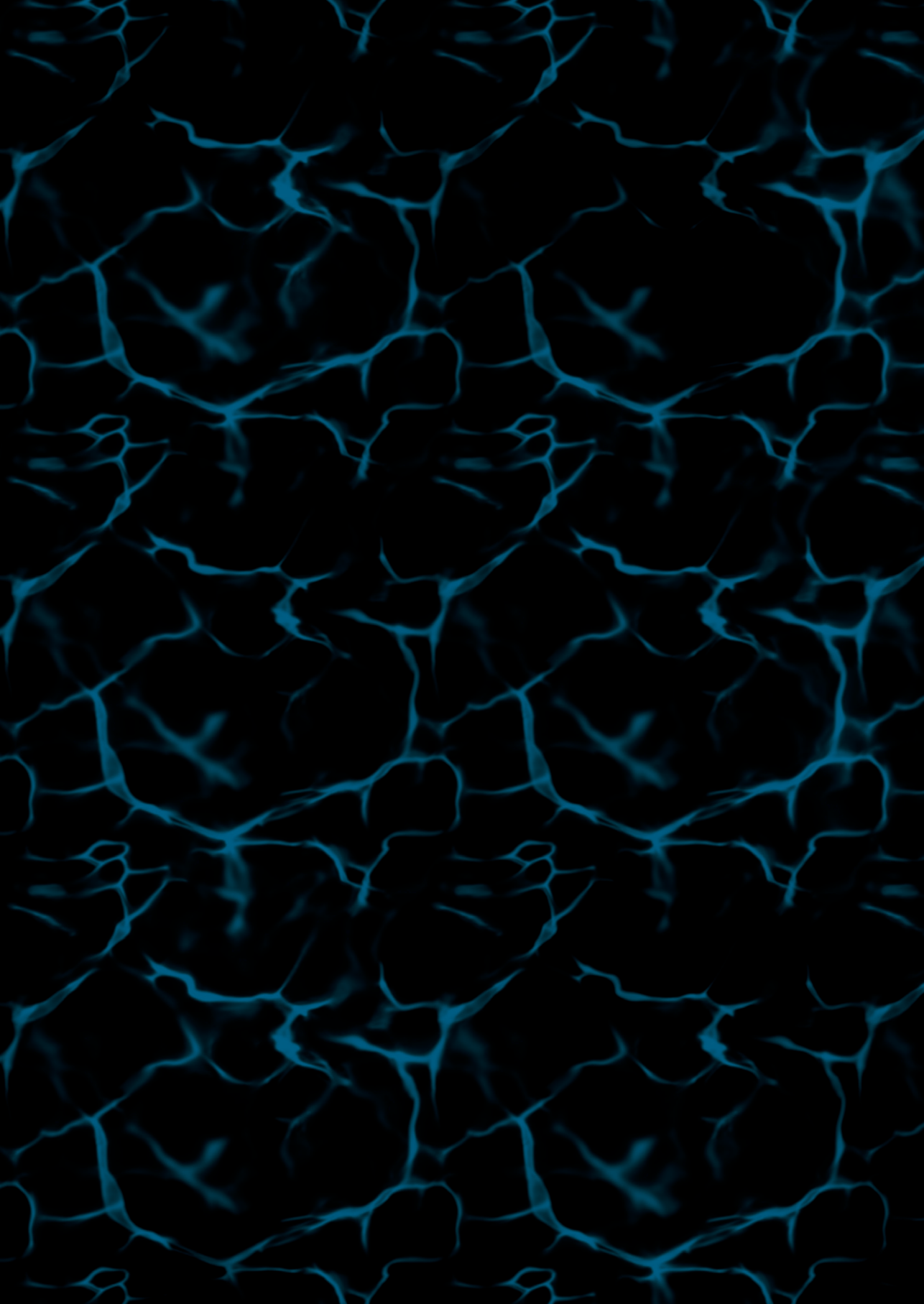
**Supplementary Figure S9:** A) Bending resistance of volumetrically printed 5% and 8% w/v gelMA tubes reinforced with 40-layer, 34° winding angle rhombus MEW meshes on two 5 mm high columns spanning 20 mm in length to evaluate the maximum deformation of the printed construct (scale bars = 3 mm). B) Plotted average maximum deformation of control samples without MEW reinforcement and reinforced tubes at both hydrogel concentrations (dotted line represents the maximum height of the columns on which the constructs were placed).



**Supplementary Figure S10:** Statistical information of bridging data shown in Supplementary Figure S9, showing two-way ANOVA analysis results for spanning-distance comparisons. \* =  $p < 0.05$ , \*\* =  $p < 0.01$ , \*\*\* =  $p < 0.001$ , \*\*\*\* =  $p < 0.0001$ .



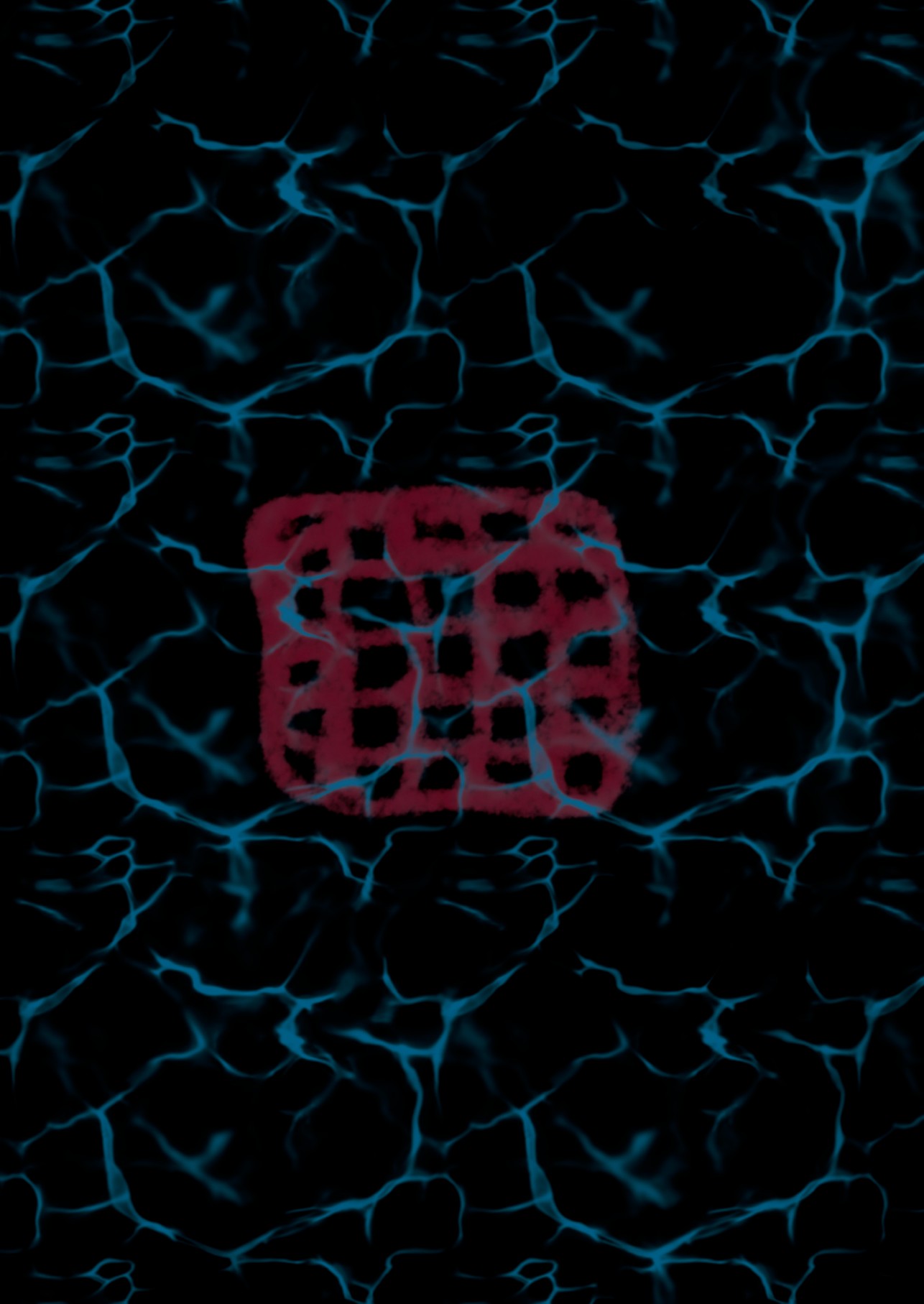
**Supplementary Figure S11:** 7-day cell viability of hbMSCs embedded in gelMA hydrogel samples reinforced with a melt electrowritten mesh, and without mesh reinforcement.



A vertical strip on the left side of the page features a microscopic image of a cell network, showing interconnected cells with blue and white tones. The rest of the page is white.

# Part II

**Development of Advanced *In Vitro*  
Model Platforms Through Biofabrication  
Approaches**





# Chapter 5

## Bioprinting of Human Liver-Derived Epithelial Organoids for Toxicity Studies

Manon C. Bouwmeester<sup>1</sup>, Paulina Núñez Bernal<sup>2</sup>,  
Loes A. Oosterhoff<sup>1</sup>, Monique van Wolferen<sup>1</sup>, Vivian  
Lehmann<sup>1,3</sup>, Monique Vermaas<sup>1</sup>, Maj-Britt Buchholz<sup>1</sup>,  
Quentin Peiffer<sup>2</sup>, Jos Malda<sup>2,1</sup>, Luc J. W. van der  
Laan<sup>4</sup>, Nynke I. Kramer<sup>5,6</sup>, Kerstin Schneeberger<sup>1</sup>,  
Riccardo Levato<sup>1,2</sup>, Bart Spee<sup>1</sup>

Published in: *Macromolecular Bioscience*. 2021. 21(12)

<sup>1</sup> Department of Clinical Sciences, Faculty of Veterinary Medicine, Utrecht University, Utrecht, The Netherlands

<sup>2</sup> Department of Orthopedics, University Medical Center Utrecht, Utrecht University, Utrecht, The Netherlands

<sup>3</sup> Division of Pediatric Gastroenterology, Wilhelmina Children's Hospital, Regenerative Medicine Center Utrecht, Utrecht, The Netherlands

<sup>4</sup> Department of Surgery, Erasmus Medical Center, Rotterdam, The Netherlands

<sup>5</sup> Institute for Risk Assessment Sciences, Utrecht University, Utrecht, The Netherlands

<sup>6</sup> Division of Toxicology, Wageningen University, Wageningen, The Netherlands

## ABSTRACT

5

There is a need for long-lived hepatic *in vitro* models to better predict drug induced liver injury (DILI). Human liver-derived epithelial organoids are a promising cell source for advanced *in vitro* models. Here, organoid technology is combined with biofabrication techniques, which holds great potential for the design of *in vitro* models with complex and customizable architectures. In the present study, porous constructs with human hepatocyte-like cells derived from organoids were generated using extrusion-based printing technology. Cell viability of bioprinted organoids remained stable for up to ten days (88–107% cell viability compared to the day of printing). The expression of hepatic marker *G6PC*, transporters *BSEP* and *ABCG2* and phase I enzyme *CYP3A4* increased compared to undifferentiated controls (expansion condition), and was comparable to non-printed controls. Exposure to acetaminophen, a well-known hepatotoxic compound, decreased cell viability of bioprinted liver organoids to 21-51% ( $p < 0.05$ ) compared to the start of exposure and elevated levels of damage marker miR-122 were observed in the culture medium, indicating the potential use of the bioprinted constructs for toxicity testing. We showed that human liver-derived epithelial organoids can be combined with a biofabrication approach, thereby paving the way to create perfusable, complex constructs which can be used as toxicology- and disease-models.

**Keywords:** extrusion-based bioprinting, drug induced liver injury, *in vitro* modeling, organoids

## INTRODUCTION

Drug-induced liver injury (DILI) is the most frequent reason for drug failure in clinical trials and post-marketing drug withdrawal.<sup>[337]</sup> Thirty percent of drug candidates are discontinued due to hepatic dysfunction even post-marketing.<sup>[338]</sup> Additionally, drug-induced liver injury accounts for more than fifty percent of the cases of acute liver failure in the United States.<sup>[339]</sup> Preclinical drug testing using rodent models allows for drug evaluation in the presence of a complete immune system and cross-talk with other organs.<sup>[340]</sup> However, significant inter-species differences in metabolic processes, disease mechanisms and modes of toxicity, hamper the extrapolation of obtained preclinical data to the human situation.<sup>[341,342]</sup>

Compared to animal models, human hepatic *in vitro* models could give more insight in specific metabolic processes and mechanisms of toxicity, and allow for an ethically less controversial model.<sup>[343]</sup> Primary human hepatocytes (PHHs) are considered the golden standard due to the representative expression levels of metabolizing enzymes and expression of liver-specific markers. However, issues with PHHs are their rapid dedifferentiation leading to decreased hepatic function *in vitro* and the limited availability of these cells.<sup>[344]</sup> Nevertheless, PHHs are still widely used and recently introduced culture strategies are able to delay the dedifferentiation process in an attempt to set up a model that can be used for long-term toxicity testing.<sup>[345-347]</sup> To overcome previously mentioned limitations of PHHs, hepatic cell lines, such as HepG2 and HepaRG, are extensively used.<sup>[348]</sup> Although advantages of hepatic tumor-derived lines are their availability and nearly unlimited growth, they generally have reduced expression of key hepatic enzymes compared to PHHs.<sup>[349]</sup> Similar to PHHs, new culture strategies exist that are able to improve the hepatic function,<sup>[350]</sup> however these cell lines are single-donor-derived and therefore do not exhibit interindividual differences. Especially in the case of the liver, a model needs to recapitulate the interindividual variation in metabolism, which is a major contributor to heterogeneity in drug clearance.<sup>[351]</sup>

Organoids have a great potential to serve as liver models as they recapitulate aspects of the native tissue architecture and function *in vitro*.<sup>[352]</sup> Organoids are cultured as three-dimensional structures that are derived from primary cells (stem cells, progenitor, and/or differentiated cells) that self-organize through cell-cell and cell-matrix interactions.<sup>[35]</sup> Epithelial organoids are single germ layer derived and under specific culture conditions expand and polarize to reproduce aspects of the native epithelium.<sup>[353]</sup> In the case of the liver, progenitor cells derived from the biliary tree can be cultured as organoids and differentiated into the cholangiocytic- and hepatocytic-lineage, indicating a true bipotential nature. In culture conditions where the Wnt/b-catenin pathway is induced, these progenitor cells from the intrahepatic biliary tree form organoids (Intrahepatic Cholangiocyte Organoids, ICOs) and upregulate a stem cell marker LGR5.<sup>[354]</sup> ICOs are

highly proliferative, expanding as cystic structures for several months while remaining genetically stable and can be produced in large scale.<sup>[55,355]</sup> Under differentiating conditions ICOs upregulate hepatocyte markers and acquire mature hepatocyte functions, such as albumin and bile acid secretion, glycogen storage, phase I and II drug metabolism, and ammonia detoxification.<sup>[355]</sup> Unlike cellular aggregates or spheroids, the organoids are cystic-like structures which, in case of hepatic differentiation, are polarized with the apical side at the inside, facing the organoid lumen.<sup>[55]</sup> As ICOs are donor-derived, they can reflect interindividual variability in metabolic activity *in vitro*. Current hepatic maturity is limited compared to primary hepatocytes as indicated by lower hepatic function (*i.e.*, albumin expression and cytochrome activity).<sup>[355]</sup> In order to improve hepatic maturation the complexity of the *in vitro* constructs can be increased, thereby more closely mimicking the native liver environment.<sup>[356]</sup> Biofabrication techniques, and more specifically bioprinting, can provide such complexity through the precise placement of biomaterial inks or bioinks to promote cellular interactions, and through the production of constructs that allow for vascularization and enhanced exchange of nutrients.<sup>[357,358]</sup>

5 The potential to converge bioprinting and self-assembled biological building units like organoids, has recently sparked attention in the biofabrication field, due to the possibility to create models at the tissue-like level scale.<sup>[109,359]</sup> Hence, novel models that benefit from both the 3D spatial control, as provided by bioprinting, and of the biological resemblance by using organoids as building blocks and bioink components, holds great potential to introduce a humanized testing platform for personalized medicine and drug screening. Here, we take the initial step towards increasing the culture complexity of human ICO's by showing that bioprinted organoids can be processed into functional liver constructs.

## RESULTS

Hepatic constructs were created with extrusion-based bioprinting using organoid-derived hepatocyte-like cells and gelatin-based hydrogel (GelMA) as a bioink. After expanding the intrahepatic cholangiocyte organoids (ICOs) in Matrigel, in order to achieve the cell amount required for the bioprinting of the liver constructs, ICOs were resuspended in GelMA at a 2-5 million cells per mL density. Cell-laden GelMA was co-printed with the sacrificial hydrogel Pluronic-127 allowing to create porous constructs (**Figure 1a**). Printed constructs consisted of printed strands of 600 to 1000  $\mu\text{m}$  with pores of 200 to 400  $\mu\text{m}$  in size (**Figure 1b**). Diffusion through the GelMA hydrogel occurred at  $> 1000 \mu\text{m}$  within minutes, as was determined by using a coloring dye (**Figure S1**). This observation indicates that the hydrogel allows an exchange of soluble compounds with molecular weight comparable or superior to the drugs used in this work, thus permitting exposure to the hydrogel-embedded organoids. Moreover, the shear thinning property of GelMA was unaffected by the presence of organoids in the hydrogel (**Supplementary Figure**

**S1**), as the trend in viscosity with increasing angular frequency was comparable to GelMA without organoids.

## Cell viability in bioprinted constructs

Hepatic differentiation of ICOs was started directly after bioprinting using differentiation media. After 10 days of culture, morphology of the organoids was assessed using an HE staining. We observed that the organoids remained within the printed GelMA struts or aligned along the edge (**Figure 1c**) with an average diameter size of  $48.2 \pm 29.0 \mu\text{m}$  (**Supplementary Figure S2**). Organoids were distributed evenly throughout the construct with an overall coverage area of  $6.4 \pm 0.4 \%$  (**Supplementary Figure S2**) of bioprinted struts. In order to assess if the printed constructs can be applied for long-term toxicity studies, we assessed the cell viability of organoids over time using an Alamar blue assay as well as a live-dead assay. The differentiated (non-proliferative) organoids remained viable over a period of 10 days (88–107% cell viability compared to printing day; **Figure 1d**) as determined using an Alamar blue assay, which is comparable to organoids plated in GelMA (non-printed). Fluorescence imaging of live/dead cells showed that the amount of viable cells is stable over time and individual dead cells, which are present on the first day after printing, decreased over time (**Figure 1e**), which is comparable to the plated control (data not shown).

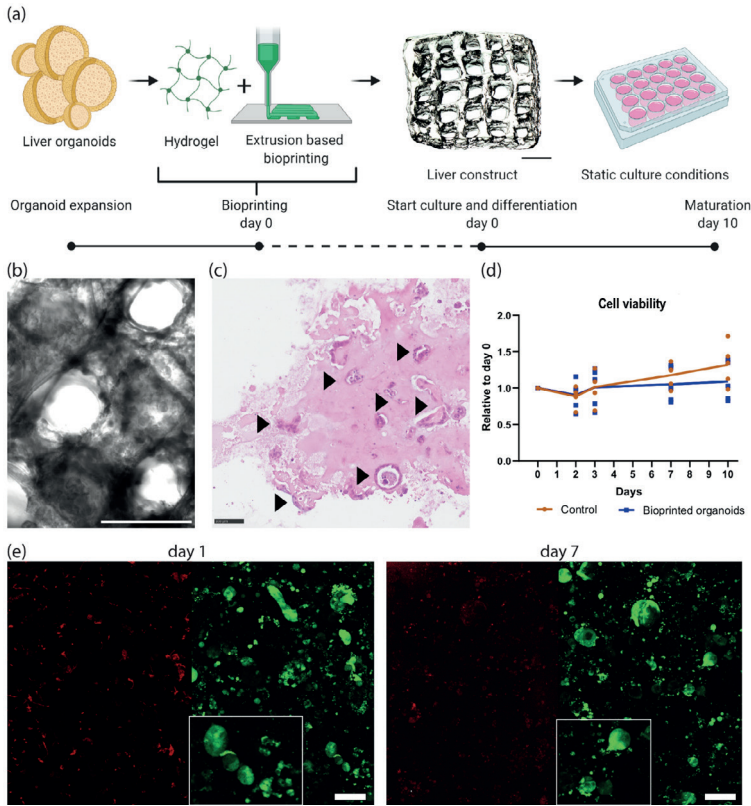


**Figure 1: Bioprinting liver constructs.** (a) Schematic overview of the experimental procedure for bioprinting liver constructs. Once expanded, liver organoids are encapsulated in hydrogel (GelMA). A porous construct was fabricated using extrusion-based bioprinting of the resulting bioink. The construct is cultured in organoid differentiation media, thus guiding organoids towards a hepatocyte-like phenotype. Scale bar = 1000  $\mu\text{m}$ . Created with BioRender.com (b) Brightfield image of the bioprinted liver construct. Scale bar = 1000  $\mu\text{m}$ . (c) HE staining of the bioprinted liver construct. Scale bar = 100  $\mu\text{m}$ . Arrowheads indicate cystic organoid structures within printed struts. Scale bar = 100  $\mu\text{m}$ , inserts are twofold higher magnification. (d) Cell viability of liver organoids in GelMA (5 donors) after plating (control; orange) and after printing (blue). Each dot represents the mean of a technical triplicate of a donor. (e) Representative image of the live/dead staining of liver organoids after printing at day 1 and 7 post-printing. Viable cells are stained in green, dead cells in red, image covers an entire printed strut.

## Post-printing hepatic functionality

Hepatic differentiation of the organoids in GelMA droplets and extrusion-based bioprinted constructs was compared to that of organoids in plated Matrigel cultures (day 10 of differentiation), by gene expression profiling and protein expression (immunofluorescence). As expected, gene expression profiling indicated a decrease of the stemness marker leucine-rich repeat-containing G-protein coupled receptor 5 (*LGR5*) compared to expansion conditions ( $p < 0.01$  for plated and printed organoids), and an

increase of hepatic markers ATP-binding cassette super-family G member 2 (*ABCG2*), bile salt export pump (*BSEP*), Glucose-6-Phosphatase Catalytic Subunit (*G6PC*), cytochrome P450 3A4 (*CYP3A4*) in differentiation conditions compared to expansion conditions (**Figure 2a**). Expression levels of *albumin*, *G6PC*, *ABCG2*, and *CYP3A4* and cytochrome P450 2E1 (*CYP2E1*) show that the use of organoid technology includes donor-to-donor variation, with one of the donors showing low expression, whereas the other donors show increased expression levels in differentiation condition (**Figure 2a**). Overall, GelMA differentiating conditions (both printed constructs and plated controls) showed similar gene expression levels for the assessed hepatic markers compared to Matrigel. Immunofluorescence analysis (**Figure 2b**) showed that the cytoskeleton marker cytokeratin 18 (CK18) is present in bioprinted liver constructs (**Supplementary Figure S3**). Expression of membrane marker E-cadherin and tight junction marker zonula occludens-1 (ZO-1; **Supplementary Figure S3**) confirm that the bioprinted organoids retain an epithelial phenotype. Additionally, expression of hepatic markers hepatic nuclear factor 4 alpha (*HNF4α*), albumin, and argininosuccinate synthase (*ASS*) show differentiation towards hepatocytes. Expression of multi drug resistance protein 1 (*MDR1*), an apical transporter, shows polarization of liver organoids, allowing for transepithelial transport. Another characteristic of hepatocytes is glycogen storage. Glycogen can be hydrolyzed during a fasting state to generate glucose. Periodic acid-Schiff staining for glycogen shows that bioprinted organoids show glycogen accumulation indicating hepatic function (**Figure 2c**).

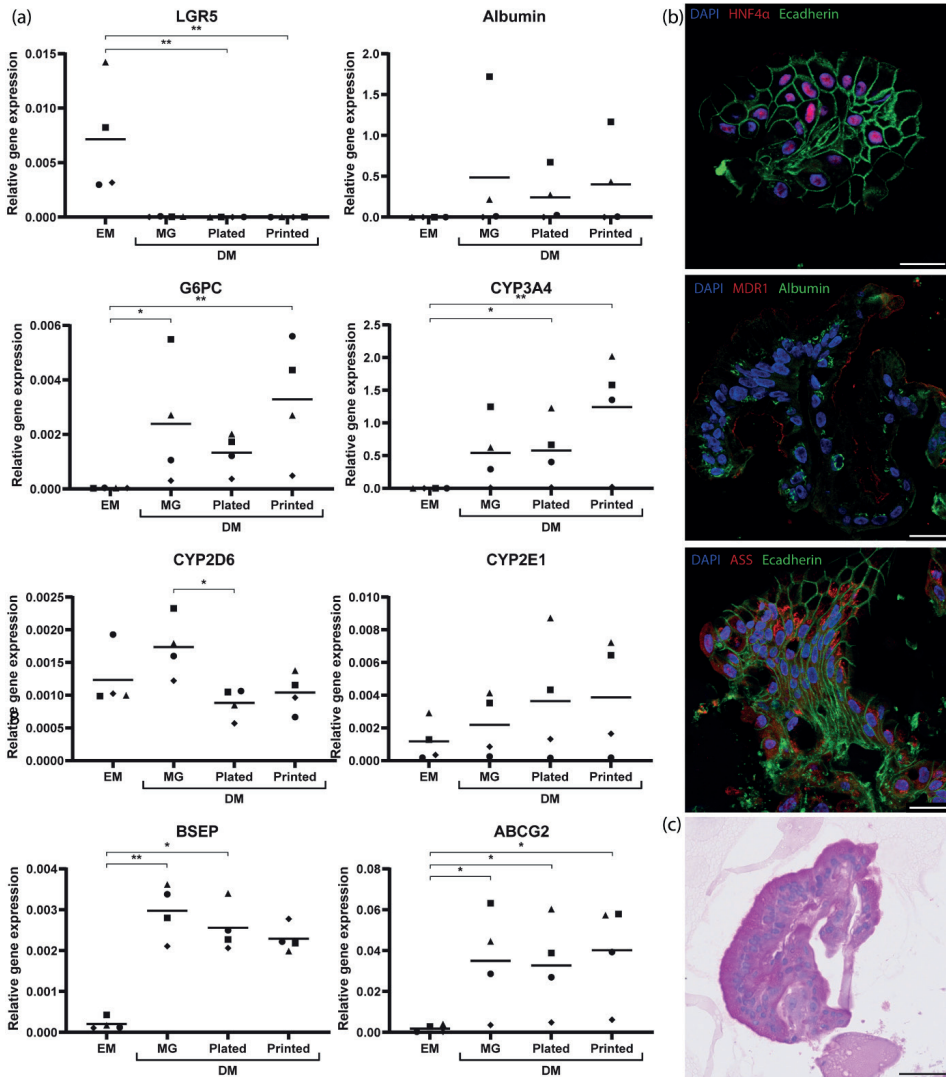


**Figure 2: Functionality assessment in liver constructs.** (a) Gene expression of liver organoids in Matrigel (MG; expansion (EM) and differentiation (DM) conditions), plated and printed in GelMA in differentiation conditions (DM). Each dot represents the mean of a technical triplicate of a donor. Relative gene expression was calculated using the reference genes GAPDH and RPS5 ( $\Delta Ct$ ). LGR5, Leucine-rich repeat-containing G-protein coupled receptor 5; G6PC, ATP-binding cassette super-family G member 2; CYP2D6, Cytochrome P450 2D6; CYP3A4, Cytochrome P450 3A4; CYP2E1, Cytochrome P450 2E1; ABCG2, Glucose-6-Phosphatase Catalytic Subunit; BSEP, Bile salt export pump (b) Immunofluorescence staining in liver constructs. Scale bar = 25  $\mu m$ . HNF4 $\alpha$ , Hepatocyte nuclear factor 4 alpha; MDR1, Multidrug resistance protein 1; ASS, Argininosuccinate synthase (c) Glycogen accumulation in liver construct. Scale bar = 50  $\mu m$ .



## Toxicity in bioprinted constructs

As a proof-of-concept that the liver constructs can be applied to predict drug toxicity, we exposed bioprinted human organoids (5 donors) to the well-known hepatotoxic compound acetaminophen (APAP) on post-printing (differentiation) day 7 (72 h at 30 mM). APAP can cause liver toxicity after biotransformation into its toxic metabolite N-acetyl-p-benzoquinone imine (NAPQI) by cytochrome P450 enzymes. Exposed organoids had a decreased cell viability to 21–45% ( $p < 0.01$ ) after 72h of exposure compared to the start of exposure (**Figure 3a**), which is comparable to APAP toxicity observed in non-printed organoids (**Supplementary Figure S4**). Fluorescence imaging of cell viability shows that after 72 h of APAP exposure, the spherical shape of the organoids is disrupted indicating cellular stress (**Figure 3b**). Additionally, levels of damage marker miRNA-122 was also measured for four donors in the media. Levels of miRNA-122 seemed elevated compared to non-exposed organoids indicating leakage of miRNA-122 into the media (**Figure 3c**). Taken together, this data suggests that bioprinted organoids contain functional cytochrome P450 enzymes which were able to biotransform APAP into its toxic metabolite NAPQI.

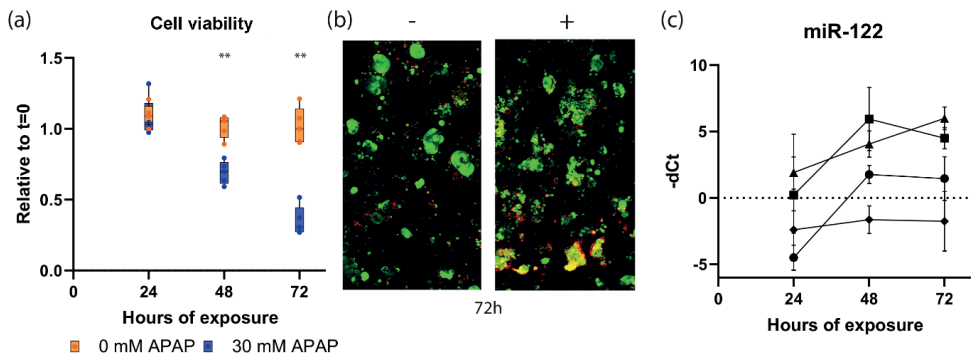


**Figure 3: Acetaminophen (APAP) toxicity in bioprinted organoids.** Exposure (72 h at 30 mM APAP) started on day 7 post-printing with organoid-derived hepatocyte like cells. (a) Cell viability of bioprinted organoids exposed to APAP relative to the cell viability at start of exposure. Bioprinted organoids exposed to 0 mM APAP (control; orange) and 30 mM (blue). Each dot represents the mean of a technical triplicate of one donor ( $n=5$ ). After 72h of exposure the cell viability of exposed organoids is significantly affected ( $p < 0.01$ ). (b) LIVE/DEAD staining of bioprinted organoids non-exposed (-, day 10 post-printing) and exposed to APAP for 72 h (+, day 10 post-printing). Viable cells are stained in green, dead cells in red. (c) Medium-levels of microRNA-122. Data are expressed as  $\log_2$  fold-change ( $-\Delta Ct$ ) using the non-exposed samples as baseline. Each symbol, representing a different donor ( $n = 4$ ), and error bars represent the mean  $\pm$  standard deviation.

## DISCUSSION

5 The present study shows the potential application of hepatocyte-like cells derived from human intrahepatic cholangiocyte organoids (ICOs) for the bioprinting of drug responsive liver models. This enables the production of liver tissue constructs that are able to metabolize compounds relevant for pharmaceutical research. To obtain such models, an extrusion-based bioprinting strategy using an organoid-laden, gelatin-based bioink was established. Bioprinted hepatocyte-like cells from ICOs with a sustained metabolic activity provide possibilities for developing more advanced post-printing culture platforms, such as bioreactors and the incorporation of microfluidic devices, which will increase functional maturation, as well as standardized testing procedures.<sup>[352,356,360]</sup> Herein, it is demonstrated that hepatic functionality of differentiated ICOs in GelMA (plated and bioprinted) is comparable to regular Matrigel cultures. As a proof of principle to show the potential of bioprinted hepatocyte-like cells from ICOs to predict *in vitro* toxicity, bioprinted constructs were exposed to acetaminophen (APAP), a well-known hepatotoxic drug.<sup>[361]</sup> Donor-derived liver organoids are hollow cystic structures that express hepatic functionality once differentiated towards the hepatic lineage.<sup>[55,355]</sup> After differentiation, the hepatocyte-like cells are polarized as indicated by specific membrane transporters at either the apical or basolateral membrane. The observed polarization (MDR1), an apical membrane transporter, does mimic the native tissue in great detail and is important in the excretion of metabolites and transepithelial transport which can be measured in the media surrounding the bioprinted construct. In non-polarized 2D cultures such transport studies are not possible.<sup>[362]</sup> The donor-derived origin of the liver organoids was visible in our expression profile as not all donors showed similar expression levels, such as CYP3A4 and CYP2E1. Interindividual differences in metabolic gene expression profile may contribute to the sensitivity to hepatotoxic drugs,<sup>[363]</sup> a feature that single-donor derived hepatic cell lines do not provide.<sup>[348]</sup>

Additionally to toxicity screening, hepatocyte-like cells from ICOs also hold great promise for therapeutic applications due to their patient-derived origin. Next to iPSCs, it is one of the few models that allows for precision medicine approaches.<sup>[360]</sup> Tissue-derived epithelial organoids have been shown to exhibit patient-specific phenotypes *in vitro*,<sup>[364]</sup> thereby enabling personalized testing of therapeutic applications. Disease modeling using patient derived liver organoids have been described for diseases such as Alagille syndrome and alpha-1 antitrypsin deficiency.<sup>[355]</sup> Moreover, patient-derived organoids have been shown to allow for genetic repair by gene editing techniques<sup>[365]</sup> and are envisioned as a clinical therapy.<sup>[366]</sup> Next to the liver-derived organoids focused on in this paper, the described bioprinting strategy can also be used in combination with tissue-derived organoids from other organs, including gall bladder, kidney, intestine and pancreas<sup>[367-369]</sup> paving the way for more *in vitro* (disease) modeling opportunities.

Although hepatocyte-like cells from ICOs are a valuable tool for studying metabolism, even after differentiation some hepatic features are still lacking resulting in an immature phenotype. By bioprinting the biological resemblance of the *in vitro* system can be improved by applying precise patterning of organoids thereby permitting control over porosity and improved nutrient and waste exchange.<sup>[370–372]</sup> Here, we used extrusion-based bioprinting, which is an affordable technique in which a wide range of materials can be used.<sup>[114,229]</sup> The bioink (organoid-laden hydrogel pre-cursor) is pushed through a needle and is used to draw the desired 3D design layer-by-layer. Extrusion-based bioprinting could potentially cause organoid disruption due to shear stress at the nozzle. However, with the printing settings optimized in this study, viability of the hepatocyte-like cells from ICOs remained stable over time and comparable to non-printed controls.

Epithelial organoids are commonly cultured in the animal-derived and thermosensitive hydrogel Matrigel, which is advantageous for organoid growth and can be printed with a cooled print head.<sup>[373]</sup> However, while Matrigel has been well established to expand organoids in culture, using other 3D matrices during the organoid maturation steps has been proven to increase hepatic differentiation of liver organoids.<sup>[374,375]</sup> Furthermore, Matrigel shows considerable batch-to-batch variations, which represents a hurdle towards generation of highly standardized and scalable *in vitro* models for pharmaceutical research.<sup>[376]</sup> In our study, the main goal was to maintain a hepatic phenotype for subsequent testing, rather than proliferation and maintenance of undifferentiated phenotypes. Thus, we selected the widely used gelatin-derived hydrogel GelMA to prepare the printable bioinks. The modified methacryloyl groups in GelMA allow irreversible photocrosslinking and highly controllable stiffness of the hydrogel.<sup>[229]</sup> Furthermore, rheological analysis showed that the used GelMA concentration has shear thinning properties, which greatly facilitates stable extrusion while minimizing cell stress during printing.<sup>[130,151]</sup> Upon addition of organoids, the material still maintained its shear thinning properties. As the selected GelMA concentration is known to give rise to relatively soft hydrogels, typically in the range  $\approx 5$  kPa.<sup>[377]</sup> Pluronic-127 was used to temporarily support the desired grid-like structure before photocrosslinking<sup>[259]</sup> and the sacrificial filaments can also serve as a template to provide channels suitable to permit vascularization at a later stage.<sup>[371]</sup> The porosity of the current lattice shaped constructs already permit close proximity of the liver organoids to the media and nutrient supply. LAP was used as photoinitiator for its cytocompatibility, herein demonstrated also when mixed with organoid-laden bioinks, and its potential to trigger crosslinking with visible light ( $\sim 405$  nm), which has been shown to permit hydrogel formation under mild and cell-friendly photo-exposure conditions.<sup>[378]</sup> Importantly, this is, to the best of our knowledge, the first report demonstrating the feasibility of bioprinting organoids derived from liver epithelium. Such liver organoids, forming lumen-rich structures, are more structurally fragile than dense spheroids and could potentially be susceptible to damage and disruption during extrusion through

a nozzle. This study indicates the feasibility and safety of bioprinting such structures without hampering their functionality and constitutes a necessary preliminary step for future studies of more complex bioprinted architectures. Taken together, extrusion-based bioprinting using GelMA in combination with a sacrificial material provide a versatile strategy for the bioprinting of a porous construct that sustains organoid viability.

Extrusion-based bioprinting of hepatic structures has been shown before using different hepatic *in vitro* models, such as tumor-derived hepatic lines,<sup>[370,371,379–381]</sup> (cryopreserved) PHHs,<sup>[382,383]</sup> and human iPSCs.<sup>[138,384]</sup> Although all cell-types have hepatocyte features, the cellular organization of these bioprinted models is different compared to the bioprinted organoid constructs. Cells can be bioprinted as single cells,<sup>[371,379–384]</sup> cellular aggregates that are forced to form (co-cultured) spheroids<sup>[370]</sup> or, in our case, as self-organizing organoids. Even though the size and level of organization of the cellular structures does not necessarily affect cell viability after bioprinting,<sup>[385]</sup> it can have an effect on hepatic functionality<sup>[138]</sup> and contribute to cellular organization within prints. Extrusion-based bioprinted intestinal-derived organoids showed that specific patterning of the organoids can stimulate self-organization.<sup>[386]</sup> Here, liver organoids also reorganized within the bioprinted constructs and did not maintain their morphological characteristics as seen in Matrigel cultures. Even though there are morphological differences, the hepatic differentiation state in bioprinted constructs was similar compared to Matrigel. The high stability of the bioprinted organoids with respect to cell viability could also be due to intrinsic cell-binding motifs present in gelatin.<sup>[387]</sup>

Next to the stability in viability and gene expression levels, histology and function are equally important. The current liver constructs do not fully recapitulate the native liver structure yet. We showed that liver organoids can be patterned via bioprinting, which provides the basis for future applications. Several important steps need to be taken to increase the complexity of the *in vitro* system which will lead to improved hepatic differentiation. This improved differentiation can be reached by co-culture with supporting liver cells<sup>[388,389]</sup> or vascular cells leading to a vascularized construct,<sup>[347]</sup> or flow perfusion,<sup>[390,391]</sup> which can be applied to the bioprinted constructs.<sup>[347]</sup> The latter can be particularly beneficial, as recent studies have shown how *in vitro* zonation can be induced by flow perfusion.<sup>[392,393]</sup> The presence of Argininosuccinate synthetase (ASS, involved in urea cycle and mainly located in the periportal area) as well as the expression of CYP enzymes (mainly located in the perivenous area), suggests that hepatocyte-like cells from ICOs are not yet zonally oriented in the bioprinted constructs. In this study, we showed that hepatocyte-like cells from ICOs maintained high metabolic activity up to at least ten days after printing, allowing for post-printing exposure assays. The combination of bioprinting and ICOs provides possibilities to increase culture complexity to provide a more physiological relevant microenvironment and thereby potentially improve the hepatic differentiation state of the organoids.

Although several liver models have been developed for the determination of hepatic toxicity, almost all models have limitations that hamper their use in toxicity screening.<sup>[344]</sup> In this study, acetaminophen-induced toxicity was observed in the liver constructs over time, although used acetaminophen concentrations were relatively high compared to literature.<sup>[370,394]</sup> This is likely mainly due to the high level of the anti-oxidant glutathione present in the organoid differentiation medium which acts as an anti-oxidant and protects against APAP toxicity.<sup>[395]</sup> Additionally, expression levels of CYP2E1, which is mainly responsible for the formation of the toxic metabolite NAPQI (in addition CYP3A4 and CYP1A2 contribute to APAP metabolism, albeit to a lesser extent),<sup>[396]</sup> are only slightly increased in differentiated liver organoids compared to expanding conditions. Improved hepatic functionality, including CYP expression, can reinforce the predictive capacity for necrotic toxicity after formation of reactive metabolites.<sup>[397,398]</sup> With improvements of hepatic functionality of the organoids and the experimental set-up, bioprinted liver organoids could result in a robust *in vitro* model to detect drug-induced effects. Acetaminophen toxicity is known to be predictable and dose-dependent as the formation of a toxic metabolite causes toxicity, however most drug-induced hepatic injury are less predictable and occur via different mechanisms.<sup>[399]</sup> By exposure of liver organoids to a selection of known hepatotoxic compounds with different toxicological mechanisms (for example formation of reactive metabolites, BSEP inhibition, mitochondrial impairment) the applicability of liver organoids in specific toxicological mechanisms can be established.<sup>[400]</sup>

## CONCLUSIONS

We aimed to develop a hepatic model that allowed spatial control using hepatocyte-like cells from ICOs and gelatin-based hydrogel as bioink. By bioprinting epithelial organoids we have taken the first step in the development of a more complex, and hence more physiologically relevant, *in vitro* model system that allows the accurate predictions of drug-induced liver injury (DILI). This study provided the basis of a humanized testing platform for personalized medicine and/or drug screening based on the creation of liver constructs through bioprinting.

## EXPERIMENTAL SECTION

**Cells and culture conditions:** Healthy liver biopsies were obtained during liver transplantation at the Erasmus Medical Center Rotterdam in accordance with the ethical standard of the institutional committee to use the tissue for research purposes (ethical approval number MEC 2014-060). The procedure was in accordance with the Helsinki Declaration of 1975 and informed consent in writing was obtained from each patient. Obtained human liver material was frozen down in Recovery Cell Freezing Medium for future experiments or used for organoid isolation directly. Organoid isolation was performed as follows: Tissue was chopped into small pieces and enzymatically digested with 0.125 mg mL<sup>-1</sup> Type II collagenase and 0.125 mg mL<sup>-1</sup> dispase in Dulbecco's Modified Eagle's Medium (DMEM) Glutamax supplemented with 0.01% v/v DNase I (Roche, Basel, Switzerland), 1% (v/v) fetal calf serum (FCS) and 1% v/v penicillin/streptomycin (P/S) at 37° C. Every hour, the supernatant was collected and fresh enzyme-supplemented media was added to the remaining tissue until only ducts and single cells were visible. Cells were washed with DMEM Glutamax (supplemented with 1% v/v FCS and 1% v/v P/S) and spun down at 453 g for 5 min. All components were obtained from Life Technologies (Carlsbad, CA, USA).

The cell suspension was cultured in Matrigel™ (Corning, New York, NY, USA) droplets in expansion medium (EM) until intrahepatic cholangiocyte organoids (ICOs) arise, as previously described.<sup>[401]</sup> In short, EM consisted of Advanced DMEM/F12 (Life Technologies) supplemented with 1% v/v penicillin-streptomycin (Life Technologies), 1% v/v GlutaMax (Life Technologies), 10 mM HEPES (4-(2-hydroxyethyl)-1-piperazineethanesulfonic acid, Life Technologies), 2% v/v B27 supplement without vitamin A (Invitrogen, Carlsbad, CA, USA), 1% v/v N2 supplement (Invitrogen), 10 mM nicotinamide (Sigma-Aldrich, St Louis, MO, USA), 1.25 mM N-acetylcysteine (Sigma-Aldrich), 10% v/v R-spondin-1 conditioned medium (the Rspo1-Fc-expressing cell line was a kind gift from Calvin J. Kuo), 10 μM forskolin (Sigma-Aldrich), 5 μM A83-01 (transforming growth factor beta inhibitor; Tocris Bioscience, Bristol, UK), 50 ng mL<sup>-1</sup> EGF (Invitrogen), 25 ng mL<sup>-1</sup> HGF (Peprotech, Rocky Hill, NJ, USA), 0.1 μg mL<sup>-1</sup> FGF10 (Peprotech) and 10 nM recombinant human (Leu15)-gastrin I (Sigma-Aldrich). Media was changed twice a week. Passaging occurred every 7-10 days at ratios ranging between 1:2 and 1:4. All cultures were kept in a humidified atmosphere of 95% air and 5% CO<sub>2</sub> at 37° C. Organoids were primed for differentiation with BMP7 (25 ng mL<sup>-1</sup>, Peprotech) through spiking EM 3 days prior to shifting to differentiation medium (DM). DM consisted of EM without R-spondin-1, FGF10 and nicotinamide, supplemented with 100 ng mL<sup>-1</sup> FGF19 (Peprotech), 500 nM A83-01 (Tocris Bioscience), 10 μM DAPT (Selleckchem, Munich, Germany), 25 ng mL<sup>-1</sup> BMP-7 (Peprotech), and 30 μM dexamethasone (Sigma-Aldrich). Organoids were kept on DM up to 10 days.

**Bioink preparation:** Gelatin-methacryloyl (GelMA) was synthesized from gelatin-derived from porcine skin (Sigma-Aldrich) as previously described.<sup>[257]</sup> In short, 10% w/v gelatin

in phosphate buffered saline (PBS) was reacted with 1:0.6 methacrylic anhydride (Sigma-Aldrich) at 50° C for 1h in order to form 80% degree of functionalization of the lysine residues. The excess of methacrylic anhydride was removed by centrifugation. The obtained GelMA solution was neutralized with NaOH and dialyzed against distilled water for 5 days, sterile-filtered, freeze-dried and stored at -20° C until further use.

The used photoinitiator in the bioink was lithium-phenyl-2,4,6-trimethylbenzoylphosphinate (LAP; Sigma-Aldrich) 0.2% w/v dissolved in DMEM/F12 (without phenol red, supplemented with 1% v/v penicillin-streptomycin, 1% v/v GlutaMax, 10 mM HEPES). Freeze-dried GelMA was dissolved (5% w/v) in the LAP-solution. The temperature of the GelMA solution was stabilized at 25° C prior to cell mixing. Organoids were mechanically fragmented and mixed with the GelMA bioink right before transferring to the bioprinting cartridge. The sacrificial material Pluronic®F-127 (Sigma-Aldrich) was dissolved in PBS (40% w/v) while incubating at 4° C under continuous agitation.

*Rheological evaluation GelMA:* The rheological properties of the hydrogel precursor solution were assessed using a DHR2 rheometer (TA Instruments, the Netherlands). To evaluate the hydrogels shear thinning properties, a stainless-steel flat plate (diameter = 20 mm) with a 200 µm plate-to-plate distance was used. GelMA in LAP-solution (65 µL of 5% w/v; previously described) was loaded and the gels complex viscosity (Pa·S) was recorded at 25°C as a function of shear rate (0.01–100 rad s<sup>-1</sup>) at a constant strain of 5% (n = 3 for GelMA control, n = 4 for cell-laden GelMA).

*Compound diffusion in GelMA:* A 5% w/v GelMA in 0.2% w/v LAP-solution was casted using a custom-designed PDMS mold and crosslinked for 10 minutes under 400 nm light exposure, to form cylindrical discs (diameter = 5 mm; height = 3 mm). To evaluate the diffusion rate of the crosslinked hydrogel construct, 10 µL of a green colored dye (MW = 534,3–561,7 g mol<sup>-1</sup>; Singh Traders, Baambrugge, the Netherlands) was pipetted on top of the cylinder to create an even fluid layer over the top face surface of the hydrogel disc. After 1, 2, 4, 6, 8, 12, 16, 24, 32 minutes samples were removed from the mold (n = 2 per time point). The migration of the dye through the gel over time was assessed using a stereomicroscope (Olympus SZ61 coupled with an Olympus DP70 digital camera; Olympus Soft Imaging Solutions GmbH, the Netherlands) by imaging cross-sections of the hydrogel cylinder at the indicated time points.

*Bioprinting settings:* The constructs were designed using a Computer Aided Design (CAD) software (BioCAD, RegenHU, Switzerland), and printed using an extrusion-based bioprinter (3D Discovery, RegenHU, Switzerland) in a sterile 5 cm Petri dish (ThermoFisher, Waltham, Massachusetts, USA). The constructs consist of horizontal strands of Pluronic®F-127 with 0.135 mm space between each strand. In between these supporting strands, the cell-laden GelMA was printed and photocrosslinked with an exposure of 45 seconds with blue-light (405 nm). Subsequent layers are printed in a layer-by-layer fashion, with a 90 degrees

rotation in the filament orientation between each layer. Pluronic®F-127 was printed at a speed of 30 mm sec<sup>-1</sup> at a pressure of 450-550 kPa. GelMA was printed at a speed of 15 mm sec<sup>-1</sup> at a pressure of 15-30 kPa. The printhead containing the cell-laden GelMA bioink was equipped with a cooling device set to 25° C. The dispensing tip was a stainless steel 27G nozzle (length 6.35 mm; Nordson, Westlake, OH, USA) for both bioinks. After printing 10 layers, the printed construct is further photocrosslinked for 10 min in a custom-made curing box containing 400 nm LED lights (000214, Groenlicht, Geldrop, the Netherlands). Pluronic®F-127 was washed away with DMEM/F12 (without phenol red, supplemented with 1% (v/v) penicillin-streptomycin, 1% (v/v) GlutaMax, 10 mM HEPES) at 4° C resulting in porous cubical shaped constructs (approximately 5x5x2 mm lwxhx). Constructs were cultured in 24 well plates (ThermoFisher) under differentiating conditions (Differentiation Medium, DM) as described for a maximum of 10 days in a humidified atmosphere of 95% air and 5% CO<sub>2</sub> at 37° C.

**Alamar Blue cell viability assay:** Cell viability of the organoids (4 donors in technical triplicate) in printed constructs and plated controls (GelMA and Matrigel) was examined through an Alamar Blue assay (ThermoFisher), a resazurin-based solution that functions as a cell health indicator. Briefly, the Alamar Blue reagent was diluted 1:10 in DMEM/F12 (phenol-red free). Cells were incubated for 2 h at 37° C. Subsequently, fluorescence intensity of the Alamar Blue solution was measured with a photospectrometer (Fluoroskan Ascent FL, ThermoFischer Scientific) at ex/em 544/570 nm.

**Cell viability:** Cell viability of printed and exposed organoids was visualized using a LIVE/DEAD Viability/Cytotoxicity Kit for mammalian cells (ThermoFisher, Catalog number: L3224). Samples were incubated with fluorescent dyes to detect live (Calcein-AM) and dead (Ethidium homodimer-1) cells. Samples were imaged using confocal laser scanning microscopy (SP8, Leica Microsystems, the Netherlands).

**Gene expression:** Prior to RNA isolation, GelMA hydrogels were broken down using QIAshredder columns according to the manufacturer's instructions (Qiagen, Hilden, Germany). RNA was isolated from liver organoids (4 donors (n=4), in triplicate) using 350 µL RNeasy lysis buffer directly added into one well of the 24 well plate followed by RNA extraction using the RNeasy micro Kit according to the manufacturer's instructions (Qiagen). cDNA synthesis was performed using iScript cDNA synthesis kit (Bio-Rad, Veenendaal, the Netherlands). Relative gene expression of selected genes was measured using RT-qPCR in a CFX-384 (Bio-Rad). Primer design, validation, RT-qPCR conditions, and data analysis was performed as previously described.<sup>[402]</sup> Normalization was performed using reference genes GAPDH and RPS5. Details of primers are listed in **Table S1**.

**Immunofluorescence:** Organoids (4 donors) were fixed in 4% w/v paraformaldehyde (PFA) with 0.1% v/v eosin and stored in 70% v/v EtOH at 4° C until further processing. Bioprinted constructs were placed in agarose before embedding to keep the constructs



integrity during the histological processing. Samples were embedded in paraffin and cut into 4  $\mu\text{m}$  sections. Sections were deparaffinized and rehydrated. After antigen retrieval (information per antibody in **Table S2**), a blocking step was performed using 10% v/v normal goat serum (Bio-Rad) in PBS for 30 min at RT. Antibodies are listed in Table S2. Incubation with primary antibodies was performed overnight at 4° C. Secondary antibodies were incubated at room temperature for 1h. Nuclei were stained with DAPI (Sigma-Aldrich) diluted 2000x in PBS. Washing steps were performed using a buffer of PBS with 0.1% Triton X-100 (Sigma-Aldrich) and 0.2% w/v Bovine Serum Albumin (Sigma). Slides were mounted using FluorSave (Merck-Millipore, Burlington, MA, USA), and images were acquired using confocal microscopy (SP8, Leica Microsystems).

*HE staining:* Morphology and distribution of organoids in printed constructs (4 donors) was evaluated by hematoxylin and eosin (H&E) staining, scanned with slide scanner (Hamamatsu Photonics, Hamamatsu-city, Japan).

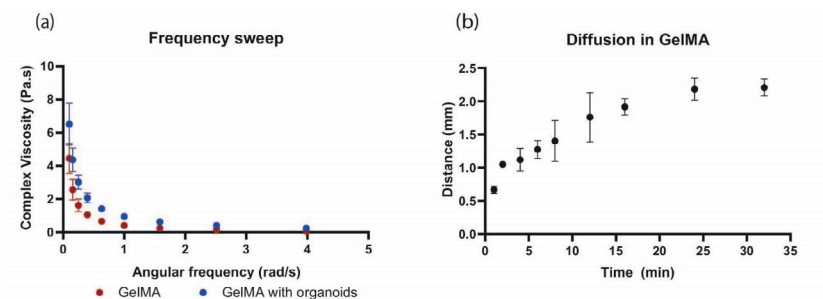
*Acetaminophen toxicity:* Acetaminophen (APAP; CAS 103-90-2, Sigma-Aldrich) was dissolved in differentiation medium as described above, using DMEM Glutamax with added factors as described for DM except Glutamax, NAC and B27. At day 7 of differentiation organoids were exposed to 30 mM APAP for 72 h (4 donors, n = 3), repeated dosing every 24 h. Metabolic activity was examined at 24, 48 and 72 h after start of exposure using the Alamar Blue assay. Medium was collected at 4, 24, 48 and 72 h of exposure to examine levels of miRNA-122 in the medium.

*Detection miRNA 122 in medium:* Total RNA was extracted from assay medium (120–160  $\mu\text{L}$ ) using the miRNeasy Serum/Plasma Kit (Qiagen) following the manufacturer's instructions. miRNA-122 was reverse-transcribed using the miScript II RT Kit (Qiagen) according to the manufacturer's protocol. Normalization of qPCR data of printed samples was performed using spiked-in synthetic *C. elegans* miR-39 (miRNeasy Serum/Plasma Spike-In Control, Qiagen). Ce\_miR-39\_1 and H2\_miR-122a\_1 miScript Primer Assays (Qiagen) were used for qPCR. The qPCR was carried out in a CFX-384 (Bio-Rad). Calculations were performed as previously described.<sup>[403]</sup> Changes of miRNA levels in supernatants were determined by comparing the Ct values in the exposed samples in comparison to the control (non-exposed) samples and expressed as  $-\Delta\text{Ct}$ .

*Statistical analysis:* For the statistical analysis of metabolic activity data, the gene expression data and the effects of acetaminophen exposure, we applied the post-hoc comparison uncorrected Dunn's test using GraphPad Prism (version 8.3.0). Significance levels are \*  $p \leq 0.05$ ; \*\*  $p \leq 0.01$  and \*\*\*  $p \leq 0.001$ .

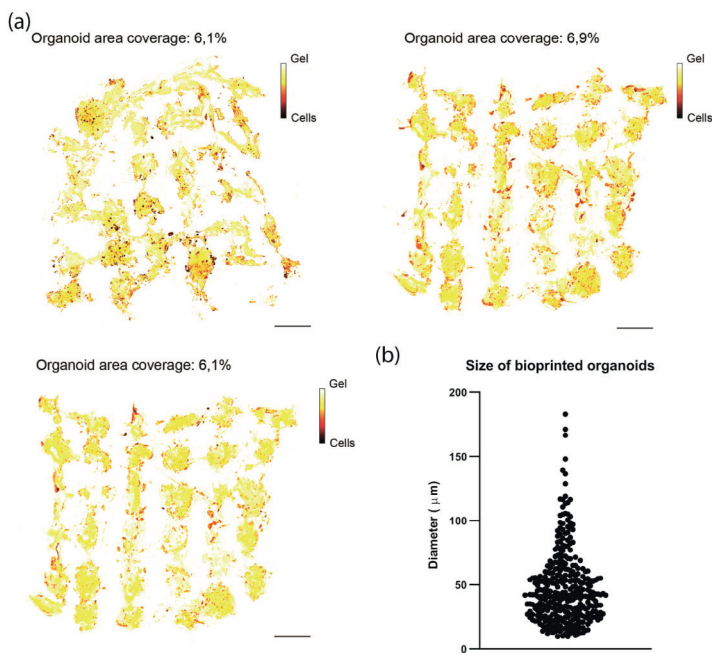
## SUPPORTING INFORMATION

## Supplementary Figures

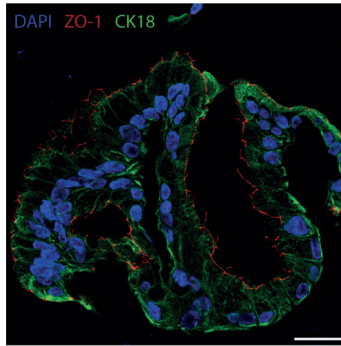


**Supplementary Figure S1:** Characterization of (a) the frequency-dependent behavior of viscosity in a 5% w/v GelMA ink with (blue) and without (red) organoids ( $n = 3$ ), and of (b) its capability to allow diffusion of solutes over time ( $n = 4$ ). Dots and error bars represent the average  $\pm$  standard deviation.

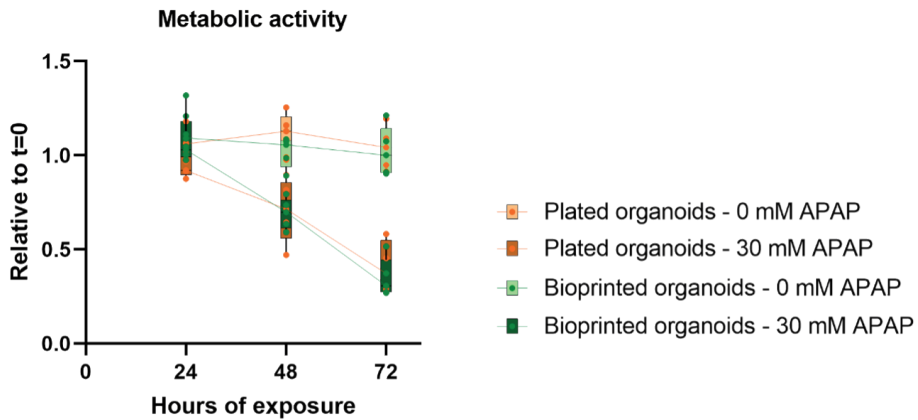
5



**Supplementary Figure S2:** Area of coverage (a) and organoid diameter (b) of the bioprinted organoids. (a) Average area of coverage is  $6.4 \pm 0.4\%$  ( $n = 3$ ). Scale bar =  $1000\ \mu\text{m}$ . Yellow: Hydrogel; Red: Cells. (b) The average diameter of bioprinted organoids is  $48.2 \pm 29.0\ \mu\text{m}$ .



**Supplementary Figure S3:** Immunofluorescence staining in liver constructs. Scale bar = 25  $\mu$ m. ZO-1, Zonula occludens-1; CK18, Cytokeratin 18.



**Supplementary Figure S4:** Cell viability of non-bioprinted (plated; orange) and bioprinted (green) liver organoids exposed to acetaminophen (APAP) relative to the cell viability at start of exposure (differentiation day 7 after plating/printing). Organoids exposed to 0 mM APAP (control; light colored box) and 30 mM (dark colored box). Each dot represents the mean of a technical triplicate of one donor (n = 5).

## Supplementary Tables

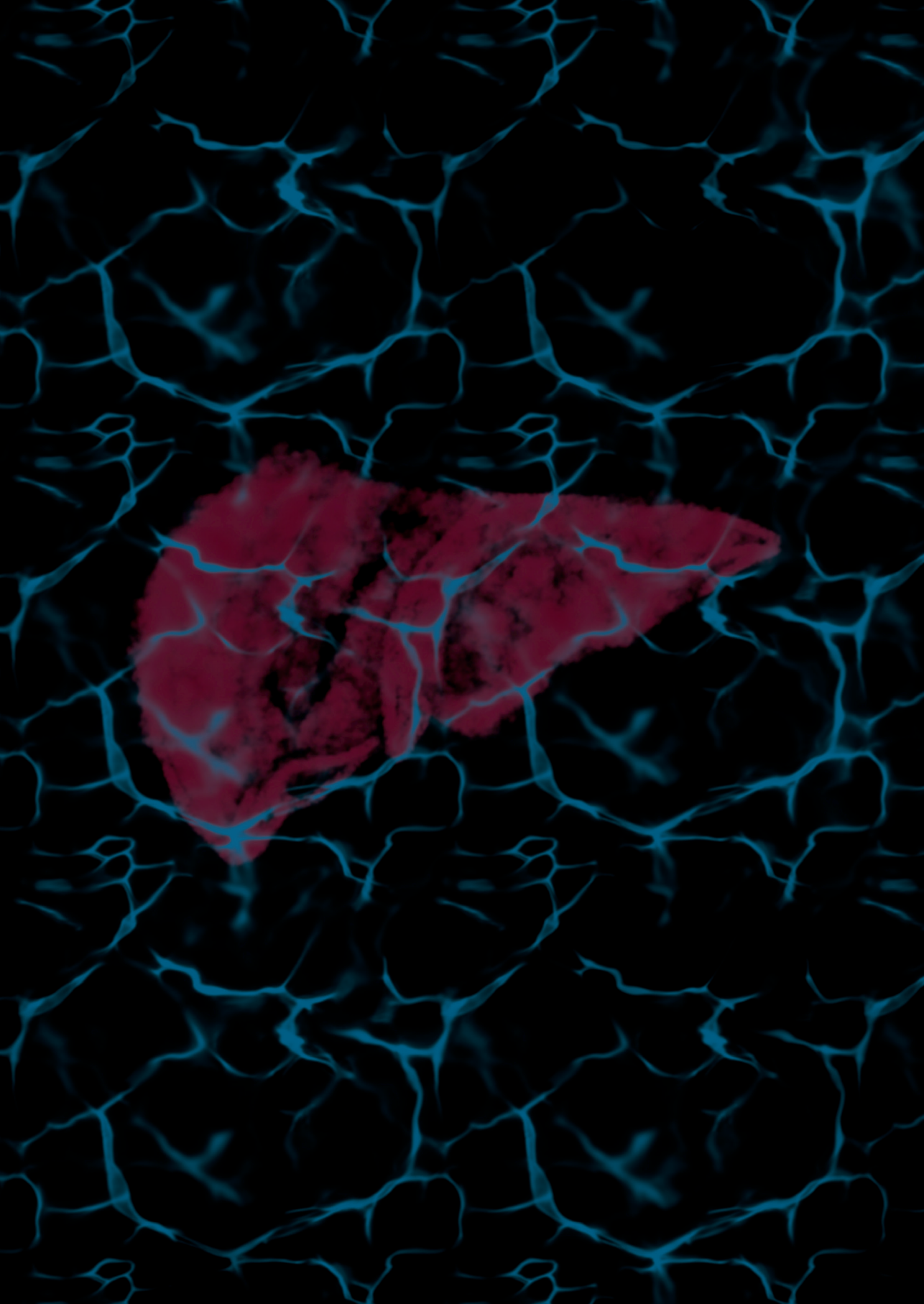
**Supplementary Table S1:** Primers used for quantitative PCR analysis.

Gene	Forward	Reverse
LGR5	GCAGTGTTACCTTCCC	GGTCCACACTCCAATTCTG
ALB	GTTCTGTACACCAAGAAAGTACC	GACCACGGATAGATAGTCTTCTG
G6PC	CGTCTTTAAGTGGATTCTCTTTGG	GTCCAGTCTCACAGGTTACAG
CYP3A4	TGATGGTCAACAGCCTGTGCTGG	CCACTGGACAAAAGCCTCCG
CYP2D6	GAGGTGCTGAATGCTGTC	AGGTCATCCTGTGCTCAG
CYP2E1	GTACACAATGGACGGTATCACC	GGAGCTTCTCTTCGATCTCAG
ABCG2	CGAGTAAAAGTGAAGAGTGGCTTT	CGAAGATTTGCCTCCACCT
BSEP	GTCATCTTGTGCTTCTTCCC	TCATTGTAAATCTGTCCCACCA

**Supplementary Table S2:** Antibodies used for immunofluorescence analysis

Primary antibodies				
Antigen	Source and cat. number	Raised in	Dilution	Antigen retrieval
MDR1	Novus Bio NBP1-90291	rabbit	1:200	TE
CK18	Santa Cruz sc-51582	mouse	1:400	Pepsin
Albumin	Sigma Aldrich A6684	mouse	1:1,000	TE
ZO-1	Invitrogen 40-2300	rabbit	1:250	Pepsin
HNF4 $\alpha$	LS Biosciences LS-B969	rabbit	1:200	TE
ASS	Aviva System Biology ARP41366_T100	rabbit	1:300	Citrate
E-cadherin	BD Bioscience 610181	w	1:100	TE / Citrate
TE: 10 mM Tris, 1 mM EDTA, 0.5% Tween 20 in PBS at pH 9.0 for 30 min at 98 °C Citrate: 10 mM citrate buffer at pH 6.0 for 30 min at 98° C Pepsin: 0.4% w/v (Dako) in 0.2 M HCl for 20 min at 37° C				
Secondary antibodies				
Antigen	Source and cat. number	Raised in	Dilution	
Anti-mouse Alexa	Life Technologies #A11029	goat	1:200	
Anti-rabbit Alexa 568	Life Technologies #A11036	goat	1:200	
Secondary antibodies were diluted in Antibody Diluent (Dako).				





# Chapter 6

## Volumetric Bioprinting of Organoids and Optically Tuned Hydrogels to Build Liver-Like Metabolic Biofactories

Paulina Núñez Bernal<sup>1\*</sup>, Manon Bouwmeester<sup>2\*</sup>, Jorge Madrid-Wolff<sup>3</sup>, Marc Falandt<sup>2</sup>, Sammy Florczak<sup>1</sup>, Nuria Ginés Rodríguez<sup>1</sup>, Yang Li<sup>1</sup>, Gabriel Größbacher<sup>1</sup>, Roos-Anne Samsom<sup>2</sup>, Monique van Wolferen<sup>2</sup>, Luc J. W. van der Laan<sup>4</sup>, Paul Delrot<sup>5</sup>, Damien Loterie<sup>5</sup>, Jos Malda<sup>1,2</sup>, Christophe Moser<sup>3</sup>, Bart Spee<sup>2</sup>, Riccardo Levato<sup>2,1</sup>

Published in: *Advanced Materials*. 2022. 34(15)

<sup>1</sup> Department of Orthopedics, University Medical Center Utrecht, Utrecht University, Utrecht, The Netherlands

<sup>2</sup> Department of Clinical Sciences, Faculty of Veterinary Medicine, Utrecht University, Utrecht, The Netherlands

<sup>3</sup> Laboratory of Applied Photonics Devices, École Polytechnique Fédéral Lausanne (EPFL), Lausanne, Switzerland

<sup>4</sup> Department of Surgery, Erasmus Medical Center, Rotterdam, The Netherlands

<sup>5</sup> Readily3D SA, EPFL Innovation Park, Lausanne, Switzerland

\* Authors contributed equally to this work

## ABSTRACT

Organ- and tissue-level biological functions are intimately linked to microscale cell-cell interactions and to the overarching tissue architecture. Together, biofabrication and organoid technologies offer the unique potential to engineer multi-scale living constructs, with cellular microenvironments formed by stem cell self-assembled structures embedded in customizable bioprinted geometries. This study introduces the volumetric bioprinting of complex organoid-laden constructs, which capture key functions of the human liver. Volumetric bioprinting via optical tomography shaped organoid-laden gelatin hydrogels into complex centimeter-scale 3D structures in under 20 seconds. Optically-tuned bioresins enabled refractive index matching of specific intracellular structures, countering the disruptive impact of cell-mediated light scattering on printing resolution. This layerless, nozzle-free technique poses no harmful mechanical stresses on organoids, resulting in superior viability and morphology preservation post-printing. Bioprinted organoids underwent hepatocytic differentiation showing albumin synthesis, liver-specific enzyme activity, and remarkably acquired native-like polarization. Organoids embedded within low stiffness gelatins ( $< 2$  kPa) were bioprinted into mathematically-defined lattices with varying degrees of pore network tortuosity, and cultured under perfusion. These structures acted as metabolic biofactories in which liver-specific ammonia detoxification could be enhanced by the architectural profile of the constructs. This technology opens up new possibilities for regenerative medicine and personalized drug testing.

**Keywords:** biofabrication; volumetric additive manufacturing; light-based 3D printing; bioresin; hydrogel



## INTRODUCTION

Laboratory-made three-dimensional (3D) living constructs that fully retain the function of human tissues and organs remain a major hope for regenerative medicine and for the development of advanced *in vitro* models for drug discovery, toxicology testing and precision medicine.<sup>[109,132]</sup> Biofabrication approaches, thanks to their ability to precisely orchestrate the three-dimensional patterning of multiple types of cells and biomaterials, have great potential to generate key architectural elements that can instruct the emergence of native functionalities in engineered tissues.<sup>[109]</sup> To date, various bioprinting techniques, a subset of biofabrication approaches in which one or several cellular components are directly incorporated in an additive manufacturing process,<sup>[110]</sup> have played a primary role in several proof-of-concept applications that showed the mimicry of salient organ functions *in vivo*, including in engineered ovaries,<sup>[221]</sup> thyroid glands,<sup>[143]</sup> and innervated skeletal muscle-like constructs.<sup>[404]</sup> The versatility and the freedom of design guaranteed by bioprinting technologies can be exploited both to generate anatomical-like as well as engineering-inspired architectures. While the exact degree of biomimicry that an engineered tissue should have right after the fabrication step is still a matter of debate, it is generally agreed that recapitulating every detail of physiological structures may not be needed, while providing cells with an environment to initiate and boost their own biological functionality is more important.<sup>[143,221,405,406]</sup> However, developing complex living structures of physiologically-relevant size (*i.e.*, dimension above the centimeter-scale) that can favorably guide cell behavior remains a major challenge. In addition, while bioprinting excels at modulating the environment surrounding the printed cells, tissue morphogenesis events *in vivo* are primarily driven by cell-cell interactions and self-assembly at the microscale, and thus cannot be directly controlled in a bioprinting strategy. Thanks to the development of organoids, which are miniaturized 3D structures that express key organ-like behavior, harnessing such cell-driven organization *in vitro* has led to a major breakthrough in biomedical research.<sup>[36]</sup> Even though organoids can also be generated from differentiated primary cells, most of the systems developed up to now arise from stem cells (harvested from adult tissue, or induced pluripotent cells).<sup>[407]</sup> Stem-cell derived systems are particularly promising due to their self-renewal capacity, helping to obtain sufficient organoid numbers for downstream applications, and due to the potential of the cells to differentiate into the multiple lineages that compose the tissue of reference.<sup>[407]</sup> However, organoid development in conventional tissue culture on Matrigel-like substrates is highly aleatory, offering no control over individual architecture, and resulting in sizes limited to the millimeter range.

In this work, we introduce a new, generalizable strategy for the light-driven volumetric bioprinting (VBP) of complex, functional organoid-laden constructs (**Figure 1A**). VBP is a layerless printing approach capable of printing positive and negative features (channels) at

high resolutions ( $41.5 \pm 2.9 \mu\text{m}$  and  $104.0 \pm 5.5 \mu\text{m}$ , respectively) (**Figures 1B-C**) and large-scale constructs previously achieving volumes of up to  $4.14 \text{ cm}^3$  in less than 30 seconds.<sup>[127]</sup> Given the novelty of the technology and of its working principle, which relies on the precise delivery of multiple tomographic light projections onto a cell-laden photopolymer, little is still known on the interplay between the cells and the precisely patterned projected light as well as on the printability requirements that a biomaterial needs to fulfill. Thus, first we investigated a new technique to engineer the optical properties of cell-laden hydrogels for VBP and unraveled its impact on printing shape fidelity. Leveraging this knowledge, in the present study VBP is combined for the first time with organoids that exhibit a microscale multicellular structure. These are herein bioprinted into centimeter-scale structures with designed architectures that facilitate access to metabolites. To meet the large cell numbers required for the volumetric bioprinting process (in the range of tens of millions of cells, at the densities shown throughout this study), a dynamic spinner flask culture system is used to establish organoid structures from human tissue samples (**Figure 1D**). As a proof-of-concept, we demonstrate the fabrication of centimeter-scale hydrogel-based objects embedding human liver epithelial organoids, obtained from primary (stem) cells found in intrahepatic bile ducts.<sup>[406]</sup> Differently from dense aggregates obtained from differentiated hepatic cells, that do not usually acquire native microarchitectural features of the liver,<sup>[408]</sup> these organoids are epithelial in nature, and form a cyst-like structure with an inner hollow lumen surrounded by a thin cell (mono)layer (**Figure 1D**).<sup>[35,355]</sup> This specific organization is especially interesting since many liver functions are dependent on hepatocyte polarization, *i.e.*, the directional transfer and secretion of compounds from and towards the apical or basolateral side of the cell. Importantly, since the specialized microarchitecture of the organoids can be easily compromised by mechanical stresses, a particular attention was placed on the ability of the printing process to preserve the self-organization of these biological building units. Thus, in this work epithelial liver organoids were selected to study how they can act as metabolically active biofactories, in which a prominent detoxification function of the liver can be modulated by the overall architecture of the construct, as defined via the volumetric printing process (**Figure 1E**).

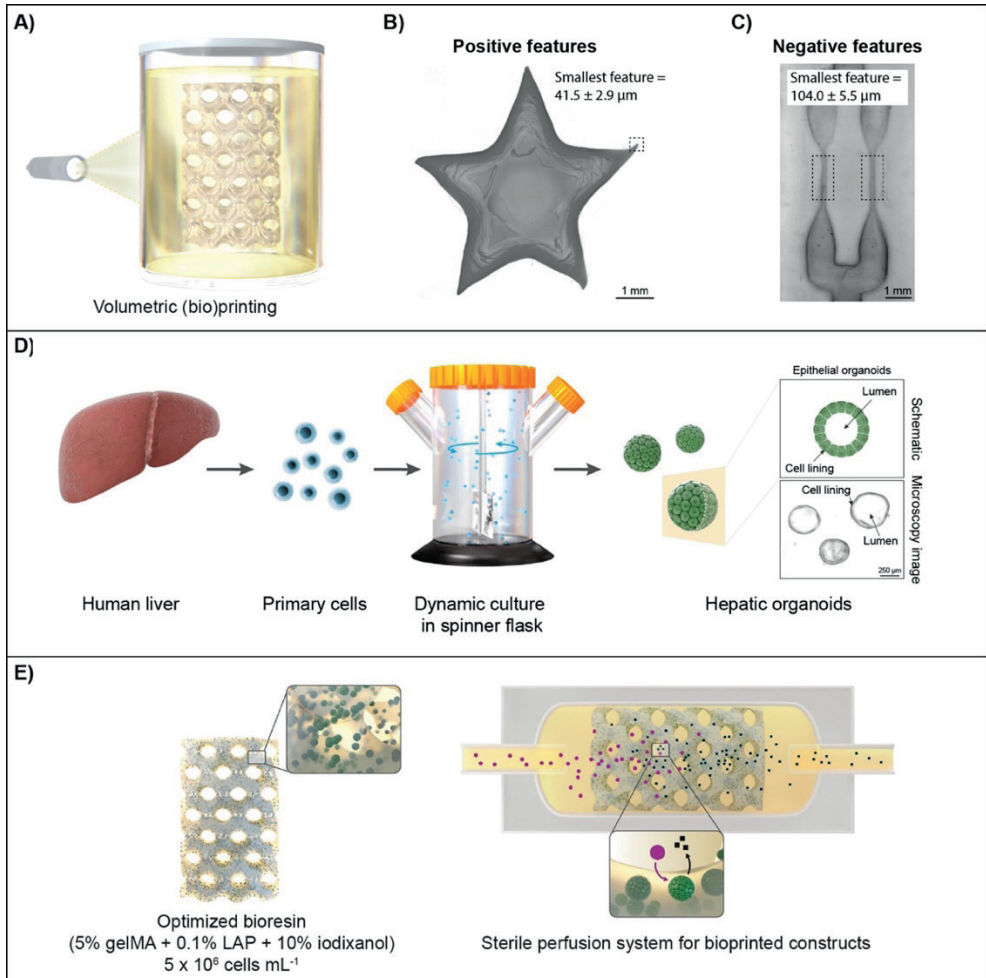


**Figure 1: Overview of the high-resolution volumetric printing process and study design.** A) Schematic representation of the volumetric printing process. B-C) Highest resolution prints of B) positive and C) fully perfusable negative features achieved with the 5% gelMA + 0.1% LAP bioresin used in this study (scale bars = 1 mm). Samples were imaged when being immersed in PBS directly after printing. D) Diagram of the hepatic organoid culture system, starting with human liver biopsies and isolation into single cells, which are then dynamically cultured in a spinner flask system to establish high yields of hollow epithelial organoid structures (microscopy image scale bar = 250  $\mu\text{m}$ ). E) Illustration of a complex, organoid-laden printed biofactory cultured under dynamic perfusion to enhance hepatic function, showing a representation of the breakdown of perfused compounds (purple circles) into metabolites (black squares).

## RESULTS AND DISCUSSION

Volumetric bioprinting is an emerging light-based technology capable of sculpting cell-laden photoresponsive hydrogels - also termed bioresins - into 3D constructs of various sizes, ranging up to several cubic centimeters, and complex geometries in a layerless fashion.<sup>[127]</sup> Leveraging the principles of tomographic additive manufacturing,<sup>[224,225]</sup> in VBP, a vat containing the bioresin is illuminated with visible light from multiple angles using a sequence of filtered backprojections of the object to be printed. While the light patterns address the whole build volume, the cumulative energy dose provided by the projections exceeds the bioresin's photocrosslinking threshold only in the geometry corresponding to the programmed object, thus building the whole construct at once. In this way, VBP yields centimeter-scale structures embedding microscale features in tens of seconds.<sup>[127]</sup> The rapid fabrication time and cell-friendly light doses are beneficial for preserving cell viability and functionality post-printing, whereas extensive printing times required to fabricate large parts can be of concern for conventional layer-by-layer manufacturing (*i.e.*, extrusion- and lithographic-based methods).<sup>[202]</sup> Moreover, via VBP, elements like overhangs, moving parts and convoluted porous networks typical of native tissues, can be easily recapitulated without the need for sacrificial or support materials, as previously reported reproducing the trabecular meshwork of cancellous bone.<sup>[127]</sup>

6 As the first step towards the fabrication of organoid-laden structures, we investigated the impact of the optical properties of the bioresin on printing resolution, in particular the ability of the cell-laden material to homogeneously transmit light. As opposed to extrusion-based bioprinting (EBB), in which printability is predominantly governed by the rheological properties of a bioink,<sup>[151,306,409,410]</sup> in VBP and other light-based approaches, such as stereolithography and digital light processing, the printing resolution is defined primarily by the photopolymerization kinetics of the material, and by the ability to precisely control the spatial distribution of the light dose within the bioresin volume. While EBB of photocrosslinkable materials requires rapid polymerization kinetics as well to ensure construct stability, in VBP the latter is key in achieving highly accurate prints. This factor is largely dependent on the resolution of the light projection, the spatial coherence of the light source, the algorithm for generating the set of patterns (for a digital micromirror device, the optical resolution is given by the effective pixel size projected in the print volume), and the presence or absence of scattering elements. The latter is of particular relevance for bioprinting applications, since cells and many subcellular structures are capable of altering the path of incident light, either causing attenuation of ballistic photons or scattering, therefore affecting printing resolution. In particular, scattered light will blur the projected tomographic images, causing an increase of the light dose in regions of the volume adjacent, but external to the part to be printed. Depending on the length of the scattering mean free path at a given wavelength (which is a measurement of the

average distance between two consecutive scattering events, thus inversely proportional to the cell density<sup>[411]</sup>, this can result in off-target polymerization and loss of resolution. In addition, the ballistic light attenuation caused by scattering decreases the addressable size of the construct in the vial.

To investigate this effect, we printed a 5% w/v gelatin methacryloyl (gelMA)-based bioresin (**Supplementary Figure S1**) supplemented with 0.1% w/v lithium phenyl-2,4,6-trimethylbenzoylphosphinate (LAP) as photoinitiator carrying either a single cell suspension of a well-known hepatic cell line (HepG2) (**Figure 2A**) or epithelial organoids derived from human liver (**Figure 2B**) in the form of a hollow disc with an S-shape filament (thickness = 500  $\mu\text{m}$ ) placed at its center (**Supplementary Figure S2**). This specific size was selected to generate filaments that could completely embed the produced organoids, even though finer printing resolution are possible as shown before in Figures 1B and C, in which resolution superior to what shown with volumetric printing up to date has been demonstrated.<sup>[224,225,291,412]</sup> In an ideal print, both the thick border of the disc and the thinner filament, herein used as a benchmark to quantify the printing resolution, should solidify at the same time after receiving the same, optimal light dose. Exceeding this optimal dose will cause overcuring of the fine feature, thickening of the filament wall, and eventually clogging of the disc. At a low cell density ( $1 \times 10^6$  individual cells  $\text{mL}^{-1}$ ) the bioresin is photocrosslinked at an exposure dose of  $250 \text{ mJ cm}^{-2}$ , and the fine features can be correctly resolved (at  $312 \text{ mJ cm}^{-2}$ ) with both single HepG2 cells and organoids. At higher cell concentrations, the minimal light dose required for crosslinking single cell suspensions rises, and the slope of the dose-thickness curve rapidly increases, narrowing the ideal printing window. Consequently, with the currently available hardware and software, printing at high cell densities is possible (as previously shown with up to  $10^7$  articular cartilage progenitor cells  $\text{mL}^{-1}$ ).<sup>[127]</sup> However, this requires a fine empirical adjustment of the delivered dose, which is often impractical when cells are available in limited amounts. A similar trend was observed for organoid-laden bioresins, although the printing process yielded a larger printability window compared to what was observed with single cells, as loss of shape fidelity in reproducing the fine feature was observed only at  $5 \times 10^6$  cells  $\text{mL}^{-1}$  (**Supplementary Figure S3**), a cell density selected for this investigation due to its already proven suitability for functional liver tissue engineering studies.<sup>[379,382,413–420]</sup> This result can be explained by the fact that liver organoids form cyst-like, hollow structures delimited by an epithelial cell monolayer.<sup>[355]</sup> Due to their relatively large size ( $\sim 300 \mu\text{m}$ ), organoids have a longer scattering mean free path, compared to single cell suspensions at any given equivalent cell concentration. Recent research efforts are introducing novel algorithms for tomographic printing that can correct for scattering events at the filtered projection-level, and thus ensure high resolution printing even in opaque media.<sup>[421]</sup> Although this has been only shown with resins carrying homogeneously-sized particles so far,<sup>[421]</sup> future translation to materials laden with cells, which have more complex light scattering profiles, will help expand the range of applications of VBP.

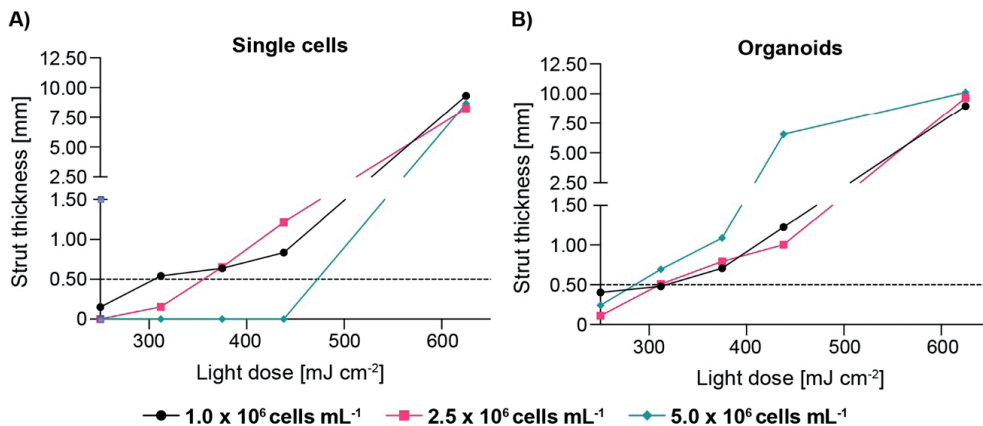


**Figure 2: Effect of single cell and organoid density on volumetric bioprinting accuracy in absence of optical corrections.** Fine feature thickness in constructs printed at increasing light doses (250–625 mJ cm<sup>-2</sup>) with bioresins containing different densities of A) single cell and B) organoid (1–5 x 10<sup>6</sup> cells mL<sup>-1</sup>). Dashed line represents the programmed feature dimension of the printed model (selected to be 500 μm to accommodate for the size of the printed organoids) (n = 3).

Cell-mediated scattering can also be addressed from the biomaterial-design perspective, by tuning the optical properties of the bioresin. In this study, we introduced a biocompatible and water-miscible refractive index matching compound, iodixanol, in order to modulate the optical performance of the gelMA-based bioresins (**Figure 3A**). Iodixanol was selected as it was proven not to harm cellular structures and tissue components, since this iodine, non-ionic compound has been applied for *in vivo* imaging,<sup>[422]</sup> as contrast agent for x-ray imaging,<sup>[423]</sup> and as an agent for the isolation of extracellular vesicles when preserving the integrity of membrane proteins is needed.<sup>[424]</sup> In principle, scattering-driven artefacts could be completely obviated, if the refractive index of the hydrogels matches that of the scattering element (*i.e.*, the cells). However, cells are highly heterogeneous, composed of several subcellular structures each characterized by its own average refractive index (**Supplementary Table S1**).<sup>[425]</sup> Furthermore, different cell types and even individual cells within the same population have a unique light scattering fingerprint. Selected concentrations of iodixanol could thus be tested to approximate the light refracting profile of key subcellular components that play a major role in light scattering at 405 nm (the wavelength used in the printer), which primarily includes the nucleus, contributing to increased ballistic light.<sup>[425]</sup>

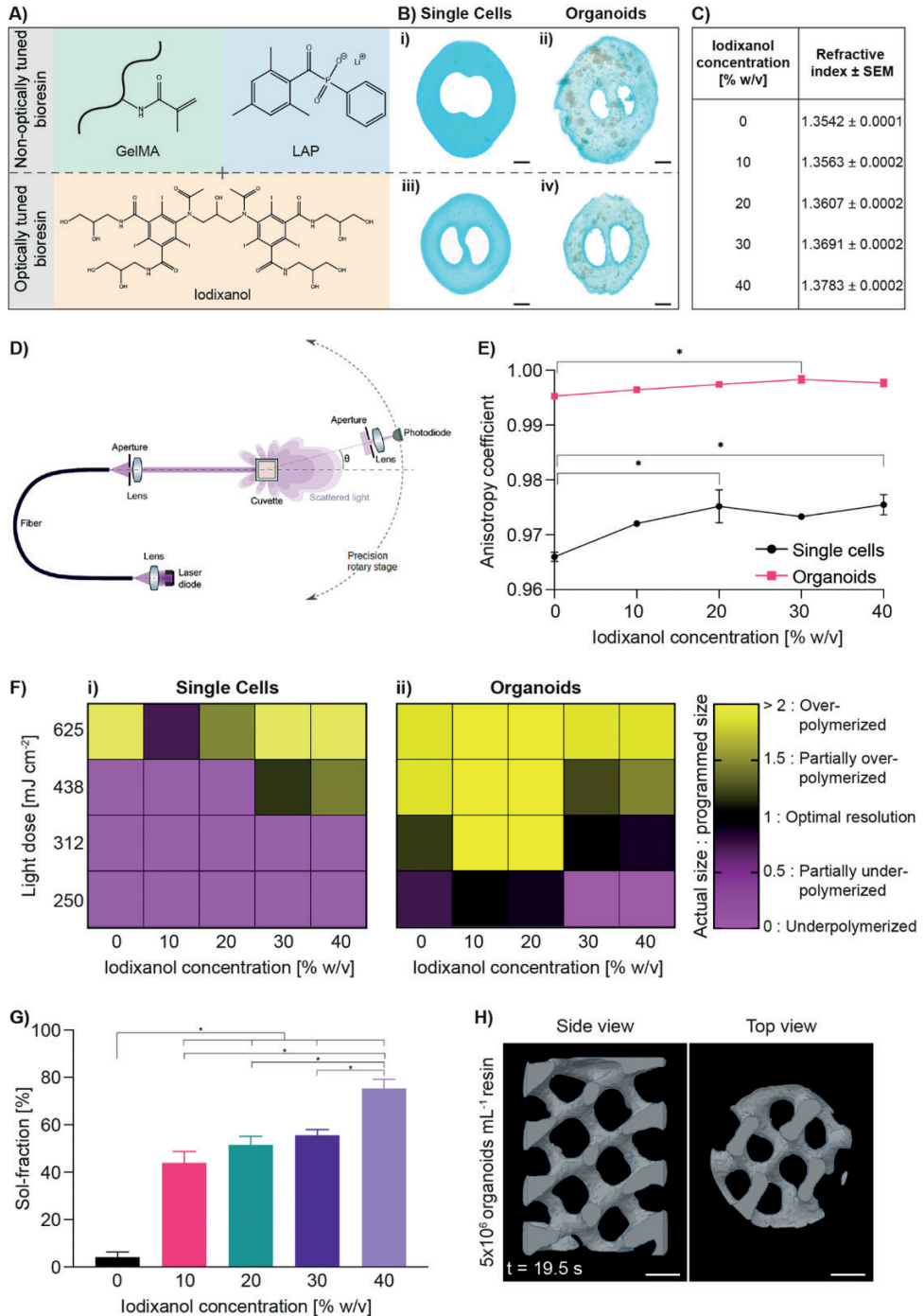


**Figure 3: Enhancing volumetric bioprinting of single cells and hepatic organoids through bioresin optical tuning with iodixanol.** A) Schematic of the bioresins used for volumetric bioprinting consisting of gelMA and

LAP, supplemented with iodixanol to optically tune the bioresin for enhanced printing accuracy in the presence of cellular structures. B) Stereomicroscopy images of i, ii) non-optimally tuned bioresin and iii), iv) iodixanol-containing bioresins for printing single cells and organoids (scale bars = 1 mm). C) Refractive index of the pristine and optically-tuned bioresins ( $n = 3$ ). D) Schematic of the light scattering measuring setup, and E) resulting anisotropy coefficient of different bioresin samples containing  $5 \times 10^6 \text{ mL}^{-1}$  single cells and organoids and increasing iodixanol content ( $n = 3$ ). F) Printability window of  $5 \times 10^6 \text{ mL}^{-1}$  single cells and organoids represented by the ratio of the printed fine feature thickness to the programmed thickness ( $n = 3$ ). G) Soluble fraction of gelMA samples containing increasing iodixanol concentrations ( $n = 3$ ). H) Side and top view of cross-sections from the 3D reconstruction of a complex bioprinted gyroidal structure with the optimized bioresin formulation carrying 10% w/v iodixanol (scale bars = 2 mm). \* = significant difference ( $p < 0.05$ ).

Supplementation with iodixanol successfully improved printing resolution both when using bioresins embedding single cells or liver organoids at  $5 \times 10^6 \text{ cells mL}^{-1}$  (**Figure 3B**), and it increased the refractive index of the bioresin in a concentration dependent manner, from 1.352 (pristine gelMA) up to 1.3783 at a 40% w/v (**Figure 3C**). The characterization of the angular light scattering profile in bioresins laden with single cells and organoids, supplemented with increasing iodixanol concentrations (**Figure 3D, E**), confirmed the experimentally found result that more optical power was directed in the forward direction. The extracellular refractive index change caused by the addition of iodixanol provides a better match to the overall refractive index of the organoids and thus light is less scattered, which is indicated quantitatively by a measured anisotropy coefficient closer to 1 (unity indicates no scattering). This effect was observed for both single cells and organoids. In terms of volumetric bioprinting, this made it possible to identify a working window for printing hepatocytic cells of 30% w/v iodixanol and organoids with as low as 10% w/v iodixanol (**Figure 3F, Supplementary Figure S4**). Importantly, the positive effect of the printing optimization via hydrogel optical tuning can be readily applied to produce thin features also when utilizing higher cell densities (herein tested with  $1.5 \times 10^7 \text{ cells mL}^{-1}$ ). This was shown by printing star-shaped hydrogel structures with the smallest resolved points measuring  $49.2 \pm 8.4 \mu\text{m}$  and  $50.5 \pm 6.0 \mu\text{m}$ , when using single cells and organoids respectively, although the organoids, given their large size exceeding the minimum print resolution, may of course protrude from the gel in the proximity of the finest features (**Supplementary Figure S5**). Notably, this approach for optical tuning of the biomaterials could potentially be combined with upcoming software-end based algorithms to further enhance printing resolution.<sup>[421]</sup>

It should be noted that, while these results apply to the liver cells tested in this study, such optimization of the refractive index of the bioresin is likely to result in a different optimal printing window when utilizing another cell population. From the chemico-physical point of view, iodixanol is intended as a fugitive additive, and it passively diffuses out of the hydrogel after crosslinking. Sol-fraction analysis revealed that in presence of iodixanol concentrations from 10 to 40% w/v, the sol fraction of the bioresins increased from  $44.0 \pm 4.7 \%$  to  $75.3 \pm 3.9\%$ , whereas pristine gelMA showed lower values ( $4.2 \pm 2.1\%$ ) (**Figure 3G**). Such high values for the mass loss after 24 h can be explained by the partial diffusion



of the refractive index matching compound out of the gels, but also indicate that part of the additive, which forms a viscous solution at room temperature, is likely still trapped in the gel and may be released over a longer time frame. Thus, to minimize the presence of this extra component in the culture environment and ensure hydrogel stability for the subsequent prints embedding liver organoids, the bioresin formulation containing the lowest amount of iodixanol (10% w/v) was selected. This optimized, optically tuned bioresin composition made it possible to resolve complex 3D structures, such as gyroidal constructs (**Figure 3H**) printed in under 20 seconds ( $195 \text{ mJ cm}^{-2}$ , 19.5 s printing time), which are otherwise not possible to bioprint with conventional extrusion methods, especially with soft materials needed for tissue culture.

Having identified a bioresin formulation for printing with high shape fidelity in presence of increasing cell concentrations, we further explored the advantages of combining VBP and organoid technology to create a bioengineered construct able to perform native-like liver function, given the critical role of the liver in maintaining systemic homeostasis. Notably, the distinguishing ability of liver epithelial organoids to capture micro-scale level architectures present in the liver, together with the fact that they can be readily obtained from individual patients and healthy donors via minimally invasive biopsies, holds potential for the development of advanced *in vitro* models for drug discovery and toxicology in personalized medicine. Such new platforms are especially needed in biomedical research, as liver damage is a primary cause for post-marketing withdrawal of new drugs,<sup>[338]</sup> a situation accentuated by the fact that current animal and cell culture models are insufficient to fully predict human physiology or donor-dependent responses.<sup>[342,426]</sup> The performance of liver organoids within the selected hydrogel upon bioprinting via VBP was investigated. Given the inherent challenge in replicating the multifaceted biosynthetic functions of native hepatocytes *in vitro*, we specifically analyzed i) the viability of the printed structures, and ii) the influence of the VBP on organoid microstructure and morphology, as a preliminary step to promote the differentiation and maturation capacity of the printed construct into hepatic-like structures.

The liver organoids used in this study were originally derived from adult stem cells positive for epithelial cell adhesion molecule (EpCAM) and for leucine-rich repeat-containing G-protein coupled receptor 5 (LGR5),<sup>[355]</sup> obtained through expansion in a dynamic stirred bioreactor.<sup>[55]</sup> Recent works further probing the *in vivo* origin of these cells suggest that these cells may be intrahepatic cholangiocytes, which display bi-potent differentiation capacity.<sup>[35]</sup> These adult cells have already been demonstrated to maintain genomic stability over multiple passages,<sup>[355]</sup> suggesting they can be an ideal source when high cell numbers are required for liver tissue engineering applications. As these hepatic organoids are available from donor tissues, they also have the potential for simulating a patient-specific response to drugs, as well as the production of catabolites or toxic compounds natively metabolized in the liver for drug discovery and toxicology studies, or serve as promising building

blocks for whole organ engineering.<sup>[427]</sup> However, when freshly isolated and expanded, these cells do not normally display specific hepatocytic phenotype commitment.<sup>[35]</sup> The liver organoids obtained from these cells are typically expanded in presence of laminin-rich basal membrane extracts (*i.e.*, Matrigel), in culture media cocktails that maintain them in a proliferative state. Their differentiation into hepatocytic structures is accompanied by an inhibition of proliferation and can be triggered by switching the media composition (key components being bone morphogenetic protein-7 and fibroblast growth factor-19).<sup>[55]</sup> This process has also been shown to be greatly influenced by mechano-chemical stimuli provided by different biomaterials and culture conditions.<sup>[428]</sup> As a first step, it was paramount to assess how organoids in differentiation media respond to the milieu defined by the VBP process.

Thus, upon printing, liver organoid-laden hydrogels were cultured in differentiation media. First, it was confirmed that iodixanol had no detrimental effect on the metabolic activity of the organoids, even when used in concentrations up to 40% w/v. In particular, all the tomographically bioprinted samples performed similarly to casted controls in absence of iodixanol, in which a slight decrement of resazurin reduction from day 1 to day 10 of culture was observed (**Figure 4A**). This was in line with what was previously observed for liver organoids cultured in differentiation conditions using other natural-origin hydrogels such as cellulose nanofibril-derived gels.<sup>[374]</sup>

The evolution of the metabolic activity over 10 days was also assessed in further detail with the optimized bioresin supplemented with 10% w/v iodixanol. The performance of constructs obtained from cells from three adult donors, was evaluated comparing samples generated via VBP, EBB, and casted gelMA (with and without iodixanol) and Matrigel controls to assess the impact of different fabrication approaches and materials (**Figure 4B**, further statistical details in **Supplementary Figure S6**). In all gelMA samples, the metabolic activity remained constant, whereas in the Matrigel control, a gradual increase was observed over the culture period. In the latter, this increment was accompanied by a higher amount of DNA in the samples (**Supplementary Table S2**). This result is coherent with the notion that Matrigel is a favorable substrate for organoid proliferation.<sup>[374]</sup>

Having demonstrated the cytocompatibility of the bioresin and of the printing process, an important objective was to evaluate if VBP could be used to preserve organoid structure, including the specific cell-cell contacts, tight junctions, and communication channels established during the organoid formation phase. During the expansion phase, organoids can reach millimeter-scale sizes, and in general, the growth to larger dimensions is regarded as an indicator of cell health.<sup>[55]</sup> As a light-based biofabrication technology, VBP does not subject cells to potentially harmful shear stresses that can instead be experienced in nozzle-based techniques.<sup>[247]</sup> Moreover, in extrusion-based bioprinting, nozzles typically displaying diameters 2-3 times larger than these organoid structures are required in order

to avoid clogging,<sup>[256]</sup> thus imposing a compromise on printing resolution. Alternatively, organoids need to be fragmented via mechanical or enzymatic disruption to enable seamless flow of the bioink during printing.<sup>[429]</sup>

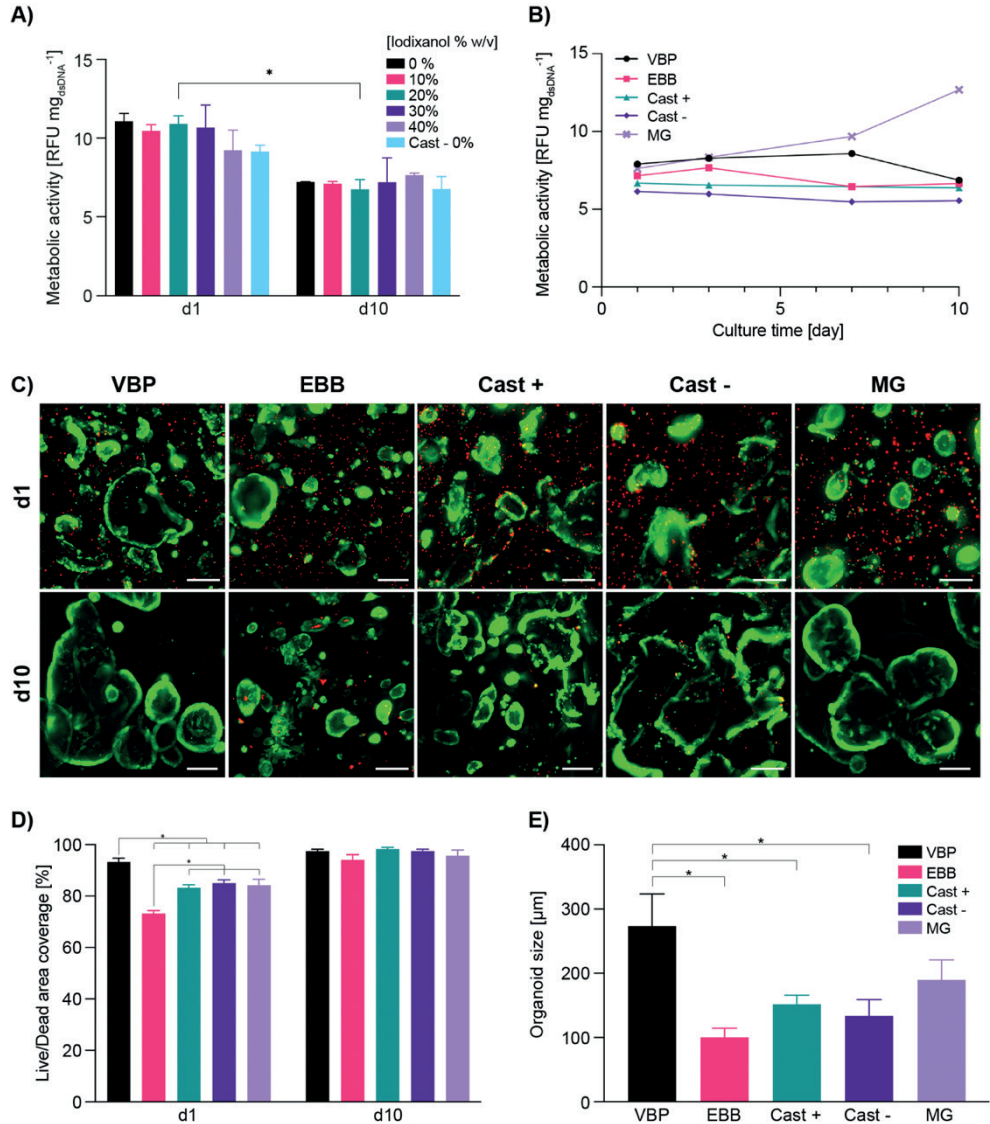


**Figure 4: Viability of volumetrically bioprinted hepatic organoids.** A) Metabolic activity of bioprinted organoids within bioresins with increasing iodixanol concentrations (0–40% w/v) over a 10-day differentiation period ( $n = 5$ ). B) Metabolic activity ( $n = 5$ ), C) Representative Live/Dead images (scale bars = 250  $\mu\text{m}$ ), D) live to dead ratio area ( $n = 3$ ) coverage, and E) average organoid sizes ( $n = 60$ ) of VBP- and EBB-printed organoids with the optically tuned bioresin (gelMA + 10% w/v iodixanol), casted gelMA samples with (Cast +) and without 10% w/v iodixanol (Cast -) and casted Matrigel (MG) samples over a 10-day differentiation period. \* = significant difference ( $p < 0.05$ ).

6

A LIVE/DEAD fluorescent staining post-printing revealed that organoids printed via VBP displayed superior viability ( $93.3 \pm 1.4\%$ ) and undisturbed average size ( $273.5 \pm 49.9 \mu\text{m}$ ) when compared to EBB ( $73.2 \pm 1.2\%$  viability,  $100.1 \pm 14.2 \mu\text{m}$  average size) one day post-printing (**Figure 4C, D, E**). Such high viability, as demonstrated by the positive staining of Calcein AM into the cells lining the hollow organoid structures, was comparable or superior to casted gelMA and Matrigel controls. Notably, for all samples, it was found that most of the dead cells were single cells shed from the organoids, which appeared in higher numbers in the samples containing fragmented cells processed via EBB. This significant difference in dead cell numbers between the VBP conditions and the other processing methods can likely be attributed to the fact that the nozzle-free nature of VBP allows for the maintenance of the structural integrity of the organoids by minimizing the shear stresses induced on these large structures through actions such as pipetting or extruding through a nozzle. The EBB samples, which show the lowest viability at day 1, exhibit high number of dead cells likely due to i) a high number of single cells resulting from the mechanical fragmentation of the organoids pre-printing that are not capable of reassembly when incorporated in the hydrogels, and ii) further organoid damage and breakdown into single cells and smaller fragments due to the shear stresses experienced during extrusion through the nozzle (**Figure 4D**). This is further supported by the significantly smaller organoid sizes observed in EBB samples during the differentiation period (**Figure 4E**). Casted organoids in gelMA and Matrigel on the other hand, only undergo shear stresses as the embedded organoids pass through the narrow pipet tip for controlled volume deposition for the casting process, instead of the extensive fragmentation of EBB-printed organoids. This is likely the reason for the significantly higher viability compared to the EBB condition. Over time, viability values reached comparable values ( $94.1\text{--}98.2\%$ ) for all experimental groups and controls. This was predominantly due to the fact that dead cells are removed from the culture environment with each media exchange, paired with the preservation of the cell viability already discussed for the biomaterials used in this study. To date, organoid shaping via bioprinting has been demonstrated via extrusion of a suspension of single stem cells, which are then led to re-form into organoids post-printing.<sup>[386]</sup> Alternatively, biofabrication of pre-generated organoids has been prevalently performed via molding,<sup>[430]</sup> individual spheroid dispensing,<sup>[143]</sup> or robotic-assisted pick-and-place techniques.<sup>[32]</sup> Although yielding impressive results in terms of generating tissues with high cell content, these approaches are limited to relatively simple 3D geometries, and rely on the printing of thick filaments/spheroids with a  $400\text{--}1000 \mu\text{m}$  diameter range to achieve simple tubular structures.<sup>[32,143,386,430]</sup> Complementing the possibilities granted by such strategies, the ability of VBP to print pristine, undamaged organoids offers an alternative to facilitate the free-form generation of intact organoid-laden constructs. Printing morphologically intact organoids can be advantageous for applications aiming to preserve the organoid pre-deposited ECM, given the increasing

evidence that cells embedded in biomaterials alter their behavior via contact with the nascent, self-synthesized ECM.<sup>[431]</sup> Even though in the context of liver tissue engineering, hepatocytes alone have limited capacity to secrete extracellular matrix proteins, this could be relevant especially when incorporating other liver-specific cell types, such as stellate cells.<sup>[432]</sup>

Next, the expression of key hepatocyte differentiation markers was investigated (**Figure 5**). Organoids from all experimental groups showed comparable levels of cytochrome 3A4 activity (which appeared significantly elevated in Matrigel-based cultures vs. EBB samples) normalized over the total protein content of the sample (**Figure 5A**), as well as gene expression levels of the same cytochrome and albumin (**Figure 5B, C**). In addition, all samples showed comparable normalized levels of various liver transaminases, such as aspartate transaminase (ASAT, involved in amino acid metabolism), gamma-glutamyl transferase (GGT, involved in drug and xenobiotic detoxification) and glutamate dehydrogenase (GLDH, involved in the urea cycle) (**Supplementary Figure S7**). The presence of such markers indicates the successful commitment towards a hepatocyte-like phenotype in VBP, EBB, and the casted controls, while only in the volumetrically bioprinted group this result was also paired with higher cell viability after printing. The evident donor-dependent variability observed in the expression levels indicate that liver organoids as *in vitro* models are better suited for personalized medicine applications or to establish bio-banks *i.e.*, to study drug susceptibility on patient groups with similar genetic make-up, as already proposed for other tissue types.<sup>[433]</sup>

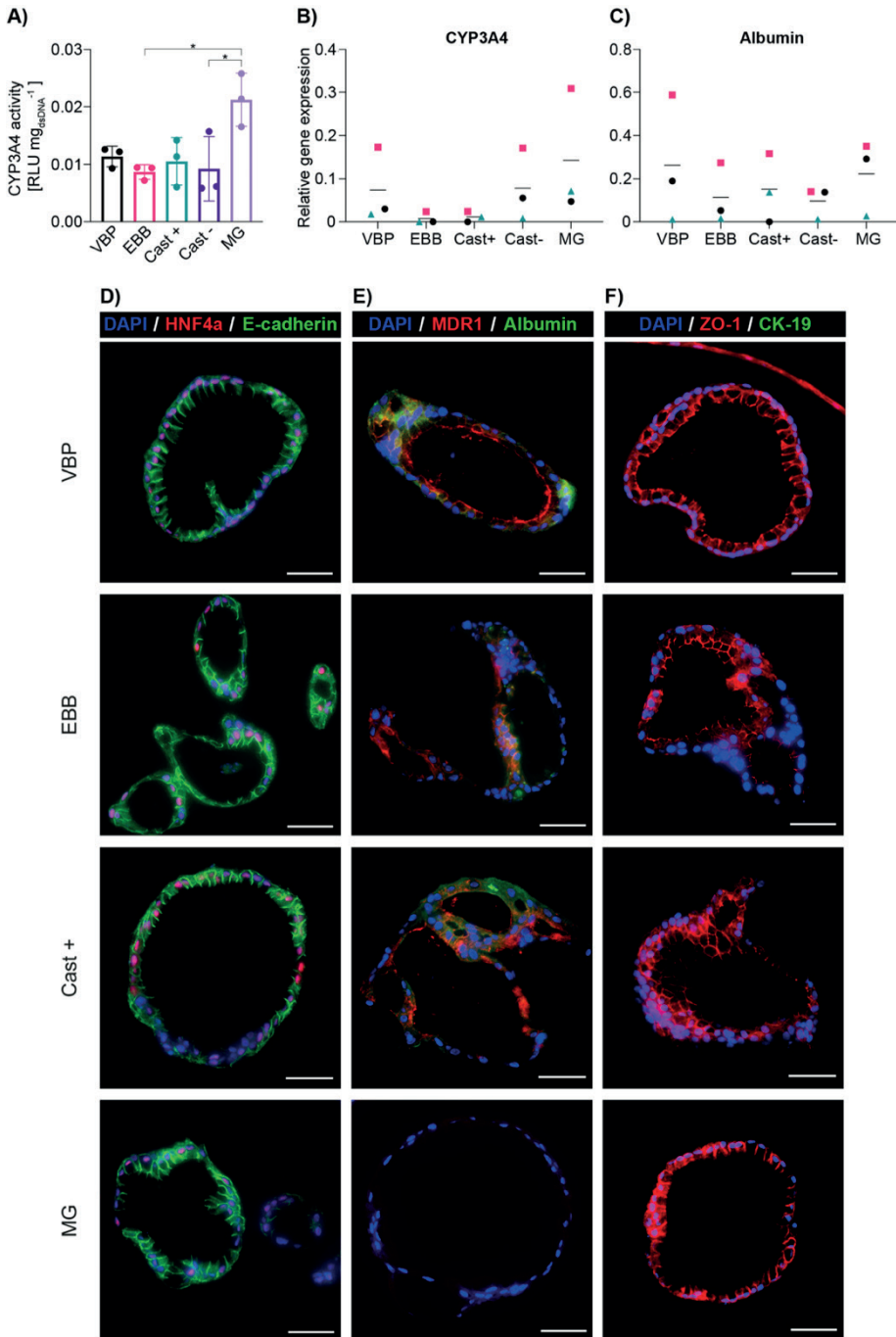


**Figure 5: Liver-specific markers in volumetrically bioprinted hepatic organoids.** A) CYP3A4 activity and relative gene expression of B) CYP3A4 and C) albumin in VBP- and EBB-printed organoids with the optically tuned bioresin, casted gelMA samples with (Cast +) and without 10% w/v iodixanol (Cast -) and casted Matrigel

(MG) samples after a 10-day differentiation period ( $n = 3$ ). Representative fluorescence images of liver-specific and organoid polarization markers D) HNF4 $\alpha$  and E-cadherin, E) MDR1 and albumin, and F) CK19 and ZO-1 in the VBP, EBB, Cast + and MG conditions after 10 days of hepatic differentiation. Scale bars = 50  $\mu\text{m}$ . Individual data points shown for 3 different donors ( $N = 3$ ). \* = significant difference ( $p < 0.05$ ).

Immunofluorescence analysis of volumetrically bioprinted organoids within the optimized gelMA-based bioresin also revealed the intracellular presence of the hepatocyte markers hepatocyte nuclear factor 4 alpha (HNF4 $\alpha$ ), E-cadherin, high-expression of albumin and tight junction protein-1 (ZO-1) (**Figures 5D, E, F**), as well as the absence of the cholangiocyte marker cytokeratin 19 (CK-19),<sup>[55]</sup> underlining the acquisition of a hepatocyte-like phenotype. Organoid morphology and glycogen storage was also visualized in all experimental groups though hematoxylin and eosin (H&E) and periodic acid-Schiff (PAS) stainings (**Supplementary Figure S8**). Extrusion-based printed samples and casted controls also showed similar patterns, albeit with some key differences. In particular, the VBP samples clearly showed a significantly higher degree organoid polarization, with the formation of an apical side in the cyst lumen for the highest percentage of organoids ( $73.9 \pm 1.8\%$ ), as evidenced by the localized expression of multidrug resistance protein 1 (MDR-1).<sup>[434]</sup> Organoid polarization is an indicator of maturation and an important feature to study the directional uptake, transport and eventual secretion of metabolites present in the native liver, which is not observed in cell lines under conventionally established culture conditions (*i.e.*, standard 2D culture of single liver cell lines, primary cells or 3D spheroid cultures). Moreover, while MDR-1 was also detected in EBB and casted gelMA controls (but not in Matrigel), quantitative analysis of the polarized organoids showed significantly impaired polarization in these groups ( $12.1 \pm 1.2\%$  for EBB,  $36.9 \pm 3.0\%$  and  $36.5 \pm 3.6\%$  for the cast+ and cast- samples respectively) as opposed to VBP-printed organoids (**Figure 5E, Supplementary Figure S9, S10**). This significant difference between VBP-printed organoids and EBB and casted controls could be attributed to the fact that in VBP, structural integrity of the organoids is not disrupted during the printing process and seemingly results in the rapid acquisition of polarity markers when the differentiation process begins. Instead, EBB and casted organoids undergo shear stresses and fragmentation during their respective fabrication processes, and have to reassemble once they have been embedded in viscous hydrogels, a condition that may impair the onset of polarity across all organoids, as suggested by our results. These findings are also supported by the comparable trends observed in organoid viability post-fabrication (**Figure 4**), in which, much like for MDR-1 polarization, EBB showed the lowest values, followed by the milder casting process. In addition, Matrigel controls were also negative for MDR-1, and notably also for albumin, even if the marker was present at a gene expression level, indicating no synthesis of this protein and indicative of a well-known common mismatch in molecular biology between mRNA levels and actual protein expression.<sup>[435–437]</sup> This result, paired with the previous finding of enhanced metabolic activity over time, further underlines how Matrigel is an ideal substrate for organoid proliferation.

On the other hand, for hepatocytic differentiation, other hydrogels<sup>[374,428,438]</sup> including gelMA as shown in this study, appear to provide a more suitable 3D environment. While the exact mechanism by which gelMA facilitates organoid differentiation remains to be elucidated, previous studies with other RGD-modified polyethyleneglycol hydrogels have identified stiffness values in the range between 1-2 kPa as beneficial for organoid growth and differentiation.<sup>[428]</sup> Conversely, the same hydrogels in softer or stiffer formulation lead to inferior organoid yield and expression of liver fibrosis markers, respectively.<sup>[428]</sup> Interestingly, gelMA-iodixanol bioresins yielded gels with compressive moduli of  $1.73 \pm 0.09$  kPa, nearly identical to the matrigel compressive modulus ( $1.72 \pm 0.09$  kPa), suggesting that mechanosensing may indeed be a contributing element to the enhanced organoid differentiation, and the biological cues provided by the gelatin-derived gelMA resin may be a key factor in creating a more permissive environment for differentiation compared to the proliferative enhancement observed in Matrigel culture systems. These soft gels are also likely a consequence of the higher sol-fraction after crosslinking, since unmodified gelMA prepared at the same prepolymer concentration with no optical tuning resulted in stiffer gels ( $5.04 \pm 0.10$  kPa) (**Supplementary Figure S11**). Notably, both gelMA resins were shown to remain biodegradable after the photocrosslinking process, as found upon exposure to a collagenase-laden media,<sup>[331]</sup> an essential characteristic of biocompatible materials used in the field of tissue engineering (**Supplementary Figure S12**).

6 Upon confirming that VBP samples in optically tuned gelMA bioresins provide a suitable environment for liver organoid differentiation, we investigated the potential of bioprinting to modulate the functionality of the organoid-laden constructs, when cultured in a dynamic perfusion setting. At first, we selected a series of 3D objects with convoluted pore distribution from a pool of mathematically defined triple periodic minimal surface structures. This class of geometries is well-known in the field of tissue engineering, as lattices belonging to this family have been investigated to produce mechanical metamaterials,<sup>[439]</sup> to maximize cell seeding in polymeric scaffolds,<sup>[440]</sup> and to promote *in vivo* bone ingrowth in biomaterials-based implants,<sup>[441]</sup> among other applications. Specifically, we selected three lattice structures with interconnected porosity: Schwarz D, Schwarz G and Schwarz P.<sup>[442–445]</sup> At a comparable volume (between 383.17 and 394.25 mm<sup>3</sup>), these structures show a decrease in surface area to volume ratio (from 2.05 to 1.88 mm<sup>-1</sup>), and decreasing average tortuosity of the porous network (from 1.32 to 1.04) respectively. (**Supplementary Figure S13, Supplementary Table S3**). Thus, the choice of these structures provide the possibility to modulate key geometrical parameters, and, under perfusion, the flow profile within the porous construct, that are paramount for the interaction between the embedded cells and the solutes within the culture media, without significantly altering the cell content and cell density. Therefore, these architectures offer an ideal platform and proof-of-concept to study the effect of the geometry imposed by the printing process on the functionality of the embedded cells.



Notably, such complex geometries are in general extremely difficult to reproduce at high resolution with extrusion technologies, especially when soft hydrogels are used as carrier materials. Hydrogel-based gyroidal structures can instead be easily printed with digital light projection bioprinting techniques, although generally requiring extended printing times that scale linearly with the height of the construct.<sup>[173]</sup>

However, printing similar convoluted structures in cell-friendly processing times and at the same time ensuring shape fidelity when using soft, cell-friendly hydrogels like the gelMA-iodixanol bioresin tested in this study remains a major challenge in the field of biofabrication. Via VBP, we could successfully generate all three Schwarz structures laden with organoids, and the construct could maintain their shape when retrieved from the printing environment and immersed in aqueous media. To facilitate handling and permit a seamless coupling of the constructs with a fluidic circuit for perfusion culture, we modified the design of the lattices. These were encased in a hydrogel made fluidic chamber, equipped with an entry and an exit port, to which plastic microfluidic tubing could be coupled. The modified design could be reproducibly printed, with a printing time ranging from 14 to 15.5 seconds, depending on the geometry (**Figure 6A**). When compared to the extensive printing times that would be needed to fabricate these same centimeter-scale structures under optimal printing conditions (between 24.7–34.0 minutes, even when using the easily printable and high-shape fidelity ink Pluronic F127, **Supplementary Figure S14**), the extremely rapid printing speed offered by VBP pose a promising advantage to overcome the detrimental effects on cell functionality that have been previously observed over extended printing times.<sup>[202]</sup> Given the high-speed printing achieved with VBP, these structures could also be printed for high-throughput analysis in a matter of minutes (**Supplementary Figure S15**). The system was first perfused with a constant flow of buffered solution supplemented with fluorescent microspheres to evaluate the flow profile within the structures. Tracking of the trajectory of the beads confirmed that these particles followed a nearly straight path in the Schwarz P lattice, as opposed to an increasingly wavy path in the other geometries (**Figure 6B**). This was quantitatively proven by the significantly larger trajectory amplitudes exhibited by the Schwarz D structure ( $0.214 \pm 0.098$  mm) compared to the G and P architectures ( $0.157 \pm 0.109$  and  $0.077 \pm 0.105$  mm respectively, **Supplementary Figure S16**). Given the constant flow rate ( $1.5 \mu\text{L min}^{-1}$ ) imposed by the pump connected to the system and a smaller equivalent cross-sectional area along the flow pathway within more convoluted lattice in the Schwarz D, the average particle speed in this system was the highest ( $0.416 \pm 0.009$  mm  $\text{s}^{-1}$ ), whereas the lowest speed was found for the Schwarz P lattice ( $0.241 \pm 0.009$ ) (**Figure 6C**). Thus, the Schwarz D and P geometries, that showed the most marked differences in terms of flow profile, were printed embedding liver organoids, and conditioned in differentiation media, prior to being connected to the perfusion system for 24 hours.

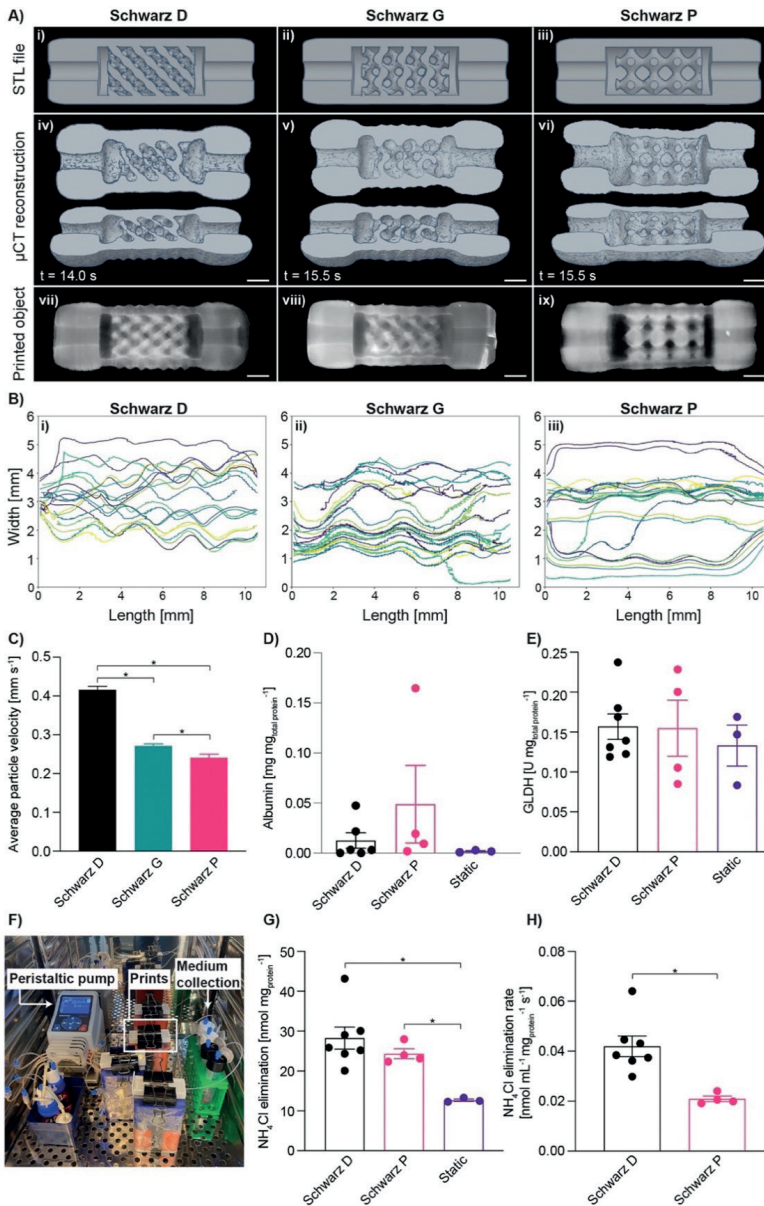


**Figure 6: Modulating hepatic organoid function through volumetric bioprinting of mathematically-derived lattices with differing flow properties.** A) Complex, perfusable architectures were successfully printed within seconds with an adjusted lattice design that enables coupling to microfluidic tubing as shown in the i-iii) STL models of the i) Schwarz D, ii) Schwarz G and iii) Schwarz P architectures. iv-vi) 3D reconstructions from  $\mu$ CT scans and vii-ix) macro-photographs showing the different complex and interconnected pore networks exhibited by the Schwarz iv,vii) D, v,viii) G, and vi,ix) P structures (scale bars = 2 mm). B) These complex architectures were shown to modulate the flow trajectory of microspheres moving through the Schwarz i) D, ii) G and iii) P prints, as well as the C) average speed of the flowing particles ( $n = 485-1210$ ). D) Albumin secretion and

E) GLDH levels of organoids embedded in Schwarz D and P architectures, after 24 hours of continuous perfusion (n = 4–8). F) Sterile perfusion setup, which enabled perfusion of differentiation medium supplemented with 1.5 mM NH<sub>4</sub>Cl through complex architectures and resulted in differing G) total NH<sub>4</sub>Cl elimination compared to statically cultured cylindrical control samples and H) architecture-dependent NH<sub>4</sub>Cl elimination rates (n=4–8). \* = significant difference ( $p < 0.05$ ).

During this time, the culture media was collected to measure the secretion of albumin and of the liver specific enzyme GLDH, which is a key player in protein catabolism, ammonia production, and in the generation of substrates for the synthesis of ATP (**Figure 6D, E, F**).<sup>[446]</sup> Albumin levels secreted over a 24 hour period of continuous flow perfusion were highest in the Schwarz P structure ( $0.061 \pm 0.051 \text{ mg mg}_{\text{total protein}}^{-1}$ ) compared to Schwarz D ( $0.013 \pm 0.008 \text{ mg mg}_{\text{total protein}}^{-1}$ ) and static controls ( $0.002 \pm 0.001 \text{ mg mg}_{\text{total protein}}^{-1}$ ) (**Figure 6D**). The total albumin production ( $3.40 \pm 1.75$  and  $17.00 \pm 13.03 \mu\text{g mL}^{-1}$  for Schwarz D and P, respectively, **Supplementary Table S4**) exhibited by the complex printed structures was also superior to previously reported experimental results from liver-like constructs, where albumin values range from  $\sim 0.004$ ,<sup>[447]</sup>  $\sim 0.3$ ,<sup>[448,449]</sup> and  $\sim 0.6 \mu\text{g mL}^{-1}$ ,<sup>[450]</sup> over longer medium collection periods of 7 – 10 days. Taking into account the total volume of medium collected in our perfusable system ( $\sim 28 \text{ mL}$ ), these highly complex VBP-printed biofactories outperform previous tissue engineering attempts in terms of albumin production. As for GLDH, printed and static constructs exhibited similar enzyme levels (**Figure 6E**). Most notably, the organoid-laden bioprinted lattices were able to actively remove ammonia from the media injected in the perfusion chamber (**Figure 6G**), a key function normally performed by the liver through the urea cycle. Ammonia detoxification was significantly higher under perfusion culture ( $33.5 \pm 5.8$  and  $24.3 \pm 1.4 \text{ nmol mg}_{\text{total protein}}^{-1}$  for Schwarz D and P, respectively) when compared to static controls ( $12.7 \pm 0.3 \text{ nmol mg}_{\text{total protein}}^{-1}$ ), suggesting that the applied flow promotes organoid function, possibly due to stimuli provided by the fluid shear stresses on the gelMA-embedded organoids. Previous studies using perfusion systems in combination with liver cell lines,<sup>[451]</sup> stem cells,<sup>[414]</sup> and differentiated primary cells<sup>[417]</sup> have shown enhanced liver-like functions in smaller-scale systems. In addition, fluid flow-induced shear stresses have demonstrated to enhance organoid maturation in different tissue engineering and organ-on-a-chip applications (*i.e.*, kidney),<sup>[452]</sup> further supporting the hypothesis that shear stimuli also played a role in our system. Importantly, in Schwarz D samples, due to the higher flow velocity compared to the Schwarz P lattice, ammonia molecules have a shorter residency time within the construct (24.0 vs. 41.5 s). Yet, ammonia elimination also occurred at a significantly faster rate, indicating that the ammonia detoxification capacity of the bioprinted organoids can be effectively boosted by the accurate selection of the architecture imposed to the organoid-laden hydrogel, in this case, using a highly convoluted, tortuous structure like the Schwarz D construct (**Figure 6H**). While it can be inferred that part of this modulation of the biological functionality in response to the engineered geometry can be due to an improved surface area available for exchange

of solutes, it is also likely that the design-driven enhancement in diffusion could directly stimulate the encapsulated liver organoids. It should also be noted that, given the design of these constructs, organoids were also present in the casing with connectors placed around the lattices, and these additions to the Schwarz structures were identical for all three architectures. Nevertheless, the variation in geometry imparted in the central part of the object was sufficient to observe a difference in terms of cell behavior during culture. In the context of our *in vitro* system, these mathematically defined lattices were shown to offer unique potential to control the fluid flow within the pores and to modulate the communication between the bioprinted organoids and solutes found in the media, leading to a modulatory effect on ammonia detoxification. Moreover, it is important to remark that, although in this specific study focused on bioprinting for *in vitro* 3D culture applications, and thus *in vivo* regenerative medicine applications go beyond the scope of this work, such user designable, bioprinted structures that can maximize the ability of the cells to interact with the surrounding nutrients and signals could have valuable applications also for producing transplantable grafts. Overall, these results underline the importance of architectural cues in the design of advanced tissue engineered and biofabricated constructs.

## CONCLUSIONS

In summary, the first phase of the study takes fundamental steps to unravel the effects of different cellular components (single cells and organoids) on the volumetric printing process, namely due to the cell-mediated light scattering and its effect on printing resolution. Using this knowledge, an optically tuned, gelatin-based bioresin was successfully developed and was able to reduce scattering through refractive index matching of specific intracellular components. This strategy is versatile, and could be potentially applied to resins used for volumetric additive manufacturing which use other photocrosslinking chemistries besides methacryloyl-based, such as thiol-ene step growth.<sup>[453]</sup> This development allowed high resolution volumetric bioprinting with increasing cell densities, and provides important knowledge on the ideal design requirements for the development of next-generation bioresins for VBP. In combination with more advanced tomographic algorithms, multi-material and multi-cellular printing approaches can be more easily established in order to increase the overall complexity of volumetrically printed architectures. Using the liver as a model tissue platform, this study demonstrated the ability to harness the advantages of both VBP and organoid technology in a single approach that resulted in the fabrication of multi-scale biofactories capable of guiding tissue-specific functions. Liver-derived organoids were successfully printed at high densities and demonstrated maintained viability and hepatic function compared to extrusion printed and casted controls. The layerless fabrication approach employed by VBP resulted in increased organoid viability post-printing, and enabled the preservation of organoid morphology and polarity compared to controls. The soft, organoid-laden bioresin was successfully sculpted into highly convoluted, mathematically-derived structures with distinct structural properties. Successful printing of these cell-laden structures in under 20 seconds and establishment of a sterile perfusion chamber allowed the printed organoids to act as biofactories capable of modulating liver-specific ammonia detoxification depending on the printed architecture. These findings demonstrate the close relationship between the shape of the constructs and their resulting biological functionality, further underlining the potential of biofabrication for advancing tissue engineering. This study, therefore, opens up new possibilities for the future development of self-sustaining biofactories that are able to carry out a wide variety to tissue-specific functions. Overall, the combination of the ultra-fast VBP process with organoid technology holds great potential for the development of advanced regenerative medicine approaches and *in vitro* model development for fundamental biology research, personalized drug screening and disease modeling.

## EXPERIMENTAL SECTION

*Materials:* GelMA (93.5% DoF) was synthesized as previously reported,<sup>[335]</sup> and used as a 5% w/v solution in phosphate buffered saline (PBS). Lithium phenyl(2,4,6-trimethylbenzoyl) phosphinate (LAP, Tokyo Chemical Industry, Japan) was added at 0.1% (w/v) as a photoinitiator to induce a photocrosslinking reaction. To perform optical tuning of the cell-laden bioresin, the gelMA and LAP solution was supplemented with different concentrations (0 – 40% w/v) of iodixanol (OptiPrep™; StemCell Technologies, Canada).

*Volumetric bioprinting procedure:* Volumetric bioprinting of different structures was achieved using a Tomolite printer (Readily3D, Switzerland). For bioprinting, single cells and hepatic organoids were embedded in different gelMA bioresins at densities of  $1 - 1.5 \times 10^7$  cells per mL and placed in Ø10 mm cylindrical borosilicate glass vials. The bioresin-filled vials were placed at 4° C to elicit thermal gelation and prevent cell sedimentation throughout the printing process. Briefly, the printing process is induced by a laser beam at 405 nm directed onto a digital micromirror device (DMD) that is modulated into tomographic projections. These projections are then imaged into the printing vials. The projections were calculated using a commercial software (Apparite, Readily3D, Switzerland) taking into account the material properties of the resin and the printing vials. The average light intensity before the printing container was  $9.98 \text{ mW cm}^{-2}$  during printing. Further details concerning the tomographic printing process can be found in literature.<sup>[127,224]</sup> Post-printing, the printer vials were heated to 37° C to melt the unpolymerized bioresin, and samples were washed with prewarmed PBS. For the printing optimization experiments, prints at different light doses were performed, by modulating the exposure time. Successful crosslinking was appreciated for doses at which the every intended feature object could be resolved and the print did not redissolve when heating the bioresin. Finally, the as-printed parts underwent 5 min of additional crosslinking in 0.1% w/v LAP in PBS solution in a CL-1000 Ultraviolet Crosslinker ( $\lambda = 365 \text{ nm}$ ; UVP, USA).

*Hepatic organoid establishment, expansion and differentiation:* Healthy liver biopsies were obtained during liver transplantation at the Erasmus Medical Center Rotterdam in accordance with the ethical standard of the institutional committee to use the tissue for research purposes (ethical approval number MEC 2014-060). The procedure was in accordance with the Helsinki Declaration of 1975 and informed consent in writing was obtained from each patient. Disposable 125-mL spinner flasks (Corning, USA) were inoculated with  $5 \times 10^6$  of the collected single cells in 20 mL expansion medium (EM), including 10% v/v Matrigel™ (Corning, New York, NY, USA) to increase organoid yield as previously described.<sup>[55]</sup> Rotation speed was set to 85 rpm. Every 2-3 days, new medium was added to the spinner flasks. After a 14-day expansion period, organoids were collected for printing and passaged into a new spinner flask. To assess the size of the organoids, aliquots from the spinner flasks were taken at the end of the culture time and imaged

with an optical microscope, measuring the diameter of at least 150 organoids per spinner flask. In order to match the printed cell densities to the single cell conditions, aliquots of the organoid suspension were mechanically fragmented and trypsinized into single cells, and were subsequently counted using an automatic cell counter. Post-printing, organoid-laden structures were cultured in hepatic differentiation media (DM) for 10 days. For single cell studies, HepG2 cell line was used, (ATCC nr. HB-8065) and cultured in T175 culture flasks in HEPG2 expansion medium, which was replenished twice a week. All cultures were kept in a humidified atmosphere of 95% air and 5% CO<sub>2</sub> at 37° C. Details of the cell isolation protocol from liver biopsies and of the culture media components are reported in the Supporting Information.

*Stereomicroscopy and computed tomography for print evaluation:* Macroscopic images of cell- and organoid-laden structures were acquired using an Olympus SZ61 stereomicroscope coupled with an Olympus DP70 digital camera (Olympus Soft Imaging Solutions GmbH, The Netherlands). Zoomed in images were cropped and pasted over a black background to eliminate background reflections.  $\mu$ CT scans were performed with a Quantum FX  $\mu$ CT (voxel size = 15  $\mu$ m<sup>3</sup>, 90 kV tube voltage, 200  $\mu$ A current, and 26 seconds of scan time, Perkin Elmer, USA). 3D reconstructions were generated with the 3D viewer plugin in Image J (n = 3-6).

*Refractive index and measurements of scattering phase function of cell suspensions:* The refractive index of bioresins with different iodixanol concentrations (n = 3) was measured with an Abbe refractometer (2WAJ, Optika, Italy). The scattering properties of the hydrogels were measured with a custom-made apparatus, as depicted in figure 3D. The principle of the setup is similar to that introduced by Hunt and Huffman.<sup>[454]</sup> The apparatus setup and anisotropy coefficient calculations are detailed in the Supporting Information.

*Metabolic activity and viability of bioprinted and cast organoids:* Cylindrical organoid-laden constructs (5 x 10<sup>6</sup> cells mL<sup>-1</sup>; 5 mm diameter x 2 mm height) were produced through i) volumetric bioprinting (170 mJ cm<sup>-2</sup>, 17.0 s printing time) with and without iodixanol (0–40 % w/v), ii) extrusion-based bioprinting with a pneumatic-driven system (25 G stainless steel nozzle, temperature = 21° C, pressure = 0.03 MPa, 3DDiscovery, REGENHU, Switzerland), iii) casting of the gelMA bioresin with and without idodixanol (10% w/v) and crosslinking for 15 minutes in a CL-1000 Ultraviolet Crosslinker ( $\lambda$  = 365 nm; UVP, USA) and iv) casting in Matrigel droplets, thermally crosslinked at 37° C for 20 minutes. Importantly, EBB-printed organoids had to be mechanically fragmented using a P200 pipette tip in order to prevent nozzle clogging prior to the fabrication step. Samples were cultured in organoid differentiation medium for 10 days, which was refreshed every two days. Metabolic activity (n = 5) was measured with a resazurin assay (resazurin sodium salt, Alfa Aesar, Germany) and normalized by double-stranded DNA content per sample quantified using a Picogreen Quant-iT assay (Thermo Fischer Scientific, The Netherlands)

after 1, 3, 7 and 10 days. Cell viability was evaluated using a LIVE/DEAD assay (Calcein, ethidium homodimer, Thermo Fischer Scientific, The Netherlands) after 1, 3 and 10 days ( $n = 3$ ), imaged by a Thunder imaging system (Leica Microsystems, Germany). For each measurement in the printing/casting comparisons, 3 donors were evaluated ( $N = 3$ ).

*Hepatic functionality assessment of bioprinted/casted constructs:* CYP3A4 activity in organoids at day 10 of differentiation was quantified using the P450-Glo CYP3A4 Assay (Promega, USA) according to the manufacturer's instructions. CYP3A4 levels were normalized to DNA amount in the samples determined with a picogreen assay ( $n = 3$ ). Gene expression of liver-specific markers (CYP3A4 and albumin) was quantified through RT-qPCR (Bio-Rad, The Netherlands) at day 10 of differentiation ( $n = 3$ ). Liver-specific and polarization marker expression upon hepatic differentiation (HNF4 $\alpha$ , ZO-1, MDR1, CK-19 and E-cadherin) were visualized through immunofluorescent stainings and imaged using a Thunder imaging system (Leica Microsystems, Germany) ( $n = 3$ ). Details of the qPCR protocol primers and of the immunohistochemical procedures are reported in the Supporting Information. Liver transaminase and GLDH present in organoid-laden constructs and secreted albumin in the culture medium were measured with the clinical chemistry analyzer Beckman AU680 (Beckman Coulter, USA) using standard protocols ( $n = 3$ ). Values were normalized to total protein content quantified through a micro-BCA protein assay kit (ThermoFischer Scientific, The Netherlands).

*Fluorescent beads tracking through complex printed structures:* Printed Schwarz D, G and P structures were placed in a custom-made PDMS mold and connected to a syringe pump using FA microfluidic tubing (IDEX Health&Science, OD 1.6 mm, ID 0.75 mm). Green fluorescent polyethylene microspheres (125 – 150  $\mu\text{m}$  diameter; Cospheric, USA) were perfused through the printed structures at a flow rate of 20  $\mu\text{L min}^{-1}$  ( $n = 3$ ). Videos of microsphere flow through the printed constructs were recorded using a custom-made imaging system (Supporting Information). The particle trajectories were calculated from the acquired videos with the Crocker and Grier algorithm,<sup>[455]</sup> using trackpy v0.5.0 (<https://zenodo.org/record/4682814>). The particles identified in each video frame were linked into trajectories using a proximity criterion. Mean particle speeds were calculated as averages between each trajectory start and end point, where the contribution of each trajectory to the overall mean speed was weighed by the trajectory length. The amplitude was calculated on a subset of the oscillations within the trajectories shown in Figure 6Bi-iii ( $n = 50$ -80). Local minima and maxima values were identified in the trajectory y positions. Amplitude was calculated as half of the distance in the direction orthogonal to the main direction of the flow from a maximum to the subsequent minimum. All code used for video analysis is available at: <https://github.com/VictorOnink/Particle-Trajectory-Analysis>.

*Ammonia elimination assay in a sterile perfusion setup:* Organoid-laden, volumetrically bioprinted Schwarz D and P structures ( $5 \times 10^6$  cells  $\text{mL}^{-1}$ , 200  $\text{mJ cm}^{-2}$ , 20.0 s printing

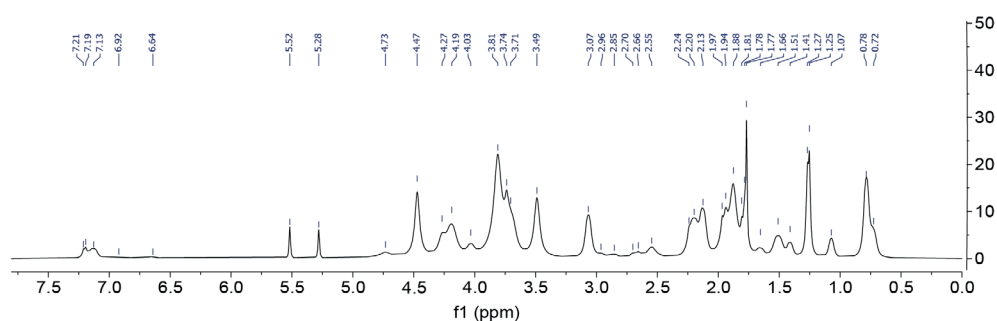


time;  $n = 8$  and  $4$  respectively) were cultured with differentiation medium for 10 days under static conditions. After 10 days the structures were transferred to a sterile flow perfusion chamber (Supplementary information) and perfused with DM supplemented with  $1.5 \text{ mM}$  ammonium chloride ( $\text{NH}_4\text{Cl}$ ) for 24 hours under continuous flow of  $20 \mu\text{L min}^{-1}$ . The fluidic chambers were cultured in sterile conditions at  $37^\circ \text{C}$ , and medium was collected for 24 hours. Ammonium chloride concentrations in the collected medium were determined using the Urea/Ammonia Assay Kit (Megazyme, Ireland). Medium samples were decolorized using activated carbon (Merck, Germany). Static controls consisted of volumetrically printed non-porous cylinders (diameter  $6 \text{ mm}$  x  $17 \text{ mm}$  height) cultured under static conditions ( $n = 3$ ). Media supplemented with  $1.5 \text{ mM}$   $\text{NH}_4\text{Cl}$  that was incubated for 24 hours without cells was used to determine the initial concentration ( $n = 3$ ). Total ammonium chloride elimination and elimination rate were normalized to the total protein content.

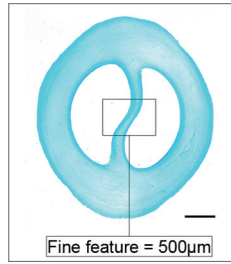
**Statistical analysis:** Results were reported as mean  $\pm$  standard error of the mean (SEM). Statistical analysis was performed using GraphPad Prism 9.0 (GraphPad Software, USA). Comparisons between experimental groups were assessed via one or two-way ANOVAs, followed by *post hoc* Bonferroni correction to test differences between groups. When normality could not be assumed, non-parametric tests were performed. Differences were found to be significant when  $p < 0.05$ .

## SUPPORTING INFORMATION

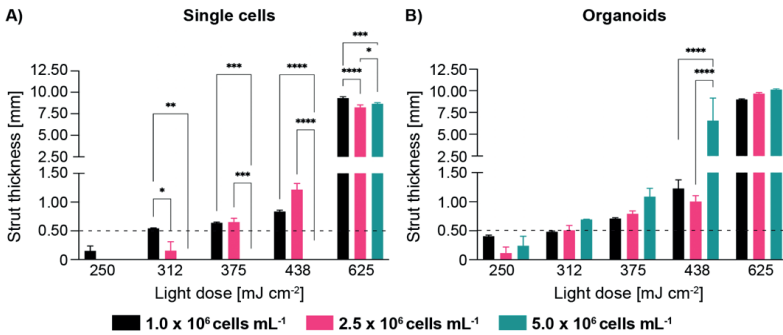
### Supplementary Figures



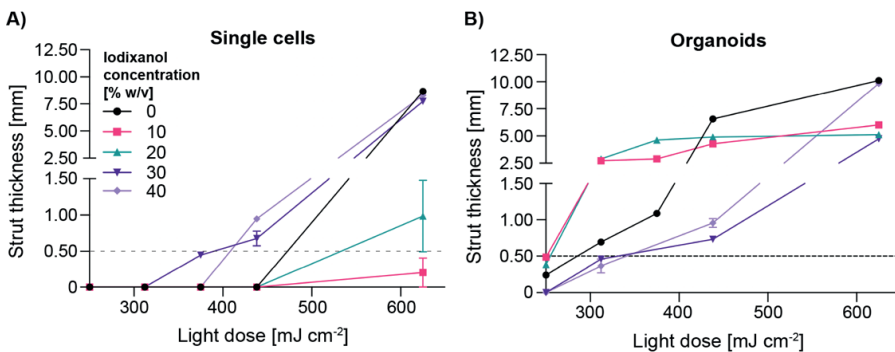
**Supplementary Figure S1: Proton nuclear magnetic resonance ( $^1\text{H-NMR}$ ) spectrum of synthesized gelatin methacryloyl in  $\text{D}_2\text{O}$ .**  $^1\text{H NMR}$  (400 MHz,  $\text{d}_2\text{o}$ )  $\delta$  7.24 – 7.10 (m, 3H), 5.52 (s, 1H), 5.28 (s, 1H), 4.73 (s, 2H), 4.47 (s, 9H), 4.27 (s, 3H), 4.19 (s, 8H), 4.03 (s, 2H), 3.81 (s, 24H), 3.72 (d,  $J = 13.3 \text{ Hz}$ , 9H), 3.49 (s, 9H), 3.07 (s, 6H), 2.55 (s, 3H), 2.22 (d,  $J = 17.1 \text{ Hz}$ , 8H), 2.13 (s, 6H), 1.95 (d,  $J = 11.6 \text{ Hz}$ , 7H), 1.88 (s, 13H), 1.78 (d,  $J = 6.4 \text{ Hz}$ , 8H), 1.51 (s, 4H), 1.41 (s, 2H), 1.26 (d,  $J = 6.7 \text{ Hz}$ , 10H), 1.07 (s, 2H), 0.78 (s, 10H).



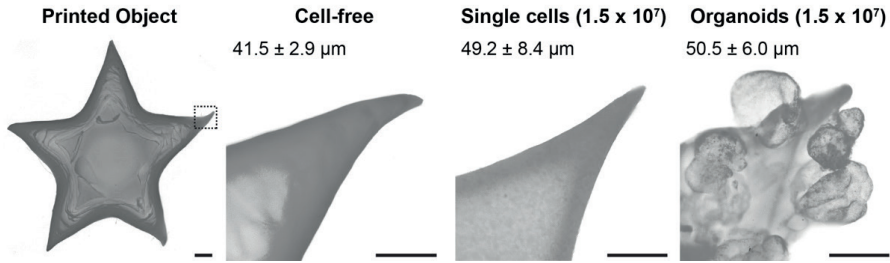
**Supplementary Figure S2: Simple structure to measure printing resolution.** Oval shaped structure with a curved inner strut representing a fine feature of 500  $\mu\text{m}$  thickness. This structure was used to assess printing resolution with cell-laden bioresins containing different cell densities and concentrations of iodixanol. Scale bar = 2 mm.



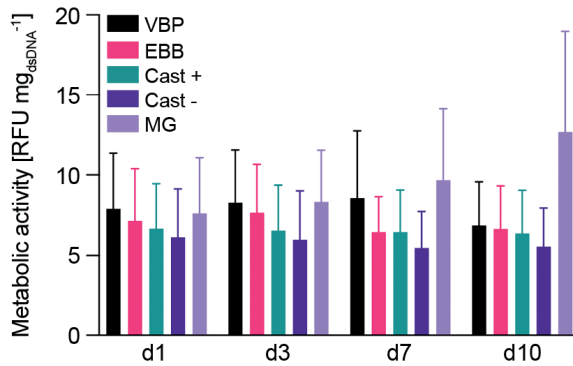
**Supplementary Figure S3: Printing accuracy of bioresins with increasing cell densities in absence of optical corrections (including SEM).** Fine feature thickness in constructs printed at increasing light doses (250–625  $\text{mJ cm}^{-2}$ ) with bioresins containing different A) single cell and B) organoid densities ( $1\text{--}5 \times 10^6 \text{ cells mL}^{-1}$ ) ( $n = 3$ ). \* = significant difference ( $p < 0.05$ ).



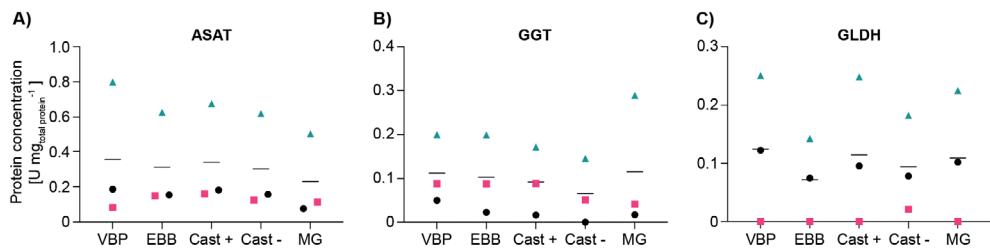
**Supplementary Figure S4: Printing accuracy of bioresins with increasing iodixanol concentrations (including SEM).** Fine feature thickness in constructs printed with  $5 \times 10^6 \text{ cells mL}^{-1}$  at increasing light doses (250–625  $\text{mJ cm}^{-2}$ ) with bioresins containing different iodixanol concentrations (0–40% w/v) ( $n = 3$ ).



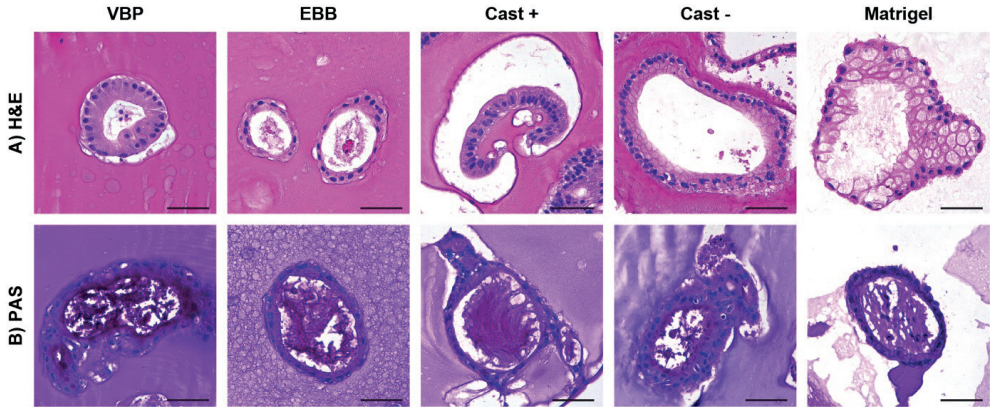
**Supplementary Figure S5: High-resolution printing with high single cell and organoid densities.** Stereomicroscopy images showing the printing of a star-shaped construct, zooming in on the fine feature points of the stars containing no cells,  $1.5 \times 10^7$  cells  $\text{mL}^{-1}$ , printed as single cells and as organoids (scale bar = 500  $\mu\text{m}$ ). The measurements reported in the panels refer to the width at the tips of the stars ( $n = 5-15$ ).



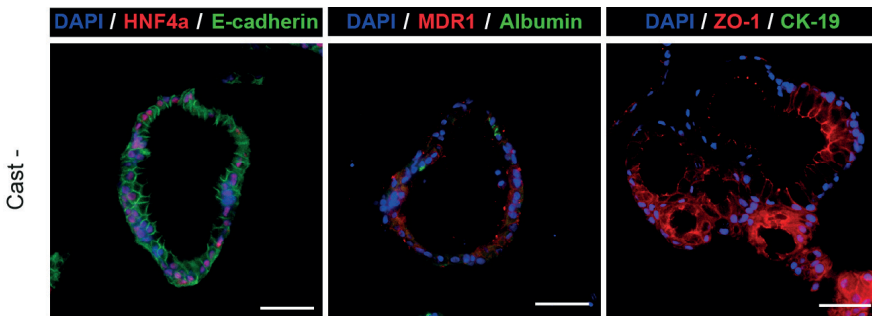
**Supplementary Figure S6: Metabolic activity of printed and casted organoids during hepatic differentiation (including SEM).** Metabolic activity of VBP- and EBB-printed organoids with the optically tuned bioresin (gelMA + 10% w/v iodixanol), casted gelMA samples with (Cast +) and without iodixanol (Cast -) and casted Matrigel (MG) samples over the 10-day differentiation period ( $n = 3$ ) ( $p < 0.05$ ).



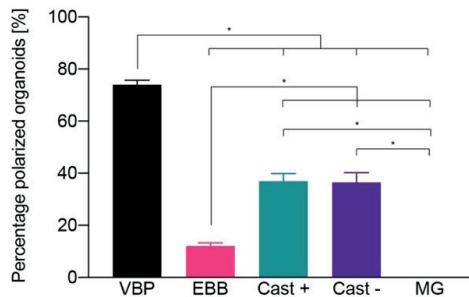
**Supplementary Figure S7: Liver transaminases levels in bioprinted and casted organoid-laden samples upon hepatic differentiation.** Levels of A) ASAT, B) GGT and C) GLDH in cell lysates of VBP- and EBB-printed organoids with the optically tuned bioresin (gelMA + 10% w/v iodixanol), casted gelMA samples with (Cast+) and without iodixanol (Cast-) and casted Matrigel (MG) samples after the 10-day differentiation period ( $n = 3$ ) ( $p < 0.05$ ).



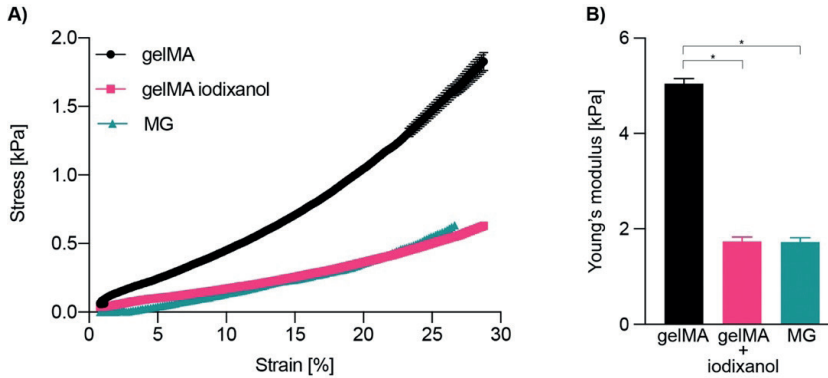
**Supplementary Figure S8: H&E and PAS staining of bioprinted and casted organoid-laden samples after hepatic differentiation.** Histological images showing A) H&E staining and B) PAS staining of VBP- and EBB-printed organoids with the optically tuned bioresin (gelMA + 10% w/v iodixanol), casted gelMA samples with (Cast+) and without iodixanol (Cast-) and casted Matrigel (MG) samples after the 10-day differentiation period.



**Supplementary Figure S9: Liver-specific markers in cast samples not supplemented with iodixanol.** Representative fluorescence images of liver-specific and organoid polarization HNF4 $\alpha$  and E-cadherin, MDR1 and albumin, and CK19 and ZO-1 in the Cast- condition after 10 days of hepatic differentiation. Scale bars = 50  $\mu$ m.



**Supplementary Figure S10: Quantitative analysis of organoid polarization based on luminal MDR-1 expression between different fabrication strategies: VBP, EBB, and casted gelMA (with and without iodixanol) and Matrigel.** (n = 160 – 255). \* = significant difference ( $p < 0.05$ ).



**Supplementary Figure S11:** A) Stress/strain curves and B) compression modulus of gelMA samples without and with (10% w/v) iodixanol and Matrigel control samples. (n = 3). \* = significant difference ( $p < 0.05$ )

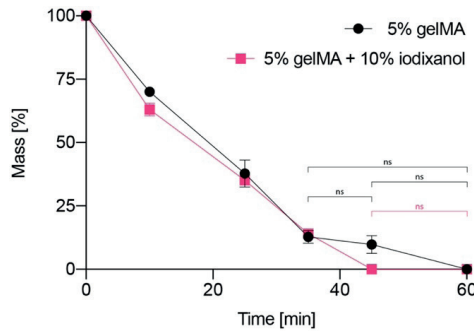
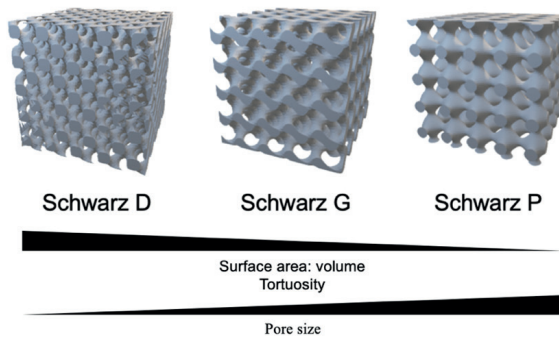
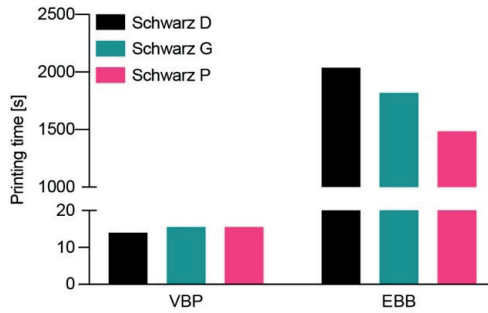


**Figure S12: Time-dependent, enzymatically accelerated degradation of pristine gelMA and gelMA supplemented with 10% w/v iodixanol.** Exposure to a collagenase solution demonstrates the gradual degradation of photocrosslinked bioresins over time. Data is represented as mass percentage with respect to the gels prior to the incubation collagenase solution. Bioresin blends were completely degraded after 60 and 45 minutes, respectively (n=3). ns = not statistically significant ( $p < 0.05$ ), all other data points are significantly different from each other within bioresin groups.



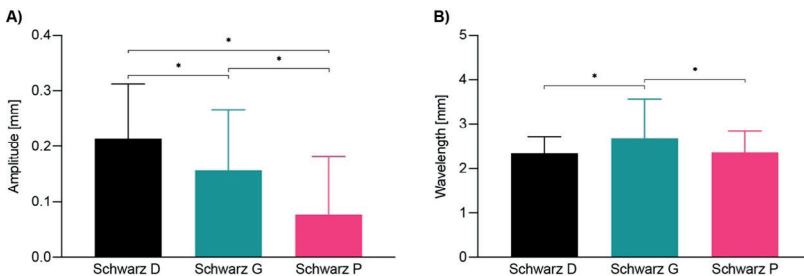
**Supplementary Figure S13: Mathematically-derived triply periodic minimal surface structures with distinct structural properties.** STL models of the selected complex architectures Schwarz D, G and P, outlining their different surface area to volume ratio, tortuosity and pore sizes.



**Supplementary Figure S14:** Printing times of Schwarz structures using different bioprinting approaches. Printing times (s) for Schwarz D, G and P structures as shown in figure 6A i-iii. VBP prints were performed with the optically tuned gelMA-based bioresin, while EBB prints, given the challenge in printing free-standing volumetric structures with such a soft material, were instead printed with a model bioink, Pluronic F-127.



**Supplementary Figure S15: High-throughput printing of highly complex, perfusable structures within minutes.** Twelve volumetrically printed constructs of complex architectures (Schwarz D, G and P) each measuring 1.7 cm in length and 6 mm in diameter with perfusable inlets printed in 180 s for high-throughput analysis of organoid activity.



**Supplementary Figure S16: Bead trajectory analysis in different Schwarz architectures.** Amplitude of the bead trajectories during perfusion at  $1.5 \mu\text{L min}^{-1}$  of Schwarz D, G and P structures ( $n = 50-80$ ). \* = significant difference ( $p < 0.05$ ).

## Supplementary Tables

**Supplementary Table S1: Refractive index of different cellular organelles.** Modified from Liu *et al.*, 2016.<sup>[425]</sup>

Organelles / intracellular matter	Refractive index
Cytosol	1.360 - 1.390
Nucleus	1.355 - 1.365
Nucleolus	1.375 - 1.385
Mitochondria	1.400 - 1.420
Lysosome	1.600

**Supplementary Table S2: dsDNA content of organoid-laden samples fabricated with different approaches.**

Total dsDNA content in: VBP- and EBB-printed organoids with the optically tuned bioresin (gelMA + 10% w/v iodixanol), casted gelMA samples with (Cast+) and without iodixanol (Cast-) and casted Matrigel (MG) samples after a 10-day differentiation period.

Fabrication method	dsDNA content [mg sample <sup>-1</sup> ]
VBP	1.45 ± 0.28
EBB	1.46 ± 0.06
Cast +	1.25 ± 0.06
Cast -	1.13 ± 0.19
MG	2.03 ± 0.22

**Supplementary Table S3: Structural and dimensional properties of mathematically-derived Schwarz structures.**

Structure	Volume (mm <sup>3</sup> )	SA : V (mm <sup>-1</sup> )	Tortuosity
Schwarz D	394.25	2.05	1.32
Schwarz G	383.17	1.98	1.05
Schwarz P	390.86	1.88	1.04

**Supplementary Table S4: Secreted albumin levels in bioprinted structures.** Total albumin production of hepatic organoids printed into different architectures during 24 hours of sterile perfusion at 20  $\mu\text{L min}^{-1}$ .

Architecture	Albumin production over 24 hrs [ $\mu\text{g mL}^{-1} \pm \text{SEM}$ ]
Schwarz D	3.40 ± 1.75
Schwarz P	17.00 ± 13.03
Cylinder (static)	1.17 ± 0.47

**Supplementary Table S5:** Primers used for quantitative PCR analysis.

Gene	Forward sequence	Reverse sequence
CYP3A4	TGATGGTCAACAGCCTGTGCTGG	CCACTGGACCAAAAGGCCTCCG
ALB	GTTCTGTTACACCAAGAAAGTACC	GACCACGGATAGATAGTCTTCTG

**Supplementary Table S6:** Primary antibodies used for immunofluorescence analysis

\*TE: 10 mM Tris, 1 mM EDTA, 0.5% Tween 20 in PBS at pH 9.0 for 30 min at 98° C

Antigen	Source and cat. number	Raised in	Dilution	Antigen retrieval*
HNF4 $\alpha$	LS Biosciences LS-B969	Rabbit	1 : 200	TE
E-cadherin	BD Bioscience 610181	Mouse	1 : 400	TE
ZO-1	Invitrogen 40-2300	Rabbit	1 : 200	TE
CK-19	Abcam Ab15463	Rabbit	1 : 500	TE
MDR1	Novus Bio NBP1-90291	Rabbit	1 : 200	TE
Albumin	Sigma A6684	Mouse	1 : 1000	TE

**Supplementary Table S7:** Secondary antibodies used for immunofluorescence analysis

\*Secondary antibodies were diluted in Antibody Diluent (Dako).

Antigen	Source and cat. number	Raised in	Dilution*
Anti-mouse Alexa 488	Life Technologies A11029	Goat	1 : 200
Anti-mouse Alexa 568	Life Technologies A11036	Goat	1 : 200



## Supplementary Methods

*GelMA characterization:*  $^1\text{H}$  NMR spectrum was measured on an Agilent 400 MR-NMR spectrometer (Agilent Technologies, USA) at 400 MHz in  $\text{D}_2\text{O}$  at  $50^\circ\text{C}$ . The degree of functionalization of the synthesized gelMA was measured using a 2,4,6-trinitrobenzenesulfonic acid (TNBSA, 5% w/v, Sigma, The Netherlands) in  $\text{H}_2\text{O}$  solution to quantify free primary amines before and after methacryloyl substitution. For the sol-fraction analysis, cylindrical constructs (6 mm diameter x 2 mm height) were printed with bioresins containing different concentrations of iodixanol ( $n = 3$ ; 0–40% w/v) and the mass loss of the resulting structures was assessed as previously described.<sup>[173]</sup>

*Cell isolation from liver biopsies:* Liver biopsies (obtained during liver transplantation at the Erasmus Medical Center Rotterdam with ethical approval number MEC 2014-060) were chopped into small pieces and enzymatically digested with  $0.125\text{ mg mL}^{-1}$  Type II collagenase and  $0.125\text{ mg mL}^{-1}$  dispase in Dulbecco's Modified Eagle's Medium (DMEM) Glutamax supplemented with 0.01% v/v DNase I (Roche, Basel, Switzerland), 1% v/v fetal calf serum (FCS) and 1% v/v penicillin/streptomycin (P/S) at  $37^\circ\text{C}$ . Every hour, the supernatant was collected and fresh enzyme-supplemented media was added to the remaining tissue until only ducts and single cells were visible. Single cells were washed with DMEM Glutamax (supplemented with 1% v/v FCS and 1% v/v P/S) and spun down at 453 g for 5 min. All components were obtained from Life Technologies (Carlsbad, CA, USA).

*Organoid expansion and differentiation medium:* Expansion medium (EM) consisted of Advanced DMEM/F12 (Life Technologies) supplemented with 1% v/v penicillin-streptomycin (Life Technologies), 1% v/v GlutaMax (Life Technologies), 10 mM HEPES (4-(2-hydroxyethyl)-1-piperazineethanesulfonic acid, Life Technologies), 2% v/v B27 supplement without vitamin A (Invitrogen, Carlsbad, CA, USA), 1% v/v N2 supplement (Invitrogen), 10 mM nicotinamide (Sigma-Aldrich, St Louis, MO, USA), 1.25 mM N-acetylcysteine (Sigma-Aldrich), 10% v/v R-spondin-1 conditioned medium (the Rspo1-Fc-expressing cell line was a kind gift from Calvin J. Kuo), 10  $\mu\text{M}$  forskolin (Sigma-Aldrich), 5  $\mu\text{M}$  A83-01 (transforming growth factor beta inhibitor; Tocris Bioscience, Bristol, UK), 50  $\text{ng mL}^{-1}$  EGF (Invitrogen), 25  $\text{ng mL}^{-1}$  HGF (Peprotech, Rocky Hill, NJ, USA), 0.1  $\mu\text{g mL}^{-1}$  FGF10 (Peprotech) and 10 nM recombinant human (Leu15)-gastrin I (Sigma-Aldrich). Differentiation medium (DM) consisted of EM without R-spondin-1, FGF10 and nicotinamide, supplemented with 100  $\text{ng mL}^{-1}$  FGF19 (Peprotech), 500 nM A83-01 (Tocris Bioscience), 10  $\mu\text{M}$  DAPT (Selleckchem, Munich, Germany), 25  $\text{ng mL}^{-1}$  BMP-7 (Peprotech), and 30  $\mu\text{M}$  dexamethasone (Sigma-Aldrich). The characterization of the micro-scale morphology of the organoids both in expansion and differentiation media via transmission electron microscopy has been extensively investigated and reported previously.<sup>[456]</sup>

*HepG2 expansion medium:* DMEM + GlutaMAX (Gibco, 31966, The Netherlands) supplemented with fetal bovine serum (FBS, 10% v/v, Gibco, 10270, The Netherlands) and penicillin/streptomycin (1%, Gibco, The Netherlands).

*Measurement of scattering phase function of cell suspensions:* In the apparatus, light from a laser diode at 405 nm (HL40033G, Ushio, Japan) is condensed by an aspherical lens (C671-TME405, Thorlabs, USA) into a multimode optical fiber (WF 70×70/115/200/400N, CeramOptec, Germany). Then, a lens (AC254-030-A-ML, Thorlabs) collimates the light at the output of the fiber. An aperture placed right after the lens limits the extension of the outgoing beam to 1 mm. The light is sent straight onto a 2 mm thick square quartz cuvette (CV10Q7FA, Thorlabs). The thickness of the cuvette was chosen so that only single scattering events were present in the hydrogel. Light scattered from the sample is collected by a photodiode (SM05PD3A, Thorlabs). The photodiodes rotate along a circumference of  $r = 250$  mm by means of a precision rotational stage (X-RSW60A-E03, Zaber, Canada). The cuvette is held static on top of the center of the circumference. The signal from the photodiode is amplified (PDA200C, Thorlabs) and digitized by a data acquisition device (USB-6003, National Instruments, USA) and recorded in a computer. A MATLAB code controls and synchronizes the laser, the rotational stage, and the data acquisition device to acquire intensities 5 times at every angle with an angular resolution of  $0.05^\circ$  between  $0^\circ$  and  $20^\circ$  (scattered light beyond this angle was 3 orders of magnitude less intense than at  $\theta = 10^\circ$ , and thus approached to zero). A python code is used to process and convert the raw measured currents on the photodiode into light intensities, and to calculate scattering properties from them. For each hydrogel, we report the anisotropy coefficient  $g$ , which is the expected value of the scattering angle ( $n = 3$ ).<sup>[457]</sup>

$$g = \langle \cos\theta \rangle$$

$$g = \int_0^\pi p(\theta) \cos(\theta) 2\pi \sin(\theta) d\theta$$

*Mechanical analysis of samples with and without iodixanol:* Compressive properties of casted bioresin cylinders (6 mm x 2 mm height) with 0 and 10% w/v iodixanol were assessed in an uniaxial, indentation-based compression test with a Dynamic Mechanical Analyzer (DMA Q800, TA Instruments, The Netherlands), equipped with a cylindrical flat piston (diameter = 2 mm). Samples were subjected to a strain ramp of  $-20$  %/min strain rate to  $-30$  % deformation ( $n = 5$ ). Young's modulus was calculated as the slope of the stress/strain curve in the 10–15% strain range.

*Enzymatic degradation assay:* To assess the enzymatic degradation of photocrosslinked resins used in this study, photocrosslinked 5% w/v gelMA and 5% w/v gelMA + 10% w/v iodixanol (cylindrical samples, diameter = 6 mm, height = 2 mm) were swollen in PBS overnight and subsequently incubated at  $37^\circ$  C in a 0.2% w/v solution of collagenase type II in Dulbecco's modified Eagle Medium (DMEM, 31966, Gibco, The Netherlands),

supplemented with 10% v/v heat-inactivated fetal bovine serum (FBS Gibco, The Netherlands), and 1% v/v penicillin and streptomycin (Life Technologies, The Netherlands). Samples were removed from the enzymatic solution at different time points (10, 25, 35, 45, and 60 min,  $n = 3$  per time point), and the mass was measured and compared to that of the hydrogels before collagenase incubation as previously described.<sup>[331]</sup>

*Gene expression analysis:* Prior to RNA isolation, GelMA hydrogels were broken down using QIAshredder columns according to the manufacturer's instructions (Qiagen, Hilden, Germany). RNA was isolated from organoids (3 donors,  $n = 3$ ) using 350  $\mu$ L RNeasy lysis buffer directly added into one well of the 24 well plate followed by RNA extraction using the RNeasy micro Kit according to the manufacturer's instructions (Qiagen). cDNA synthesis was performed using iScript cDNA synthesis kit (Bio-Rad, Veenendaal, the Netherlands). Relative gene expression of selected genes was measured using RT-qPCR in a CFX-384 (Bio-Rad). Primer design, validation, RT-qPCR conditions, and data analysis was performed as previously described (primer sequences are detailed in **Supplementary Table S5**).<sup>[402]</sup> Normalization was performed using reference gene 60S ribosomal protein L19 (RPL19).

*Albumin secretion:* To determine organoid albumin secretion medium was collected during the differentiation period of 10 days to examine total albumin secretion ( $n = 3$ ). The culture medium was collected and concentrated using Amicon Ultra centrifugal filters (Amicon, Germany). The concentration of albumin was then determined using a DxC-600 Beckman chemistry analyzer (Beckman Coulter, USA). Values were normalized for total protein content.

*Liver transaminase levels:* Enzyme activity levels were determined by lysing the samples (3 donors,  $n = 3$ ) with Milli-Q water (Merck, Millipore, Burlington, MA, USA). Subsequently, aspartate transaminase (ASAT), gamma-glutamyl transferase (GGT) and glutamate dehydrogenase (GLDH) were measured with the clinical chemistry analyzer Beckman AU680 (Beckman Coulter, USA) using standard protocols. Values were normalized for total protein content.

*Immunofluorescence:* Cell-laden discs ( $N = 3$ ,  $n = 3$ ) were fixed in 4% w/v paraformaldehyde (PFA) and stored in 70% (v/v) EtOH at 4°C until further processing. Samples were embedded in paraffin and cut into 5  $\mu$ m sections. Sections were deparaffinized and rehydrated. After antigen retrieval (information per antibody in **Supplementary Table S6**), a blocking step was performed using 10% v/v normal goat serum (Bio-Rad) in PBS for 30min at RT. Antibodies are listed in **Supplementary Table S6**. Incubation with primary antibodies was performed overnight at 4° C. Secondary antibodies were incubated at room temperature for 1 h (listed in **Supplementary Table S7**). Nuclei were stained with DAPI (Sigma-Aldrich) diluted 2000x in PBS. Washing steps were performed using a buffer of PBS with 0.1% v/v Triton X-100 (Sigma-Aldrich) and 0.2% w/v Bovine Serum Albumin (Sigma, The Netherlands). Slides were mounted using FluorSave (Merck-Millipore, USA), and images

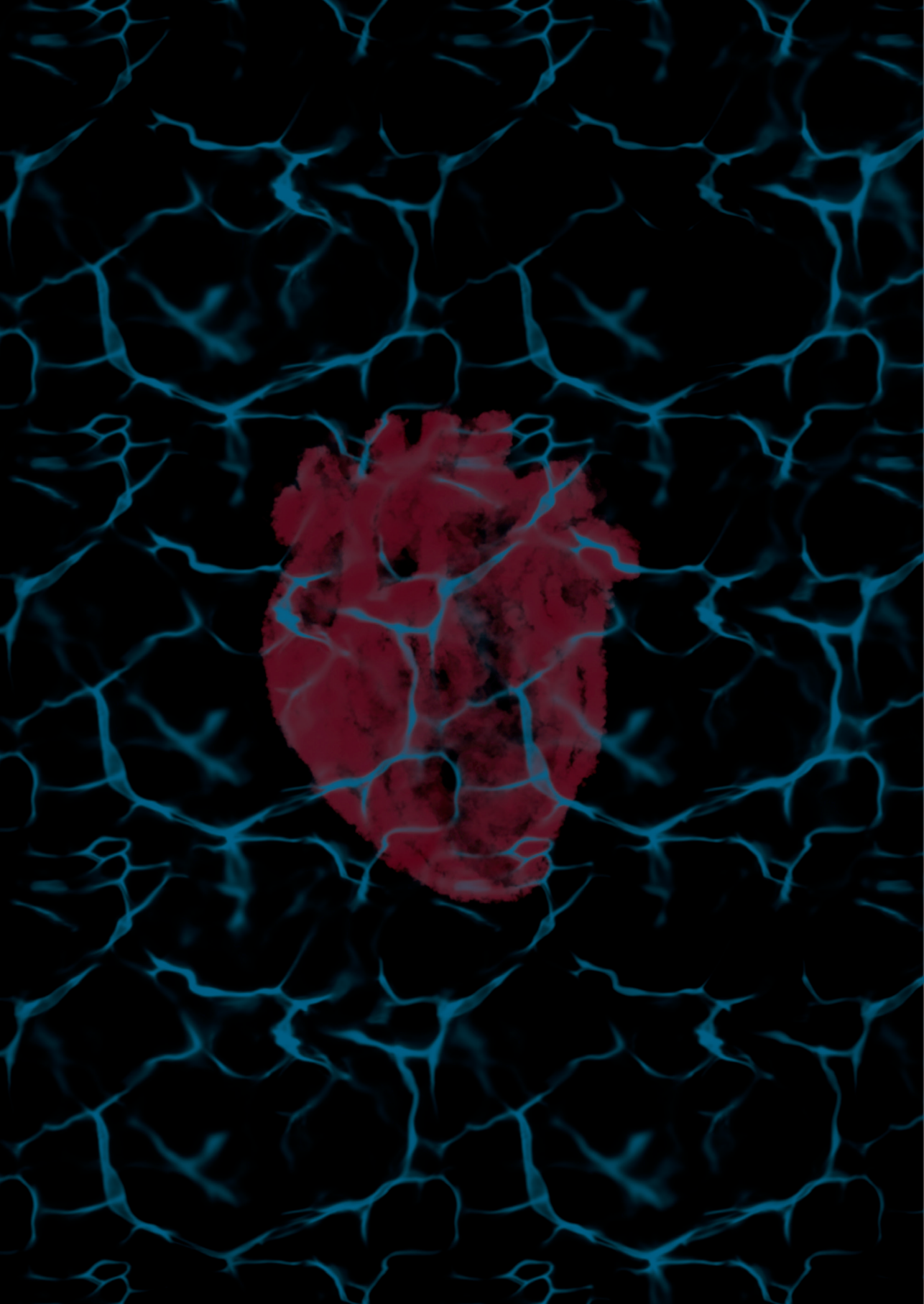
were acquired using a Thunder imaging system (Leica Microsystems, Germany).

*Extrusion-based printing attempt of Schwarz structures:* Schwarz D, G and P structures encased in a perfusable chamber as shown in Figure 6A i-iii were printed with a pneumatic-driven system (27 G stainless steel nozzle, temperature = 21° C, pressure = 0.2 MPa, feed rate = 25 mm s<sup>-1</sup>, 3DDiscovery, REGENHU, Switzerland) using model in Pluronic F-127 (Sigma-Aldrich, The Netherlands). Support structures were printed with the same material under the same printing parameters to ensure the structure was successfully printed and remained stable. Printing time was recorded for comparison to VBP printing times.

*Fluorescent Microsphere Imaging in Perfusable System:* The fluorescent microspheres were illuminated using a 405nm laser source (USHIO HL40033G) driven at 500 ± 50 mW. The beam was first collimated using a f = 6.33mm 0.68NA mounted aspheric lens (Thorlabs C330TMD-A) then passed through an engineered square diffuser (Thorlabs ED1-S20-MD). This produced a homogeneously illuminated surface with a square, top-hat illumination profile under which the samples were placed. A monochromatic camera (Basler a2A1920-160umPRO) with a 25mm lens (Basler C125-2522-5M-P f25mm) and 455nm longpass filter (Thorlabs FGL455) was used to perform the imaging. The longpass filter acted to reduce the background signal of the laser illumination, such as not to overwhelm the emission signal of the excited microspheres.

*Sterile perfusion system for assessment of organoid ammonia elimination:* Volumetrically printed constructs were assembled into custom-made PDMS mold fitted in a custom-designed Polylactic acid (PLA) flow chamber prepared by Ultimaker S3 FDM 3D printer (Ultimaker, The Netherlands). For a leakproof flow chamber, the PFA microfluidic tubing (IDEX Health&Science, OD 1.6 mm, ID 0.75 mm) was guided through the side walls of the chamber and the hollow inlet/outlet printed within the hydrogel construct, followed by applying UV crosslinkable glue (Norland Optical Adhesive NOA 63; Norland Products, USA) around the connection between the PDMS mold and the tubing under 5 min UV exposure with a handheld lamp ( $\lambda = 365$  nm; Vilber Lourmat, Eberhardzell, Germany) solely on the connection zone. A 4-channel peristaltic pump (ISMATEC Regio ICC, 12 rollers, 3-stop tubing ID 2.54 mm) was applied to perfuse 4 flow chambers independently at the flow rate of 20  $\mu\text{L min}^{-1}$  per chamber for 24 hours within an incubator. An inlet reservoir of organoid differentiation medium (DM) supplemented with 1.5 mM of ammonium chloride was closed with a solvent cap (Diba Industries, 3\*1/4"-28 UNF, GL32) which connected two PFA tubing for perfusion plus one syringe filter (0.2 mm) to prevent both particulate contamination and the evaporation of medium. The PFA tubing both from the flow chamber inlet and the solvent caps was fitted with the pumping tubing via a 1/4"-28 barbed adapter (IDEX Health&Science) coupled with a standard union (P-620, IDEX Health&Science), and the PFA tubing from the flow chamber outlet was connected to a microfluidic reservoir adapter (Elveflow, 2/4 port) which collected the fluid from each chamber towards individual 50 mL falcon tubes.





# Chapter 7

## Volumetric Printing Hollow Bi-Chambered Heart Structures for the Next Generation of Clinically Relevant Cardiac *In Vitro* Models

Nino Chirico<sup>1\*</sup>, Paulina Núñez Bernal<sup>2\*</sup>, Gabriel Größbacher<sup>2\*</sup>, Aina Cervera i Barea<sup>1</sup>, Sammy Florczak<sup>2</sup>, Josh Mesfin<sup>3</sup>, Jianan Wang<sup>3</sup>, Inge Dokter<sup>1</sup>, Christian J. B. Snijders Blok<sup>1</sup>, Karen Christman<sup>3</sup>, Joost Sluijter<sup>1</sup>, Jos Malda<sup>2,4</sup>, Riccardo Levato<sup>4,2#</sup>, Alain van Mil<sup>1#</sup>

In preparation.

<sup>1</sup> Department of Cardiology, Experimental Cardiology Laboratory, University Medical Center Utrecht, Utrecht University, Utrecht, The Netherlands

<sup>2</sup> Department of Orthopedics, University Medical Center Utrecht, Utrecht University, Utrecht, The Netherlands

<sup>3</sup> Department of Bioengineering, Sanford Consortium for Regenerative Medicine, University of California, San Diego, California, USA

<sup>4</sup> Department of Clinical Sciences, Faculty of Veterinary Medicine, Utrecht University, Utrecht, The Netherlands

\* Authors contributed equally to this work

# Indicates shared senior authorship

## ABSTRACT

Cardiovascular diseases are the leading cause of death worldwide, with a high failure rate in the development of new therapies. Current *in vitro* models, such as two-dimensional cell culture and engineered heart tissues, have limitations in simulating cell-cell and cell-microenvironment interactions and in evaluating functional and structural changes typical of cardiac diseases in shape-accurate systems. In this study, we present a novel approach in the development of a three-dimensional cardiac *in vitro* model for the study of cardiovascular diseases, which combines multi-material volumetric bioprinting and human induced pluripotent stem cell-derived cardiomyocytes to create a scalable, bi-chambered heart construct. To achieve a mechanically stable print capable of resisting the heart's native pumping action in future studies, material properties were optimized to create a two-material construct with differing mechanical properties. The freedom of design of volumetric bioprinting also enabled the fabrication of different structures mimicking different cardiomyopathies. The multi-material printing process was shown to still allow physiological and diseased cellular gene expression responses to external stimuli such as an induced cryoinjury meant to mimic the onset of myocardial ischemia, as shown through ribonucleic acid (RNA) sequencing. Here, as a response to cryoinjury, the cells embedded within the volumetrically bioprinted heart showed gene-level signs of adverse matrix remodeling, as observed also in ischemic heart tissue. Furthermore, the printed models were shown to be compatible with medical imaging technologies like magnetic resonance imaging, highlighting the potential for clinically-relevant analyses in future studies. Further optimization of the platform is required, focusing on enhancing cell-cell contact within the printed model to improve coordinated beating, the development of more complex disease models, and the inclusion of other cell types and tissues to create more complex and realistic *in vitro* models of the cardiovascular system. Addressing this will lead to the creation of a tool that allows for the accurate study of the underlying mechanisms and development and progression of cardiovascular diseases *in vitro*, for use in high-throughput drug screening and personalized medicine.

**Keywords:** multi-material volumetric bioprinting, engineered heart tissues, iPSC-derived cardiomyocytes



## INTRODUCTION

Cardiovascular diseases, including myocardial infarction, are the leading cause of death worldwide with heavy disease burden.<sup>[458]</sup> In recent years, several therapies have gone through the drug development pipeline and reached the market. However, there is a major struggle to deliver compounds that can truly prevent chronic heart damage, and restore cardiovascular function, and many drug candidates never make it through clinical trials. Wherein the general drug discovery process experiences very high failure rates as well, with 89% candidate drugs failing immediately upon entering the clinical testing phase,<sup>[2]</sup> this phenomenon is exacerbated in the cardiac field partially due to the complexity and costs of acquiring clinically relevant data necessary to assess functional and structural improvements.<sup>[459]</sup> The latter can be associated with the limits in translating *in vitro* models evidence into functional clinically relevant measurements.<sup>[460]</sup> Several *in vitro* models have been developed and are now used to evaluate cardiac toxicity and the efficacy of new therapies.<sup>[461]</sup> These platforms extend from simplified two-dimensional (2D) models, where cells are seeded on the tissue culture plates, to advanced three-dimensional (3D) models such as engineered heart tissues (EHTs)<sup>[16]</sup>. Two-dimensional models can give elementary and mechanistic information about the tested drug at the cellular level; however, they lack the ability to simulate the complex 3D cell microenvironment.<sup>[16]</sup> Three-dimensional models that enable the precise patterning of multiple cell types relevant to the tissue/organ of interest within extracellular matrix (ECM) mimicking matrices such as hydrogels can better represent the native cell-to-cell and cell-matrix interactions, thus yielding higher physiologically relevant functions.<sup>[12]</sup> Furthermore, current EHTs can give adequate information on drug efficacy by evaluating contraction forces and other relevant clinical characteristics (such as action potential measurements, receptor expression, and more)<sup>[462]</sup>, but provide limited information on morphological adaptations given their architectural simplicity. The absence of a hollow multi-chamber structure in particular severely hinders the ability to evaluate key functional and structural outcomes of the developed heart tissue (*i.e.*, contractility, heart volume, ventricle size, etc.). These structural factors are of utmost importance for several cardiovascular diseases, as alterations in heart morphology are commonly used in clinics to evaluate pathology progression; most often using echocardiogram and magnetic resonance imaging (MRI) as non-invasive methods to assess these parameters. To address this current gap in existing EHT platforms, the field of biofabrication has come forth as a viable set of enabling technologies that enable the precise patterning of complex biological units into hierarchical architectures that better mimic native structures.<sup>[110]</sup>

While several biofabrication approaches have sought to recreate cardiac tissues, several challenges have arisen in the last years in truly mimicking the functionality and architecture of the heart.<sup>[463]</sup> From a technological standpoint, most functional bioprinted cardiac

7

tissue constructs are small and represent only a small region of the heart wall, to be used as potential cardiac patches.<sup>[464,465]</sup> While some advanced models have been created, that incorporate cardiac and endothelial cells to create partially vascularized heart tissue,<sup>[466,467]</sup> or enhance the mechanical properties of the printed construct,<sup>[200,466,468]</sup> conventional layer-by-layer bioprinting approaches pose a limit on the size and complexity of printed models. Recent advances in extrusion-based printing approaches have allowed for far more complex native heart models to be printed, by carrying out the printing process inside a support bath that enables the creation of hollow chambers and convoluted structures without the usual drawbacks of conventional extrusion printing. In this way, large, human-sized acellular heart models have been printed with high anatomical accuracy.<sup>[469]</sup> Smaller, cellularized heart models have also been printed this way, but either lack the compartmentalization of the native heart<sup>[470]</sup> or clinically relevant cardiac functionality outputs.<sup>[471]</sup> All these examples relying on layer-by-layer, nozzle extrusion bioprinting bring about significant drawbacks when upscaling and incorporating further design complexity to printed models. The creation of larger constructs would result in longer printing times, which can have detrimental effects on cell survival and function, especially when working with sensitive cells that require a high control of their culture environment. To overcome this problem, a novel tomography-based printing approach called volumetric bioprinting (VBP) allows for the creation of highly complex, cell-laden structures in tens of seconds.<sup>[127]</sup> In VBP, a sequence of tomographic light projections of the desired object are directed towards a light-sensitive bioresin, sculpting the structure in a single-step, thus facilitating the creation of convoluted structures such as overhangs, hollow chambers, etc., in a matter of seconds. Given the contactless nature of this approach, even large (hundreds of micrometers) and fragile cellular structures such as organoids have been successfully printed into highly convoluted, centimeter-scale structures without impairing cell viability, function or morphology.<sup>[286]</sup> Previous studies have shown the possibility to print contractile cells using this approach, yielding sporadic, localized contractions within VBP bioresins.<sup>[291]</sup> These key advantages over conventional 3D bioprinting methods make this approach promising for the processing of other highly sensitive cell types into complex, native-like structures.

Here, we combined VBP and a previously established co-culture of human induced pluripotent stem cell-derived cardiomyocytes (hiPSC-CMs) and human fetal cardiac fibroblasts (hfCFs)<sup>[466]</sup> to develop a scalable, multi-material bi-chambered heart construct. From a technological perspective, we demonstrated the principles of multi-material VBP to create a mechanically competent structure with a mechanically stable material to enable handling and support of the printed structure, and a softer material that enables cell growth and function. The potential to print more complex, asymmetrical heart models using this approach to mimic various structural cardiomyopathies was also explored. To demonstrate that cells embedded within the volumetrically bioprinted

heart remain viable and reactive to external stimuli, a cryoinjury was performed on the heart wall to mimic the onset of myocardial ischemia, and its effects on gene expression were assessed at a whole-genome level as a proof of concept. Furthermore, from a translational perspective, the compatibility of the bioprinted heart with the widely used magnetic resonance imaging (MRI) technology was demonstrated, enabling conventional clinical analysis of the printed structure. All in all, we elucidate the potential of such a complex printed model for the study of cardiomyopathies, cardiac injury and potential treatment strategies in the future and highlight the current limitations and challenges of this biofabrication technology, which will need to be tackled to advance these heart constructs towards biomedical applications.

## RESULTS AND DISCUSSION

One of the biggest drawbacks of cardiac *in vitro* models to date is the lack of ventricular compartmentalization. On the one hand, 2D cell culture models do not resemble the 3D structure of the native heart at all, and the more complex tissue engineered constructs, due to processing limitations, make the building of hollow, perfusable chambers extremely difficult and time consuming. Especially with the use of soft polymers that facilitate cell-cell interactions and coordinated beating motion, maintaining complex 3D structures post-printing is a common challenge with conventional tissue engineering strategies.<sup>[128,144]</sup> Here, VBP was used to overcome this limitation and develop a bi-chambered heart model, rapidly produced in tens of seconds, with anatomically-derived wall thicknesses (**Figure 1A - D**). Another challenge in cardiac tissue engineering is that of providing mechanical stability of EHTs, while also using low stiffness materials, suitable for muscle cell culture. To date, often a compromise between stiff, strain resisting matrices that support the beating and long-term stability of the construct, and soft matrices that facilitate cellular interconnections, elongation and migration must be made.<sup>[128]</sup> To address these challenges, the volumetrically bioprinted heart was fabricated using two different materials (**Figure 1B, C**). First, a stiff supporting resin consisting of 15% w/v gelatin methacryloyl (gelMA) supplemented with 0.1% w/v lithium phenyl(2,4,6-trimethylbenzoyl)phosphinate (LAP), which aids in increased shape fidelity of the printed structure and enables handling and hanging of the construct from a custom-made forklift structure to keep the constructs upright and prevent the collapse of one or both chambers (**Figure 1D**). Furthermore, this supporting region will also facilitate future functional readouts like ejection fraction quantification and incorporation within bioreactor systems. Second, a cell bioresin consisting of 5% w/v gelMA blend with 10% v/v iodixanol and 0.1% w/v LAP, providing a softer environment for cells to mature in. The volumetrically bioprinted heart structures could successfully be resolved in just over 20 seconds, and exhibited two hollow chambers separated by a septum.

Recent studies have shown the potential of multi-material VBP, some using sequential printing of the first material, a washing step to remove the uncrosslinked resin, followed by a second volumetric printing step of the second material,<sup>[472,473]</sup> or the incorporation of a second printing approach, such as embedded extrusion bioprinting.<sup>[474]</sup> However, as shown in a recently published study outlining different approaches towards multi-material VBP, printing two resins in a single step requires some adjustments to their optical properties,<sup>[473][473]</sup> as well as the establishment of a strong interface that holds both materials together post-printing. The first step towards creating the multi-material bioprinted heart was to optimize a resin interface that would allow for the seamless connection between both support and cell-laden components through a protocol adjusting the thermal gelation of both resins (**Figure 1E**). First attempts at printing the two materials in a single printing step, with the support resin being immediately cooled to induce thermal gelation over the cell bioresin, were not successful. The pre-cooled cell bioresin which was immediately supplemented with a second layer of support resin above did not create a blended interface, suggesting that both materials were physically separated from each other (**Figure 1Fi**), and led to the heart structure breaking into two separate parts after washing (**Figure 1Fii**). Therefore, the interface protocol was adjusted by prewarming the support resin to 40° C (as opposed to a physiological temperature of 37° C to prevent the resin from cooling too much during pipetting at room temperature) before gently pipetting it over the already gelated cell bioresin. The cell bioresin was pre-gelated to prevent immediate mixing of the two materials, but the pre-warmed support resin induced a partial melting of the surface of the cell bioresin, creating a blended interface where the materials mixed to ensure good integration between the two parts of the volumetrically bioprinted heart (**Figure 1E, Fiii**). Using this approach, the two bioprinted heart regions remained attached post-printing, creating a stable, multi-material construct in a single step (**Figure 1Fiv**). Standardization of this approach with controllable heating rings to modulate the temperature of both materials independently and precisely is an important next step towards the upscaling of this model's fabrication throughput.

Another important aspect needed to ensure a homogenous printed structure was matching the optical properties of both bioresins, to prevent printing inaccuracies arising from different light beam behavior through each of the bioprinted heart regions. For this, the refractive index (RI) of the cell bioresin had to be adjusted to match that of the support resin (1.355, the highest RI of the two). To achieve this, the cell bioresin was supplemented with varying degrees of iodixanol, a biocompatible compound previously shown to modulate the RI of VBP bioresins. As the iodixanol concentration in the cell bioresin increased, so did the refractive index (from  $1.342 \pm 0.00$  with no supplemented iodixanol to  $1.405 \pm 0.004$  with the addition of 40% v/v iodixanol). Of all concentrations tested, the 10% v/v iodixanol condition ( $1.355 \pm 0.000$ ) was selected for further studies, as it matched

the RIs of both resins perfectly (**Figure 1G**). As an added value, this concentration has already been shown to efficiently enhance printing resolution in the presence of high single cell and organoid densities, as well as yield a decrease in the stiffness of pure gelMA that can have a positive effect on the viability and function of sensitive cell types<sup>[286]</sup> Importantly, this refractive index matching step can be applied to a wide variety of bioresins with differing optical properties. For example, should different cell types or scattering elements in one of the two resins require higher iodixanol concentrations for optimal printability, the second resin could also be supplemented with iodixanol to achieve matching RIs.

This difference in mechanical properties between the two resins is clearly shown in the compressive and tensile behavior of the two individual resins, and the intermediate behavior of the interface region of printed structures (**Figure H - J**). The compressive properties of a flat multi-material print consisting of the cell bioresin, support resin and thermally induced interface region (**Figure 1H**) all show significantly different properties, with the cell bioresin exhibiting the lowest Young's modulus ( $4.16 \pm 0.43$  kPa) of the construct, with the support resin exhibiting 2.8-fold higher compressive properties ( $11.85 \pm 1.30$  kPa), and the interface, being a blend of both resins, exhibiting an intermediate Young's modulus ( $6.80 \pm 0.38$  kPa) (**Figure 1I**). These properties confirm that the two resins provide different mechanical properties to the volumetrically bioprinted heart – a softer resin to facilitate cellular survival and function, and a stiff resin to facilitate handling of the construct and to provide structural stability when the printed sample is fixed to the forklift structure. The stiffness of the interface, an intermediate between the support and cell resins, suggests that the thermal protocol described above indeed leads to a homogeneous blend of the two materials. In terms of tensile properties, the support resin exhibited a significantly higher tensile modulus ( $200.65 \pm 41.88$  kPa) compared to the cell bioresin ( $14.00 \pm 1.71$  kPa), an important feature for the heart structure to withstand the hanging position from the forklift over the duration of culture (**Figure 1J**). The incorporation of these two mechanically different resins in a single construct, with a strong thermally induced interface, pave the way for various applications relevant to cardiovascular research using this complex 3D model, with properties that aim to withstand physiological cell functions.

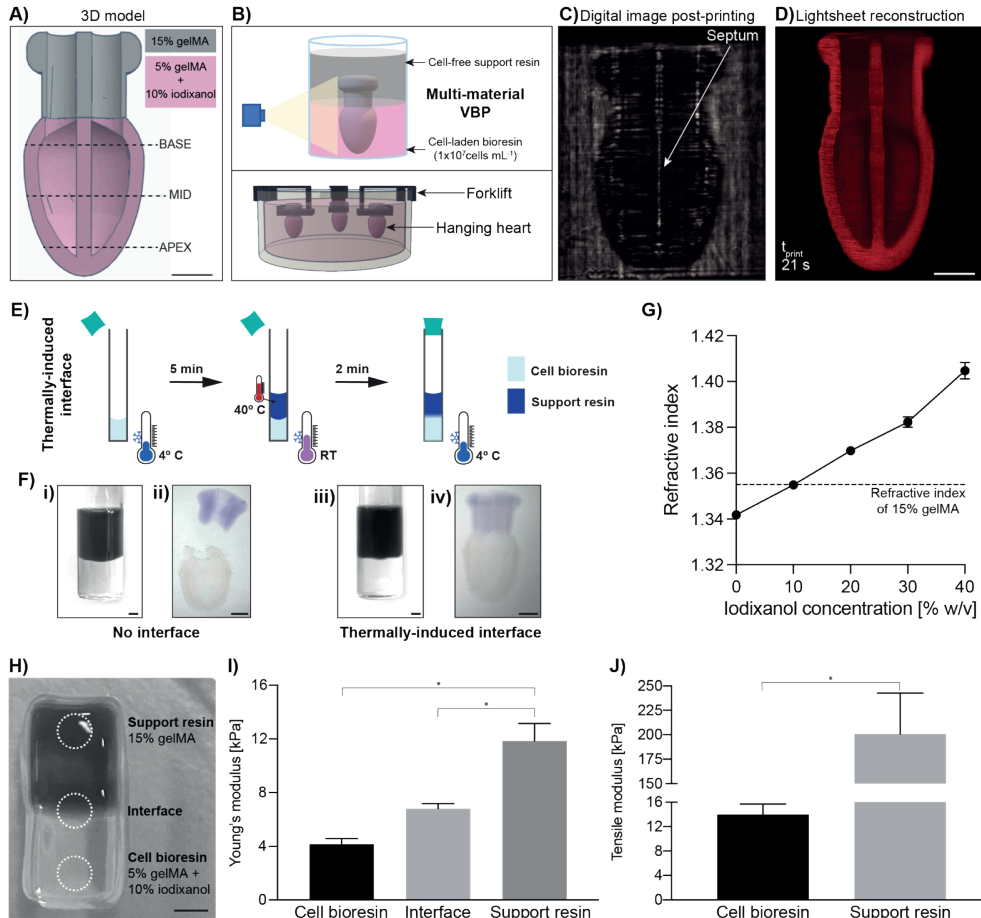


**Figure 1: Volumetric bioprinting of two-chamber heart model.** A) A 2-chamber heart model consisting of a top cell-free region made of 15% w/v gelMA + 0.1% w/v LAP (support resin) and the heart chamber structures made of 5% w/v gelMA + 10% v/v iodixanol + 0.1% w/v LAP and a  $1 \times 10^7$  iPSC-derived cardiomyocyte/fibroblast co-culture (cell bioresin) (scale bar = 2 mm). B) Graphical overview of the multi-material volumetric bioprinting process employed to fabricate the multi-material heart constructs, by precisely placing the material interface over the desired regions of the computer-aided design (CAD) model. The printed hearts were then hung on a petri dish using a custom-made forklift structure to mimic the heart's vertical orientation. C) Digital image of a volumetrically printed heart model acquired immediately post-printing and D) a cross-sectional view of the 3D reconstruction of the printed volumetric heart obtained through lightsheet imaging (scale bar = 2 mm). E) Graphical representation of the thermally-induced interface formation between the cell bioresin and the support resin by gradually melting the cell bioresin with a pre-warmed support resin ( $40^\circ \text{C}$ ) for two minutes to create a blended interface. F) Digital images of the volumetric printer vials (i,iii) without a thermally induced interface (i) and with the thermal interface protocol (iii), and the resulting volumetric heart prints (ii) without and (iv) with the thermally-induced interface (scale bars = 2 mm). G) Refractive index measurements of the cell bioresin blends supplemented with increasing concentrations of iodixanol (0–40% v/v). The red box represents the refractive index range of the support resin. H) Stereomicroscopy image of the printed gel strip consisting of cell bioresin and support resin, with a thermally induced interface region (scale bar = 2 mm; dotted circles represent the regions subjected to the compression testing protocol). I) Young's modulus of the printed structures' cell bioresin, interface and support resin regions and J) the tensile modulus of the printed cell and support resins. \* =  $p < 0.05$ .

The design of the volumetrically bioprinted heart, a simplified bi-chambered construct, was based on anatomical heart wall thickness measurements obtained from patient MRI scans, where the base region of the heart is the widest, narrowing at the mid-section and widening again at the apex of the heart. A scaled-down version mimicking these ratios in wall thickness was fabricated using the volumetric printer through the multi-material approach described herein. A comparison between the original CAD model consisting of these wall thickness variations was made with the volumetrically bioprinted structures, using 3D renderings from lightsheet scans (**Figure 2A, B**). The overall printing accuracy of the bioprinted heart model exhibited thickness variations ranging from  $\pm 12.4\%$  at the base,  $\pm 6.0\%$  at the mid-section and  $\pm 5.5\%$  at the apex compared to the original design. Despite this variation, the overall wall thickness gradient observed in anatomical heart measurements was reproduced in the bioprinted heart, with the base ( $909.0 \pm 52.4 \mu\text{m}$ ), mid-section ( $912.0 \pm 31.7 \mu\text{m}$ ) and apex ( $964.6 \pm 37.3 \mu\text{m}$ ) mimicking the narrowing and widening of the native heart walls (**Figure 2B**). Furthermore, a comparison of the regions of the printed structure with the most variation compared to the CAD model showed that the biggest deviations occur where the septum connects with the outer heart wall, forming a protruding bump to appear along this side of the print (**Figure 2C**). This results from an additional accumulation of light at the corners of objects where features of different dimensions intersect, and currently a topic of study in the field of volumetric printing, with new algorithm corrections being developed recently.<sup>[475]</sup>

Having established the possibility to print multi-material bi-chambered constructs that mimic the basic compartmentalization of the heart, the freedom of design provided by VBP was further exploited to develop more complex, asymmetrical structures. Drawing from the structural changes that often occur with various cardiomyopathies, we demonstrate the possibility of printing these heart models with one-sided enlarged chamber (**Figure 2Di, iv**) or a shrunken chamber with a thickened wall (**Figure 2Dii, v**), which could be used to mimic the cardiac deformations observed in dilated and hypertrophic cardiomyopathies, respectively. In the future, these models could be used to evaluate various clinical parameters *in vitro* to better understand the structural impact of these pathologies. To further expand on the achievable printing complexity of the VBP process, the printing of a four-chambered anatomical replica of the heart was also printed with this approach (**Figure 2Diii, vi**). Upon further characterization and optimization of the simple volumetrically bioprinted heart system, these more complex models could bring about important improvements upon existing cardiac disease models, potentially replicating patient-specific structures with high accuracy to study disease and potential treatments *in vitro*. Furthermore, the high printing speeds characteristic of VBP could also be harnessed for the high-throughput study of this models for preclinical testing and patient-specific applications (**Supplementary Figure S1**).

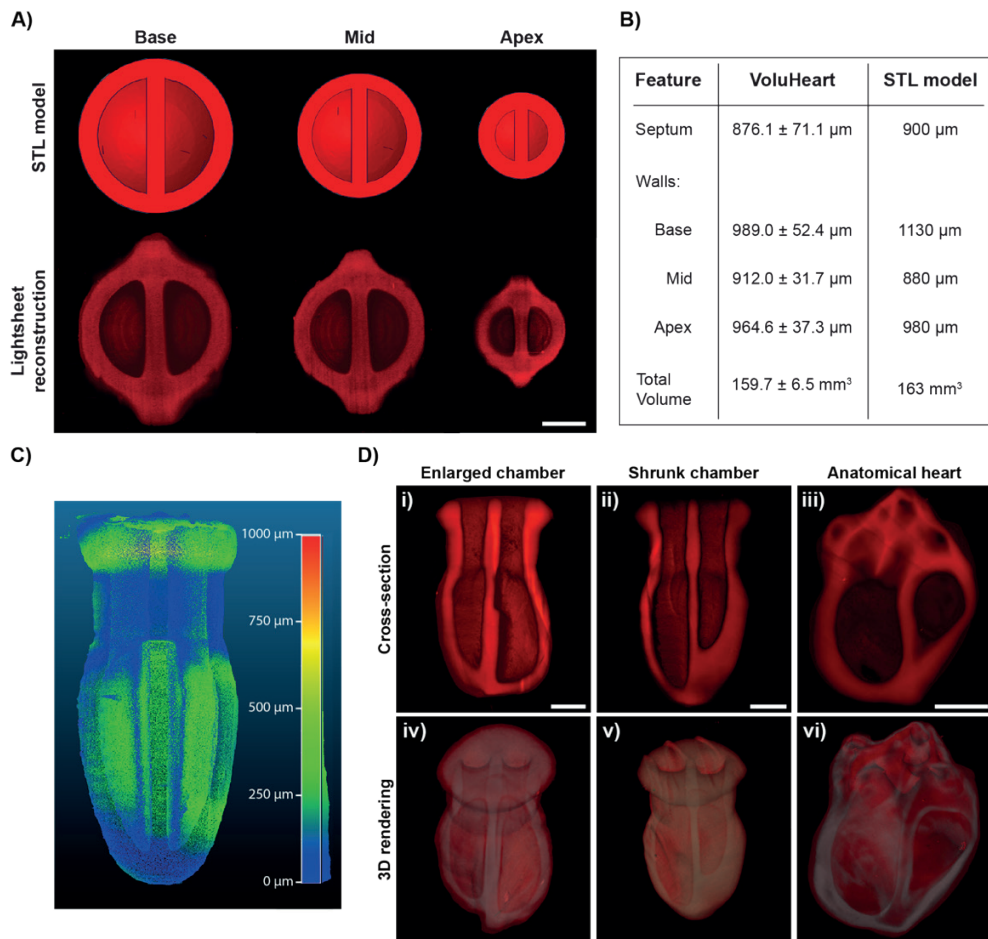


**Figure 2: Printing accuracy of anatomically derived heart wall thicknesses and mimicking structural cardiomyopathies.** A) Transversal cross-sectional view of the heart CAD model vs. the VBP hearts at the base, mid and apex regions of the heart and B) comparison of feature sizes and print volume compared to the original CAD model. C) Cloud-to-cloud distance difference map showing the size variation of the volumetric heart compared to the original CAD model. D) Cross-sectional views and full 3D renderings of complex heart models depicting: an enlarged chamber, a shrunk chamber and an anatomical heart model (without valve structures) obtained through lightsheet microscopy (scale bars = 2 mm).

After optimization of the printed heart's fabrication process, post-printing cellular behavior was assessed. The addition of iodixanol, as previously shown,<sup>[286]</sup> allowed for the successful printing of the model's features at the employed density of  $1 \times 10^7$  cells  $\text{mL}^{-1}$ . Although the low stiffness of iodixanol-supplemented gelMA is in line with what has been reported in previous work to facilitate the establishment of intercellular connections in cardiomyocytes,<sup>[476]</sup> the currently used cell loading density, which is among the highest achievable through optical tuning of VBP bioresins,<sup>[286]</sup> is well below what has been previously used to facilitate coordinated beating.<sup>[466]</sup> This resulted in the volumetrically



bioprinted heart lacking the capability of undergoing coordinated beating motion, likely due to the absence of densely interconnected cells resulting from the suboptimal density of the printed bioresin. It is noteworthy that, in randomly distributed regions of the printed structures where cells were more densely interconnected, contractile activity was observed, supporting the fact that the bioresin platform employed here does enable iPSC-CM connectivity, albeit in dispersed, localized areas only (**Supplementary Video S1**). In its current form, the cell-laden heart construct lacked the coordinated contractile forces to allow for the investigation of relevant clinical outputs such as ejection fraction, electrophysiological parameters, and other key clinical information. The limitations and possible improvements for this volumetrically bioprinted heart platform are thoroughly discussed in the following section (**Model Limitations and Perspectives**). Nonetheless, the responsiveness of the printed cellular co-culture to external stimuli was investigated to determine if the fabrication steps would hinder such processes. To assess such cellular responses, a unilateral cryoinjury on the heart wall was induced to induce cardiomyocyte loss and scar formation, resembling the signs of myocardial ischemia (MI). This approach has been employed *in vivo* to study cardiac regeneration and MI treatment strategies.<sup>[477–481]</sup> In this proof-of-concept study, screening of transcriptional changes via RNA sequencing within the volumetrically bioprinted heart constructs that were either cryoinjured ( $n = 4$ ) or left untreated was performed to evaluate the biological response to the induced injury as a proof of concept (**Figure 3**). Differential expression analysis led us to find a total of 96 differentially expressed genes (70 upregulated, 26 downregulated), determined via a  $\log_2$  fold change greater than or equal to 1.5 (upregulated) or a  $\log_2$  foldchange less than or equal to -1.5, with a Benjamini-Hochberg false-discovery rate of  $q < 0.05$ . All differentially expressed genes are displayed via Volcano plot. (**Figure 3A**). To further understand what differentially expressed genes were signaling, we performed gene enrichment analyses with the EnrichR package on gene ontology (GO) terms with a false-discovery rate of  $q < 0.05$ . Based on hierarchical clustering of each sample, the differentially expressed genes cluster by sample condition. In cryoinjured samples, differentially expressed genes were found to be enriched in extracellular structure and matrix organization (COMP, COL8A2, ADAMTS16) (**Figure 3B**). Response to transforming growth factor beta (WNT2, ADAMTSL2, PMEPA2) was also found to be upregulated due to cryoinjury, suggesting ECM remodeling processes occurring (**Figure 3B**). This phenomenon is also represented by ECM component genes (FN1, COL8A2, COL10A1, COL22A1, MFAP4) which were more highly expressed in cryoinjured samples (**Supplementary Figure S2**). Finally, in control samples, gene ontology enrichment elicited cellular communication and positive regulation of cell population proliferation (BMP2, FGFR2, IQGAP3, IL1R1) (**Supplementary Figure S3**), suggesting normal cellular processes occur in uninjured samples. Thus, these data provide evidence that a fibrotic response, at least at gene level, takes place in cryoinjured samples, with subsequent signs of matrix remodeling and *de novo* ECM deposition, as commonly

observed in clinical models of myocardial infarction.<sup>[482]</sup> While conventional clinical outputs were difficult to evaluate given the cell density limitations of the developed heart platform, this cellular response to cryoinjury is a promising observation that suggests the cells embedded within the printed structure retain key functions and exhibit the ability to undergo matrix remodeling in response to localized damage.

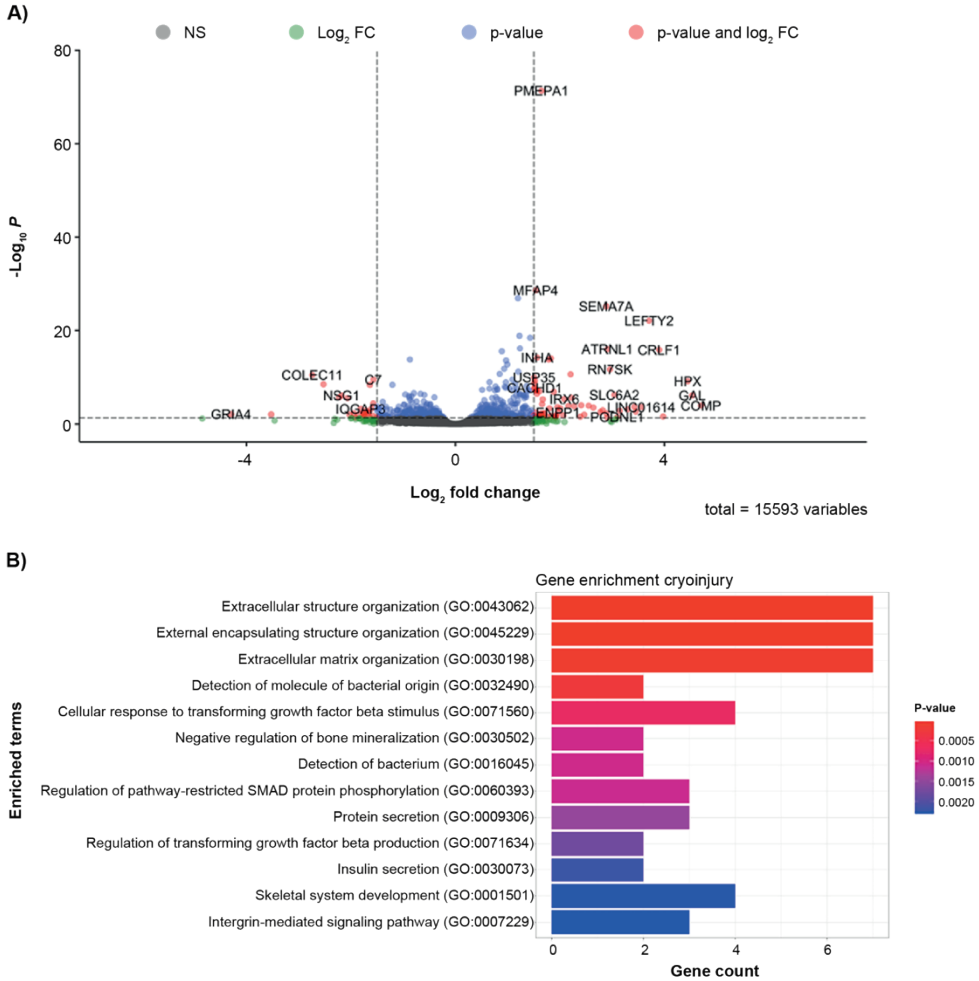


**Figure 3: RNA sequencing of cryoinjured vs. control volumetrically bioprinted heart samples.** A) Volcano plot of differentially expressed genes between cryoinjury treatment and control volumetrically bioprinted heart samples. Differentially expressed genes were determined via DeSeq2, where upregulated genes have > 1.5 log<sub>2</sub>FC and adjusted p-value < 0.05 and downregulated genes have < 1.5 log<sub>2</sub>FC and adjusted p-value < 0.05. B) GO Enrichment of Cryoinjury Treatment Genes; all 70 differentially expressed genes unique to cryoinjury treatment were subjected to Gene Ontology (Biological Processes 2021) enrichment.

Despite the biological drawbacks in terms of starting cell density of the volumetrically bioprinted heart platform, an important advantage of this approach, pending

improvements to cell interconnectivity and the induction of contractile activity, is its compatibility with widely used medical imaging technologies. Cardiovascular diseases are characterized by alterations in heart morphology linked to decreased function, and a common clinical practice is to evaluate such changes to monitor pathology progression, often using echocardiography and MRI.<sup>[483–485]</sup> Nevertheless, current *in vitro* systems present limited capability to mimic these morphological changes or apply these analysis techniques. The developed volumetrically bioprinted heart platform, with its advanced compartmentalized architecture and its water-based hydrogel composition enable the use of MRI imaging to monitor the morphological profile of the printed constructs. Herein, both cell-free and cell-laden heart constructs could be imaged with MRI technology immersed in their own cell culture medium (**Figure 4**). This in-medium imaging enabled the construct's chambers to remain open and prevented the collapse of the lower stiffness cell-bioresin regions of the construct, allowing for an accurate 3D representation of the mini hearts. In this way, conventional clinical slicing of the resulting MRI scans was possible, enabling the visualization of the volumetrically bioprinted heart from various transversal slices along the cardiac short-axis (SAX) of the base, mid-region and apex of the structures (**Figure 4A**). Similarly, the scans could be sliced along the cardiac long-axis (LAX) and the cardiac 4-chamber axis (**Figure 4B**). In the latter, the septum dividing the bioprinted heart's chambers can be clearly visualized. This compatibility with medical imaging techniques conventionally used in cardiology increases the clinical relevance of this platform as a future *in vitro* model. Upon enhancement of the biological capabilities of the model, this imaging analysis could be employed to monitor morphological changes of the platform over time, together with the pertinent quantitative analyses to evaluate changes in heart volume and length, individual chamber volumes as well as heart wall and septum thickness.

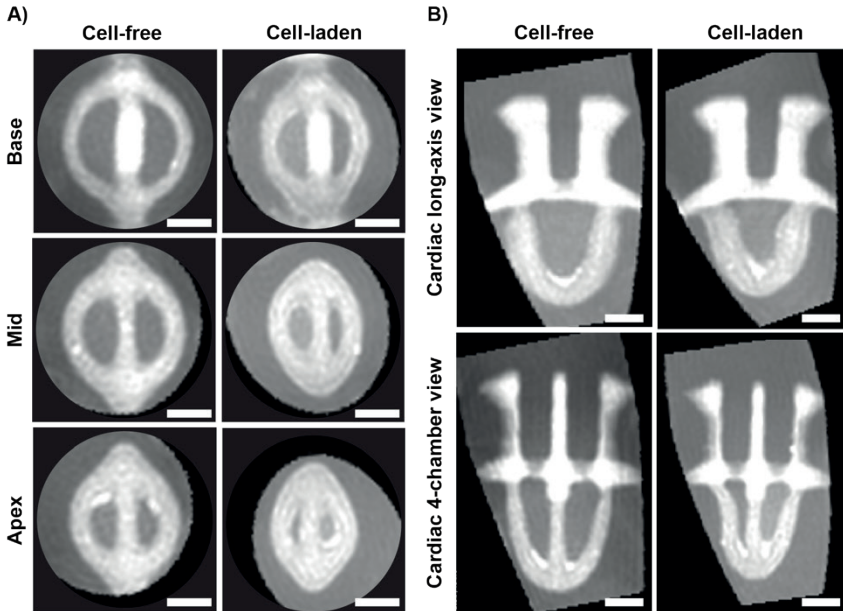


**Figure 4: MRI imaging of cell-free and cell-laden volumetrically bioprinted heart constructs.** A) Transversal, short-axis slices of representative cell-free and cell-laden volumetrically bioprinted heart constructs with separate slices of the base, mid and apex regions of the structure. B) MRI slices of the cell-free and cell-laden bioprinted hearts from a long-axis view and a 4-chamber view, where the dividing septum between the two independent chambers of the heart model are visible. Scale bars = 2 mm.

## MODEL LIMITATIONS AND PERSPECTIVES

Current *in vitro* models, such as 2D cell culture and engineered heart tissues, have limitations in mimicking the intricate macrostructural properties of cardiac tissue mimics. It is, therefore, necessary to develop a new generation of *in vitro* models with high architectural control to more predictively evaluate the efficacy of new therapies for cardiovascular disease, thus reducing the high failure rates of clinical trials. While VBP of the heart model presents a high-speed, contactless approach to process the sensitive iPSC-CMs employed in this model, the achievable cell densities and resulting cell-cell contact required to induce continuous and coordinated beating, resulting in actual fluid ejection, are not yet possible with VBP, due to the optical demands of the process itself. While previous studies with this co-culture employ densities of up to  $6 \times 10^7$  cells mL<sup>-1</sup>,<sup>[466]</sup> the current model could be correctly printed with 6-times less cells. Algorithms to correct scattering-induced artefacts,<sup>[421]</sup> alternative light sources that allow homogenous beam paths through a cell-laden suspension, the already employed optical adjustment of the bioresin,<sup>[286]</sup> or a combination of these approaches should be studied further to more significantly mitigate the cell density limitation of the VBP process and facilitate increased cell-cell interactions that allow the construct to function as a mini heart. Alternatively, strategies to guide cellular alignment and organization such as fiber reinforcement,<sup>[200,466,472]</sup> growth factor patterning,<sup>[486]</sup> or stimuli-responsive nanoparticles that can become highly aligned,<sup>[219]</sup> could help enhance cell interconnectivity without requiring such high cellular densities. In this way, the volumetrically bioprinted heart's full potential could be realized, and allow for the incorporation of other clinical outputs to study cardiomyopathies, such as action potential, beating rate, calcium handling evaluation, optical mapping, and even ejection fraction. In the present study, another important limitation was the induction of the cryoinjury itself. Given the manual fashion in which the injury was created, and the large tool (frozen spatula) used in this study, it was extremely challenging to thermally induce a small and precise injury on one chamber of the bioprinted heart and keep track of the injured region during imaging and subsequent sample analysis. Alternative ways to induce a superficial injury without penetrating through the heart wall should be further investigated (*i.e.* the use of a focused laser beam, or a blunt microneedle, with the additional aid of a stereotactic microscope to precisely position the injury) as well as a design change to ensure the injury site can be traced back during and after culture.

## CONCLUSIONS

This study presents a new approach to print cardiac *in vitro* models that capture key anatomical architectures using, for the first time, the combination of volumetric bioprinting and human iPSC-CMs. The bioprinted heart utilizes volumetric bioprinting to create scalable, bi- or multi-chamber heart constructs at high printing speeds. By introducing multi-material printing, and taking advantage of VBP's design freedom, this *in vitro* heart platform can be built with region-dependent mechanical properties, forming a) a high stiffness zone that can facilitate handling and withstand a hanging position and b) a low stiffness zone suitable for cell encapsulation. This approach could also be used to create models representative of structural deformations of the heart, as well as the native 4-chambered heart structure, posing great promise for potential disease modeling and patient specific research and treatment development. Cells embedded within the volumetrically bioprinted heart also demonstrated their post-printing responsiveness to external stimuli, as shown through the gene expression-level indication of matrix remodeling exhibited after cryoinjury, resembling the cellular response during myocardial ischemia. Notably, the bioprinted heart demonstrated compatibility with MRI imaging, a widely used medical imaging technique used in the field of cardiology for diagnostic and disease monitoring purposes, making it a promising *in vitro* modeling platform upon further development.

While the enhancement of cellular density and cell-to-cell contact is needed for further optimization of this model to enable further incorporation of clinically-relevant readouts, we highlight the potential of the volumetrically bioprinted heart as a tool for studying the underlying mechanisms and evolution of cardiovascular diseases *in vitro*. This platform provides a more architecturally realistic model than traditional 2D models and previously developed EHTs and has the potential to be used in high-throughput drug screening and personalized medicine, ultimately facilitating the development of new therapies. Further studies should focus on the establishment of a fully coordinated beating platform, the introduction of complex injury/disease models, as well as the inclusion of other cell types such as endothelial and epicardial cells to create more complex and realistic *in vitro* models of the heart. Future developments can also include the combination of this advanced model with heart valves and a pressure-volume (PV) loop system, to provide additional information to mimic other aspects of cardiovascular diseases, such as hypertension, valve fibrosis, or heart failure.

## EXPERIMENTAL SECTION

**Materials:** As the base bioresin for volumetric (bio)printing, gelatin methacryloyl (gelMA; 93.5% DoF) was synthesized as previously reported.<sup>[335]</sup> GelMA solutions were made in phosphate-buffered saline (PBS) at the required concentrations for each region of the volumetrically bioprinted heart construct. As photoinitiator, 0.1% w/v lithium phenyl(2,4,6-trimethylbenzoyl)phosphinate (LAP, Tokyo Chemical Industry, Japan) was supplemented to the hydrogel precursor solution to initiate the photocrosslinking reaction. To match the refractive index of the cells incorporated into the bioresin, 10% w/v iodixanol (OptiPrep, StemCell Technologies, Canada) was supplemented to the cell-laden bioresin.

**Human iPSC culture and differentiation:** Three healthy Caucasian fully characterized human iPSCs lines generated from peripheral blood mononuclear cells by using the insertion-free Sendai virus reprogramming method were used: UKKi032-C (NP0141-31B), UKKi037-C (NP0144-41), and NP0143-18 UKKi036-C.<sup>[487]</sup> All these cell lines have been deposited in the European Bank for iPSCs (EBiSC, <https://ebisc.org/>) and are registered in the online registry for human PSC lines hPSCreg (<https://hpscereg.eu/>). iPSCs were cultured on growth factor reduced Matrigel (Corning) in Essential 8 medium refreshed daily. Cells were passaged every 4–5 days with  $0.5 \times 10^{-3}$  M EDTA (Thermo Fisher Scientific). iPSCs were differentiated into iPSC-CMs using a GiWi differentiation protocol adapted from Chirico et al.,<sup>[488]</sup> and subsequently expanded following Maas et al. protocol.<sup>[489]</sup> In the differentiation process, we included a purification and a replating step to generate a high-purity cardiomyocyte population.

**Primary cell culture:** Human fetal cardiac fibroblasts (hfCFs) were isolated as described previously<sup>[490]</sup>. hfCFs were cultured in fibroblast medium until 70–80% confluency and passaged in a 1:4 ratio before experimental use. hfCF medium consisted of DMEM ([+] 4.5 g D-Glucose, L-Glutamine, [-] Pyruvate; Gibco, 41965-039) supplemented with 10% fetal bovine serum (FBS; Biowest S1810-500) and 1% penicillin-streptomycin (pen/strep; Gibco, 15-140-122).

**Volumetric heart bioprinting – multimaterial refractive index matching:** To achieve a seamless interface between the two resins present in the volumetric heart, the optical properties of the cell bioresin (base 5% w/v gelMA + 0.1% w/v LAP) were matched to that of pristine 15% w/v gelMA + 0.1% w/v LAP (support resin) using iodixanol (0 – 40% v/v iodixanol). The refractive index of the resulting 5% gelMA blends ( $n = 3$ ) and the support resin was measured using a digital refractometer (MA871; Milwaukee Instruments, Hungary) using the pre-crosslinked hydrogel solution to select the optimal iodixanol concentration.

**Volumetric heart bioprinting:** iPSC-CMs were detached using TrypLE Select Enzyme 10X (Gibco), hfCFs were dislodged using Trypsin (Gibco) and mixed in a 10:1 ratio (90% iPSC-CMs : 10% hfCFs). Cells were then spun down and resuspended in a 5% w/v gelMA, 10% v/v

iodixanol and 0.1% w/v LAP hydrogel precursor solution (cell bioresin). Subsequently, 500  $\mu\text{L}$  of this cell bioresin was gently pipetted inside a pre-cooled 10 mm diameter borosilicate glass vial to prevent cell sedimentation. The bioresin was further gelated in ice water for 5 minutes. Afterwards, the vials were taken out of the ice water and 500  $\mu\text{L}$  of pre-warmed (40° C) support resin (15% w/v gelMA and 0.1% w/v LAP) was pipetted just above the layer of cell bioresin. The vials were then kept at room temperature for 2 minutes to ensure a homogenous interface region was formed, and they were then cooled in ice water again. Volumetric bioprinting of the heart constructs was then carried out using a commercial Tomolite v1.0 (Readily3D, Switzerland) printer. Briefly, the vial was placed so that the interface of the heart STL model corresponded with the resin interface and a 405 nm laser beam was then directed towards a digital micromirror device that in turn modulated the tomographic projections of the model onto the rotating printer vial. Each region (support and cell-laden) received a different light dose to ensure homogenous printing of the heart model. After printing, the construct was gently washed with prewarmed medium to remove uncrosslinked GelMA and incubated in construct medium. After one hour, constructs were hanged using a custom-made, 3D printed forklift and transferred to a 3.5 cm Petri dish (ThermoFischer Scientific, The Netherlands) with prewarmed construct medium. 75% of the construct culture medium was changed every other day.

*Mechanical characterization of multi-material constructs:* To measure the compressive properties of printed structures consisting of both the support resin and cell bioresin employed in the volumetric heart, a 2980 Dynamic Mechanical Analyzer was used (DMA; Q800, TA Instruments, The Netherlands) equipped with a cylindrical flat piston (diameter = 2 mm). Flat multi-material structures were printed as previously described ( $n = 5$ ), forming a stable interface through thermal control of both resins. Using the 2 mm indenter, the compressive properties of the constructs were measured per region (one measurement of the support resin, one of the cell bioresin and one of the interface, carefully placed in the middle of the interface region). Each region was subjected to a strain ramp of  $-20\% \text{ min}^{-1}$  strain rate until 30% deformation. Young's Modulus was calculated as the slope of the stress/strain curve in the 10-15% strain range. Similarly, the same DMA device was used with a tensile test clamp to assess the tensile properties of the different resins. 3 cm long strips with a thickness of 0.5 mm were printed with each resin composition, secured to each end of the clamp, and subjected to a force ramp of  $0.05 \text{ N min}^{-1}$  force rate until reaching 10 N or until the sample yielded ( $n = 6$ ). The tensile modulus was also calculated as the slope of the resulting stress/strain curve in the 10-15% strain range.

*Volumetric heart imaging and analysis:* Volumetrically printed samples were imaged using a custom-made lightsheet microscope after staining with a Cy3.5-PEG-SH fluorescent dye (5kD; Biopharma PEG) and 3D renderings of the lightsheet scans were made with the image analysis software FIJI.<sup>[491]</sup> To show the printing accuracy between the printed hearts and the original CAD model, a 3D triangular mesh editing software (CloudCompare V2.11) was



used.<sup>[492]</sup> Both STL files (print reconstruction and original design) were manually aligned by selecting different referential points in each mesh. Then, the distance between the meshes was computed using the cloud-to-cloud distance (Hausdorff distance algorithm), which is a measurement for comparing image segmentations between two set points.<sup>[493]</sup> The difference map was then created to see the overall print variation from the original STL file.

*Volumetric heart cryoinjury:* Seven days after seeding, the volumetrically bioprinted hearts were transferred one by one on a clean Petri dish without medium. A sterile steel microspoon previously submerged in liquid nitrogen was gently placed on one of the ventricles for ten seconds. The constructs were subsequently transferred back into their support and cultured until further analysis.

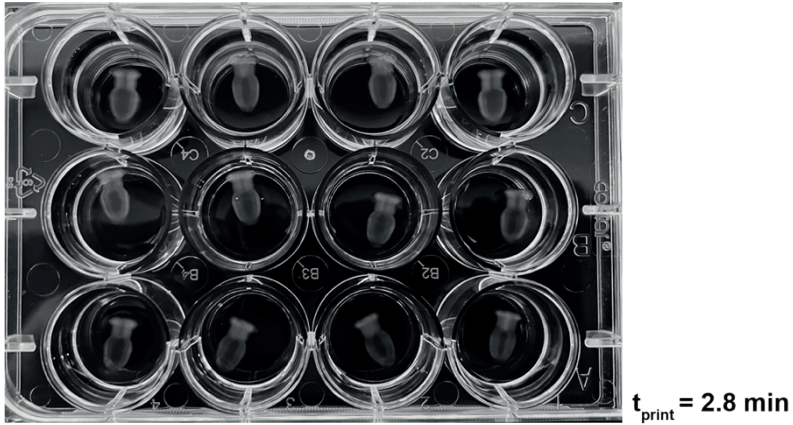
*RNA isolation and sequencing:* 7 days after inflicting the cryoinjury, the volumetrically bioprinted hearts were digested for RNA isolation and bulk RNA sequencing were performed on control and cryoinjury samples (n = 4). First, samples were digested in collagenase to isolate the cellular material from the bioresin. Samples were incubated in sterile DMEM medium supplemented with 1% wt/v penicillin streptomycin and 1% wt/v collagenase type 2 enzyme (Worthington Biochemical, USA) for 8 minutes under stirring conditions. The resulting cell pellets were resuspended in 100  $\mu$ L TRIZOL solution (ThermoFischer Scientific, The Netherlands) and stored frozen at  $-80^{\circ}$  C until sequencing. RNA extraction, cDNA library preparation (CEL-Seq2 protocol<sup>[494]</sup>) quality control for aRNA and cDNA, and sequencing on a NextSeq500 High output 1  $\times$  75 bp paired end run a sequencing depth of 10 million reads/sample were performed by Single Cell Discoveries B.V. (Utrecht, The Netherlands).

*Differential gene expression and gene set enrichment analysis:* Differential gene expression and normalization between cryoinjured and control bioprinted heart samples was evaluated using the DESeq2 package in R. Significance was set with a false-discovery rate Benjamini-Hochberg correction with a q-value < 0.05, average  $\log_2$  fold-changes > 1.5 for upregulated genes relative to control, and average  $\log_2$  fold-changes < -1.5 for downregulated genes relative to controls. The heatmap of significant genes was created with the heatmap package in R, displaying the top 20 variably expressed genes across samples. The EnhancedVolcano package in R was used to create volcano plots depicting the top differentially expressed genes with the lowest q-values, the highest  $\log_2$  fold-changes for upregulated genes, and the lowest  $\log_2$  fold-changes for downregulated genes. Gene set enrichment analysis via gene ontology (GO) enrichment terms (GO Biological Processes 2021, GO Molecular Function 2021, and GO Cellular Component 2021 gene sets) was performed using the enrichR package in R, with significance cut-off for enrichment at q < 0.05 and a false discovery rate by Benjamini-Hochberg correction. The top 10 enriched GO terms per gene list were plotted via EnrichR.

*MRI imaging, data processing and quantification:* MRI experiments were performed at a Varian 9.4 T magnet with OpenVnmrJ. To obtain a whole volume view of the volumetrically bioprinted hearts a 3D balanced SSFP sequence was used (TR/TE 15.4/7.7 ms, flip angle 40°, FOV 30x10x10 mm<sup>3</sup>, 150x50x50 pts (resolution 200x200x200 μm<sup>3</sup>), nt 4, repeated 4 times (0, 90, 180 and 270 phase shifts) and total acquisition time is about 10 min). Data processing was performed using MATLAB® (MathWorks®) and tools from FSL (FMRIB Software Library v6.0). Data were zero-filled to twice the size before Fourier-transformation, leading to an isotropic spatial resolution in the images of 100 micrometer. The 3D-volume images obtained from the balanced SSFP sequence showed a high signal intensity for the construct culture medium and lower signal intensities for the tissue matrix and the heart tissue, where the matrix base appeared to be most dense. Signal intensity of the image was inverted to allow a better observation of the heart tissue, which becomes higher in signal intensity because of this procedure. Masks were generated for three perpendicular slices through the volumetric heart, and these were manually edited to remove areas not containing the heart. The masks were used to seed a snake algorithm, an iterative region-growing image segmentation program (activecontour in MATLAB) that automatically segments the heart. The ventricles within the volumetric heart were filled with culture medium and were detected by filling the holes in the mask of the volumetric heart and subtracting the original mask from the filled one. One of the heart images was manually oriented orthogonally and this image was used as a reference for linear registration of the other hearts (using FLIRT of FSL). The last step allows visual comparison of the registered hearts and compartmentalization of different regions of the heart (base, left ventricle, right ventricle).

## SUPPORTING INFORMATION

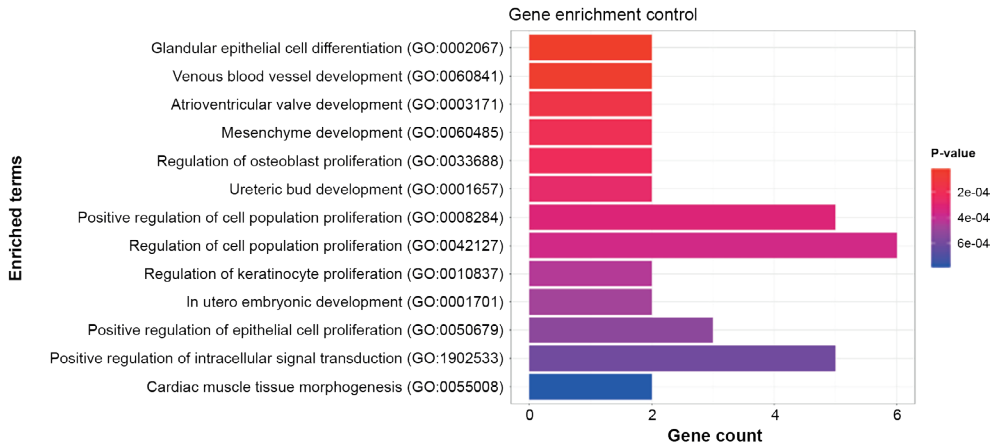
### Supplementary Figures



**Supplementary Figure S1:** High-throughput volumetric bioprinting of 12x volumetrically bioprinted heart models in under 3 minutes.



**Supplementary Figure S2:** Heatmap of cryoinjured versus control volumetrically bioprinted heart samples. Differentially expressed genes (92 total, 70 upregulated, 26 downregulated) were plotted on a heatmap, and all 4 replicates of cryoinjury and control conditions were clustered together per treatment.

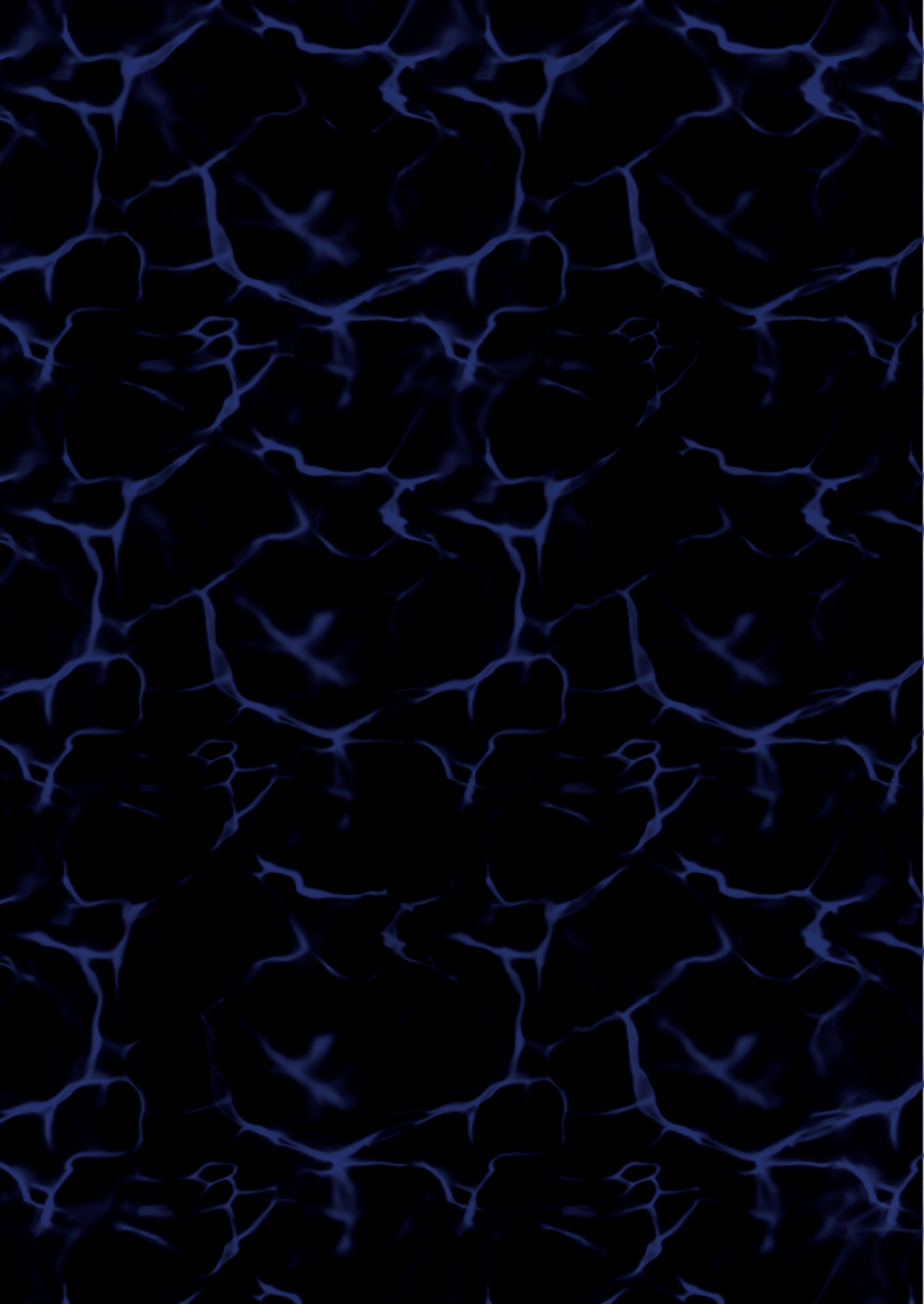


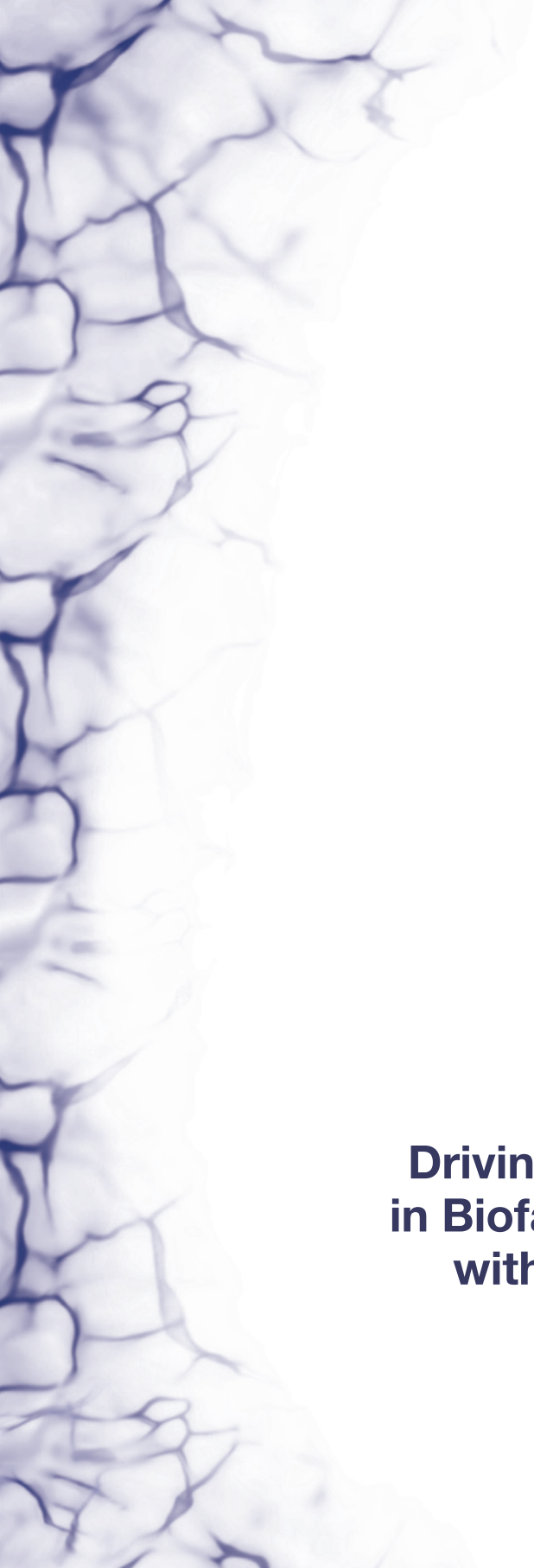
**Supplementary Figure S3:** GO Enrichment of Control Treatment Genes. All 26 differentially expressed genes unique to control treatment were subjected to Gene Ontology (Biological Processes 2021) enrichment.

## Supplementary Video

**Supplementary Video S1:** High cell density region of a volumetrically bioprinted iPSC-CM/hfCF laden structure, exhibiting contractile activity.

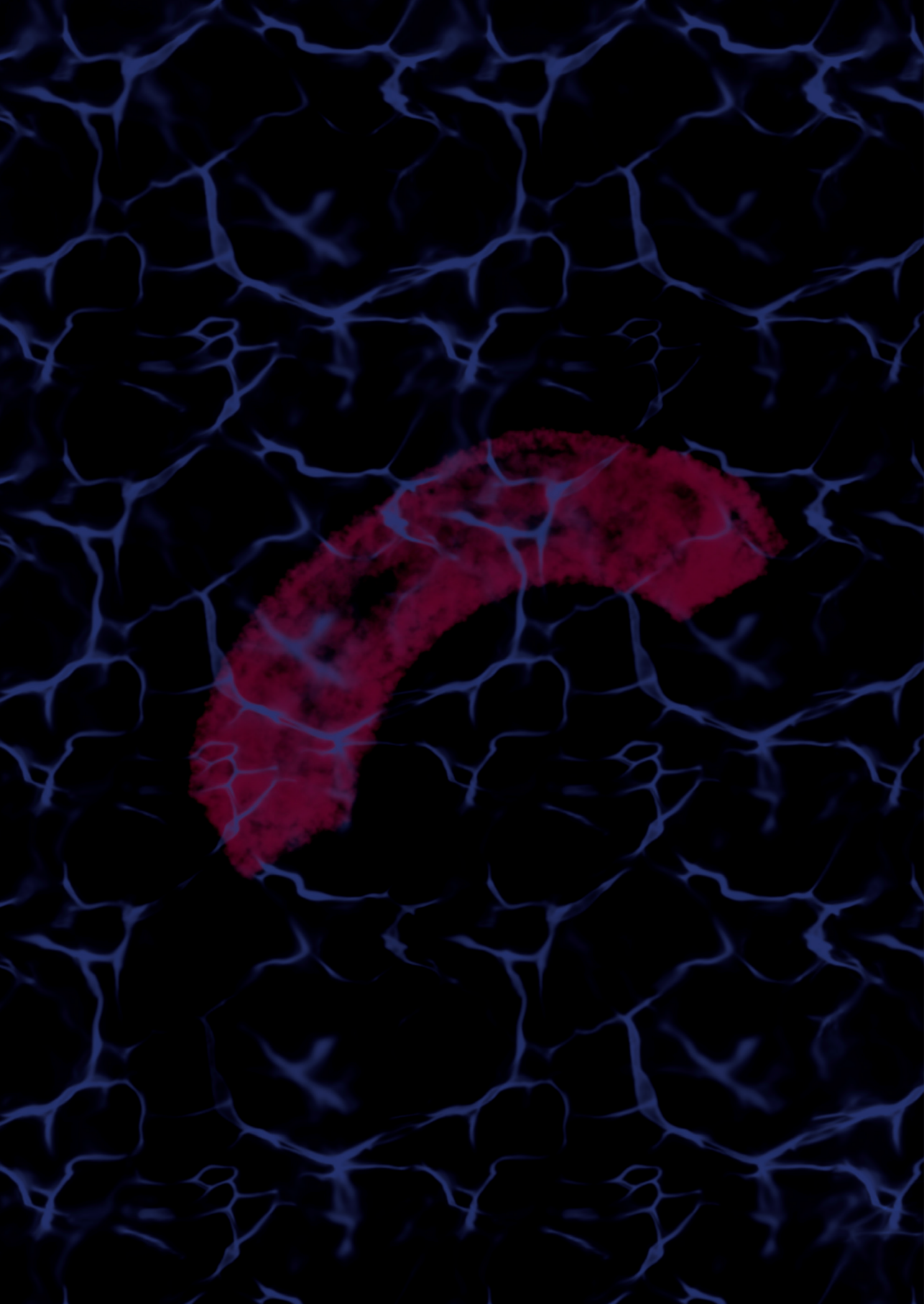






# Part III

**Driving Tissue Biomimicry  
in Biofabricated Structures  
with Smart Biomaterials**





# Chapter 8

## Biofunctionalization of 3D Printed Collagen with Bevacizumab-Loaded Microparticles Targeting Pathological Angiogenesis

Anna Abbadessa<sup>1,2</sup>, Paulina Nuñez Bernal<sup>3</sup>, Giorgio Buttitta<sup>1,2</sup>, Alfredo Ronca<sup>4</sup>, Ugo D'Amora<sup>4</sup>, Carla Zihlmann<sup>5</sup>, Niklaus Stiefel<sup>5</sup>, Luigi Ambrosio<sup>4</sup>, Jos Malda<sup>3,6</sup>, Riccardo Levato<sup>3,6</sup>, José Crecente-Campo<sup>1,2</sup>, María José Alonso<sup>1,2</sup>

Published in: *Journal of Controlled Release*. 2023. 360

<sup>1</sup>Center for Research in Molecular Medicine and Chronic Diseases (CIMUS), IDIS Research Institute, Universidade de Santiago de Compostela, Santiago de Compostela, Spain

<sup>2</sup>Department of Pharmacology, Pharmacy and Pharmaceutical Technology, School of Pharmacy, Campus Vida, Universidade de Santiago de Compostela, Santiago de Compostela, Spain

<sup>3</sup>Department of Orthopaedics, University Medical Center Utrecht, Utrecht, the Netherlands

<sup>4</sup>Institute of Polymers, Composites and Biomaterials, National Research Council (IPCB-CNR), Naples, Italy

<sup>5</sup>Geistlich Pharma AG, Wolhusen, Switzerland

<sup>6</sup>Department of Clinical Sciences, Faculty of Veterinary Medicine, Utrecht University, Utrecht, the Netherlands

## ABSTRACT

Pathological angiogenesis is a crucial attribute of several chronic diseases such as cancer, age-related macular degeneration, and osteoarthritis (OA). In the case of OA, pathological angiogenesis mediated by the vascular endothelial growth factor (VEGF), among other factors, contributes to cartilage degeneration and to implants rejection. In line with this, the use of the anti-VEGF bevacizumab (BVZ) has been shown to prevent OA progression and support cartilage regeneration. The aim of this work was to functionalize a medical grade collagen with poly (lactic-co-glycolic acid) (PLGA) microparticles containing BVZ via three-dimensional (3D) printing to target pathological angiogenesis. First, the effect of several formulation parameters on the encapsulation and release of BVZ from PLGA microparticles was studied. Then, the anti-angiogenic activity of released BVZ was tested in a 3D cell model. The 3D printability of the microparticle-loaded collagen ink was tested by evaluating the shape fidelity of 3D printed structures. Results showed that the release and the encapsulation efficiency of BVZ could be tuned as a function of several formulation parameters. In addition, the released BVZ was observed to reduce vascularization by human umbilical vein endothelial cells. Finally, the collagen ink with embedded BVZ microparticles was successfully printed, leading to shape-stable meniscus-, nose- and auricle-like structures. Taken altogether, we defined the conditions for the successful combination of BVZ-loaded microparticles with the 3D printing of a medical grade collagen to target pathological angiogenesis.

**Keywords:** anti-angiogenic effect, protein delivery, PLGA, 3D printing

## INTRODUCTION

Pathological angiogenesis is a crucial attribute of cancer and several chronic inflammatory diseases, such as age-related macular degeneration (AMD) and osteoarthritis (OA).<sup>[495,496]</sup> In cancer, new vessels develop by sprouting from pre-existing vessels leading to an abnormal vasculature with a disorganized architecture and a high vascular permeability, among other features.<sup>[495]</sup> In AMD, a chronic retinal disease, new abnormal vessels originating from the vascularized choroid invade the retinal space, leading to death of photoreceptors and irreversible blindness.<sup>[496]</sup> More recently, pathological angiogenesis has also been linked to OA, a chronic inflammatory disease characterized by the damage of the articular cartilage, pain, and reduced mobility. The association between pathological angiogenesis and OA has emerged following the observation that OA patients present vasculature in the articular cartilage and in the inner meniscus, which normally are avascular structures.<sup>[497]</sup> As in cancer and in AMD, also in OA, members of the vascular endothelial growth factor (VEGF) family play a key role, among other factors.<sup>[495,497]</sup> In OA, this angiogenic process is associated to a progressive breakdown of the extracellular matrix (ECM) and tissue degeneration.<sup>[497,498]</sup> In fact, one of the effects of VEGF is the stimulation of the degrading enzymes matrix metalloproteinases (MMPs) and the inhibition of the tissue inhibitors of the matrix metalloproteinases (TIMP).<sup>[498,499]</sup> Moreover, the VEGF-mediated cellular invasion can cause premature resorption of implanted cartilage scaffolds *in vivo*, via monocyte chemoattraction.<sup>[500]</sup> These observations highlight the importance of modulating the VEGF activity during OA and when a scaffold-mediated regeneration of avascular cartilage and fibrocartilage is sought.

Bevacizumab (BVZ) is a full-length, humanized, recombinant monoclonal antibody against all isoforms of VEGF-A. It was approved by the Food and Drug Administration (FDA) for the treatment of the advanced stage of colon, lung, kidney, and brain cancers, and it is also used as an off-label drug for the treatment of AMD.<sup>[501,502]</sup> Recently, BVZ has also emerged as a promising active factor to block pathological angiogenesis and support regeneration in OA cartilage.<sup>[503–505]</sup> As an example, BVZ was reported to support the repair of articular cartilage in an osteochondral defect model in rabbits.<sup>[506]</sup> Moreover, BVZ was found to preserve scaffold long-term stability *in vivo*.<sup>[500]</sup> Despite these promising *in vivo* results, the incorporation of BVZ in three-dimensional (3D) printed scaffolds for their use in regenerative medicine has not been explored yet.

In this study, we biofunctionalized a medical grade collagen with BVZ-loaded microparticles to target pathological angiogenesis as that found in OA cartilage and meniscus. Moreover, we tested the processability of this composite material via 3D printing, a widely explored technology for the fabrication of customized scaffolds in tissue engineering. The rationale behind the use of polymeric microparticles is the prevention of the premature degradation of BVZ and its controlled release upon implantation of the scaffolds.<sup>[507]</sup> In this sense, it has

been argued that for the efficient VEGF blockage in the context of OA cartilage, it would be important to achieve a continuous delivery of BZV for 2-3 weeks<sup>[500,506]</sup>. To achieve such profile, we selected microparticles made of poly(lactic-co-glycolic acid) (PLGA), a polymer known for its capacity to control the release of biological drugs, including BVZ.<sup>[508-515]</sup>

In our study, a medical grade porcine collagen material that has already been applied in clinical procedures for cartilage, bone regeneration and wound healing<sup>[516-520]</sup> was selected for the production of the scaffold using 3D printing. This technique was selected because it allows the design and manufacturing of customized complex structures by the layer-by-layer deposition of printable materials, *i.e.*, inks, that may carry cells and active factors.<sup>[521-526]</sup> Remarkably, 3D printing allows for the spatial distribution of these elements to recreate naturally occurring gradients, as those present in the articular cartilage and meniscus.<sup>[527,528]</sup> For example, the human meniscus presents an outer vascularized zone (the red zone) that gradually turns into an avascular inner zone (the white zone, outer-inner gradient), whereas articular cartilage is avascular and presents several horizontal zones that differ in terms of cell morphology and density, as well as in the content and arrangement of the ECM components (bottom-up gradient). For such anisotropic tissues, 3D printing can allow a spatio-specific distribution of active factors throughout tissue-engineered scaffolds to mimic zone-specific features. This can be important to recreate an appropriate milieu for cell differentiation and tissue ingrowth.<sup>[528,529]</sup> Taken altogether, we combined BVZ micro-encapsulation and 3D printing to fabricate medical grade scaffolds loaded with anti-angiogenic microparticles targeting pathological angiogenesis, as that found in OA cartilage and meniscus. Remarkably, this approach may be potentially extended to other diseases with pathological angiogenesis, such as cancer and AMD.

## RESULTS AND DISCUSSION

### 8

### Effect of surfactants in the organic phase on the encapsulation and release of BZV from PLGA microparticles - Formulation screening 1

First, an explorative screening (16 formulations) involving different non-ionic surfactants at different concentrations and in combination with two different PLGA molecular weights (**Supplementary Table S1** and **Supplementary Figure S1**) was carried out. From this study, the five most interesting formulations in terms of EE and release profile were selected for the formulation screening 1 (**Table 1**). In this screening, the effect of different surfactants (Pluronic® F-68, Pluronic® L-64, Tween® 80 and Span® 60), used at different concentrations, was investigated.

**Table 1:** Effect of surfactants and their concentration in the organic phase on the BVZ encapsulation efficiency (EE) of PLGA microparticles (formulation screening 1). The concentration of BVZ in the inner water phase (w1) was 28.9 mg mL<sup>-1</sup> (0.2 mL), the concentration of capped PLGA (14 kDa) in the organic phase was 50 mg mL<sup>-1</sup> (1 mL). In the abbreviations, S1 indicates screening 1, and the last 4 characters refer to the name of the surfactant and concentration used. Standard deviation values of the average diameter indicate particle size variability within a given batch.

Sample	Surfactant in the organic phase	Surfactant concentration (mg mL <sup>-1</sup> )	Average diameter (µm)	EE (%)
S1-PF50	Pluronic® F-68 (HLB=28.0)	50	6.5 ± 7.4	53 ± 3
S1-PL150	Pluronic® L-64 (HLB=15.0)	150	1.5 ± 0.3	48 ± 3
S1-TW25	Tween® 80 (HLB=15.0)	25	2.3 ± 0.7	39 ± 0
S1-TW50		50	2.5 ± 1.3	22 ± 2
S1-SP50	Span® 60 (HLB=4.3)	50	2.7 ± 1.4	83 ± 4

The EE values presented a broad range (22-83%) as a function of the surfactant hydrophilic/lipophilic balance (HLB). This can be appreciated by comparing the formulations S1-PF50, S1-TW50 and S1-SP50, prepared using the same concentration in the organic phase of three different surfactants with different HLB values, *i.e.*, Pluronic® F-68 (HLB = 28.0), Tween® 80 (HLB = 15.0) and Span® 60 (HLB = 4.3), respectively. Formulations prepared with Span® 60 showed the highest values of EE, *i.e.*, 83%. This finding is in line with the results reported in previous literature, where the high encapsulation of hydrophilic drugs into poly(D,L-lactide) (PLA) and PLGA microspheres in the presence of Span® 60 was attributed to the low HLB of this surfactant, which makes it an ideal stabilizing agent for water-in-oil interfaces.<sup>[530,531]</sup> By increasing the HLB from 4.3 (Span® 60) to 15.0 (Tween® 80), the EE values dramatically decreased down to 22%. By further increasing the HLB to 28.0 (Pluronic® F-68), the EE values increased again up to 53%. This trend is in line with the observations by Dinarvand *et al.* regarding the encapsulation of a hydrophilic drug into PLA microparticles.<sup>[530]</sup> The lower EE found for the formulations made with Tween® 80 can be attributed to its higher HLB, as compared to that of Span® 60 and, therefore, to its inferior capacity for the stabilization of the primary emulsion (w1/o). On the other hand, the moderate EE values found for the formulations made with the most hydrophilic surfactant of the study, *i.e.*, Pluronic® F-68 demonstrated that the EE can also benefit from the stabilization of the secondary emulsion (o/w2), mediated by the migration of these surfactants to the o/w2 interface, which reduces the amount of protein adsorbed onto the microparticles surface.<sup>[530]</sup> Moreover, surfactants with high HLB may interact with the PVA present in the outer water phase, forming a gel-like stabilizing barrier.<sup>[530]</sup>

Previous studies reported in literature have shown that the EE values of BVZ into PLGA nano- and microparticles fabricated by the double emulsion technique are usually higher than 80%.<sup>[512,513,532,533]</sup> However, it must be noted that in these studies uncapped PLGA is used, for which we have also found similarly high values of EE. These high values of EE

are likely due to the electrostatic interactions between the positively charged BVZ and the negatively charged PLGA carboxyl end groups. In this study, we preferred the use of capped PLGA, since the uncapped polymer did not support the desired release kinetics.

The BVZ release profiles of the tested formulations significantly differed as a function of the surfactant HLB and concentration (**Figure 1a, b**). Formulations made with poloxamers (Pluronic® F-68 and Pluronic® L-64) showed a release kinetics, characterized by an initial burst release phase during the first 2-3 days followed by a slower release until day 21. These formulations showed the lowest burst release (percentage of BVZ released by day 2 was 11% and 15%, for S1-PF50 and S1-PL150, respectively) and the lowest total percentage of BVZ released by day 21 (16% and 22% for S1-PF50 and S1-PL150, respectively). Overall, the burst release of BVZ increased when the surfactant HLB decreased. This can be appreciated by comparing the formulations S1-PF50, S1-TW50 and S1-SP50, which organic phases contain the same concentration of three different surfactants with different HLB values, *i.e.*, Pluronic® F-68 (HLB = 28.0), Tween® 80 (HLB = 15.0) and Span® 60 (HLB = 4.3), respectively. Indeed, the percentage of BVZ released by day 2 was 11%, 29%, and 39%, for S1-PF50, S1-TW50 and S1-SP50, respectively. This trend can be explained by considering the different distribution of the surfactant and the protein within the PLGA matrix. Surfactants with a low HLB tend to position themselves preferentially towards the oily PLGA-containing phase, whereas those with a high HLB tend to diffuse towards the water phase, which causes a correspondent displacement of the entrapped protein.<sup>[530]</sup> Therefore, in the former case, the fraction of the protein that the surfactant displaces from the core and that ends up onto the microparticle surface is much higher. This explains the much higher burst release of BVZ observed when using surfactants with a lower HLB. The formulation S1-SP50 showed the highest burst release and the highest value of total BVZ released by day 21 (*i.e.*, 41%), however between day 5 and day 21 only a minor percentage of BVZ was released, which could be due to the absence of release or to the degradation of the protein molecules. S1-PL150 was the best performing formulation in terms of providing a constant release of BVZ from day 5 to day 21 (distributive release profiles shown in **Supplementary Figure S3**) and, hence, was selected for further evaluation by ELISA and by cellular *in vitro* studies.

It must be noted that all formulations exhibited incomplete release of BZV, a result in line with previously reported data on the release of BVZ from PLGA particles.<sup>[508,512,513]</sup> For instance, Sousa *et al.* reported a total 15% BZV release over the first 7 days.<sup>[513]</sup> A low amount of total BZV release (< 10%) was also observed by Varshochian *et al.* during the first 21 days.<sup>[512]</sup> This incomplete protein release often noted for PLGA particles has been found to be dependent on the protein isoelectric point and protein size, as well as on the PLGA charge density and particle porosity.<sup>[513]</sup> The incomplete release of BVZ observed in our study is likely due to protein/polymer interactions, as previously described for protein-loaded PLGA particles.<sup>[534–537]</sup> Indeed, all formulations showed an insoluble residue at the

end of the study. The presence of a residue originated by protein/polymer interactions has been previously reported for PLGA microparticles.<sup>[535]</sup> To understand the role of BVZ on the generation of this residue, in a separate experiment, BVZ-loaded and blank microparticles made with a fast-degrading uncapped PLGA with a molecular weight of 2 kDa were prepared and monitored for 21 days. This PLGA type was selected because a complete PLGA degradation was expected for 21 days. This is important to exclude that the residue generation was due to undegraded PLGA matrix. Importantly, BVZ-loaded formulations showed an insoluble residue at day 21, whereas no residue was observed for the blank formulations (**Supplementary Figure S4**). This confirms that the presence of BVZ into PLGA microparticles triggered the formation of insoluble complexes. In this context, an interesting aspect is to analyse whether these BVZ/PLGA interactions are established during the formulation process or also after that BVZ has been released (post-release BVZ adhesion onto PLGA residual particles). To answer this question, a separate experiment was performed. BVZ was dissolved in the release medium, incubated with blank microparticles, and free BVZ in the supernatant was quantified at day 0 and 7. No significant adhesion of BVZ was observed in this experiment. Therefore, the observed incomplete release cannot be attributed to post-release BVZ-PLGA interactions, but to an actual lack of BVZ release due to protein-polymer interactions that occur during the formulation and incubation process.

ELISA/Bradford comparative studies allowed to quantify the active protein (ELISA quantification) as a percentage of the total protein released (Bradford quantification, **Figure 1c, d**). These studies showed that the percentage of active protein for the selected formulation (namely, S1-PL150) ranged between 26 and 35%, depending on the time point under consideration. The partial protein inactivation observed in our study is in line with the results of Varshochian *et al.* who reported a protein inactivation of up to 79% during the first 21 days in an *in vitro* release study.<sup>[512]</sup> Importantly, the same authors found a much higher amount of active protein released in an *ex-vivo* model. This highlights the intrinsic limitations of *in vitro* release studies and the need to complement *in vitro* release data with other protein activity assays.

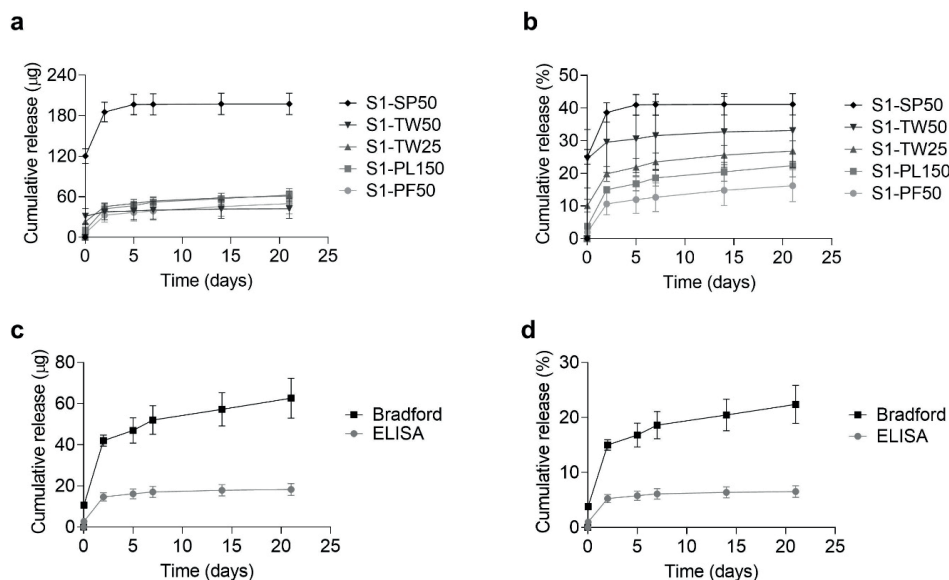


**Figure 1: BVZ release profiles of the formulations prepared in the formulation screening 1.** BVZ cumulative release of all formulations in a)  $\mu\text{g}$  and b) % as a function of time. BVZ release profiles according to the Bradford assay and ELISA of the formulation S1-PL150. Cumulative release in c)  $\mu\text{g}$  and d) % as a function of time. In the abbreviations, S1 indicates screening 1, whereas the last 4 characters refer to the name of the surfactant and to the concentration used (**Table 1**).

## Effect of the PLGA/BVZ and Tween® 80/BVZ ratios on the encapsulation and release of BVZ from PLGA microparticles - Formulation screening 2

The aim of the formulation screening 2 was to study the effect of the PLGA/BVZ ratio and the Tween® 80/BVZ ratio on the EE and release kinetics when the surfactant is dissolved in the primary water phase (w1) (**Table 2**). In this screening, Tween has been preferred over Pluronic because, according to the literature, it has been previously mixed in aqueous phases for BVZ micro- and nanoencapsulation, with a beneficial effect on the EE and stability.<sup>[538,539]</sup> Span has been excluded due to its insolubility in water.



**Table 2:** Effect of the PLGA/BVZ and Tween® 80/BVZ ratios on the encapsulation efficiency (EE) and microparticle size (formulation screening 2). Different PLGA/BVZ ratios were obtained by varying the volume of the primary water phase w1 (fixed BVZ concentration = 25 mg mL<sup>-1</sup>) and the concentration of capped PLGA (36 kDa) in the organic phase (fixed volume = 500 µL), whereas different Tween® 80/PLGA ratios were obtained by varying the concentration of Tween® 80 (58 or 116 mg mL<sup>-1</sup>) in w1. In the abbreviation, S2 indicates screening 2 and PB indicates the PLGA/BVZ ratio. For the formulations PB25, a and b indicate that the same PLGA/BVZ ratio was achieved using different volumes of w1 and different concentrations of PLGA in the organic phase; whereas for the formulations PB7, a and b indicate that the formulations have a different Tween® 80/BVZ ratio. Standard deviation values of the average diameter indicate particle size variability within a given batch.

Sample	Volume w1 (mL)	PLGA concentration (mg mL <sup>-1</sup> )	PLGA/BVZ ratio	TW80/BVZ ratio	Average diameter (µm)	EE (%)
S2-PB50	0.1	250	50	2.3	107 ± 57	93 ± 7
S2-PB25a	0.2	250	25	2.3	81 ± 35	82 ± 1
S2-PB25b	0.1	125	25	2.3	39 ± 13	78 ± 8
S2-PB12	0.2	125	12.5	2.3	55 ± 21	75 ± 2
S2-PB7a	0.2	75	7.5	2.3	53 ± 22	62 ± 8
S2-PB7b	0.2	75	7.5	4.6	42 ± 21	85 ± 1

The EE presented values between 62 and 93%, depending on the composition (**Table 2**). Overall, the EE increased when the PLGA/BVZ ratio increased. This general trend is in agreement with the results reported previously regarding protein delivery from PLGA microparticles,<sup>[515]</sup> and can be explained by the fact that an increase in the PLGA/BVZ ratio implies a lower BVZ diffusion from the internal water phase to the external one due to a lower BVZ gradient. Moreover, in our study an increase in the PLGA/BVZ ratio was also obtained by increasing the PLGA concentration, which causes an increase in the viscosity of the organic phase that, in turn, reduces the BVZ diffusion toward the external water phase.<sup>[515]</sup> Furthermore, by increasing the PLGA concentration, bigger particles were obtained. This likely caused a decrease in the BVZ leakage due to the relatively lower superficial area of bigger particles.

By comparing the formulations S2-PB7a and S2-PB7b, it can be noted that an increase in the TW80/BVZ ratio from 2.3 to 4.6 caused a significant increase in the EE (from 62 to 85%). This is in line with the findings reported by Narayana *et al.*, who also found higher EE by increasing Tween 80 concentration.<sup>[538]</sup> Overall, the values of EE in the formulations of the screening 2 (**Table 2**) were higher than those found in the formulation screening 1 (**Table 1**), likely due to the bigger particle size (40-100 µm vs 1-5 µm) and the milder homogenization used in the formulation screening 2.

All formulations showed a sustained release of BVZ during the first 21 days (cumulative release curves in **Figure 2** and distributive release curves in **Supplementary Figure S5**). In line with previously reported data on BVZ release from PLGA particles, the release was accelerated by decreasing the PLGA/BVZ ratio (from 50 to 7.5) and by decreasing the

particle size (from 100 to 40  $\mu\text{m}$ ).<sup>[508]</sup> The formulation S2-PB7b, which had the lowest PLGA/BVZ ratio and the highest Tween® 80/BVZ ratio, released the highest amount of BVZ at day 21 (126  $\mu\text{g}$ , 21%). This result indicates that the decrease in the PLGA/BVZ ratio and the increase in the Tween® 80/BVZ ratio had a synergistic effect in boosting BVZ release. For this reason, the formulation S2-PB7b was selected for further *in vitro* cellular studies. Remarkably, the percentage of active protein in the total released protein was higher than that found in the screening 1, ranging between 50 and 64% depending on the time point under consideration. Such difference is likely explained by the milder homogenization procedure employed in the screening 2 compared to the screening 1 (vortex at 2200 rpm vs Ultra Turrax 11200 rpm), and a more protective role of the higher PLGA concentration and of the surfactant in the primary water phase used in the screening 2.

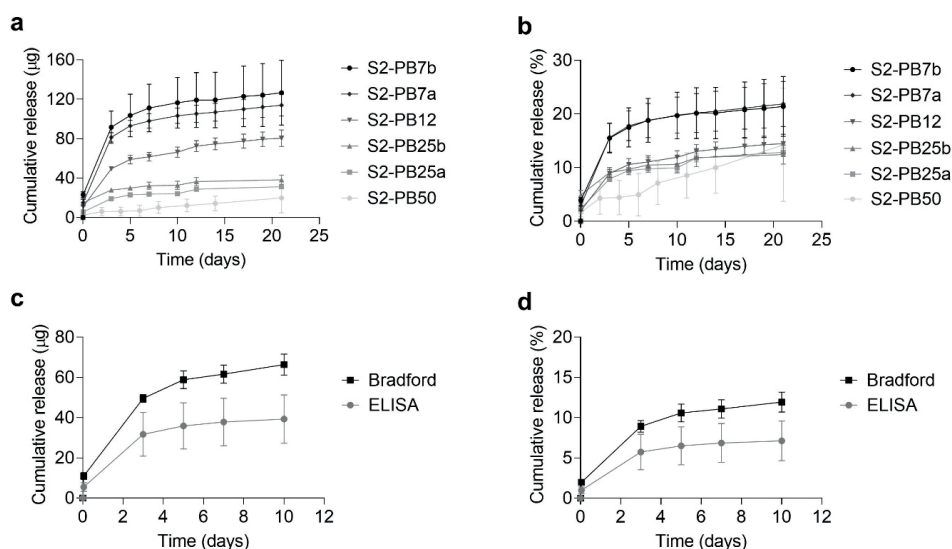


**Figure 2: BVZ release profiles of the formulations prepared in formulation screening 2.** BVZ cumulative release of all formulations in a)  $\mu\text{g}$  and b) % as a function of time. BVZ release profiles according to the Bradford assay and ELISA of the formulation S2-PB12. Cumulative release in c)  $\mu\text{g}$  and d) % as a function of time. In the abbreviations, S2 indicates formulation screening 2 and PB indicates the PLGA/BVZ ratio (**Table 2**).

## Morphology of BVZ-loaded microparticles

The formulations S1-PL150 and S2-PB7b, selected for the *in vitro* cellular studies, were also visualized by FESEM. The BVZ-loaded microparticles of the formulation S1-PL150 had a diameter of about 1  $\mu\text{m}$  and presented a rougher surface and a less spherical shape than the blank microparticles prepared using the same method (**Figure 3a, b**). This result indicates that the presence of BVZ affects the particle morphology, likely due to a partial BVZ/PLGA phase separation during solvent evaporation which causes dimples on the

surface.<sup>[508,540]</sup> The appearance of the BVZ-loaded microparticles after 21 days of release study was very similar to the one of the microparticles at day 0 (**Figure 3c**), which indicates that no visible particle degradation has occurred during that time frame.

BVZ-loaded microparticles from the formulation S2-PB7b had an average diameter of 40  $\mu\text{m}$ , a spherical shape, and a rough and highly porous surface (**Figure 3d, e**). We hypothesize that this high porosity is due to the lower PLGA/BVZ ratio and higher content of Tween<sup>®</sup> 80 used in this formulation compared to the other formulations prepared in the formulation screening 2. In line with this, BVZ-loaded microparticles of the formulation S2-PB50, which had the highest PLGA/BVZ ratio and the lowest amount of Tween<sup>®</sup> 80, showed a non-porous surface (**Figure 3f**). The observed particle porosity further supports the higher burst release of BVZ from S2-PB7b compared to S2-PB50.

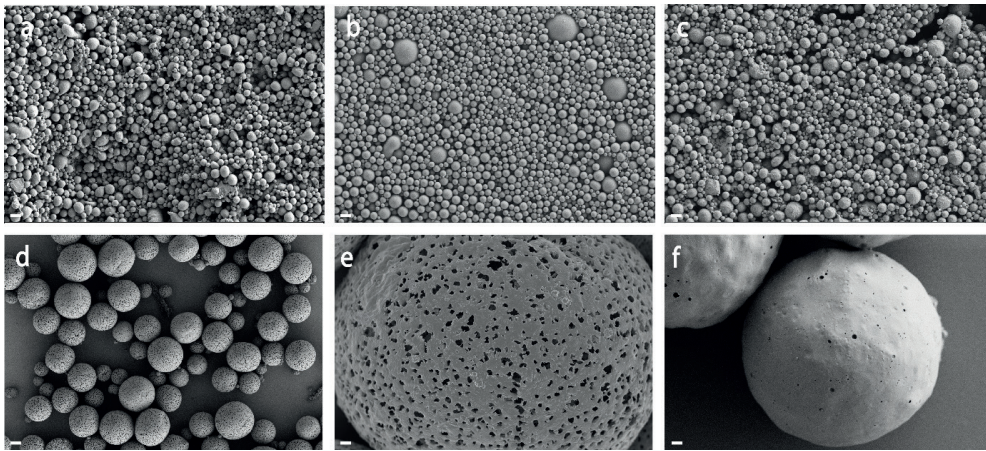


**Figure 3: FESEM images of microparticles.** Formulation S1-PL150 (a-c). a) BVZ-loaded microparticles at day 0, b) blank microparticles at day 0, c) BVZ-loaded microparticles at day 21. BVZ-loaded microparticles of the formulation S2-PB7b at day 0 (d-e). f) BVZ-loaded microparticles of the formulation S2-PB50 at day 0. Scale bar = 2  $\mu\text{m}$  for all photographs, except for the photograph d whose scale bar = 20  $\mu\text{m}$ .

### *In vitro* cellular activity

In order to determine the bioactivity of the microencapsulated BVZ, the anti-angiogenic activity of the two selected microparticle formulations (namely, S1-PL150 and S2-PB7b) was tested on GFP-labelled human umbilical vascular endothelial cells (GFP-HUVECs) and human bone marrow-derived mesenchymal stromal cells (hbMSC)-laden fibrin gels (**Figure 4a**). This cellular co-culture has previously been shown to elicit HUVEC-driven network formation.<sup>[127,336]</sup> This process is aided by the presence of hbMSCs that differentiate into pericytes and provide support to the forming capillary networks.<sup>[248,336]</sup> Fibrin gel was selected as a cell carrier due to the high reproducibility of its properties and the simple casting procedure that facilitates high-throughput studies. Moreover, fibrin gels have

previously shown an ability to support endothelial proliferation, cell attachment and migration, leading to the formation of capillary-like structures.<sup>[336,541–543]</sup> As opposed to 2D cell culture models, cell encapsulation in a 3D matrix can provide a more physiologically relevant environment that is more permissive for angiogenesis to occur.<sup>[541]</sup>

Firstly, we identified the active dose range of BVZ (10–100  $\mu\text{g mL}^{-1}$ ) at which anti-angiogenic effects were initially observed within the cell-laden fibrin droplets (**Supplementary Figure S6**). From there, and considering the BVZ release profile of the selected formulations, we deduced that an amount of 10 mg of microparticles/well would be appropriate to study the anti-angiogenic capacity of our two selected formulations, as well as their effect on cell metabolism over a 7 day culture (**Figure 4**). The fluorescent images and corresponding software-based output images representing the vessels and junctions present in the fibrin gel show a clear recession of the HUVEC network in the presence of soluble BVZ (positive control) or BVZ-loaded microparticles compared to the BVZ-free controls consisting of blank microparticles and fibrin only (**Figure 4b**).

The quantitative analysis of these images further supports this observation as it shows a statistically significant decrease in the average vessel area (approximately a 1.3-fold decrease, **Figure 4c**), average vessel length (approximately a 2-fold decrease, **Figure 4d**) and total number of cellular junctions (approximately a 2-fold decrease, **Figure 4e**), when comparing the results obtained with BVZ versus the BVZ-free controls. Furthermore, the anti-angiogenic effect observed for both microparticle formulations confirms that a significant percentage of the released BVZ retains its activity. In fact, the effect of soluble BVZ that is supplemented to the medium with each media change (a cumulative amount of 80  $\mu\text{g}$  BVZ throughout the culture period) does not show any significant variation compared to both BVZ-loaded microparticle formulations tested (expected cumulative release of active BVZ  $\leq 100 \mu\text{g}$ ) in either of the aforementioned vessel analysis outputs. This result is in line with previous research that showed the anti-angiogenic effect of released BVZ from different micro/nanoparticle studies.<sup>[514,533,543]</sup> These observations suggest that the gradual and sustained release of BVZ from microparticles is an effective strategy to achieve a controlled anti-angiogenic effect.

Importantly, despite the significant anti-angiogenic effect elicited by the introduction of BVZ in the co-culture system, neither the concentration, nor the way of BVZ supplementation (soluble BVZ supplemented to the media or BVZ released from microparticles) appeared to have a toxic effect on the established co-culture. Indeed, a constant metabolic activity (with values of fluorescence ranging from 8.8 to 10.4) was observed for all experimental conditions throughout the 7-day experiment (**Figure 4f**). This observation is also in line with a previous study that employed similar BVZ concentrations (0.1 - 10,000  $\mu\text{g mL}^{-1}$ ) and showed no detrimental effect on HUVEC cell viability in the BVZ-concentration range used throughout the present study.<sup>[514]</sup>

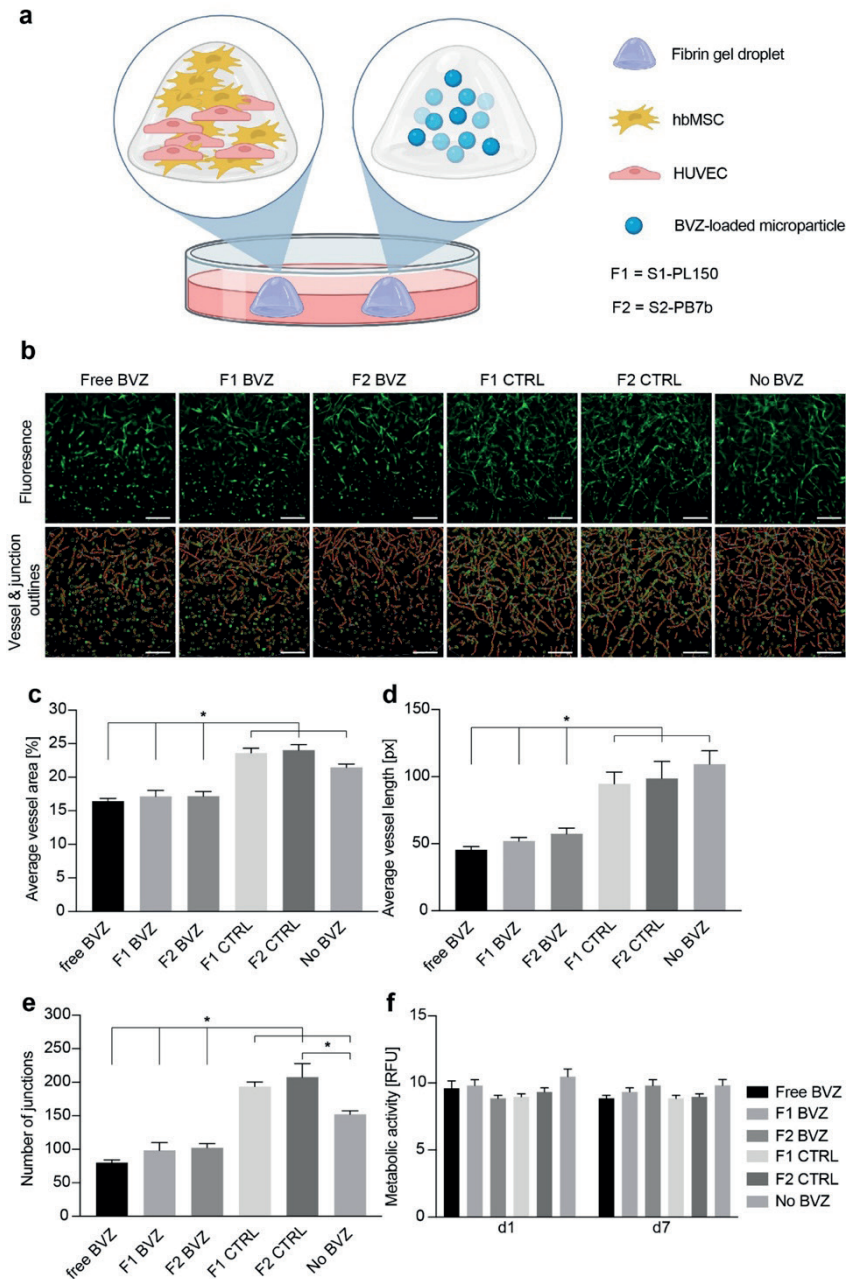


**Figure 4: Anti-angiogenic effect of BVZ-loaded microparticles on GFP-HUVECs and hbMSCs 3D co-culture model.** a) Scheme of the *in vitro* model based on fibrin gel droplets loaded with GFP-HUVECs, hbMSCs and BVZ microparticles. b) Fluorescent images of the vascular networks formed by the GFP-HUVECs within the fibrin gels after 7 days in culture in the presence of free BVZ (cumulative amount of  $80 \mu\text{g mL}^{-1}$ ), two formulations of BVZ-loaded and blank microparticles (10 mg of microparticles/well), as well as BVZ-free controls (top panel).

The AngioTool output diagrams showing the vessel outlines (red) and the cellular junctions (blue), scale bars = 250  $\mu\text{m}$  (bottom panel). c) Average vessel area, d) average vessel length and e) number of junctions of vascular networks formed in the casted fibrin gels as calculated through the AngioTool software ( $n = 4-6$ ) \* = significant difference ( $p < 0.05$ ). f) Metabolic activity of the 3D co-culture over a 7-day period, under the same experimental conditions ( $n = 4 - 6$ ) \* = significant difference ( $p < 0.05$ ) (f). For simplicity, the two tested formulations S1-PL150 and S2-PB7b are referred to as F1 and F2, respectively.

### 3D printing of medical grade collagen biofunctionalized with BVZ-loaded microparticles

The cellular studies reported above showed a statistically comparable activity of the formulations S1-PL150 and S2-PB7b. Following this observation, the formulation S1-PL150 was used for further 3D printing studies for two technical reasons. Firstly, microparticles of the formulation S1-PL150 are more versatile for 3D printing applications because they have a smaller diameter than those of the formulation S2-PB7b (approx. 1  $\mu\text{m}$  vs 40  $\mu\text{m}$ ). Secondly, formulation S1-PL150 has a faster preparation protocol and easier handling.

To assess the 3D printability of the microparticle-loaded collagen ink, a filament collapse test and a filament fusion test were performed.<sup>[306]</sup> In these tests, the filaments of the microparticle-loaded collagen ink were compared to those of the blank collagen ink (control). No filament collapse was observed after printing and over time for any of the two inks (*i.e.*, with and without microparticles, **Figure 5a, b**), suggesting that the presence of BVZ-loaded microparticles at a concentration of 4.0 % (w/w) did not affect the 3D printability of the collagen ink. The fact that no filament collapse was observed even at the highest gap distance of 1.6 cm, suggests that, if needed, an increase of particle concentration up to a certain extent could be implemented without expecting any detrimental effect on the 3D printability. This would allow, for example, an increase in the dose of BVZ/scaffold, if required by the specific application, animal model and implantation site in future studies. Results from the filament fusion test showed that for the two inks, there was a similar relationship between the infill increase and the filament gap closure (**Figure 5c**). Furthermore, an increase in the infill density (input parameter controlled by the used software) from 50 to 90% resulted in a decrease of the line spacing in the printed pattern, and a clear filament fusion was observed only when using the highest infill value of 90%. For this reason, to ensure an adequate porosity, an infill value of 70% was considered the most appropriate for subsequent experiments where grid like structures were fabricated (**Figure 5d**).

The SEM imaging on cross-sections of 3D printed, chemically cross-linked collagen scaffolds containing BVZ-loaded PLGA microparticles showed a uniform distribution of the spherical microparticles in the scaffold (**Figure 5e, f**). SEM images of cross-sections of blank 3D printed, chemically cross-linked collagen scaffolds (controls) are shown in the Supporting Information (**Supplementary Figure S7**).

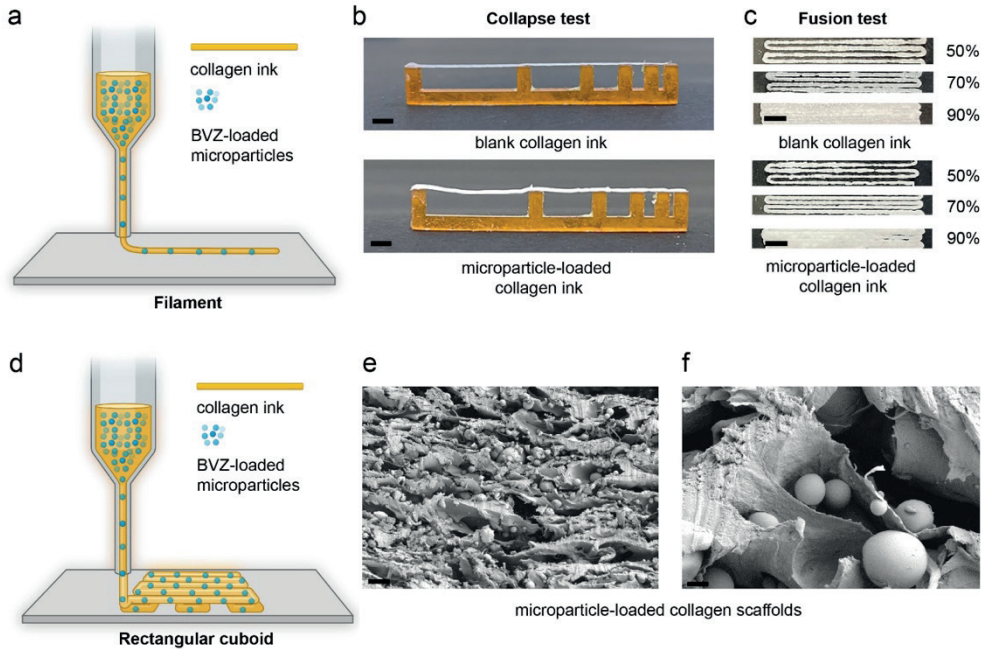


**Figure 5: 3D printing of microparticle-loaded collagen ink and collagen scaffolds.** a) 3D printing of a single filament of the microparticle-loaded collagen ink and blank collagen ink (control) in b) a filament collapse test (scale bar = 4 mm) and c) a filament fusion test (scale bar = 4 mm). Results for the filament fusion test are shown for three different infill values, *i.e.*, 50, 70 and 90%. d) 3D printing of multi-layer rectangular cuboids for the fabrication of microparticle-loaded collagen scaffolds. e, f) Cross-sections of microparticle-loaded collagen scaffolds after chemical cross-linking and freeze-drying, as visualized by SEM (e, scale bar = 20  $\mu\text{m}$  and f, scale bar = 2  $\mu\text{m}$ ).

To assess the 3D printability of the microparticle-loaded collagen ink toward the generation of clinically relevant shapes, we fabricated meniscus-like structures with the typical C-shape and a wedge-like vertical cross-section, as well as human nose- and auricle-like structures based on generic models (**Figure 6a - c**). All 3D printed structures preserved high shape fidelity and were stable over time in PBS, without being chemically cross-linked. Importantly, these structures were 3D printed without a supporting thermoplastic frame or a sacrificial material. The bottom-up fabrication was obtained by the progressive small increments of subsequent layers without intermediate steps of chemical cross-linking. Remarkably, with this procedure both nasal and auricle cavities remained hollow highlighting the printing stability of the microparticle-loaded collagen ink.

The successful 3D printing of these complex structures demonstrated that the applicability of the ink under study could be potentially extended to different tissues for a broad application in tissue engineering. These findings are a valuable effort toward addressing the constant clinical need for personalized medicine in tissue engineering which requires 3D (bio-)printable materials for the fabrication of high-resolution, patient-specific scaffolds.

In the last decade, the use of 3D printed collagen inks has been widely reported for tissue engineering application, *i.e.*, for cartilage and bone regeneration.<sup>[522,544,545]</sup> Usually, collagen is used alone or blended with other materials to obtain synergetic effects on mechanical and biochemical properties. However, most of these studies cover the 3D printing of simple 3D structures, usually rectangular cuboids, or cylinders. Only a few recent papers demonstrated the possibility to print more complex, hollow structures using collagen-based inks, without supporting materials.<sup>[521,524,546]</sup> It is important to mention that these studies do not include the ink biofunctionalization through drug-loaded delivery systems, *i.e.*, nano- or microparticles which can be a valuable tool for the final *in vivo* performance of the implant. On the other hand, studies that focus on the 3D printing of collagen inks functionalized with nano- and micro-sized drug delivery systems are limited to bone regeneration only and do not consider the possibility of fabricating complex, hollow structures.<sup>[547-549]</sup> In conclusion, our overview of the data reported in the literature to date confirms the novelty of the work described herein, consisting of a combination of an anti-angiogenic drug delivery system with a medical grade collagen ink for the 3D printing of complex, hollow structures without supporting materials. Future studies will investigate the release kinetics of BVZ from microparticle-loaded collagen scaffolds. In this context, we can hypothesize that the highly porous structure of the collagen scaffold and its interconnected pores are expected to allow the diffusion of the BVZ released from the microparticles *in vitro*. In an *in vivo* setting, when the scaffold is locally implanted, BVZ release kinetics may be affected by additional factors, such as the scaffold infiltration by endogenous components *i.e.*, plasma and cells, and the formation of a fibrin clot. Remarkably, the studied biomaterial is made of FDA-approved and clinically used components, *i.e.*, Avastin<sup>®</sup> (bevacizumab), medical grade collagen from Geistlich Pharma AG and PLGA. This will potentially accelerate the next steps of investigations toward the clinical translation of the proposed biomaterial.



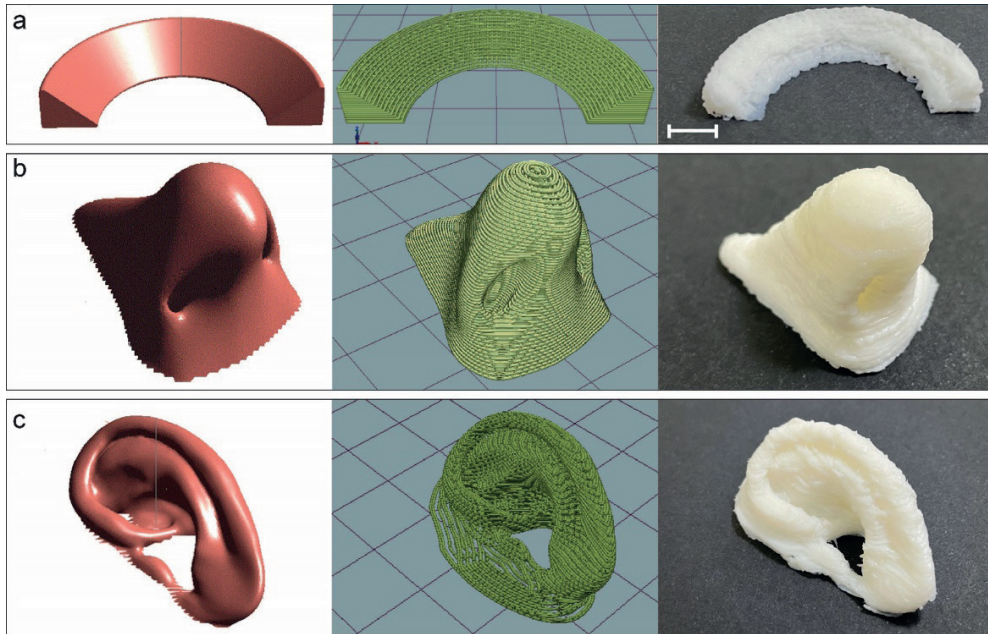


**Figure 6: 3D printing of biomimicking complex structures.** Structures resembling the human a) meniscus, b) nose and c) auricle, obtained by a multi-layer deposition of BVZ microparticle-loaded collagen ink through a “Rokit Invivo 4D2” bioprinter. 3D models based on the STL file (red, left), 3D models showing the printing pattern based on the GCode (green, center), and 3D printed structures (white, right) are shown. Scale bar = 1 cm.

## CONCLUSIONS

In this study, we achieved the biofunctionalization of a 3D printed, medical grade collagen with BVZ-loaded microparticles to target pathological angiogenesis, as that found in the articular cartilage and meniscus of OA patients. Our findings are of relevance considering the growing interest in the biofunctionalization of tissue engineering constructs by the inclusion of growth factors and other biomolecules. Since these signalling molecules require a molecule-specific spatiotemporal delivery, the combination of 3D printing (spatial control) and drug delivery strategies (temporal control), as explored in this study, is an essential tool for the development of novel tissue constructs with high performance. Likewise, we are currently investigating a similar approach to distribute microparticles loaded with different active factors (pro-angiogenic vs anti-angiogenic) throughout meniscus scaffolds to mimic its outer-inner gradient.

## EXPERIMENTAL SECTION

*Materials:* Ester-terminated PLGA (capped PLGA) Resomer® RG 502 25G (D,L-Lactide:Glycolide ratio = 50 : 50,  $M_n = 6880$  Da,  $M_w = 14700$  Da) and Resomer® RG 503 25G (D,L-Lactide:Glycolide ratio = 50 : 50,  $M_n = 12100$  Da,  $M_w = 35800$  Da) were supplied by Evonik. Polyvinyl alcohol (PVA) was purchased by Nippon Gohsei, whereas poloxamer 184 (Pluronic® L64) and kolliphor® HS 15 were supplied by BASF. Dichloromethane (DCM), dimethylsulphoxide (DMSO) and sodium azide were purchased by Scharlau, whereas phosphate-buffer saline (PBS) was purchased from Fischer Scientific. The anti-angiogenic BVZ (Avastin®) was kindly donated by mAbxience-GH Genhelix. Recombinant human VEGF 165 was supplied by Peprotech, goat anti-human IgG horseradish peroxidase (HRP)-conjugated by Jackson ImmunoResearch and sodium hyaluronate (molecular weight = 290 kDa) by Bloomage Biotech. Tween® 80 and Tween® 20 were purchased from Merck, and 2,2'-azino-di-(3-ethylbenzthiazoline sulfonic acid) (ABTS) from Roche. Green fluorescent protein-expressing human umbilical vein endothelial cells (GFP-HUVECs) were supplied by Angio-Proteomie (USA). Endothelial Growth Medium-2 (EGM-2) and Endothelial Basal Medium-2 + SingleQuots were purchased from Lonza (The Netherlands), whereas Dulbecco Modified Eagle Medium (DMEM) + GlutaMAX (31966), fetal bovine serum (FBS, 10% v/v, 10270), penicillin/streptomycin (p/s 1%) and N-2-hydroxyethylpiperazine-N-2-ethane sulfonic acid (HEPES, 15630080) from Gibco (The Netherlands). Fibrinogen (F8630) and thrombin (T4648) were supplied by Sigma-Aldrich, bovine serum albumin by Roche, resazurin sodium salt by Alfa Aesar (Germany). Porcine, decellularized medical-grade collagen composed of collagen type I, type III and elastin, and purified as described in the patent Bio-Gide (EP1676592) was donated by Geistlich Pharma AG (Wolhusen, Switzerland). All other chemicals were supplied by Sigma-Aldrich.

*Experimental design:* Firstly, a formulation study was carried out to identify the parameters that allow the fabrication of BVZ-loaded microparticles with high encapsulation efficiency (EE) and with a BVZ sustained release over the first 21 days. Secondly, two selected formulations were tested *in vitro* in a 3D vascularization model to study the anti-angiogenic activity of released BVZ and its effect on cellular metabolic activity. Thirdly, we studied the effect of microparticles on the 3D printability of a medical grade collagen ink and evaluated the feasibility of fabricating complex structures.

*Preparation of BVZ-loaded microparticles:* Microparticles composed of capped PLGA were prepared according to the water-in-oil-in-water double emulsion-solvent evaporation method as previously reported,<sup>[550]</sup> with some modifications. The detailed protocol used in the formulation screenings 1 and 2 is reported in Supporting Information. The formulation parameters used as variables are reported in **Tables 1 and 2**. The encapsulation efficiency (EE), defined as the percentage of entrapped protein versus total protein, was calculated using either a direct method or an indirect method, as reported in Supporting Information.

*In vitro release study:* Microparticles were dispersed in PBS (5 mg mL<sup>-1</sup>) enriched with sodium azide and Tween® 20 (further referred to as release medium) and incubated at 37° C under mild agitation. At predefined time intervals, microparticles were centrifuged at 4° C for 30 minutes using a speed of 10000 g (Centrifuge 5430R Eppendorf, formulation screening 1) or precipitated by sedimentation (formulation screening 2). Supernatants were taken and analysed for protein quantification. The pellets were resuspended in fresh release medium and incubated as explained above. The released BVZ at each time point was quantified by a Bradford protein assay according to the manufacturer's protocol. Calibration curves were obtained using freshly prepared solutions of BVZ in the release medium, and by reading the absorbance at 595 and 466 nm by a Synergy H1 Hybrid Multi-Mode Reader (BioTeck). The ratio between the 2 absorbance values was used to build the calibration curve and to calculate BVZ concentration in the samples. For selected formulations, the released BVZ at different time points was also quantified by an enzyme-linked immunosorbent assay (ELISA), according to a protocol reported in the Supporting Information.

*Particle size and morphology:* Microparticles were visualized by using an Olympus IX51 optical microscope, equipped with an Olympus DP72 camera. The samples were prepared by placing 10 µL of a particle suspension (5 mg mL<sup>-1</sup>) on a microscope slide and covered by a coverslip. The average particle diameter was determined by measuring the circumference of at least 70 microparticles, with an Olympus cellSens standard 1.16 software according to a 3-point circle identification method. Microparticle morphology of selected formulations was studied using Field Emission Scanning Electron Microscopy (FESEM). To this end, a volume of 25 µL of a microparticle suspension (5 mg mL<sup>-1</sup>) was deposited on a silicon wafer previously attached on top of a carbon-taped aluminium stub. Microspheres were air-dried overnight and then sputter-coated with a 5-nm coating of Iridium. Finally, microparticles were visualized using a FESEM microscope (Ultra plus FESEM, ZEISS), in a regime of high void.

*Cell isolation and culture:* GFP-HUVECs were used in co-culture with human bone marrow-derived mesenchymal stromal cells (hbMSCs) to evaluate the anti-angiogenic effect of selected formulations of BVZ-loaded microparticles. hbMSCs were isolated from bone marrow aspirates obtained from consenting patients as previously described.<sup>[248]</sup> The procedures to isolate human tissue and cells were approved by the research ethics committee of the University Medical Center Utrecht. GFP-HUVECs were cultured in EGM-2 medium containing Endothelial Basal Medium-2 + SingleQuots, 100 U mL<sup>-1</sup>-100 µg mL<sup>-1</sup> PenStrep, and 10% heat-inactivated FBS. HbMSCs were cultured in DMEM + GlutaMAX supplemented with FBS (10% v/v) and p/s 1%. All cells were cultured at 37° C and 5% CO<sub>2</sub>.

*Casting of GFP-HUVECs and hbMSC-laden fibrin gels:* GFP-HUVECs and hbMSCs co-cultures were embedded in 3D fibrin gel droplets consisting of 6.6 mg mL<sup>-1</sup> of fibrinogen and 2 U mL<sup>-1</sup> of thrombin. GFP-HUVECs were encapsulated at a density of 2.5 x 10<sup>6</sup> cells mL<sup>-1</sup> of gel

and hbMSCs were encapsulated at a density of  $5 \times 10^6$  cells  $\text{mL}^{-1}$  of gel. To this end, the cell pellet was suspended in fibrinogen dissolved in saline supplemented with 1% w/v bovine serum albumin and 10 mM HEPES. The cell-laden fibrinogen solution was then mixed with thrombin dissolved in DMEM supplemented with p/s. Fibrin gel droplets of a volume of 20  $\mu\text{L}$  were casted directly on the surface of a culture plate and incubated for 20 minutes at 37° C to allow complete gelation. The droplets were cultured in EGM-2 medium for 7 days in the presence of fibrin-encapsulated blank or BVZ-loaded microparticles (10 mg of microparticles/60  $\mu\text{L}$  of fibrin gel) or BVZ-supplemented medium (10  $\mu\text{g mL}^{-1}$ ) (**Figure 4a**). Medium was refreshed every 2 days. Two formulations of BVZ-loaded microparticles were tested, namely S1-PL150 and S2-PB7b, that were selected from the formulation screenings 1 and 2, respectively.

*Evaluation of cell metabolism and anti-angiogenic activity:* Metabolic activity of cell-laden droplets cultured in the presence of free BVZ, BVZ-loaded, and blank microparticles was assessed through a resazurin assay after 1 and 7 days in culture ( $n = 4 - 6$ ). Cell-laden droplets cultured in the presence of free BVZ, BVZ-loaded, and blank microparticles were evaluated for their angiogenic capacity after 7 days in culture ( $n = 4 - 6$ ). Samples were fixed in 4% v/v neutral buffered formalin, and fluorescent images of the GFP-HUVEC networks were acquired using a Thunder imaging system (Leica Microsystems, Germany). The vessel area coverage, average vessel length and junction number were calculated using the vessel analysis software AngioTool.<sup>[551]</sup>

*Preparation of the blank and microparticle-loaded collagen ink:* A blank collagen ink was prepared by dissolving medical-grade collagen in PBS at 12.5 % w/w. The mixture was manually stirred with a spatula and the pH was lowered to 3.5 using ortho-phosphoric acid 85% to yield a smooth slurry. The slurry was further homogenized using a static mixer and finally centrifuged to remove air bubbles. For the preparation of the microparticle-loaded collagen ink, BVZ-loaded microparticles of a selected formulation, namely S1-PL150, were dispersed in the exact weight of PBS to obtain a final particle concentration of 4% w/w referred to the total slurry. The particle suspension was gently mixed for 10 seconds, added to the collagen powder, and further homogenized as explained above for the blank collagen ink. Before 3D printing, the ink was heated up to 30° C for at least 10 min.

*Assessment of 3D printability:* The 3D printability of the microparticle-loaded collagen ink was compared to that of the blank collagen ink in a filament collapse and a filament fusion test.<sup>[306]</sup> For the filament collapse test, a platform with pillars ( $l \times w \times h = 2.0 \times 2.0 \times 4.0$  mm<sup>3</sup>) placed at known gap distances (1.0, 2.0, 4.0, 8.0, and 16.0 mm) was fabricated using a Perfactory Mini digital light projection 3D printer (Envisiontec, Germany) as previously reported<sup>[306]</sup>. Over these gaps, a single gel filament was deposited using a Rokit Invivo 4D2 bioprinter (Rokit Healthcare Inc., South Korea) equipped with a syringe dispenser and a

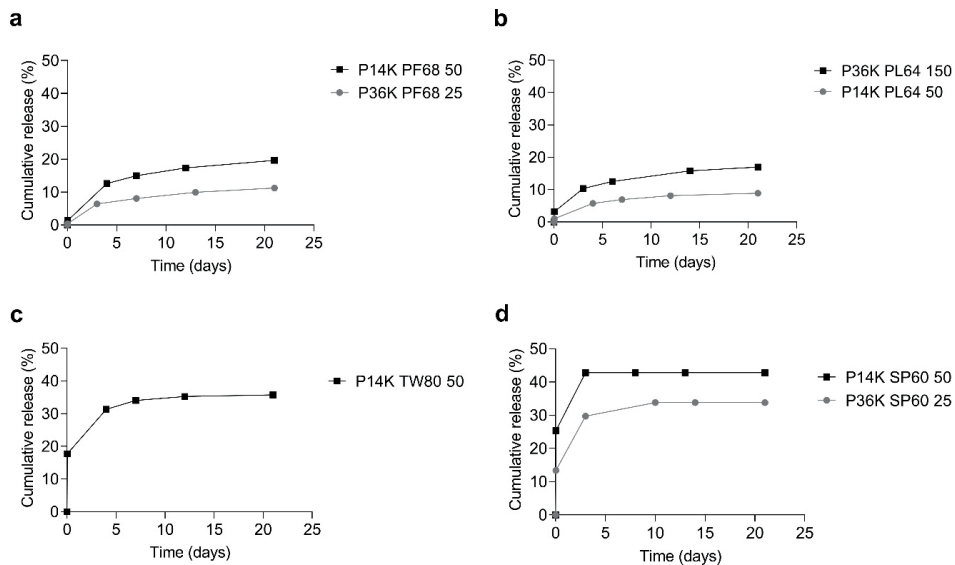
1.80 firmware. To this aim, the blank or the microparticle-loaded collagen ink was loaded into a Luer-Lock glass syringe (10 mL) with an inner diameter of 15.5 mm and extruded using a 0.61 mm needle (GA 20), a deposition speed of 4 mm/s, a layer thickness of 0.4 mm and a printing temperature of 25° C. In the filament fusion test, three different patterns were used, each one corresponding to a specific infill of 50, 70 and 90%. From the GCode analysis, it was found that the filament distances for the proposed infill of 50, 70 and 90% were 0.60, 0.27 and 0.06 mm, respectively. To perform the fusion test of the blank and the microparticle-loaded collagen ink, the same printing parameters of the filament collapse test were employed. Top-down pictures were obtained using a Nikon digital camera directly after printing, as no apparent deformation was observed at this time point.

*Microparticle distribution and 3D printing of anatomically shaped structures:* To analyze the microparticle distribution throughout the 3D printed collagen scaffolds, rectangular cuboids (13 x 13 x 5 mm) with an infill of 70% were fabricated using a Rokit Invivo 4D2 bioprinter. To this end, either the microparticle-loaded ink, or the blank collagen ink (as control), was loaded into a Luer-Lock glass syringe and 3D printed using the printing parameters reported in section 2.10. The input print pattern was sliced using a NewCreatorK 1.57.70 software. To preserve structural stability, the obtained samples were immersed in an aqueous solution of NaCl (100 mg mL<sup>-1</sup>) for 1 h, washed three times in PBS for 2 h, and pH-adjusted to 7.4. Subsequently, samples were freeze-dried and chemically crosslinked with 1-Ethyl-3-(3-dimethylaminopropyl)carbodiimide (EDC) and *N*-hydroxysuccinimide (NHS) as described in the patent US2016166737A1. After cross-linking, washing steps in phosphate buffer at elevated pH and subsequent flushing steps were applied. Importantly, these steps allow the full inactivation of EDC and NHS, and permit to wash out remaining degradation products. Finally, samples were freeze-dried, conditioned at 22° C and at 55% of relative humidity for 2 h, and sterilized by the company STERIS (Däniken, Switzerland) using X-ray irradiation at 22-33 kGy. Slices (thickness = 1 mm) of freeze-dried samples were fixed on top of a carbon-taped aluminium stub, sputter-coated with a 5 nm coating of Iridium and visualized by a FESEM, as reported in section 2.5 for the visualization of microparticles. Finally, to show the feasibility of a clinically relevant printing process, complex anatomically shaped structures resembling the human meniscus, nose and auricle were printed based on generic models with a 70% infill.

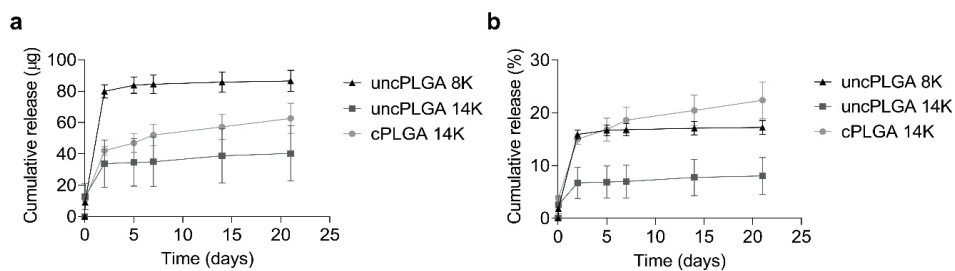
*Statistics:* Results were reported as mean ± standard error of the mean (S.E.M.). Statistical analysis of vessel network characterization and cellular metabolic activity was performed using GraphPad Prism 9.0 (GraphPad Software, USA). Comparisons between experimental groups were assessed via one- (vessel network characterization) or two-way (metabolic activity) ANOVAs, followed by post hoc Bonferroni correction to test differences between groups. Normality was checked with a Shapiro-Wilk test. Differences were found to be significant when  $p < 0.05$ .

## SUPPORTING INFORMATION

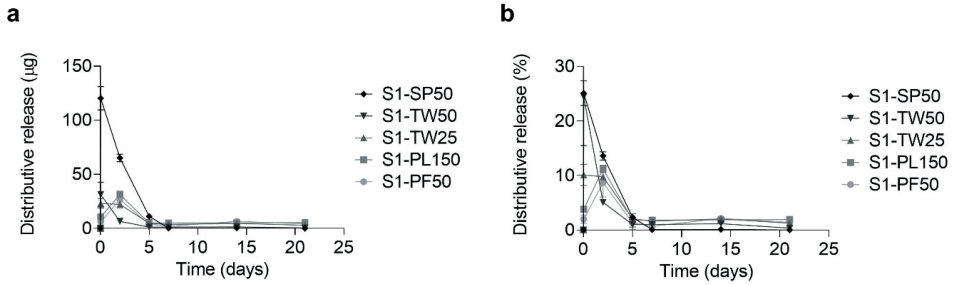
### Supplementary Figures



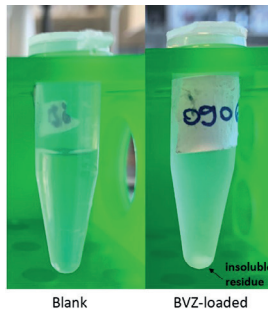
**Supplementary Figure S1:** BVZ release profiles of 7 formulations of the exploratory screening, selected based on the values of encapsulation efficiency (EE). Data are reported according to the Bradford assay.



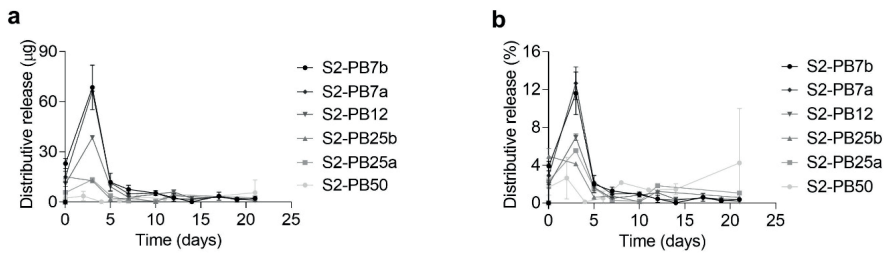
**Supplementary Figure S2:** BVZ release profiles of the formulations prepared to study the effect of the capping group (composition reported in Table S2). a) Cumulative release (µg) of BVZ over time, and b) cumulative release (%) of BVZ over time. Data according to the Bradford assay.



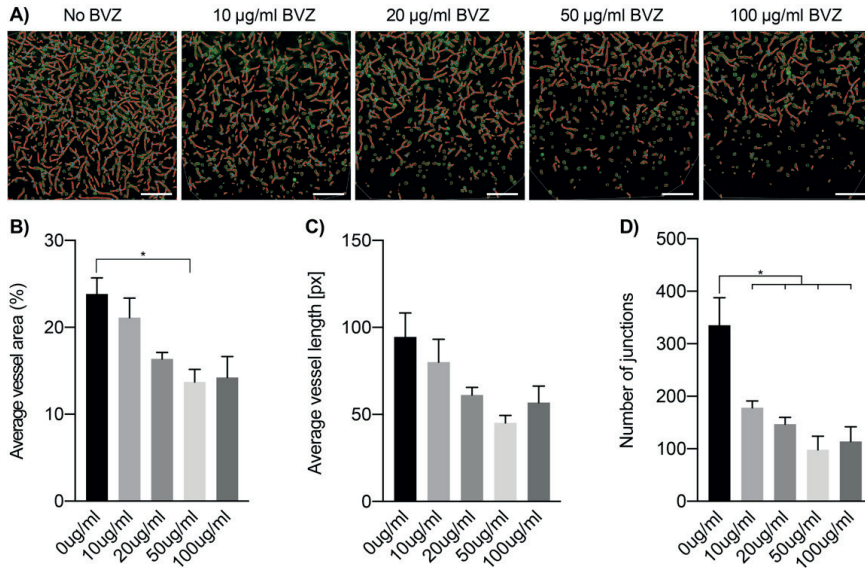
**Supplementary Figure S3:** BVZ release profiles according to the Bradford assay of the formulations prepared in the formulation screening 1 (composition reported in **Table 1**). a) Distributive release ( $\mu\text{g}$ ) of BVZ over time, and b) distributive release (%) of BVZ over time.



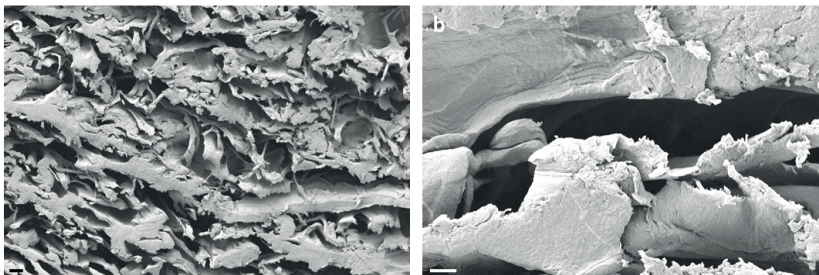
**Supplementary Figure S4:** Formulations made with uncapped PLGA with a molecular weight of 2 kDa after 21 days of incubation. In the blank formulation (left), microparticles are visually completely degraded and solubilized, whereas the BVZ-loaded formulation (right) showed the presence of an insoluble residue.



**Supplementary Figure S5:** BVZ release profiles according to the Bradford assay of the formulations prepared in the formulation screening 2 (composition reported in **Table 2**). a) Distributive release ( $\mu\text{g}$ ) of BVZ over time, and b) distributive release (%) of BVZ over time.



**Supplementary Figure S6:** Identification of the active dose range of BVZ in the *in vitro* model based on a co-culture of HUVECs and hbMSC. a) Angiotool vessel formation analysis after a 7 day culture of HUVECs-hbMSCs laden fibrin gels supplemented with increasing concentrations of free BVZ (0–100  $\mu\text{g mL}^{-1}$ ) (scale bars = 250  $\mu\text{m}$ ). b) Average vessel area, c) average vessel length and d) number of junctions of vascular networks formed in these co-cultures (n = 3). \* = significant difference ( $p < 0.05$ ).



**Supplementary Figure S7:** Cross-sections of blank collagen scaffolds after chemical cross-linking and freeze-drying, as visualized by SEM (a, scale bar = 10  $\mu\text{m}$  and b, scale bar = 2  $\mu\text{m}$ ).



## Supplementary Tables

**Supplementary Table S1:** Composition and encapsulation efficiency (EE) of the formulations tested in the exploratory screening, preliminary to the formulation screening 1. Surfactants with different hydrophilic-lipophilic balance (HLB) and chemical structure were dissolved in the organic phase at different concentrations (25–150 mg mL<sup>-1</sup>) to fabricate microparticles made of capped PLGA of two different molecular weights (36 and 14 kDa). Bevacizumab (BVZ) concentration in the primary water phase was 28.9 mg mL<sup>-1</sup> (0.2 mL) and PLGA concentration in the organic phase was 50 mg mL<sup>-1</sup> (1 mL). Formulations highlighted in bold are those selected for further release studies.

PLGA	Surfactant	Surfactant (mg mL <sup>-1</sup> )	EE (%)	Abbreviation
36 kDa	Pluronic® F-68 (HLB=28.0)	<b>25</b>	<b>70</b>	<b>P36K PF68 25</b>
		50	57	P36K PF68 50
		150	22	P36K PF68 150
	Tween® 20 (HLB=16.7)	25	16	P36K TW20 25
		50	7	P36K TW20 50
	Pluronic® L-64 (HLB=15.0)	25	66	P36K PL64 25
		50	48	P36K PL64 50
		<b>150</b>	<b>82</b>	<b>P36K PL64 150</b>
	Span® 60 (HLB=4.3)	<b>25</b>	<b>88</b>	<b>P36K SP60 25</b>
		50	89	P36K SP60 50
14 kDa	Pluronic® F-68 (HLB=28.0)	<b>50</b>	<b>57</b>	<b>P14K PF68 50</b>
	Pluronic® L-64 (HLB=15.0)	<b>50</b>	<b>65</b>	<b>P14K PL64 50</b>
	Tween® 80 (HLB=15.0)	<b>50</b>	<b>31</b>	<b>P14K TW80 50</b>
		150	21	P14K TW80 150
	Span® 60 (HLB=4.3)	25	79	P14K SP60 25
		<b>50</b>	<b>90</b>	<b>P14K SP60 50</b>

**Supplementary Table S2:** Formulations prepared to study the effect of the PLGA capping group and molecular weight. The concentration of Bevacizumab (BVZ) in the primary water phase was 28.9 mg mL<sup>-1</sup> (0.2 mL), the concentration of PLGA in the organic phase was 50 mg mL<sup>-1</sup> (1 mL), and a single surfactant, *i.e.*, PL64 was used in a fixed concentration of 150 mg mL<sup>-1</sup> in the organic phase, for all formulations. EE indicates the encapsulation efficiency.

Abbreviation	PLGA capping group	PLGA MW	EE (%)
cPLGA 14K	capped	14	48 ± 3
uncPLGA 14K	uncapped	14	87 ± 4
uncPLGA 8K	uncapped	8	87 ± 2

## Supplementary Methods and Results

### Preparation of bevacizumab (BVZ)-loaded microparticles

For the fabrication of BVZ-loaded PLGA microparticles (formulation screenings 1 and 2), capped PLGA (*i.e.*, ester-terminated) was preferred over uncapped PLGA (*i.e.*, acid-terminated), since the free carboxyl group of the latter induces higher BVZ/PLGA interactions and an unsuitable BVZ release kinetics.

*Formulation screening 1:* Microparticles composed of PLGA (capped, 14 kDa) were prepared according to the water-in-oil-in-water double emulsion-solvent evaporation method as previously reported,<sup>[550]</sup> with some modifications. In detail, a primary water phase containing BVZ (200  $\mu\text{L}$ ) was emulsified into the organic phase (1 mL) containing PLGA dissolved in DCM (50 mg mL<sup>-1</sup>). The primary water phase consisted of BVZ dissolved in a buffer (28.9 mg mL<sup>-1</sup>) as obtained from the supplier, whereas the organic phase was a PLGA solution enriched with a surfactant (type and concentration of surfactants are reported in Table 1, main manuscript). The first emulsification step was carried out using a Digital Sonifier 450 (Branson) at 15% amplitude (approximately equivalent to 15 Watt) for 15 seconds, in presence of a cold-water bath. The obtained first emulsion was further emulsified into a secondary water phase containing poly (vinyl alcohol) (PVA, 5 mL, 10 mg mL<sup>-1</sup>), using an Ultra Turrax T25 Digital (IKA), equipped with a S 25 N – 10 G dispersing tool at 11,200 rpm for 30 seconds. The double emulsion was then transferred into a more diluted PVA solution (10 mL, 3 mg mL<sup>-1</sup>) and stirred for 2 h to allow solvent evaporation and solidification of the microparticles. Microparticles were washed with milliQ water and collected via centrifugation (Optima™ L-100 XP ultracentrifuge equipped with a fixed angle 45 Ti rotor, Beckman Coulter). To this aim, microparticles were spun down at 30000 g for 30 minutes at 4°C. After the removal of the supernatant, microparticles were dispersed in an appropriate medium for the *in vitro* release study (section 2.4, main manuscript.). Alternatively, microparticles were dispersed in milliQ water and freeze-dried prior to cellular *in vitro* studies or 3D printing studies. Blank microparticles were prepared according to the same protocol replacing the BVZ solution with PBS.

*Formulation screening 2:* Microparticles composed of PLGA (capped, 36 kDa) were prepared according to the water-in-oil-in-water double emulsion-solvent evaporation method as previously reported,<sup>[550]</sup> with some modifications. In detail, a primary water phase containing BVZ (100 or 200  $\mu\text{L}$ ) was emulsified into the organic phase (500  $\mu\text{L}$ ) containing PLGA dissolved in DCM (75, 125 or 250 mg mL<sup>-1</sup>). The primary water phase was a physical mixture of BVZ (25 mg mL<sup>-1</sup>) and Tween® 80 (58 or 116 mg mL<sup>-1</sup>) in phosphate buffer saline (PBS, pH 7.4, 25 mM), enriched with small amounts of sodium hyaluronate (0.5 mg mL<sup>-1</sup>) and Kolliphor® HS 15 (2.5 mg mL<sup>-1</sup>). This mixture was chosen since it has been previously found beneficial for antibody delivery when included in the formulation of

antibody-loaded nanocapsules developed in our group.<sup>[552]</sup> The organic phase was a plain PLGA solution in DCM. Different PLGA/BVZ ratios were obtained by varying the volume of the primary water phase and the concentration of PLGA in the organic phase, whereas different Tween® 80/PLGA ratios were obtained by varying the concentration of Tween® 80 in the primary water phase (Table 2, main manuscript). The first emulsification step was carried out using a Digital Sonifier 450 (Branson) at 15% amplitude (approximately equivalent to 15 Watt) for 15 s, in presence of a cold-water bath. The obtained first emulsion was further emulsified into a secondary water phase containing PVA (5 mL, 10 mg mL<sup>-1</sup>), using a vortex at 2200 rpm for 1 min. The double emulsion was then transferred into a more diluted PVA solution (33 mL, 3 mg mL<sup>-1</sup>) and stirred for 2 h to allow solvent evaporation and solidification of the microparticles. Microparticles were washed three times with milliQ water and collected via centrifugation (Centrifuge 5430R Eppendorf). After each washing step, microparticles were centrifuged for 5 minutes at 4°C using a speed of 2000 g for all formulations, except for the formulations S2-PB7a and S2-PB7b (Table 2, main manuscript) for which a speed of 5000 g was used. After the removal of the supernatant, microparticles were dispersed in milliQ water and freeze-dried prior release study, *in vitro* cellular studies, or 3D printing studies. Blank microparticles were prepared according to the same protocol replacing the BVZ solution with PBS.

### Encapsulation efficiency (EE) of BVZ-loaded microparticles

The EE is defined as the percentage of the entrapped protein out of the total protein, and it was calculated using a direct method (formulation screening 1) or an indirect method (formulation screening 2).

*Direct method:* Microparticles were completely hydrolysed under basic conditions, according to a previously described method by Sah et al.,<sup>[553]</sup> with some modifications. In detail, 500 µL of DMSO was added to 5 mg of microparticles and agitated by vortex until clear appearance. Then, the mixture was stirred under an orbital agitation at r.t. for 1h. Subsequently, 2.5 mL of NaOH 0.05M was added, homogenized by vortex, and left under magnetic stirring for 1 hour at r.t. Formulations containing the hydrophobic Span 60 did not result in clear solutions after the hydrolysis. Therefore, these formulations were centrifuged for 30 minutes, at 30000 g, at 4° C (Optima™ L-90K ultracentrifuge, Beckman Coulter) to yield a clear supernatant. Aliquots of the clear supernatants were appropriately diluted using a mixture of DMSO/NaOH 0.05M (1:5) as diluent and analysed by the Bradford protein assay (Bio-Rad Laboratories GmbH), according to the manufacturer's protocol. A solution of DMSO/NaOH 0.05M (1:5) was also used as diluent to obtain an 8-point calibration curve of BVZ. The absorbance reading was performed using a Synergy H1 Hybrid Multi-Mode Reader (BioTeck) set at 595 and 466 nm, and the ratio between the 2 absorbance values was used to build the calibration curve and to calculate the BVZ concentration in the samples.

*Indirect method:* The amount of BVZ lost in the supernatant during washing was quantified via the Bradford protein assay, and the entrapped BVZ was calculated by subtracting the lost BVZ from the total protein. To avoid the interference of the supernatant components in the protein assay, the supernatant derived from blank microparticles was used to appropriately dilute samples and to prepare BVZ solutions for the calibration curve. The Bradford protein assay was carried out according to the manufacturer's protocol. The absorbance reading was performed using a Synergy H1 Hybrid Multi-Mode Reader (BioTeck) set at 595 and 466 nm, and the ratio between the 2 absorbance values was used to build the calibration curve and to calculate the BVZ concentration in the samples.

### Enzyme-linked immunosorbent assay (ELISA)

A high protein-binding capacity polystyrene ELISA plate (ThermoFischer Scientific) was coated with 100  $\mu\text{L}$  of a VEGF (Recombinant Human VEGF165) solution at 0.05  $\mu\text{g mL}^{-1}$  in a coating buffer (1.59  $\text{mg mL}^{-1}$   $\text{Na}_2\text{CO}_3$ , 2.94  $\text{mg mL}^{-1}$   $\text{NaHCO}_3$ , and 0.50  $\text{mg mL}^{-1}$   $\text{NaN}_3$ , pH 9.6) and incubated overnight at 4 °C. After washing (with Tween® 20 in PBS 0.05% v/v), the plate was blocked with 300  $\mu\text{L}$  of a blocking solution (washing buffer supplemented with skimmed milk 2% w/v) per well for 2 h at 37° C under orbital stirring at 300 rpm. Subsequently, samples and standards were appropriately diluted in the release medium, dispensed after plate washing and incubated under orbital stirring at 300 rpm and 37 °C for one hour. After washing, 100  $\mu\text{L}$  of the secondary antibody solution (0.08  $\mu\text{g mL}^{-1}$  of goat anti-human IgG HRP-conjugated) was added to the plate and incubated for 1 h at 37 °C. After a final washing step, 50  $\mu\text{L}$  of substrate (2,2'-Azino-bis(3-ethylbenzthiazoline-6-sulfonic acid), ABTS) was added to each well and the absorbance at 405 nm was recorded during the following 30 minutes by using a Synergy H1 Hybrid Multi-Mode Reader (BioTeck). The standard curve was created by processing the data recovered after 30 minutes, using GraphPad Prism 9 to generate a 4-parameter logistic (4-PL) curve-fit.

## 8

### Exploratory screening of a single surfactant (preliminary to the formulation screening 1)

*Experimental design:* The aim of this exploratory screening was to identify the main trends of encapsulation efficiency (EE) and release profile as a function of the surfactant hydrophilic-lipophilic balance (HLB), chemical structure and concentration, when using two different molecular weights (36 and 14 kDa) of capped PLGA. To this aim, 16 formulations (n=1) were prepared by using 5 different surfactants varying in chemical structure and HLB, namely Pluronic® F-68 (HLB = 28.0), Tween® 20 (HLB = 16.7), Pluronic® L-64 (HLB = 15.0), Tween® 80 (HLB = 15.0), and Span® 60 (HLB = 4.7) (Table S1). Microparticles were prepared as described in section 1 of this document. The surfactant was dissolved in the organic phase together with PLGA at concentrations ranging between 25 and 150  $\text{mg mL}^{-1}$ , while keeping constant the concentration of BVZ (28.9  $\text{mg mL}^{-1}$ ) and that of PLGA (50  $\text{mg mL}^{-1}$ ).

*Effect of a single surfactant on the EE:* The values of EE obtained for all formulations are reported in **Supplementary Table S1**. Overall, the values of EE broadly ranged between 7% and 90% as a function of the surfactant chemical structure, HLB and concentration in the organic phase. For all water-soluble surfactants, *i.e.*, Pluronic® F-68, Tween® 20, Pluronic® L-64 and Tween® 80, the EE decreased by increasing the surfactant concentration, except for P36K-PL64 150, for which an exceptionally high EE (*i.e.*, 82%) was found when using the highest concentration of surfactant (150 mg mL<sup>-1</sup>). This trend can be likely explained by the fact that the use of a higher amount of surfactant causes its higher diffusion toward the external water phase, which may drive a higher premature leaching of BVZ. On the contrary, when using the lipophilic Span® 60, the high values of EE (79-90%) can be explained by the lack of surfactant diffusion and by its greater capacity of stabilizing water-in-oil-interfaces. A more detailed discussion about the effect of the surfactant HLB on the EE is reported in the manuscript. Comparing formulations made with the same type and concentration of surfactant and two different molecular weights of capped PLGA (14 and 36 kDa), it can be noted that the EE values were not significantly affected by the PLGA molecular weight, except in the cases where 50 mg/mL of Pluronic® L-64 or 25 mg mL<sup>-1</sup> of Span® 60 were used. In these two cases, the decrease of PLGA molecular weight caused an increase of EE when using Pluronic® L-64 and a decrease of EE when using Span® 60. For each surfactant and each PLGA molecular weight, the formulation with the highest value of EE was selected for further release studies (formulations highlighted in bold in **Supplementary Table S1**). In the cases where comparable values of EE were obtained, the formulation with the lowest concentration of surfactant was preferred. Formulations containing Tween®20 were excluded because of the very low values of EE (< 20%).

*Effect of a single surfactant on the release kinetics of BVZ:* The release profile of BVZ varied as a function of surfactant HLB, chemical structure and concentration in the organic phase (**Supplementary Figure S1**). Formulations made of poloxamers (Pluronic® F-68 and Pluronic® L-64) showed a release kinetics characterized by an initial burst release phase during the first 3 days followed by a slower release until day 21. Compared to other surfactants tested in this study, formulations made of poloxamers showed the lowest percentage of BVZ released at day 0 (0.4-3.2%) and the lowest total percentage of BVZ released until day 21 (8.9-19.6%). The amount of total BVZ released increased by increasing the amount of surfactant, likely due to a higher surfactant diffusion toward the external water phase. Although Pluronic® L-64 and Tween® 80 share the same HLB, formulations made of these two surfactants significantly differ in terms of BVZ release kinetics. Indeed, the formulation made of Tween® 80 showed a much higher burst release percentage at day 0 (17.7% vs 1.0%) and a much higher total percentage of BVZ released at day 21 (35.8% vs 8.9%) compared to the formulation made with the same amount of Pluronic® L-64 and the same PLGA molecular weight (14 kDa). This highlights that the HLB is not the only parameter affecting the release kinetics but also the surfactant chemical

structure plays a major role, likely because it dictates different chemical interactions that the surfactant can establish with BVZ and PLGA.

Formulations made of Span® 60 showed the highest percentage of BVZ released at day 0 (13.4-25.4%) and the highest percentage of total BVZ released until day 21 (33.8-42.8%) of this study. For all formulations made with Span 60, the burst release increased by increasing the surfactant concentration. Moreover, after the high burst release phase a much flatter plateau was observed compared to the other formulations of this study. This highlights a better capacity of water-soluble surfactants to support a sustained release of BVZ from PLGA microparticles.

*Selection of formulations for the formulation screening 1:* This exploratory screening ( $n = 1$ ) allowed the selection of 5 formulations for the formulation screening 1 ( $n = 3$ ), based on the results on EE and release profile. For each surfactant, the formulation with the best release profile (the highest percentage of BVZ released over the first 21 days) was selected among those having the highest EE values. Following this criterion, the selected formulations resulted those made using 50 mg mL<sup>-1</sup> of surfactant, except for the formulation containing Pluronic® L-64, which contained 150 mg mL<sup>-1</sup> of surfactant. Only for the formulation made of Tween® 80, two different surfactant concentrations were selected (*i.e.*, 25 and 50 mg mL<sup>-1</sup>) to study in triplicate the effect of surfactant concentration. For a fair comparison, all formulations of the formulation screening 1 were prepared by using PLGA with a molecular weight of 14 kDa.

## Effect of the capping group on the EE and release profile of BVZ

*Materials:* Acid-terminated PLGA Resomer® RG 502 H 25G (D,L-Lactide:Glycolide ratio = 50:50,  $M_n = 6320$  Da,  $M_w = 14100$  Da) was supplied by Evonik, whereas acid-terminated PLGA AP081 (D,L-Lactide:Glycolide ratio = 50:50,  $M_n = 5112$  Da,  $M_w = 7760$  Da) was purchased from PolySciTech®. Particles were prepared as described in section 1.1 of this document, except for the fact that particles were isolated by centrifugation at 49000 g for 30 minutes at 4°C. EE was calculated as described in section 2.1 of this document. *In vitro* release study was carried out as described the main manuscript.

*5.2. Effect of PLGA capping group and molecular weight:* The values of EE of the formulations made with uncapped PLGA were much higher than those found when using capped PLGA (87% vs 48%) and no difference was observed between the two molecular weights used (Table S2). The higher encapsulation of BVZ when using uncapped PLGA compared to capped PLGA can be attributed to the establishment of electrostatic interactions between the positively charged BVZ (isoelectric point 8.3) and the negatively charged carboxyl end groups of uncapped PLGA. This is in accordance with previously reported studies where the EE of BVZ when using uncapped PLGA was higher than 80%.<sup>[512,513,532,533]</sup> Unfortunately, formulations made with uncapped PLGA showed a burst release of BVZ during the

first two days, followed by virtually no release up to day 21. Burst release increased by decreasing PLGA molecular weight (percentage of BVZ released by day 2 was 7% and 16%, when using PLGA with a molecular weight of 14 kDa and 8 kDa, respectively). This is in line with previous literature, and it is explained by the higher hydrophilicity of lower molecular weight PLGA, which causes a higher water uptake and burst release of hydrophilic drugs.<sup>[554,555]</sup> By comparing formulations made with capped and uncapped PLGA of the same molecular weight (cPLGA 14K and uncPLGA 14K), a beneficial effect of the capping group on the release kinetics of BVZ can be observed. In fact, formulations made with capped PLGA released BVZ in a faster and more sustained manner. The absence of a sustained release observed for the formulations made with uncapped PLGA can be explained by the establishment of strong electrostatic interactions between the positively charged BVZ and negatively charged end groups of PLGA. This makes these formulations not suitable for our purpose and therefore, formulations made with uncapped PLGA were no further investigated.





# Chapter 9

## **Spatial-Selective Volumetric 4D Printing and Single-Photon Grafting of Biomolecules within Centimeter-Scale Hydrogels via Tomographic Manufacturing**

Marc Falandt<sup>1</sup>, Paulina Núñez Bernal<sup>2</sup>, Oksana Dudaryeva<sup>2</sup>, Sammy Florczak<sup>2</sup>, Gabriel Größbacher<sup>2</sup>, Matthias Schweiger<sup>1</sup>, Alessia Longoni<sup>2</sup>, Coralie Greant<sup>3,4</sup>, Marisa Assunção<sup>2</sup>, Olaf Nijssen<sup>1</sup>, Sandra van Vlierberghe<sup>3,4</sup>, Jos Malda<sup>2,1</sup>, Tina Vermonden<sup>5</sup>, Riccardo Levato<sup>1,2</sup>

Published in: *Advanced Materials Technologies*. 2023. 8(15)

<sup>1</sup> Department of Clinical Sciences, Faculty of Veterinary Medicine, Utrecht University, Utrecht, The Netherlands

<sup>2</sup> Department of Orthopedics, University Medical Center Utrecht, Utrecht University, Utrecht, The Netherlands

<sup>3</sup> Polymer Chemistry & Biomaterials Group, Centre of Macromolecular Chemistry, Department of Organic & Macromolecular Chemistry, Faculty of Sciences, Ghent University, Ghent, Belgium

<sup>4</sup> BIO INX BV, Ghent, Belgium

<sup>5</sup> Department of Pharmaceutical Sciences (UIPS), Faculty of Science, Utrecht University, Utrecht, The Netherlands

## ABSTRACT

Conventional additive manufacturing and biofabrication techniques are unable to edit the chemico-physical properties of the printed object post-printing. Herein, a new approach is presented, leveraging light-based volumetric printing as a tool to spatially pattern any biomolecule of interest in custom-designed geometries even across large, centimeter-scale hydrogels. As biomaterial platform, a gelatin norbornene resin is developed with tunable mechanical properties suitable for tissue engineering applications. The resin can be volumetrically printed within seconds at high resolution ( $23.68 \pm 10.75 \mu\text{m}$ ). Thiol-ene click chemistry allows on-demand photografting of thiolated compounds post-printing, from small to large (bio)molecules (*i.e.*, fluorescent dyes or growth factors). These molecules are covalently attached into printed structures using volumetric light projections, forming 3D geometries with high spatiotemporal control and  $\sim 50 \mu\text{m}$  resolution. As a proof-of-concept, vascular endothelial growth factor is locally photografted into a bioprinted construct and demonstrated region-dependent enhanced adhesion and network formation of endothelial cells. This technology paves the way towards the precise spatiotemporal biofunctionalization and modification of the chemical composition of (bio)printed constructs to better guide cell behavior, build bioactive cues gradients. Moreover, it opens future possibilities for 4D printing to mimic the dynamic changes in morphogens presentation natively experienced in biological tissues.

**Keywords:** volumetric additive manufacturing; biofabrication; photopatterning; light-based printing; 4D printing

## INTRODUCTION

Three-dimensional (3D) printing technologies have rapidly become fundamental tools for biomedical research and personalized implant generation. These technologies have exceptional ability to generate biomaterials-based constructs with customized architecture and precise spatial patterning of different biocompatible materials and living cells (*i.e.*, via biofabrication technologies including bioprinting).<sup>[556,557]</sup> Key applications of biofabricated structures that mimic salient features of native tissues include patient-specific *in vitro* models for drug discovery, and implantable constructs for regenerative medicine.<sup>[558]</sup>

A main limitation of current bioprinting technologies is the lack of control over the temporal evolution of the printed structures. In fact, the physico-chemical properties of printed objects cannot be edited with precise spatiotemporal control after printing. Geometrical changes in various polymers and hydrogel-based 3D structures have so far been achieved using stimuli-responsive materials and shape memory polymers as building blocks. These approaches have often been defined as four-dimensional (4D) printing, with time being the fourth dimension.<sup>[559]</sup> Typically, these strategies include the induction of predictable and desired changes in stiffness, architecture, or size of constructs post-printing upon exposure to heat,<sup>[560]</sup> ions,<sup>[561]</sup> ultrasounds,<sup>[562]</sup> or electromagnetic fields.<sup>[563]</sup> These geometrical changes are especially useful in the field of soft robotics,<sup>[564]</sup> and to mechanically stimulate cells during tissue culture.<sup>[565]</sup> On the other hand, time-dependent, on-demand modifications of the biochemical properties of the printed structure remain particularly challenging. Precise spatial control over the biochemical composition of a construct would allow for the gradual presentation of different growth factors and morphogens into local cell environments, thus enabling local control of (stem) cell fate, mimicking environmental changes naturally occurring during developmental, healing, and degenerative processes. In the field of 3D printed hydrogel for tissue engineering applications, capturing the physico-chemical composition of the native extracellular matrix (ECM) remains an important objective. In fact, tissue ECM displays unique region-dependent mechanical properties, and it also acts as a depot of biologically active biochemical signals. These are both in the form of peptide sequences embedded in the ECM polymeric backbone, as well as through the release and presentation of growth factors tethered to specific domains in ECM proteins and glycans. Several elegant hydrogel-based systems have been designed to be readily functionalized with such bioactive sequences during their preparation. Often, these systems result in the isotropic distribution of bioactive cues that are effective in steering cell behavior.<sup>[566,567]</sup> Alternatively, post-curing in photopolymers can be leveraged to graft molecules of interest onto pre-fabricated structures, homogeneously in specific regions in which the still reactive material is present, as shown for example in studies processing non-hydrogel materials.<sup>[568,569]</sup>

To date, spatio-selective chemical grafting of bioactive molecules has been typically performed in tissue cultures exploiting the contactless nature of light-based fabrication technologies, for example with lithographic techniques,<sup>[156,570,571]</sup> which permit projections of 2D patterns, and via multiphoton lithography.<sup>[572,573]</sup> The latter, albeit showing exceptionally high resolution ( $< 1 \mu\text{m}$ ), is limited by the working distance of the objective used in the device, which rarely exceeds 1 mm, thus preventing photochemical editing of larger objects.

In the present study, we introduce a new visible light-mediated technology to precisely imprint volumetric 3D patterns of fluorescent moieties and biological molecules within cubic centimeter-scale hydrogels, leveraging the potential of tomographic printing. This approach enables the generation of geometrically defined patterns of biologically active species for directing cell behavior, which can be introduced arbitrarily at any time point after hydrogel crosslinking and printing.

Previously, our group demonstrated the possibility to produce complex, hydrogel-based cell-free or cell-laden constructs of clinically relevant size in mere seconds, via Volumetric Bioprinting (VBP).<sup>[127]</sup> This novel light-based printing method, inspired by computed tomography, generates whole objects in a layer-less fashion (as opposed to conventional layer-by-layer 3D printing).<sup>[127,224,225]</sup> This permits high-speed printing, while still achieving printing resolution in the range of  $\approx 40\text{-}50 \mu\text{m}$ , even when printing in the presence of cells and complex cellular aggregates like organoids.<sup>[286]</sup> In Volumetric Printing (VP), also called Volumetric Additive Manufacturing (VAM), a digital micromirror device shapes (visible) light into filtered back projections of the object to be printed, as instructed by a tomographic reconstruction algorithm. The projections are sent to a rotating volume of a photoresponsive material at specific angles, and the resulting light dose accumulation allows for selective crosslinking of the resin into the desired 3D object. While this concept has been so far applied for photocrosslinking and 3D printing, volumetric printing can be more broadly envisioned as a technique to spatially confine any light-triggered chemical reaction. In addition, as long as the printing resin is sufficiently transparent to the desired wavelength, the photoreaction could be conducted at any point in time post-manufacture of a given object, in a non-invasive and biocompatible manner.

To demonstrate this concept, in this study, we selected gelatin as a base material due to its known biocompatibility and possibility to source it with low endotoxin content, which makes it potentially translatable for medical and pharmaceutical use.<sup>[574]</sup> Moreover, gelatin allows for a broad array of chemical modifications, to accurately modulate its degradation profile and mechanical properties.<sup>[160,575]</sup> As a platform material, we prepared and characterized a thiol-ene photocrosslinkable norbornene-modified gelatin (gelNOR), which enables the generation of covalent hydrogel structures displaying complex geometries via volumetric printing. Thiol-ene click chemistry has gained increasing

attention in the field of 3D printing and tissue engineering, as it yields hydrogels with highly homogenous network composition and mesh size. As the thiol-ene reaction progresses via a step-growth mechanism, the physical characteristics of the network can be reproducibly controlled by selecting the thiol-bearing crosslinker (length, molecular weight, number of reactive groups), network density, Degree of Functionalization (DoF) and the thiol-to-norbornene ratio.<sup>[195]</sup> Given the accurate control over the crosslinking kinetics and reaction termination upon removal of light irradiation, it is also readily possible to contextually control the amount of unreacted norbornene groups, which remain available for secondary reactions (*i.e.*, in this case, photografting) even after network percolation. Next, we subjected the volumetrically printed object to a second volumetric printing step in the presence of desired thiolated biomolecules of interest, a precise chemical editing can be performed locally at any point in time, decorating the hydrogel construct with 3D convoluted photopatterns (**Figure 1**). To ensure high spatial resolution during the photografting process, the interaction between tomographic light dose, initiator concentration and inhibiting antioxidant compounds was thoroughly characterized. As a proof-of-concept of biological functionality, a hydrogel chip with a perfusable channel was produced and assessed for cell adhesion, spatio-selective proliferation and promoted self-assembly of endothelial cells seeded within the channel, in response to volumetrically grafted patterns of vascular endothelial growth factor (VEGF), a key chemokine in angiogenesis. Overall, this novel approach paves the way towards the production of future tissue culture scaffolds and biofabricated constructs that can be gradually modified to match the evolving, dynamic requirements of cells during tissue culture and maturation, thus offering a new toolbox towards the engineering of functional living tissues.

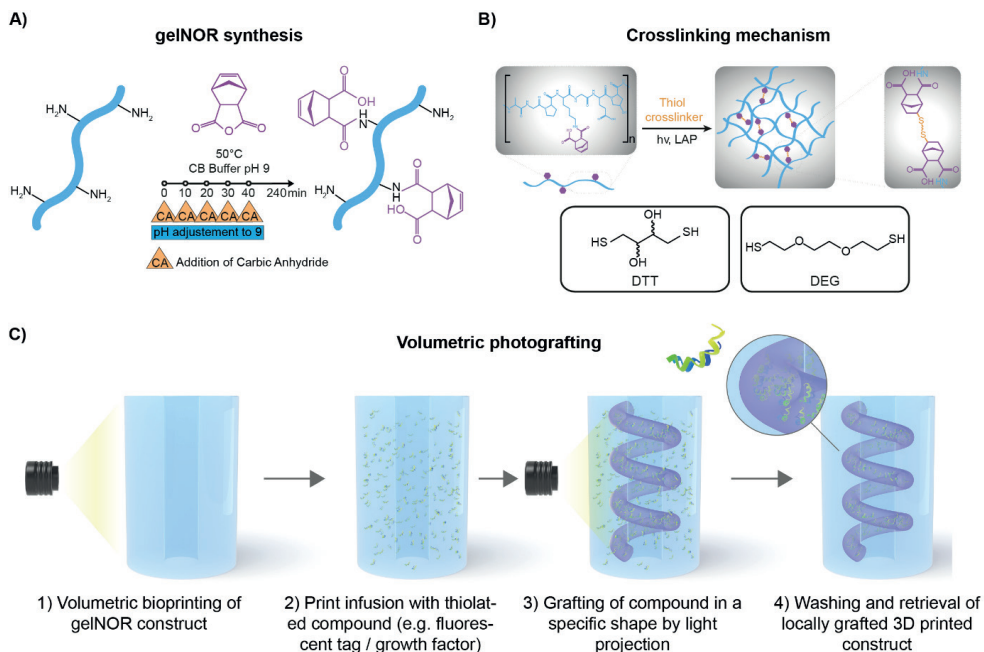


**Figure 1: Overview of gelNOR synthesis and crosslinking reaction, and volumetric photografting process.**

A) Synthesis of gelNOR with addition of carbic anhydride at multiple timepoints. B) Schematic representation of the crosslinking mechanism of gelNOR with a dithiolated crosslinker, showing the two crosslinkers used in this study, DTT and DEG. C) Schematic representation of the volumetric photografting technique including volumetric printing, the infusion strategy with a thiolated compounds, and a second volumetric projection step for volumetric photografting of these compounds into complex structures within a gelNOR construct using covalent thiol-ene chemistry.

## RESULTS AND DISCUSSION

As a starting point, gelNOR was selected as it satisfies multiple requirements, namely: i) the compatibility with light-based 3D printing processes, to provide architectural control over 3D printed scaffolds of an arbitrary geometry, ii) the printing of structures with tunable mechanical properties across a broad range of stiffness relevant for tissue culture, via screening different di-thiolated molecules, and iii) the ability to be used for photografting of any molecule bearing a free thiol group, such as those found in cysteine residues in native proteins. First, we screened an array of hydrogel formulations by varying crosslinker length and thiol-ene ratio, while keeping a constant 5 w/v% gelNOR concentration with 80% degree of norbornene functionalization, to maximize the amount of norbornene groups (**Supplementary Figure S1**). In addition, a relatively high degree of functionalization maximizes the number of reactive groups available for post-crosslinking during the volumetric photografting process. We thoroughly characterized a broad

library of hydrogel formulations with tunable mechanical properties, by introducing two crosslinkers displaying different length: dithiothreitol (DTT) and a dithiolated diethyleneglycol (DEG), at different thiol-to-norbornene ratios (**Figure 2**). To evaluate the general trend in the crosslinking kinetics of these hydrogel formulations, photorheology was performed (**Figure 2A**). We noticed that for all formulations crosslinking of the hydrogels start immediately upon the moment of light exposure and progresses with similar kinetics. This suggests that, in the range tested herein, the crosslinker length does not significantly influence the crosslinking kinetics of the hydrogel, which is in line with previous research.<sup>[576]</sup> However, varying the thiol-to-norbornene ratio, provided a clear difference in crosslinking kinetics between the samples, with 1:1 thiol-to-norbornene ratio yielding the fastest crosslinking kinetics (under 12 seconds to reach 80% of complete crosslinking). For hydrogels with a 4:5 thiol-ene ratio the crosslinking was achieved in under 24 seconds and for the 3:5 thiol-ene ratio crosslinking was achieved in under 36 seconds. The step-growth mechanism of gelNOR is known to provide rapid crosslinking, resulting from ring strain relief, especially when compared with hydrogels formed with a chain-growth mechanism, like gelMA.<sup>[291,576]</sup> Consequently, this allows to control the mesh size of the formed hydrogel network without greatly affecting the reaction kinetics, by changing the length of the crosslinker while maintaining constant the thiol-ene ratio. The soluble fraction (sol-fraction), which represents the amount of uncrosslinked polymer that washes out of the hydrogel network, of varying gelNOR formulations showed no significant difference for different crosslinkers or thiol-to-norbornene ratios (**Figure 2B**). Hydrogels formed with DTT as crosslinker displayed a sol-fraction of  $12.58 \pm 4.95\%$ ,  $10.76 \pm 4.03\%$ , and  $6.04 \pm 2.39\%$  for thiol-ene ratios 1:1, 4:5, and 3:5, respectively. Hydrogels formed with DEG as crosslinker provided a sol-fraction of  $9.94 \pm 4.04\%$ ,  $7.00 \pm 2.05\%$ , and  $4.78 \pm 3.78\%$  for the thiol-ene ratios 1:1, 4:5, and 3:5, respectively. All these measurements showed no significant difference. Dynamic mechanical analysis (DMA) was performed to determine the compressive modulus of the different hydrogel formulations (**Figure 2C**). Notably, a significant decrease in stiffness was observed as the thiol-to-norbornene ratios decreased in DTT samples ( $6.30 \pm 0.29$  kPa,  $4.94 \pm 0.70$  kPa, and  $3.53 \pm 0.79$  kPa for the thiol-ene ratios 1:1, 4:5, and 3:5) and between the 1:1 thiol-ene ratio ( $5.26 \pm 0.13$  kPa) the 4:5 ratio ( $3.62 \pm 0.12$  kPa), and the 3:5 ratio ( $2.52 \pm 0.08$  kPa) for DEG crosslinked samples. This was to be expected since a 1:1 thiol-ene ratio would provide a maximal crosslinking of the polymer network and thus the stiffest gels, while at 4:5 and 3:5, thiol-ene ratios there is an excess of norbornene groups that do not participate in the network. As for the effect of crosslinker length on the compressive properties of the hydrogels, a significant increase in stiffness (1.36-fold) was observed in DTT samples compared to DEG at the 4:5 thiol-to-norbornene ratio. This mechanical versatility supports previously data shown for this bioresin and demonstrates that the mechanical properties of gelNOR hydrogels can be easily tailored to specific needs by adjusting either the thiol-ene ratio, and/or the length of

the thiol crosslinker.<sup>[291,576,577]</sup> Considering the wide range of biomechanical requirements for culturing cells from different native tissues and organs, the mechanical versatility exhibited by gelNOR is of great interest to create stable, mechanically competent scaffolds for different tissue engineering applications.<sup>[578]</sup> In terms of the stress relaxation response of the materials, all the formulations showed a predominantly elastic behavior, in line with the characteristics of covalent hydrogels, with minimal relaxation, and high retention of the peak stress upon application of a constant strain (**Figure 2D, Supplementary Figure S2**). The swelling ratio of the hydrogel formulations differed significantly, both for crosslinker length and thiol-to-norbornene ratio (**Figure 2E**). The swelling ratios for the hydrogels with DTT as crosslinker were  $14.47 \pm 0.62$ ,  $16.84 \pm 0.42$ , and  $20.18 \pm 1.07$  for thiol-ene ratios 1:1, 4:5, 3:5, respectively. For the hydrogels with DEG as crosslinker we measured the swelling ratio to be  $17.71 \pm 1.28$ ,  $19.66 \pm 0.33$ , and  $23.02 \pm 0.87$  for the thiol-ene ratios 1:1, 4:5, and 3:5, respectively. These results show that the hydrogels with a 1:1 thiol-ene ratio have a significant difference with varying crosslinker length, where the longer DEG has a higher swelling ratio than the shorter DTT crosslinker, probably also because DEG has a more hydrophilic profile than DTT. Furthermore, the measurement showed a significant difference in varying thiol-ene ratios for the formulations with DTT as crosslinker, where we see that the lower the crosslinker density, the higher the swelling ratio. This indicates the higher crosslinking density to be effectively formed for the 1:1 thiol-ene ratio, as compared to the other thiol-ene ratios. To confirm that the tunability of mechanical and physical properties of the hydrogels did not hinder sample stability over time, the rate of degradation of the different gelNOR formulations was evaluated in the presence of low collagenase concentrations (**Figure 2F**). The results of this accelerated degradation test, showed that all hydrogel formulations could be completely enzymatically degraded with a similar kinetics in a 60-minute timeframe, therefore suggesting the potential for cultured cells to remodel the gelatin matrix.



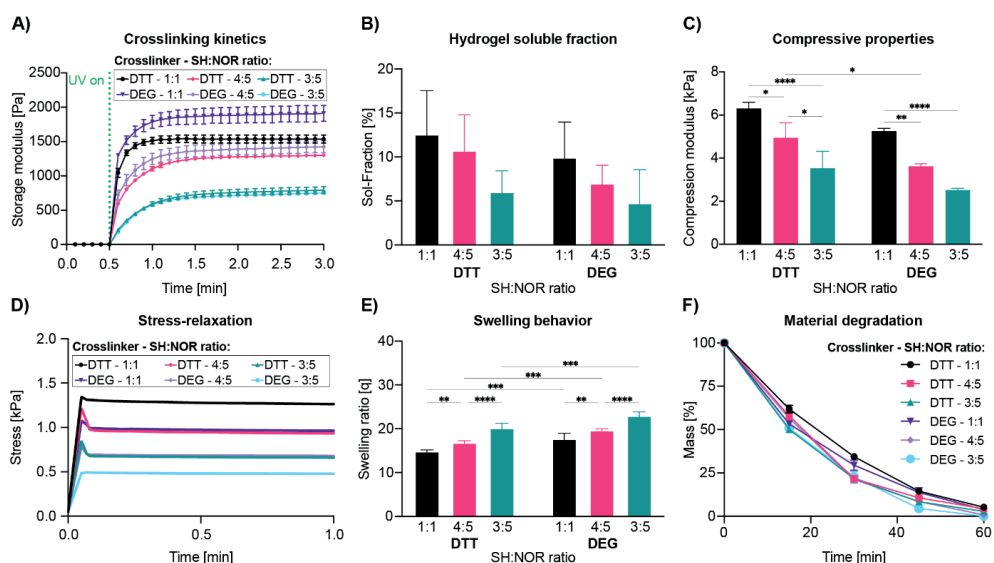


**Figure 2: Mechanical and physical characterization of 5 w/v% gelNOR bioresins using different crosslinkers (DTT or DEG) at varying thiol-ene ratios (1:1, 4:5, or 3:5) keeping the LAP concentration consistent at 0.1 w/v%, showing A) Photorheological time sweep measurements displaying the crosslinking kinetics (n = 3). B) Soluble fraction of different gelNOR formulations (n = 5). C) Compressive Young's modulus (n = 3). D) Stress-relaxation evolution graphs (n =). E) Swelling behavior (n = 5). F) Material degradation in collagenase solution at 37°C (n = 3). \* =  $p < 0.05$ , \*\* =  $p < 0.01$ , \*\*\* =  $p < 0.001$ , \*\*\*\* =  $p < 0.0001$ .**

Next, having available this set of photoresponsive hydrogels, the potential for shaping them into complex architectures through volumetric printing was investigated. For this, the formulation yielding 1:1 thiol-norbornene ratio and DTT as a crosslinker was used, as it was the one showing the highest mechanical stability and stiffness, thus allowing to maximize the ease of handling during printing and photografting. Light-based biofabrication technologies, such as stereolithography,<sup>[579]</sup> digital light projection printing,<sup>[331]</sup> and multiphoton lithography,<sup>[580]</sup> enable printing at higher resolution (nanometers to tens of micrometers)<sup>[121]</sup> and superior freedom of design compared to extrusion printing. In fact, being nozzle-free, light-based techniques sculpt photoresponsive materials, enabling the production of convoluted geometries recurrent in biological tissues (*i.e.*, templates of vascular networks) that cannot be readily produced with conventional extrusion techniques. With the recent introduction of volumetric printing, such complex geometries can now also be produced with a resolution in the range of few tens of micrometers, while printing centimeter-sized objects in less than 20 seconds (**Figure 3**). To date, this technology has been applied to produce architecturally complex objects made of light-sensitive hydrogels,<sup>[127,286,291]</sup> polymeric acrylic and thiol-ene resins,<sup>[225,453]</sup> elastomers,<sup>[412]</sup> nanoparticle-laden materials,<sup>[421]</sup> and glass.<sup>[581]</sup> In this study, we successfully achieved high printing resolutions with the selected gelNOR formulation of  $23.68 \pm 10.75 \mu\text{m}$  for positive features (*i.e.*, spikes), and of  $176.01 \pm 36.34 \mu\text{m}$ , printing open, perfusable channels within

a soft hydrogel matrix (**Figure 3A, B**). These findings show the highest printing resolution of positive features to date, and complement the high-speed, high-resolution printing of gelatin norbornene materials previously reported using this printing technique.<sup>[291]</sup> Based on these printing conditions, more complex scaffolds were accurately resolved, from a mathematically derived gyroidal structure to torus knot shaped channels (**Figure 3D, 3E**). These highly convoluted structures were printed in less than 15 seconds, further underlining the ability of volumetric printing and of the gelNOR bioresin to rapidly and consistently produce architecturally complex, porous 3D structures. Printing accuracy was shown to be extremely high for both positive and negative feature constructs showing no significant difference in volume between the digital model and the printed object itself (gyroid: 69.40 mm<sup>3</sup> model vs. 71.95 ± 2.11 mm<sup>3</sup> print; torus knot channels: 154.73 mm<sup>3</sup> model vs. 169.85 ± 13.34 mm<sup>3</sup> print) (**Figure 3F**).

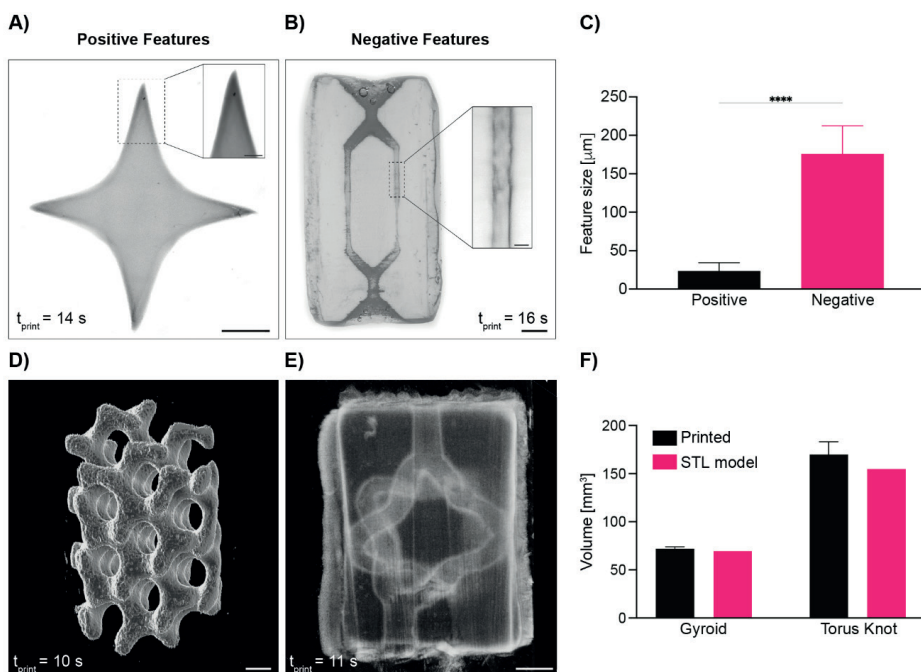


**Figure 3. Volumetric printing resolution and accuracy using gelNOR bioresins.** Stereomicroscopy images of A) positive and B) fully perfusable negative features achieved with the 1:1 DTT gelNOR formulation (scale bars = 1 mm; zoomed scale bar = 250 μm), and C) quantification of this maximum resolution (n = 3 independent samples, n = 10 technical replicates). Light-sheet 3D images of D) mathematically derived gyroid structure printed with gelNOR and E) hollow torus knot channel fabricated via VP using the 1:1 DTT gelNOR formulation (scale bars = 1 mm). F) Volume comparison between original STL file and the printed construct of the gyroid and torus knot structures (n = 3). \*\*\*\* = p < 0.0001.

Building on the high-resolution printability of the gelNOR resin, we then investigated the potential to functionalize the printed constructs by covalently crosslinking single thiol-bearing molecules on the gelatin backbone in a spatioselective fashion across centimeter-

scale objects. During the volumetric printing process of hydrogels, light irradiation is on purpose prematurely stopped to avoid crosslinking of out-of-target regions of the build volume, which could lead to printing artefacts. Consequently, the hydrogel reaches enough network percolation to be considered stable, however the maximum crosslinking density is not achieved, and if necessary, can be reached only with a post curing process.<sup>[127,286]</sup> This feature is especially desirable for enabling secondary reactions post-printing, such is the case of photografting onto still available norbornene groups. As a first step, we thoroughly characterized the photografting process and how to modulate its accuracy, taking advantage of both the tomographic printing principle and the reactivity of the photoresin with thiols (**Figure 4**). For this purpose, we selected as a model molecule a fluorescent Cy3 tagged polyethylene glycol (PEG) chain functionalized with a single thiol moiety, which could be easily visualized and analyzed to determine photografting accuracy and intensity and exhibited stable fluorescence levels over time (Cy3-PEG-SH; 5 kDa; **Supplementary Figure S3**). As first step, it was first confirmed that the Cy3-PEG-SH compound could be covalently bound to the gelNOR network. To assess this, gelNOR cylinders were infused with the grafting cocktail (containing Cy3-PEG-SH and LAP as photoinitiator) and were either irradiated with light from the volumetric printer (2000 mJ/cm<sup>2</sup>), or left in the dark. As shown by fluorescence imaging, the photoexposed samples retained a stable level of fluorescence intensity over multiple days of incubation in PBS. Conversely, the Cy3-PEG-SH rapidly diminished over time in non-photoexposed samples (**Figure 4A**). A quantitative assessment of the fluorescence measured in the PBS used to wash the hydrogels further corroborated this observation, displaying 6-fold higher fluorescence signal in the eluates from the non-illuminated controls already after 1 day of incubation, showing a rapid release of the PEG probe as opposed to a stable incorporation facilitated by the volumetric printer (**Supplementary Figure S4**). Furthermore, quantitative analysis of the grafted and non-grafted samples demonstrated that for the grafting conditions selected in this experiment, the tethered mono-thiolated Cy3-PEG-SH was found to be in the range of  $30.92 \pm 2.06 \mu\text{M}$  concentration, and samples infused in the grafting cocktail but not photografted, showed non-detectable dye concentrations. (**Supplementary Figure S5**). Next, in order to ensure spatial control over the 3D patterns imparted during volumetric photografting, a thorough characterization of the reaction was performed. During the tomographic printing process, in fact, it is important to keep in mind that the whole hydrogel volume is exposed to light, by delivering an anisotropic, 3D dose distribution. With the aim to correctly confine the photografting reaction within the desired region dictated by the STL file, an optimal process would show high grafting specificity, which is a parameter measuring the contrast between in-target binding and off-target binding. As testing platform, gelNOR cylinders previously infused with a grafting cocktail were exposed to a series of disc-shaped tomographic projections using the volumetric printing set up and delivering to each disk

a different light dose (750–2000 mJ/cm<sup>2</sup>), to screen grafting specificity, intensity, and degree of off-target grafting (**Figure 4B, Supplementary Figure S6**). It was initially observed that by simply adjusting the light dose delivered to the printed construct (750–2000 mJ/cm<sup>2</sup>) and photoinitiator concentration (0.6–1.0% w/v), covalent photografting could be achieved, but the Cy3 dye was detected at nearly equal amounts everywhere across the light path traversing the hydrogel with low spatial specificity, likely due to the high reactivity of the gelNOR system (**Supplementary Figure S7**). We therefore hypothesized that slowing down the reaction kinetics by adding a free-radical inhibitor to the grafting cocktail, could help minimize unwanted off-target events. In this study, we chose (2,2,6,6-tetramethylpiperidin-1-yl)oxidanyl (TEMPO) as inhibiting compound, since it has been previously used to enhance resolution in volumetric printing in combination with norbornene-based, non-hydrogel resins.<sup>[453]</sup> At relatively high concentrations, TEMPO can act as a pro-oxidant and elicit cytotoxicity on bacterial and mammalian cells,<sup>[582]</sup> however, this compound has been also proven to induce a protective effect for cells from oxidation-induced cell death,<sup>[583]</sup> and to act as a ROS scavenger,<sup>[584]</sup> when used in the safe concentration range also tested in our study (0.006 - 0.01 w/v%).<sup>[582,585]</sup> At the lower average light dose tested (750–1250 mJ/cm<sup>2</sup>), regardless of the TEMPO concentration, low specificity ratios were still observed ( $0.804 \pm 0.05$  -  $1.825 \pm 0.08$ ) and correlated with low grafting overall (both in- and off-target, **Figure 4C - E, Supplementary Figure S8**), the latter being indicative of limited reaction efficiency, in line with the inhibiting action of TEMPO. At higher light doses, instead, sufficient free radicals can be generated within the region of interest in the hydrogel, resulting in an improved contrast over the surrounding regions, which instead receive a lower dose as programmed by the tomographic algorithm and are therefore more affected by the presence of TEMPO (**Figure 4F - H, Supplementary Figure S8**). Specifically, for the highest tested light dose (2000 mJ/cm<sup>2</sup>) and using the formulation consisting of 1.0% w/v LAP and 0.008% w/v TEMPO, grafting specificity of  $2.388 \pm 0.06$  (2.1-fold higher than what was found without TEMPO) could be achieved, while also showing the highest in-target fluorescence intensity ( $4.473 \pm 0.11$  times higher than the background), and a low off-target intensity of  $1.568 \pm 0.26$  (with 1 being the value of the native autofluorescence of the hydrogel). Altogether these measurements showed the grafting cocktail consisting of 1.0% w/v LAP and 0.008% w/v TEMPO allows for the most specific photografting to be achieved, while exhibiting dose-dependent intensity changes and greatly reducing off-target grafting. Having optimized the grafting cocktail to achieve highly specific spatial patterning of our fluorescent molecule, we explored the potential to photograft more complex architectures, and assessed the effect of light dose grafting specificity of the Cy3-PEG-SH compound. To assess this, a tubular spiral was grafted surrounding a central channel within a printed cylinder (**Figure 4I, J**). This structure was successfully patterned and visualized in 3D (**Figure 4I - J**). Previously, it has been shown in several studies employing the VP approach that different architectures,

depending on their feature heterogeneity and size, require different light doses to be accurately resolved using this tomography-based approach.<sup>[286]</sup> In the case of photografting of complex objects, a light dose sweep was performed to determine whether grafting specificity was in any way affected by light dose. We showed that, albeit the highest grafting specificity for the spiral pattern was found at 1500 mJ/cm<sup>2</sup>, there was no significant difference for the other tested selected light doses, which also managed to resolve the spiral structure. This could suggest that the optimal formulation of the infusion cocktail may yield a broad, robust window for grafting such convoluted geometry at high specificity (**Figure 4K**). On top of this large grafting window at different doses, our gelNOR photografting system also yielded high resolutions of the grafted objects within our volumetric prints. A grafted spiral starting at 5 mm in width ( $5.04 \pm 0.08$  mm grafted resolution) that gradually became thinner in width until reaching a resolution of 1 pixel in the digital file reached a fully grafted resolution of  $57.20 \pm 1.66$   $\mu\text{m}$  (**Figure 4L**). This high level of resolution could be of particular impact and interest to produce patterns of bioactive molecules mimicking the micro-scale organization of biochemical components found in native biological tissues even at a scale close to the size of a single mammalian cell.

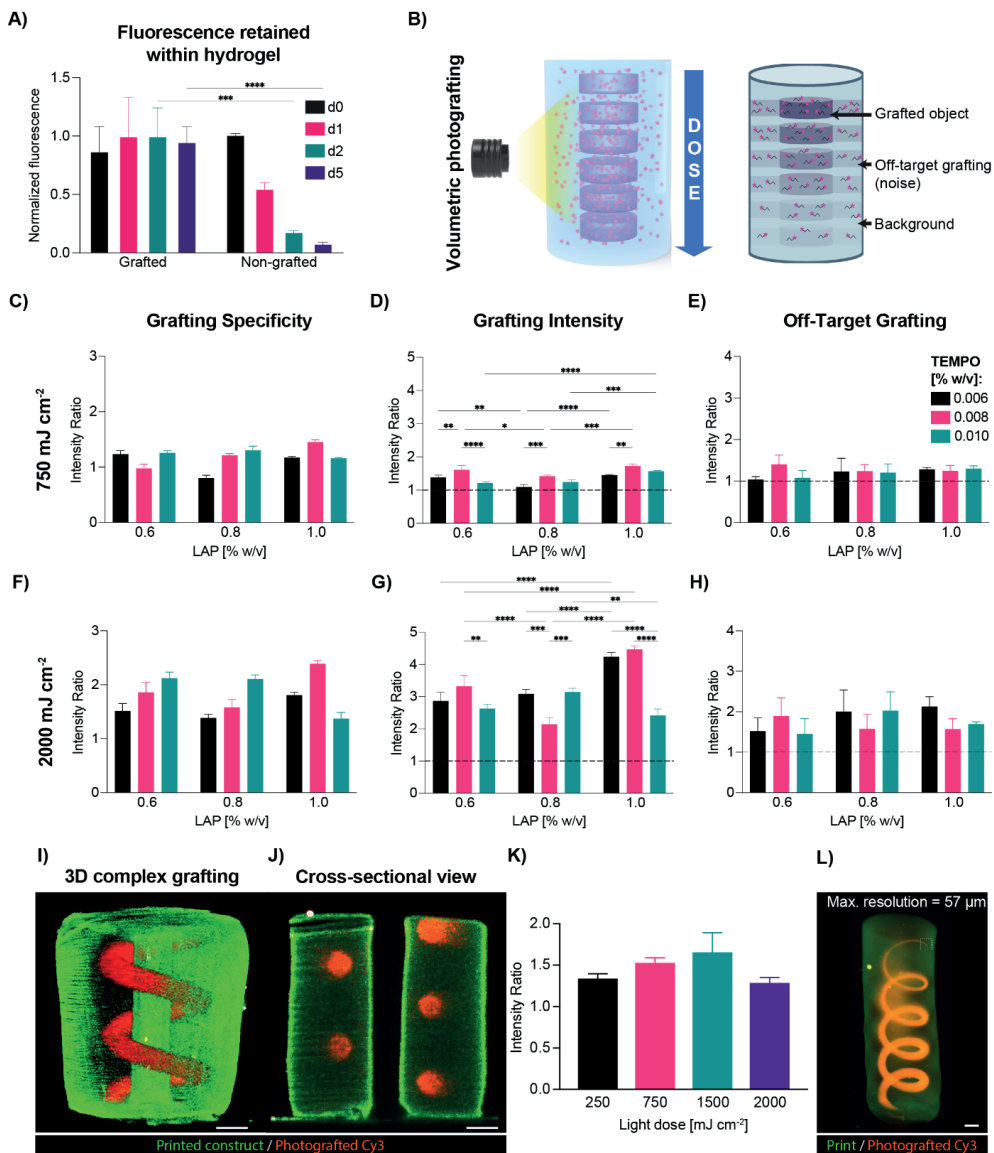


**Figure 4: Optimization of the volumetric photografting of thiolated fluorescent compounds.** A) Schematic representation of grafting optimization of gelNOR with Cy3-PEG-SH at different light doses, photoinitiator and crosslinking inhibitor concentrations. B) Normalized fluorescence intensity ( $\lambda = 580$  nm) of grafted and non-grafted gelNOR hydrogels at different time points of washing with PBS ( $n = 3$  technical replicates). C, F) Grafting specificity as ratio of intensity of the region of interest vs. unwanted crosslinking, D, G) Grafting intensity as ratio between the intensity of the region of interest and the background (dotted line represents the baseline gelNOR autofluorescence) and E, H) Off-target grafting as ratio between the intensity of the unwanted photografted regions and the background of gelNOR (dotted line represents the baseline gelNOR autofluorescence). Samples were grafted at a dose of 750 or 2000 mJ/cm<sup>2</sup> with different infusion mix concentrations (ranging from 0.6 to 1.0% w/v LAP and 0.006 to 0.010% w/v TEMPO, with 0.06% w/v Cy3-PEG-SH) ( $n = 3$  technical replicates). I) 1

3D lightsheet reconstruction and J) cross-sectional view of a photografted Cy3-PEG-SH spiral inside a gelNOR construct with a central channel (scale bar = 1 mm). K) Grafting specificity of the photografted spiral at different light doses (250, 750, 1500 and 2000 mJ/cm<sup>2</sup>). L) 3D image of photografted coil structure of gradually decreasing width, starting at 5 mm, and measurement of maximum photografting resolution (scale bar = 1 mm). \* =  $p < 0.05$ , \*\* =  $p < 0.01$ , \*\*\* =  $p < 0.001$ , \*\*\*\* =  $p < 0.0001$ .

Having established a successful protocol for photografting structures at high resolution, a range of different structures with varying feature sizes and degrees of complexity were accurately grafted (**Figure 5, Supplementary Figure S9**). A highly tortuous, mathematically derived gyroidal structure surrounding a central hollow channel within a printed gelNOR cylinder (**Figure 5Ai**), a spiral structure surrounding a hollow channel (**Figure 5Aii**), an interlocked chain structure with subunits in different axial orientations (**Figure 5Aiii**), the name of our research lab “Levato” spelled vertically along a gelNOR cylinder (**Figure 5Aiv**), and a random vessel structure (**Figure 5Av**) were successfully grafted using the previously optimized grafting cocktail. Moreover, since most tissues present highly diverse types of proteins and growth factors critical for tissue function that are heterogeneously distributed along the same area, the possibility to graft multiple compounds in a spatially defined regions within the same printed object were also investigated. Here, a spiral shape was first grafted with Cy3-PEG-SH. Subsequently, another grafting process was performed, using a Cy5-PEG-SH, which was imprinted in the shape of vertically aligned cylinders (**Figure 5Avi**). Grafting specificity of these complex geometries was measured for the gyroid ( $4.04 \pm 0.70$ ), spiral ( $3.54 \pm 0.64$ ), interlocked chain ( $2.09 \pm 0.45$ ), “Levato” ( $2.18 \pm 0.33$ ), and the random vessel ( $1.88 \pm 0.69$ ) (**Figure 5B**). Furthermore, grafting intensity of the complex geometries was measured for the gyroid ( $4.27 \pm 0.80$ ), spiral ( $3.80 \pm 0.44$ ), interlocked chain ( $4.05 \pm 0.36$ ), “Levato” ( $3.98 \pm 0.29$ ), and the random vessel ( $3.99 \pm 0.14$ ) (**Figure 5C**). The fact that both sets of values are within the same range as those observed in Figure 4 for simpler structures, further supports our previous observation that when using the optimized grafting cocktail, this process is extremely reproducible and as shown here, applicable to a wide range of architectures (**Figure 5B**). Variations in grafting specificity shown in **Figure 5B** are a phenomenon dependent on the tomographic reconstruction algorithm used for volumetric printing. As described in the previous literature,<sup>[224]</sup> when delivering light doses from multiple angles following a Radon transform and filtered-backprojections-based algorithm, the exact light dose delivered in every voxel oscillates around the average light dose set by the user. As a result, regions at the borders of the construct, especially in presence of sharp corners, tend to receive slightly higher doses and react faster. Printing (and herein, grafting) artefacts caused by this phenomenon could be resolved with dedicated corrections of the tomographic algorithm, as previously shown.<sup>[224]</sup> Despite this phenomenon, we demonstrate the possibility to accurately photograft complex patterns, even within more convoluted 3D printed structures, like an Atlas statue (**Figure 5D**) and a mathematically derived gyroid (**Figure 5E**). All in all, this fast method of grafting complex 3D patterns

of several thiol-functionalized molecules can greatly increase the possibility of editing large hydrogel-based constructs in a spatiotemporally controlled fashion via sequential volumetric printing. Noteworthy to mention that thiol-ene chemistry is not the only possibility for photografting small molecules into a hydrogel system. In this study, thiol-ene chemistry was chosen since gelNOR is mechanically tunable and in many biological molecules there are cysteine residues capable of forming covalent networks through this thiol-ene chemistry. Other photochemistries could be studied for covalently grafting molecules to a hydrogel *i.e.*, di-tyrosine oxidation,<sup>[335]</sup> photolysis of aromatic azides,<sup>[586]</sup> or selectively cleaving areas in a gelatin hydrogel,<sup>[576,587]</sup> which could further expand the library of functionalizing compounds that are usable with this volumetric photografting approach, to further enhance the biochemical profile of bioprinted scaffolds.



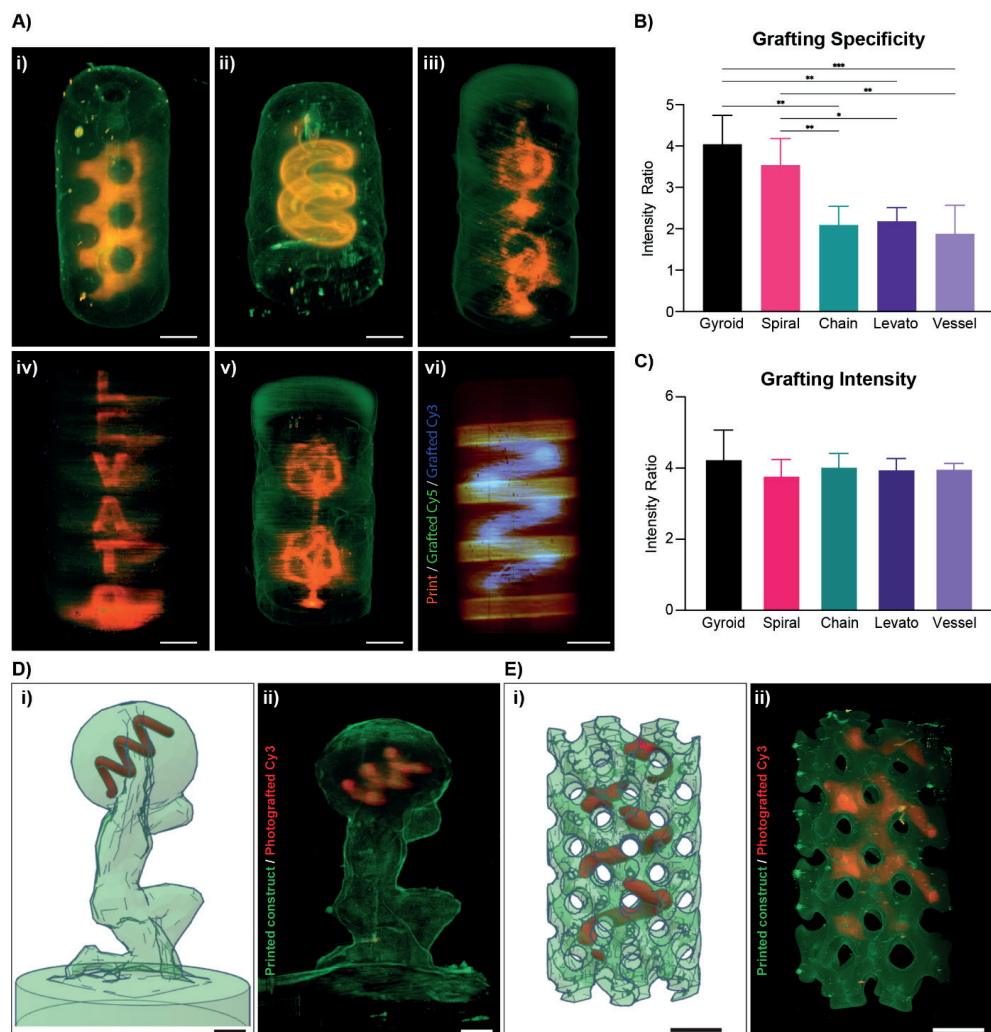


**Figure 5: Volumetric photografting of complex structures.** Photografting and analysis of geometries with different feature sizes and degrees of complexity. A) 3D image reconstructions of i) a mathematically derived gyroid, ii) a spiral, iii) interlocked chain model, iv) research lab name spelled vertically, v) and a random interconnected vascular structure grafted with Cy3-PEG-SH onto cylindrical gelNOR volumetric prints and vi) double dye grafting with Cy3-PEG-SH (spiral, blue) and Cy5-PEG-SH (discs, green) onto cylindrical gelNOR volumetric prints. B) Grafting specificity of complex grafting structures ( $n = 3$  samples), and C) grafting intensity of complex grafting structures ( $n = 3$  samples). D,i) STL file of an Atlas statue (green; CC BY-SA 3.0) volumetrically printed with gelNOR and a photografted Cy3-PEG-SH spiral (red). ii) Lightsheet 3D reconstruction of the printed gelNOR model (green) and the photografted spiral (red). E,i) STL file of a mathematically derived gyroid structure volumetrically printed with gelNOR (green) and a photografted Cy3-PEG-SH spiral (red). ii) Lightsheet 3D reconstruction of the printed gelNOR model (green) and the photografted spiral (red). Scale bars = 2 mm.

Besides the tethering of fluorescent compounds for easy visualization and optimization of the photografting process, this approach can also be used to covalently attach

proteins or growth factors within the printed structures for guiding cell fate with spatiotemporal control. While covalent grafting of biomolecules could have an effect on protein bioactivity, the use of norbornene moieties for thiol-ene photoclick chemistry has previously been shown to enable thiolated protein immobilization, with several growth factors showing maintained bioactivity post immobilization.<sup>[588–592]</sup> As a proof-of-concept, we volumetrically grafted vascular endothelial growth factor (VEGF) within a tissue engineered macrochannel, aiming to improve the adhesion and sprouting capacity of human umbilical vein endothelial cells (HUVECs) within an uncoated lumen. VEGF expresses synergistic interactions with the integrin adhesion receptors guiding vessel growth and maturation, as well as endothelial cell survival by the regulation of anti-apoptotic factor expression in these cells *in vivo*.<sup>[593–595]</sup> This proangiogenic growth factor is routinely used in endothelial growth culture medium to selectively enhance vascularization in *in vitro* engineered models as well.<sup>[596–600]</sup> VEGF has an uneven amount of cysteine residues and can be covalently coupled to a free norbornene onto the gelNOR network through the optimized photografting approach presented here. A volumetrically printed vascular chip, consisting of a central lumen of 1.5 mm in diameter, was fabricated to assess the effect of photografted VEGF on seeded HUVECs adhesion, interconnectivity and sprouting capabilities (**Figure 6A**). Given the short half-life of recombinant VEGF protein, cell performance in the grafted and non-grafted regions of the printed samples was evaluated after 3 days to ensure the proangiogenic effects of the tethered growth factor were captured, in the presence of either VEGF-free (VEGF<sup>-</sup>) or VEGF-supplemented (VEGF<sup>+</sup>) medium. To ensure that only the effects of VEGF incorporation were analyzed, the non-grafted regions of the prints were post-cured at the same light dose that was used to graft the VEGF, resulting in homogenous mechanical properties throughout the construct (**Supplementary Figure S10**). After 3 days of culture, clear differences in HUVEC adhesion and interconnectivity were observed in the VEGF-photografted regions cultured in both VEGF<sup>+</sup> and VEGF<sup>-</sup> culture media (**Figure 6B, C, Supplementary Figure S11**). In VEGF<sup>-</sup>, HUVEC adhesion in the grafted regions of the lumen was significantly enhanced compared to non-grafted areas, as shown by the increased average cell coverage in the grafted ( $84.06 \pm 6.36\%$ ) vs. non-grafted regions ( $35.72 \pm 2.43\%$ ) (**Figure 6B**). In samples cultured with VEGF<sup>+</sup> medium, the difference in the average HUVEC area coverage was less pronounced but showed significant differences between VEGF-grafted ( $83.71 \pm 3.87\%$ ) and non-grafted ( $54.46 \pm 8.57\%$ ) regions (**Figure 6B**) suggesting that in terms of cell adhesion to the hydrogel, the tethered VEGF provides a superior stimulation compared to free VEGF. Further, VEGF supplementation in the media did not significantly increase the coverage in the grafted regions of the construct, suggesting the absence of, or weak cumulative effects of the grafted and free soluble VEGF. Similarly, VEGF grafting had a significant effect on the cell interconnectivity showing a higher number of inter-cluster junctions compared to regions lacking the covalently bound VEGF molecules in the absence of VEGF in the

culture medium ( $309.00 \pm 104.65$  in VEGF-grafted region vs.  $145.40 \pm 49.07$  in non-grafted regions) (**Figure 6C**). These effects were conserved across VEGF<sup>+</sup> and VEGF<sup>-</sup> conditions. These observations suggest that the covalently tethered VEGF may provide a better support for HUVEC adhesion and growth compared to supplementation of soluble VEGF, at least in these initial stages of culture. The VEGF grafting could potentially be repeated over time to steer the vascular growth volumetrically printed constructs in real time in order to obtain more controlled multi-scale vascular structures. Further, after only 3 days, the photografted VEGF facilitated HUVEC infiltration into the printed hydrogel, as shown by the significantly higher spanning depth of the cells from the inner edge of the lumen into the bulk hydrogel ( $130.77 \pm 25.83 \mu\text{m}$  in VEGF-grafted regions vs.  $35.42 \pm 7.73 \mu\text{m}$  in non-grafted regions) (**Figure 6D, E**). This observed cell infiltration was observed across the whole perimeter of the lumen (**Figure 6F**) and across the entire length of the printed channel (**Figure 6G**) in the grafted regions, while being completely absent in the non-grafted regions of the vascular chip model. These observations are encouraging, given that a pro-angiogenic effect is clearly seen in the VEGF-grafted regions of the lumen, where the growth factor acts as a chemoattractant capable not only of enhancing cell adhesion to an uncoated printed lumen, but also facilitates cell sprouting into the bulk hydrogel in the early days of culture. Since these effects are seen in both VEGF<sup>-</sup> and VEGF<sup>+</sup> medium, this strongly suggests that the covalently bound VEGF molecules retain sufficient bioactivity to steer the behavior of the seeded HUVECs. This grafting step could potentially be repeated over time to achieve different degrees of vascular growth volumetrically printed constructs and obtain more controlled multi-scale vascular structures.

Overall, this study proves the feasibility of grafting biologically functional compounds like growth factors, allowing these to maintain their bioactivity and guide cell fate with exceptional spatiotemporal control. Despite the demonstrated potential of this volumetric photografting technique, the infancy of this approach leaves room for future developments and exploration. To further boost the potential of the photografting process, a wider library of chemically editable bioresins suitable for VBP should be developed, and the stability and long-term functionality of different grafted compounds should be elucidated in more depth. Importantly, in terms of future perspectives, the biocompatibility of the grafting conditions towards cell viability and function should be assessed in long-term culture conditions to further evaluate translatability for potential regenerative medicine applications. Furthermore, with such future developments, the possibility to continuously edit the printed construct with different bioactive molecules during culture (*i.e.*, to replenish the growth factor content over time, or to change its localization over time), can also be explored to more closely mimic certain developmental and tissue repair processes.

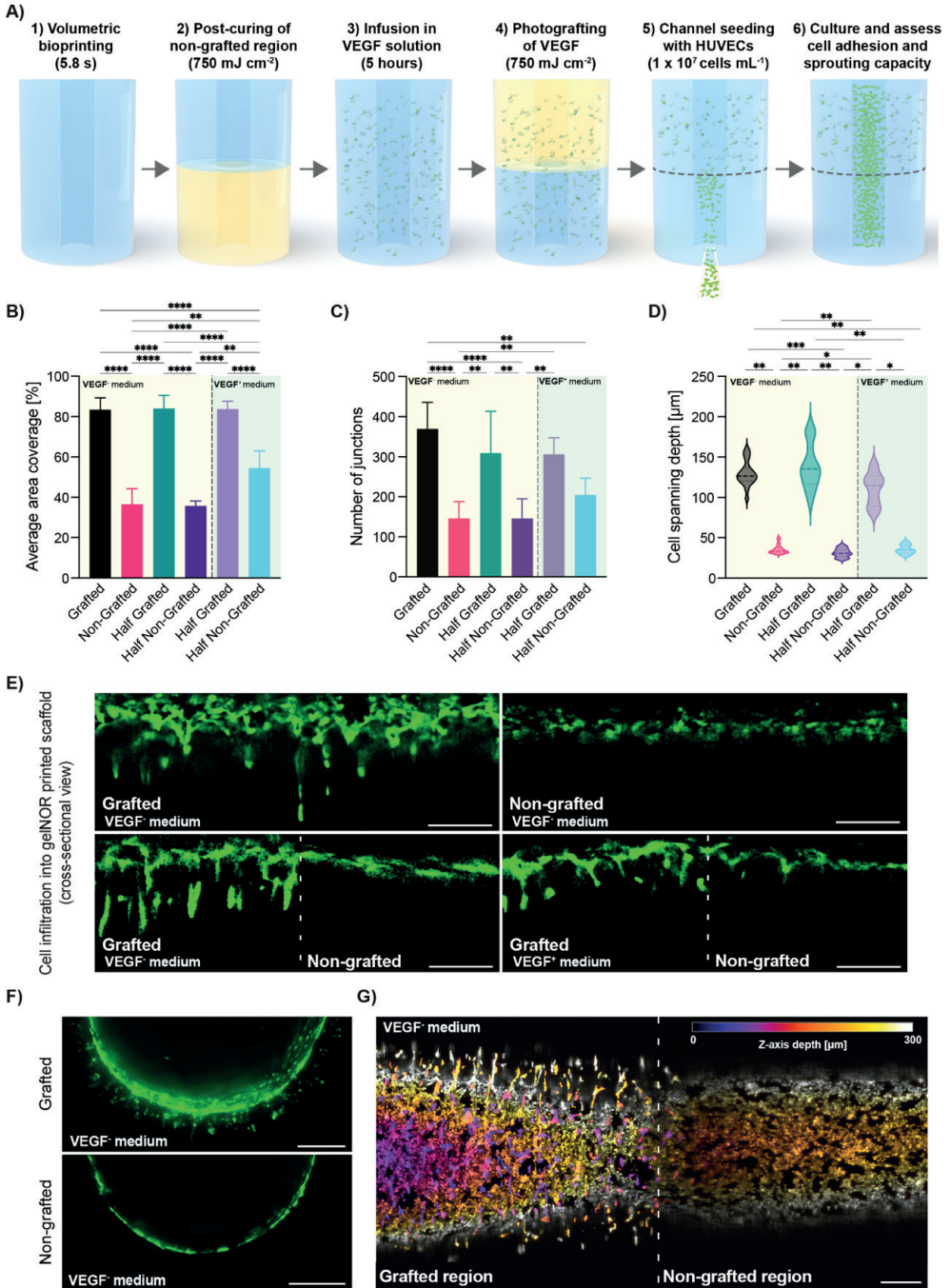


**Figure 6: Photografting functional VEGF growth factor as proof-of-concept assay to guide endothelial cell adhesion, interconnectivity and sprouting.** A) Schematic diagram of the sterile process with which VEGF was photografted onto half of a vascular chip model consisting of a central channel within a gelNOR cylinder. B)

Average area coverage and C) number of junctions of interconnected HUVEC clusters in the VEGF-grafted and non-grafted regions of the vascular chip cultured in VEGF-free and VEGF-supplemented medium after 3 days in culture ( $n = 3$ ). D) Average HUVEC spanning depth from the channel wall into the VEGF-grafted and non-grafted regions of the vascular chip, cultured in VEGF-free and VEGF-supplemented medium after 3 days in culture ( $n = 3$ ). E) Confocal images of horizontal cross-sections of the channel wall of the vascular chip seeded with HUVECs, showing various degrees of cell sprouting into the printed hydrogel. F) Confocal images of the vertical cross-section of the seeded vascular chip channel in grafted and non-grafted regions cultured in VEGF-free medium. G) Tile scan maximum projection image of a confocal z-stack the vascular tube showing the boundary between the grafted and non-grafted regions (indicated by a dotted line). The color code indicates the z-axis depth, depicting how cells in all imaged layers can sprout in the surrounding hydrogel matrix. Scale bars = 250  $\mu\text{m}$ . \* =  $p < 0.05$ , \*\* =  $p < 0.01$ , \*\*\* =  $p < 0.001$ , \*\*\*\* =  $p < 0.0001$ .

## CONCLUSIONS

In this study we demonstrated a new technological solution to create volumetric, 3D patterns of biological molecules within large, centimeter-scale hydrogels via tomographic printing and using visible light and bio-orthogonal thiol-ene chemistry. The selected material platform, gelNOR, was shown to possess highly controllable mechanical properties (through the adjustment of crosslinker length and resin DoF), and was shown to be printable via VBP, achieving a high printing resolution (20-30  $\mu\text{m}$  for positive features). We demonstrated that these versatile gelNOR bioresins are suitable for the photografting of complex shapes onto volumetrically printed hydrogel constructs, as demonstrated by the controlled grafting of fluorescent dyes within gelNOR prints using tomographic projections, therefore allowing to both sculpt the architecture of the hydrogel and locally edit its chemical composition with high resolution (in the range of 50  $\mu\text{m}$ ). Through the extensive optimization of the grafting cocktail formulations (containing the thiolated compounds, crosslinking inhibitor TEMPO and LAP photoinitiator) and the light dose delivered to the printed object, we achieved, for the first time, effective and precise photografting of both small dyes and large bioactive molecules, achieving  $\mu\text{m}$ -scale resolution of the grafted structures within centimeter-scale constructs while using a single-photon approach. As a proof of concept, we further applied this photografting principle to covalently tether the bioactive, pro-angiogenic growth factor VEGF to selectively guide and confine endothelial cell growth in the grafted, biofunctionalized areas. Improved cell adhesion and early formation of endothelial cell connections were observed preferentially in the biofunctionalized regions of the printed chip construct. Given that these observations match those of cells exposed to unbound VEGF molecules, this study indicates that the grafting process preserves bioactivity of the growth factors and opens the door for further characterization and tissue engineering applications. Overall, this work takes the first step in the characterization and development of smart materials that allow spatiotemporally precise biochemical editing. In combination with the ultra-fast VBP technique, this photografting approach holds great promise to bring about the creation of biofabricated scaffolds that can better guide cell fate and behavior and therefore more closely mimic the complex biochemical environment of native tissues and organs.

## EXPERIMENTAL SECTION

*Materials:* Gelatin from porcine skin (type A, X-Pure low endotoxin content) was kindly provided by Rousselot Biomedical (Ghent, Belgium). Commercial grade gelNOR (type B, Bovine hide, DoF 60%) was kindly provided by BIO INX BV (Zwijnaarde, Belgium). Cellulose dialysis membrane tubes (molecular weight cutoff = 12 kDa) were purchased from Sigma-Aldrich. Lithium phenyl-2,4,6-trimethylbenzoylphosphinate (LAP) was purchased from Tokyo Chemical Industry (Tokyo, Japan). Cy3-PEG-SH and Cy5-PEG-SH (Mw = 5 kDa) were purchased from Biopharma PEG (Watertown, USA). All other chemicals were obtained from Sigma-Aldrich unless stated otherwise.

*GelNOR synthesis:* Type A gelatin was dissolved in a CB-Buffer (carbonate-bicarbonate buffer pH 9, 0.1 M concentration) to reach a 10% w/v concentration. This solution was heated to 50° C for the gelatin to dissolve and kept at this constant temperature throughout the synthesis. To reach a desired degree of functionalization (DoF), 0.2 g (1.2 mmol) of carbic anhydride (CA) per gram of gelatin was used in the reaction. The CA was added every 10 minutes for a total of 5 times starting at  $t = 0$ . After every addition of CA, the pH of the reaction was stabilized with 5 M NaOH to reach a pH of 9. After 240 minutes (DoF 80%) from the first addition of CA, the reaction was stopped by centrifuging the solution at 4000 rpm at room temperature for 5 minutes. Afterwards the pH was stabilized to 7.4 using 1 M HCl. To benchmark the custom-synthesized gelNOR we used a commercial grade gelNOR kindly supplied by BIO INX BV (Zwijnaarde, Belgium) which exhibited comparable mechanical properties (**Supplementary Figure S12**) and grafting accuracy (**Supplementary Figure S13**) as the custom-synthesized hydrogel. The solution was diluted to reach a 5% w/v concentration of gelatin and dialyzed against MilliQ water for 4 days at 4° C. After the dialysis, the solution was further diluted with MilliQ to reach a final concentration of 2.5% w/v. The solution was then heated to 50° C and sterile filtered. Next, the solution was frozen at -80° C, and lyophilized in a freeze dryer (Alpha 1-4 LSCbasic, Chris) to yield the dry product.

*Degree of functionalization quantification:* 2,4,6-trinitrobenzene sulfonic acid (TNBSA) assay was performed for the quantification of the amount of free amine groups present in the gelatin before and after functionalization. A glycine standard curve, to determine the amino group concentration, was prepared with concentrations of 0, 0.8, 8, 16, 32, 64  $\mu\text{g mL}^{-1}$ . Gelatin samples were dissolved in 1.6  $\text{mg mL}^{-1}$  of 0.1 M  $\text{NaHCO}_3$  buffer. Subsequently, 0.5 mL of the sample was mixed with 0.5 mL of a 0.1% w/v TNBSA solution in the buffer and incubated at 37° C for 2 h. Next, the reaction was stopped by the addition of 0.25 mL of 1 M HCl and 0.5 mL of 10% w/v sodium dodecyl sulfate (SDS). The absorbance of the samples was measured by a CLARIOstar Plus® (BMG Labtech, Germany) plate reader at  $\lambda = 335$  nm. The amount of free amines was calculated to be 0.3371 mmol per g of gelatin, based on the TNBSA results ( $n > 5$ ).

*Sample preparation for hydrogel crosslinking:* Unless stated otherwise all experiments are conducted using gelNOR hydrogel supplemented with the following components to achieve photocrosslinking. GelNOR stock solutions were made in PBS at a 10% w/v concentration. LAP stock solution was made in PBS at a 1% w/v concentration. A stock solution of dithiothreitol (DTT) or 2,2'-(ethylenedioxy)diethanethiol (DEG) was prepared in PBS at a 100 mM concentration. To facilitate complete dissolution, all stock solutions were heated to 37° C. Afterwards, the stock solutions were mixed and diluted with PBS to reach a final concentration of 5% w/v gelatin-based material, 0.1% w/v LAP, and the tunable ratio of thiol crosslinker to norbornene as needed for each experiment (1:1, 4:5, or 3:5 thiol-ene ratio).

*Mechanical analysis:* GelNOR solutions from different aliquots of the same synthesis batch were casted in a cylindrical mold (6 mm diameter, 2 mm height), and crosslinked for 10 minutes (CI-1000, Ultraviolet Crosslinker,  $\lambda = 365$  nm,  $I = 8$  mW/cm<sup>2</sup> UVP, USA). Samples were washed in PBS at 37° C overnight to reach equilibrium swelling. To assess the compressive properties, the samples ( $n = 5$ ) were subjected to a strain ramp at 20% min<sup>-1</sup> strain rate until 30% deformation using a dynamic mechanical analyzer (DMA Q800, TA Instruments, The Netherlands). The compression modulus was calculated as the slope of the stress/strain curve in the 10–15% linear strain range. To assess the viscoelastic properties, the samples ( $n = 5$ ) were subjected to a strain recovery measurement at a constant 20% strain for 2 minutes and then left for recovery for 1 minute, with a preload force of 0.0010 N. The elasticity index was calculated as the ratio between the recovered stress and the maximal stress under constant strain.

*Photorheology:* Photorheology experiments on gelNOR precursor solutions to determine the crosslinking kinetics were assessed using a DHR2 rheometer (TA Instruments, The Netherlands). Time sweep experiments were performed at a frequency of 10.0 Hz, angular frequency of 62.83 rad/s, with 5.0% constant strain at 21° C ( $n = 3$ ). A volume of 100  $\mu$ L of gel was used with a gap size of 300  $\mu$ m. A 20.0 mm parallel EHP stainless steel plate was used as geometry. 30 seconds after the start of the measurement, the light source was activated (1200mha, AOMEES, China,  $\lambda = 365$  nm, intensity of 24 mW/cm<sup>2</sup> for the remaining 2.5 minutes).

*Soluble fraction and swelling ratio:* The sol-fraction and swelling ratio experiment was performed according to a recent publication.<sup>[173]</sup> Briefly, to assess sol-fraction of the gelNOR hydrogel formulation, cylindrical samples produced from different aliquots of the same synthesis batch (6 mm diameter, 3 mm height,  $n = 5$ ) were weighed immediately after crosslinking for their initial mass. Next, samples were placed in PBS and placed in the incubator at 37° C overnight. The next day, the hydrogel samples were weighed again, and their mass was measured as  $mass_{wet,t0}$ . Subsequently the hydrogels were lyophilized, and the dry mass ( $mass_{dry,t0}$ ) was measured. The samples were stored in PBS again to ensure

swelling of the dry gels and placed in the incubator at 37° C overnight. The wet mass of the hydrogels was measured as  $mass_{wet,t1}$ . The samples were lyophilized, and the mass of the dry samples was measured as  $mass_{dry,t1}$ . The sol-fraction of the hydrogel formulations was calculated with the following formula:

$$Sol - fraction [\%] = \frac{mass_{dry,t0} - mass_{dry,t1}}{mass_{dry,t0}} \cdot 100$$

**Formula 1:** Sol-fraction formula for analysis of the crosslinking properties of the gelNOR formulations.

The swelling ratio of the hydrogel formulations was calculated with the following formula:

$$Swelling\ ratio\ (q) = \frac{mass_{wet,t1}}{mass_{dry,t1}}$$

**Formula 2:** Swelling ratio for analysis of the swelling behavior of the gelNOR hydrogel formulations.

*Enzymatic degradation assay.* GelNOR hydrogels were swollen in PBS overnight and subsequently incubated in a 0.2% w/v collagenase type II in Dulbecco's modified Eagle Medium (DMEM, 31966, Gibco, The Netherlands) supplemented with 10% v/v heat-inactivated fetal bovine serum (FBS Gibco, The Netherlands), and 1% v/v penicillin and streptomycin (Life Technologies, The Netherlands) at 37° C. Samples were removed from the enzymatic solution at different time points (15, 30, 45, and 60 minutes, n = 3 independent samples per time point). The mass of the hydrogel samples was measured and compared to the initial mass of the hydrogels before enzymatic incubation to determine the degradation rate of samples over time.

*Volumetric printing:* GelNOR solutions were dispensed into cylindrical borosilicate glass vials (Ø 10 mm), which were then loaded into a commercial volumetric 3D printer (Tomolite V1, Readily3D, Switzerland), equipped with a 405 nm laser, set to deliver an average light intensity of 11.98 mW/cm<sup>2</sup> within the printing volume. Prior to printing, the samples were cooled to 4° C to achieve physical gelation of the gelatin-based materials. Custom-designed STL files were loaded into the printer software (Apparite, Readily3D, Switzerland). After the printing process, the vials were heated to 37°C and washed gently with 37° C PBS to retrieve the prints. To ensure homogenous crosslinking, the sample was submerged in 0.1% w/v solution of LAP in PBS and irradiated for 1 minute in a UV oven.

*Volumetric photografting:* Printed constructs were subjected to a second printing step to induce spatio-selective photografting. Samples were printed at equimolar amounts of thiol to norbornene at a 5% w/v gelNOR concentration. Next, the printed samples were washed with PBS overnight, and infused with a fluorescent probe molecule, Cy3-PEG-SH (0.06 w/v%). To characterize the photografting reaction, several formulations of the infusion mix were prepared containing varying amounts of LAP (0.6, 0.8, or 1.0%



w/v concentration) and (2,2,6,6-Tetramethylpiperidin-1-yl)oxyl (TEMPO) (0, 0.006, 0.008, or 0.01% w/v concentration), as inhibitor of the thiol-ene grafting reaction. The printed constructs were infused with the infusion mix at 4° C for 2 hours. Next, the gels were placed back into the printing vials with a small amount of gelatin (5% w/v in PBS) to ensure thermal gelation and fixation of the construct inside the vial. The grafting process was performed in the printer, by loading STL files of the pattern to be grafted into the Apparite software, and performing a new tomographic light exposure step, to induce the 3D patterning of the fluorescent Cy3-PEG-SH in the programmed geometry. For the characterization of the volumetric grafting reaction, an array of vertically aligned cylindrical disks (3 mm diameter 1 mm height) were grafted within a gelNOR cylinder (6 mm diameter, 20 mm height), with every disk exposed to a different dose (dose range: 250, 750, 1250, 1500, 1750, and 2000 mJ/cm<sup>2</sup>) (**Figure 4A**). The accuracy of the photografting process was assessed imaging cross-sections of these samples with a fluorescence microscope (Leica Microsystems, Germany), and the fluorescence intensity within the grafted regions of interest was compared to that of off-target areas. To assess the accuracy of photografting, 3 different ratios were calculated using the following formulas:

$$\text{Grafting Specificity} = \frac{\text{Fluorescence of interest region}}{\text{Fluorescence of side bands}}$$

**Formula 3:** Grafting specificity formula for analysis of grafted GelNOR hydrogels with fluorescent dyes.

$$\text{Grafting Intensity} = \frac{\text{Fluorescence of interest region}}{\text{Hydrogel autofluorescence (background)}}$$

**Formula 4:** Grafting intensity formula for analysis of grafted GelNOR hydrogels with fluorescent dyes.

$$\text{Off - target grafting} = \frac{\text{Fluorescence of side bands}}{\text{Hydrogel autofluorescence (background)}}$$

**Formula 5:** Off-target grafting formula for analysis of grafted GelNOR hydrogels with fluorescent dyes.

Using optimized grafting parameters, complex, arbitrary 3D patterns of the Cy3-PEG-SH were imparted within custom designed, 3D printed objects. Finally, the constructs were washed with PBS for a maximum of 5 days, until the uncrosslinked dye was completely removed from the gel. Subsequently, the photografted constructs were imaged with a light-sheet microscope. To demonstrate the possibility of grafting multiple molecules in a sequential fashion, a second grafting process was also performed using Cy5-PEG-SH as a fluorescent dye, using the same components of the grafting cocktail.

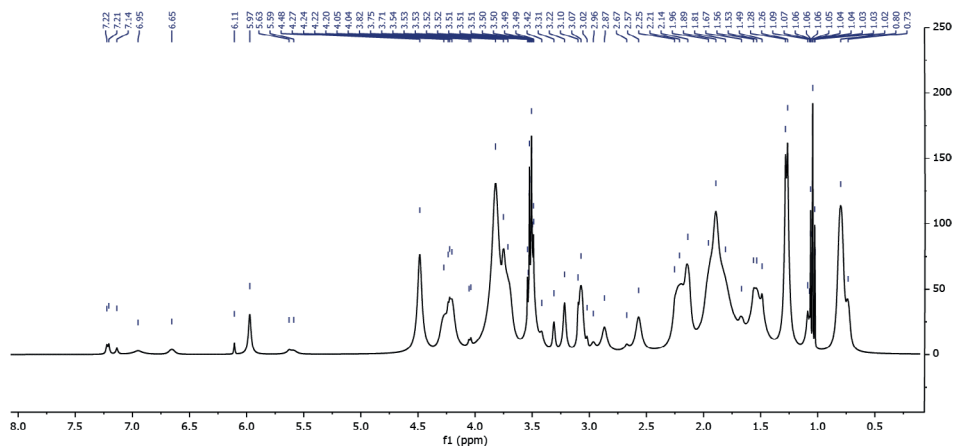
*Volumetric grafting of VEGF and cell culture assays:* Cylindrical constructs with a perfusable channel spanning through the center of the construct were volumetrically printed as described above, and a pro-angiogenic growth factor was photografted on the bottom half of these constructs (n = 4 replicates samples, single HUVEC donor line). To ensure homogenous mechanical properties in the grafted and non-grafted regions, the bottom

half (non-grafted) of the construct was post-cured immediately after printing at the same light dose that was subsequently used during photografting (750 mJ/cm<sup>2</sup>). Samples were then washed and incubated overnight at 4°C in an infusion mix of LAP (1% w/v), TEMPO (0.008% w/v), and recombinant human vascular endothelial growth factor (1000 ng mL<sup>-1</sup>; VEGF<sub>165</sub>, PeproTech). The volumetric photografting process was conducted as described above to deliver an average light dose of 750 mJ/cm<sup>2</sup> to the top half of the construct and generate constructs with anisotropic VEGF patterning. The constructs were then washed at 37° C for 5 hours to remove excess, non-grafted VEGF. Green fluorescent protein (GFP)-tagged human umbilical vein endothelial cells (GFP-HUVECs, Angio-Proteomie, Boston, USA, passage 5) were seeded into the channel within the printed construct at a concentration of 10<sup>7</sup> cells mL<sup>-1</sup>. To ensure homogenous seeding through the round channel, the samples were placed in rectangular PDMS molds and rotated 90° every 15 minutes for the first hour of culture. Cell-seeded constructs were cultured in Endothelial Cell Growth Medium-2 (EGM-2) containing Endothelial Basal Medium-2 + SingleQuots (except VEGF), 100 U mL<sup>-1</sup>-100 µg mL<sup>-1</sup> PenStrep, and 10% heat-inactivated FBS. Samples were cultured at 37° C and 5% CO<sub>2</sub>, medium was refreshed every day. To assess the effect of non-grafted VEGF, the full EGM-2 medium (including VEGF) was used for control samples. On day 3, fluorescent images of the GFP-HUVEC growing along the printed channels were acquired via confocal laser scanning microscopy (SPX8, Leica Microsystems, The Netherlands). The HUVEC area coverage and cell spanning depth (distance from inner side of the lumen to the outer edge of the lumen, or sprouting cells) were measured with Fiji,<sup>[491]</sup> and junction numbers were analyzed using the vessel analysis software AngioTool.<sup>[551]</sup>

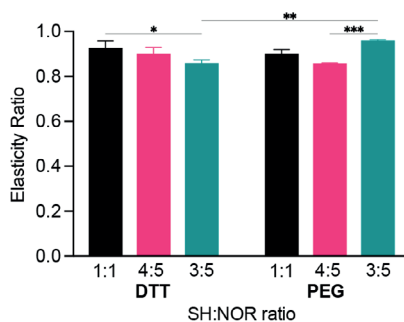
*Statistics:* Results were reported as mean ± standard deviation (SD). Statistical analysis was performed using GraphPad Prism 9 (GraphPad Software, USA). Comparisons between experimental groups were assessed via one or two-way ANOVAs, followed by post hoc Bonferroni correction to evaluate differences between groups. When normality could not be assumed, non-parametric tests were performed. Differences were found to be significant when  $p < 0.05$ .

## SUPPORTING INFORMATION

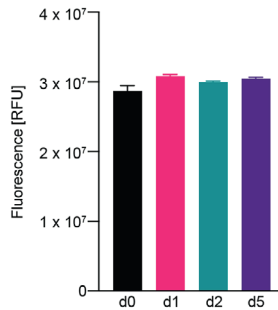
## Supplementary Figures



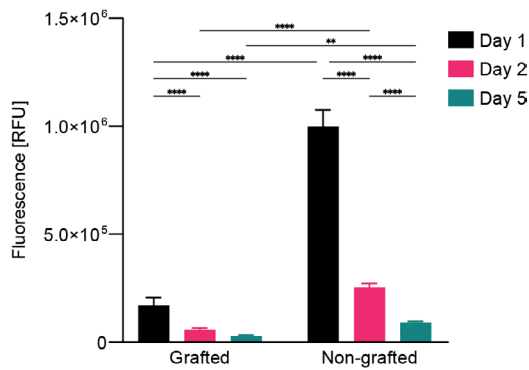
**Supplementary Figure S1:**  $^1\text{H}$ -NMR spectrum of gelNOR in  $\text{D}_2\text{O}$ .  $^1\text{H}$  NMR (400 MHz,  $\text{D}_2\text{O}$ )  $\delta$  = 5.97 (s, 1H), 4.48 (s, 3H), 4.30 – 4.18 (m, 3H), 3.82 (s, 10H), 3.75 (s, 0H), 3.71 (s, 2H), 3.52 (dd,  $J$  = 7.4, 3.8 Hz, 1H), 3.50 (s, 3H), 3.22 (s, 1H), 3.07 (s, 2H), 2.87 (s, 1H), 2.57 (s, 1H), 2.21 (s, 3H), 2.14 (s, 2H), 1.96 (s, 1H), 1.89 (s, 8H), 1.81 (s, 6H), 1.58 – 1.51 (m, 4H), 1.49 (s, 1H), 1.27 (d,  $J$  = 7.5 Hz, 5H), 1.11 – 1.00 (m, 2H), 0.80 (s, 5H), 0.73 (s, 1H).



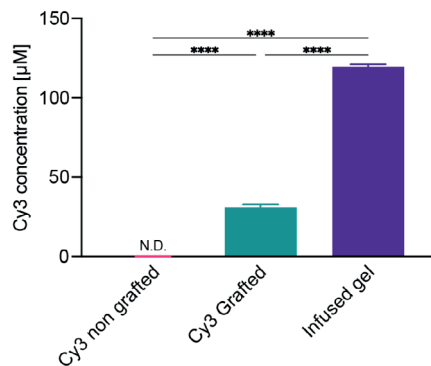
**Supplementary Figure S2:** Elasticity ratio of gelNOR hydrogels employing crosslinkers of different lengths and different thiol-to-norbornene molar ratios as measured by DMA as a result of stress-relaxation measurements ( $n = 3$ ). \* =  $p < 0.05$ , \*\* =  $p < 0.01$ , \*\*\* =  $p < 0.001$ .



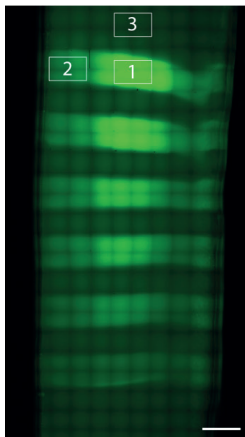
**Supplementary Figure S3:** Fluorescent intensity of the infusion mix after infusing of the hydrogel samples at different time points. Showing no significant decrease in fluorescence over time (n = 3).



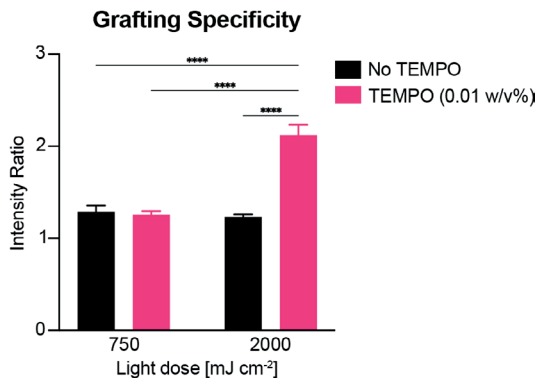
**Supplementary Figure S4:** Fluorescent intensity of washing water of both grafted and non-grafted gelNOR hydrogels at different time points (n = 5). \*\* = p < 0.01, \*\*\* = p < 0.001, \*\*\*\* = p < 0.0001.



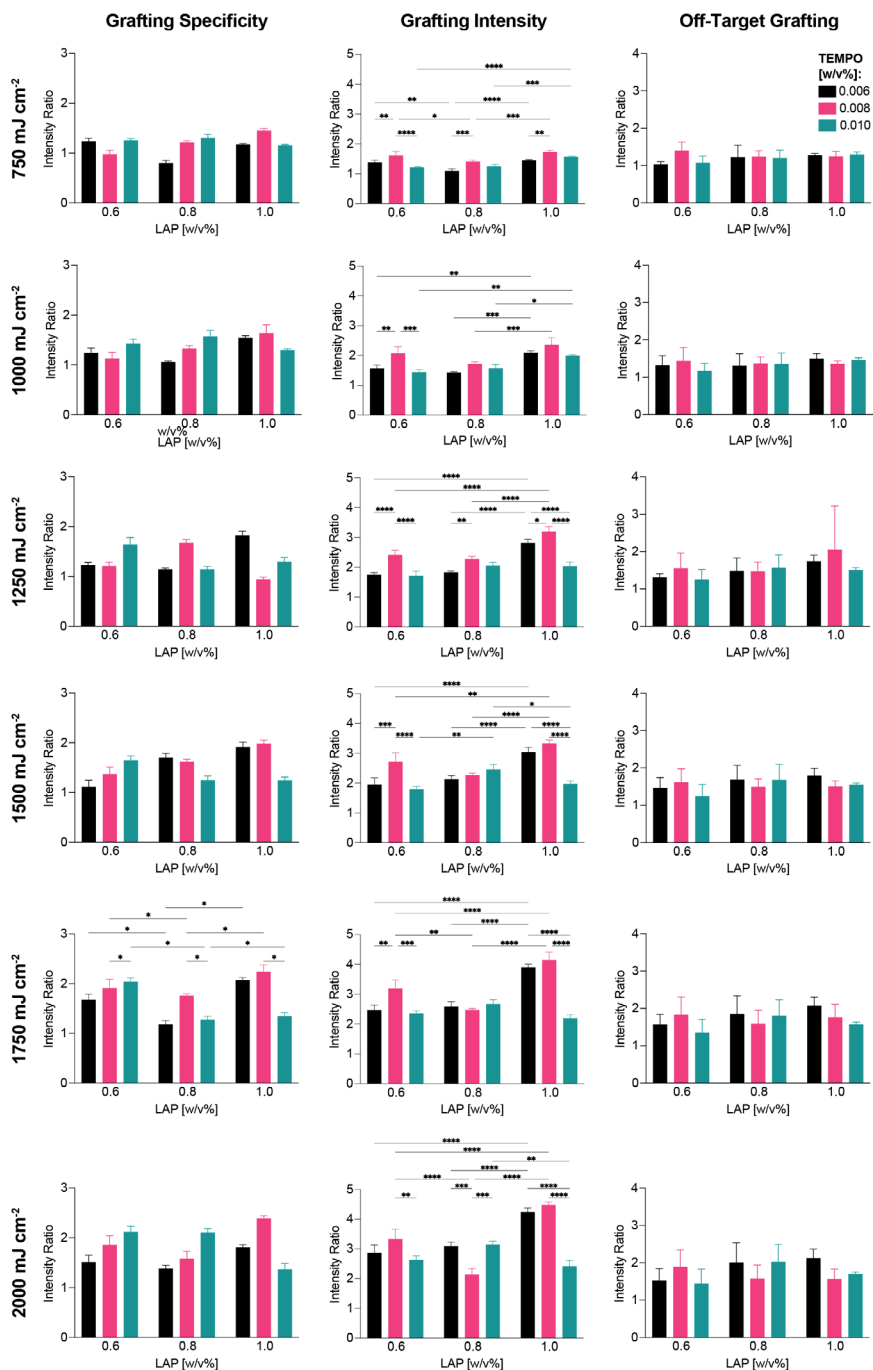
**Supplementary Figure S5.** Cy3-PEG-SH concentration quantification of non-infused, non-grafted and grafted gelNOR hydrogels after washing. The hydrogel samples were enzymatically degraded using 0.2% w/v collagenase, after which the fluorescent intensity was measured and the concentration of dye inside the hydrogel was calculated (n = 3). N.D. = Not Detected. \*\*\*\* = p < 0.0001.



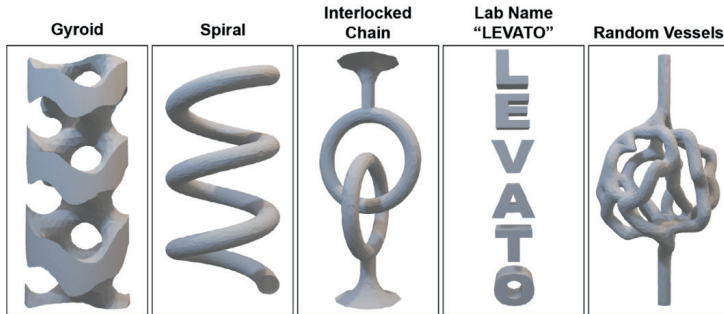
**Supplementary Figure S6:** Fluorescence image of gelNOR cylinder as used for grafting optimization used in **Figure 4** to optimize photografting, explaining how the ratios were measured. Area 1 is used to measure the intensity of the intended photografting region. Area 2 is used to measure intensity off-target grafting of the unwanted regions. Area 3 is used to measure the intensity of the background. From these values, the grafting specificity (ratio of area 1 vs. area 2), grafting intensity (ratio of area 1 vs. area 3), and off-target grafting (ratio of area 2 vs. area 3) was measured. This image is from a gelNOR hydrogel with a formulation consisting of 1.0% w/v LAP, 0.006% w/v TEMPO, and 0.06% w/v Cy3-PEG-SH. Scale bar = 1 mm.



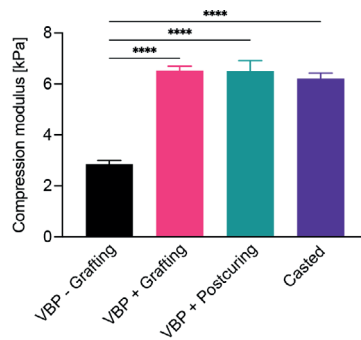
**Supplementary Figure S7:** Grafting specificity of Cy3-PEG-SH on gelNOR hydrogels without radical scavenger TEMPO and with 0.010% w/v TEMPO included in the grafting cocktail, with a stable photoinitiator concentration (0.6% w/v LAP) and at two volumetric printing light doses (750 and 2000 mJ/cm<sup>2</sup>) (n = 3). \*\*\*\* = p < 0.0001



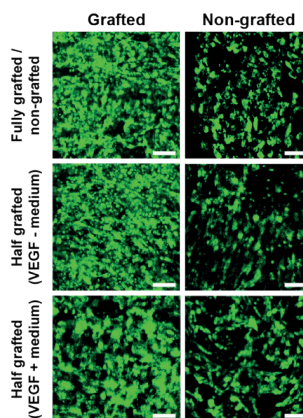
**Supplementary Figure S8:** Full grafting optimization (specificity, intensity and off-target grafting) of Cy3-PEG-SH on gelNOR hydrogels at different light doses (750 – 2000 mJ/cm<sup>2</sup>), photoinitiator (0.6 - 1.0% w/v) and crosslinking inhibitor concentrations (0.006 - 0.010% w/v) (n = 3). \* = p < 0.05, \*\* = p < 0.01, \*\*\* = p < 0.001, \*\*\*\* = p < 0.0001.



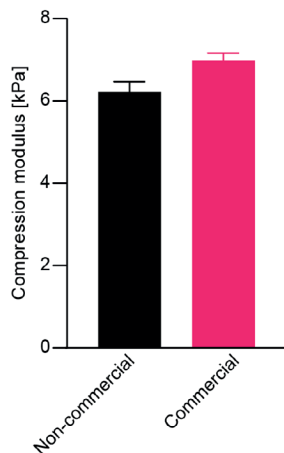
**Supplementary Figure S9:** STL models of the structures grafted onto gelNOR hydrogels in **Figure 5**. A gyroid, spiral, interlocked chain, lab name "LEVATO", and a random vessel-like network.



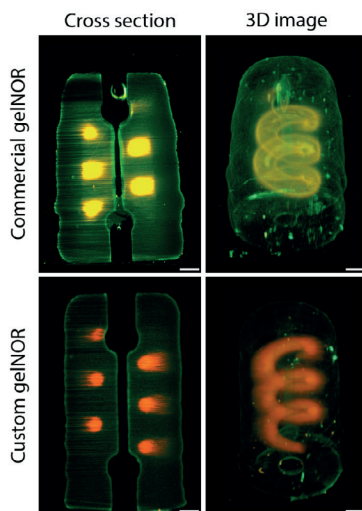
**Supplementary Figure S10.** Compression modulus of volumetrically printed 5% w/v gelNOR hydrogels using DTT as crosslinker in a 1:1 thiol-ene ratio with 0.1% w/v LAP as photoinitiator. Comparison of the compression modulus between non-grafted, grafted with Cy3-PEG-SH (750 mJ/cm<sup>2</sup>), and post-cured (750 mJ/cm<sup>2</sup>) and casted samples (n = 3) in absence of the thiolated PEG probe. \*\*\*\* = p < 0.0001.



**Supplementary Figure S11:** Representative confocal images of HUVECs (GFP-positive) seeded on portions of the lumen of the printed vascular chip model (n = 3 biological replicates). Scale bars = 100  $\mu$ m.



**Supplementary Figure S12:** Compression modulus comparison between commercially available gelNOR from BIO INX B.V. and custom synthesized non-commercially available gelNOR crosslinked under identical conditions (1:1 SH:NOR ratio using DTT as a crosslinker + 0.1% w/v LAP). Young's modulus for both gels showed no significant differences (n = 5).



**Supplementary Figure S13:** Comparison of complex photografting of a spiral structure around a hollow channel, between commercially available gelNOR (supplied by BIO INX B.V.) and custom made gelNOR. Showing no differences in photografting application both in cross-sectional view as in 3D view. Samples were exposed to same infusing concentration (0.06% w/v Cy3, 1.0% w/v LAP, and 0.008% w/v TEMPO) and same light dose (750 mJ/cm<sup>2</sup>). Scalebar = 1 mm.



## Supplementary Methods

*Nuclear magnetic resonance (NMR):* The  $^1\text{H}$ -NMR spectrum of the gelatin-based materials was measured by NMR (400 MHz, Agilent 400 MR-NMR, Agilent technologies, USA). The material was dissolved in  $\text{D}_2\text{O}$  at a 4% w/v concentration. NMR was not used to calculate the DoF of the material since a big overlap occurs with the material and the functionalized groups, leading to inaccurate calculation of the DoF following this method ( $n = 3$  independently synthesized batches). NMR was used as a purity check of the material.

*Cy3 concentration quantification:* Cylindrical gelNOR (5% w/v, 1:1 thiol-ene ratio) samples with a volume of 100  $\mu\text{L}$  were prepared. These samples were infused with the Cy3-PEG-SH infusion mix as described previously. The hydrogels were photografted at a dose of 750  $\text{mJ}/\text{cm}^2$ . Samples were treated in 4 different conditions: 1) non-infused hydrogel, 2) infused hydrogel which was not grafted, 3) hydrogel which was infused and grafted and 4) freshly infused hydrogel without washing (to determine the initial loading concentration of Cy3-PEG-SH). After photografting samples were washed in PBS for 2 days at 4° C. Subsequently, the hydrogels were enzymatically degraded using 0.2 w/v% collagenase solution at 37° C for 1 hour. The fluorescent intensity for all conditions was measured with a CLARIOstar Plus® (BMG Labtech, Germany) plate reader with excitation at  $\lambda = 530$  nm, and emission at  $\lambda = 580$  nm. From this measurement, the concentration of fluorescent dye in the hydrogel formulation was calculated using a known standard curve (**Supplementary Figure S5**).





# **Chapter 10**

## **General Discussion and Future Perspectives**



In the current healthcare landscape, enhancing the efficiency of the drug discovery pipeline is of utmost importance to counter the increasing incidence of chronic diseases and the differential patient response to drugs and other treatment strategies. In order to improve the efficacy of the drug discovery process, the development of advanced preclinical testing strategies that better mimic healthy and diseased human processes is necessary to ensure that candidate drugs and therapies can be more accurately studied before transitioning into the very costly clinical trial phase.<sup>[5,6,460]</sup> With governmental and social initiatives encouraging the development of animal-free research that can overcome the low-predictability of human conditions shown in various animal models,<sup>[7-9]</sup> the field of biofabrication provides advanced fabrication technologies that could fill the translational gap of human-based *in vitro* models in the advanced phases of the preclinical testing pipeline. However, while the existing biofabrication techniques have enabled the creation of structurally complex, three-dimensional (3D) biological tissue analogues,<sup>[109,110,112]</sup> the current state of the field has encountered several key obstacles that still hinder the achievement of functionally predictable and accurate *in vitro* models that are needed as late-stage preclinical testing platforms. Throughout this thesis, several steps have been taken towards fulfilling the aim of developing “**new biofabrication approaches, encompassing 3D bioprinting technologies, powerful biological building blocks, and smart biomaterials, that facilitate the development of advanced human *in vitro* models with native tissue-like functionality**”. In the three overarching sections, different challenges in the development of advanced biofabricated *in vitro* platforms have been addressed and will be further discussed below.

## ADVANCED BIOPRINTING STRATEGIES FOR MIMICKING NATIVE TISSUE ORGANIZATION

Existing biofabrication strategies exhibit significant limitations in their basic working principles that hinder the architectural complexity and ensuing shape-function relationships of bioprinted tissue analogues, which have thus far hampered their adoption as standardized preclinical and clinical research models. To recapitulate native tissues from a functional perspective, it is crucial to mimic their biochemical composition in a structurally accurate way, mimicking the micro-scale and bulk shape of tissues to enable intricate multicellular interactions and matrix organization that gives rise to tissue-specific functionalities, as well as providing the mechanical stability required for *in vitro* tissues to mature and resist physiological stresses. **Part I** of this thesis focused on the development of novel bioprinting techniques that provide enhanced control over various of these features. **Chapter 2** introduced a novel approach, cell electrowriting (CEW), that enables the precise, high-resolution patterning of cell-laden, naturally derived biopolymers through an adaptation of the melt electrowriting (MEW) process.

It has long been established that resolving the microscale features of native tissues is instrumental in replicating salient elements of native cellular organization, extracellular matrix structure and the cell-cell and cell-matrix interactions, features that are essential to the functionality of many tissue engineered constructs.<sup>[107,109,601]</sup> While other bioprinting approaches have been shown to achieve such single-cell patterning resolutions such as cell electrospinning,<sup>[181,602]</sup> multiphoton printing<sup>[161,174,603]</sup> and laser induced-forward transfer,<sup>[604]</sup> this approach introduces a high degree of positional control over cell patterning within continuous biopolymer fibers, providing intricate cellular organization and controlled directionality at the microscale. Such an approach could potentially be applied in future mechanobiology studies, where the interaction of cells with their fibrous microenvironment and the resulting effects on cellular alignment and orientation are essential to induce native-like functions. Mechanobiological processes of cells within highly aligned tissues such as cardiac, vascular, and musculoskeletal tissues, have been extensively studied using fibrous substrates and provided insights into the molecular mechanisms involved in microscale tissue organization.<sup>[605-607]</sup> Therefore, the high architectural control over cellularized fiber deposition and cell directionality in CEW could be a valuable additional biofabrication tool to gain further understanding into microscale cellular processes occurring in tunable microarchitectures. However, a drawback of CEW and principally of all high-resolution approaches, capable of patterning cells and materials at single-cell resolutions, is the inherent limitation regarding achievable print sizes. This severely hinders their scalability when it comes to developing multi-scale tissue mimics that also resemble the bulk shape and multicellular composition of their native counterparts. Furthermore, while the presented CEW process could potentially be performed with various natural and synthetic hydrogels, the various material requirements of electrohydrodynamic processes (viscosity, conductivity, surface tension, and fiber stabilization processes),<sup>[276]</sup> makes the development of CEW-compatible materials that are also optimal for cell culture a challenging effort. As observed in conventional printing approaches,<sup>[128]</sup> achieving optimally printable material properties for CEW (*i.e.* high viscosity, reduced ion and salt hydrogel content), can have detrimental effects on cell viability and behavior unless a compromise between printability and cell compatibility is made. As possible directions to expand the library of CEW-printable materials, the development and optimization of highly viscous hydrogels is required, through the incorporation of high molecular weight polymers or the addition of viscosity enhancers as shown in this chapter. However, to still enable high cell viability and functionality, material modifications such as the incorporation of dynamic or supramolecular bonds could be a valuable addition to enhance cell stretching and migration within these more printable biomaterials.

On the one hand, approaches such as cell electrowriting may be beneficial to induce a high degree of cellular organization in a small region of a tissue of interest and study fundamental

processes, for example, those dependent on cell signaling and mechanobiology. However, CEW-based and other high-resolution printing methods may not be the best suited to provide the complex 3D macroenvironments that can better encompass multiple cell types and gradients of biochemical and mechanical cues as observed *in vivo* given their long processing times. Even conventional lower-resolution layerwise approaches (*i.e.*, extrusion bioprinting) that are widely used in the field of biofabrication undergo a significant increase in processing times as the print volume is increased, hampering the upscaling of bioprinted constructs that can replicate the complex macroscopic shape-to-function relationships of native tissues.<sup>[121]</sup> In **Chapter 3**, the volumetric bioprinting (VBP) approach was first introduced, bringing about a paradigm shift from the conventional layer-by-layer manufacturing approach towards a single-step printing process. This radical change in printing modality was achieved through the use of coordinated sequences of tomographic back projections directed towards light-sensitive polymers, yielding highly convoluted 3D structures when the cumulative dose from these projections surpassed the material's crosslinking threshold.<sup>[224,225]</sup> Here, cell-laden, centimeter-scale structures could be bioprinted in tens of seconds, exhibiting the fastest printing speeds in the field of biofabrication to date. Not only was VBP shown to be scalable while maintaining such short printing times and high cell viability, but the design freedom of the technique also proved to be far greater than as seen in layerwise techniques, where overhangs or free-standing objects are extremely difficult to resolve, especially in short processing times to prevent impairments to cellular functionality. These features make this printing modality a great addition to the bioprinting toolkit, where replicating the convoluted macro-architectures of native tissues can be achieved in a matter of seconds, facilitating the fabrication of clinically-relevant sized structures. Nonetheless, the development of this technique does not overcome all drawbacks of the bioprinting process. Since its inception, a wide range of volumetrically printable materials has been developed.<sup>[608]</sup> However, in the context of biocompatible hydrogel based bioresins for cell encapsulation, significant challenges remain, especially when aiming to develop materials that facilitate cell migration and support the cells' own ability to self-assemble into tissue-like structures. Most types of hydrogels that facilitate these cellular behaviors typically display low stiffnesses and relatively low polymer content. When volumetrically printing these soft materials, especially into convoluted structures with large channels or overhanging features, maintaining the shape fidelity of these structures is an important challenge that must be addressed in order to develop stable complex-shaped tissue analogues.

There is, therefore, a need to optimize the volumetric bioprinting approach and material library to facilitate the fabrication of convoluted cell-laden hydrogel structures that exhibit optimal cell behavior while maintaining high shape fidelity post-printing. Hydrogel reinforcement with thermoplastic polymer structures,<sup>[167,271,284,609]</sup> printing of multiple materials with varying mechanical properties,<sup>[135,170,610]</sup> or the development of hybrid

hydrogel biomaterials with higher stiffness that can facilitate cell migration and matrix remodeling through the incorporation of dynamic bonds,<sup>[611-613]</sup> are concepts that have been employed in conventional extrusion bioprinting methods with significant success. To achieve construct stability and shape fidelity of volumetrically bioprinted constructs, the convergence of melt electrowriting with volumetric printing (VolMEW) presented in **Chapter 4** presents one of various approaches to enhance the mechanical stability of printed structures. In this converged approach, the mechanical properties of low-stiffness hydrogel prints were significantly enhanced through the incorporation of tubular MEW meshes, as well as the shape stability of tubes with open macro channels (> 3 millimeters). While such a reinforcing approach has demonstrated similar mechanical enhancement of tubular cell-seeded constructs without a hydrogel component,<sup>[284]</sup> the incorporation of VBP in this case generates the possibility of developing highly complex tubular architectures that can be used to mimic various tissue-specific features (*i.e.*, intestinal tube with villi, fenestrated and branching vascular structures) and disease models (*i.e.*, stenosis of blood vessels and other tissues). The concept of technology convergence as presented in this chapter has been the focus of ample research in recent years in the field of biofabrication, due to the need to develop advanced approaches that can mimic the intricate hierarchy of native tissues, which often requires structural and biomechanical properties that individual bioprinting approaches cannot currently provide.<sup>[131]</sup>

Within the scope of the volumetric printing process, this multi-technology convergence has recently been explored to address some of the major drawbacks of this novel approach as well as other light-based printing technologies. For example, an alternative approach to reinforce volumetrically printed structures demonstrated the combination of materials with differing mechanical properties through the combination of embedded extrusion bioprinting of stiff hydrogel patterns within granular hydrogels and the subsequent volumetric bioprinting of the support bath into complex architectures.<sup>[474]</sup> Another example of technology convergence addressed the limit on the achievable resolution of VBP (>20  $\mu\text{m}$  positive features and >100  $\mu\text{m}$  negative features), which has hindered the creation of multi-scale printed structures to date. Rizzo *et al.*, demonstrated the feasibility of combining the high-speed printing of large VBP constructs with perfusable macrochannels with the subsequent 2-photon ablation of high-resolution ( $\sim 2 \mu\text{m}$ ) microchannels.<sup>[614]</sup> The resulting convoluted and multi-scale tubular networks greatly resemble native vascular structures, but given the short working depth of the 2-photon ablation process ( $\sim 500 \mu\text{m}$ ), such a converged approach will be challenging to upscale. In its current form, such an approach can only be used to pattern thin constructs of the border regions of larger VBP-produced structures. An alternative material-based approach to push the micro-scale resolution of volumetric bioprinting is presented in **Annex I**. Here, thermally responsive, photocrosslinkable hydrogels were developed for volumetric bioprinting. Post-printing thermal treatment of these developed resins facilitated the



creation of high-resolution prints, achieving the highest resolution of negative features to date with this printing approach ( $< 40 \mu\text{m}$ ). While the printing resolution of 2-photon ablation and other multiphoton strategies remains higher, the material-approach described here provides the full extent of the freedom of design offered by VBP, without the penetration depth restrictions posed by these other approaches.<sup>[615-617]</sup> With further optimization of the shrinking process of these hydrogels, and with increased control over temperature-dependent shrinking differences,<sup>[618]</sup> further steps can be taken towards the creation of multiscale volumetric structures.

Overall, the chapters outlined in this part of the thesis have made significant strides towards tackling key fabrication-centered challenges towards the creation of advanced bioprinted constructs that can serve as the next generation of *in vitro* platforms. However, there are further aspects related to the biological functionality and maturation of bioprinted structures that are crucial in the development of precise and predictive platforms utilizing these advanced printing techniques.

## INCORPORATING ADVANCED BIOLOGICAL BUILDING BLOCKS WITHIN THE BIOPRINTING PROCESS IN TISSUE-SPECIFIC PLATFORMS

Native tissue function arises from an intricate cascade of multicellular interactions with their surrounding 3D environment, where signaling and mechanical cues are regulated by constant feedback loops. Mimicking this complex 3D microenvironment goes beyond printing anatomically accurate architectures. It requires the mimicry of native cellular organization and interactions that single cell types or multicellular co-cultures of stem or primary cells cannot easily recapitulate without the body's intricate biochemical guidance. To complement the fabrication-based advances for creating complex 3D structures presented in Part I of this thesis, **Part II** aimed at incorporating cutting-edge biological tools to enhance cellular function and maturation within complex 3D architectures. As illustrated by the growing trend of converging complementary bioprinting approaches to harness their respective advantages, the same principle applies to the convergence of different *in vitro* modeling technologies. In this case, the freedom of design offered by bioprinting can be further leveraged through the incorporation of advanced pre-organized cellular assemblies and microtissues, such as tissue-like spheroids and organoid technology, to increase the biological mimicry of the resulting structures.<sup>[139,142,619,620]</sup> In this thesis, one of the model organs chosen to explore this convergence of bioprinting with advanced biological building blocks was the liver, given its critical role in blood detoxification and maintenance of systemic homeostasis and its importance in the field of toxicology and the drug discovery process. Replicating this organ's highly

complex multicellular and multifunctional nature has been a major challenge in the field of tissue engineering, and significant drawbacks remain regarding the mimicry of the 3D organization and intercellular interactions of previously developed models.<sup>[621,622]</sup> In **Chapter 5**, the possibility of creating highly functional bioprinted liver models that exhibit physiologically-relevant functions was demonstrated through the incorporation of human-derived liver organoids, which hold great expansion capacity while maintaining genetic stability, multilineage differentiation capabilities and exhibit liver-specific markers and functions.<sup>[623]</sup> Organoids, which are three-dimensional structures derived from self-organizing (pluripotent) stem cells, progenitor, and/or differentiated cells exhibit superior recapitulation of the native tissue organization and function due to their enhanced cell-cell and cell-matrix interactions.<sup>[35]</sup> These structures have emerged as powerful tools for understanding organ development, modeling diseases, and testing potential therapeutics in patient-specific 3D organized platforms. The inclusion of organoids as biological building blocks in the bioprinting process can aid in overcoming some limitations of organoid technology related to size, vascularization, and architectural complexity, with bioprinted scaffolds providing support and spatial guidance to enhance the controllability of organoid growth and the emergence of higher-level functional characteristics.<sup>[39,46,51,56]</sup> Few studies have explored this potential synergy, but there is already significant evidence that spatial patterning of organoid structures via bioprinting,<sup>[386]</sup> and other methods to control the architecture and microenvironment properties surrounding them,<sup>[624,625]</sup> can have organoid can guide and enhance tissue morphogenesis *in vitro*. In this first study presented in **Chapter 5**, liver organoids were bioprinted with extrusion bioprinting technology, to enable the precise positioning of these complex 3D cellular structures into an open pore architecture that would result in higher oxygen and nutrient supply to the organoids and potentially increase their metabolic exchange rate compared to non-printed samples. These printed organoid structures demonstrated differentiation capacity into metabolizing hepatocytes capable of responding to the presence of common drug compounds. However, the significant morphological damage induced on the organoids to facilitate extrusion, as well as from the shear stresses of the extrusion nozzle, the large inter-donor variability, and the relatively simple grid-like architecture printed with the soft bioinks needed to favor organoid function posed significant limitations to the process and did not show significant advantages over conventional casting methods. Nonetheless, it opened the possibility of shaping such complex structures into controllable 3D shapes while maintaining their basic functions and differentiation potential.

10 With the development of VBP described in this thesis, this new and contactless printing approach posed an optimal opportunity to further enhance the architectural complexity into which organoids could be encapsulated, with the aim to elicit shape-dependent metabolic behaviors and develop functional liver units (**Chapter 6**). Here, the VBP process was first optimized to enable the incorporation of increased single cell and

organoid densities in line with previous liver *in vitro* models to better replicate native liver functions and enabled the printing of highly complex liver organoid-laden structures.<sup>[413–415]</sup> By optically tuning the gelatin methacryloyl bioresin to reduce the light scattering phenomenon shown to impact printing resolution, the tuned bioresin did not only enhance printing resolution in the presence of cells, but also resulted in a soft (2 kPa) matrix for the organoids to grow in, within the stiffness range of healthy liver tissue, as determined by conventional clinical guidelines.<sup>[626]</sup> The growing importance of optical and crosslinking properties, and photons-materials interactions in light-based printing, including phenomena like light scattering, underscores the demand for new materials or the modification of existing ones that align with these technologies.<sup>[421]</sup> These efforts are particularly significant due to the increased attention these technologies are receiving, owing to their superior design flexibility and in the case of VBP, its scalability.<sup>[119,120]</sup> While extrusion printing methods are not strongly influenced by the optical properties of a bioink (rheological properties like shear thinning and viscosity play a much larger role on printability),<sup>[130]</sup> VBP has its specific requirements in terms of bioresin transparency, absorbance, crosslinking kinetics and refractive index homogeneity to ensure accurate and high-resolution printing. Therefore, the design, characterization and application of a compatible bioresin library is crucial to expand the range of matrices that can be incorporated into cell-laden prints. In the present study, the soft, optically tuned bioresins that proved to facilitate organoid survival and function could still be shaped into complex architectures without undergoing structural artefacts resulting from the collapse of stacking layers typically observed in layerwise methods. Volumetrically bioprinted organoid structures not only retained their differentiation capacity, but in this case, due to the stress-free printing method, the structural integrity of the organoids was maintained, showing highly organized, polarized structures compared to casted samples. When further shaped into complex, mathematically defined architectures with distinct structural properties,<sup>[444,627]</sup> and cultured in a dynamic perfusion system to provide mild mechanical cues throughout culture, these *in vitro* liver units exhibited a shape-dependent capacity to metabolize common waste products depending on the architectural shapes into which they were placed. This study highlights the importance of the bioprinting process in creating convoluted shapes designed to guide and control biological function and is a clear example of how a combination of advanced tools (bioprinting, organoids, and perfusion systems) can bring about enhanced tissue-like functionality. Drawing from design concepts stemming from different disciplines, such as water purification membrane or dialysis device fabrication,<sup>[444,445]</sup> efforts should be placed to further explore the design and modeling different structural compositions and their effect on flow, shear stresses and nutrient and oxygen supply within bioprinted structures. While the metabolic rates observed here are in line with previous literature,<sup>[414,417,451]</sup> characterizing the overall effect of such liver units in an *in vivo* setting would be beneficial to assess the physiological

relevance of the developed platform, not just as a preclinical model, but potentially as a regenerative implant capable of recovering the metabolic capacity of the liver. This shape-to-function relationship provided by the bioprinting of predefined architectures can be further combined with the possibility to develop patient-specific organoids for various tissues.<sup>[36,37,352,628,629]</sup> This synergy of technologies would present an exciting possibility for personalized disease modeling, drug screening and development of tailored regenerative therapies.

To further explore the design freedom of VBP and its compatibility with other advanced biological tools, **Chapter 7** showcases the development of multi-material, induced pluripotent stem cell (iPSC)-derived cardiomyocyte laden heart model. In this instance, another highly versatile cellular technology is introduced into the VBP system. Induced pluripotent stem cells hold immense promise in regenerative medicine and biomedical research. These cells, derived from adult somatic cells possess the ability to transform into virtually any cell type in the human body. iPSCs provide a unique, ethically sourced platform for modeling diseases, screening drugs, and studying developmental processes.<sup>[630]</sup> Despite challenges regarding the standardization of generation and differentiation protocols, their patient-specific nature of these cells, like organoids, offer the potential to tailor treatments to individual patients.<sup>[630,631]</sup> The resulting iPSC-laden *in vitro* heart platform exhibited great design versatility, creating various simplified bi-chambered models with differing chamber volumes, as well as an anatomically shaped 4-chambered heart model. To create a mechanically competent construct, two mechanically distinct bioresins were printed, and enabled the maintenance of cellular function of iPSC-derived cardiomyocytes. While the developed heart platform proved to be compatible with medical imaging techniques, and some beating cell patches were observed throughout the construct and exhibited responsiveness to external damage cues, the maximum cellular density employed with this printing technique did not support sufficient cell-cell contacts to induce coordinated beating, and thus the evaluation of other clinically relevant outputs of the platform. Further development of the model is necessary to leverage the architectural advantages of VBP with the biological power provided by these iPSC cells.<sup>[488,489]</sup> For such approaches, where intricate cell alignment and contact is needed, various avenues could be considered, from the combination of optical and algorithmic<sup>[421]</sup> light scattering correction strategies to increase the processable cell densities with VBP and the use of infrared wavelengths displaying high penetration depth through cells and other opaque components, to the direct guidance of printed cells to self-assemble and align in predetermined orientations using growth factor gradient patterning along the heart walls,<sup>[277,566,568,569]</sup> embedding cells within highly aligned fiber meshes that guide their growth and alignment,<sup>[466,468,486]</sup> or through the direct orientation of cells through the manipulation of acoustic,<sup>[142]</sup> magnetic,<sup>[219,632]</sup> or electrical fields.<sup>[59,240]</sup>

All in all, **Part II** of this thesis employed the fabrication concepts developed in **Part I**

and incorporated advanced biological tools into the bioprinting processes, yielding tissue-specific platforms that exhibit native-like functional outputs and a high degree of control over architecture, which is shown to be a key factor in modulating biological activity of highly organized cellular structures. By harnessing the distinct advantages of self-assembled 3D cellular structures like organoids, or the powerful induced pluripotent stem cell technology within such complex architectures, important steps have been taken towards more precise control over cell fate. Nonetheless, in order to orchestrate the intricate developmental processes of tissues, more advanced approaches that incorporate biochemical cues into these complex structures are needed to achieve accurate models that encompass their multicellular and multifunctional nature.

## ENHANCING CELL FATE REGULATION THROUGH THE DEVELOPMENT OF SMART BIOMATERIALS

Beyond the incorporation of self-assembled cellular units to increase the mimicry of the cell-cell interactions characteristic of native tissues, a fundamental aspect required to ensure accurate functional outputs of *in vitro* platforms is the incorporation of spatially organized biochemical cues to guide cell behavior. In the body, signaling pathway activation and inhibition arises as a result of highly orchestrated multicellular and multi-tissue interactions, setting up tissue and organ development, as well as their subsequent functions. *In vitro*, without the constant feedback loops of surrounding tissues and multiple cell types organized in a hierarchical fashion, it is crucial to provide such biochemical cues in the correct timing and region of tissue engineered constructs. **Part III** of this thesis explored material-based approaches that facilitate the controlled delivery of bioactive cues to bioprinted constructs to enhance the localized control over cellular functions. **Chapter 8** shows the development of a controlled release system for bioactive compounds with cell fate guidance effects, consisting of biodegradable microparticles that could be incorporated into printable bioinks for their precise positioning within bioprinted structures. By combining the widely explored concept of controlled drug delivery<sup>[633–635]</sup> with the positional accuracy of 3D bioprinting, this study highlights the possibility to modulate the spatial and temporal presentation of bioactive compounds to cells already spatially patterned into tissue-specific organizations. In this particular study, the use of medical grade and FDA approved materials for both the microparticles, loaded anti-angiogenic drug and the collagen bioink also demonstrates the clinical translatability of such an approach. Nonetheless, while the speed and efficiency of release can be tailored through modifications of the microparticle formulation, there are limits to the controllability and long-term efficiency of this approach, especially where carefully coordinated bioactive factor availability, concentrations and positional accuracy are crucial to emulate native tissue heterogeneity. Furthermore, the precise localization and

distribution of these microparticles is limited by the resolution of the extrusion printing process in this case, resulting in functionalized regions ranging in the hundreds of micrometers, which may exceed the required resolution to pattern microscale gradients of bioactive compounds. Combining these microparticles with higher resolution technologies could be a solution to achieve higher control over the biofunctionalized regions. Approaches like electrowriting or laser-induced forward transfer (LIFT), where superior encapsulation resolutions of these particles could be achieved, could bring about higher positional control over this controlled release process. Furthermore, drawing from the ample research performed in the field of controlled drug delivery strategies, further improvements to enhance the specificity and temporal control over the process could be undertaken. One alternative is the combination of particles that allow differential release rates of one or more compounds. For example, hydrogel microspheres for controlled release have been developed with highly tuneable degradation rates.<sup>[636]</sup> Such controlled delivery approaches have also been used to achieve the delivery of living cells to therapeutic target regions, for instance, for controlled cardiac progenitor cell delivery and grafting in ischemic heart regions.<sup>[636]</sup> Furthermore, the printed material itself could be developed as a controlled release platform, as previously shown through the chemical modification of ceramic materials to tune the degradation and release rate of compounds embedded within.<sup>[637]</sup> Alternative methods in which the release of bioactive compounds is achieved through specific environmental stimuli like pH,<sup>[638,639]</sup> temperature,<sup>[639]</sup> or magnetic cues<sup>[640]</sup> for example could be employed to further refine the positional and temporal specificity of the compound release process.

To overcome some of these challenges, **Chapter 9** focuses on the development of an alternative approach to biofunctionalize 3D printed structures post printing with high positional accuracy and at high spatial resolutions. By leveraging the crosslinking capabilities of a previously employed gelatin-based hydrogel (gelatin norbornene)<sup>[212,278,291,576,641]</sup> not only to induce photopolymerization of this resin in a volumetric printer, but also to photopattern thiolated bioactive compounds throughout the polymer backbone, mechanically and chemically tunable printed objects could be fabricated. Similar photopatterning concepts have been previously explored to “decorate” hydrogel-based 3D structures with various material chemistries,<sup>[568,572,573,642]</sup> including thiol-ene materials<sup>[641]</sup> as shown in this study. The majority of these approaches employ photomasking and light-based techniques like 2-photon polymerization technologies to create spatially defined biofunctionalized regions within hydrogel structures. However, these types of approaches pose distinct types of challenges when it comes to creating large and convoluted, precisely biofunctionalized printed constructs. In photomasking technologies, the resulting biofunctionalized patterns do not fully capture the 3D complexity observed in native developmental processes. These patterned structures provide no control over the z-directional architecture of the grafted regions, meaning

that resulting structures are just projected two-dimensional (2D) patterns, thus lacking the convoluted 3D complexity that can be achieved with more advanced light-based approaches.<sup>[572]</sup> On the other hand, another employed approach to photopattern biomolecules within hydrogels is 2-photon lithography. In studies demonstrating this approach, the 3D resolution of grafted structures is significantly enhanced, given the design freedom in across all planes that is possible in this approach. However, as with several multi-photon approaches, the working depth of this approach is rather limited (< 1 mm for various studies employing hydrogels)<sup>[614,615,643]</sup> and approximately 2-3 mm for microscopy applications.<sup>[644,645]</sup> This means that convoluted 3D printed structures of clinically relevant sizes could not be biofunctionalized with full spatial freedom. While the depth penetration of multiphoton approaches has been increased by employing alternative lens set-ups and immersion platforms to reduce light scattering,<sup>[617]</sup> the maximum achievable structure sizes of 7 mm in height compromise the submicron resolutions characteristic of these approaches, and are still very time consuming.<sup>[617]</sup> Thus the biochemical guidance provided by these approaches would be limited to small scale regions of organs or tissues, failing to capture tissue-wide complexity. In the case of the volumetric photopatterning approach developed in **Chapter 9**, through the leveraging of the tomographic back projections used in the volumetric printing process, spatially complex patterns of thiolated compounds could be achieved within seconds, through the entire depth of volumetrically printed structures. In this way, the incorporation of growth factors and their maintained bioactivity was shown to modulate vascular growth in printing constructs and could be used for a wide range of applications. Multiple bioactive compounds could potentially be incorporated in distinct regions of printed structures, guiding the response of single cell types of more advanced biological units in a highly controlled spatial manner, as demonstrated with model fluorescent compounds in this thesis. Similarly, this process can also be performed on demand during different stages of the print maturation period to selectively induce differential cellular responses over time, simply by repeating the photopatterning process with newly infused compounds. In this way, orchestrating complex signaling cascades in a spatiotemporal manner could be achieved to induce time-dependent changes in cell behavior, to better replicate complex native growth, developmental and disease processes *in vitro*. With the addition of this elegant patterning approach, the combination of the various innovative elements of the biofabrication process introduced in this thesis (scalable bioprinting processes, shape-dependent control over self-assembled cellular units, and the ability to chemically edit the surrounding matrix of these complex biological components) open the door to creating the next generation of *in vitro* models with heightened architectural, biological and biochemical properties.

## FUTURE PERSPECTIVES

The different studies presented in this thesis sought to improve specific gaps and drawbacks of existing biofabrication approaches, tackling key fabrication, biological and biochemical demands to enhance the biomimicry of *in vitro* platforms. Herein, we demonstrated the development of new technologies and the convergence of existing tools and techniques into complementary processes that enrich the biofabrication toolbox, to enable biomedical scientists to build more complex *in vitro* models that more closely capture salient features of (human) biology. At the same time, several challenges remain open in the field, and will require further, future research efforts to address all the considerations required to create more physiologically relevant *in vitro* platforms that could become standardized candidates for the advanced preclinical testing phase in the current drug development landscape.

Beyond achieving tissue-like functionality through the incorporation of advanced cellular components and a myriad of relevant biochemical and biomechanical cues, a major challenge in the field of biofabrication, and *in vitro* modeling in general, is the incorporation of vasculature into these platforms to provide adequate nutrient and oxygen supply, as well as intra- and inter-tissue transport. Hand in hand with this challenge is the establishment of interconnected platforms that represent various tissue units that, in the body, act in synchrony and are in constant communication through innervation and vasculature. The multi-scale resolution of various bioprinting techniques has been abundantly exploited to replicate the convoluted, multi-scale vascular networks within tissue-specific structures.<sup>[325,646]</sup> Recent approaches have demonstrated that a combination of techniques, such as the printing of macrochannels and subsequent chemoattracting strategies to guide capillary formation,<sup>[598,647]</sup> or the 2-photon ablation-based patterning of perfusable templates to induce cell infiltration,<sup>[648]</sup> provide significantly more native-like multi-scale vascular networks, rather than attempting to fabricate such complex networks with single techniques. To incorporate such complex vascular networks within the large volumetrically printed platforms shown in this thesis, VBP-compatible approaches to induce vascular network formation must be developed. Similar chemoattracting approaches, using the photopatterning approach demonstrated in **Chapter 9** could serve to direct capillary formation within printed structures, for example. Furthermore, the incorporation of vascularization-promoting cells and materials in reproducible stochastic micropatterns using chaotic flows<sup>[649,650]</sup> for instance, could aid in creating prints with embedded, interconnected vascular structures. An important step to achieving vascularized structures lies in the development of compatible VBP materials that possess the stiffness and topographical properties optimal for vascular growth. For example, the use of photosensitive hydrogels with controllable porosity, dynamic bonds that facilitate cell-induced matrix remodeling or stable low molecular weight polymers could aid in



enhancing volumetric print vascularization. The recently developed Embedded extrusion Volumetric Printing (EmVP) process, in which materials of different mechanical properties and cell types can be differentially patterned, first through embedded printing within microgel resins and subsequently through VBP, could be another approach to introduce vascular networks into larger, complex architectures.<sup>[474]</sup> Along this same line of materials, the use of granular hydrogels consisting of microgel units for VBP or any other bioprinting technique has been a widely studied concept, as these highly tuneable materials can elicit a wide range of cellular behaviors through simple modifications like packing density, material stiffness and molecular weight, microgel shape and annealing strength, and material choice itself.<sup>[651–655]</sup> Due to their tuneable mechanics and the intrinsic porosity that forms at the gaps between microgels, these materials should be further studied for their potential to create complex and interconnected vascular networks.<sup>[656,657]</sup>

Regarding the multi-tissue interconnectivity that is essential to understand systemic processes and diseases, the multi-organ-on-a-chip microphysiological systems (MPS) that have been recently developed in the field of tissue engineering<sup>[104–106,658]</sup> pose a useful starting point for adoption in the biofabrication process. Creating looped perfusable systems that connect relevant bioprinted tissue units together as recently shown for MPS,<sup>[659]</sup> each connected through a central intricate vascular network to enable inter-tissue transport and signaling, could be of great value to obtain more relevant clinical outcomes. For instance, in order to understand the drug toxicity effects of newly developed candidates, creating such arrays of the digestive and renal systems for instance, could provide unique insights into the delivery, absorption, breakdown and excretion of orally administered drugs. An MPS-based example of such interconnected, multi-tissue system developed a heart-lung-liver platform that was exhibited tissue-specific functions when cultured independently and in interconnected flow loops.<sup>[660]</sup> Interestingly, this model demonstrated a differential, detrimental response of the heart component of the platform to a lung-cancer drug when connected to the other organs compared to direct exposure to the drug in an independent loop, showcasing the advantage these interconnected platforms in the investigation of systemic processes.<sup>[660]</sup> Further incorporation multi-tissue interconnectivity and the development of sensors for advanced monitoring can provide a much more accurate understanding of these processes than an animal study for instance, and considering the patient-specific origin of organoids and other stem cell technologies, such systems could be used to create tailored treatment strategies for patients in the future and gradually reduce the need for animal experimentation.

Naturally, the implementation of the technologies discussed throughout this thesis as reliable and reproducible stages of the preclinical testing pipeline require more than just the aforementioned technology-centered developments. Given the young age of biofabrication as a research field, the vast majority of the biomaterials and resulting tissue analogues created with bioprinting approaches have not yet undergone the basic safety

and biocompatibility tests required to start the certification process as advanced therapy medicinal products (ATMPs). While more of the fundamental research in the field has started to transition towards preclinical applications, and first steps have been taken towards the first clinical trial of a biofabricated implant, several quality control and regulatory hurdles remain that thus far, hinder the widespread application of these technologies in the biomedical and pharmaceutical industries. The first issue to consider is the need for reproducibility and for quality control in 3D bioprinting processes. Slightly differing printer set-ups, variability in material properties from commercial or in-house origins, inter-user method variability and human error all pose significant drawbacks in the translatability of advanced bioprinting techniques. The introduction of artificial intelligence,<sup>[661]</sup> quality control sensors,<sup>[662]</sup> and methodology standardization are necessary additions to all classes of bioprinting technologies, including the ones presented in this thesis to automate and standardize biofabrication processes. Undergoing similar approaches to standardize material production and safety assessments is essential to ensure that these promising technologies continue to take steps closer to patients and industry. Furthermore, looking towards the establishment of *in vitro* platforms that can aid in the reduction of animal experimentation by providing biofabricated humanized models of high physiological accuracy, it is crucial to undergo long-term validation of recently developed systems to ensure these are in line with clinical outcomes and existing results from the immense collection of data from decades of animal experiments and the more basic *in vitro* models used to date.

A major topic of debate that remains within the field that can greatly impact these regulatory and standardization obstacles revolves around the extent of complexity that must be directly crafted through tissue engineering and biofabrication technologies. While biofabrication approaches can continuously be redesigned to create more and more complex architectures, the more elements (fabrication-, biology- and material-related) that are incorporated into the process, the more arduous standardization and regulatory approval processes can become. A careful balance between exploiting these technologies to mimic every last aspect of target tissues, and reducing the overall process complexity of these approaches by providing few, yet powerful cues to guide tissue self-organization is of utmost importance to ensure biofabrication strategies can take the next step towards clinical and pharmaceutical applicability.<sup>[663]</sup> It is also noteworthy that, depending on the intended application of such biofabricated models (*i.e.*, transplantation vs. clinical model), the regulatory and standardization requirements will differ significantly. Biofabricated *in vitro* platforms could already draw from the guidelines that are emerging in the organ-on-a-chip field, where models are fit-for-purpose, to screen a specific range of drugs, diseases, or molecular pathways, and thus the required model complexity can be tailored per application. All in all, advanced biofabrication strategies, though not ideal for the early high-throughput testing stage of the preclinical process due to their complexity and

time-intensive manufacturing, hold significant potential for the more advanced phases of the pipeline. With adequate functional and regulatory optimization, these strategies can become valuable in elucidating complex tissue-specific and systemic drug responses given the higher-level functionality they provide, offering valuable insights into drug efficacy and safety.

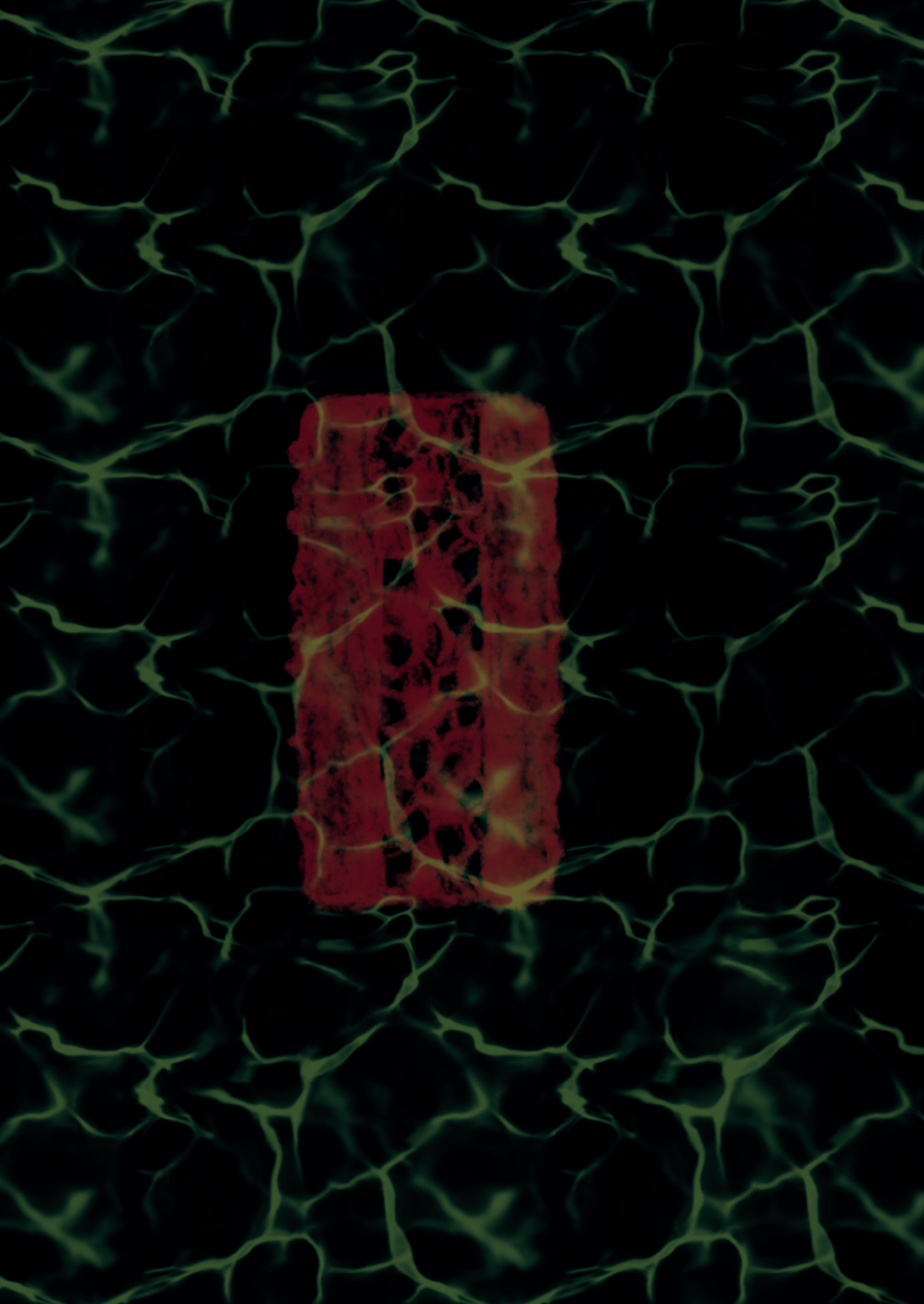
## CONCLUSION

This thesis introduced significant advancements within the field of biofabrication for the generation of human *in vitro* models with tissue-like functionality. Through a comprehensive exploration that tackled challenges related to fundamental bioprinting principles, the biological intricacies, and the biochemical and material property requirements of bioprinted structures to better recapitulate native tissues, the developments described here have expanded the toolkit of biofabrication approaches. By introducing novel technologies, including the pioneering, layerless volumetric bioprinting strategy, and synergizing new and existing advanced printing approaches to harness their unique advantages, this thesis showcases a variety of functional bioprinted tissue models that enable the study of biological processes *in vitro*. The fabrication and thorough exploration of volumetric bioprinting, distinguished by its scalability, unparalleled design freedom, compatibility with advanced biological tools, and a growing library of smart materials, chart new paths toward the creation of clinically-relevant testing platforms. The bioprinted, tissue-specific *in vitro* models presented here offer enhanced physiological accuracy and predictability, as well as the potential to incorporate patient-specific elements for personalized medicine. The toolkit developed in this thesis represents a crucial stride in bridging the translational gap of tissue-engineered *in vitro* models, particularly in the context of preclinical testing. Tackling the emerging challenges in navigating the regulatory landscape of the biomedical sector, the future of biofabricated *in vitro* models certainly holds promise as these innovative approaches continue to evolve in the coming years.





# **Annex**



# Annex 1

## Thermal Shrinking of Biopolymeric Hydrogels for High Resolution Volumetric Printing

Martina Viola<sup>1,2</sup>, Paulina Núñez Bernal<sup>2\*</sup>, Marta G. Valverde<sup>3\*</sup>, Jaap van Trijp<sup>1</sup>, Jaimie Hak<sup>1</sup>, Carl.C.L. Schuurmans<sup>1</sup>, Cornelus F. van Nostrum<sup>1</sup>, Rosalinde Masereeuw<sup>3</sup>, Silvia Mihaila<sup>3</sup>, Jos Malda<sup>2,4</sup>, Riccardo Levato<sup>2,4</sup>, Tina Vermonden<sup>1</sup>

<sup>1</sup> Department of Pharmaceutical Sciences (UIPS), Faculty of Science, Utrecht University, Utrecht, The Netherlands

<sup>2</sup> Department of Orthopedics, University Medical Center Utrecht, Utrecht University, Utrecht, The Netherlands

<sup>3</sup> Department of Pharmacology, Utrecht University, Utrecht, the Netherlands

<sup>4</sup> Department of Clinical Sciences, Faculty of Veterinary Medicine, Utrecht University, Utrecht, The Netherlands

\* Authors contributed equally to this work





## INTRODUCTION

Tissues and organs are composed of highly organized, multiscale structures that give rise to specific functions essential for systemic homeostasis, from the micro-scale organization of cells and their surrounding extracellular matrix (ECM) to the bulk macro-scale architectures that facilitate the exchange of nutrients, oxygen and waste through various organs and regulate tissue-specific functions. Mimicking this multiscale organization is key to develop accurate *in vitro* tissue mimics that can be used to study development and disease, and in the future, be suitable for regenerative clinical strategies.<sup>[109,325]</sup> The field of biofabrication poses unique advantages to address this challenge, as it enables the precise placement of cells and biomaterials into highly organized structures through the use of various three-dimensional (3D) bioprinting or bioassembly approaches.<sup>[110]</sup> The rapid development of 3D bioprinting approaches with distinct working principles, material properties and resolution capabilities, has made it so that a wide array of bioengineered constructs mimicking specific tissue and organ functions have been developed in the last decades.<sup>[109,111,112,133]</sup> Extrusion-based bioprinting,<sup>[114,664]</sup> inkjet bioprinting,<sup>[117,118,665]</sup> sacrificial material-based techniques,<sup>[666]</sup> and light-assisted processes,<sup>[119,120,667,668]</sup> are amongst the most widely used in the field. When aiming to develop multi-scale constructs, it is often the high resolution structures that pose a greater technical challenge using these printers, and are largely limited by material properties of the bioinks employed (*i.e.*, stiffness, post-printing material stability and shape fidelity), and the working principle of the fabrication strategy itself (*i.e.*, resulting Barus effect of extruded materials resulting in filament thickening, overcuring of light-sensitive resins in light-based approaches, and a wide array of process specific parameters).<sup>[121,128]</sup> When it comes to high-resolution printing, multiphoton laser polymerization and ablation have been the most promising given their high precision, in which submicrometer regions of the bioresin can be photocrosslinked upon the simultaneous absorption of two or more photons.<sup>[580,648,669,670]</sup> However, the working principle of these approaches makes them extremely time consuming, only producing small units in the span of several hours, making the upscaling of these printed structures into clinically relevant-sized models very challenging. Furthermore, the existing library of photoresponsive hydrogels compatible with such techniques is rather limited still, especially those that support cellular function.<sup>[671–673]</sup>

Besides the achievement of high-resolution structures, to successfully transition any of these techniques to functional *in vitro* models and potential clinical applications, it is important to have a fabrication process that both facilitates complex structure creation and allows for short processing times, allowing for scalable production.<sup>[674]</sup> Despite notable advancements, there remains a strong demand for a more optimal method to prepare micron-scale structures within engineered tissues, be it from a fabrication perspective or through the development of smart materials that can be tailored to achieve these high

resolutions.

In the case of smart materials, stimuli-responsive hydrogels are receiving considerable attention due to their ability to display rapid changes in swelling behavior in response to external stimuli, such as changes in temperature, pH, solvent composition and electric field.<sup>[152]</sup> Within these emerging types of smart biomaterials, thermo-responsive hydrogels are widely researched polymer systems that exhibit temperature-dependent behavior. These hydrogels can respond rapidly to changes in temperature resulting in an increase or decrease of their volume (swelling or de-swelling).<sup>[675–677]</sup> Poly(N-isopropylacrylamide) (PNIPAM) is one of the most widely studied and used temperature-sensitive materials, composed of hydrophilic (amide groups) and hydrophobic (isopropyl groups) side groups, which shows lower critical solution temperature (LCST) behavior around 32°C in aqueous environment.<sup>[677–679]</sup> When the LCST is reached, PNIPAM undergoes conformational changes, resulting in decreased solubility and wettability. Specifically, above the LCST, the hydrophilic bonds between water and amide groups are broken, resulting in the release of water and self-assembly of PNIPAM.<sup>[680–682]</sup> This process is reversible, meaning that when the environmental temperature is lowered below the LCST, the PNIPAM chains revert back to their coiled form. This transition of rehydration restore the solubility, and recovers their original wettability.<sup>[682]</sup>

PNIPAM has already been introduced to fabricate stimuli-responsive, high-resolution structures.<sup>[679,683]</sup> Using a microfluidic system to create tubular structures, PNIPAM's water expulsion properties at high temperatures demonstrated a significant reduction in the wall thickness of these constructs. By doing so, the inner diameter of the channels increased, mimicking the process of vasodilation.<sup>[679]</sup> A similar, but more recent technique uses PNIPAM to decrease the overall volume (inner diameter and wall thickness) of simple tubular structures made of hydrogels and sacrificial materials, resulting in shrunken tubular structures with high cell viability over 7 days (human umbilical vein endothelial cells).<sup>[618]</sup>

In this study, we sought to exploit the thermal shrinking properties of PNIPAM within a volumetric printing (VP) process to create high-resolution bioprinted structures. Volumetric printing is a layer-less approach that facilitates the printing of highly convoluted geometries in tens of seconds.<sup>[127]</sup> This is achieved through the delivery of a sequence of tomographic light projections of a desired 3D object onto a photosensitive resin. Upon sufficient light accumulation in the desired regions of the resin volume, covalent crosslinking of the resin yields a solid 3D printed structure in a single step, with a high freedom of design. Volumetric printing of cellular structures (volumetric bioprinting), has been demonstrated on various occasions, reporting the possibility to print viable and functional cells and organoids,<sup>[127,286]</sup> and to sculpt the latter into complex, function-modulating architectures.<sup>[286]</sup> The potential to create complex multi-material

constructs,<sup>[473]</sup> combine the VP approach with other printing strategies, like embedded bioprinting for further multi-material and multi-cellular applications,<sup>[474]</sup> two-photon ablation to create microchannels within VP-printed structures,<sup>[614]</sup> and melt electrowriting to enhance the mechanical stability of printed hydrogel structures,<sup>[472]</sup> has also been recently demonstrated. In the field of material chemistry however, the use of smart, stimuli responsive bioresins has been limited to date. While chemically editable hydrogels have been recently shown to facilitate spatiotemporal growth factor patterning,<sup>[335]</sup> the use of stimuli-responsive materials that elicit conformational or chemical changes of volumetrically printed structures is still unexplored. Herein, the novel VP approach and the shrinking capabilities of PNIPAM-based materials will be converged to fabricate freeform, high-resolution structures. To facilitate cell adhesion to this thermosensitive hydrogel, we supplemented these hydrogels with two different biopolymeric, photocrosslinkable materials with methacryloyl moieties, gelatin methacryloyl (gelMA) or silk fibroin methacryloyl (silkMA). GelMA and silkMA have been covalently crosslinked with NIPAM through light induced radical polymerization to form a polymeric network (gelMA-NIPAM and silkMA-NIPAM, respectively), in which the gelMA or silkMA chains acts as a bridge between the PNIPAM backbone. The shrinking capacity of the resulting printed hydrogels was investigated upon exposure to 37° C (as shown in **Figure 1A**).

In this study, our goal was to explore a new category of thermosensitive materials for use as bioresins in a volumetric printing set-up and thus achieve clinically relevant-sized 3D structures with high-resolution features. By combining the temperature-sensitive shrinking capacity of gelMA-NIPAM or silkMA-NIPAM hydrogels with the volumetric 3D printer the goal is to further push the resolution of this technique to be able to create multi-scale tissue mimics for tissue engineering applications (**Figure 1B**).

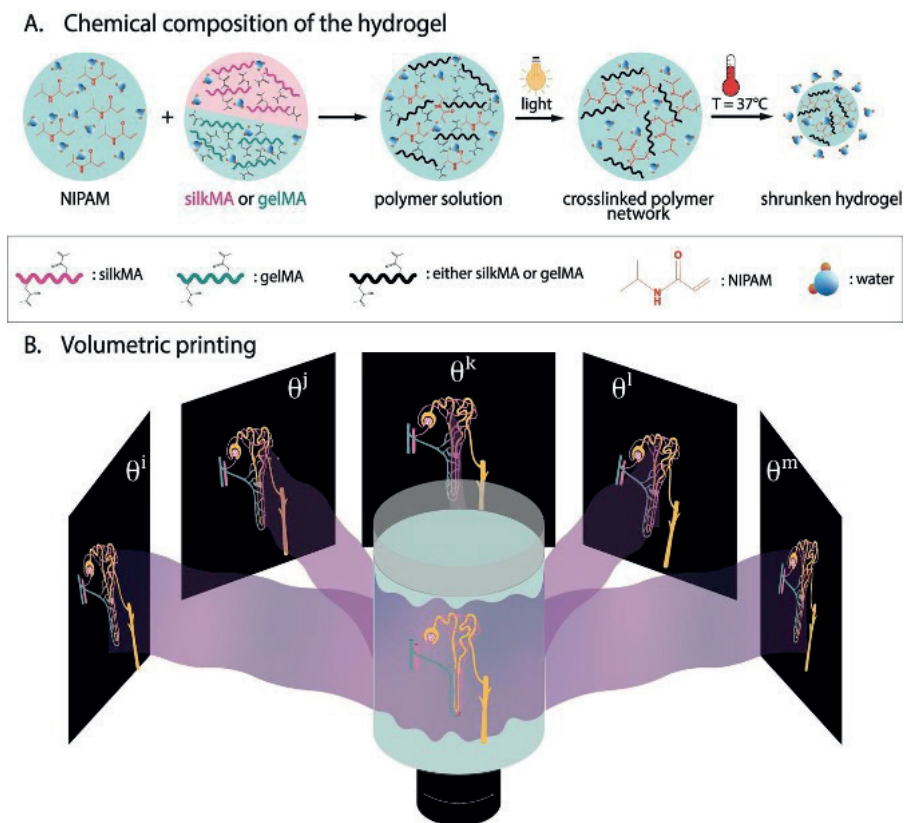


**Figure 1:** Schematic representation of the overall process: A) Chemical composition of the two hydrogels gelMA-NIPAM or silkMa-NIPAM and B) visual representation of the tomography-based light projections of a nephron structure in volumetric printing.

## RESULTS AND DISCUSSION

PNIPAM-derived hydrogel blends have previously been investigated for applications in tissue engineering, with differing ratios of supplemented gelMA to introduce greater bioactivity to these thermosensitive materials.<sup>[618]</sup> Said research has focused on developing shrinking tubular structures with gelMA-NIPAM that have showed promising vasculogenic effects *in vivo*, demonstrating temperature- and NIPAM:gelMA ratio-dependent shrinking behaviors.<sup>[618]</sup> In this study, the printability of this material with VP is explored for the first time, as well as the first-time characterization of photocrosslinkable methacrylated silk fibroin as another potential shrinkable biopolymer. The use of these widely used biopolymers opens the door to a wide variety of tissue engineering applications given their intrinsic biocompatibility and, especially important for silk, its unique mechanical

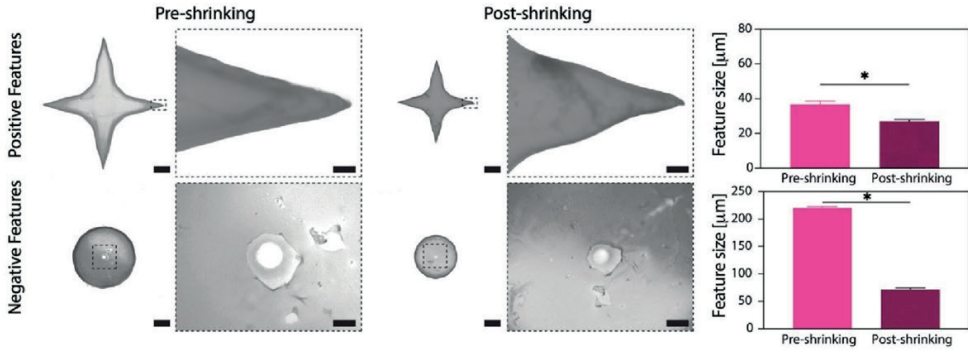
properties.<sup>[158,684–687]</sup> Since silk fibroin possesses side groups on its polymer chain (attributed to the presence of lysines, tyrosines and serines), functionalization of the polymer backbone has previously been demonstrated. In fact, the methacrylation of silk fibroin, a process optimized by Kim et al., highlighted the possibility of tuning the degree of methacrylation (DoM) of silk fibroin, in a glycidil methacrylate concentration-dependent manner (in the range of 22-40 % DoM).<sup>[234]</sup>

The potential to thermally control the shrinking of PNIPAM-derived hydrogels is highly interesting in the field of biofabrication, when it comes to the 3D printing of high-resolution features, as a material-driven approach to produce micro-scale positive and negative features. While some printing approaches like multi-photon laser ablation<sup>[648,670,688,689]</sup> or digital light processing<sup>[235,331,332]</sup> have proven to achieve high-resolution features in the range of tens of micrometers using biocompatible hydrogels, these approaches are largely limited by the time required to print clinically-relevant sized structures for *in vitro* modeling or potential implantation. The recently introduced volumetric printing approach allows for the single-step printing of large and complex architectures in a matter of seconds.<sup>[127]</sup> VP allows for the processing of a wide variety of photoresponsive hydrogels, and theoretically, allows for a nominal resolution up to approximately 25-30  $\mu\text{m}$ , based on the optical components employed in the system (*i.e.*, pixel size in the digital micromirror device).<sup>[224]</sup> However, the inherent entropy of radical-mediated polymerization reactions (used for all volumetrically printed materials to date) has proven to hinder the achievable printing resolution of this technology.<sup>[286,291,486]</sup>

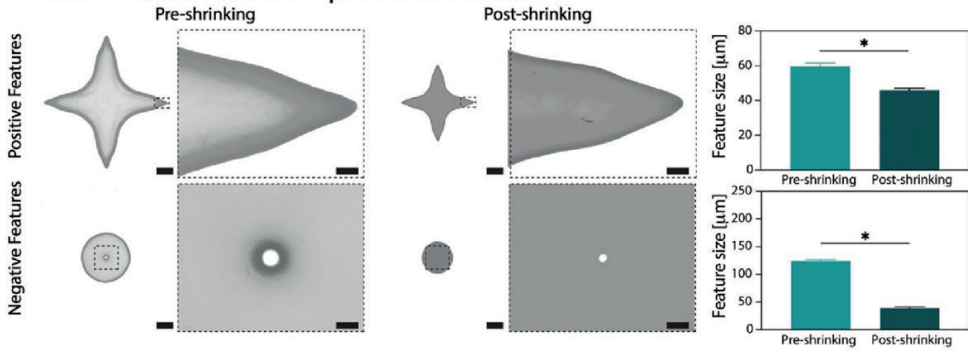
The volumetrically printed silkMA-NIPAM and gelMA-NIPAM structures demonstrated significant resolution increases for both positive and negative features (**Figure 2**). SilkMA-NIPAM showed a significant resolution enhancement of simple positive (from  $36.7 \pm 1.9$  to  $27.0 \pm 1.0$   $\mu\text{m}$ ;  $t_{\text{print}} = 13.4$  s) and negative (from  $220.3 \pm 2.5$  to  $71.5 \pm 3.1$   $\mu\text{m}$ ;  $t_{\text{print}} = 11.8$  s) features after overnight shrinking at the optimal temperature of  $37^\circ\text{C}$  (**Figure 2A**). Interestingly, these shrinking hydrogels enable the fabrication of positive features that match the optical resolution limit of the volumetric printer, and negative features also exhibit a high shrinking factor (3.1-fold). Similarly, gelMA-NIPAM exhibited a significant enhancement of print resolution (**Figure 2B**). While positive features (shrinking from  $59.6 \pm 2.1$  to  $46.0 \pm 1.1$   $\mu\text{m}$ ;  $t_{\text{print}} = 14.2$  s) did not achieve as high a resolution as silkMA-NIPAM prints, the negative features achieved post-shrinking (from  $123.8 \pm 2.7$  to  $39.1 \pm 2.3$   $\mu\text{m}$ ;  $t_{\text{print}} = 12.6$  s) are, to date, the highest open channels created with a volumetric printer, highlighting the advantage of the post-printing shrinkage induced by the incorporation of PNIPAM, a process that does not require a change in the VP process itself. Another recently developed approach to enhance the printing resolution of VP has been explored, and consists of the incorporation of different lenses with various magnification capabilities to reduce the size of the volumetric projections and thus yield higher resolution features. However, this approach still did not yield the negative feature

resolution shown in the present study (with the highest magnification lenses employed achieving features of 240-380  $\mu\text{m}$  features). While higher magnification lenses can be used to further push this resolution, the introduction of these into the printer set up also result in an overall reduction in size of the printable object.<sup>[614]</sup> Furthermore, the possibility to create high-resolution microchannels within volumetrically printed bulk structures has been demonstrated through the incorporation of a sequential 2-photon ablation step, which allowed the fabrication of negative features down to 1  $\mu\text{m}$  in size.<sup>[614]</sup> However, the working depth of the 2-photon ablation process shown in this study is limited to 500  $\mu\text{m}$ , thus posing significant limitations on the size of the volumetrically printed structure that can be “edited” with these sequentially fabricated microchannels. Furthermore, the creation of complex structures was far more time consuming than the conventional VP approach, with working volumes of 0.02  $\text{mm}^3$  taking over 10 minutes to fully ablate into open channels.<sup>[614]</sup> The printing of shrinkable bioresins shown in this study, which requires no modification of the optical set up of the volumetric printer and relies solely on the processing time of VP rather than the introduction of a second processing approach, is thus a promising approach for achieving high resolution features using this high-speed printing technique.

**A. SilkMA-NIPAM Volumetric printed structures**



**B. GelMA-NIPAM Volumetric printed structures**



**C. Volumetric printed complex structures**

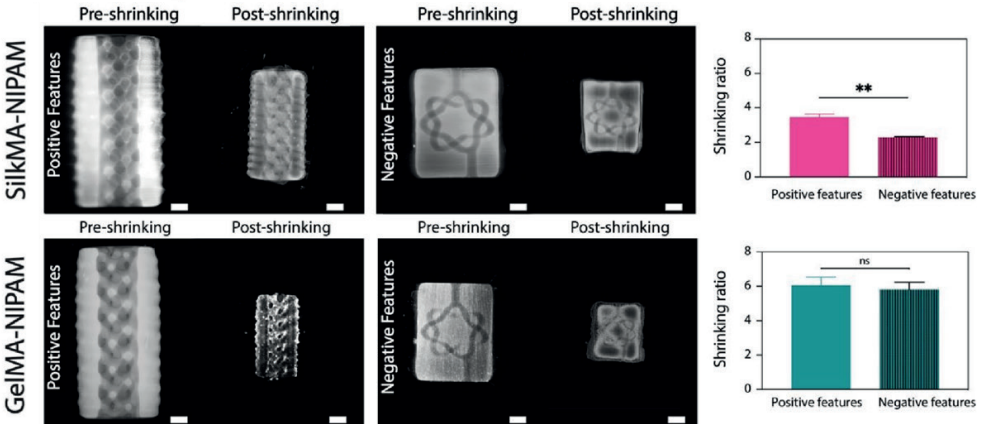


**Figure 2:** Volumetric printing of thermally shrinkable structures. Simple VP structures consisting of positive and negative features in a pre- and post-shrinking (overnight at 37°C) state, as well as quantitative measurements of these feature sizes made of A) silkMA-NIPAM and B) gelMA-NIPAM (Scale bar low magnification = 1 mm, high magnification = 200  $\mu\text{m}$ ). C) Complex VP structures printed with silkMA-NIPAM (top row) and GelMA-NIPAM (bottom row), consisting of positive features (gyroid) and negative features (hollow torus knot) before and after shrinking (scale bar = 1 mm). \* =  $p < 0.05$ , \*\* =  $p < 0.01$ .

To demonstrate the ability to create more convoluted architectures consisting of complex struts and channels, and their ability to shrink into stable structures while maintaining high shape fidelity, both silkMA- and gelMA-based thermosensitive materials were used to volumetrically print larger, more intricate shapes. A gyroid structure, consisting of a complex network of repeating pore units, and a hollow torus knot shape with an inlet and outlet to allow perfusion were printed. For both materials, these larger, bulkier structures also underwent shrinking post-printing (**Figure 2C**). For silkMA, the gyroid ( $t_{\text{print}} = 17$  s), representing a complex positive feature structure, underwent shrinking by a factor of  $3.5 \pm 0.2$ , and the hollow torus knot network ( $t_{\text{print}} = 18.6$  s by a factor of  $2.3 \pm 0.1$ ), with all channels and features remaining distinct and open in the case of the channel structures. GelMA-NIPAM in this case, experienced a much higher shrinking ratio for both gyroid ( $t_{\text{print}} = 17$  s) and torus knot ( $t_{\text{print}} = 19$  s) ( $6.1 \pm 0.5$  and  $5.8 \pm 0.4$  respectively), indicating a more pronounced shrinking capacity of the gelatin-supplemented material in the chosen structures. This observation could be based on the printing technique itself. In the VP process, the desired regions of the bioresin are irradiated long enough to barely surpass the gelation threshold of the material, to prevent polymerization of the surrounding unwanted regions of the resin. This means the photocrosslinking of the hydrogel is stopped earlier than in regular casted constructs, where the gel is completely polymerized, and thus higher amounts of the polymer remain uncrosslinked in the printed conditions. After this crosslinking step, the unreacted polymer is washed out with warm phosphate buffered saline (PBS) and the resulting construct is then post-cured to finish the crosslinking mechanism leading to a stable hydrogel. Since gelatin is a more hydrophilic polymer than silk, uncrosslinked gelatin can more readily be washed out of the underpolymerized construct before the full polymerization of the construct takes place. This in turn leads to a final hydrogel with a lower crosslinking density than its more hydrophobic silkMA-supplemented counterpart. This lower crosslinking density for the gelMA-NIPAM hydrogels explains why they exhibit a larger shrinking capacity, since a lower crosslinking density leads to higher water content within the hydrogel network, and therefore increased water expulsion occurs at  $37^\circ\text{C}$ . Since silkMA is the more hydrophobic of the two biopolymers, this effect is decreased, as less of the initially uncrosslinked polymer immediately after VP is washed out before the post-curing step. Overall, this data demonstrates the ability to volumetrically print highly complex PNIPAM-based structures whose volume and feature sizes can be thermally controlled. The shrinking properties observed in this study can be carefully controlled through the selection of the resin composition (hydrophobic vs. hydrophilic supplements such as silkMA and gelMA, respectively) and/or the thermal cues provided to achieve a wide array of construct sizes for different applications. These observations open a wide range of possibilities for incorporating multiscale structures with both high-resolution positive and negative features, as well as fabrication times in the range of tens of seconds that can facilitate the creation of clinically-relevant sized constructs that more closely mimic native tissues.



## CONCLUSIONS

In this study, the library of materials for volumetric printing is further expanded with two photocrosslinkable, thermosensitive proteinaceous biomaterials, PNIPAM hydrogels supplemented with widely used biopolymers silkMA and gelMA. Both materials, upon surpassing the lower critical solution temperature of PNIPAM (32° C) exhibited a reversible shrinking behavior due to water expulsion resulting from a decrease in solubility and wettability of PNIPAM. Here, we demonstrate the compatibility of these materials with the ultra-fast volumetric printing approach. With these thermoresponsive materials, the current printing resolution of positive features was pushed to the limits of the theoretical optical resolution achievable with the printer ( $< 30 \mu\text{m}$ ), and in terms of negative resolution, the gelMA-NIPAM blend under shrinkage at 37° C achieved the highest resolution of open channels reported to date using VP ( $< 40 \mu\text{m}$  diameter). Apart from this significant enhancement in simple positive and negative feature resolution, both materials could also be printed into highly tortuous gyroid structures and convoluted perfusable channel networks, exhibiting up to a 6-fold shrinking factor of these complex constructs. Gelatin and silk are widely used natural polymers in the field of tissue engineering and biofabrication, given their biocompatibility and in the case of silk, its unique mechanical properties. Thus, considering the great potential of the high-speed fabrication of complex, high-resolution structures with VP, it is crucial to investigate the compatibility of these materials with different cell types in the near future. In doing so, these newly established volumetrically printable materials could lead to the high-throughput generation of complex, multi-scale structures with controllable shrinking characteristics, opening new doors the creation of tissue mimics that can provide the next step in implantable and *in vitro* modeling platforms for biomedical applications.

## EXPERIMENTAL SECTION

*Gelatin methacryloyl synthesis:* Synthesis of gelMA with was performed according to previously reported procedures.<sup>[17]</sup> Briefly, 10 g of porcine skin type A gelatin ( $\sim 300$  bloom) was dissolved in 100 mL of phosphate-buffered saline solution (PBS) (pH 7.4) at 50° C for one hour. Methacrylic anhydride (MA) was added dropwise in a 0.8 mL g<sup>-1</sup> ratio of MA to gelatin and left to stir for 2 hours at 50° C. Upon completion, the solution was diluted with PBS to a concentration of 200 mL g<sup>-1</sup> gelatin followed by dialysis (MWCO: 12-15 kDa, Spectrum Lab Inc.) against deionized water at 40° C for 5 days. Lyophilization resulted in a white powder.

*Methacrylate silk fibroin synthesis:* Silk degumming was based on protocol by Rockwood *et al.*<sup>[191]</sup> and silk fibroin (SF) methacrylation was based on protocol by Kim *et al.*<sup>[234]</sup> Briefly, *Bombyx Mori* silk cocoons (Evrosilk, Czech Republic) were cut using scissors and silkworm was disposed of. A 0.02 M Na<sub>2</sub>CO<sub>3</sub> solution was brought to a boil and 5 grams of clean, cut open cocoons were boiled for exactly 5 minutes to remove the sericine layer. The degummed SF fibers were rinsed in cold deionized water and dried on aluminium foil overnight. SF (5 grams) was then dissolved in 9.3 M LiBr (Acros Organics) at 60° C. After 1-hour glycidyl methacrylate (1.12g, 7.9 mmol) was added and the solution was left to stir for 3 hours. SilkMA was purified by dialysis against deionized water for 3 days using cellulose dialysis tubes (MWCO 3.5 kDa, Sigma Aldrich) at 4° C. The dialyzed solution was centrifuged to remove impurities and stored as liquid solution at 4° C.

*Preparation of gelMA-NIPAM and silkMA-NIPAM hydrogels:* GelMA stock solution 10% w/v was dissolved in PBS at 50° C for an hour and stored at 4° C. NIPAM stock solutions in PBS of 10% w/v were prepared and stored at 4° C. To reach a concentration of 10%w/v, SF was dialyzed overnight against a 40% w/v polyethylene glycol (PEG) (6 kDa) aqueous solution using cellulose dialysis tubes (MWCO 3.5 kDa, Sigma Aldrich). The concentrated silkMA solution was stored at 4° C for no more than one week. GelMA or silkMA stock solutions were combined with NIPAM stock solution in different ratios (1:1, 1:2, 1:3, 1:4 and 1:5). However, the 1:4 ratio was chosen for further experiments with 0.1% w/v lithium phenyl 2-4-6-trimethylbenzoyl phosphinate (LAP) (TCI chemicals, Hong Kong) as photo-initiator to produce a pre-gel solution. Pre-gel solutions were cast in open-topped cylindrical moulds (1 x 8 or 3 x 8 mm). The moulds were placed under Bluepoint 4 UV lamp (Honle UV technology AG, Germany) and irradiated for 40 seconds at a 5 cm distance (light intensity ~390 mW at the light source).

*Hydrogel shrinking kinetics:* Hydrogel disks (d = 8 mm, h = 2 mm, ~100 µl) were prepared as described before in a 1:4 GelMA-NIPAM and SilkMA-NIPAM ratios. Hydrogels were placed in 12 multi-well plates with 4 mL of PBS and incubated at 33° C and 37° C. Photos were taken at precisely timed timepoints from the moment the hydrogel was added to the warm PBS (33° C and 37° C) and images were analysed using ImageJ software (1. 53e, National institute of health, USA).

*Measurements of rheological and mechanical properties:* The crosslinking kinetics of the hydrogels were evaluated with a Discovery HR-2 Rheometer (TA Instruments, Etten-Leur, The Netherlands) equipped with a light guide attached to a BluePoint 4 lamp (Honle UV technology) using a 20 mm plate-plate geometry. Time sweeps were performed for 5 minutes at 10% strain and 1Hz angular frequency at 25° C, the lamp was switched on after 1 minutes for 30 seconds. Data were processed with TRIOS software (version 5.0).

Furthermore, hydrogel disks (d = 8 mm, h =3 mm, ~150 µL) were prepared. Rheological properties were determined the same rheometer equipped with a Peltier plate for

temperature control and solvent trap to prevent evaporation. All samples were measured using a plate-plate geometry (aluminium, 20 mm diameter). Data were processed with TRIOS software (version 5.0). Oscillation amplitude sweeps were performed to determine appropriate strain for oscillation frequency sweep. Oscillation frequency sweeps (strain 10%, frequency 0.1 to 100 Hz) were performed at 25° C, 33° C and 37° C.

Compression tests were performed on a 2980 DMA (Q800, TA Instruments, the Netherlands). Compression tests were performed using a three-step protocol: equilibration 25° C (or 33° or 37° C), isothermal for 3 minutes, compressive force ramp 2N/min up to 5N (n = 3). From the obtained data the young modulus was calculated as the slope of  $\sigma/\epsilon$  between 0% and 20%.

*Volumetric printing:* GelMA-NIPAM (2% w/v and 8% w/v respectively) and SilkMA-NIPAM (2% w/v and 8% w/v respectively) solutions supplemented with 0.1% w/v lithium phenyl 2-4-6-trimethylbenzoyl phosphinate (LAP; TCI chemicals, Hong Kong) were dispensed into cylindrical borosilicate glass vials ( $\varnothing$  10 mm), which were then loaded into a commercial volumetric 3D printer (Tomolite V1, Readily3D, Switzerland) equipped with a 405 nm laser, set to deliver an average light intensity of 10.13 mW cm<sup>-2</sup> within the printing volume. Prior to printing, the samples were cooled to 4° C to achieve physical gelation of the resins. In the case of SilkMA, which does not thermally gelate, 1% w/v porcine gelatin (25 mg mL<sup>-1</sup>; porcine skin type A gelatin (~300 bloom) was added to the final resin blend to allow for thermal gelation to occur pre-printing and prevent artefacts due to sedimentation of the polymerized structure over time. Custom-designed stereolithography (STL) files were loaded into the printer software (Apparite, Readily3D, Switzerland). After the printing process, the vials were heated to 30° C to melt the unpolymerized resin and washed gently with PBS to retrieve the prints. To ensure homogenous crosslinking, the samples were submerged in 0.1% w/v solution of LAP in PBS and irradiated for 5 minutes in a CL-1000 Ultraviolet Crosslinker ( $\lambda$  = 365 nm; UVP, USA). Afterwards, samples were submerged in PBS and incubated at 37° C overnight to induce shrinking. To analyze the print resolution achievable pre- and post-shrinking, an Olympus SZ61 stereomicroscope coupled with an Olympus DP70 digital camera (Olympus Soft Imaging Solutions GmbH, The Netherlands) was used to image the printed structures, which were stained using Alcian Blue solution for better visualization. To visualize the complex prints in 3D, samples were imaged using a custom-built lightsheet microscope. All images were processed, for feature and volume measurements, as well as generation of 3D renderings of light-sheet scans, using the image analysis software FIJI.<sup>[491]</sup>

*Statistical analysis:* Graphpad PRISM v.9.4.1 was used for analysing and graphing data. Data are shown as mean  $\pm$  SD, unless otherwise stated. Statistical significance was tested by unpaired t-test with Welch's correction.





# References



## REFERENCES

- [1] O. J. Wouters, M. McKee, J. Luyten, *JAMA - Journal of the American Medical Association* **2020**, 323, DOI 10.1001/jama.2020.1166.
- [2] G. A. Van Norman, *JACC Basic Transl Sci* **2019**, DOI 10.1016/j.jacbts.2019.10.008.
- [3] S. M. Paul, D. S. Mytelka, C. T. Dunwiddie, C. C. Persinger, B. H. Munos, S. R. Lindborg, A. L. Schacht, *Nat Rev Drug Discov* **2010**, 9, 203.
- [4] R. Franco, A. Cedazo-Minguez, *Front Pharmacol* **2014**, 5 JUN, DOI 10.3389/fphar.2014.00146.
- [5] P. P. Adhikary, Q. Ul Ain, A. C. Hocke, S. Hedtrich, *Nat Rev Mater* **2021**, 6, DOI 10.1038/s41578-021-00305-z.
- [6] A. Loewa, J. J. Feng, S. Hedtrich, *Nature Reviews Bioengineering* **2023**, DOI 10.1038/s44222-023-00063-3.
- [7] P. Mukherjee, S. Roy, D. Ghosh, S. K. Nandi, *Lab Anim Res* **2022**, 38, DOI 10.1186/s42826-022-00128-1.
- [8] H. R. Ferdowsian, N. Beck, *PLoS One* **2011**, 6, DOI 10.1371/journal.pone.0024059.
- [9] J. J. Han, *Artif Organs* **2023**, 47, DOI 10.1111/aor.14503.
- [10] I. Beloglazova, E. Zubkova, K. Dergilev, Y. Goltseva, Y. Parfyonova, *Cells* **2022**, 11, DOI 10.3390/cells11203278.
- [11] I. Yuste, F. C. Luciano, E. González-Burgos, A. Lalatsa, D. R. Serrano, *Pharmacol Res* **2021**, 169, DOI 10.1016/j.phrs.2021.105626.
- [12] G. Abdelsayed, D. Ali, A. Malone, J. Saidi, M. Myneni, K. Rajagopal, F. H. Cheema, A. Hameed, *Applications in Engineering Science* **2022**, 12, DOI 10.1016/j.apples.2022.100115.
- [13] S. D. Collins, G. Yuen, T. Tu, M. A. Budzinska, K. Spring, K. Bryant, N. A. Shackel, in *Hepatocellular Carcinoma*, **2019**.
- [14] K. Duval, H. Grover, L. H. Han, Y. Mou, A. F. Pegoraro, J. Fredberg, Z. Chen, *Physiology* **2017**, 32, DOI 10.1152/physiol.00036.2016.
- [15] M. Kapałczyńska, T. Kolenda, W. Przybyła, M. Zajączkowska, A. Teresiak, V. Filas, M. Ibbs, R. Bliźniak, Ł. Łuczewski, K. Lamperska, *Archives of Medical Science* **2018**, 14, DOI 10.5114/aoms.2016.63743.
- [16] C. Jensen, Y. Teng, *Front Mol Biosci* **2020**, 7, DOI 10.3389/fmolb.2020.00033.
- [17] J. W. Nichol, S. T. Koshy, H. Bae, C. M. Hwang, S. Yamanlar, A. Khademhosseini, *Biomaterials* **2010**, 31, DOI 10.1016/j.biomaterials.2010.03.064.
- [18] K. Y. Lee, D. J. Mooney, *Chem Rev* **2001**, 101, 1869.
- [19] G. Huskin, J. Chen, T. Davis, H.-W. Jun, *Tissue Eng Regen Med* **2023**, 20, 523.
- [20] S. Y. Lee, I. S. Koo, H. J. Hwang, D. W. Lee, *SLAS Discovery* **2023**, 28, DOI 10.1016/j.slasd.2023.03.006.
- [21] A. Cacciamali, R. Villa, S. Dotti, *Front Physiol* **2022**, 13, DOI 10.3389/fphys.2022.836480.
- [22] Y. Park, K. M. Huh, S. W. Kang, *Int J Mol Sci* **2021**, 22, DOI 10.3390/ijms22052491.
- [23] X. Y. Tang, S. Wu, D. Wang, C. Chu, Y. Hong, M. Tao, H. Hu, M. Xu, X. Guo, Y. Liu, *Signal Transduct Target Ther* **2022**, 7, DOI 10.1038/s41392-022-01024-9.
- [24] K. Białkowska, P. Komorowski, M. Bryszewska, K. Miłowska, *Int J Mol Sci* **2020**, 21, DOI 10.3390/ijms21176225.
- [25] N. Timmins, S. Dietmair, L. Nielsen, *Angiogenesis* **2004**, 7, DOI 10.1007/s10456-004-8911-7.
- [26] X. Cui, Y. Hartanto, H. Zhang, *JR Soc Interface* **2017**, 14, DOI 10.1098/rsif.2016.0877.
- [27] R. Z. Lin, H. Y. Chang, *Biotechnol J* **2008**, 3, DOI 10.1002/biot.200700228.
- [28] Z. Chen, S. Han, A. Sanny, D. L. K. Chan, D. van Noort, W. Lim, A. H. M. Tan, S. Park, *J Nanobiotechnology* **2022**, 20, DOI 10.1186/s12951-021-01213-8.
- [29] S. J. Han, S. Kwon, K. S. Kim, *Cancer Cell Int* **2021**, 21, DOI 10.1186/s12935-021-01853-8.
- [30] M. Ingelman-Sundberg, V. M. Lauschke, *Basic Clin Pharmacol Toxicol* **2022**, 130, DOI 10.1111/bcpt.13587.
- [31] E. Elje, M. Hesler, E. Rundén-Pran, P. Mann, E. Mariussen, S. Wagner, M. Dusinska, Y. Kohl, *Mutat Res Genet Toxicol Environ Mutagen* **2019**, 845, DOI 10.1016/j.mrgentox.2019.03.006.
- [32] A. C. Daly, M. D. Davidson, J. A. Burdick, *Nat Commun* **2021**, 12, DOI 10.1038/s41467-021-21029-2.
- [33] A. C. Daly, D. J. Kelly, *Biomaterials* **2019**, 197, 194.

- [34] M. Yeo, S. J. Chae, G. H. Kim, *Theranostics* **2021**, *11*, DOI 10.7150/THNO.53928.
- [35] A. Marsee, F. J. M. Roos, M. M. A. Verstegen, F. Roos, M. Verstegen, H. Clevers, L. Vallier, T. Takebe, M. Huch, W. C. Peng, S. Forbes, F. Lemaigre, E. de Koning, H. Gehart, L. van der Laan, B. Spee, S. Boj, P. Baptista, K. Schneeberger, C. Soroka, M. Heim, S. Nuciforo, K. Zaret, Y. Saito, M. Lutolf, V. Cardinale, B. Simons, S. van IJzendoorn, A. Kamiya, H. Chikada, S. Wang, S. J. Mun, M. J. Son, T. T. Onder, J. Boyer, T. Sato, N. Georgakopoulos, A. Meneses, L. Broutier, L. Boulter, D. Grün, J. IJzermans, B. Artegiani, R. van Boxtel, E. Kuijk, G. Carpino, G. Peltz, J. Banales, N. Man, L. Aloia, N. LaRusso, G. George, C. Rimland, G. Yeoh, A. Grappin-Botton, D. Stange, N. Prior, J. E. E. Tirnitz-Parker, E. Andersson, C. Braconi, N. Hannan, W. Y. Lu, S. Strom, P. Sancho-Bru, S. Ogawa, V. Corbo, M. Lancaster, H. Hu, S. Fuchs, D. Hendriks, S. J. Forbes, L. J. W. van der Laan, *Cell Stem Cell* **2021**, *28*, 816.
- [36] H. Clevers, *Cell* **2016**, *165*, DOI 10.1016/j.cell.2016.05.082.
- [37] M. Hofer, M. P. Lutolf, *Nat Rev Mater* **2021**, *6*, 402.
- [38] T. Sato, H. Clevers, *Science (1979)* **2013**, *340*, DOI 10.1126/science.1234852.
- [39] L. Shariati, Y. Esmaeili, S. Haghjooy Javanmard, E. Bidram, A. Amini, *Stem Cells* **2021**, *39*, DOI 10.1002/stem.3379.
- [40] K. L. Fair, J. Colquhoun, N. R. F. Hannan, *Philosophical Transactions of the Royal Society B: Biological Sciences* **2018**, *373*, DOI 10.1098/rstb.2017.0217.
- [41] X. Lu, J. Yang, Y. Xiang, *Cell Regeneration* **2022**, *11*, DOI 10.1186/s13619-021-00103-6.
- [42] J. Liang, X. Li, Y. Dong, B. Zhao, *Cell Transplant* **2022**, *31*, DOI 10.1177/09636897221124481.
- [43] P. Van Mourik, J. M. Beekman, C. K. Van Der Ent, *European Respiratory Journal* **2019**, *54*, DOI 10.1183/13993003.02379-2018.
- [44] P. O. Frappart, K. Walter, J. Gout, A. K. Beutel, M. Morawe, F. Arnold, M. Breunig, T. F. E. Barth, R. Marienfeld, L. Schulte, T. Ettrich, T. Hackert, M. Svinarenko, R. Rösler, S. Wiese, H. Wiese, L. Perkhofor, M. Müller, A. Lechel, B. Sainz, P. C. Hermann, T. Seufferlein, A. Kleger, *United European Gastroenterol J* **2020**, *8*, DOI 10.1177/2050640620905183.
- [45] N. Sachs, A. Papaspyropoulos, D. D. Zomer-van Ommen, I. Heo, L. Böttinger, D. Klay, F. Weeber, G. Huelsz-Prince, N. Iakobachvili, G. D. Amatngalim, J. de Ligt, A. van Hoeck, N. Proost, M. C. Viveen, A. Lyubimova, L. Teeven, S. Derakhshan, J. Korving, H. Begthel, J. F. Dekkers, K. Kumawat, E. Ramos, M. F. van Oosterhout, G. J. Offerhaus, D. J. Wiener, E. P. Olimpio, K. K. Dijkstra, E. F. Smit, M. van der Linden, S. Jaksani, M. van de Ven, J. Jonkers, A. C. Rios, E. E. Voest, C. H. van Moorsel, C. K. van der Ent, E. Cuppen, A. van Oudenaarden, F. E. Coenjaerts, L. Meyaard, L. J. Bont, P. J. Peters, S. J. Tans, J. S. van Zon, S. F. Boj, R. G. Vries, J. M. Beekman, H. Clevers, *EMBO J* **2019**, *38*, DOI 10.15252/embj.2018100300.
- [46] C. Caiazza, S. Parisi, M. Caiazza, *Biology (Basel)* **2021**, *10*, DOI 10.3390/biology10090835.
- [47] A. Papaspyropoulos, M. Tsolaki, N. Foroglou, A. A. Pantazaki, *Front Pharmacol* **2020**, *11*, DOI 10.3389/fphar.2020.00396.
- [48] B. Nugraha, M. F. Buono, L. von Boehmer, S. P. Hoerstrup, M. Y. Emmert, *Clin Pharmacol Ther* **2019**, *105*, DOI 10.1002/cpt.1286.
- [49] H. Wang, *Front Synaptic Neurosci* **2018**, *10*, DOI 10.3389/fnsyn.2018.00015.
- [50] T. Miyoshi, K. Hiratsuka, E. G. Saiz, R. Morizane, *Developmental Dynamics* **2020**, *249*, DOI 10.1002/dvdy.22.
- [51] Y. Li, P. Tang, S. Cai, J. Peng, G. Hua, *Cell Regeneration* **2020**, *9*, DOI 10.1186/s13619-020-00059-z.
- [52] G. Schwank, B. K. Koo, V. Sasselli, J. F. Dekkers, I. Heo, T. Demircan, N. Sasaki, S. Boymans, E. Cuppen, C. K. Van Der Ent, E. E. S. Nieuwenhuis, J. M. Beekman, H. Clevers, *Cell Stem Cell* **2013**, *13*, DOI 10.1016/j.stem.2013.11.002.
- [53] S. Y. Graeber, P. van Mourik, A. M. Vonk, E. Kruiesselbrink, S. Hirtz, C. K. van der Ent, M. A. Mall, J. M. Beekman, *Am J Respir Crit Care Med* **2020**, *202*, DOI 10.1164/rccm.202004-1200LE.
- [54] Y. Sun, Q. Ding, *Protein Cell* **2017**, *8*, DOI 10.1007/s13238-016-0368-0.



- [55] K. Schneeberger, N. Sánchez-Romero, S. Ye, F. G. van Steenbeek, L. A. Oosterhoff, I. Pla Palacin, C. Chen, M. E. van Wolferen, G. van Tienderen, R. Lieshout, H. Colemonts-Vroninks, I. Schene, R. Hoekstra, M. M. A. Verstegen, L. J. W. van der Laan, L. C. Penning, S. A. Fuchs, H. Clevers, J. De Kock, P. M. Baptista, B. Spee, *Hepatology* **2020**, *72*, 257.
- [56] M. Nikolaev, O. Mitrofanova, N. Broguiere, S. Geraldo, D. Dutta, Y. Tabata, B. Elci, N. Brandenberg, I. Kolotuev, N. Gjorevski, H. Clevers, M. P. Lutolf, *Nature* **2020**, *585*, DOI 10.1038/s41586-020-2724-8.
- [57] V. D. L. Putra, K. A. Kilian, M. L. Knothe Tate, *Commun Biol* **2023**, *6*, DOI 10.1038/s42003-022-04320-w.
- [58] D. Cortes, C. D. McTiernan, M. Ruel, W. Franco, C. Chu, W. Liang, E. J. Suuronen, E. I. Alarcon, *Sci Rep* **2020**, *10*, DOI 10.1038/s41598-020-67169-1.
- [59] S. Parittotokkaporn, *Med Eng Phys* **2022**, *105*, DOI 10.1016/j.medengphy.2022.103815.
- [60] P. J. Nicksic, D. T. Donnelly, M. Hesse, S. Bedi, N. Verma, A. J. Seitz, A. J. Shoffstall, K. A. Ludwig, A. M. Dingle, S. O. Poore, *Front Bioeng Biotechnol* **2022**, *10*, DOI 10.3389/fbioe.2022.793945.
- [61] N. Nikolić, S. W. Görgens, G. H. Thoresen, V. Aas, J. Eckel, K. Eckardt, *Acta Physiologica* **2017**, *220*, DOI 10.1111/apha.12830.
- [62] D. Petta, V. Basoli, D. Pellicciotta, R. Tognato, J. Barcik, C. Arrigoni, E. Della Bella, A. R. Armiento, C. Candrian, R. G. Richards, M. Alini, M. Moretti, D. Eglin, T. Serra, *Biofabrication* **2020**, *13*, DOI 10.1088/1758-5090/abbb9c.
- [63] A. G. Athanassiadis, Z. Ma, N. Moreno-Gomez, K. Melde, E. Choi, R. Goyal, P. Fischer, *Chem Rev* **2022**, *122*, DOI 10.1021/acs.chemrev.1c00622.
- [64] Y. Pan, X. Du, F. Zhao, B. Xu, *Chem Soc Rev* **2012**, *41*, DOI 10.1039/c2cs15315g.
- [65] A. C. Manjua, J. M. S. Cabral, C. A. M. Portugal, F. C. Ferreira, *Sci Technol Adv Mater* **2021**, *22*, DOI 10.1080/14686996.2021.1927834.
- [66] A. Marrella, M. Iafisco, A. Adamiano, S. Rossi, M. Aiello, M. Barandalla-Sobrados, P. Carullo, M. Miragoli, A. Tampieri, S. Scaglione, D. Catalucci, *J R Soc Interface* **2018**, *15*, DOI 10.1098/rsif.2018.0236.
- [67] C. Mueller, M. Trujillo-Miranda, M. Maier, D. E. Heath, A. J. O'Connor, S. Salehi, *Adv Mater Interfaces* **2021**, *8*, DOI 10.1002/admi.202001167.
- [68] C. Roque, N. Pinto, M. Vaz Patto, G. Baltazar, *J Neurosci Res* **2021**, *99*, DOI 10.1002/jnr.24792.
- [69] S. M. Naqvi, L. M. McNamara, *Front Bioeng Biotechnol* **2020**, *8*, DOI 10.3389/fbioe.2020.597661.
- [70] M. Aragona, T. Panciera, A. Manfrin, S. Giulitti, F. Michielin, N. Elvassore, S. Dupont, S. Piccolo, *Cell* **2013**, *154*, DOI 10.1016/j.cell.2013.07.042.
- [71] S. Correia Carreira, M. Taghavi, E. Pavez Lorié, J. Rossiter, *ACS Biomater Sci Eng* **2021**, *7*, DOI 10.1021/acsbiomaterials.0c01448.
- [72] I. Uzieliene, D. Bironaite, P. Bernotas, A. Sobolev, E. Bernotiene, *Int J Mol Sci* **2021**, *22*, DOI 10.3390/ijms22189690.
- [73] J. and K.-L. B. and M. U. Wiesmann Hans Peter and Neunzehn, in *Fundamentals of Tissue Engineering and Regenerative Medicine* (Ed.: J. and W. H. P. and M. T. Meyer Ulrich and Handschel), Springer Berlin Heidelberg, Berlin, Heidelberg, **2009**, pp. 633–646.
- [74] G. Mattei, S. Giusti, A. Ahluwalia, *Processes* **2014**, *2*, DOI 10.3390/pr2030548.
- [75] M. Ginai, R. Elsby, C. J. Hewitt, D. Surry, K. Fenner, K. Coopman, *Drug Discov Today* **2013**, *18*, DOI 10.1016/j.drudis.2013.05.016.
- [76] A. Šećerović, A. Ristaniemi, S. Cui, Z. Li, A. Soubrier, M. Alini, S. J. Ferguson, G. Weder, S. Heub, D. Ledroit, S. Grad, *ACS Biomater Sci Eng* **2022**, *8*, DOI 10.1021/acsbiomaterials.2c00330.
- [77] C. F. Bellani, J. Ajeian, L. Duffy, M. Miotto, L. Groenewegen, C. J. Connon, *Front Nutr* **2020**, *7*, DOI 10.3389/fnut.2020.575146.
- [78] Z. Li, Z. Lin, S. Liu, H. Yagi, X. Zhang, L. Yocum, M. Romero-Lopez, C. Rhee, M. J. Makarczyk, I. Yu, E. N. Li, M. R. Fritch, Q. Gao, K. B. Goh, B. O'Donnell, T. Hao, P. G. Alexander, B. Mahadik, J. P. Fisher, S. B. Goodman, B. A.

- Bunnell, R. S. Tuan, H. Lin, *Advanced Science* **2022**, *9*, DOI 10.1002/advs.202105909.
- [79] P. F. Costa, C. Vaquette, J. Baldwin, M. Chhaya, M. E. Gomes, R. L. Reis, C. Theodoropoulos, D. W. Hutmacher, *Biofabrication* **2014**, *6*, DOI 10.1088/1758-5082/6/3/035006.
- [80] S. Gabetti, B. Masante, A. Cochis, G. Putame, A. Sanginario, I. Armando, E. Fiume, A. C. Scalia, F. Daou, F. Baino, S. Salati, U. Morbiducci, L. Rimondini, C. Bignardi, D. Massai, *Sci Rep* **2022**, *12*, DOI 10.1038/s41598-022-18075-1.
- [81] M. Gensler, A. Leikeim, M. Möllmann, M. Komma, S. Heid, C. Müller, A. R. Boccaccini, S. Salehi, F. Groeber-Becker, J. Hansmann, *PLoS One* **2020**, *15*, DOI 10.1371/journal.pone.0242615.
- [82] D. E. Ingber, *Nat Rev Genet* **2022**, *23*, DOI 10.1038/s41576-022-00466-9.
- [83] H. Chen, Z. Luo, X. Lin, Y. Zhu, Y. Zhao, *Nano Res* **2023**, DOI 10.1007/s12274-023-5651-9.
- [84] P. Admane, K. B. Ghaghada, L. Devkota, P. Sarkar, A. Badachhpe, P. Bhandari, A. Annapragada, Z. Starosolski, *Bioprinting* **2023**, *29*, DOI 10.1016/j.bprint.2022.e00249.
- [85] J. P. Wikswo, *Exp Biol Med* **2014**, *239*, DOI 10.1177/1535370214542068.
- [86] A. Manz, N. Graber, H. M. Widmer, *Sens Actuators B Chem* **1990**, *1*, DOI 10.1016/0925-4005(90)80209-I.
- [87] D. C. Duffy, J. C. McDonald, O. J. A. Schueller, G. M. Whitesides, *Anal Chem* **1998**, *70*, DOI 10.1021/ac980656z.
- [88] H. G. Yi, H. Lee, D. W. Cho, *Bioengineering* **2017**, *4*, DOI 10.3390/bioengineering4010010.
- [89] V. Carvalho, I. Gonçalves, T. Lage, R. O. Rodrigues, G. Minas, S. F. C. F. Teixeira, A. S. Moita, T. Hori, H. Kaji, R. A. Lima, *Sensors* **2021**, *21*, DOI 10.3390/s21093304.
- [90] E. M. J. Verpoorte, B. H. Van Der Schoot, S. Jeanneret, A. Manz, H. M. Widmer, N. F. De Rooij, *Journal of Micromechanics and Microengineering* **1994**, *4*, DOI 10.1088/0960-1317/4/4/009.
- [91] D. E. Ingber, *Advanced Science* **2020**, *7*, DOI 10.1002/advs.202002030.
- [92] K. M. Bircsak, R. DeBiasio, M. Miedel, A. Alsebah, R. Reddinger, A. Saleh, T. Shun, L. A. Verneti, A. Gough, *Toxicology* **2021**, *450*, DOI 10.1016/j.tox.2020.152667.
- [93] I. Francis, J. Shrestha, K. R. Paudel, P. M. Hansbro, M. E. Warkiani, S. C. Saha, *Drug Discov Today* **2022**, *27*, DOI 10.1016/j.drudis.2022.06.004.
- [94] Y. Zhu, L. Sun, Y. Wang, L. Cai, Z. Zhang, Y. Shang, Y. Zhao, *Advanced Materials* **2022**, *34*, DOI 10.1002/adma.202108972.
- [95] D. Zhang, L. Qiao, *VIEW* **2023**, *4*, DOI 10.1002/VIW.20220037.
- [96] S. Myram, B. Venzac, B. Lapin, A. Battistella, F. Cayrac, B. Cinquin, C. Cavaniol, G. Groppero, I. Bonnet, S. Demolombe, S. Descroix, S. Coscoy, *Front Bioeng Biotechnol* **2021**, *9*, DOI 10.3389/fbioe.2021.624553.
- [97] D. Wang, M. Gust, N. Ferrell, *Sensors* **2022**, *22*, DOI 10.3390/s22186889.
- [98] V. Guarino, A. Zizzari, M. Bianco, G. Gigli, L. Moroni, V. Arima, *Biofabrication* **2023**, *15*, DOI 10.1088/1758-5090/acb571.
- [99] M. Mir, S. Palma-Florez, A. Lagunas, M. J. López-Martínez, J. Samitier, *ACS Sens* **2022**, *7*, DOI 10.1021/acssensors.2c00333.
- [100] S. Piluso, Y. Li, F. Abinzano, R. Levato, L. Moreira Teixeira, M. Karperien, J. Leijten, R. van Weeren, J. Malda, *Trends Biotechnol* **2019**, *37*, DOI 10.1016/j.tibtech.2019.03.003.
- [101] M. Rothbauer, S. Schobesberger, R. Byrne, H. P. Kiener, S. Tögel, P. Ertl, *Osteoarthritis Cartilage* **2020**, *28*, DOI 10.1016/j.joca.2020.02.135.
- [102] R. X. Z. Lu, B. F. L. Lai, N. Rafatian, D. Gustafson, S. B. Campbell, A. Banerjee, R. Kozak, K. Mossman, S. Mubareka, K. L. Howe, J. E. Fish, M. Radisic, *Lab Chip* **2022**, *22*, DOI 10.1039/d1lc00817j.
- [103] F. Chesnais, J. Joel, J. Hue, S. Shakib, L. Di Silvio, A. E. Grigoriadis, T. Coward, L. Veschini, *Lab Chip* **2023**, *23*, DOI 10.1039/d2lc00930g.
- [104] A. Sontheimer-Phelps, B. A. Hassell, D. E. Ingber, *Nat Rev Cancer* **2019**, *19*, DOI 10.1038/s41568-018-0104-6.
- [105] S. Syama, P. V. Mohanan, *Trends Food Sci Technol* **2021**, *110*, DOI 10.1016/j.tifs.2021.02.049.
- [106] C. D. Edington, W. L. K. Chen, E. Geishecker, T. Kassis, L. R. Soenksen, B. M. Bhushan, D. Freake, J. Kirschner, C.

- Maass, N. Tsamandouras, J. Valdez, C. D. Cook, T. Parent, S. Snyder, J. Yu, E. Suter, M. Shockley, J. Velazquez, J. J. Velazquez, L. Stockdale, J. P. Papps, I. Lee, N. Vann, M. Gamboa, M. E. Labarge, Z. Zhong, X. Wang, L. A. Boyer, D. A. Lauffenburger, R. L. Carrier, C. Communal, S. R. Tannenbaum, C. L. Stokes, D. J. Hughes, G. Rohatgi, D. L. Trumper, M. Cirit, L. G. Griffith, *Sci Rep* **2018**, *8*, DOI 10.1038/s41598-018-22749-0.
- [107] M. Boareto, *Dev Biol* **2020**, *460*, DOI 10.1016/j.ydbio.2019.12.008.
- [108] C. M. Nelson, M. J. Bissell, *Annu Rev Cell Dev Biol* **2006**, *22*, DOI 10.1146/annurev.cellbio.22.010305.104315.
- [109] R. Levato, T. Jungst, R. G. Scheuring, T. Blunk, J. Groll, J. Malda, *Advanced Materials* **2020**, *32*, DOI 10.1002/adma.201906423.
- [110] J. Groll, T. Boland, T. Blunk, J. A. Burdick, D. W. Cho, P. D. Dalton, B. Derby, G. Forgacs, Q. Li, V. A. Mironov, L. Moroni, M. Nakamura, W. Shu, S. Takeuchi, G. Vozzi, T. B. F. Woodfield, T. Xu, J. J. Yoo, J. Malda, *Biofabrication* **2016**, *8*, DOI 10.1088/1758-5090/8/1/013001.
- [111] L. Moroni, J. A. Burdick, C. Highley, S. J. Lee, Y. Morimoto, S. Takeuchi, J. J. Yoo, *Nat Rev Mater* **2018**, *3*, DOI 10.1038/s41578-018-0006-y.
- [112] L. Moroni, T. Boland, J. A. Burdick, C. De Maria, B. Derby, G. Forgacs, J. Groll, Q. Li, J. Malda, V. A. Mironov, C. Mota, M. Nakamura, W. Shu, S. Takeuchi, T. B. F. Woodfield, T. Xu, J. J. Yoo, G. Vozzi, *Trends Biotechnol* **2018**, *36*, DOI 10.1016/j.tibtech.2017.10.015.
- [113] W. C. Wilson, T. Boland, *Anatomical Record - Part A Discoveries in Molecular, Cellular, and Evolutionary Biology* **2003**, *272*, DOI 10.1002/ara.10057.
- [114] I. T. Ozbolat, M. Hospodiuk, *Biomaterials* **2016**, *76*, DOI 10.1016/j.biomaterials.2015.10.076.
- [115] S. Boularaoui, G. Al Hussein, K. A. Khan, N. Christoforou, C. Stefanini, *Bioprinting* **2020**, *20*, DOI 10.1016/j.bprint.2020.e00093.
- [116] Y. S. Zhang, G. Haghiashtiani, T. Hübscher, D. J. Kelly, J. M. Lee, M. Lutolf, M. C. McAlpine, W. Y. Yeong, M. Zenobi-Wong, J. Malda, *Nature Reviews Methods Primers* **2021**, *1*, DOI 10.1038/s43586-021-00073-8.
- [117] X. Li, B. Liu, B. Pei, J. Chen, D. Zhou, J. Peng, X. Zhang, W. Jia, T. Xu, *Chem Rev* **2020**, *120*, DOI 10.1021/acs.chemrev.0c00008.
- [118] D. ke Zhao, H. qi Xu, J. Yin, H. yong Yang, *Journal of Zhejiang University: Science A* **2022**, *23*, DOI 10.1631/2023.A2200569.
- [119] R. Levato, O. Dudaryeva, C. E. Garciamendez-Mijares, B. E. Kirkpatrick, R. Rizzo, J. Schimelman, K. S. Anseth, S. Chen, M. Zenobi-Wong, Y. S. Zhang, *Nature Reviews Methods Primers* **2023**, *3*, DOI 10.1038/s43586-023-00231-0.
- [120] M. Lee, R. Rizzo, F. Surman, M. Zenobi-Wong, *Chem Rev* **2020**, *120*, DOI 10.1021/acs.chemrev.0c00077.
- [121] T. Zandrini, S. Florczak, R. Levato, A. Ovsianikov, *Trends Biotechnol* **2022**, DOI 10.1016/j.tibtech.2022.10.009.
- [122] A. C. Daly, K. S. Lim, *Trends Biotechnol* **2023**, *41*, DOI 10.1016/j.tibtech.2022.11.007.
- [123] T. D. Brown, P. D. Dalton, D. W. Hutmacher, *Prog Polym Sci* **2016**, *56*, 116.
- [124] T. D. Brown, P. D. Dalton, D. W. Hutmacher, *Advanced Materials* **2011**, *23*, 5651.
- [125] G. Hochleitner, T. Jüngst, T. D. Brown, K. Hahn, C. Moseke, F. Jakob, P. D. Dalton, J. Groll, *Biofabrication* **2015**, *7*, DOI 10.1088/1758-5090/7/3/035002.
- [126] O. Gryshkov, M. Müller, S. Leal-Marín, V. Mutsenko, S. Suresh, V. M. Kapralova, B. Glasmacher, in *J Phys Conf Ser*, **2019**.
- [127] P. N. Bernal, P. Delrot, D. Loterie, Y. Li, J. Malda, C. Moser, R. Levato, *Advanced Materials* **2019**, *31*, DOI 10.1002/adma.201970302.
- [128] J. Malda, J. Visser, F. P. Melchels, T. Jüngst, W. E. Hennink, W. J. A. Dhert, J. Groll, D. W. Hutmacher, *Advanced Materials* **2013**, *25*, 5011.
- [129] J. Groll, J. A. Burdick, D. W. Cho, B. Derby, M. Gelinsky, S. C. Heilshorn, T. Jüngst, J. Malda, V. A. Mironov, K. Nakayama, A. Ovsianikov, W. Sun, S. Takeuchi, J. J. Yoo, T. B. F. Woodfield, *Biofabrication* **2019**, *11*, DOI 10.1088/1758-5090/aeec52.

- [130] T. Jungst, W. Smolan, K. Schacht, T. Scheibel, J. Groll, *Chem Rev* **2016**, *116*, DOI 10.1021/acs.chemrev.5b00303.
- [131] M. Castilho, M. de Ruijter, S. Beirne, C. C. Villette, K. Ito, G. G. Wallace, J. Malda, *Trends Biotechnol* **2020**, *38*, 1316.
- [132] V. Mironov, T. Trusk, V. Kasyanov, S. Little, R. Swaja, R. Markwald, *Biofabrication* **2009**, *1*, DOI 10.1088/1758-5082/1/2/022001.
- [133] K. A. Van Kampen, R. G. Scheuring, M. L. Terpstra, R. Levato, J. Groll, J. Malda, C. Mota, L. Moroni, *Biofabrication: From Additive Manufacturing to Bioprinting*, **2019**.
- [134] M. B. Ginzberg, R. Kafri, M. Kirschner, *Science (1979)* **2015**, *348*, DOI 10.1126/science.1245075.
- [135] M. Rocca, A. Fragasso, W. Liu, M. A. Heinrich, Y. S. Zhang, *SLAS Technol* **2018**, *23*, DOI 10.1177/2472630317742071.
- [136] X. Zeng, Z. Meng, J. He, M. Mao, X. Li, P. Chen, J. Fan, D. Li, *Acta Biomater* **2022**, *140*, DOI 10.1016/j.actbio.2021.11.048.
- [137] N. V. Mekhileri, G. Major, K. Lim, I. Mutreja, K. Chitchoitan, E. Phillips, G. Hooper, T. Woodfield, *Adv Healthc Mater* **2023**, *12*, DOI 10.1002/adhm.202201581.
- [138] E. Goulart, L. C. De Caires-Junior, K. A. Telles-Silva, B. H. S. Araujo, S. A. Rocco, M. Sforca, I. L. De Sousa, G. S. Kobayashi, C. M. Musso, A. F. Assoni, D. Oliveira, E. Caldini, S. Raia, P. I. Lelkes, M. Zatz, *Biofabrication* **2020**, *12*, DOI 10.1088/1758-5090/ab4a30.
- [139] D. N. Heo, B. Ayan, M. Dey, D. Banerjee, H. Wee, G. S. Lewis, I. T. Ozbolat, *Biofabrication* **2021**, *13*, DOI 10.1088/1758-5090/abc1bf.
- [140] D. Banerjee, Y. P. Singh, P. Datta, V. Ozbolat, A. O'Donnell, M. Yeo, I. T. Ozbolat, *Biomaterials* **2022**, *291*, DOI 10.1016/j.biomaterials.2022.121881.
- [141] P. Rawal, D. M. Tripathi, S. Ramakrishna, S. Kaur, *BioDes Manuf* **2021**, *4*, DOI 10.1007/s42242-020-00124-1.
- [142] H. Chen, Z. Wu, Z. Gong, Y. Xia, J. Li, L. Du, Y. Zhang, X. Gao, Z. Fan, H. Hu, Q. Qian, Z. Ding, S. Guo, *Adv Healthc Mater* **2022**, *11*, DOI 10.1002/adhm.202102784.
- [143] E. A. Bulanova, E. V. Koudan, J. Degosserie, C. Heymans, F. D. A. S. Pereira, V. A. Parfenov, Y. Sun, Q. Wang, S. A. Akhmedova, I. K. Sviridova, N. S. Sergeeva, G. A. Frank, Y. D. Khesuani, C. E. Pierreux, V. A. Mironov, *Biofabrication* **2017**, *9*, DOI 10.1088/1758-5090/aa7fdd.
- [144] D. Kilian, T. Ahlfeld, A. R. Akkineni, A. Lode, M. Gelinsky, *MRS Bull* **2017**, *42*, DOI 10.1557/mrs.2017.164.
- [145] K. P., D. B., A. F.H., H. N.T., A. S.K., C. B.R., *Crit Rev Ther Drug Carrier Syst* **2015**, *32*.
- [146] J. Parrish, K. Lim, B. Zhang, M. Radisic, T. B. F. Woodfield, *Trends Biotechnol* **2019**, *37*, DOI 10.1016/j.tibtech.2019.04.009.
- [147] H. Lee, D. W. Cho, *Lab Chip* **2016**, *16*, DOI 10.1039/c6lc00450d.
- [148] K. Fetah, P. Tebon, M. J. Goudie, J. Eichenbaum, L. Ren, N. Barros, R. Nasiri, S. Ahadian, N. Ashammakhi, M. R. Dokmeci, A. Khademhosseini, *Progress in Biomedical Engineering* **2019**, *1*, DOI 10.1088/2516-1091/ab23df.
- [149] K. Thakare, L. Jerpseth, Z. Pei, A. Elwany, F. Quek, H. Qin, *Journal of Manufacturing and Materials Processing* **2021**, *5*, DOI 10.3390/JMMP5030091.
- [150] F. Yu, D. Choudhury, *Drug Discov Today* **2019**, *24*, DOI 10.1016/j.drudis.2019.03.025.
- [151] A. Schwab, R. Levato, M. D'Este, S. Piluso, D. Eglin, J. Malda, *Chem Rev* **2020**, *120*, 11028.
- [152] N. Sood, A. Bhardwaj, S. Mehta, A. Mehta, *Drug Deliv* **2016**, *23*, DOI 10.3109/10717544.2014.940091.
- [153] M. A. Mohamed, A. Fallahi, A. M. A. El-Sokkary, S. Salehi, M. A. Akl, A. Jafari, A. Tamayol, H. Fenniri, A. Khademhosseini, S.T. Andreadis, C. Cheng, *Prog Polym Sci* **2019**, *98*, DOI 10.1016/j.progpolymsci.2019.101147.
- [154] R. Raman, B. Bhaduri, M. Mir, A. Shkumatov, M. K. Lee, G. Popescu, H. Kong, R. Bashir, *Adv Healthc Mater* **2016**, *5*, 610.
- [155] L. A. Sawicki, A. M. Kloxin, *Journal of Visualized Experiments* **2016**, *2016*, DOI 10.3791/54462.
- [156] J. A. Shadish, G. M. Benuska, C. A. DeForest, *Nat Mater* **2019**, DOI 10.1038/s41563-019-0367-7.
- [157] M. J. Webber, P. Y. W. Dankers, *Macromol Biosci* **2019**, *19*, DOI 10.1002/mabi.201800452.

- [158] K. Numata, S. Yamazaki, T. Katashima, J. A. Chuah, N. Naga, T. Sakai, *Macromol Biosci* **2014**, *14*, DOI 10.1002/mabi.201300482.
- [159] B. J. Klotz, D. Gawlitta, A. J. W. P. Rosenberg, J. Malda, F. P. W. Melchels, *Trends Biotechnol* **2016**, *34*, 394.
- [160] J. Van Hoorick, L. Tytgat, A. Dobos, H. Ottevaere, J. Van Erps, H. Thienpont, A. Ovsianikov, P. Dubruel, S. Van Vlierberghe, *Acta Biomater* **2019**, DOI 10.1016/j.actbio.2019.07.035.
- [161] J. Van Hoorick, P. Gruber, M. Markovic, M. Tromayer, J. Van Erps, H. Thienpont, R. Liska, A. Ovsianikov, P. Dubruel, S. Van Vlierberghe, *Biomacromolecules* **2017**, *18*, 3260.
- [162] J. A. Brassard, M. P. Lutolf, *Cell Stem Cell* **2019**, *24*, 860.
- [163] Y. J. No, M. Castilho, Y. Ramaswamy, H. Zreiqat, *Advanced Materials* **2020**, *32*, DOI 10.1002/adma.201904511.
- [164] S. Sart, T. Ma, Y. Li, *Biores Open Access* **2014**, *3*, DOI 10.1089/biores.2014.0012.
- [165] K. H. Vining, D. J. Mooney, *Nat Rev Mol Cell Biol* **2017**, *18*, DOI 10.1038/nrm.2017.108.
- [166] G. Charras, E. Sahai, *Nat Rev Mol Cell Biol* **2014**, *15*, DOI 10.1038/nrm3897.
- [167] M. Castilho, A. van Mil, M. Maher, C. H. G. Metz, G. Hochleitner, J. Groll, P. A. Doevendans, K. Ito, J. P. G. Sluijter, J. Malda, *Adv Funct Mater* **2018**, *28*, DOI 10.1002/adfm.201803151.
- [168] A. Deglincerti, F. Etoc, M. C. Guerra, I. Martyn, J. Metzger, A. Ruzo, M. Simunovic, A. Yoney, A. H. Brivanlou, E. Siggia, A. Warmflash, *Nat Protoc* **2016**, *11*, DOI 10.1038/nprot.2016.131.
- [169] T. Luo, K. Mohan, P. A. Iglesias, D. N. Robinson, *Nat Mater* **2013**, *12*, DOI 10.1038/nmat3772.
- [170] W. Liu, Y. S. Zhang, M. A. Heinrich, F. De Ferrari, H. L. Jang, S. M. Bakht, M. M. Alvarez, J. Yang, Y. C. Li, G. Trujillo-de Santiago, A. K. Miri, K. Zhu, P. Khoshakhlagh, G. Prakash, H. Cheng, X. Guan, Z. Zhong, J. Ju, G. H. Zhu, X. Jin, S. R. Shin, M. R. Dokmeci, A. Khademhosseini, *Advanced Materials* **2017**, *29*, DOI 10.1002/adma.201604630.
- [171] C. Norotte, F. S. Marga, L. E. Niklason, G. Forgacs, *Biomaterials* **2009**, *30*, 5910.
- [172] M. Yanez, J. Rincon, A. Dones, C. De Maria, R. Gonzales, T. Boland, *Tissue Eng Part A* **2015**, *21*, DOI 10.1089/ten.tea.2013.0561.
- [173] K. S. Lim, R. Levato, P. F. Costa, M. D. Castilho, C. R. Alcalá-Orozco, K. M. A. Van Dorenmalen, F. P. W. Melchels, D. Gawlitta, G. J. Hooper, J. Malda, T. B. F. Woodfield, *Biofabrication* **2018**, *10*, DOI 10.1088/1758-5090/aac00c.
- [174] A. Dobos, J. Van Hoorick, W. Steiger, P. Gruber, M. Markovic, O. G. Andriotis, A. Rohatschek, P. Dubruel, P. J. Thurner, S. Van Vlierberghe, S. Baudis, A. Ovsianikov, *Adv Healthc Mater* **2019**, 1900752.
- [175] E. Ehler, S. N. Jayasinghe, *Analyst* **2014**, *139*, 4449.
- [176] M. Hu, R. Deng, K. M. Schumacher, M. Kurisawa, H. Ye, K. Purnamawati, J. Y. Ying, *Biomaterials* **2010**, *31*, DOI 10.1016/j.biomaterials.2009.10.002.
- [177] H. Chen, Y. Liu, Q. Hu, *Exp Cell Res* **2015**, *338*, DOI 10.1016/j.yexcr.2015.08.007.
- [178] J. He, X. Zhao, J. Chang, D. Li, *Small* **2017**, *13*, DOI 10.1002/smll.201702626.
- [179] X. Zhao, J. He, F. Xu, Y. Liu, D. Li, *Virtual Phys Prototyp* **2016**, *11*, DOI 10.1080/17452759.2016.1139378.
- [180] J. Li, S. Wu, E. Kim, K. Yan, H. Liu, C. Liu, H. Dong, X. Qu, X. Shi, J. Shen, W. E. Bentley, G. F. Payne, *Biofabrication* **2019**, *11*, DOI 10.1088/1758-5090/ab06ea.
- [181] S. L. Sampson, L. Saraiva, K. Gustafsson, S. N. Jayasinghe, B. D. Robertson, *Small* **2014**, *10*, DOI 10.1002/smll.201300804.
- [182] S. N. Jayasinghe, J. Auguste, C. J. Scotton, *Advanced Materials* **2015**, *27*, DOI 10.1002/adma.201503001.
- [183] M. G. Yeo, J. H. Ha, H. J. Lee, G. H. Kim, *Acta Biomater* **2016**, *38*, DOI 10.1016/j.actbio.2016.04.017.
- [184] X. Li, Z. Li, L. Wang, G. Ma, F. Meng, R. H. Pritchard, E. L. Gill, Y. Liu, Y. Y. S. Huang, *ACS Appl Mater Interfaces* **2016**, *8*, DOI 10.1021/acsami.6b07797.
- [185] V. Liaudanskaya, L. Gasperini, D. Maniglio, A. Motta, C. Migliaresi, *Tissue Eng Part C Methods* **2015**, *21*, DOI 10.1089/ten.tec.2014.0228.
- [186] D. Nahm, F. Weigl, N. Schaefer, A. Sancho, A. Frank, J. Groll, C. Villmann, H. W. Schmidt, P. D. Dalton, R.

- Luxenhofer, *Mater Horiz* **2020**, *7*, DOI 10.1039/c9mh01654f.
- [187] J. H. Jordahl, L. Solorio, H. Sun, S. Ramcharan, C. B. Teeple, H. R. Haley, K. J. Lee, T. W. Eyster, G. D. Luker, P. H. Krebsbach, J. Lahann, *Advanced Materials* **2018**, *30*, DOI 10.1002/adma.201707196.
- [188] D. J. Wu, N. H. Vonk, B. A. G. Lamers, M. Castilho, J. Malda, J. P. M. Hoefnagels, P. Y. W. Dankers, *Eur Polym J* **2020**, *141*, DOI 10.1016/j.eurpolymj.2020.110099.
- [189] G. Steinhoff, *Regenerative Medicine - From Protocol to Patient: 1. Biology of Tissue Regeneration: Third Edition*, **2016**.
- [190] L. Gu, Y. Jiang, J. Hu, *Advanced Materials* **2019**, *31*, DOI 10.1002/adma.201904311.
- [191] D. N. Rockwood, R. C. Preda, T. Yücel, X. Wang, M. L. Lovett, D. L. Kaplan, *Nat Protoc* **2011**, *6*, DOI 10.1038/nprot.2011.379.
- [192] M. Montinaro, V. Fasano, M. Moffa, A. Camposeo, L. Persano, M. Lauricella, S. Succi, D. Pisignano, *Soft Matter* **2015**, *11*, DOI 10.1039/c4sm02708f.
- [193] X. Cui, B. G. Soliman, C. R. Alcalá-Orozco, J. Li, M. A. M. Vis, M. Santos, S. G. Wise, R. Levato, J. Malda, T. B. F. Woodfield, J. Rnjak-Kovacina, K. S. Lim, *Adv Healthc Mater* **2020**, *9*, DOI 10.1002/adhm.201901667.
- [194] K. S. Lim, B. S. Schon, N. V. Mekhileri, G. C. J. Brown, C. M. Chia, S. Prabakar, G. J. Hooper, T. B. F. Woodfield, *ACS Biomater Sci Eng* **2016**, *2*, 1752.
- [195] S. Bertlein, G. Brown, K. S. Lim, T. Jungst, T. Boeck, T. Blunk, J. Tessmar, G. J. Hooper, T. B. F. Woodfield, J. Groll, *Advanced Materials* **2017**, *29*, DOI 10.1002/adma.201703404.
- [196] B. G. Soliman, G. C. J. Lindberg, T. Jungst, G. J. Hooper, J. Groll, T. B. F. Woodfield, K. S. Lim, *Adv Healthc Mater* **2020**, DOI 10.1002/adhm.201901544.
- [197] P. Gambhire, R. M. Thakkar, *Phys Rev E Stat Nonlin Soft Matter Phys* **2012**, *86*, DOI 10.1103/PhysRevE.86.036301.
- [198] I. Hayati, A. I. Bailey, T. F. Tadros, *Nature* **1986**, *319*, DOI 10.1038/319041a0.
- [199] G. Hochleitner, A. Youssef, A. Hrynevich, J. N. Haigh, T. Jungst, J. Groll, P. D. Dalton, *BioNanoMaterials* **2016**, *17*, DOI 10.1515/bnm-2015-0022.
- [200] M. Castilho, D. Feyen, M. Flandes-Iparraguirre, G. Hochleitner, J. Groll, P. A. F. Doevendans, T. Vermonden, K. Ito, J. P. G. Sluijter, J. Malda, *Adv Healthc Mater* **2017**, *6*, DOI 10.1002/adhm.201700311.
- [201] W. Liu, M. A. Heinrich, Y. Zhou, A. Akpek, N. Hu, X. Liu, X. Guan, Z. Zhong, X. Jin, A. Khademhosseini, Y. S. Zhang, *Adv Healthc Mater* **2017**, *6*, DOI 10.1002/adhm.201601451.
- [202] M. de Ruijter, A. Ribeiro, I. Dokter, M. Castilho, J. Malda, *Adv Healthc Mater* **2019**, *8*, 1800418.
- [203] G. Collins, J. Federici, Y. Imura, L. H. Catalani, *J Appl Phys* **2012**, *111*, DOI 10.1063/1.3682464.
- [204] F. M. Wunner, M. L. Wille, T. G. Noonan, O. Bas, P. D. Dalton, E. M. De-Juan-Pardo, D. W. Huttmacher, *Advanced Materials* **2018**, *30*, DOI 10.1002/adma.201706570.
- [205] M. Yeo, G. H. Kim, *Acta Biomater* **2020**, *107*, DOI 10.1016/j.actbio.2020.02.042.
- [206] E. L. Gill, S. Willis, M. Gerigk, P. Cohen, D. Zhang, X. Li, Y. Y. S. Huang, *ACS Appl Mater Interfaces* **2019**, *11*, DOI 10.1021/acsami.9b01258.
- [207] B. Yi, H. Zhang, Z. Yu, H. Yuan, X. Wang, Y. Zhang, *J Mater Chem B* **2018**, *6*, DOI 10.1039/c8tb00535d.
- [208] M. Wang, H. J. Jin, D. L. Kaplan, G. C. Rutledge, *Macromolecules* **2004**, *37*, DOI 10.1021/ma048988v.
- [209] S. N. Jayasinghe, S. Irvine, J. R. McEwan, *Nanomedicine* **2007**, *2*, DOI 10.2217/17435889.2.4.555.
- [210] M. J. Hoogduijn, J. C. Van Den Beukel, L. C. M. Wiersma, J. Ijzer, *BMJ (Online)* **2013**, *347*, DOI 10.1136/bmj.f6833.
- [211] L. Li, J. Eyckmans, C. S. Chen, *Nat Mater* **2017**, *16*, 1164.
- [212] Z. Muñoz, H. Shih, C. C. Lin, *Biomater Sci* **2014**, *2*, 1063.
- [213] V. H. M. Mouser, A. Abbadessa, R. Levato, W. E. Hennink, T. Vermonden, D. Gawlitta, J. Malda, *Biofabrication* **2017**, *9*, 15026.
- [214] J. Crest, A. Diz-Muñoz, D. Y. Chen, D. A. Fletcher, D. Bilder, *Elife* **2017**, *6*, DOI 10.7554/eLife.24958.
- [215] H. Donnelly, M. Salmeron-Sanchez, M. J. Dalby, *J R Soc Interface* **2018**, *15*, DOI 10.1098/rsif.2018.0388.

- [216] N. Gjorevski, N. Sachs, A. Manfrin, S. Giger, M. E. Bragina, P. Ordóñez-Morán, H. Clevers, M. P. Lutolf, *Nature* **2016**, *539*, 560.
- [217] S. A. Matarazzo, *PLoS One* **2015**, *10*(3), e0120436.
- [218] G. Bahcecioglu, N. Hasirci, B. Bilgen, V. Hasirci, *Biofabrication* **2019**, *11*, DOI 10.1088/1758-5090/aaf707.
- [219] R. Tognato, A. R. Armiento, V. Bonfrate, R. Levato, J. Malda, M. Alini, D. Eglin, G. Giancane, T. Serra, *Adv Funct Mater* **2019**, *29*, DOI 10.1002/adfm.201804647.
- [220] H. W. Kang, S. J. Lee, I. K. Ko, C. Kengla, J. J. Yoo, A. Atala, *Nat Biotechnol* **2016**, *34*, 312.
- [221] M. M. Laronda, A. L. Rutz, S. Xiao, K. A. Whelan, F. E. Duncan, E. W. Roth, T. K. Woodruff, R. N. Shah, *Nat Commun* **2017**, *8*, DOI 10.1038/ncomms15261.
- [222] M. Müller, E. Öztürk, Ø. Arlov, P. Gatenholm, M. Zenobi-Wong, *Ann Biomed Eng* **2017**, *45*, 210.
- [223] J. K. Hohmann, M. Renner, E. H. Waller, G. von Freymann, *Adv Opt Mater* **2015**, *3*, 1488.
- [224] D. Loterie, P. Delrot, C. Moser, *Nat Commun* **2020**, *11*, DOI 10.1038/s41467-020-14630-4.
- [225] B. E. Kelly, I. Bhattacharya, H. Heidari, M. Shusteff, C. M. Spadaccini, H. K. Taylor, *Science (1979)* **2019**, *363*, 1075.
- [226] M. Shusteff, A. E. M. Browar, B. E. Kelly, J. Henriksson, T. H. Weisgraber, R. M. Panas, N. X. Fang, C. M. Spadaccini, *Sci Adv* **2017**, *3*, DOI 10.1126/sciadv.aao5496.
- [227] A. C. Kak, M. Slaney, G. Wang, *Med Phys* **2002**, *29*, 107.
- [228] A. K. Miri, D. Nieto, L. Iglesias, H. Goodarzi Hosseinabadi, S. Maharjan, G. U. Ruiz-Esparza, P. Khoshakhlagh, A. Manbachi, M. R. Dokmeci, S. Chen, S. R. Shin, Y. S. Zhang, A. Khademhosseini, *Advanced Materials* **2018**, *30*, DOI 10.1002/adma.201800242.
- [229] B. J. Klotz, D. Gawlitta, A. J. W. P. Rosenberg, J. Malda, F. P. W. Melchels, *Trends Biotechnol* **2016**, *34*, 394.
- [230] G. L. Ying, N. Jiang, S. Maharjan, Y. X. Yin, R. R. Chai, X. Cao, J. Z. Yang, A. K. Miri, S. Hassan, Y. S. Zhang, *Advanced Materials* **2018**, DOI 10.1002/adma.201805460.
- [231] L. Ouyang, J. A. Burdick, W. Sun, *ACS Appl Mater Interfaces* **2018**, *10*, 12424.
- [232] L. Ouyang, C. B. Highley, W. Sun, J. A. Burdick, *Advanced Materials* **2017**, *29*, DOI 10.1002/adma.201604983.
- [233] C. Xu, W. Lee, G. Dai, Y. Hong, *ACS Appl Mater Interfaces* **2018**, *10*, 9969.
- [234] S. H. Kim, Y. K. Yeon, J. M. Lee, J. R. Chao, Y. J. Lee, Y. B. Seo, M. T. Sultan, O. J. Lee, J. S. Lee, S. Il Yoon, I. S. Hong, G. Khang, S. J. Lee, J. J. Yoo, C. H. Park, *Nat Commun* **2018**, *9*, DOI 10.1038/s41467-018-03759-y.
- [235] B. Grigoryan, S. Paulsen, D. Corbett, D. Sazer, C. L. Fortin, A. Zaita, P. Greenfield, N. Calafat, J. Gounley, A. Ta, F. Johansson, A. Randles, J. J. Rosenkrantz, J. Louis-Rosenberg, Peter. Galie, K. Stevens, J. Miller, *Science (1979)* **2019**, *364*, 458.
- [236] R. Holmes, X. Bin Yang, A. Dunne, L. Florea, D. Wood, G. Tronci, *Polymers (Basel)* **2017**, *9*, DOI 10.3390/polym9060226.
- [237] J. R. Tumbleston, D. Shirvanyants, N. Ermoshkin, R. Januszewicz, A. R. Johnson, D. Kelly, K. Chen, R. Pinschmidt, J. P. Rolland, A. Ermoshkin, E. T. Samulski, J. M. DeSimone, *Science (1979)* **2015**, *347*, 1349.
- [238] A. Kirillova, R. Maxson, G. Stoychev, C. T. Gomillion, L. Ionov, *Advanced Materials* **2017**, *29*, DOI 10.1002/adma.201703443.
- [239] S. Miao, H. Cui, M. Nowicki, L. Xia, X. Zhou, S. J. Lee, W. Zhu, K. Sarkar, Z. Zhang, L. G. Zhang, *Adv Biosyst* **2018**, *2*, DOI 10.1002/adbi.201800101.
- [240] S. R. Shin, B. Migliori, B. Miccoli, Y. C. Li, P. Mostafalu, J. Seo, S. Mandla, A. Enrico, S. Antona, R. Sabarish, T. Zheng, L. Pirrami, K. Zhang, Y. S. Zhang, K. T. Wan, D. Demarchi, M. R. Dokmeci, A. Khademhosseini, *Advanced Materials* **2018**, *30*, DOI 10.1002/adma.201704189.
- [241] W. Y. Lim, G. Lloyd, S. Bhattacharyya, *Heart* **2017**, *103*, 1934.
- [242] M. Wehner, R. L. Truby, D. J. Fitzgerald, B. Mosadegh, G. M. Whitesides, J. A. Lewis, R. J. Wood, *Nature* **2016**, *536*, 451.
- [243] M. Bartnikowski, N. J. Bartnikowski, M. A. Woodruff, K. Schrobback, T. J. Klein, *Acta Biomater* **2015**, *27*, 66.

- [244] N. E. Fedorovich, M. H. Oudshoorn, D. van Geemen, W. E. Hennink, J. Alblas, W. J. A. Dhert, *Biomaterials* **2009**, *30*, 344.
- [245] E. R. Ruskowitz, C. A. Deforest, *ACS Biomater Sci Eng* **2019**, *5*, 2111.
- [246] V. H. M. Mouser, R. Levato, A. Mensinga, W. J. A. Dhert, D. Gawlitta, J. Malda, *Connect Tissue Res* **2018**, DOI 10.1080/03008207.2018.1553960.
- [247] A. Blaeser, D. F. Duarte Campos, U. Puster, W. Richtering, M. M. Stevens, H. Fischer, *Adv Healthc Mater* **2016**, *5*, 326.
- [248] I. Pennings, L. A. van Dijk, J. van Huuksloot, J. O. Fledderus, K. Schepers, A. K. Braat, E. C. Hsiao, E. Barruet, B. M. Morales, M. C. Verhaar, A. J. W. P. Rosenberg, D. Gawlitta, *J Tissue Eng Regen Med* **2019**, *13*, DOI 10.1002/term.2807.
- [249] B. Lorber, W. K. Hsiao, I. M. Hutchings, K. R. Martin, *Biofabrication* **2014**, *6*, DOI 10.1088/1758-5082/6/1/015001.
- [250] V. Chan, P. Zorlutuna, J. H. Jeong, H. Kong, R. Bashir, *Lab Chip* **2010**, *10*, 2062.
- [251] A. J. Almarza, K. A. Athanasiou, *Ann Biomed Eng* **2004**, *32(1)*, 2.
- [252] J. L. Puetzer, L. J. Bonassar, *Tissue Eng Part A* **2016**, *22*, 907.
- [253] C. K. F. Chan, G. S. Gulati, R. Sinha, J. V. Tompkins, M. Lopez, A. C. Carter, R. C. Ransom, A. Reinisch, T. Wearda, M. Murphy, R. E. Brewer, L. S. Koepke, O. Marecic, A. Manjunath, E. Y. Seo, T. Leavitt, W. J. Lu, A. Nguyen, S. D. Conley, A. Salhotra, T. H. Ambrosi, M. R. Borrelli, T. Siebel, K. Chan, K. Schallmoser, J. Seita, D. Sahoo, H. Goodnough, J. Bishop, M. Gardner, R. Majeti, D. C. Wan, S. Goodman, I. L. Weissman, H. Y. Chang, M. T. Longaker, *Cell* **2018**, *175*, 43.
- [254] S. Greuel, G. Hanci, M. Böhme, T. Miki, F. Schubert, M. Sittinger, C. Mandenius, K. Zeilinger, N. Freyer, *Cell Prolif* **2019**, *52*, DOI 10.1111/cpr.12604.
- [255] U. Martin, *Adv Drug Deliv Rev* **2017**, *120*, 108.
- [256] R. Levato, J. Visser, J. a Planell, E. Engel, J. Malda, M. a Mateos-Timoneda, *Biofabrication* **2014**, *6*, 35020.
- [257] F. P. W. Melchels, M. M. Blokzijl, R. Levato, Q. C. Peiffer, M. De Ruijter, W. E. Hennink, T. Vermonden, J. Malda, *Biofabrication* **2016**, *8*, 35004.
- [258] K. S. Lim, B. J. Klotz, G. C. J. Lindberg, F. P. W. Melchels, G. J. Hooper, J. Malda, D. Gawlitta, T. B. F. Woodfield, *Macromol Biosci* **2019**, *19*, e1900098.
- [259] R. Levato, W. R. Webb, I. A. Otto, A. Mensinga, Y. Zhang, M. van Rijen, R. van Weeren, I. M. Khan, J. Malda, *Acta Biomater* **2017**, *61*, DOI 10.1016/j.actbio.2017.08.005.
- [260] R. C. Stewart, A. N. Patwa, H. Lusic, J. D. Freedman, M. Wathier, B. D. Snyder, A. Guermazi, M. W. Grinstaff, *J Med Chem* **2017**, *60*, 5543.
- [261] B. J. Klotz, K. S. Lim, Y. X. Chang, B. G. Soliman, I. Pennings, F. P. W. Melchels, T. B. F. Woodfield, A. J. W. P. Rosenberg, J. Malda, D. Gawlitta, *Eur Cell Mater* **2018**, *35*, 335.
- [262] F. P. W. Melchels, J. Feijen, D. W. Grijpma, *Biomaterials* **2010**, *31*, 6121.
- [263] H. W. Kang, S. J. Lee, I. K. Ko, C. Kengla, J. J. Yoo, A. Atala, *Nat Biotechnol* **2016**, *34*, 312.
- [264] S. L. Ding, X. Liu, X. Y. Zhao, K. T. Wang, W. Xiong, Z. L. Gao, C. Y. Sun, M. X. Jia, C. Li, Q. Gu, M. Z. Zhang, *Bioact Mater* **2022**, *17*, 81.
- [265] N. V. Mekhileri, K. S. Lim, G. C. J. Brown, I. Mutreja, B. S. Schon, G. J. Hooper, T. B. F. Woodfield, *Biofabrication* **2018**, *10*, DOI 10.1088/1758-5090/aa9ef1.
- [266] A. C. Daly, D. J. Kelly, *Biomaterials* **2019**, *197*, 194.
- [267] M. Nakamura, A. Kobayashi, F. Takagi, A. Watanabe, Y. Hiruma, K. Ohuchi, Y. Iwasaki, M. Horie, I. Morita, S. Takatani, *Tissue Eng* **2005**, *11*, DOI 10.1089/ten.2005.11.1658.
- [268] P. D. Dalton, *Curr Opin Biomed Eng* **2017**, *2*, 49.
- [269] T. M. Robinson, D. W. Hutmacher, P. D. Dalton, *Adv Funct Mater* **2019**, *29*, DOI 10.1002/adfm.201904664.
- [270] M. Tavafoghi, M. A. Darabi, M. Mahmoodi, R. Tutar, C. Xu, A. Mirjafari, F. Billi, W. Swieszkowski, F. Nasrollahi, S. Ahadian, V. Hosseini, A. Khademhosseini, N. Ashammakhi, *Biofabrication* **2021**, *13*, DOI 10.1088/1758-



- 5090/ac0b9a.
- [271] J. Visser, F. P. W. Melchels, J. E. Jeon, E. M. Van Bussel, L. S. Kimpton, H. M. Byrne, W. J. A. Dhert, P. D. Dalton, D. W. Hutmacher, J. Malda, *Nat Commun* **2015**, *6*, DOI 10.1038/ncomms7933.
- [272] N. Abbasi, A. Abdal-Hay, S. Hamlet, E. Graham, S. Ivanovski, *ACS Biomater Sci Eng* **2019**, *5*, 3448.
- [273] M. Castilho, G. Hochleitner, W. Wilson, B. Van Rietbergen, P. D. Dalton, J. Groll, J. Malda, K. Ito, *Sci Rep* **2018**, *8*, DOI 10.1038/s41598-018-19502-y.
- [274] J. C. Kade, P. D. Dalton, *Adv Healthc Mater* **2021**, *10*, DOI 10.1002/adhm.202001232.
- [275] R. Sanchez Diaz, J. R. Park, L. L. Rodrigues, P. D. Dalton, E. M. De-Juan-Pardo, T. R. Dargaville, *Adv Mater Technol* **2022**, *7*, DOI 10.1002/admt.202100508.
- [276] T. M. Robinson, D. W. Hutmacher, P. D. Dalton, *Adv Funct Mater* **2019**, *29*, DOI 10.1002/adfm.201904664.
- [277] M. J. Ainsworth, O. Lotz, A. Gilmour, A. Zhang, M. J. Chen, D. R. McKenzie, M. M. M. Bilek, J. Malda, B. Akhavan, M. Castilho, *Adv Funct Mater* **2022**, DOI 10.1002/adfm.202206583.
- [278] M. Castilho, R. Levato, P. N. Bernal, M. De Ruijter, C. Y. Sheng, J. Van Duijn, S. Piluso, K. Ito, J. Malda, *Biomacromolecules* **2021**, *22*, 855.
- [279] E. McColl, J. Groll, T. Jungst, P. D. Dalton, *Mater Des* **2018**, *155*, 46.
- [280] T. D. Brown, A. Slotsch, L. Thibaudeau, A. Taubenberger, D. Loessner, C. Vaquette, P. D. Dalton, D. W. Hutmacher, *Biointerphases* **2012**, *7*, 1.
- [281] T. Jungst, M. L. Muerza-Cascante, T. D. Brown, M. Standfest, D. W. Hutmacher, J. Groll, P. D. Dalton, *Polym Int* **2015**, *64*, 1086.
- [282] A. M. van Genderen, K. Jansen, M. Kristen, J. van Duijn, Y. Li, C. C. L. Schuurmans, J. Malda, T. Vermonden, J. Jansen, R. Masereeuw, M. Castilho, *Front Bioeng Biotechnol* **2021**, *8*, DOI 10.3389/fbioe.2020.617364.
- [283] Z. Qiao, M. Lian, Y. Han, B. Sun, X. Zhang, W. Jiang, H. Li, Y. Hao, K. Dai, *Biomaterials* **2021**, *266*, DOI 10.1016/j.biomaterials.2020.120385.
- [284] T. Jungst, I. Pennings, M. Schmitz, A. J. W. P. Rosenberg, J. Groll, D. Gawlitta, *Adv Funct Mater* **2019**, *29*, DOI 10.1002/adfm.201905987.
- [285] F. Afghah, N. B. Iyison, A. Nadernezhad, A. Midi, O. Sen, B. Saner Okan, M. Culha, B. Koc, *Adv Healthc Mater* **2022**, *11*, DOI 10.1002/adhm.202102068.
- [286] P. N. Bernal, M. Bouwmeester, J. Madrid-Wolff, M. Falandt, S. Florczak, N. G. Rodriguez, Y. Li, G. Größbacher, R. Samsom, M. van Wolferen, L. J. W. van der Laan, P. Delrot, D. Loterie, J. Malda, C. Moser, B. Spee, R. Levato, *Advanced Materials* **2022**, *34*, DOI 10.1002/adma.202270112.
- [287] M. Bartnikowski, T. R. Dargaville, S. Ivanovski, D. W. Hutmacher, *Prog Polym Sci* **2019**, *96*, DOI 10.1016/j.progpolymsci.2019.05.004.
- [288] N. Golafshan, E. Vorndran, S. Zaharievski, H. Brommer, F. B. Kadumudi, A. Dolatshahi-Pirouz, U. Gbureck, R. van Weeren, M. Castilho, J. Malda, *Biomaterials* **2020**, *261*, DOI 10.1016/j.biomaterials.2020.120302.
- [289] P. Diloksumpan, F. Abinzano, M. de Ruijter, A. Mensinga, S. Plomp, I. Khan, H. Brommer, I. Smit, M. Dias Castilho, P. R. van Weeren, J. Malda, R. Levato, *Journal of Trial and Error* **2021**, *2*, DOI 10.36850/e3.
- [290] A. Daghery, J. A. Ferreira, J. Xu, N. Golafshan, D. Kaigler, S. B. Bhaduri, J. Malda, M. Castilho, M. C. Bottino, *Bioact Mater* **2023**, *19*, DOI 10.1016/j.bioactmat.2022.04.013.
- [291] R. Rizzo, D. Ruetsche, H. Liu, M. Zenobi-Wong, *Advanced Materials* **2021**, *33*, DOI 10.1002/adma.202102900.
- [292] J. Gehlen, W. Qiu, G. N. Schädli, R. Müller, X. H. Qin, *Acta Biomater* **2022**, DOI 10.1016/j.actbio.2022.06.020.
- [293] D. B. Camasão, D. Mantovani, *Mater Today Bio* **2021**, *10*, DOI 10.1016/j.mtbio.2021.100106.
- [294] J. Schöneberg, F. De Lorenzi, B. Theek, A. Blaeser, D. Rommel, A. J. C. Kuehne, F. Kießling, H. Fischer, *Sci Rep* **2018**, *8*, DOI 10.1038/s41598-018-28715-0.
- [295] P. Zilla, D. Bezuidenhout, P. Human, *Biomaterials* **2007**, *28*, 5009.
- [296] M. Stekelenburg, M. C. M. Rutten, L. H. E. H. Snoeckx, F. P. T. Baaijens, *Dynamic Straining Combined with Fibrin Gel Cell Seeding Improves Strength of Tissue-Engineered Small-Diameter Vascular Grafts*, **2009**.

- [297] X. Li, H. Zhao, *J Biomater Appl* **2019**, *33*, 1017.
- [298] C. M. Brennan, K. F. Eichholz, D. A. Hoey, *Biomedical Materials (Bristol)* **2019**, *14*, DOI 10.1088/1748-605X/ab49f2.
- [299] A. B. McCosker, M. E. Snowdon, R. Lamont, M. A. Woodruff, N. C. Paxton, *Adv Mater Technol* **2022**, DOI 10.1002/admt.202200259.
- [300] E. Pickering, N. C. Paxton, A. Bo, B. O'Connell, M. King, M. A. Woodruff, *Adv Eng Mater* **2022**, *24*, DOI 10.1002/adem.202200479.
- [301] V. Kasjanovs, I. Ozolanta, B. Purina, *Mechanics of Composite Materials* **1999**, *35*, DOI 10.1007/BF02257246.
- [302] N. Pien, M. Bartolf-Kopp, L. Parmentier, J. Delaey, L. De Vos, D. Mantovani, S. Van Vlierberghe, P. Dubruel, T. Jungst, *Macromol Mater Eng* **2022**, *307*, DOI 10.1002/mame.202200097.
- [303] N. Diban, S. Haimi, L. Bolhuis-Versteeg, S. Teixeira, S. Miettinen, A. Poot, D. Grijpma, D. Stamatialis, *Acta Biomater* **2013**, *9*, 6450.
- [304] V. Thomas, X. Zhang, Y. K. Vohra, *Biotechnol Bioeng* **2009**, *104*, 1025.
- [305] K. W. M. Boere, J. Visser, H. Seyednejad, S. Rahimian, D. Gawlitta, M. J. Van Steenberghe, W. J. A. Dhert, W. E. Hennink, T. Vermonden, J. Malda, *Acta Biomater* **2014**, *10*, DOI 10.1016/j.actbio.2014.02.041.
- [306] A. Ribeiro, M. M. Blokzijl, R. Levato, C. W. Visser, M. Castilho, W. E. Hennink, T. Vermonden, J. Malda, *Biofabrication* **2018**, *10*, DOI 10.1088/1758-5090/aa90e2.
- [307] C. Xie, Q. Gao, P. Wang, L. Shao, H. Yuan, J. Fu, W. Chen, Y. He, *Mater Des* **2019**, *181*, DOI 10.1016/j.matdes.2019.108092.
- [308] W. G. Roberts, G. E. Palade, *Cancer Res* **1997**, *57*, 765.
- [309] S. C. Satchell, F. Braet, *Am J Physiol Renal Physiol* **2009**, *296*, 947.
- [310] J. Bernier-Latmani, C. Mauri, R. Marcone, F. Renevey, S. Durot, L. He, M. Vanlandewijck, C. Maclachlan, S. Davanture, N. Zamboni, G. W. Knott, S. A. Luther, C. Betsholtz, M. Delorenzi, C. Brisken, T. V. Petrova, *Nat Commun* **2022**, *13*, DOI 10.1038/s41467-022-31571-2.
- [311] G. Grevers, U. Herrmann, *Oto-Rhino-Laryngology Fenestrated Endothelia in Vessels of the Nasal Mucosa An Electron-Microscopic Study in the Rabbit*, **1987**.
- [312] S. Parab, R. E. Quick, R. L. Matsuoka, *Elife* **2021**, *10*, 1.
- [313] M. Kaya, L. Chang, A. Truong, M. W. Brightman, *Exp Neurol* **1996**, *142*, DOI 10.1006/exnr.1996.0174.
- [314] F. Benz, S. Liebner, in *Handb Exp Pharmacol*, Springer Science And Business Media Deutschland GmbH, **2022**, pp. 3–31.
- [315] P. A. Stewart, K. Hayakawa, E. Hayakawa, C. L. Farrell, R. F. Del Maestro, *Acta Neuropathol (Berl) A Quantitative Study of Blood-Brain Barrier Permeability Ultrastructure in a New Rat Glioma Model\**, **1985**.
- [316] P. M. Bungay, N. Burfitt, K. Sritharan, L. Muir, S. L. Khan, M. C. De Nunzio, K. Lingam, A. Huw Davies, *J Vasc Surg* **2011**, *54*, DOI 10.1016/j.jvs.2011.05.115.
- [317] B. M. Stanley, J. B. Semmens, M. Lawrence-Brown, M. A. Goodman, D. E. Hartley, *Fenestration in Endovascular Grafts for Aortic Aneurysm Repair: New Horizons for Preserving Blood Flow in Branch Vessels*, **2001**.
- [318] T. F. Browne, D. Hartley, S. Purchas, M. Rosenberg, G. Van Schie, M. Lawrence-Brown, *A Fenestrated Covered Suprarenal Aortic Stent*, **1999**.
- [319] M. Gallois, T. Gidenne, L. Fortun-Lamothe, I. Le Huerou-Luron, J. P. Lallès, *Reprod Nutr Dev* **2005**, *45*, DOI 10.1051/rnd:2005008.
- [320] W. J. Kim, G. H. Kim, *Theranostics* **2020**, *10*, DOI 10.7150/thno.41225.
- [321] R. Abbasi, T. B. Lefevre, A. D. Benjamin, I. J. Thornton, J. N. Wilking, *Lab Chip* **2021**, *21*, DOI 10.1039/d1lc00135c.
- [322] A. Augello, C. De Bari, *Hum Gene Ther* **2010**, *21*, DOI 10.1089/hum.2010.173.
- [323] K. Kurpinski, H. Lam, J. Chu, A. Wang, A. Kim, E. Tsay, S. Agrawal, D. V. Schaffer, S. Li, *Stem Cells* **2010**, *28*, DOI 10.1002/stem.319.

- [324] T. Wang, Z. Xu, W. Jiang, A. Ma, *Int J Cardiol* **2006**, *109*, DOI 10.1016/j.ijcard.2005.05.072.
- [325] L. de Silva, P. N. Bernal, A. J. W. Rosenberg, J. Malda, R. Levato, D. Gawlitta, *Acta Biomater* **2022**, DOI 10.1016/j.actbio.2022.08.051.
- [326] D. B. Kolesky, K. A. Homan, M. A. Skylar-Scott, J. A. Lewis, *Proc Natl Acad Sci U S A* **2016**, *113*, 3179.
- [327] L. Ouyang, J. P. K. Armstrong, Q. Chen, Y. Lin, M. M. Stevens, *Adv Funct Mater* **2020**, *30*, DOI 10.1002/adfm.201908349.
- [328] L. Shao, Q. Gao, C. Xie, J. Fu, M. Xiang, Y. He, *Biofabrication* **2020**, *12*, DOI 10.1088/1758-5090/ab7e76.
- [329] C. Dikyol, M. Altunbek, B. Koc, *J Mater Res* **2021**, *36*, DOI 10.1557/s43578-021-00254-x.
- [330] M. A. Skylar-Scott, S. G. M. Uzel, L. L. Nam, J. H. Ahrens, R. L. Truby, S. Damaraju, J. A. Lewis, *Sci Adv* **2019**, *5*, DOI 10.1126/sciadv.aaw2459.
- [331] R. Levato, K. S. Lim, W. Li, A. U. Asua, L. B. Peña, M. Wang, M. Falandt, P. N. Bernal, D. Gawlitta, Y. S. Zhang, T. B. F. Woodfield, J. Malda, *Mater Today Bio* **2021**, *12*, DOI 10.1016/j.mtbio.2021.100162.
- [332] W. Zhu, X. Qu, J. Zhu, X. Ma, S. Patel, J. Liu, P. Wang, C. S. E. Lai, M. Gou, Y. Xu, K. Zhang, S. Chen, *Biomaterials* **2017**, *124*, 106.
- [333] B. Kang, J. Shin, H. J. Park, C. Rhyou, D. Kang, S. J. Lee, Y. sup Yoon, S. W. Cho, H. Lee, *Nat Commun* **2018**, *9*, DOI 10.1038/s41467-018-07823-5.
- [334] G. Cedillo-Servin, O. Dahri, J. Meneses, J. van Duijn, F. Sage, J. Silva, A. Pereira, F. D. Magalhães, J. Malda, N. Geijsen, M. Castilho, *BioRxiv* **2023**, DOI 10.1101/2023.01.19.524679.
- [335] K. S. Lim, F. Abinzano, P. N. Bernal, A. Albillos Sanchez, P. Atienza-Roca, I. A. Otto, Q. C. Peiffer, M. Matsusaki, T. B. F. Woodfield, J. Malda, R. Levato, *Adv Healthc Mater* **2020**, *9*, DOI 10.1002/adhm.201901792.
- [336] M. L. Terpstra, J. Li, A. Mensinga, M. De Ruijter, M. H. P. Van Rijen, C. Androulidakis, C. Galiotis, I. Papantoniou, M. Matsusaki, J. Malda, R. Levato, *Biofabrication* **2022**, *14*, DOI 10.1088/1758-5090/ac6282.
- [337] V. B. Siramshetty, J. Nickel, C. Omieczynski, B. O. Gohlke, M. N. Drwal, R. Preissner, *Nucleic Acids Res* **2016**, *44*, DOI 10.1093/nar/gkv1192.
- [338] W. M. Lee, *Medical Progress Drug-Induced Hepatotoxicity*, **2003**.
- [339] G. Ostapowicz, R. J. Fontana, F. V. Schiødt, A. Larson, T. J. Davern, S. H. B. Han, T. M. McCashland, A. O. Shakil, J. E. Hay, L. Hynan, J. S. Crippin, A. T. Blei, G. Samuel, J. Reisch, W. M. Lee, R. Santyanarayana, C. Caldwell, L. Shick, N. Bass, S. Rouillard, E. Atillasoy, S. Flamm, K. G. Benner, H. R. Rosen, P. Martin, R. Stribling, E. R. Schiff, M. B. Torres, V. Navarro, B. McGuire, R. Chung, D. Abraczinskas, J. Dienstag, *Ann Intern Med* **2002**, *137*, DOI 10.7326/0003-4819-137-12-200212170-00007.
- [340] M. R. McGill, H. Jaeschke, *Biochim Biophys Acta Mol Basis Dis* **2019**, *1865*, DOI 10.1016/j.bbadis.2018.08.037.
- [341] F. Ballet, *Digestive Diseases* **2015**, *33*, DOI 10.1159/000374093.
- [342] H. Olson, G. Betton, D. Robinson, K. Thomas, A. Monro, G. Kolaja, P. Lilly, J. Sanders, G. Sipes, W. Bracken, M. Dorato, K. Van Deun, P. Smith, B. Berger, A. Heller, *Regulatory Toxicology and Pharmacology* **2000**, *32*, 56.
- [343] M. J. Gómez-Lechón, L. Tolosa, I. Conde, M. T. Donato, *Expert Opin Drug Metab Toxicol* **2014**, *10*, DOI 10.1517/17425255.2014.967680.
- [344] P. Godoy, N. J. Hewitt, U. Albrecht, M. E. Andersen, N. Ansari, S. Bhattacharya, J. G. Bode, J. Bolleyn, C. Borner, J. Böttger, A. Braeuning, R. A. Budinsky, B. Burkhardt, N. R. Cameron, G. Camussi, C. S. Cho, Y. J. Choi, J. Craig Rowlands, U. Dahmen, G. Damm, O. Dirsch, M. T. Donato, J. Dong, S. Dooley, D. Drasdo, R. Eakins, K. S. Ferreira, V. Fonsato, J. Fraczek, R. Gebhardt, A. Gibson, M. Glanemann, C. E. P. Goldring, M. J. Gómez-Lechón, G. M. M. Groothuis, L. Gustavsson, C. Guyot, D. Hallifax, S. Hammad, A. Hayward, D. Häussinger, C. Hellerbrand, P. Hewitt, S. Hoehme, H. G. Holzhütter, J. B. Houston, J. Hrach, K. Ito, H. Jaeschke, V. Keitel, J. M. Kelm, B. Kevin Park, C. Kordes, G. A. Kullak-Ublick, E. L. Lecluyse, P. Lu, J. Luebke-Wheeler, A. Lutz, D. J. Maltman, M. Matz-Soja, P. McMullen, I. Merfort, S. Messner, C. Meyer, J. Mwinyi, D. J. Naisbitt, A. K. Nussler, P. Olinga, F. Pampaloni, J. Pi, L. Pluta, S. A. Przyborski, A. Ramachandran, V. Rogiers, C. Rowe, C. Schelcher, K. Schmich, M. Schwarz, B. Singh, E. H. K. Stelzer, B. Stieger, R. Stöber, Y. Sugiyama, C. Tetta, W. E. Thasler,

- T. Vanhaecke, M. Vinken, T. S. Weiss, A. Widera, C. G. Woods, J. J. Xu, K. M. Yarborough, J. G. Hengstler, *Arch Toxicol* **2013**, *87*, DOI 10.1007/s00204-013-1078-5.
- [345] V. M. Lauschke, R. Z. Shafagh, D. F. G. Hendriks, M. Ingelman-Sundberg, *Biotechnol J* **2019**, *14*, DOI 10.1002/biot.201800347.
- [346] J. Fraczek, J. Bolleyn, T. Vanhaecke, V. Rogiers, M. Vinken, *Arch Toxicol* **2013**, *87*, DOI 10.1007/s00204-012-0983-3.
- [347] M. Ruoß, M. Vosough, A. Königsrainer, S. Nadalin, S. Wagner, S. Sajadian, D. Huber, Z. Heydari, S. Ehnert, J. G. Hengstler, A. K. Nussler, *Food and Chemical Toxicology* **2020**, *138*, DOI 10.1016/j.fct.2020.111188.
- [348] J. V. Castell, R. Jover, C. P. Martínez-Jiménez, M. J. Gómez-Lechón, *Expert Opin Drug Metab Toxicol* **2006**, *2*, DOI 10.1517/17425255.2.2.183.
- [349] S. N. Hart, Y. Li, K. Nakamoto, E. A. Subileau, D. Steen, X. B. Zhong, *Drug Metabolism and Disposition* **2010**, *38*, DOI 10.1124/dmd.109.031831.
- [350] M. N. Ashraf, M. W. Asghar, Y. Rong, M. R. Doschak, T. K. L. Kiang, *Eur J Drug Metab Pharmacokinet* **2019**, *44*, DOI 10.1007/s13318-018-0533-3.
- [351] S. F. Zhou, J. P. Liu, B. Chowbay, *Drug Metab Rev* **2009**, *41*, DOI 10.1080/03602530902843483.
- [352] F. Schutgens, H. Clevers, *Annual Review of Pathology: Mechanisms of Disease* **2020**, *15*, DOI 10.1146/annurev-pathmechdis-012419-032611.
- [353] T. Sato, R. G. Vries, H. J. Snippert, M. Van De Wetering, N. Barker, D. E. Stange, J. H. Van Es, A. Abo, P. Kujala, P. J. Peters, H. Clevers, *Nature* **2009**, *459*, 262.
- [354] L. Planas-Paz, T. Sun, M. Pikiolek, N. R. Cochran, S. Bergling, V. Orsini, Z. Yang, F. Sigoillot, J. Jetzer, M. Syed, M. Neri, S. Schuierer, L. Morelli, P. S. Hoppe, W. Schwarzer, C. M. Cobos, J. L. Alford, L. Zhang, R. Cuttat, A. Waldt, N. Carballido-Perrig, F. Nigsch, B. Kinzel, T. B. Nicholson, Y. Yang, X. Mao, L. M. Terracciano, C. Russ, J. S. Reece-Hoyes, C. Gubser Keller, A. W. Sailer, T. Bouwmeester, L. E. Greenbaum, J. J. Lugas, F. Cong, G. McAllister, G. R. Hoffman, G. Roma, J. S. Tchorz, *Cell Stem Cell* **2019**, *25*, DOI 10.1016/j.stem.2019.04.005.
- [355] M. Huch, H. Gehart, R. Van Boxtel, K. Hamer, F. Blokzijl, M. M. A. Verstegen, E. Ellis, M. Van Wenum, S. A. Fuchs, J. De Ligt, M. Van De Wetering, N. Sasaki, S. J. Boers, H. Kemperman, J. De Jonge, J. N. M. Ijzermans, E. E. S. Nieuwenhuis, R. Hoekstra, S. Strom, R. R. G. Vries, L. J. W. Van Der Laan, E. Cuppen, H. Clevers, *Cell* **2015**, *160*, 299.
- [356] C. Chen, A. Soto-Gutierrez, P. M. Baptista, B. Spee, *Gastroenterology* **2018**, *154*, DOI 10.1053/j.gastro.2018.01.066.
- [357] G. H. Underhill, S. R. Khetani, *CMGH* **2018**, *5*, DOI 10.1016/j.jcmgh.2017.11.012.
- [358] K. Schneeberger, B. Spee, P. Costa, N. Sachs, H. Clevers, J. Malda, *Biofabrication* **2017**, *9*, DOI 10.1088/1758-5090/aa6121.
- [359] K. T. Lawlor, J. M. Vanslambrouck, J. W. Higgins, A. Chambon, K. Bishard, D. Arndt, P. X. Er, S. B. Wilson, S. E. Howden, K. S. Tan, F. Li, L. J. Hale, B. Shepherd, S. Pentoney, S. C. Presnell, A. E. Chen, M. H. Little, *Nat Mater* **2021**, *20*, DOI 10.1038/s41563-020-00853-9.
- [360] T. Takahashi, *Annu Rev Pharmacol Toxicol* **2019**, *59*, DOI 10.1146/annurev-pharmtox-010818-021108.
- [361] H. Jaeschke, M. L. Bajt, A. Ramachandran, in *Comprehensive Toxicology*, **2018**.
- [362] S. C. Ramaiahgari, M. W. Den Braver, B. Herpers, V. Terpstra, J. N. M. Commandeur, B. Van De Water, L. S. Price, *Arch Toxicol* **2014**, *88*, DOI 10.1007/s00204-014-1215-9.
- [363] D. Utkarsh, C. Loretz, A. P. Li, *Chem Biol Interact* **2016**, *255*, DOI 10.1016/j.cbi.2015.12.013.
- [364] H. S. Kruitwagen, L. A. Oosterhoff, I. G. W. H. Vernooij, I. M. Schraal, M. E. van Wolferen, F. Bannink, C. Roesch, L. van Uden, M. R. Molenaar, J. B. Helms, G. C. M. Grinwis, M. M. A. Verstegen, L. J. W. van der Laan, M. Huch, N. Geijsen, R. G. Vries, H. Clevers, J. Rothuizen, B. A. Schotanus, L. C. Penning, B. Spee, *Stem Cell Reports* **2017**, *8*, DOI 10.1016/j.stemcr.2017.02.015.
- [365] I. F. Schene, I. P. Joore, R. Oka, M. Mokry, A. H. M. van Vugt, R. van Boxtel, H. P. J. van der Doef, L. J. W. van

- der Laan, M. M. A. Verstegen, P. M. van Hasselt, E. E. S. Nieuwenhuis, S. A. Fuchs, *Nat Commun* **2020**, *11*, DOI 10.1038/s41467-020-19136-7.
- [366] F. Sampaziotis, D. Muraro, O. C. Tysoe, S. Sawiak, T. E. Beach, E. M. Godfrey, S. S. Upponi, T. Brevini, B. T. Wesley, J. Garcia-Bernardo, K. Mahbubani, G. Canu, R. Gieseck, N. L. Berntsen, V. L. Mulcahy, K. Crick, C. Fear, S. Robinson, L. Swift, L. Gambardella, J. Bargehr, D. Ortman, S. E. Brown, A. Osnato, M. P. Murphy, G. Corbett, W. T. H. Gelson, G. F. Mells, P. Humphreys, S. E. Davies, I. Amin, P. Gibbs, S. Sinha, S. A. Teichmann, A. J. Butler, T. C. See, E. Melum, C. J. E. Watson, K. Saeb-Parsy, L. Vallier, *Science (1979)* **2021**, *371*, DOI 10.1126/science.aaz6964.
- [367] F. J. M. Roos, M. M. A. Verstegen, L. Muñoz Albarinos, H. P. Roest, J. W. Poley, G. W. M. Tetteroo, J. N. M. IJzermans, L. J. W. van der Laan, *Front Cell Dev Biol* **2021**, *8*, DOI 10.3389/fcell.2020.630492.
- [368] F. Schutgens, M. B. Rookmaaker, T. Margaritis, A. Rios, C. Ammerlaan, J. Jansen, L. Gijzen, M. Vormann, A. Vonk, M. Viveen, F. Y. Yengej, S. Derakhshan, K. M. de Winter-de Groot, B. Artegiani, R. van Boxtel, E. Cuppen, A. P. A. Hendrickx, M. M. van den Heuvel-Eibrink, E. Heitzer, H. Lanz, J. Beekman, J. L. Murk, R. Masereeuw, F. Holstege, J. Drost, M. C. Verhaar, H. Clevers, *Nat Biotechnol* **2019**, *37*, DOI 10.1038/s41587-019-0048-8.
- [369] T. Sato, D. E. Stange, M. Ferrante, R. G. J. Vries, J. H. Van Es, S. Van Den Brink, W. J. Van Houdt, A. Pronk, J. Van Gorp, P. D. Siersema, H. Clevers, *Gastroenterology* **2011**, *141*, DOI 10.1053/j.gastro.2011.07.050.
- [370] N. S. Bhise, V. Manoharan, S. Massa, A. Tamayol, M. Ghaderi, M. Miscuglio, Q. Lang, Y. S. Zhang, S. R. Shin, G. Calzone, N. Annabi, T. D. Shupe, C. E. Bishop, A. Atala, M. R. Dokmeci, A. Khademhosseini, *Biofabrication* **2016**, *8*, 14101.
- [371] S. Massa, M. A. Sakr, J. Seo, P. Bandaru, A. Arneri, S. Bersini, E. Zare-Eelanjegh, E. Jalilian, B. H. Cha, S. Antona, A. Enrico, Y. Gao, S. Hassan, J. P. Acevedo, M. R. Dokmeci, Y. S. Zhang, A. Khademhosseini, S. R. Shin, *Biomicrofluidics* **2017**, *11*, DOI 10.1063/1.4994708.
- [372] T. Grix, A. Ruppelt, A. Thomas, A. K. Amler, B. P. Noichl, R. Lauster, L. Kloke, *Genes (Basel)* **2018**, *9*, DOI 10.3390/genes9040176.
- [373] J. E. Snyder, Q. Hamid, C. Wang, R. Chang, K. Emami, H. Wu, W. Sun, *Biofabrication* **2011**, *3*, DOI 10.1088/1758-5082/3/3/034112.
- [374] M. Krüger, L. A. Oosterhoff, M. E. van Wolferen, S. A. Schiele, A. Walther, N. Geijsen, L. De Laporte, L. J. W. van der Laan, L. M. Kock, B. Spee, *Adv Healthc Mater* **2020**, DOI 10.1002/adhm.201901658.
- [375] B. J. Klotz, L. A. Oosterhoff, L. Utomo, K. S. Lim, Q. Vallmajo-Martin, H. Clevers, T. B. F. Woodfield, A. J. W. P. Rosenberg, J. Malda, M. Ehrbar, B. Spee, D. Gawlitta, *Adv Healthc Mater* **2019**, *8*, DOI 10.1002/adhm.201900979.
- [376] G. Benton, I. Arnaoutova, J. George, H. K. Kleinman, J. Koblinski, *Adv Drug Deliv Rev* **2014**, *79*, DOI 10.1016/j.addr.2014.06.005.
- [377] W. Schuurman, P. A. Levett, M. W. Pot, P. R. van Weeren, W. J. A. Dhert, D. W. Hutmacher, F. P. W. Melchels, T. J. Klein, J. Malda, *Macromol Biosci* **2013**, *13*, 551.
- [378] A. K. Nguyen, P. L. Goering, V. Reipa, R. J. Narayan, *Biointerphases* **2019**, *14*, DOI 10.1116/1.5095886.
- [379] L. E. Bertassoni, J. C. Cardoso, V. Manoharan, A. L. Cristino, N. S. Bhise, W. A. Araujo, P. Zorlutuna, N. E. Vrana, A. M. Ghaemmaghami, M. R. Dokmeci, A. Khademhosseini, *Biofabrication* **2014**, *6*, DOI 10.1088/1758-5082/6/2/024105.
- [380] T. Hiller, J. Berg, L. Elomaa, V. Röhrs, I. Ullah, K. Schaar, A. C. Dietrich, M. A. Al-Zeer, A. Kurtz, A. C. Hocke, S. Hippenstiel, H. Fechner, M. Weinhart, J. Kurreck, *Int J Mol Sci* **2018**, *19*, DOI 10.3390/ijms19103129.
- [381] M. Gori, S. M. Giannitelli, M. Torre, P. Mozetic, F. Abbruzzese, M. Trombetta, E. Traversa, L. Moroni, A. Rainer, *Adv Healthc Mater* **2020**, *9*, DOI 10.1002/adhm.202001163.
- [382] A. Mazzocchi, M. Devarasetty, R. Huntwork, S. Soker, A. Skardal, *Biofabrication* **2019**, *11*, DOI 10.1088/1758-5090/aae543.
- [383] L. M. Norona, D. G. Nguyen, D. A. Gerber, S. C. Presnell, E. L. LeCluyse, *Toxicological Sciences* **2016**, *154*, 354.

- [384] A. Faulkner-Jones, C. Fyfe, D. J. Cornelissen, J. Gardner, J. King, A. Courtney, W. Shu, *Biofabrication* **2015**, *7*, DOI 10.1088/1758-5090/7/4/044102.
- [385] C. D. Roche, P. Sharma, A. W. Ashton, C. Jackson, M. Xue, C. Gentile, *Front Bioeng Biotechnol* **2021**, *9*, DOI 10.3389/fbioe.2021.636257.
- [386] J. A. Brassard, M. Nikolaeov, T. Hübscher, M. Hofer, M. P. Lutolf, *Nat Mater* **2021**, *20*, 22.
- [387] N. Davidenko, C. F. Schuster, D. V. Bax, R. W. Farndale, S. Hamaia, S. M. Best, R. E. Cameron, *J Mater Sci Mater Med* **2016**, *27*, DOI 10.1007/s10856-016-5763-9.
- [388] H. Lee, S. Chae, J. Y. Kim, W. Han, J. Kim, Y. Choi, D. W. Cho, *Biofabrication* **2019**, *11*, DOI 10.1088/1758-5090/aaf9fa.
- [389] X. Ma, C. Yu, P. Wang, W. Xu, X. Wan, C. S. E. Lai, J. Liu, A. Koroleva-Maharajh, S. Chen, *Biomaterials* **2018**, *185*, DOI 10.1016/j.biomaterials.2018.09.026.
- [390] S. S. Bale, J. T. Borenstein, *Drug Metabolism and Disposition* **2018**, *46*, DOI 10.1124/dmd.118.083055.
- [391] A. J. Foster, B. Chouhan, S. L. Regan, H. Rollison, S. Amberntsson, L. C. Andersson, A. Srivastava, M. Darnell, J. Cairns, S. E. Lazic, K. J. Jang, D. B. Petropolis, K. Kodella, J. E. Rubins, D. Williams, G. A. Hamilton, L. Ewart, P. Morgan, *Arch Toxicol* **2019**, DOI 10.1007/s00204-019-02427-4.
- [392] J. W. Allen, S. R. Khetani, S. N. Bhatia, *Toxicological Sciences* **2005**, *84*, DOI 10.1093/toxsci/kf052.
- [393] J. Ahn, J. H. Ahn, S. Yoon, Y. S. Nam, M. Y. Son, J. H. Oh, *J Biol Eng* **2019**, *13*, DOI 10.1186/s13036-019-0148-5.
- [394] Y. Zhou, J. X. Shen, V. M. Lauschke, *Front Pharmacol* **2019**, *10*, DOI 10.3389/fphar.2019.01093.
- [395] J. Xu, S. Oda, T. Yokoi, *Toxicology in Vitro* **2018**, *48*, DOI 10.1016/j.tiv.2018.01.019.
- [396] E. Yoon, A. Babar, M. Choudhary, M. Kutner, N. Pysopoulos, *J Clin Transl Hepatol* **2016**, *4*, DOI 10.14218/JCTH.2015.00052.
- [397] C. Lin, S. R. Khetani, *Biomed Res Int* **2016**, *2016*, DOI 10.1155/2016/1829148.
- [398] A. J. S. Ribeiro, X. Yang, V. Patel, R. Madabushi, D. G. Strauss, *Clin Pharmacol Ther* **2019**, *106*, DOI 10.1002/cpt.1458.
- [399] C. Goldring, A. Norris, N. Kitteringham, M. D. Aleo, D. J. Antoine, J. Heslop, B. A. Howell, M. Ingelman-Sundberg, R. Kia, L. Kamalian, S. Koerber, J.-C. Martinou, A. Mercer, J. Moggs, D. J. Naisbitt, C. Powell, J. Sidaway, R. Sison-Young, J. Snoeys, B. van de Water, P. B. Watkins, R. J. Weaver, A. Wolf, F. Zhang, B. K. Park, *Appl In Vitro Toxicol* **2015**, *1*, DOI 10.1089/aivt.2015.0001.
- [400] S. Dragovic, N. P. E. Vermeulen, H. H. Gerets, P. G. Hewitt, M. Ingelman-Sundberg, B. K. Park, S. Juhila, J. Snoeys, R. J. Weaver, *Arch Toxicol* **2016**, *90*, DOI 10.1007/s00204-016-1845-1.
- [401] M. Huch, H. Gehart, R. van Boxtel, K. Hamer, F. Blokzijl, M. M. A. Verstegen, E. Ellis, M. van Wenum, S. A. Fuchs, J. de Ligt, M. van de Wetering, N. Sasaki, S. J. Boers, H. Kemperman, J. de Jonge, J. N. M. Ijzermans, E. E. S. Nieuwenhuis, R. Hoekstra, S. Strom, R. R. G. Vries, L. J. W. van der Laan, E. Cuppen, H. Clevers, *Cell* **2015**, *160*, 299.
- [402] F. G. van Steenbeek, B. Spee, L. C. Penning, A. Kummeling, I. H. M. van Gils, G. C. M. Grinwis, D. van Leenen, F. C. P. Holstege, M. Vos-Loohuis, J. Rothuizen, P. A. J. Leegwater, *PLoS One* **2013**, *8*, DOI 10.1371/journal.pone.0057973.
- [403] E. M. Kroh, R. K. Parkin, P. S. Mitchell, M. Tewari, *Methods* **2010**, *50*, DOI 10.1016/j.ymeth.2010.01.032.
- [404] J. H. Kim, I. Kim, Y. J. Seol, I. K. Ko, J. J. Yoo, A. Atala, S. J. Lee, *Nat Commun* **2020**, DOI 10.1038/s41467-020-14930-9.
- [405] I. Martin, J. Malda, N. C. Rivron, *Curr Opin Organ Transplant* **2019**, *24*, 1.
- [406] P. L. Lewis, R. M. Green, R. N. Shah, *Acta Biomater* **2018**, *69*, 63.
- [407] J. Kim, B. K. Koo, J. A. Knoblich, *Nat Rev Mol Cell Biol* **2020**, *21*, 571.
- [408] S. P. Harrison, S. F. Baumgarten, R. Verma, O. Lunov, A. Dejneka, G. J. Sullivan, *Front Med (Lausanne)* **2021**, *8*, DOI 10.3389/fmed.2021.574047.
- [409] N. Paxton, W. Smolan, T. Böck, F. Melchels, J. Groll, T. Jungst, *Biofabrication* **2017**, *9*, DOI 10.1088/1758-5090/

- aa8dd8.
- [410] C. Echalié, R. Levato, M. A. A. Mateos-Timoneda, O. Castaño, S. Déjean, X. Garric, C. Pinese, D. Noël, E. Engel, J. Martinez, A. Mehdi, G. Subra, *RSC Adv* **2017**, 7, DOI 10.1039/c6ra28540f.
- [411] P. Arjmand, O. Katz, S. Gigan, M. Guillon, *Opt Express* **2021**, DOI 10.1364/oe.412640.
- [412] D. Loterie, P. Delrot, C. Moser, **2018**, 1.
- [413] S. P. Rebelo, R. Costa, M. Estrada, V. Shevchenko, C. Brito, P. M. Alves, *Arch Toxicol* **2015**, DOI 10.1007/s00204-014-1320-9.
- [414] V. Starokozhko, M. Hemmingsen, L. Larsen, S. Mohanty, M. Merema, R. C. Pimentel, A. Wolff, J. Emnéus, A. Aspegren, G. Groothuis, M. Dufva, *J Tissue Eng Regen Med* **2018**, DOI 10.1002/term.2659.
- [415] J. Christoffersson, C. Aronsson, M. Jury, R. Selegård, D. Aili, C. F. Mandenius, *Biofabrication* **2019**, 11, DOI 10.1088/1758-5090/aaf657.
- [416] M. Kehtari, B. Zeynali, M. Soleimani, M. Kabiri, E. Seyedjafari, *Artif Cells Nanomed Biotechnol* **2018**, 46, 161.
- [417] M. B. Esch, J. M. Prot, Y. I. Wang, P. Miller, J. R. Llamas-Vidales, B. A. Naughton, D. R. Applegate, M. L. Shuler, *Lab Chip* **2015**, 15, 2269.
- [418] R. Taymour, D. Kilian, T. Ahlfeld, M. Gelsinsky, A. Lode, *Sci Rep* **2021**, 11, DOI 10.1038/s41598-021-84384-6.
- [419] H. Lee, W. Han, H. Kim, D. H. Ha, J. Jang, B. S. Kim, D. W. Cho, *Biomacromolecules* **2017**, 18, 1229.
- [420] S. Hong, J. M. Song, *Biomater Sci* **2021**, 9, 5939.
- [421] J. Madrid-Wolff, A. Boniface, D. Loterie, P. Delrot, C. Moser, *Advanced Science* **2022**, 9, DOI 10.1002/adv.202105144.
- [422] T. Boothe, L. Hilbert, M. Heide, L. Berninger, W. B. Huttner, V. Zaburdaev, N. L. Vastenhouw, E. W. Myers, D. N. Drechsel, J. C. Rink, *Elife* **2017**, 6, DOI 10.7554/eLife.27240.
- [423] B. Pouran, V. Arbabi, R. L. Bleys, P. René van Weeren, A. A. Zadpoor, H. Weinans, *J Biomech* **2017**, 52, DOI 10.1016/j.jbiomech.2016.12.025.
- [424] M. I. Zonneveld, M. J. C. van Herwijnen, M. M. Fernandez-Gutierrez, A. Giovanazzi, A. M. de Groot, M. Kleinjan, T. M. M. van Capel, A. J. A. M. Sijts, L. S. Taams, J. Garssen, E. C. de Jong, M. Kleerebezem, E. N. M. Nolte-’t Hoen, F. A. Redegeld, M. H. M. Wauben, *J Extracell Vesicles* **2021**, DOI 10.1002/jev2.12071.
- [425] P. Y. Liu, L. K. Chin, W. Ser, H. F. Chen, C. M. Hsieh, C. H. Lee, K. B. Sung, T. C. Ayi, P. H. Yap, B. Liedberg, K. Wang, T. Bourouina, Y. Leprince-Wang, *Lab Chip* **2016**, DOI 10.1039/c5lc01445j.
- [426] S. P. den Braver-Sewradj, M. W. den Braver, M. van Dijk, Y. Zhang, S. J. Dekker, L. Wijaya, N. P. E. Vermeulen, L. Richert, J. N. M. Commandeur, J. C. Vos, *Curr Drug Metab* **2018**, 19, 370.
- [427] P. G. Alexander, R. Gottardi, H. Lin, T. P. Lozito, *Diseases*, **2017**.
- [428] G. Sorrentino, S. Rezakhani, E. Yildiz, S. Nuciforo, M. H. Heim, M. P. Lutolf, K. Schoonjans, *Nat Commun* **2020**, 11, DOI 10.1038/s41467-020-17161-0.
- [429] M. C. Bouwmeester, P. N. Bernal, L. A. Oosterhoff, M. E. van Wolferen, V. Lehmann, M. Vermaas, M.-B. Buchholz, Q. C. Peiffer, J. Malda, L. J. W. van der Laan, N. I. Kramer, K. Schneeberger, R. Levato, B. Spee, *Macromol Biosci* **2021**, 21, DOI 10.1002/mabi.202100327.
- [430] Y. Liu, C. Dabrowska, A. Mavousian, B. Strauss, F. Meng, C. Mazzaglia, K. Ouaras, C. Macintosh, E. Terentjev, J. H. Lee, Y. Y. S. Huang, *Advanced Science* **2021**, DOI 10.1002/adv.202003332.
- [431] S. A. Ferreira, M. S. Motwani, P. A. Faull, A. J. Seymour, T. T. L. Yu, M. Enayati, D. K. Taheem, C. Salzlechner, T. Haghghi, E. M. Kania, O. P. Oommen, T. Ahmed, S. Loaiza, K. Parzych, F. Dazzi, O. P. Varghese, F. Festy, A. E. Grigoriadis, H. W. Auner, A. P. Snijders, L. Bozec, E. Gentleman, *Nat Commun* **2018**, 9, DOI 10.1038/s41467-018-06183-4.
- [432] R. Ouchi, S. Togo, M. Kimura, T. Shinozawa, M. Koido, H. Koike, W. Thompson, R. A. Karns, C. N. Mayhew, P. S. McGrath, H. A. McCauley, R. R. Zhang, K. Lewis, S. Hakozaiki, A. Ferguson, N. Saiki, Y. Yoneyama, I. Takeuchi, Y. Mabuchi, C. Akazawa, H. Y. Yoshikawa, J. M. Wells, T. Takebe, *Cell Metab* **2019**, 30, 374.
- [433] N. Sachs, J. de Ligt, O. Kopper, E. Gogola, G. Bounova, F. Weeber, A. V. Balgobind, K. Wind, A. Gracanin, H.

- Begthel, J. Korving, R. van Bortel, A. A. Duarte, D. Lelieveld, A. van Hoeck, R. F. Ernst, F. Blokzijl, I. J. Nijman, M. Hoogstraal, M. van de Ven, D. A. Egan, V. Zinzalla, J. Moll, S. F. Boj, E. E. Voest, L. Wessels, P. J. van Diest, S. Rottenberg, R. G. J. Vries, E. Cuppen, H. Clevers, *Cell* **2018**, *172*, 373.
- [434] R. J. Schulze, M. B. Schott, C. A. Casey, P. L. Tuma, M. A. McNiven, *Journal of Cell Biology* **2019**, DOI 10.1083/jcb.201903090.
- [435] C. Vogel, E. M. Marcotte, *Nat Rev Genet* **2012**, DOI 10.1038/nrg3185.
- [436] T. Maier, M. Güell, L. Serrano, *FEBS Lett* **2009**, *583*, 3966.
- [437] R. De Sousa Abreu, L. O. Penalva, E. M. Marcotte, C. Vogel, *Mol Biosyst* **2009**, *5*, 1512.
- [438] S. Ye, J. W. B. Boeter, M. Mihajlovic, F. G. van Steenbeek, M. E. van Wolferen, L. A. Oosterhoff, A. Marsee, M. Caiazzo, L. J. W. van der Laan, L. C. Penning, T. Vermonden, B. Spee, K. Schneeberger, *Adv Funct Mater* **2020**, *30*, DOI 10.1002/adfm.202000893.
- [439] S. J. P. Callens, C. H. Arns, A. Kuliesh, A. A. Zadpoor, *Adv Funct Mater* **2021**, *31*, DOI 10.1002/adfm.202101373.
- [440] F. P. W. Melchels, B. Tonnarelli, A. L. Olivares, I. Martin, D. Lacroix, J. Feijen, D. J. Wendt, D. W. Grijpma, *Biomaterials* **2011**, *32*, 2878.
- [441] A. Paré, B. Charbonnier, P. Tournier, C. Vignes, J. Veziers, J. Lesoeur, B. Laure, H. Bertin, G. De Pinieux, G. Cherrier, J. Guicheux, O. Gauthier, P. Corre, D. Marchat, P. Weiss, *ACS Biomater Sci Eng* **2020**, *6*, 553.
- [442] S. C. Kapfer, S. T. Hyde, K. Mecke, C. H. Arns, G. E. Schröder-Turk, *Biomaterials* **2011**, *32*, 6875.
- [443] T. Femmer, A. J. C. Kuehne, M. Wessling, *Chemical Engineering Journal* **2015**, *273*, 438.
- [444] Y. Jung, S. Torquato, *Phys Rev E Stat Nonlin Soft Matter Phys* **2005**, *72*, DOI 10.1103/PhysRevE.72.056319.
- [445] N. Thomas, N. Sreedhar, O. Al-Ketan, R. Rowshan, R. K. Abu Al-Rub, H. Arafat, *Desalination* **2018**, *443*, 256.
- [446] A. Plaitakis, E. Kalef-Ezra, D. Kotzamani, I. Zaganas, C. Spanaki, *Biology (Basel)* **2017**, *6*, DOI 10.3390/biology6010011.
- [447] M. Krüger, L. A. Oosterhoff, M. E. van Wolferen, S. A. Schiele, A. Walther, N. Geijsen, L. De Laporte, L. J. W. van der Laan, L. M. Kock, B. Spee, *Adv Healthc Mater* **2020**, DOI 10.1002/adhm.201901658.
- [448] G. Hong, J. Kim, H. Oh, S. Yun, C. M. Kim, Y. M. Jeong, W. S. Yun, J. H. Shim, I. Jang, C. Y. Kim, S. Jin, *Advanced Materials* **2021**, *33*, DOI 10.1002/adma.202102624.
- [449] D. Kang, G. Hong, S. An, I. Jang, W. Yun, J. Shim, **2020**, *1905505*, 1.
- [450] M. Cuvellier, F. Ezan, H. Oliveira, S. Rose, J. C. Fricain, S. Langouët, V. Legagneux, G. Baffet, *Biomaterials* **2021**, *269*, DOI 10.1016/j.biomaterials.2020.120611.
- [451] Y. S. Kim, A. Asif, A. R. Chethikkattuveli Salih, J. W. Lee, K. N. Hyun, K. H. Choi, *Biomedicines* **2021**, DOI 10.3390/biomedicines9101369.
- [452] K. A. Homan, N. Gupta, K. T. Kroll, D. B. Kolesky, M. Skylar-Scott, T. Miyoshi, D. Mau, M. T. Valerius, T. Ferrante, J. V Bonventre, J. A. Lewis, R. Morizane, *Nat Methods* **2019**, DOI 10.1038/s41592-019-0325-y.
- [453] C. C. Cook, E. J. Fong, J. J. Schwartz, D. H. Porcincula, A. C. Kaczmarek, J. S. Oakdale, B. D. Moran, K. M. Champley, C. M. Rackson, A. Muralidharan, R. R. McLeod, M. Shusteff, *Advanced Materials* **2020**, *32*, DOI 10.1002/adma.202003376.
- [454] A. J. Hunt, D. R. Huffman, *Review of Scientific Instruments* **1973**, *44*, 1753.
- [455] J. C. Crocker, D. G. Grier, *J Colloid Interface Sci* **1996**, *179*, 298.
- [456] V. Lehmann, I. F. Schene, A. I. Ardisasmita, N. Liv, T. Veenendaal, J. Klumperman, H. P. J. van der Doef, H. J. Verkade, M. M. A. Verstegen, L. J. W. van der Laan, J. J. M. Jans, N. M. Verhoeven-Duif, P. M. van Hasselt, E. E. S. Nieuwenhuis, B. Spee, S. A. Fuchs, *J Inherit Metab Dis* **2022**, *45*, DOI 10.1002/jimd.12450.
- [457] D. Fukutomi, K. Ishii, K. Awazu, *Opt Rev* **2016**, *23*, 291.
- [458] J. S. Rana, S. S. Khan, D. M. Lloyd-Jones, S. Sidney, *J Gen Intern Med* **2021**, *36*, DOI 10.1007/s11606-020-06070-z.
- [459] M. McClellan, N. Brown, R. M. Califf, J. J. Warner, *Circulation* **2019**, *139*, DOI 10.1161/CIR.0000000000000652.
- [460] A. A. Seyhan, *Transl Med Commun* **2019**, *4*, DOI 10.1186/s41231-019-0050-7.



- [461] A. Mathur, Z. Ma, P. Loskill, S. Jeeawoody, K. E. Healy, *Adv Drug Deliv Rev* **2016**, *96*, DOI 10.1016/j.addr.2015.09.011.
- [462] G. Vunjak Novakovic, T. Eschenhagen, C. Mummery, *Cold Spring Harb Perspect Med* **2014**, *4*, a014076.
- [463] C. D. Roche, R. J. L. Brereton, A. W. Ashton, C. Jackson, C. Gentile, *European Journal of Cardio-thoracic Surgery* **2020**, *58*, DOI 10.1093/ejcts/ezaa093.
- [464] R. Gaetani, D. A. M. Feyen, V. Verhage, R. Slaats, E. Messina, K. L. Christman, A. Giacomello, P. A. F. M. Doevendans, J. P. G. Sluijter, *Biomaterials* **2015**, *61*, DOI 10.1016/j.biomaterials.2015.05.005.
- [465] J. Jang, H. J. Park, S. W. Kim, H. Kim, J. Y. Park, S. J. Na, H. J. Kim, M. N. Park, S. H. Choi, S. H. Park, S. W. Kim, S. M. Kwon, P. J. Kim, D. W. Cho, *Biomaterials* **2017**, *112*, DOI 10.1016/j.biomaterials.2016.10.026.
- [466] M. J. Ainsworth, N. Chirico, M. de Ruijter, A. Hrynevich, I. Dokter, J. P. G. Sluijter, J. Malda, A. van Mil, M. Castilho, *Biofabrication* **2023**, *15*, 035025.
- [467] F. Maiullari, M. Costantini, M. Milan, V. Pace, M. Chirivi, S. Maiullari, A. Rainer, D. Baci, H. E. S. Marei, D. Seliktar, C. Gargioli, C. Bearzi, R. Rizzi, *Sci Rep* **2018**, *8*, DOI 10.1038/s41598-018-31848-x.
- [468] M. Kristen, M. J. Ainsworth, N. Chirico, C. F. T. van der Ven, P. A. Doevendans, J. P. G. Sluijter, J. Malda, A. van Mil, M. Castilho, *Adv Healthc Mater* **2020**, *9*, DOI 10.1002/adhm.201900775.
- [469] E. Mirdamadi, J. W. Tashman, D. J. Shiwerski, R. N. Palchesko, A. W. Feinberg, *ACS Biomater Sci Eng* **2020**, *6*, DOI 10.1021/acsbmaterials.0c01133.
- [470] A. Lee, A. R. Hudson, D. J. Shiwerski, J. W. Tashman, T. J. Hinton, S. Yerneni, J. M. Bliley, P. G. Campbell, A. W. Feinberg, *Science (1979)* **2019**, *365*, DOI 10.1126/science.aav9051.
- [471] N. Noor, A. Shapira, R. Edri, I. Gal, L. Wertheim, T. Dvir, *Advanced Science* **2019**, *6*, DOI 10.1002/advs.201900344.
- [472] G. Größbacher, M. Bartolf-Kopp, C. Gergely, P. N. Bernal, S. Florczak, M. de Ruijter, N. G. Rodriguez, J. Groll, J. Malda, T. Jungst, R. Levato, *Advanced Materials* **2023**, DOI 10.1002/adma.202300756.
- [473] P. Chansoria, D. Rüttsche, A. Wang, H. Liu, D. D'Angella, R. Rizzo, A. Hasenauer, P. Weber, W. Qiu, N. B. M. Ibrahim, N. Korshunova, X. H. Qin, M. Zenobi-Wong, *Advanced Science* **2023**, DOI 10.1002/advs.202300912.
- [474] D. Ribezzi, M. Gueye, S. Florczak, F. Dusi, D. de Vos, F. Manente, A. Hierholzer, M. Fussenegger, M. Caiazzo, T. Blunk, J. Malda, R. Levato, *Advanced Materials* **2023**, DOI 10.1002/adma.202301673.
- [475] A. Orth, D. Webber, Y. Zhang, K. L. Sampson, H. W. de Haan, T. Lacelle, R. Lam, D. Solis, S. Dayanandan, T. Waddell, T. Lewis, H. K. Taylor, J. Boisvert, C. Paquet, *Nat Commun* **2023**, *14*, DOI 10.1038/s41467-023-39886-4.
- [476] N. J. Kaiser, R. J. Kant, A. J. Minor, K. L. K. Coulombe, *ACS Biomater Sci Eng* **2019**, *5*, DOI 10.1021/acsbmaterials.8b01112.
- [477] M. Alonzo, M. Delgado, C. Cleetus, S. A. Kumar, V. Thakur, M. Chattopadhyay, B. Joddar, *Acta Histochem* **2020**, *122*, DOI 10.1016/j.acthis.2020.151624.
- [478] K. Breckwoldt, F. Weinberger, S. Pecha, B. Geertz, J. Starbatty, A. Hansen, T. Eschenhagen, *Cardiovasc Res* **2014**, *103*, DOI 10.1093/cvr/cvu087.1.
- [479] R. K. Li, Z. Q. Jia, R. D. Weisel, F. Merante, D. A. G. Mickle, *J Mol Cell Cardiol* **1999**, *31*, DOI 10.1006/jmcc.1998.0882.
- [480] S. Sankar, M. Jayabalan, R. Methodious, M. Ibrahim, *Free Radic Biol Med* **2021**, *177*, DOI 10.1016/j.freeradbiomed.2021.08.151.
- [481] C. von Bibra, A. Shibamiya, B. Geertz, E. Querdel, M. Köhne, T. Stüdemann, J. Starbatty, F. N. Schmidt, A. Hansen, B. Hiebl, T. Eschenhagen, F. Weinberger, *J Mol Cell Cardiol* **2022**, *166*, DOI 10.1016/j.yjmcc.2022.01.007.
- [482] V. Talman, H. Ruskoaho, *Cell Tissue Res* **2016**, *365*, DOI 10.1007/s00441-016-2431-9.
- [483] A. Furber, J. J. Le Jeune, *Medicamundi* **1991**, *36*.
- [484] A. M. Agha, P. Parwani, A. Guha, J. B. Durand, C. A. Iliescu, S. Hassan, N. L. Palaskas, G. Gladish, P. Y. Kim, J. Lopez-Mattei, *Open Heart* **2018**, *5*, DOI 10.1136/openhrt-2018-000881.
- [485] G. Constantine, K. Shan, S. D. Flamm, M. U. Sivananthan, *Lancet* **2004**, *363*, DOI 10.1016/S0140-

- 6736(04)16509-4.
- [486] M. Falandt, P. N. Bernal, O. Dudaryeva, S. Florczak, G. Größbacher, M. Schweiger, A. Longoni, C. Greant, M. Assunção, O. Nijssen, S. van Vlierberghe, J. Malda, T. Vermonden, R. Levato, *Adv Mater Technol* **2023**, DOI 10.1002/admt.202300026.
- [487] S. Hamad, D. Derichsweiler, S. Papadopoulos, F. Nguemo, T. Šarić, A. Sachinidis, K. Brockmeier, J. Hescheler, B. J. Boukens, K. Pfannkuche, *Theranostics* **2019**, *9*, DOI 10.7150/thno.32058.
- [488] N. Chirico, E. L. Kessler, R. G. C. Maas, J. Fang, J. Qin, I. Dokter, M. Daniels, T. Šarić, K. Neef, J. W. Buikema, Z. Lei, P. A. Doevendans, J. P. G. Sluijter, A. van Mil, *Stem Cell Res Ther* **2022**, *13*, DOI 10.1186/s13287-022-03209-z.
- [489] R. G. C. Maas, S. Lee, M. Harakalova, C. J. B. Snijders Blok, W. R. Goodyer, J. Hjortnaes, P. A. F. M. Doevendans, L. W. Van Laake, J. van der Velden, F. W. Asselbergs, J. C. Wu, J. P. G. Sluijter, S. M. Wu, J. W. Buikema, *STAR Protoc* **2021**, *2*, DOI 10.1016/j.xpro.2021.100334.
- [490] T. C. L. Bracco Gartner, J. M. Stein, D. E. P. Muylaert, C. V. C. Bouten, P. A. Doevendans, A. Khademhosseini, W. J. L. Suyker, J. P. G. Sluijter, J. Hjortnaes, *Tissue Eng Part C Methods* **2021**, *27*, DOI 10.1089/ten.tec.2020.0298.
- [491] J. Schindelin, I. Arganda-Carreras, E. Frise, V. Kaynig, M. Longair, T. Pietzsch, S. Preibisch, C. Rueden, S. Saalfeld, B. Schmid, J. Y. Tinevez, D. J. White, V. Hartenstein, K. Eliceiri, P. Tomancak, A. Cardona, *Nat Methods* **2012**, *9*, DOI 10.1038/nmeth.2019.
- [492] F. Adams, T. Qiu, A. Mark, B. Fritz, L. Kramer, D. Schlager, U. Wetterauer, A. Miernik, P. Fischer, *Ann Biomed Eng* **2017**, *45*, 963.
- [493] P. Zarrintaj, S. Manouchehri, Z. Ahmadi, M. R. Saeb, A. M. Urbanska, D. L. Kaplan, M. Mozafari, *Carbohydr Polym* **2018**, *187*, DOI 10.1016/j.carbpol.2018.01.060.
- [494] T. Hashimshony, N. Senderovich, G. Avital, A. Klochendler, Y. de Leeuw, L. Anavy, D. Gennert, S. Li, K. J. Livak, O. Rozenblatt-Rosen, Y. Dor, A. Regev, I. Yanai, *Genome Biol* **2016**, *17*, DOI 10.1186/s13059-016-0938-8.
- [495] P. Carmeliet, R. K. Jain, *Nature* **2000**, *407*, DOI 10.1038/35025220.
- [496] A. Chopdar, U. Chakravarthy, D. Verma, *BMJ* **2003**, *326*, 485.
- [497] P. I. Mapp, D. A. Walsh, *Nat Rev Rheumatol* **2012**, *8*, DOI 10.1038/nrrheum.2012.80.
- [498] T. Matsumoto, G. M. Cooper, B. Gharaibeh, L. B. Meszaros, G. Li, A. Usas, F. H. Fu, J. Huard, *Arthritis Rheum* **2009**, *60*, DOI 10.1002/art.24443.
- [499] W. Petersen, T. Pufe, C. Stärke, T. Fuchs, S. Kopf, M. Raschke, R. Becker, B. Tillmann, *Annals of Anatomy* **2005**, *187*, DOI 10.1016/j.aanat.2005.04.010.
- [500] M. Centola, F. Abbruzzese, C. Scotti, A. Barbero, G. Vadalà, V. Denaro, I. Martin, M. Trombetta, A. Rainer, A. Marsano, *Tissue Eng Part A* **2013**, *19*, DOI 10.1089/ten.tea.2012.0455.
- [501] S. M. Kaiser, S. Arepalli, J. P. Ehlers, *J Exp Pharmacol* **2021**, *13*, DOI 10.2147/JEPS259298.
- [502] T. Bro, M. Derebecka, Ø. K. Jørstad, A. Grzybowski, *Graefes Archive for Clinical and Experimental Ophthalmology* **2020**, *258*, DOI 10.1007/s00417-019-04569-8.
- [503] S. Lee, J. G. E. Nemeño, J. I. Lee, *Tissue Eng Part B Rev* **2016**, *22*, DOI 10.1089/ten.teb.2015.0300.
- [504] S. K. Chibule, K. Rajagopal, N. Walter, V. Dutt, V. Madhuri, *Indian J Orthop* **2022**, *56*, DOI 10.1007/s43465-021-00434-1.
- [505] W. Li, J. Lin, Z. Wang, S. Ren, X. Wu, F. Yu, J. Weng, H. Zeng, *J Orthop Translat* **2019**, *19*, DOI 10.1016/j.jot.2019.04.002.
- [506] T. Nagai, M. Sato, T. Kutsuna, M. Kokubo, G. Ebihara, N. Ohta, J. Mochida, *Arthritis Res Ther* **2010**, *12*, DOI 10.1186/ar3142.
- [507] S. Kobsa, W. M. Saltzman, *Pediatr Res* **2008**, *63*, DOI 10.1203/PDR.0b013e318165f14d.
- [508] F. Li, *Open Ophthalmol J* **2012**, *6*, DOI 10.2174/1874364101206010054.
- [509] J. Liu, X. Zhang, G. Li, F. Xu, S. Li, L. Teng, Y. Li, F. Sun, *Int J Nanomedicine* **2019**, *14*, DOI 10.2147/IJN.S217038.
- [510] C. K. Pan, C. Durairaj, U. B. Kompella, O. Agwu, S. C. N. Oliver, H. Quiroz-Mercado, N. Mandava, J. L. Olson, *Journal of Ocular Pharmacology and Therapeutics* **2011**, *27*, DOI 10.1089/jop.2010.0158.

- [511] J. Pandit, Y. Sultana, M. Aqil, *Artif Cells Nanomed Biotechnol* **2017**, *45*, DOI 10.1080/21691401.2016.1243545.
- [512] R. Varshochian, M. Jeddi-Tehrani, A. R. Mahmoudi, M. R. Khoshayand, F. Atyabi, A. Sabzevari, M. R. Esfahani, R. Dinarvand, *European Journal of Pharmaceutical Sciences* **2013**, *50*, DOI 10.1016/j.ejps.2013.07.014.
- [513] F. Sousa, A. Cruz, P. Fonte, I. M. Pinto, M. T. Neves-Petersen, B. Sarmento, *Sci Rep* **2017**, *7*, DOI 10.1038/s41598-017-03959-4.
- [514] X. P. Zhang, J. G. Sun, J. Yao, K. Shan, B. H. Liu, M. Di Yao, H. M. Ge, Q. Jiang, C. Zhao, B. Yan, *Biomedicine and Pharmacotherapy* **2018**, *107*, DOI 10.1016/j.biopha.2018.08.092.
- [515] S. Mohammadi-Samani, B. Taghipour, *Pharm Dev Technol* **2015**, *20*, DOI 10.3109/10837450.2014.882940.
- [516] D. G. Armstrong, D. P. Orgill, R. D. Galiano, P. M. Glat, J. P. Kaufman, M. J. Carter, L. A. DiDomenico, C. M. Zelen, *Int Wound J* **2022**, *19*, DOI 10.1111/iwj.13715.
- [517] F. G. Usuelli, L. de Girolamo, M. Grassi, R. D'Ambrosi, U. A. Montrasio, M. Boga, *Arthrosc Tech* **2015**, *4*, DOI 10.1016/j.eats.2015.02.010.
- [518] F. Schwarz, A. Hegewald, N. Sahm, J. Becker, *Clin Oral Implants Res* **2014**, *25*, DOI 10.1111/clr.12220.
- [519] J. Becker, B. Al-Nawas, M. O. Klein, H. Schliephake, H. Terheyden, F. Schwarz, *Clin Oral Implants Res* **2009**, *20*, DOI 10.1111/j.1600-0501.2008.01689.x.
- [520] A. K. Schlegel, H. Möhler, F. Busch, A. Mehl, *Biomaterials* **1997**, *18*, DOI 10.1016/S0142-9612(96)00175-5.
- [521] Y. Zhang, S. T. Ellison, S. Duraivel, C. D. Morley, C. R. Taylor, T. E. Angelini, *Bioprinting* **2021**, *21*, DOI 10.1016/j.bprint.2020.e00121.
- [522] X. Yang, Z. Lu, H. Wu, W. Li, L. Zheng, J. Zhao, *Materials Science and Engineering C* **2018**, *83*, DOI 10.1016/j.msec.2017.09.002.
- [523] E. V. Isaeva, E. E. Beketov, G. A. Demyashkin, N. D. Yakovleva, N. V. Arguchinskaya, A. A. Kisel, T. S. Lagoda, E. P. Malakhov, A. N. Smirnova, V. M. Petriev, P. S. Eremin, E. O. Osidak, S. P. Domogatsky, S. A. Ivanov, P. V. Shegay, A. D. Kaprin, *Int J Mol Sci* **2022**, *23*, DOI 10.3390/ijms23052703.
- [524] S. Rhee, J. L. Puetzer, B. N. Mason, C. A. Reinhart-King, L. J. Bonassar, *ACS Biomater Sci Eng* **2016**, *2*, 1800.
- [525] Y. W. Koo, E. J. Choi, J. Y. Lee, H. J. Kim, G. H. Kim, S. H. Do, *Journal of Industrial and Engineering Chemistry* **2018**, *66*, DOI 10.1016/j.jiec.2018.05.049.
- [526] C. F. Lee, Y. H. Hsu, Y. C. Lin, T. T. Nguyen, H. W. Chen, S. C. Nabilla, S. Y. Hou, F. C. Chang, R. J. Chung, *Polymers (Basel)* **2021**, *13*, DOI 10.3390/polym13183123.
- [527] O. Messaoudi, C. Henrionnet, K. Bourge, D. Loeuille, P. Gillet, A. Pinzano, *Cells* **2021**, *10*, DOI 10.3390/cells10010002.
- [528] A. Abbadessa, J. Crecente-Campo, M. J. Alonso, *Tissue Eng Part B Rev* **2021**, *27*, DOI 10.1089/ten.teb.2020.0096.
- [529] T. Karimi, D. Barati, O. Karaman, S. Moeinzadeh, E. Jabbari, *Integrative Biology (United Kingdom)* **2015**, *7*, DOI 10.1039/c4ib00197d.
- [530] R. Dinarvand, S. H. Moghadam, A. Sheikhi, F. Atyabi, *J Microencapsul* **2005**, *22*, DOI 10.1080/02652040400026392.
- [531] M. C. Benítez, J. I. Espada, D. Fernandes, D. H. P. De La Ossa, M. E. Gil-Alegre, *J Surfactants Deterg* **2014**, *17*, DOI 10.1007/s11743-013-1505-x.
- [532] R. Varshochian, M. Riaz-Esfahani, M. Jeddi-Tehrani, A. R. Mahmoudi, S. Aghazadeh, M. Mahbod, M. Movassat, F. Atyabi, A. Sabzevari, R. Dinarvand, *J Biomed Mater Res A* **2015**, *103*, DOI 10.1002/jbm.a.35446.
- [533] F. Sousa, A. Cruz, I. M. Pinto, B. Sarmento, *Acta Biomater* **2018**, *78*, DOI 10.1016/j.actbio.2018.07.040.
- [534] J. Panyam, M. M. Dali, S. K. Sahoo, W. Ma, S. S. Chakravarthi, G. L. Amidon, R. J. Levy, V. Labhasetwar, *Journal of Controlled Release* **2003**, *92*, DOI 10.1016/S0168-3659(03)00328-6.
- [535] N. Samadi, A. Abbadessa, A. Di Stefano, C. F. Van Nostrum, T. Vermonden, S. Rahimian, E. A. Teunissen, M. J. Van Steenberghe, M. Amidi, W. E. Hennink, *Journal of Controlled Release* **2013**, *172*, DOI 10.1016/j.jconrel.2013.05.034.

- [536] G. Crotts, T. G. Park, in *J Microencapsul*, **1998**.
- [537] T. G. Park, W. Lu, G. Crotts, *Journal of Controlled Release* **1995**, *33*, DOI 10.1016/0168-3659(94)00084-8.
- [538] S. Narayana, M. Gulzar Ahmed, A. Nasrine, *Mater Today Proc* **2022**, *68*, DOI 10.1016/j.matpr.2022.06.179.
- [539] E. Peira, G. Chindamo, D. Chirio, S. Sapino, S. Oliaro-bosso, E. Rebba, P. Ivanchenko, M. Gallarate, *Pharmaceutics* **2021**, *13*, DOI 10.3390/pharmaceutics13020258.
- [540] K. Park, A. Otte, F. Sharifi, J. Garner, S. Skidmore, H. Park, Y. K. Jhon, B. Qin, Y. Wang, *Journal of Controlled Release* **2021**, *329*, DOI 10.1016/j.jconrel.2020.10.044.
- [541] L. García-Fernández, S. Halstenberg, R. E. Unger, M. R. Aguilar, C. J. Kirkpatrick, J. San Román, *Biomaterials* **2010**, *31*, DOI 10.1016/j.biomaterials.2010.07.022.
- [542] K. T. Morin, R. T. Tranquillo, *Exp Cell Res* **2013**, *319*, DOI 10.1016/j.yexcr.2013.06.006.
- [543] L. Bédouet, V. Verret, S. Louguet, E. Servais, F. Pascale, A. Beilvert, M. T. Baylatry, D. Labarre, L. Moine, A. Laurent, *Int J Pharm* **2015**, *484*, DOI 10.1016/j.ijpharm.2015.02.039.
- [544] H. Suo, J. Zhang, M. Xu, L. Wang, *Materials Science and Engineering C* **2021**, *123*, DOI 10.1016/j.msec.2021.111963.
- [545] H. Lee, G. H. Yang, M. Kim, J. Y. Lee, J. T. Huh, G. H. Kim, *Materials Science and Engineering C* **2018**, *84*, DOI 10.1016/j.msec.2017.11.013.
- [546] C. C. Clark, J. Aleman, L. Mutkus, A. Skardal, *Bioprinting* **2019**, *16*, DOI 10.1016/j.bprint.2019.e00058.
- [547] F. Banche-Niclot, C. Licini, G. Montalbano, S. Fiorilli, M. Mattioli-Belmonte, C. Vitale-Brovvarone, *Polymers (Basel)* **2022**, *14*, DOI 10.3390/polym14050857.
- [548] G. Montalbano, G. Borciani, G. Cerqueni, C. Licini, F. Banche-Niclot, D. Janner, S. Sola, S. Fiorilli, M. Mattioli-Belmonte, G. Ciapetti, C. Vitale-Brovvarone, *Nanomaterials* **2020**, *10*, DOI 10.3390/nano10091681.
- [549] F. Banche-Niclot, G. Montalbano, S. Fiorilli, C. Vitale-Brovvarone, *Int J Mol Sci* **2021**, *22*, DOI 10.3390/ijms22041718.
- [550] D. Blanco, M. J. Alonso, *European Journal of Pharmaceutics and Biopharmaceutics* **1998**, *45*, DOI 10.1016/S0939-6411(98)00011-3.
- [551] E. Zudaire, L. Gambardella, C. Kurcz, S. Vermeren, *PLoS One* **2011**, *6*, DOI 10.1371/journal.pone.0027385.
- [552] A. Molina-Crespo, A. Cadete, D. Sarrio, M. Gamez-Chiachio, L. Martinez, K. Chao, A. Olivera, A. Gonella, E. Diaz, J. Palacios, P. K. Dhal, M. Besev, M. Rodríguez-Serrano, M. L. G. Bermejo, J. C. Triviño, A. Cano, M. García-Fuentes, O. Herzberg, D. Torres, M. J. Alonso, G. Moreno-Bueno, *Clinical Cancer Research* **2019**, *25*, DOI 10.1158/1078-0432.CCR-18-2381.
- [553] H. Sah, *J Pharm Sci* **1997**, *86*, DOI 10.1021/js960363q.
- [554] M. J. Alonso, R. K. Gupta, C. Min, G. R. Siber, R. Langer, *Vaccine* **1994**, *12*, DOI 10.1016/0264-410X(94)90092-2.
- [555] A. H. Ghassemi, M. J. Van Steenbergen, H. Talsma, C. F. Van Nostrum, D. J. A. Crommelin, W. E. Hennink, *Pharm Res* **2010**, *27*, DOI 10.1007/s11095-010-0205-8.
- [556] R. Levato, T. Jungst, R. G. Scheuring, T. Blunk, J. Groll, J. Malda, *Advanced Materials* **2020**, *32*, DOI 10.1002/adma.201906423.
- [557] J. Groll, T. Boland, T. Blunk, J. A. Burdick, D. W. Cho, P. D. Dalton, B. Derby, G. Forgacs, Q. Li, V. A. Mironov, L. Moroni, M. Nakamura, W. Shu, S. Takeuchi, G. Vozzi, T. B. F. Woodfield, T. Xu, J. J. Yoo, J. Malda, *Biofabrication* **2016**, *8*, 013001.
- [558] K. J. Wolf, J. D. Weiss, S. G. M. Uzel, M. A. Skylar-Scott, J. A. Lewis, *Cell Stem Cell* **2022**, *29*, DOI 10.1016/j.stem.2022.04.012.
- [559] B. Gao, Q. Yang, X. Zhao, G. Jin, Y. Ma, F. Xu, *Trends Biotechnol* **2016**, *34*, 746.
- [560] M. Mehrpouya, H. Vahabi, S. Janbaz, A. Darafsheh, T. R. Mazur, S. Ramakrishna, *Polymer (Guildf)* **2021**, *230*, 124080.
- [561] P. Cao, L. Tao, J. Gong, T. Wang, Q. Wang, J. Ju, Y. Zhang, *ACS Appl Polym Mater* **2021**, *3*, 6167.

- [562] G. Li, Q. Yan, H. Xia, Y. Zhao, *ACS Appl Mater Interfaces* **2015**, *7*, 12067.
- [563] R. Tognato, A. R. Armiento, V. Bonfrate, R. Levato, J. Malda, M. Alini, D. Eglin, G. Giancane, T. Serra, *Adv Funct Mater* **2019**, *29*, 1804647.
- [564] M. López-Valdeolivas, D. Liu, D. J. Broer, C. Sánchez-Somolinos, *Macromol Rapid Commun* **2018**, *39*, DOI 10.1002/marc.201700710.
- [565] S. Camarero-Espinosa, L. Moroni, *Nat Commun* **2021**, *12*, DOI 10.1038/s41467-021-21325-x.
- [566] W. Mulyasasmita, L. Cai, R. E. Dewi, A. Jha, S. D. Ullmann, R. H. Luong, N. F. Huang, S. C. Heilshorn, *Journal of Controlled Release* **2014**, *191*, DOI 10.1016/j.jconrel.2014.05.015.
- [567] C. M. Madl, S. C. Heilshorn, *Chemistry of Materials* **2019**, *31*, DOI 10.1021/acs.chemmater.9b02485.
- [568] I. Roppolo, F. Frascella, M. Gastaldi, M. Castellino, B. Ciubini, C. Barolo, L. Scaltrito, C. Nicosia, M. Zanetti, A. Chiappone, *Polym Chem* **2019**, *10*, DOI 10.1039/c9py00962k.
- [569] A. Cosola, A. Chiappone, M. Sangermano, *Mol Syst Des Eng* **2022**, DOI 10.1039/d2me00059h.
- [570] P. M. Gawade, J. A. Shadish, B. A. Badeau, C. A. DeForest, *Advanced Materials* **2019**, *31*, DOI 10.1002/adma.201902462.
- [571] J. Lowry Curley, S. R. Jennings, M. J. Moore, *Journal of Visualized Experiments* **2011**, DOI 10.3791/2636.
- [572] I. Batalov, K. R. Stevens, C. A. DeForest, *Proc Natl Acad Sci U S A* **2021**, *118*, DOI 10.1073/pnas.2014194118.
- [573] N. Broguiere, I. Lüchtefeld, L. Trachsels, D. Mazunin, R. Rizzo, J. W. Bode, M. P. Lutolf, M. Zenobi-Wong, *Advanced Materials* **2020**, *32*, DOI 10.1002/adma.201908299.
- [574] W. M. G. A. C. Groen, L. Utomo, M. Castilho, D. Gawlitta, J. Malda, P. R. van Weeren, R. Levato, N. M. Korthagen, *Int J Mol Sci* **2020**, DOI 10.3390/ijms21228571.
- [575] T. Buie, J. McCune, E. Cosgriff-Hernandez, *Trends Biotechnol* **2020**, *38*, DOI 10.1016/j.tibtech.2019.12.005.
- [576] J. van Hoorick, A. Dobos, M. Markovic, T. Gheysens, L. van Damme, P. Gruber, L. Tytgat, J. van Erps, H. Thienpont, P. Dubruel, A. Ovsianikov, S. van Vlierberghe, *Biofabrication* **2020**, DOI 10.1088/1758-5090/abc95f.
- [577] J. Van Hoorick, P. Gruber, M. Markovic, M. Rollot, G. J. Graulus, M. Vagenende, M. Tromayer, J. Van Erps, H. Thienpont, J. C. Martins, S. Baudis, A. Ovsianikov, P. Dubruel, S. Van Vlierberghe, *Macromol Rapid Commun* **2018**, *39*, DOI 10.1002/marc.201800181.
- [578] T. R. Cox, J. T. Erler, *DMM Disease Models and Mechanisms* **2011**, *4*, DOI 10.1242/dmm.004077.
- [579] I. Karakurt, A. Aydoğdu, S. Çikrikçi, J. Orozco, L. Lin, *Int J Pharm* **2020**, *584*, DOI 10.1016/j.ijpharm.2020.119428.
- [580] A. Dobos, F. Gantner, M. Markovic, J. van Hoorick, L. Tytgat, S. van Vlierberghe, A. Ovsianikov, *Biofabrication* **2020**, *13*, DOI 10.1088/1758-5090/abb063.
- [581] J. T. Toombs, M. Luitz, C. C. Cook, S. Jenne, C. C. Li, B. E. Rapp, F. Kotz-Helmer, H. K. Taylor, *Science (1979)* **2022**, *376*, DOI 10.1126/science.abm6459.
- [582] X. Guo, R. A. Mittelstaedt, L. Guo, J. G. Shaddock, R. H. Heflich, A. H. Bigger, M. M. Moore, N. Mei, *Toxicology in Vitro* **2013**, *27*, DOI 10.1016/j.tiv.2013.02.019.
- [583] D. I. Pattison, M. Lam, S. S. Shinde, R. F. Anderson, M. J. Davies, *Free Radic Biol Med* **2012**, *53*, DOI 10.1016/j.freeradbiomed.2012.08.578.
- [584] J. Li, J. Zhang, Y. Chen, N. Kawazoe, G. Chen, *ACS Appl Mater Interfaces* **2017**, *9*, DOI 10.1021/acsami.7b12486.
- [585] X. Guo, J. E. Seo, S. M. Bryce, J. A. Tan, Q. Wu, S. L. Dial, M. M. Moore, N. Mei, *Toxicological Sciences* **2018**, *163*, DOI 10.1093/toxsci/kfy022.
- [586] A. Ovsianikov, Z. Li, A. Ajami, J. Torgersen, W. Husinsky, J. Stampfl, R. Liska, *Appl Phys A Mater Sci Process* **2012**, *108*, DOI 10.1007/s00339-012-6964-9.
- [587] S. Sayer, T. Zandrini, M. Markovic, J. Van Hoorick, S. Van Vlierberghe, S. Baudis, W. Holthöner, A. Ovsianikov, *Sci Rep* **2022**, *12*, DOI 10.1038/s41598-022-11612-y.
- [588] J. D. McCall, K. S. Anseth, *Biomacromolecules* **2012**, *13*, DOI 10.1021/bm300671s.
- [589] B. V. Sridhar, N. R. Doyle, M. A. Randolph, K. S. Anseth, *J Biomed Mater Res A* **2014**, *102*, DOI 10.1002/

- jbm.a.35115.
- [590] B. V. Sridhar, J. L. Brock, J. S. Silver, J. L. Leight, M. A. Randolph, K. S. Anseth, *Adv Healthc Mater* **2015**, *4*, DOI 10.1002/adhm.201400695.
- [591] G. Wang, N. Yuan, N. Li, Q. Wei, Y. Qian, J. Zhang, M. Qin, Y. Wang, S. Dong, *ACS Appl Mater Interfaces* **2022**, *14*, DOI 10.1021/acsmi.2c06159.
- [592] J. D. Weaver, D. M. Headen, J. Aquart, C. T. Johnson, L. D. Shea, H. Shirwan, A. J. García, *Sci Adv* **2017**, *3*, DOI 10.1126/sciadv.1700184.
- [593] N. Ferrara, H. P. Gerber, J. LeCouter, *Nat Med* **2003**, *9*, DOI 10.1038/nm0603-669.
- [594] Y. An, W. J. Liu, P. Xue, Y. Ma, L. Q. Zhang, B. Zhu, M. Qi, L. Y. Li, Y. J. Zhang, Q. T. Wang, Y. Jin, *Cell Death Dis* **2018**, *9*, DOI 10.1038/s41419-017-0082-8.
- [595] Q. Ge, H. Zhang, J. Hou, L. Wan, W. Cheng, X. Wang, D. Dong, C. Chen, J. Xia, J. Guo, X. Chen, X. Wu, *Mol Med Rep* **2018**, *17*, DOI 10.3892/mmr.2017.8059.
- [596] M. T. Poldervaart, H. Gremmels, K. Van Deventer, J. O. Fledderus, F. C. Öner, M. C. Verhaar, W. J. A. Dhert, J. Alblas, *Journal of Controlled Release* **2014**, *184*, 58.
- [597] T. Takei, S. Sakai, T. Ono, H. Ijima, K. Kawakami, *Biotechnol Bioeng* **2006**, *95*, DOI 10.1002/bit.20903.
- [598] X. Wang, D. T. T. Phan, A. Sobrino, S. C. George, C. C. W. Hughes, A. P. Lee, *Lab Chip* **2016**, *16*, DOI 10.1039/c5lc01050k.
- [599] R. R. Chen, E. A. Silva, W. W. Yuen, D. J. Mooney, *Pharm Res* **2007**, *24*, DOI 10.1007/s11095-006-9173-4.
- [600] F. E. Freeman, P. Pitacco, L. H. A. van Dommelen, J. Nulty, D. C. Browe, J. Y. Shin, E. Alsberg, D. J. Kelly, *Sci Adv* **2020**, *6*, DOI 10.1126/sciadv.abb5093.
- [601] P. Mozetic, S. M. Giannitelli, M. Gori, M. Trombetta, A. Rainer, *J Biomed Mater Res A* **2017**, *105*, 2582.
- [602] E. Ehler, S. N. Jayasinghe, *Analyst* **2014**, *139*, 4449.
- [603] A. Dobos, J. Van Hoorick, W. Steiger, P. Gruber, M. Markovic, O. G. Andriotis, A. Rohatschek, P. Dubrue, P. J. Thurner, S. Van Vlierbergh, S. Baudis, A. Ovsianikov, *Adv Healthc Mater* **2019**, 1900752.
- [604] L. Koch, A. Deiwick, J. Soriano, B. Chichkov, *Int J Bioprint* **2022**, *9*, DOI 10.18063/IJB.V9I2.672.
- [605] I. Jorba, D. Mostert, L. H. L. Hermans, A. Van Der Pol, N. A. Kurniawan, C. V. C. Bouten, *Tissue Eng Part C Methods* **2021**, *27*, DOI 10.1089/ten.tec.2020.0342.
- [606] C. A. Dessalles, C. Leclech, A. Castagnino, A. I. Barakat, *Commun Biol* **2021**, *4*, DOI 10.1038/s42003-021-02285-w.
- [607] F. E. Uslu, C. D. Davidson, E. Mailand, N. Bouklas, B. M. Baker, M. S. Sakar, *Advanced Materials* **2021**, *33*, DOI 10.1002/adma.202102641.
- [608] J. Madrid-Wolff, J. Toombs, R. Rizzo, P. N. Bernal, D. Porcincula, R. Walton, B. Wang, F. Kotz-Helmer, Y. Yang, D. Kaplan, Y. S. Zhang, M. Zenobi-Wong, R. R. McLeod, B. Rapp, J. Schwartz, M. Shusteff, H. Talyor, R. Levato, C. Moser, *MRS Commun* **2023**, DOI 10.1557/s43579-023-00447-x.
- [609] J. H. Galarraga, R. C. Locke, C. E. Witherel, B. D. Stoeckl, M. Castilho, R. L. Mauck, J. Malda, R. Levato, J. A. Burdick, *Biofabrication* **2022**, *14*, DOI 10.1088/1758-5090/ac3acb.
- [610] S. Hassan, E. Gomez-Reyes, E. Enciso-Martinez, K. Shi, J. G. Campos, O. Y. P. Soria, E. Luna-Cerón, M. C. Lee, I. Garcia-Reyes, J. Steakelum, H. Jeelani, L. E. Garcia-Rivera, M. Cho, S. S. Cortes, T. Kamperman, H. Wang, J. Leijten, L. Fiondella, S. R. Shin, *ACS Appl Mater Interfaces* **2022**, *14*, DOI 10.1021/acsmi.2c12585.
- [611] B. Yang, K. Wei, C. Loebel, K. Zhang, Q. Feng, R. Li, S. H. D. Wong, X. Xu, C. Lau, X. Chen, P. Zhao, C. Yin, J. A. Burdick, Y. Wang, L. Bian, *Nat Commun* **2021**, *12*, DOI 10.1038/s41467-021-23120-0.
- [612] O. Jeon, Y. Bin Lee, S. J. Lee, N. Guliyeva, J. Lee, E. Alsberg, *Bioact Mater* **2022**, *15*, DOI 10.1016/j.bioactmat.2021.11.025.
- [613] H. S. Kim, C. Kim, K. Y. Lee, *J Biomed Mater Res A* **2022**, *110*, DOI 10.1002/jbm.a.37325.
- [614] R. Rizzo, D. Rüttsche, H. Liu, P. Chansoria, A. Wang, A. Hasenauer, M. Zenobi-Wong, *Adv Mater Technol* **2023**, *8*, DOI 10.1002/admt.202201871.

- [615] A. K. Miri, I. Mirzaee, S. Hassan, S. Mesbah Oskui, D. Nieto, A. Khademhosseini, Y. S. Zhang, *Lab Chip* **2019**, 19, DOI 10.1039/c8lc01037d.
- [616] D. M. Zuev, A. K. Nguyen, V. I. Putlyaev, R. J. Narayan, *Bioprinting* **2020**, 20, DOI 10.1016/j.bprint.2020.e00090.
- [617] K. Obata, A. El-Tamer, L. Koch, U. Hinze, B. N. Chichkov, *Light Sci Appl* **2013**, 2, DOI 10.1038/lisa.2013.72.
- [618] S. Li, W. Wang, W. Li, M. Xie, C. Deng, X. Sun, C. Wang, Y. Liu, G. Shi, Y. Xu, X. Ma, J. Wang, *Adv Funct Mater* **2021**, 31, DOI 10.1002/adfm.202102685.
- [619] H. Zhao, Y. Chen, L. Shao, M. Xie, J. Nie, J. Qiu, P. Zhao, H. Ramezani, J. Fu, H. Ouyang, Y. He, *Small* **2018**, 14, DOI 10.1002/sml.201802630.
- [620] T. Jiang, J. G. Munguia-Lopez, S. Flores-Torres, J. Grant, S. Vijayakumar, A. De Leon-Rodriguez, J. M. Kinsella, *Sci Rep* **2017**, 7, DOI 10.1038/s41598-017-04691-9.
- [621] Z. Heydari, P. Pooyan, P. Bikmulina, A. Pozdnyakov, V. Fomin, H. Seydi, A. Shpichka, P. Timashev, M. Vosough, *Bioprinting* **2022**, 27, DOI 10.1016/j.bprint.2022.e00208.
- [622] T. Agarwal, B. Subramanian, T. K. Maiti, *ACS Biomater Sci Eng* **2019**, 5, DOI 10.1021/acsbiomaterials.9b00745.
- [623] S. Nantasanti, A. de Bruin, J. Rothuizen, L. C. Penning, B. A. Schotanus, *Stem Cells Transl Med* **2016**, 5, DOI 10.5966/sctm.2015-0152.
- [624] N. Gjorevski, M. Nikolaev, T. E. Brown, O. Mitrofanova, N. Brandenberg, F. W. DelRio, F. M. Yavitt, P. Liberali, K. S. Anseth, M. P. Lutolf, *Science (1979)* **2022**, DOI 10.1126/science.aaw9021.
- [625] C. M. Madl, S. C. Heilshorn, *Annu Rev Biomed Eng* **2018**, 20, 21.
- [626] S. Mueller, *Hepat Med* **2010**, DOI 10.2147/hmer.s7394.
- [627] D. J. Yoo, *International Journal of Precision Engineering and Manufacturing* **2014**, 15, 1657.
- [628] J. Augustyniak, A. Bertero, T. Coccini, D. Baderna, L. Buzanska, F. Caloni, *Journal of Applied Toxicology* **2019**, 39, DOI 10.1002/jat.3815.
- [629] S. Kim, A. N. Cho, S. Min, S. Kim, S. W. Cho, *Adv Ther (Weinh)* **2019**, 2, DOI 10.1002/adtp.201800087.
- [630] Y. Shi, H. Inoue, J. C. Wu, S. Yamanaka, *Nat Rev Drug Discov* **2017**, 16, DOI 10.1038/nrd.2016.245.
- [631] H. Okano, M. Nakamura, K. Yoshida, Y. Okada, O. Tsuji, S. Nori, E. Ikeda, S. Yamanaka, K. Miura, *Circ Res* **2013**, 112, DOI 10.1161/CIRCRESAHA.111.256149.
- [632] A. Omidinia-Anarkoli, S. Boesveld, U. Tuvshindorj, J. C. Rose, T. Haraszti, L. De Laporte, *Small* **2017**, 13, DOI 10.1002/sml.201770191.
- [633] S. Adepu, S. Ramakrishna, *Molecules* **2021**, 26, DOI 10.3390/molecules26195905.
- [634] N. Kamaly, B. Yameen, J. Wu, O. C. Farokhzad, *Chem Rev* **2016**, 116, DOI 10.1021/acs.chemrev.5b00346.
- [635] J. Kost, R. Langer, *Trends Biotechnol* **1984**, 2, DOI 10.1016/0167-7799(84)90007-6.
- [636] D. A. M. Feyen, R. Gaetani, J. Deddens, D. van Keulen, C. van Opbergen, M. Poldervaart, J. Alblas, S. Chamuleau, L. W. van Laake, P. A. Doevendans, J. P. G. Sluijter, *Adv Healthc Mater* **2016**, 5, DOI 10.1002/adhm.201500861.
- [637] A. Lode, C. Wolf-Brandstetter, A. Reinstorf, A. Bernhardt, U. König, W. Pompe, M. Gelsinsky, *J Biomed Mater Res A* **2007**, 81, DOI 10.1002/jbm.a.31024.
- [638] P. Gupta, K. Vermani, S. Garg, *Drug Discov Today* **2002**, 7, DOI 10.1016/S1359-6446(02)02255-9.
- [639] Q. Zhang, Y. Du, M. Yu, L. Ren, Y. Guo, Q. Li, M. Yin, X. Li, F. Chen, *Carbohydr Polym* **2022**, 277, DOI 10.1016/j.carbpol.2021.118880.
- [640] M. Sabz, R. Kamali, S. Ahmadizade, *IEEE Trans Magn* **2020**, 56, DOI 10.1109/TMAG.2020.2987998.
- [641] T. Göckler, S. Haase, X. Kempter, R. Pfister, B. R. Maciel, A. Grimm, T. Molitor, N. Willenbacher, U. Schepers, *Adv Healthc Mater* **2021**, DOI 10.1002/adhm.202100206.
- [642] W. M. Gramlich, I. L. Kim, J. A. Burdick, *Biomaterials* **2013**, 34, DOI 10.1016/j.biomaterials.2013.08.089.
- [643] A. Ovsianikov, A. Deiwick, S. Van Vlierberghe, M. Pflaum, M. Wilhelmi, P. Dubrue, B. Chichkov, *Materials* **2010**, 4, DOI 10.3390/ma4010288.

- [644] L. Kazmierski, M. Maj, *Physical Sciences Reviews* **2023**, *8*, DOI 10.1515/psr-2019-0061.
- [645] P.W. Winter, A. G. York, D. D. Nogare, M. Ingaramo, R. Christensen, A. Chitnis, G. H. Patterson, H. Shroff, *Optica* **2014**, *1*, DOI 10.1364/optica.1.000181.
- [646] F. Fazal, S. Raghav, A. Callanan, V. Koutsos, N. Radacsi, *Biofabrication* **2021**, DOI 10.1088/1758-5090/ac0963.
- [647] J. Son, S. J. Hong, J. W. Lim, W. Jeong, J. H. Jeong, H. W. Kang, *Small Methods* **2021**, *5*, DOI 10.1002/smt.202100632.
- [648] N. Brandenburg, M. P. Lutolf, *Advanced Materials* **2016**, *28*, DOI 10.1002/adma.201601099.
- [649] D. Bulnes-Abundis, L. M. Carrillo-Cocom, D. Aráiz-Hernández, A. García-Ulloa, M. Granados-Pastor, P. B. Sánchez-Arreola, G. Murugappan, M. M. Alvarez, *Biotechnol Bioeng* **2013**, *110*, DOI 10.1002/bit.24780.
- [650] M. M. Alvarez, P. E. Arratia, F. J. Muzzio, *Canadian Journal of Chemical Engineering* **2002**, *80*, DOI 10.1002/cjce.5450800418.
- [651] A. C. Daly, *Adv Healthc Mater* **2023**, DOI 10.1002/adhm.202301388.
- [652] Z. Ataie, S. Kheirabadi, J. W. Zhang, A. Kedzierski, C. Petrosky, R. Jiang, C. Vollberg, A. Sheikhi, *Small* **2022**, *18*, DOI 10.1002/smll.202202390.
- [653] D. Rommel, M. Mork, S. Vedaraman, C. Bastard, L. P. B. Guerzoni, Y. Kittel, R. Vinokur, N. Born, T. Haraszti, L. De Laporte, *Advanced Science* **2022**, *9*, DOI 10.1002/adv.202270060.
- [654] M. H. Kim, D. Banerjee, N. Celik, I. T. Ozbolat, *Biofabrication* **2022**, *14*, DOI 10.1088/1758-5090/ac4dd8.
- [655] C. S. O'Bryan, T. Bhattacharjee, S. L. Marshall, W. Gregory Sawyer, T. E. Angelini, *Bioprinting* **2018**, *11*, DOI 10.1016/j.bprint.2018.e00037.
- [656] A. L. Torres, S. J. Bidarra, D. P. Vasconcelos, J. N. Barbosa, E. A. Silva, D. S. Nascimento, C. C. Barrias, *Biomaterials* **2020**, *228*, DOI 10.1016/j.biomaterials.2019.119554.
- [657] Y. Fang, Y. Guo, M. Ji, B. Li, Y. Guo, J. Zhu, T. Zhang, Z. Xiong, *Adv Funct Mater* **2022**, *32*, DOI 10.1002/adfm.202109810.
- [658] T. Satoh, S. Sugiura, K. Shin, R. Onuki-Nagasaki, S. Ishida, K. Kikuchi, M. Kakiki, T. Kanamori, *Lab Chip* **2017**, *18*, 115.
- [659] K. Ronaldson-Bouchard, D. Teles, K. Yeager, D. N. Tavakol, Y. Zhao, A. Chramiec, S. Tagore, M. Summers, S. Stylianou, M. Tamargo, B. M. Lee, S. P. Halligan, E. H. Abaci, Z. Guo, J. Jacków, A. Pappalardo, J. Shih, R. K. Soni, S. Sonar, C. German, A. M. Christiano, A. Califano, K. K. Hirschi, C. S. Chen, A. Przekwas, G. Vunjak-Novakovic, *Nat Biomed Eng* **2022**, *6*, DOI 10.1038/s41551-022-00882-6.
- [660] A. Skardal, S. V. Murphy, M. Devarasetty, I. Mead, H. W. Kang, Y. J. Seol, Y. S. Zhang, S. R. Shin, L. Zhao, J. Aleman, A. R. Hall, T. D. Shupe, A. Kleensang, M. R. Dokmeci, S. Jin Lee, J. D. Jackson, J. J. Yoo, T. Hartung, A. Khademhosseini, S. Soker, C. E. Bishop, A. Atala, *Sci Rep* **2017**, *7*, DOI 10.1038/s41598-017-08879-x.
- [661] Z. Jin, Z. Zhang, X. Shao, G. X. Gu, *ACS Biomater Sci Eng* **2021**, DOI 10.1021/acsbomaterials.0c01761.
- [662] M. C. McCorry, K. F. Reardon, M. Black, C. Williams, G. Babakhanova, J. M. Halpern, S. Sarkar, N. S. Swami, K. A. Mirica, S. Boermeester, A. Underhill, *Biofabrication* **2023**, *15*, DOI 10.1088/1758-5090/ac94a1.
- [663] S. J. Hollister, *Biofabrication* **2009**, *1*, DOI 10.1088/1758-5082/1/1/012001.
- [664] L. Ouyang, J. P. K. Armstrong, Y. Lin, J. P. Wojciechowski, C. Lee-Reeves, D. Hachim, K. Zhou, J. A. Burdick, M. M. Stevens, *Sci Adv* **2020**, *6*, DOI 10.1126/sciadv.abc5529.
- [665] B. Derby, *J Mater Chem* **2008**, *18*, 5717.
- [666] M. A. Skylar-Scott, S. G. M. Uzel, L. L. Nam, J. H. Ahrens, R. L. Truby, S. Damaraju, J. A. Lewis, *Biomanufacturing of Organ-Specific Tissues with High Cellular Density and Embedded Vascular Channels*, **2019**.
- [667] W. L. Ng, J. M. Lee, M. Zhou, Y. W. Chen, K. X. A. Lee, W. Y. Yeong, Y. F. Shen, *Biofabrication* **2020**, DOI 10.1088/1758-5090/ab6034.
- [668] L. Brigo, A. Urciuolo, S. Giullitti, G. Della Giustina, M. Tromayer, R. Liska, N. Elvassore, G. Brusatin, *Acta Biomater* **2017**, *55*, 373.
- [669] A. Ovsianikov, S. Mühleder, J. Torgersen, Z. Li, X. H. Qin, S. Van Vlierberghe, P. Dubruel, W. Holthöner, H.



- Redl, R. Liska, J. Stampfl, *Langmuir* **2014**, *30*, 3787.
- [670] K. A. Heintz, M. E. Bregenzer, J. L. Mantle, K. H. Lee, J. L. West, J. H. Slater, *Adv Healthc Mater* **2016**, *5*, DOI 10.1002/adhm.201670093.
- [671] Y. S. Zhang, Q. Pi, A. M. van Genderen, *Journal of Visualized Experiments* **2017**, *2017*, DOI 10.3791/55957.
- [672] K. A. Homan, D. B. Kolesky, M. A. Skylar-Scott, J. Herrmann, H. Obuobi, A. Moisan, J. A. Lewis, *Sci Rep* **2016**, *6*, DOI 10.1038/srep34845.
- [673] N. Y. C. Lin, K. A. Homan, S. S. Robinson, D. B. Kolesky, N. Duarte, A. Moisan, J. A. Lewis, *Proc Natl Acad Sci U S A* **2019**, *116*, DOI 10.1073/pnas.1815208116.
- [674] J. B. Lee, D. H. Kim, J. K. Yoon, D. B. Park, H. S. Kim, Y. M. Shin, W. Baek, M. L. Kang, H. J. Kim, H. J. Sung, *Nat Commun* **2020**, *11*, DOI 10.1038/s41467-020-14480-0.
- [675] H. Huang, X. Qi, Y. Chen, Z. Wu, *Saudi Pharmaceutical Journal* **2019**, *27*, DOI 10.1016/j.jsps.2019.08.001.
- [676] T. K. Sastri, V. N. Gupta, S. Chakraborty, S. Madhusudhan, H. Kumar, P. Chand, V. Jain, B. Veeranna, D. V. Gowda, *Gels* **2022**, *8*, DOI 10.3390/gels8050316.
- [677] F. Doberenz, K. Zeng, C. Willems, K. Zhang, T. Groth, *J Mater Chem B* **2020**, *8*, DOI 10.1039/c9tb02052g.
- [678] Y. Pei, J. Chen, L. Yang, L. Shi, Q. Tao, B. Hui, J. Li, *J Biomater Sci Polym Ed* **2004**, *15*, DOI 10.1163/156856204323046852.
- [679] K. B. C. Imani, D. Kim, D. Kim, J. Yoon, *Langmuir* **2018**, *34*, DOI 10.1021/acs.langmuir.8b02687.
- [680] G. Graziano, *Int J Biol Macromol* **2000**, *27*, DOI 10.1016/S0141-8130(99)00122-1.
- [681] A. Gandhi, A. Paul, S. O. Sen, K. K. Sen, *Asian J Pharm Sci* **2015**, *10*, DOI 10.1016/j.ajps.2014.08.010.
- [682] I. Chakraborty, K. Mukherjee, P. De, R. Bhattacharyya, *Journal of Physical Chemistry B* **2018**, *122*, DOI 10.1021/acs.jpcc.8b02179.
- [683] D. Kim, A. Jo, K. B. C. Imani, D. Kim, J. W. Chung, J. Yoon, *Langmuir* **2018**, *34*, DOI 10.1021/acs.langmuir.8b00453.
- [684] S. K. Singh, B. K. Bhunia, N. Bhardwaj, S. Gilotra, B. B. Mandal, *Mol Pharm* **2016**, DOI 10.1021/acs.molpharmaceut.6b00672.
- [685] P. G. Chao, S. Yodmuang, X. Wang, L. Sun, D. L. Kaplan, G. Vunjak-Novakovic, *J Biomed Mater Res B Appl Biomater* **2010**, *95*, 84.
- [686] J. Melke, S. Midha, S. Ghosh, K. Ito, S. Hofmann, *Acta Biomater* **2016**, *31*, 1.
- [687] M. Xie, L. Lian, X. Mu, Z. Luo, C. E. Garciamendez-Mijares, Z. Zhang, A. López, J. Manríquez, X. Kuang, J. Wu, J. K. Sahoo, F. Z. González, G. Li, G. Tang, S. Maharjan, J. Guo, D. L. Kaplan, Y. S. Zhang, *Nat Commun* **2023**, *14*, DOI 10.1038/s41467-023-35807-7.
- [688] M. B. Applegate, J. Coburn, B. P. Partlow, J. E. Moreau, J. P. Mondia, B. Marelli, D. L. Kaplan, F. G. Omenetto, D. A. Weitz, *Proc Natl Acad Sci U S A* **2015**, *112*, DOI 10.1073/pnas.1509405112.
- [689] C. K. Arakawa, B. A. Badeau, Y. Zheng, C. A. DeForest, *Advanced Materials* **2017**, *29*, DOI 10.1002/adma.201703156.

## List of Abbreviations

2D: Two-Dimensional  
3D: Three-Dimensional  
4D: Four-Dimensional  
ABCG2: ATP-Binding Cassette Super-Family G Member 2  
ABTS: Azino-di-(3-ethylbenzthiazoline sulfonic acid)  
ACPCs: Articular Chondroprogenitor Cells  
AMD: Age-Related Macular Degeneration  
APAP: Acetaminophen  
ASAT: Aspartate Transaminase  
ASS: Argininosuccinate Synthase  
BVZ: Bevacizumab  
CA: Carbic Anhydride  
CAD: Computer Aided Design  
CEW: Cell Electrowriting  
CK-19: Cytokeratin 19  
CK18: Cytokeratin 18  
CLIP: Continuous Liquid Interface Printing  
CT: Computed Tomography  
DILI: Drug Induced Liver Injury  
DMA: Dynamic Mechanical Analyzer  
DM: Differentiation Media  
DMEM: Dulbecco Modified Eagle Medium  
DoF: Degree of Functionalization  
DoM: Degree of Methacrylation  
DMSO: Dimethylsulphoxide  
DTT: Dithiothreitol  
EBB: Extrusion-Based Bioprinting  
ECFCs: Endothelial Colony Forming Cells  
ECM: Extracellular Matrix  
EDC: 1-Ethyl-3-(3-dimethylaminopropyl)carbodiimide  
EE: Encapsulation Efficiency  
EGM-2: Endothelial Growth Medium-2  
ELISA: Enzyme-linked Immunosorbent Assay  
EmVP: Embedded Extrusion Volumetric Printing  
EU: European Union  
FBS: Fetal Bovine Serum  
FESEM: Field Emission Scanning Electron Microscopy  
FDA: Food and Drug Administration

FCS: Fetal Calf Serum  
G6PC: Glucose-6-Phosphatase Catalytic Subunit  
GAGs: Glycosaminoglycans  
GelMA: Gelatin Methacryloyl  
GelNOR: Gelatin Norbornene  
GFP: Green Fluorescent Protein  
GGT: Gamma-Glutamyl Transferase  
GLDH: Glutamate Dehydrogenase  
GO: Gene Ontology  
H&E: Hematoxylin and Eosin  
HEPES: (4-(2-hydroxyethyl)-1-piperazineethanesulfonic acid  
HLB: Hydrophilic/Lipophilic Balance  
HRP: Horseradish Peroxidase  
HNF4 $\alpha$ : Hepatic Nuclear Factor 4 Alpha  
HUVECs: Human Umbilical Vein Endothelial Cells  
iPSC: Induced Pluripotent Stem Cell  
iPSC-CM: Induced Pluripotent Stem Cell-Derived Cardiomyocytes  
IR: Infrared  
ISBF: International Society for Biofabrication  
LAP: Lithium Phenyl-2,4,6-trimethylbenzoyl-phosphinate  
LiBr: Lithium Bromide  
LAX: Cardiac Long-Axis  
LCST: Lower Critical Solution Temperature  
LIFT: Laser-Induced Forward Transfer  
MA: Methacrylic Anhydride  
MDR1: Multi Drug Resistance Protein 1  
MEW: Melt Electrowriting  
MG: Matrigel  
MI: Myocardial Ischemia  
MMP: Matrix Metalloproteinase  
MRI: Magnetic Resonance Imaging  
MSCs: Mesenchymal Stromal Cells  
Multi-OoC: Multi-Organ-On-A-Chip  
NaOH: Sodium Hydroxide  
NAMs: New Approached Methodologies  
NAPQI: N-acetyl-p-benzoquinone Imine  
NHS: N-hydroxysuccinimide  
NMR: Nuclear Magnetic Resonance  
OA: Osteoarthritis

P/S and Pen/Strep: Penicilin/Streptomycin  
PAS: Periodic Acid-Schiff  
PDMS: Polydimethylsiloxane  
PEG: Polyethylene Glycol  
PEO: Polyethylene Oxide  
PHH: Primary Human Hepatocytes  
PLA: Polylactic Acid  
PLGA: Poly(lactic-co-glycolic acid)  
PVA: Polyvinyl Alcohol  
PVA-MA: Polyvinyl Alcohol Methacrylate  
PV: Pressure-Volume  
RI: Refractive Index  
RNA: Ribonucleic acid  
Ru: Tris(2,2-bipyridyl)dichlororuthenium(II) Hexahydrate  
SAX: Cardiac Short-Axis  
SEM: Scanning Electron Microscopy  
SLA: Stereolithography  
SPS: Sodium Persulfate  
SAX: Cardiac Short-Axis  
TPI: Transitie Proefdiervrije Innovatie  
TRITC: Tetramethylrhodamine  
TNBSA: 2,4,6-trinitrobenzenesulfonic Acid  
UV: Ultraviolet  
UTS: Ultimate Tensile Stress  
VAM: Volumetric Additive Manufacturing  
VBP: Volumetric Bioprinting  
VEGF: Vascular Endothelial Growth Factor  
VP: Volumetric Printing  
 $\mu$ CT: Micro-computed tomography

## Summary

As the global average life expectancy increases, so does the incidence of chronic diseases, which carry a heavy economic toll on society and compromises patients' quality of life. This increased disease incidence, and the inherent biological variation of human has put the drug discovery and development pipeline to the test, calling for the adaptation of its rules and regulations to reduce the ever-increasing failure rates of new drugs. The staggering growth of the pharmaceutical industry in the last decades, and the high expenditure required to bring a new drug to the market is set to become an unsustainable issue in the coming years. The costs of the drug discovery process are further exacerbated due to the fact that an estimated 89% candidate drugs fail only after entering the highly costly clinical testing phase. Therefore, in recent years, far more attention has been focused on improving the predictive capacity of the preclinical testing phase within the pipeline, where most drug discovery testing culminates in animal testing, the current gold standard to ensure drug safety and efficacy before human trials. A general consensus on the need for more complex and predictive human disease models has emerged and become a priority for both scientists and policy makers in the past decade. Supporting this paradigm shift in preclinical testing practices, various initiatives at national and European Union (EU)-wide levels have sought to develop programs to push forward the transition towards animal-free research. From the development of governmental initiatives like the Transitie Proefdiervrije Innovatie (TPI; transition animal-free innovation), to the creation of non-profit foundations such as Proefdiervrij in The Netherlands, the European Medicine Agency has also implemented steps to facilitate the adoption of New Approached Methodologies (NAMs) aimed to replace animal experimentation in pharmaceutical research. This, together with the congressional approval of the U.S. Food and Drug Administration (FDA) Modernization Act 2.0 on January 2023, which allows for alternative complex in vitro model use in the advanced preclinical phases, have recently opened the gateway to reduce the need for animal experimentation.

Biofabrication is a novel, technology-driven field that has come to the forefront of tissue engineering and regenerative medicine strategies for the development of advanced in vitro models, as it facilitates the precise patterning of cellularized materials into complex architectures. Biofabrication, a multidisciplinary field that bridges biology, materials science and engineering is "the automated generation of biologically functional products with structural organization from living cells, bioactive molecules, biomaterials, cell aggregates such as micro-tissues, or hybrid cell-material constructs, through Bioprinting or Bioassembly and subsequent tissue maturation processes". The last decades have seen the rapid development of various bioprinting modalities, each possessing different key features such as printing resolution, design freedom and material requirements, opening the door to the development of architecturally complex in vitro platforms where multi-

cellular and multi-material structures can easily be created.

Considering the need for more complex preclinical models to bridge the existing translational gap between commonly used 2D *in vitro* models, animal testing and clinical trials, the overarching aim of this thesis was “to develop new biofabrication approaches, encompassing 3D bioprinting technologies, powerful biological building blocks, and smart biomaterials, that facilitate the development of advanced human *in vitro* models with native tissue-like functionality.” Addressing three key challenges pertaining to this aim, from a fabrication, biological complexity and material-based perspectives, this thesis was divided into three parts. **Part I** focused on the development of advanced bioprinting techniques that address different limitations of existing bioprinting processes. In **Chapter 2**, the resolution limit of most conventional bioprinting approaches was tackled through the development of cell electrowriting (CEW), a new bioprinting approach that uses a voltage-driven printing head to fabricate high resolution, cell-laden hydrogel fibers with diameters comparable or even smaller than single cells (down to 5  $\mu\text{m}$ ). **Chapter 3**, addressed the restricted design freedom exhibited by most layer-by-layer manufacturing approaches, as well as the long printing times required to create clinically-relevant sized constructs. The development of volumetric bioprinting (VBP) as a cell-friendly, layerless approach introduced a significant enhancement in design freedom of hydrogel-based constructs and enables the ultra-fast fabrication of centimeter-scale complex living structures. The hydrogel structures developed with this technique however, as observed with a variety of tissue engineering approaches, exhibit rather limited mechanical properties which may hinder the functionality and stability of these prints. To address this, **Chapter 4** demonstrated the possibility to converge Volumetric Printing and Melt ElectroWriting in a new approach termed VolMEW. The introduction of cylindrical melt electrowritten scaffolds (precisely organized thermoplastic microfibers) into the VBP process resulted in the enhancement of mechanical properties of the complex printed hydrogel structures.

Shifting attention to the biological complexity introduced within biofabricated structures and their application for organ-specific *in vitro* model development, **Part II** highlights two target organs for which platforms of various complexity levels were developed: the liver and the heart. **Chapter 5** demonstrated the extrusion bioprinting of human liver-derived organoids in a gelatin based bioink into simple 3D structures that could be perfused with various toxic compounds, exhibiting toxicity-dependent organoid death. However, these large and fragile organoids were fragmented and exhibited significant cell death post-printing due to the shear stresses characteristic of extrusion printing techniques. To address this key limitation, while still harnessing the potential of organoid technology, **Chapter 6** showed, for the first time, the VBP of high-density organoid-laden structures which retain their morphology and function post-printing. Accurate printing of liver organoids into complex, structurally defined models and their incorporation into perfusable bioreactors

showed the potential to modulate metabolic function based on the printed architecture, highlighting the importance of 3D shape in cellular function. In **Chapter 7**, a bi-chambered, multi-material heart model with native wall thickness gradients was volumetrically printed with induced pluripotent stem cell-derived cardiomyocytes, another powerful tool in cardiac tissue engineering. The design freedom of VBP enabled the fabrication of numerous variations of the heart model to mimic different structural cardiomyopathies. Furthermore, an induced cryoinjury to mimic myocardial infarction showed promising biological signs of scar tissue formation and extracellular matrix remodeling, opening the door to the creation of clinically relevant cardiac *in vitro* models.

With promising observations regarding the use of VBP and other biofabrication approaches for *in vitro* model development, **Part III** focused on further driving tissue mimicry of bioprinted structures through the development of new classes of smart biomaterials or “bioresins” that allow for the control of cell fate and/or structural properties of the material and cell culture environment. **Chapter 8** showed a controlled drug delivery tool through the fabrication of printable microcapsules capable of guiding endothelial cell behavior. The addition of 3D printing allowed for the precise patterning of these particles into complex architectures relevant for tissue engineering. **Chapter 9** introduced a chemically editable gelatin norbornene (gelNOR) bioresin for VBP that not only exhibited highly tunable mechanical properties, but also enabled the covalent attachment of thiolated proteins or growth factors with high spatiotemporal control. With this material, precise localized control over cell behavior was achieved and presented a first step towards mimicking complex developmental chemical cues. In **Annex I** the library of VBP resins was further expanded through the development of thermoresponsive materials that exhibit temperature-dependent shrinking properties. These printable resins achieved the highest resolutions with VBP shown to date and exhibit great promise in the development of multi-scale bioprinted structures.

Overall, these compiled works demonstrate how, through the combination of various aspects in the biofabrication field (advanced printing approaches, human-based biological tools and smart materials), physiologically relevant *in vitro* platforms can be developed and take the next step towards filling the translational gap currently hindering drug development and disease modeling.

## Samenvatting

Naarmate de wereldwijde gemiddelde levensverwachting toeneemt, neemt ook de incidentie van chronische ziekten toe, die een zware economische tol eisen op de samenleving en de kwaliteit van leven van patiënten aantasten. Deze toegenomen ziekte-incidentie, samen met de inherente biologische variatie van de mens, heeft de ontdekking en ontwikkeling van geneesmiddelen op de proef gesteld, waardoor de aanpassing van regels en voorschriften nodig is om de steeds toenemende faalpercentages van nieuwe medicijnen te verminderen. De verbazingwekkende groei van de farmaceutische industrie in de afgelopen decennia en de hoge uitgaven die nodig zijn om een nieuw medicijn op de markt te brengen, dreigen een onhoudbaar probleem te worden in de komende jaren. De kosten van het geneesmiddelenontdeckingsproces worden verder verergerd doordat naar schatting 89% van de kandidaat-geneesmiddelen pas faalt nadat ze de zeer kostbare klinische testfase zijn ingegaan. Daarom is er in recente jaren veel meer aandacht besteed aan het verbeteren van de voorspellende capaciteit van de preklinische testfase binnen de pijplijn, waar de meeste geneesmiddelentests uitmonden in dierproeven, de huidige gouden standaard om de veiligheid en werkzaamheid van geneesmiddelen te waarborgen voordat ze op mensen worden getest. Een algemene consensus over de noodzaak van meer complexe en voorspellende menselijke ziektemodellen is ontstaan en is een prioriteit geworden voor zowel wetenschappers als beleidsmakers in het afgelopen decennium.

Ter ondersteuning van deze paradigmaverschuiving in preklinische testpraktijken hebben verschillende initiatieven op nationaal en Europees niveau programma's ontwikkeld om de overgang naar dierproefvrij onderzoek te bevorderen. Van de ontwikkeling van overheidsinitiatieven zoals Transitie Proefdiervrije Innovatie (TPI) tot de oprichting van non-profitstichtingen zoals Proefdiervrij in Nederland, heeft ook het Europees Geneesmiddelenbureau stappen ondernomen om de overname van nieuwe benaderde methodologieën (NAM's) gericht op het vervangen van dierproeven in farmaceutisch onderzoek te vergemakkelijken. Dit, samen met de goedkeuring van de U.S. Food and Drug Administration (FDA) Modernization Act 2.0 in januari 2023, die het gebruik van alternatieve complexe in vitro modellen in de geavanceerde preklinische fasen toestaat, heeft recentelijk de weg geopend om de behoefte aan dierproeven te verminderen.

Biofabricatie is een nieuw, op technologie gebaseerd vakgebied dat naar voren is gekomen in weefseltechnologie en regeneratieve geneeskunde strategieën voor de ontwikkeling van geavanceerde in vitro modellen, omdat het de precieze vormgeving van gecellulariseerde materialen in complexe architectuur vergemakkelijkt. Biofabricatie, een multidisciplinair vakgebied dat biologie, materiaalkunde en techniek met elkaar verbindt, is "de geautomatiseerde ontwikkeling van biologisch functionele producten met structurele organisatie uit levende cellen, bioactieve moleculen, biomaterialen,



celaggregaten zoals microweefsels, of hybride cel-materiaalconstructies, via bioprinten of bioassemblage en daaropvolgende weefsel maturatieprocessen". De afgelopen decennia was er snelle ontwikkeling van verschillende bioprintmodaliteiten, elk met verschillende belangrijke kenmerken zoals printkwaliteit, ontwerprijheid en materiaalvereisten, waardoor de ontwikkeling van architectonisch complexe *in vitro* platformen mogelijk is waar multicellulaire en multimateriële structuren gemakkelijk kunnen worden gecreëerd.

Rekening houdend met de behoefte aan complexere preklinische modellen om de bestaande translationele kloof tussen veelgebruikte 2D *in vitro* modellen, dierproeven en klinische proeven te overbruggen, was het overkoepelende doel van deze scriptie "om nieuwe biofabricatiebenaderingen te ontwikkelen, waaronder 3D-bioprinttechnologieën, krachtige biologische bouwstenen en slimme biomaterialen, die de ontwikkeling van geavanceerde menselijke *in vitro* modellen met functionaliteit vergelijkbaar met native weefsel faciliteren." Om deze doelstelling aan te pakken, vanuit een fabricage-, biologische complexiteit- en materiaalgericht perspectief, was deze scriptie verdeeld in drie delen.

**Deel I** richtte zich op de ontwikkeling van geavanceerde bioprinttechnieken die verschillende beperkingen van bestaande bioprintprocessen aanpakken. In **Hoofdstuk 2** werd de resolutiegrens van de meeste conventionele bioprintbenaderingen aangepakt door de ontwikkeling van cel-electrowriting (CEW), een nieuwe bioprintbenadering die een spanningsgestuurde printkop gebruikt om hoogwaardige, cel geladen hydrogelfibers te fabriceren met diameters vergelijkbaar met, of zelfs kleiner dan cellen (tot 5 µm). **Hoofdstuk 3** richtte zich op de beperkte ontwerprijheid van de meeste laagsgewijze productiebenaderingen, evenals de lange printtijden die nodig zijn om constructies van klinisch relevant formaat te maken. De ontwikkeling van volumetrisch bioprinten (VBP) als een celvriendelijke, laagrijke benadering introduceerde een aanzienlijke verbetering in het ontwerprijheid van op hydrogel gebaseerde constructies en maakte de ultrasnelle fabricage van complexe structuren op centimeterschaal mogelijk. De hydrogelstructuren ontwikkeld met deze techniek vertoonden echter, zoals waargenomen bij verschillende hydrogel gebaseerde weefsel engineering, nogal beperkte mechanische eigenschappen die de functionaliteit en stabiliteit van deze prints kunnen belemmeren. Om dit aan te pakken, toonde **Hoofdstuk 4** de mogelijkheid om Volumetric Printing en Melt Electrowriting (MEW) samen te voegen in een nieuwe benadering die VolMEW wordt genoemd. De introductie van cilindrische steigers gemaakt met MEW (nauwkeurig geplaatste microvezels) in het VBP-proces resulteerde in de verbetering van de mechanische eigenschappen van de complexe geprinte hydrogelstructuren.

Met de aandacht verschoven naar de biologische complexiteit geïntroduceerd binnen bio-gefabriceerde structuren en hun toepassing voor de ontwikkeling van orgaanspecifieke *in vitro* modellen, benadrukt **Deel II** twee doelorganen waarvoor platformen van verschillende complexiteitsniveaus werden ontwikkeld: de lever en

het hart. **Hoofdstuk 5** toonde de extrusie-bioprinting van door de mens afgeleide leverorganoiden in een op gelatine gebaseerde bioinkt in eenvoudige 3D-structuren die konden worden geperfuseerd met verschillende toxische stoffen en die organoïde dood vertoonden afhankelijk van de toxiciteit. Deze grote en kwetsbare organoiden waren echter gefragmenteerd en vertoonden aanzienlijke celdood na het printen als gevolg van de schuifspanningen die kenmerkend zijn voor extrusie-gebaseerde printtechnieken. Om deze belangrijke beperking aan te pakken, maar nog steeds gebruikmakend van de potentie van organoïdtechnologie, toonde **Hoofdstuk 6** voor het eerst de VBP van organoïde-beladen structuren met hoge dichtheid die hun morfologie en functie behielden na het printen. Het nauwkeurig printen van leverorganoïden in complexe, structureel gedefinieerde modellen en hun opname in perfuseerbare bioreactoren toonde het potentieel om de metabole functie te moduleren op basis van de geprinte architectuur, waarbij het belang van de 3D-vorm in cellulair functioneren werd benadrukt. In **Hoofdstuk 7** werd een twee-kamer, multi-materiaal hartmodel met inheemse wanddiktegradiënten volumetrisch geprint met cardiomyocyten afgeleid van geïnduceerde pluripotente stamcellen, een ander krachtig instrument in hartweefsel regeneratie. De ontwerprijheid van VBP maakte de fabricage van talloze variaties van het hartmodel mogelijk om verschillende structurele cardiomyopathieën na te bootsen. Bovendien liet een geïnduceerde cryoletsel om myocardinfarct na te bootsen veelbelovende biologische tekenen van littekenweefselvorming en extracellulaire matrix remodellering zien, wat de weg opent naar de creatie van klinisch relevante cardiale *in vitro* modellen.

Met veelbelovende waarnemingen over het gebruik van VBP en andere biofabricatiebenaderingen voor de ontwikkeling van *in vitro* modellen, richtte **Deel III** zich op het verder bevorderen van weefsel nabootsing van biogeproduceerde structuren door de ontwikkeling van nieuwe klassen slimme biomaterialen of "bioharsen" die de controle over de celbestemming en/of structurele eigenschappen van het materiaal en de cel kweekomgeving mogelijk maken. **Hoofdstuk 8** toonde een werktuig voor gecontroleerd geneesmiddelf afgifte door de fabricage van printbare microcapsules die het gedrag van endotheliale cellen kunnen sturen. De toevoeging van 3D-printen maakte de precieze vormgeving van deze deeltjes in complexe architectuur mogelijk die relevant is voor weefseltechnologie. **Hoofdstuk 9** introduceerde een chemisch bewerkbare gelatine norbornene (gelNOR) biohars voor VBP die niet alleen zeer instelbare mechanische eigenschappen vertoonde, maar ook de covalente bevestiging van thiolhoudende eiwitten of groeifactoren met hoge controle mogelijk maakte in zowel tijd als ruimte. Met dit materiaal werd precieze gelokaliseerde controle over cellgedrag bereikt en werd een eerste stap gezet naar het nabootsen van complexe ontwikkelingschemische signalen. In **Bijlage I** werd de bibliotheek van VBP-harsen verder uitgebreid door de ontwikkeling van thermoresponsieve materialen die temperatuurafhankelijke krimpeigenschappen

vertonen. Deze printbare harsen bereikten de hoogste resoluties met VBP tot nu toe getoond en tonen grote belofte in de ontwikkeling van multiscale gebioprintestructuren.

Over het algemeen tonen deze samengevoegde werken aan hoe, door de combinatie van verschillende aspecten in het biofabricatieveld (geavanceerde printbenaderingen, op menselijke biologie gebaseerde gereedschappen en slimme materialen), fysiologisch relevante *in vitro* platforms kunnen worden ontwikkeld en de volgende stap kunnen zetten naar het overbruggen van de huidige translationele kloof die de ontwikkeling van geneesmiddelen en ziektemodellering belemmert.

## Resumen

A medida que la esperanza de vida experimenta un incremento a nivel global, se observa simultáneamente un aumento en la incidencia de enfermedades crónicas. Dichas patologías conllevan un considerable impacto económico en la sociedad, comprometiendo la calidad de vida de los pacientes. La elevada prevalencia en enfermedades crónicas, combinada con la variación biológica intrínseca en los seres humanos, ha puesto a prueba el proceso de descubrimiento y desarrollo de medicamentos, requiriendo la adaptación de la normativa y regulación para mitigar las crecientes tasas de fracaso en el descubrimiento de nuevos fármacos. El notable crecimiento que ha experimentado la industria farmacéutica en las últimas décadas y los considerables gastos que requiere llevar un nuevo medicamento al mercado están destinados a convertirse en un problema insostenible en los años venideros. Los costos asociados a este proceso se ven exacerbados debido al hecho de que el 89% de los potenciales medicamentos fallan después de entrar en la costosa fase de ensayos clínicos. En consecuencia, se ha dirigido especial atención durante los últimos años a mejorar la capacidad predictiva en la fase preclínica de la cadena de desarrollo farmacéutico. En esta etapa se realiza la mayor parte de experimentación enfocada al descubrimiento de nuevos fármacos, culminando en ensayos con animales, siendo éste el modelo de investigación estándar vigente para garantizar la seguridad y eficacia de los medicamentos antes de su utilización en ensayos humanos. Surge pues un consenso general sobre la urgente necesidad de nuevos modelos para la investigación de enfermedades humanas más complejas y predictivos, convirtiéndose en una prioridad tanto en el ámbito científico como político en la última década. Apoyando esta evolución de paradigma en las prácticas de ensayos preclínicos, diversas iniciativas nacionales (como en los Países Bajos) y de la Unión Europea han buscado desarrollar programas que impulsen la investigación libre de la utilización de animales. Desde el establecimiento de iniciativas gubernamentales como la Transitie Proefdiervrije Innovatie (TPI; Investigación Libre de Animales) hasta la creación de fundaciones sin fines de lucro como Proefdiervrij en los Países Bajos, la Agencia Europea de Medicamentos también ha implementado medidas para facilitar la adopción de New Approached Methodologies (NAM; Metodologías con Nuevo Enfoque) destinadas a reemplazar la experimentación en animales por una libre de ellos. Adicionalmente, en enero de 2023, se aprobó el Acta de Modernización 2.0 de la Administración de Alimentos y Medicamentos de EE. UU., la cual autoriza el uso de modelos *in vitro* más sofisticados como alternativa en fases preclínicas avanzadas. De esta forma queda abierta la puerta a disminuir la dependencia de la experimentación con animales en el ámbito farmacéutico.

La biofabricación es una disciplina emergente e innovadora, impulsada por tecnología de vanguardia en ingeniería de tejidos y medicina regenerativa. Es utilizada en el desarrollo de avanzados y más complejos modelos *in vitro*, ya que permite producir con precisión

materiales ya celularizados, siguiendo arquitecturas de gran complejidad. Se considera un campo multidisciplinario que integra biología con ciencias de materiales e ingeniería, es “la generación automatizada de productos biológicamente funcionales con organización estructural a partir de células vivas, moléculas bioactivas, biomateriales, agregados celulares como microtejidos o construcciones híbridas de células y materiales, mediante la Bioimpresión o Bioensamblaje y subsiguientes procesos de maduración tisular”. En las últimas décadas, las distintas modalidades de bioimpresión han experimentado un rápido desarrollo, cada una centrada en características clave distintas, como son la resolución de impresión, la libertad de diseño y requisitos de materiales. Estos avances favorecen así el desarrollo de plataformas *in vitro* arquitectónicamente complejas, posibilitando la creación de estructuras multicelulares y multimateriales de manera más accesible y eficiente.

Debido a la necesidad de desarrollar nuevas plataformas preclínicas de mayor complejidad para reducir el sesgo traslacional existente entre los modelos comúnmente empleados *in vitro* bidimensionales, los ensayos en animales y los ensayos clínicos, el objetivo principal de esta tesis fue “desarrollar nuevos procesos de biofabricación que abarquen desarrollos tecnológicos de bioimpresión 3D, la incorporación de bloques biológicos avanzados y de biomateriales inteligentes, que faciliten el desarrollo de modelos avanzados *in vitro* con funcionalidad fisiológica”. Abordando tres desafíos clave acerca de este objetivo, desde una perspectiva de fabricación, complejidad biológica y basada en materiales, esta tesis se dividió en tres partes. La **Parte I** se centró en el desarrollo de técnicas avanzadas de bioimpresión y las limitaciones intrínsecas de los procesos asociados. En el **Capítulo 2** se abordaron las limitaciones en resolución en la mayoría de las técnicas convencionales de bioimpresión a través del desarrollo de electroescritura de células (CEW, del inglés Cell ElectroWriting), un nuevo método que utiliza una cabeza de impresión impulsada por voltaje para imprimir con alta resolución fibras de hidrogel con células de diámetros similares o incluso inferiores a los de una célula (hasta 5  $\mu\text{m}$ ). El **Capítulo 3** se enfocó en las restricciones de libertad de diseño exhibidas por la mayoría de las técnicas de fabricación capa por capa, así como los extensos tiempos de impresión requeridos para crear estructuras de tamaño clínicamente relevante. Se introduce la técnica de bioimpresión volumétrica (VBP) como un enfoque libre de capas y propicio para la impresión de células, lo cual supuso una mejora significativa en la libertad de diseño de modelos impresos en hidrogel y permite la fabricación ultrarrápida de estructuras complejas celularizadas a escala centimétrica. Sin embargo, dichas estructuras, como se observa en varios métodos de ingeniería de tejidos, exhiben propiedades mecánicas bastante limitadas que pueden obstaculizar su funcionalidad y estabilidad. Con el fin de solucionar dicho problema, el **Capítulo 4** demostró la posibilidad de fusionar la impresión volumétrica y la electroescritura de fusión en un nuevo enfoque denominado VolMEW (del inglés, Volumetric Printing and Melt ElectroWriting). La introducción de andamios cilíndricos

producidos mediante la técnica de electroescritura de fusión (microfibras termoplásticas depositadas y organizadas con gran precisión) en el proceso de VBP resultó en la mejora de las propiedades mecánicas de las impresiones en hidrogel.

Centrando la atención en la complejidad biológica presente en los productos biofabricados y su potencial aplicación en el desarrollo de modelos *in vitro* para órganos específicos, la **Parte II** de esta tesis presenta dos órganos objetivo para los cuales se diseñaron plataformas de diversos niveles de complejidad: el hígado y el corazón. El **Capítulo 5** evidenció que es posible la bioimpresión por extrusión de organoides derivados de hígado humano, embebidos en un biotinta basada en gelatina, para la fabricación de estructuras tridimensionales simples que podrían perfundirse con diversos compuestos tóxicos, mostrando que la mortalidad de los organoides era dependiente de toxicidad. Sin embargo, estos organoides grandes y frágiles se fragmentaron y mostraron una significativa mortalidad celular postimpresión debido a las tensiones mecánicas características de las técnicas de impresión por extrusión. Para abordar esta limitación sustancial mientras aún se exploraba el potencial del uso de organoides, el **Capítulo 6** mostró por vez primera la VBP de estructuras densas en organoides capaces de mantener su morfología y función tras la impresión. La impresión de forma precisa de organoides hepáticos en modelos complejos y estructuralmente definidos, así como su incorporación en biorreactores perfusibles, ha mostrado el potencial para modular la función metabólica en función de la arquitectura impresa. Esto destaca la importancia de la forma tridimensional en la función celular. En el **Capítulo 7**, se imprimió volumétricamente un modelo de corazón multicámara y multimaterial incorporando gradientes fisiológicos de grosor de la pared cardiaca con cardiomiocitos derivados de células madre pluripotentes inducidas, una herramienta de gran utilidad en la ingeniería de tejidos cardíacos. La libertad de diseño proporcionada por la VBP permitió la creación de numerosas variaciones del modelo de corazón para imitar diferentes cardiomiopatías estructurales. Por ejemplo, se simuló un infarto de miocardio practicando una lesión por crioinducción en uno de los modelos y mostró signos biológicos prometedores de formación de tejido cicatricial y remodelación de la matriz extracelular. Este hallazgo allana el camino a la creación de modelos cardíacos *in vitro* clínicamente relevantes.

Con descubrimientos prometedores sobre el uso de la VBP y otros métodos de biofabricación para el desarrollo de modelos *in vitro*, la **Parte III** se centró en ahondar en la imitación de tejidos de estructuras bioimpresas mediante el desarrollo de nuevos biomateriales inteligentes o bioresinas. Estas permiten el control del funcionamiento celular y/o propiedades estructurales del material y del propio entorno de cultivo celular. En el **Capítulo 8** se presentó una herramienta de administración de medicamentos controlada mediante la fabricación de microcápsulas imprimibles capaces de guiar el comportamiento de células endoteliales. El uso de la impresión 3D permitió la incorporación de dichas partículas en arquitecturas de gran complejidad relevantes en

el ámbito de la ingeniería de tejidos. El **Capítulo 9** introdujo una nueva bioresina de gelatina norborneno (gelNOR), editable químicamente en la VBP la cual no solo mostró propiedades mecánicas altamente ajustables, sino que también permitió la unión covalente de proteínas tioalquiladas o factores de crecimiento con un elevado control espaciotemporal. Con este material se logró un control localizado y preciso sobre el comportamiento celular, marcando un primer paso hacia la imitación de señales químicas de desarrollo. En el **Anexo I**, se muestra la ampliación de la biblioteca de resinas de VBP mediante la utilización y desarrollo de materiales termosensibles que exhiben propiedades de contracción dependientes de la temperatura. Estas resinas imprimibles fueron capaces de alcanzar las mayores resoluciones con VBP registradas hasta la fecha y significan un gran hallazgo para el desarrollo de estructuras bioimpresas a múltiples escalas.

En términos generales, estos estudios demuestran cómo mediante la combinación de diversos elementos en el ámbito de la biofabricación (mediante enfoques de impresión avanzados, herramientas biológicas centradas en seres humanos y materiales inteligentes) posibilita el desarrollo de plataformas in vitro de gran relevancia fisiológica. Este enfoque representa un paso significativo hacia la reducción de la brecha traslacional que actualmente limita el avance en el desarrollo de medicamentos y la modelización de enfermedades.

## Acknowledgements

As cheesy as it sounds, it wasn't just about the journey that brought me to the completion of this book, because I owe so much of this to the incredible company I had through it all! The people I have met along the way have taught me an immeasurable amount of things about science and life, and I hope that, to some extent, I have managed to do the same. These pages aren't nearly enough to express my love and appreciation for all of you that have come along in this journey, but I have done my best. Obviously, I left this to the last minute before sending the book to print, so if I forgot something or someone, my deepest apologies! I love you all!

### *Promotor and co-promotor*

Dear Prof. dr. ir. Malda,

Dear **Jos**, Meneer, Uber Professor,

If anyone asked me 5 years ago where and what I'd be doing now, I would never have imagined this! Under your guidance, I have learned how to be an independent researcher, I have found a love for teaching I didn't know I had, and I have had the freedom to embark on amazing scientific projects that I would have never thought were possible. Thank you so much for giving me the chance to stay in this amazing team after my master's was finished, to carry out my PhD under your supervision, to dedicate some of that time to education and improving the learning experience of our master students, and overall, thank you for putting up with all the loud madness, shotjes, and questionable Dutch speaking that comes with working with me. If there is one thing I want to highlight in this small paragraph is thanking you for your continuous support. Never throughout this amazing, oftentimes difficult journey have I felt like I didn't have you in my corner, and for that, I am forever grateful. I am excited to continue working together and see where we take these amazing research and educational endeavors next, working as always, as a team!

Dear Dr. ir. Levato,

Dear **Riccardo**,

It seems like ages ago when you came into the MEW lab to ask me if I'd like to go to Switzerland with you for a few days to test some of our light-sensitive gels on a cool new technique you had come across in a pre-print! It still amazes me how far we have come as a group and how, thanks to your supervision, I have developed as a researcher these last years. The way you think about science is not just inspiring to watch, it has also pushed me to grow and develop qualities without which, this PhD thesis would not have been possible. I am so grateful for your supervision. You have gone above and beyond since my



very first days as a PhD student, always providing support in matters of the lab and outside of it as well, pushing me to be better every day. The trust and support you have given me as the research group has grown is something I treasure, and is one of the key reasons why I love my job. Thanks for creating an atmosphere not just for scientific innovation, but also for some healthy doses of fun, sometimes slightly violent retreat activities and most importantly, bringing together a diverse group of very different people that care and learn from each other every day. From the bottom of my heart, thank you for everything, and I can't wait for what is to come in these next steps.

#### *Review Committee*

I would like to thank Prof. dr. **Beekman**, Prof. dr. **Masereeuw**, Prof. dr. ir. **Moroni**, Prof. dr. **Ovsianikov** and Prof. dr. **Salvatori**, for taking the time to read and evaluate this thesis. I look forward to engaging in fruitful discussions with all of you, and gain new insights from your different areas of expertise.

#### *Paranymphs*

Dear **Mylène**, I'm not sure this acknowledgement section is enough to cover the many reasons why you are my science hero and one of my dearest friends. Since the day we first interacted, on a small adventure to the autoclave, to this very day (whenever you are reading this), you have always been one of the kindest, most selfless people I have ever met. When you add to the equation the fact that you are one of the most amazing scientists I have had the pleasure to learn from and work with, I can't think of a better person to have met at the right time of my studies. Doing my last master's internship with you taught me how to think like a researcher, made me feel way more confident in my scientific skills, and cemented the idea of doing a PhD in my mind. Your unwavering support in and outside the lab has made a massive impact on my life these last years, somehow you have a knack of making me feel like I can do anything! I know I can always count on you, and I couldn't be happier to have you by my side at my defense, and in the next amazing research endeavors! Thanks for being an amazing example in the way I do science and share knowledge, I can't wait to keep watching you do amazing things and work on cool new projects together!

Dear **Marc**, I never thought the poopy head that rejected my birthday brownies on his first day was going to become one of my closest friends and paranymph, or that I would have the honor of standing by your side as the witness at your wedding! We so quickly clicked on so many levels when you started bribing me with cookies; our ultra-focused efficiency at the lab, our obsessive love for dogs, our affinity for beer o'clocks, our endless conversations (mostly in baby voice) and slightly concerning shopaholic

tendencies (shoes? bags? truffle?), among others. In a short time, you have been by my side through the good and not so good times, and I cannot tell you how much I appreciate your friendship. I am so happy we managed to get in a couple of chapters in this thesis together, and cannot wait to see you complete your amazing PhD and become an even more wonderful scientist in the years to come.

### *Colleagues*

If I look back at my decision to pursue a PhD instead of leaving for industry (which I claimed I would do till almost the very last minute), one of the biggest reasons for that was the amazing team and atmosphere that I got to live in during my master's. A massive thank you to all past and current members of the lab that make the good days amazing, and the hard days just a little bit more enjoyable! You are all a big part of this thesis!

To all members of the **VoluTeam**, your multidisciplinary backgrounds really make the magic happen. It is a real gift to bring such different people together and make awesome science while having a good time, thank you! **Sammy**, we were the original VoluTeam for a while there, thanks for all the help with the mysterious world of physics and CAD design (you have made me CONSIDER not using TinkerCAD). To a lot more tea evenings! **Marc**, thanks for not blowing the lab up (yet), and for all the help with teaching the kiddos. **Davide**, your love for science is infectious and our chaotic brainstorm sessions inspire me to think big or go home, I will keep waiting for the big start-up so you can hire me in a couple years. **Marième**, I cannot imagine what our cell culture would be without you, thanks for all the brainstorming, and for letting me tag along your supervision successes! **Gabs**, my little baby that is older and waaay taller than me, I love working with you on all things. Your problem-solving skills are a force of nature, and I hope we keep the sweat shop open for business many more years. Thanks for all the fun and support these last years! **Núria**, I'm not quite sorry that New Zealand didn't work out, because I got to work with you and witness first hand what an amazing and hard working researcher you are! MINI-JOINT and LIFT expert, I have no doubt you will have an amazing PhD, thanks for all the amazing and crazy times and hilarious cat pictures. **Maj**, thanks for the fun times working with mathematically-derived boobs and super cool chips and organoids, and also, for the constant supply of chocolate when times get tough! **Pere**, or boring Pere as you would say, I cannot really agree with your assessment from what I have seen in the last year you've worked here, it has been lots of fun to get to know you! Thanks for the paella masterclass and all your help with pancreas knowledge. **Ale**, I am so very glad I got a second chance to get to know you at the RMCU and that this time around, we get to work on cool projects together. You are an amazing colleague and a wonderful friend, thank you for all your help these months! **Estée**, thanks your kindness and for the energy you bring to the lab, and for encouraging us to sit and enjoy the moment during lunchtime :P

To the **Biofabrication and Orthopaedics Teams**, past and current members, I greatly appreciate all your amazing scientific input, the very fun times at Meneer Malda's house, and the amazing atmosphere you all bring to the lab. **Brenda**, it's safe to say I would not even be in this country if it weren't for your efforts and patience dealing with my constant visa chaos! Thank you for always being there to help with all my questions and student assistant requests, for our never short conversations about everything, and for the lovely dinners! The lab wouldn't be the same without you! **Mattie**, I think there is no lab without you, the sheer panic that spreads when you are about to go on holidays is a clear enough sign :P Thanks for all your help in the lab, excellent food recommendations, amazing photography skills and for all the chats in between experiments. You are so amazing I'll even accept your dislike of dogs! **Anneloes**, thank you for all your help with cell culture experiments, and all the fun chats while sharing a flow cabinet. **Elianne**, thanks for keeping the lab in order with your cake points, help with cell culture and for all the fun times in and outside the lab. To the newer members of the cartilage engineering team, **Lennard, Aylin, Alba, Antonia, Marlena** it's been great getting to know you all these last few months. **ICAT team: Joost, Eva, Jonelle, Michal** and **Josse**, thanks for welcoming me into the team these last months and pushing me to take a harder look at research from a translational perspective, all the best with the ICAT's future endeavors and the big move to the new lab! **Margo**, thanks for sharing the dECM meniscus project with me. It was a cool concept that we got to explore with some amazing students. Our Dutch/Australian conference with **Gabriel** and **Marc** was one for the history books too! **Martina**, thank you for the fun collaboration on the shrinking paper, and all your insights in chemistry, mechanical testing and more! **Gerardo**, always a pleasure to have another Mexican in the lab for good laughs and a bigger supply of Mexican candy, thanks for all the fun times! **Jaqueline**, thanks for all the BKO accountability, I think our constant reminders to each other about the portfolio significantly accelerated the whole process! To the original (**Leanne, Madi, Flu, Marc**) and adapted (**Marc, Gabs, Ale, Myl**) office gang, thanks for all the random chats, insanity evenings, sporadic shopping in between experiments, and running supply of cookies and chocolate! Lab's finest (**Madi, Flor, Quentin**), it has been a while, but the PhD journey would have been very boring without you guys, and without our daily Genmab coffee routines to get us going through the after-lunch dip :) Special mention to the three most instrumental people during my pre-PhD journey: **Iris Otto**, you gave me my first shot at this whole research thing. I learned so much from you during my first master's internship, and your passion for science, teaching and communication have stuck with me throughout my PhD. I would certainly not be here today without your guidance and advice, a massive thank you for that! **Mylène**, funny how a casual conversation at Ortho drinks I wasn't invited to turned into a life changing internship and this awesome book a few years later! Thanks for believing in me and giving me the fun CEW challenge! Last but not least, the one that dragged me to these ortho drinks in the

first place, thank you **Flor** for your friendship and trust at work and outside, it was so nice to have another latin presence at the lab in the early days! You welcomed me into the lab and your family, let me steal my **Canela** for the weekend, taught me how to cook a real Argentinian steak and made life at the lab a ton of fun! To the rest of current and past team members, **Meng, Yang, Iris P, Susanna, Jasper, Margot, Jasmijn, Nasim, Inge vH, Paweena, Paula, Miguel** thanks for all the good memories and fun lab times!

### *Collaborators*

This thesis is the result of amazing collaborative efforts in and outside the UMC Utrecht. A big thank you to everyone involved in this research, for your efforts, kindness and eagerness to drive scientific innovation forward.

To the EPFL team, **Paul, Damien, Jorge, and Chris**, I think this thesis would be very different without you guys! Thank you for trusting me and giving me full reign to fill your office with cell culture supplies, for hosting me that one crazy month in 2019 and for sharing your amazing expertise, and being open to learn some cell stuff from my side! I have enjoyed every collaboration and visit from you guys, and look forward to even more future collaborations.

To the Clinical Sciences department of the Faculty of Veterinary Sciences, it was a pleasure and great learning experience to work together in two of the chapters of this thesis. **Manon**, thank you for all your work on the organoid side of our Liver VBP paper, and for the fun chats about hamsters and dogs! **Roos-Anne** and **Monique**, thanks for teaching me the basics of organoid culture and helping with all the different analyses for the paper! Thank you **Kerstin** for the brainstorming and liver expertise while working on the VBP paper. **Bart**, since my master's writing assignment I have been learning about the amazing world of liver regeneration from you, thank you for your trust and support in this awesome collaboration!

Thank you to the experimental cardiology team, **Nino, Aina, Inge D, Alain** and **Joost** for your support in the volumetric heart project. **Nino**, it was slightly nervewrecking trying not to kill the cardiomyocytes, but I think we made some big steps towards making some tiny beating volumetric hearts! Looking forward to completing this project in the future!

To the Pharmaceutical Sciences team, **Martina** and **Tina**, thank you for the nice collaborations, your knowledge in material chemistry has proven invaluable for several chapters of this thesis. Thank you **Mies** as well for saving my life when working with the DMA and rheometer for days on end in the early days of my PhD.

To the Pharmacology team, **Marta, Silvia** and **Roos**, thank you for the collaboration on the thermal shrinking gel chapter, and for the many discussions and brainstorms about experiments, *in vitro* models and more! Looking forward to more work together.

Thank you to **Leanne** and **Debby** for the constant collaborations and advice! Your expertise in bone and vascular tissue engineering are one of a kind! I really enjoyed working on the review together, and greatly appreciate all the help you both provide in many other projects!

To the Würzburg biofabrication team, **Tomasz, Michael, Csaba, Jürgen**, thank you for all the hard work and willingness to collaborate on the VolMEW paper, it was a wonderful opportunity to amplify the strength of this amazing technique! Thanks for all the brainstorming and input, for the education-related insights and the fun conference evenings!

A big thanks to all members of the MEFISTO consortium. Since the very start of my PhD, this consortium has been an ongoing learning experience, where I got to travel, learn how to function in a large international consortium, and got to meet and work with lots of amazing researchers. Particular thanks to the USC team for leading the fruitful collaboration presented in this thesis. Thanks **Anna, Alfonso, José**, and **María José**. Thanks also to **Elizaveta, Nik, Carla, Girish, Alfredo, Ugo** for the interesting work and fun times.

To my education gurus, thank you **Debby** and **Joost** for taking me along all the basics of running a master's program. **Debby**, I am so glad we can work together on the course and workshops, and love the chance to chat over coffee while preparing presentations and assignments, thank you for all the advice and help! **Joost**, you know all the ins and outs of the intro course, and I thank you for taking the time to get me up to speed, and be open to all kinds of wild suggestions and changes!

Una mención a **Grissel y Mario**. Gracias por todo el trabajo que hacen para poner a México en el mapa del mundo de biofabricación. Me entusiasma la idea de poder trabajar juntos en el futuro, y les agradezco la cálida bienvenida en Monterrey!

### *Students*

My PhD journey wouldn't be complete without the students I have supervised and coordinated in the last years. Sharing tips and knowledge, and helping you grow into amazing scientists is a large part of why I love what I do. **Sophie** and **Maud**, thank you for your work on the dECM meniscus project, there were many horse legs involved, and you guys handled them like pros! **Essa**, interrupted by COVID, but thanks for starting up the work with joint co-cultures and a great research proposal! **Núria, Enri, Demi** and **Leyla**, the MINI-JOINT team! It has been a massive student effort, with lots of bone differentiation problems and leaky platforms, but you all brought unique ways to tackle these issues and learned a lot, thank you! **Gabs**, me and your other mom were so proud of how you managed to make something out of PCU, which was as annoying as amorphous

polymers go! Thanks for all the laughs and hard work! **Vainius**, thank you for your help getting us started with microparticle printing, I enjoyed our endless brainstorm sessions a lot! **Klement**, thank you for all your hard work on the supramolecular project, and all those long days casting hundreds of gels. **Mar**, only starting now but thanks for all your hard work and AH goodies to keep the brain going during the long days! **Renate** and **Harry** thank you for your work in your writing assignments, it was great to get a different perspective on volumetric biofabrication and the world of *in vitro* models! **Kianti**, **Gerwinho**, **Bastiaan** and **Devon**, you were not officially my students, but I loved being there to help when needed, and being called sensei from time to time! Thanks to my e-course student assistants for making my life so easy: **Gerwin**, **Ninouk**, **Bastiaan**, **Maud**, and **Charlie**. Finally, thank you to all the **biofabulous master students** that have had to bear with me learning the ropes of program coordination, it makes me so happy to see each and everyone of you grow and achieve amazing things, know that I'm always in your corner and celebrate all your successes! **Enri**, **Jim**, **Isabelle**, **Laura BZ**, **Michael**, **Zena**, **Natacha**, **Charlie**, **Demi**, **Leyla**, **Douwe**, **Mar**, **Seb**, **Teebz**, **Laura BN**, **Claudia**, **Setayesh**, **Vainius**, **Luka**, **Nadine**, **Dora**, **Ángela**, **Mark**, and **Vasil**. And all my fake biofabs (you know who you are)!

### *Friends*

The crazy hours spent at the lab would have taken a bigger toll if I didn't have amazing friends to go home to during the majority of my PhD. Big shout out to all the tenants of The House. **D**, after your creepy window stalking the first day we met, I would never imagine I would now consider you my sister. Thank you for always being there (even with a crazy eye) and for all the love you give to me and my family! I know I can count on you for anything, and I thank you so much for that! **Carli**, since UCU, you have been one of my rocks, thank you for your support and friendship, the countless hours of chatting about serious and insane things, cooking Mexican food, drinking tequila, watching movies, and more, the house was a home because of you! **Sebas**, you silly goose, thanks for all the hours baking and cooking, it kinda saved our sanity during COVID. Thanks for always being there for me and for your amazing dance moves and hilarious dark humor! **Jonne**, kakaawwh, through thick and thin, you have been my bestestest bud and I am so happy I met you! Thanks for all the football madness, poop and fart jokes, house band adventures and for sharing in all the crazy stuff I do, love you to bits!

To my foodies, you have kept me sane throughout this long journey and I am so grateful you guys are part of my life! **Leanne**, first things first, to say butter chicken changed my life would be the understatement of the century! Thank you for introducing me to a whole new world of delicious food and even better company. Thanks for the endless chats, all the fun and insane evenings, the fun office moments when we would all spontaneously buy

tons of expensive things online for no reason whatsoever, and for your endless support (with a solid mix of jokes in the mix). I love you and I love being your friend. **Madi**, laaaamy, it's been an amazing and insane ride since that summer school in Heidelberg where lamy of the lab was first created, and we tried the best schnitzel on Earth! Having you in the lab all these years was so much fun, and it made the long days far more bearable when there was always a bit of time for lamy, googly eyes, coffees, and more. Your company and support these years have been invaluable to me, and I will miss having you around. Love you lots! Thanks for making this book look so amazing!

A la mejor manada de idiotas, **Carla, Sebas, y Mariana**, gracias por mantener el espíritu latino vivo en estas tierras. Gracias por las ricas cenas, por las clases de historia de la música latina, y por su amistad! Es muy bonito sentirse más cerca de casa con ustedes!

To the Corcle of Life, I somehow wish I'd met you all sooner, but you have filled these last months of my PhD with laughter, pasta and ridiculousness. Dear **Charlie**, I'm so very happy I met you woomn. You might ace the world record for how quickly two people become such close friends. From that first match of immunowars to Madrid, and eeeverything in between. Watching you grow as a scientist and get sassier and sassier this year is a great example why I love being a program coordinator! From the bottom of my pisces heart, thank you so much for all your support these last months, and thanks for not letting this book be a black and white cover kind of situation, I wouldn't have any other cover artist! **Martacita**, from a very serious-looking person interviewing us for an internship, to redoing my garden together and trying to kill you on a scooter, I am thankful for all the fun times and all your support in and outside the lab. You will be an amazing researcher and I can't wait to see it all! **Elena**, my dear fake biofab student, I cannot tell you how happy I am that you came to my house when I wasn't there! One pasta was all it took to get to know your amazing pop-culture knowledge, find Vic's Harry Potter soulmate, and share maaaany insane memories in a very short time! **Mar**, thank you for all the fun times at the lab, the AH baked goods in the mornings, after-work shenanigans and the amazing dog sitting (Sam really appreciated being carried across the street)!

Nee-yaw-kee team, just thinking of our chaotic dinner plans makes me smile! Dear **Marième**, I am so grateful to call you my friend, and probably far more thankful that your first night in Utrecht didn't make you flee the country forever (Sam does NOT apologize) :P There is just something amazing in having a friend that you know is always there for you and will tell you things as they are when you need to hear them, and at the same time can also just sit in silence reading a book like a hippie commune. I love our daily greetings and that we get to work together on amazing secret service projects, thank you for everything! **Davide**, Dade, thank you for always confusing me with your humor and Batman shenanigans, it keeps me sharp! Thanks for sharing your delicious Italian food, for always asking how I'm doing and always being down for a coffee and a chat or brainstorm!

To my UCU family, you guys all made my life in The Netherlands amazing enough to hang around for a while, and I will cherish all of your friendships and football shenanigans forever, thanks for being there through my masters and PhD chaos! Soulmate **Steph**(anie Frida Mathea Hosman), **Jonne, Doortje, Celeste, Doke, Maud, Julia, Inger, Tess.**

**Marc** and **Mariëlle**, I am so happy to have another couple of old boring people to hang out with and just play board games, watch trashy Dutch TV and have amazingly chill dog weekends with (we won't talk about the jacuzzi). You guys are amazing!

A lot of the time spent outside the lab was spent eating lots of delicious food. Thank you **Nino, Marisa, Aoife** and **Madi** for all the amazing pasta nights and delicious desserts. I think we're almost ready to open a restaurant :)

The end of my master's/start of PhD was an amazing time of latin music and dancing! Here's to the Macumba gang **Celia, Jara, Dani, Ane A, Quentin and Flor**, thanks for all the fun and crazy times in the last years!

To **Tanja**, thank you for keeping me fed and making an amazing atmosphere to get some work done on some of the chapters of my thesis. Going to Noen has always made me feel like a local in this city, and I love our hugs!

Way back when I was still deciding what my future would look like, my time at ISD has nothing but great memories and friendships that I will treasure all my life, despite the distance! **Omer, Marc, Conny, Natalia, Nik, Tia, Savannah**, you made a huge impact on who I am today. **Dr. Harnish**, your amazing way of teaching is something I take with me everywhere, and I think it makes me a better teacher, thank you for the amazing psychology stories and support! **Frank**, football is the one thing that kept me grounded and helped me adapt to life abroad, your trust and belief in me meant so much to me! **Ms. Wildeman**, your HL biology class shaped my future decisions, and brought me where I am today, thank you for your infectious enthusiasm for science!

### *Furry family*

Anyone that has talked to me for more than 2 minutes knows that dogs have been an instrumental part of my sanity before and during my PhD. Not that they will ever read it, but thank you to the loves of my life **Sam** and **Tony** for making everything ok, even when it's not. You both make me and all our friends smile by just existing, what trait to have in life! To the dog of my life, **Skippy**, you taught me how to be a good dog mom, love you forever. **Canelita**, my first dog friend in the Netherlands, I'll miss you always. **Chip, Toby, Lucy, Fito, Dasha, Queen, Phyllis, Kyra, Bob, Sparks** there's no such thing as too many dogs, you all bring immeasurable joy to my life. Shout out to the cats in my life that I appear not to like, but actually really do: **Maní, Benito, Paul Anka, Baby G, Mirris, Bruno, Poppy, Nicky, Pinya, and Elvis.**



*Human family*

**Vic**, never did I expect that you would be such an enormous part of my life when we met in Düsseldorf. You bring a very necessary calm to my baseline level of chaos, and without you a lot of things would not make a lot of sense. You have been so important in keeping me sane through this PhD journey. Thanks to you, I have been able to put my full effort into this job that I love, while having a beautiful house with you and two beautiful dogs. Never doubt how deserving you are of this amazing life, and how much I love you, thank you for making this book possible.

A mis titos, **Victoria y Antonio**, y abuelufa, **Yolanda**, ya no están pero todo lo que aprendí de ustedes, y todo el amor y las porras que me echaron viven en mi corazón, y comparto y los pienso en cada logro y cada sonrisa.

**Kiki, Rodri y Paulina pequeña**, gracias por siempre estar ahí en los momentos importantes, por llevarme a partidos de fut y por siempre enseñarme que es bueno llevar a nuestro niño interior muy en la superficie! Tía **Tere**, no me puedo imaginar una vida sin conocerte. Todo tu amor y cariño me llenan de felicidad y certeza de que no hay que compartir sangre con alguien para que sean una grandísima parte de tu familia! Gracias por siempre apoyarme y quererme tanto!

**Juan, Saloua, Adam, Sami, Montse, y Pedro grande** gracias por siempre estar ahí para ayudarme de este lado del Atlántico! Tener a la familia cerca siempre hace las cosas más sencillas, con comidas de locura, partidos de fútbol con Sami y visitas al Masnou! **Diego**, grillo, gracias por tantas aventuras de chiquitos, por todos los partidos de fut y locuras! **Rebe**, gracias por toda una vida de aventuras y cariño! Sé que siempre puedo contar contigo y papá para lo que sea, y que aunque estemos un un poco lejos, siempre están ahí conmigo. Tía **Gaby**, gracias por siempre estar y por todo tu amor y cariño, no hay nada en el mundo como tu comida, especialmente tu pozole! **Manuel**, vieji, creo que nadie más va a entender este libro como tú! Siempre has sido mi ídolo en serio. Tu inteligencia y capacidad de concretar ideas es una de las cosas que más admiro de tí, y que me ha inspirado en este trabajo, gracias! A mis bebés jóvenes que a diario me enseñan nuevas formas de ver la vida, **Rebe Jr.**, gracias por enseñarme todo sobre el balance vida/trabajo y por todo tu amor querida hermanita pequeña que es mas alta que yo! **Bikini**, cómo te admiro de verdad. Verte cantar, bailar, actuar, escribir, y todo lo que haces me inspira a ser siempre una mejor versión de mi misma bebé! **Vale**, moñita, tu pasión es infecciosa. Gracias por enseñarme a dar todo por tus sueños, a trabajar día y noche cuando es necesario, y a ser valiente frente a nuevos desafíos. **Vere**, manini, gracias por siempre estar ahí, eres de mis personas favoritas en el mundo. Contigo me divierto como con nadie, y sé que siempre cuento contigo para lo que necesite. Gracias por ser como eres, siempre me inspiras a ser yo misma sin importar lo que piense el mundo.

**Luis**, papi, gracias por siempre estar ahí. Siempre has sido un gran papá, y sé que cuando necesito ayuda, un abrazo o unas porras para seguir adelante, sólo hace falta levantar el teléfono y llamarte para escuchar todo el apoyo que necesito! Gracias por creer en mí y apoyarme en todo lo que hago, el doctorado, el fútbol, y todas las obsesiones de la infancia (Pokemons y todo lo demás). Eres un gran ejemplo para mí, siempre trabajador, amable y cariñoso. Gracias por todo siempre!

**Pit**, no sé si las palabras pueden expresar la gratitud que te tengo. Sin tener responsabilidad alguna, siempre me has dado alas y le has soplado al viento para ayudarme a volar. Gracias por traernos a Europa, eso me cambió de tantas formas que nunca hubiera imaginado. Gracias por darme la libertad de estudiar donde quisiera, vivir aquí y conocer a la gente que he conocido cambió mi forma de ver el mundo. Gracias por siempre darme libros, y ponerme películas y canciones nuevas, eso me abrió la mente a perspectivas diferentes. Este trabajo te lo debo en gran parte a ti, gracias por siempre creer en mí!

**Hilda**, abuelita, nada me da más orgullo que darte este libro y asegurarte que cada hora de trabajo, cada vez que me levanto después de caerme, y cada vez que levanto la voz por algo en lo que creo, tú estás justo detrás de mí. Siempre has sido y serás mi más grande protectora y fan número uno. Contigo detrás mío (y unas cuantas veladoras!) no hay obstáculo en el mundo que no pueda superar, por eso este librote que te dedico con todo mi amor y agradecimiento por enseñarme las cosas importantes de la vida. Gracias por inspirarme a ser mejor cada día!

**Claudia**, mamá, que te voy a decir en este libro que no sepas! No hay espacio en esta sección para agradecerte por todo lo que me has dado y enseñado en la vida, pero me has hecho una persona fuerte, trabajadora y bastante buena onda que ha tenido la fortuna de rodearse de gente buena, mucha de ella en las páginas de esta tesis! Eres mi más grande inspiración en el mundo, y todo el trabajo en este libro es el producto de todo tu amor y apoyo incondicional. Gracias por absolutamente todo, te dedico cada palabra como siempre!



## List of publications

This thesis is based on the following publications

Miguel Dias Castilho\*, Riccardo Levato\*, Paulina Núñez Bernal, Myléne de Ruijter, Christina Y. Sheng, Joost van Duijn, Susanna Piluso, Keita Ito, Jos Malda. **Hydrogel-Based Bioinks for Cell Electrowriting of Well-organized Living Structures with Micrometer-Scale Resolution.** *Biomacromolecules*. 2021 Jan; 22 (2); 855-866. DOI: 10.1021/acs.biomac.0c01577

Paulina Núñez Bernal\*, Paul Delrot\*, Damien Loterie\*, Yang Li, Jos Malda, Christophe Moser, Riccardo Levato. **Volumetric Bioprinting of Complex Living-Tissue Constructs within Seconds.** *Advanced Materials*. 2019 Aug; 31 (42); 1904209. DOI: 10.1002/adma.201904209

Gabriel Größbacher\*, Michael Bartolf-Kopp\*, Csaba Gergely\*, Paulina Núñez Bernal\*, Sammy Florczak, Myléne de Ruijter, Núria Ginés Rodriguez, Jürgen Groll, Jos Malda, Tomasz Jüngst#, Riccardo Levato#. **Volumetric Printing across Melt Electrowritten Scaffolds Fabricates Multi-Material Living Constructs with Tunable Architecture and Mechanics.** *Advanced Materials*. 2023 Apr; 35 (32); 2300756. DOI: 10.1002/adma.202300756

Manon C. Bouwmeester, Paulina Núñez Bernal, Loes A. Oosterhoff, Monique van Wolferen, Vivian Lehmann, Monique Vermaas, Maj-Britt Buchholz, Quentin Peiffer, Jos Malda, Luc J. W. van der Laan, Nynke I. Kramer, Kerstin Schneeberger, Riccardo Levato, Bart Spee. **Bioprinting of Human Liver-Derived Epithelial Organoids for Toxicity Studies.** *Macromolecular Bioscience*. 2021 Sep; 21 (12); 2100327. DOI: 10.1002/mabi.202100327

Paulina Núñez Bernal\*, Manon Bouwmeester\*, Jorge Madrid-Wolff, Marc Falandt, Sammy Florczak, Nuria Ginés Rodriguez, Yang Li, Gabriel Größbacher, Roos-Anne Samsom, Monique van Wolferen, Luc van der Laan, Paul Delrot, Damien Loterie, Jos Malda, Christophe Moser, Bart Spee, Riccardo Levato. **Volumetric Bioprinting of Organoids and Optically Tuned Hydrogels to Build Liver-Like Metabolic Biofactories.** *Advanced Materials*. 2022 Feb; 34 (15); 2110054. DOI: 10.1002/adma.202110054

Nino Chirico\*, Paulina Núñez Bernal\*, Gabriel Größbacher\*, Aina Cervera i Barea, Sammy Florczak, Josh Mesfin, Jianan Wang, Inge Dokter, Christian J. B. Snijders Blok, Karen Christman, Joost Sluijter, Jos Malda, Riccardo Levato#, Alain van Mil#. **Volumetric Printing Hollow Bi-Chambered Heart Structures for the Next Generation of Clinically Relevant Cardiac *In Vitro* Models.** *In preparation*

Anna Abbadessa, [Paulina Núñez Bernal](#), Giorgio Buttitta, Alfredo Ronca, Ugo D'Amora, Carla Zihlmann, Niklaus Stiefel, Luigi Ambrosio, Jos Malda, Riccardo Levato, José Crecente-Campo, María José Alonso. **Biofunctionalization of 3D Printed Collagen with Bevacizumab-Loaded Microparticles Targeting Pathological Angiogenesis.** *Journal of Controlled Release.* 2023 Aug; 360; 747-758. DOI: 10.1016/j.jconrel.2023.07.017

Marc Falandt, [Paulina Núñez Bernal](#), Oksana Dudaryeva, Sammy Florczak, Gabriel Groessbacher, Matthias Schweiger, Alessia Longoni, Coralie Greant, Marisa Assunção, Olaf Nijssen, Sandra van Vlierberghe, Jos Malda, Tina Vermonden, Riccardo Levato. **Spatial-Selective Volumetric 4D Printing and Single-Photon Grafting of Biomolecules within Centimeter-Scale Hydrogels via Tomographic Manufacturing.** *Advanced Materials Technologies.* 2023 May; 8; 2300026. DOI: 10.1002/admt.202300026

Martina Viola, Marta G. Valverde\*, [Paulina Núñez Bernal](#)\*, Jacobus P. van Trijp, Jaimie Hak, Carl C. L. Schuurmans, Cornelus F. van Nostrum, Rosalinde Masereeuw, Silvia M. Mihăila, Jos Malda, Riccardo Levato, Tina Vermonden. **Thermal Shrinking of Biopolymeric Hydrogels for High Resolution 3D Printing of Kidney Tubules.** *Submitted*

\* Authors contributed equally to this work

# Indicates shared senior authorship

Publications not included in this thesis

- Khoon S. Lim\*, Florencia Abinzano\*, [Paulina Núñez Bernal](#), Ane Albillos Sanchez, Pau Atienza-Roca, Iris A. Otto, Quentin C. Peiffer, Michiya Matsusaki, Tim B. F. Woodfield, Jos Malda, Riccardo Levato. **One-step Photoactivation of a Dual-Functionalized Bioink as Cell Carrier and Cartilage-Binding Glue for Chondral Regeneration.** *Advanced Healthcare Materials*. 2020 Apr; 9 (15); 1901792. DOI: 10.1002/adhm.201901792
- Riccardo Levato, Khoon S. Lim, Wanlu Li, Ane Urigoitia Asua, Laura Blanco Peña, Mian Wang, Marc Falandt, [Paulina Núñez Bernal](#), Debby Gawlitta, Yu Shrike Zhang, Tim B. F. Woodfield, Jos Malda. **High-Resolution Lithographic Biofabrication of Hydrogels with Complex Microchannels from Low-Temperature-Soluble Gelatin Bioresins.** *Materials Today Bio*. 2021 Sep; 12; 100162. DOI: 10.1016/j.mtbio.2021.100162
- Iris A. Otto, [Paulina Núñez Bernal](#), Margot Rikkers, Mattie H. P. van Rijen, Anneloes Mensinga, Moshe Kon, Corstiaan C. Breugem, Riccardo Levato, Jos Malda. **Human Adult, Pediatric and Microtia Auricular Cartilage Harbor Fibronectin-Adhering Progenitor Cells with Regenerative Ear Reconstruction Potential.** *iScience*. 2022 Sep; 25 (9); 104979. DOI: 10.1016/j.isci.2022.104979
- Leanne de Silva, [Paulina Núñez Bernal](#), AJW Rosenberg, Jos Malda, Riccardo Levato, Debby Gawlitta. **Biofabricating the Vascular Tree in Engineered Bone Tissue.** *Acta Biomaterialia*. 2023 Jan; 156; 250-268. DOI: 10.1016/j.actbio.2022.08.051
- Bram G. Soliman, Alessia Longoni, Mian Wang, Wanlu Li, [Paulina Núñez Bernal](#), Alessandro Cianciosi, Gabriella C. J. Lindberg, Jos Malda, Jürgen Groll, Tomasz Jungst, Riccardo Levato, Jelena Rnjak-Kovacina, Tim B. F. Woodfield, Yu Shrike Zhang, Khoon S. Lim. **Programming Delayed Dissolution Into Sacrificial Bioinks For Dynamic Temporal Control of Architecture within 3D-Bioprinted Constructs.** *Advanced Functional Materials*. 2023 Jan; 33 (8); 2210521. DOI: 10.1002/adfm.202210521
- Jorge Madrid-Wolff, Joseph Toombs, Riccardo Rizzo, [Paulina Núñez Bernal](#), Dominique Porcincula, Rebecca Walton, Bin Wang, Frederik Kotz-Helmer, Yi Yang, David Kaplan, Yu Shrike Zhang, Marcy Zenobi-Wong, Robert R. McLeod, Bastian Rapp, Johanna Schwartz, Maxim Shusteff, Hayden Talyor, Riccardo Levato, Christophe Moser. **A Review of Materials Used in Tomographic Volumetric Additive Manufacturing.** *MRS Communications*. 2023 Aug. DOI: 10.1557/s43579-023-00447-x



## Curriculum Vitae

Paulina Núñez Bernal was born on the 4th of March 1995 in Mexico City, Mexico. She graduated with honors from the International School of Düsseldorf (Germany) in 2013, having completed the International Baccalaureate program. In 2013, she started her undergraduate education at the International Honors College of Utrecht University, University College Utrecht (The Netherlands). She graduated magna cum laude in 2016 with a major in Biomedical Sciences and a minor in Clinical Psychology.



In 2016, she began her master's degree in Regenerative Medicine and Technology at Utrecht University and TU Eindhoven. In her first year, she worked under the supervision of dr. Iris Otto, in the Biofabrication group led by Prof. dr. ir. Jos Malda within the Orthopaedics department of the University Medical Center Utrecht. This internship consisted of the characterization of a novel stem cell progenitor population in the human auricle. During this research project, she developed a strong interest in the field of biofabrication and sought to expand her skills in this rapidly evolving field in the second half of her master's program. Paulina then performed an internship under the supervision of dr. Mylène de Ruijter and dr. ir. Miguel Castilho within the same department. Here she worked on the development of a new high-resolution cell printing approach based on the principles of electrohydrodynamic printing. After finalizing her master's degree, she became a research analyst in this group to finalize this master's project, which culminated in a published article and a European patent for this new technology. Additionally, she conducted literature research into the combination of gene editing technologies with liver-derived, patient-specific organoids for the treatment of inherited metabolic liver diseases, under the supervision of dr. Bart Spee. In 2018, Paulina graduated with a Master's Degree in Biomedical Sciences (Regenerative Medicine and Technology) from Utrecht University.

Paulina started her PhD in April 2019 at the Department of Orthopedics at the UMC Utrecht, under the supervision of Prof. dr. ir. Jos Malda and dr. ir. Riccardo Levato. During this time she was actively involved and played a leading role in various national and international research collaborations, and was part of the European consortium MEFISTO (European Union's Horizon 2020 research and innovation programme under grant agreement No 814444). In recognition of her outstanding contributions to the field, Paulina was honored with the New Investigator Award in 2022 by the International Society of Biofabrication. Outside of her academic research, Paulina has also been involved in education since



the start of the PhD track, and obtained her University Teaching Qualification (UTQ) in 2022. She is currently the program coordinator of the international master's program in Biofabrication, where she also coordinates two courses embedded within this master's. Furthermore, between June and December 2023, Paulina joined the Innovation Center for Advanced Technologies (ICAT) as a project coordinator. Paulina will continue her research and educational roles at the Department of Orthopedics at the UMC Utrecht as a postdoctoral researcher.



